FERMILAB-Proposal-830

CDF/DOC/PUBLIC/1172

Proposal For an Upgraded CDF Detector

The CDF Collaboration

October 9, 1990

Abstract

A major upgrade is proposed for the CDF detector in order to exploit fully the physics opportunities of high luminosity running at the Fermilab Collider.

Contents

1 Introduction **8**

2 Physics Accomplishments **16**

2.1 The 1987 Run 16

2.2 The 1988-89 Run 22

3 Planned Physics Program **32**

3.1 Electro-Weak Physics 32

3.2 Top Quark Physics 44

3.3 QCD Physics 52

3.4 B Physics 60

3.5 Exotic Physics 69

3.6 Rare Processes 71

4 Hardware Upgrades **74**

4.1 Tevatron Upgrade 78

4.2 Plug and Forward Calorimeters 80

4.2.1 Plug Scintillation Calorimeter 80

4.2.2 Gas Calorimeters 99

4.3 Central Drift Chamber 101

4.4 Vertex Time Projection Chambers 102

4.5 Silicon Vertex Detectors 104

4.6 Muon Systems 109

4.7 Data Acquisition Electronics 119

4.8 Level 3 Trigger: Online Analysis and Event Filtering 130

4.9 Online Computing: RUN_CONTROL 136

4.10 Offline Computing 138

4.11 Miscellaneous Systems 141

5 Cost Projections **142**

5.1 Budget: Plug Calorimeter 142

5.2 Budget: Silicon Vertex Detector 144

5.3 Budget: Muon Detectors 145

5.4 Budget: Data Acquisition System 146

5.5 Budget: Online Computing 150

5.6 Budget: Miscellaneous 151

5.7 Budget Summary 152
5.8 Budget: Test Beam 153
5.9 Budget: Offline Computing and Data Storage 154

6 Participating Institutions and Physicists 156

List of Figures

1-1 Schematic of Proposed CDF Detector Evolution 12
1-2 Evolution of $\eta - \phi$ coverage for electrons 13
1-3 Evolution of $\eta - \phi$ coverage for muons 14
1-4 Evolution of Tracking Coverage for Triggers vs. θ. 15
2-1 Inclusive Charged Particle Cross Section vs. P_T 18
2-2 $dN_{ch}/d\eta$ at $\eta = 0$ 18
2-3 Inclusive Jet Cross Section 19
2-4 Inclusive K_s^0 Cross Section 19
2-5 D^* Production in Jets 20
2-6 Jet-Broadening Parameter, Q_T 20
2-7 Two Jet Differential Cross Sections 21
2-8 Jet Fragmentation 21
2-9 $Z^0 \rightarrow e^+e^-$ Invariant Mass Plot for Calorimeter Data 25
2-10 Z $\rightarrow \mu^+\mu^-$ Invariant Mass Plot for Tracking Data 25
2-11 P_T Distributions for $W^\pm \rightarrow \mu^\pm\nu$) and $W^\pm \rightarrow e^\pm\nu$ 26
2-12 M_t Distributions for $W^\pm \rightarrow e^\pm\nu$ and $W^\pm \rightarrow \mu^\pm\nu$) 26
2-13 Transverse Mass Plots for the $e^\pm$ + jets Top Quark Search 27
2-14 $P_t(\mu)$ vs. $E_t(e)$ for the $e^\pm\mu^\pm$ Top Quark Search 27
2-15 P_T Distribution for Isolated Photons 28
2-16 Transverse Momentum Distributions for the Gauge Bosons 28
2-17 Transverse Energy Distribution for Jets 29
2-18 Dijet Mass Spectrum 29
2-19 Distribution of Trijet Energy Fractions 30
2-20 Values of σB for $W \rightarrow e\nu$ and $Z \rightarrow e^+e^-$ 30
2-21 $B \rightarrow J/\psi$-K and $B \rightarrow J/\psi$-K* Mass Spectrum 31
3-1 Constraints on M_{top} by M_W 34
3-2 Forward-Backward Asymmetry in Z $\rightarrow e^+e^-$ 37
3-3 Predicted M_{top} Dependence of $\sin^2\theta_W^{afb}$ 38
3-4 Charge Asymmetry in W $\rightarrow \ell\nu_\ell$ 39
3-5 Total Cross Section for High-Mass Z' Production 40
3-6 Limits on Quark-Lepton Compositeness from Drell-Yan Cross Section . . . 42
3-7 Top Quark Production at 1.8 TeV vs. Top Mass 44
3-8 Expected number of $t\bar{t} \rightarrow e\mu$ events 45
3-9 Expected number of events from $t\bar{t} \rightarrow e^+e^-$ and $t\bar{t} \rightarrow \mu^+\mu^-$ 46
3-10 Expected number of events for $t\bar{t} \rightarrow$ lepton + jets 48

3-11 CDF Efficiency for Detecting $t\bar{t}$ With b Tagging 49
3-12 The branching ratio for $t \rightarrow W + b$ for charged Higgs Models 51
3-13 Inclusive Jet Cross Section 53
3-14 Jet Cross Section vs. Clustering Cone Radius 54
3-15 Comparison of Jet Cross Section with Leading Order QCD 54
3-16 High Energy End of Inclusive Jet Cross Section 55
3-17 Dijet Invariant Mass Spectrum from CDF 56
3-18 Cross Section for High-Mass Dijet Resonances 56
3-19 Highest E_T Direct Photon Candidate 57
3-20 Integral Cross Section for Direct Photons 57
3-21 P_T Distribution for W Compared to Theory 58
3-22 P_T Distribution for Z Compared to Theory 59
3-23 Invariant Mass Spectrum $K^-\pi^+$ $(K^+\pi^-)$ 61
3-24 Invariant mass spectrum for $e^-K^-\pi^+$ $(e^+K^+\pi^-)$ 61
3-25 B^0 Mixing Distributions vs. B Momentum 67
3-26 B^0 Mixing Distributions vs. Lepton Momentum 68
4-1 A cutaway view of the CDF detector for 1993 77
4-2 Side View of Existing CDF Detector 81
4-3 Side View of Upgraded CDF Detector 82
4-4 Energy Resolution of the 3 × 3-tower EM calorimeter 84
4-5 Position Scan of the 3 × 3-tower EM calorimeter 85
4-6 Minimum Ionizing Signal for the Naked 40 Tile Stack 86
4-7 Plug Segmentation in $\eta - \phi$ 88
4-8 Energy deposition profiles in a double layer of 2-mm round fibers at $5.1X_0$ from 10 GeV EGS electron showers. 90
4-9 Deviations from true position using a double layer of 2-mm scintillating fibers, predicted by 10 GeV EGS electron showers. The algorithm used is simply to take the energy-weighted mean position of all fibers having energy above some threshold. 91
4-10 Reconstructed fiber detector position versus beam position: preliminary CDF test beam results. 93
4-11 An $\eta - \phi$ arrangement of scintillating fibers for the shower-maximum position detector. The ϕ fibers are divided in 15° slices to match the segmentation of the CDF hardware trigger. The actual segmentation is 30 times finer than that shown. 93
4-12 A spiral arrangement of scintillating fibers for the shower-maximum position detector. The actual segmentation is 30 times finer than that shown. 94
4-13 Scintillating Tile With Waveshifting Optical Fiber 96

4-14 Drawing of SVX detector. 104
4-15 Expected SVX Impact Parameter Resolution. 105
4-16 SVX Test Beam Event. 106
4-17 Muon Toroid Coverage vs. Polar Angle 110
4-18 Muon Toroid Resolution vs. Polar Angle 111
4-19 Muon Toroid Structure: Radial-Axial Diagram 113
4-20 Muon Toroid Resolution vs. Momentum 117
4-21 DAQ System Overview Block Diagram 121
4-22 Diagram of Calorimeter Front-End Electronics 124
4-23 Block Diagram of DAQ Connections to Level-3 (1989) 132
4-24 Block Diagram of DAQ Connections to Level-3 (1991) 133
4-25 Diagram of a Level-3 Silicon Graphics Box (1991) 134
4-26 Block Diagram of DAQ Connections to Level-3 (1993) 135

List of Tables

3-1 Projected Uncertainties in the $W \rightarrow e\,\nu$ Mass Measurement 33
3-2 Projected Uncertainties in the $W \rightarrow \mu\,\nu$ Mass Measurement 33
3-3 Projected Uncertainties in the R_e Measurement 35
3-4 Projected Uncertainties in the R_μ Measurement 36
3-5 Projected Uncertainties in the $\mathrm{Sin}^2\theta_W^{AFB}$ $Z^0 \rightarrow e^+e^-$ Measurement 37
3-6 Projected Uncertainties in the $\mathrm{Sin}^2\theta_W^{AFB}$ $Z^0 \rightarrow \mu^+\mu^-$ Measurement 38
3-7 Z' Total and Partial Cross Sections 41
3-8 Gauge Boson Pair Total Cross Sections 43
4-1 CDF Detector Systems Channnel Count 76
4-2 Tevatron Bunch Spacing Parameters 78
4-3 Overview of Proposed Calorimeter Upgrade 87
4-4 Features and Benefits of Proposed Calorimeter Upgrade. 99
4-5 CDF Muon System Coverage 109
4-6 Dimuon triggers: $t\bar{t} \rightarrow \mu^+\mu^- + \mathrm{X}$ 112
4-7 Muon Toroids: Bend Angles and Sagittas 116
4-8 Muon Toroids: Trigger Rates 116
4-9 Level-3 Parameters 130
5-1 Tile Scintillator Plug Budget 143
5-2 Silicon Vertex Detector Costs 144
5-3 Forward Muon Budget 145
5-4 Data Acquisition Electronics Budget 147
5-5 Level 1,2 Budget 148
5-6 Level 3 Budget 149
5-7 Online Computing Budget 150
5-8 Budget for Miscellaneous Items 151
5-9 CDF Upgrade Budget Summary 152
5-10 Test Beam Budget 153
5-11 Offline Computing Budget for the 1991 Run 155
5-12 Offline Computing Budget for the 1993 Run 155

1 Introduction

The Collider Detector at Fermilab (CDF) has been used to exploit the unique physics opportunities of the Fermilab Tevatron I project, where counter-rotating beams of protons and antiprotons collide at 1.8 TeV in the center-of-mass. Until the next millenium, this will likely remain the highest energy for particle physics experiments at an accelerator.

Fermilab has an ambitious program of improvements to the Tevatron which will upgrade its performance and extend its physics reach during the coming years. In order for CDF to exploit the opportunities provided by accelerator improvements, a number of its systems must be substantially upgraded - detectors, electronics, data acquisition (DAQ) and analysis facilities. This document presents the motivation for such an upgrade, its scope for each subsystem, and the resources needed to accomplish it.

CDF, a powerful, general purpose detector system, has been operated during three periods of collider operation. In October, 1985, a brief test at very low luminosity yielded the first detected collisions at the Tevatron. During 1987, an engineering run produced $\sim 25nb^{-1}$ of integrated luminosity and a variety of physics results. During a year-long run starting in June, 1988, the Tevatron surpassed its design luminosity, reaching $\sim 2 \times 10^{30}/\text{cm}^2$-sec, and CDF wrote $\sim 4500\, nb^{-1}$ of data to magnetic tape. At this writing, results of the analysis of these data are being presented at conferences and published in journals. These are discussed in Section 2.

The projected improvements in the luminosity of the Tevatron collider, $\mathcal{L} \sim 5 \times 10^{30}/\text{cm}^2$-sec or higher in 1991 and $\mathcal{L} \sim 5 \times 10^{31}/\text{cm}^2$-sec or higher by 1995, offer CDF considerably extended physics reach. A definitive search for the top quark will be possible. Either it will be found and its properties studied, or far-reaching revisions in the standard model will be necessary. Further improvements in our measurements of the mass, width and decays of the $W^{\pm}$ will also provide stringent tests of the Standard Model. All four electo-weak bosons, $W^{\pm}$, Z^0 and γ can be used to probe the short-range behavior of partons. CDF has recently demonstrated a capability for B-physics, and this new opportunity will be explored vigorously. Limits will be extended on parton compositeness and the existence of supersymmetric and other exotic particles. Section 3 describes the physics goals for future CDF operation in more detail.

In order to confront the combined challenges of the upgraded Tevatron and the physics opportunities it offers, CDF must undergo a staged improvement program.

At present, in the configuration used for the 1988-89 run, the detector consists of electromagnetic and hadronic calorimeters covering nearly 4π solid angle around the interaction region in a tower geometry. A large, superconducting solenoidal magnet containing drift chambers measures the momentum of charged particles and gives visual reconstruction of the event. Muon chambers around the perimeter of the central detector and iron-toroidal magnets at each end identify muons. Details of the detector design, construction and performance can be found in the original design report[1] and in published papers.[2-26]

Upgrades in progress for the 1991 run are described in Ref. 27. Some are required for CDF to function at $\mathcal{L} \sim 5 \times 10^{30}/\text{cm}^2$-sec and others will improve its physics capabilities

by extending the kinematic region covered, by increasing the detector's resolving power and background rejection and by enhancing its reliability. The modifications include extensive front end electronics changes, replacement of the Vertex Time Projection Chamber, and implementation of the Silicon Vertex Detector which was part of the original CDF design. The central muon upgrade (CMUP) will improve rejection of hadron punch-through in the region already covered ($0 \leq |\eta| \leq 0.7$), and the muon coverage will be extended (CMEX) to cover the region $0.7 \leq |\eta| \leq 1.1$. The cause of breakdown problems at the edges of the plug gas calorimeters has been identified and they are being repaired. This will improve coverage for electrons in the region $1.1 \leq |\eta| \leq 1.3$. Pre-radiators will be added to the central electromagnetic calorimeters to improve identification of γ's and π^0's. The Central Tracking Chamber will be operated at lower gain to extend its lifetime and some changes to the pre-amps may be needed. A segment processor (CPT) for track-finding in the CTC will be implemented to add to the Level 2 trigger capabilities. A higher rate of throughput will be needed in the DAQ system. This means replacing the prototype wire-wrap Event Builder used in 1988-89 with a printed-circuit version which incorporates a number of improvements based on operating experience. The Level 3 online computer farm is undergoing a major upgrade to deal with higher rates and additional tasks imposed on it. Increases in online computing power for control and monitoring are needed, as well as a substantial increase in offline analysis capacity.

This proposal is concerned principally with the "1993" run. The overview at the end of this section lists the upgrades proposed for that time scale. Some subsystem upgrades are mandated by the shorter bunch spacing (395 nsec) of the upgraded Tevatron. Others are necessary because of further improvements in luminosity up to $\mathcal{L} \sim 5 \times 10^{31}/\text{cm}^2$-sec, which is a key ingredient in extending the Tevatron Collider's physics capability. The proposed detector upgrades will undergo extensive evaluation in this year's test beam run.

We wish to emphasize the importance of R&D resources and test beam time for studies of large-scale prototype detectors early in 1991.

Figure 1-1 shows schematically the evolution of the detector from 1989 to 1991 and proposed changes for 1993. Figures 1-2 (for electrons) and 1-3 (for muons) show the improvements in detector and trigger coverage in the form of $\eta - \phi$ plots. Figure 1-4 shows the θ coverage for various trigger levels for the three runs. Section 4 contains more detailed discussions of each of the proposed hardware upgrades. The budget and a list of participating institutions and physicists are presented in Sections 5 and 6.

Beyond the 1993 run, the Tevatron luminosity is expected to increase further, and consideration is being given to an even shorter bunch spacing - ~200 nsec. The 1993 upgrade plans for scintillation calorimeters, muon detectors and the digital portions of the DAQ system take this into account, and these systems should function well in 1995 and beyond. The front end electronics described below are designed for 395 nsec bunch spacing. We estimate roughly $4M added cost to change the presently planned front end electronics capability from 395 nsec to ~200 nsec bunch spacing. Some present systems which require no upgrade for 1993 may run into problems thereafter. For example, the central tracking drift chamber and vertex time projection chamber may require substantial modification or replacement for runs in 1995 and beyond. This is particularly true if the ~200 nsec

bunch space option is adopted. Such modifications could, at the same time, significantly enhance our heavy flavor capabilities. For example, extending the rapidity coverage for tracking and improving momentum resolution would be natural for the B spectroscopy that we have started. The SVX is a first-generation device. There may be major improvements in the technology available for runs beyond 1993, allowing a much more powerful device. Additional fast signals from the detector can be made available to the Level-2 trigger to improve background rejection, and new trigger technologies will be available. Finally, we do not know what the status of the top quark search will be. It may be that heavy flavor physics will dictate the needs for upgrades as much as accelerator changes. The results from this coming run will teach us as much about new directions as the results from the last run have. Who thought two years ago that we would be doing B and χ spectroscopy in addition to the top search?

The design, construction and operation of this facility are being carried out by a consortium of physicists from the following institutions in the United States, Italy and Japan: Argonne National Laboratory; Brandeis University; University of California at Los Angeles, University of Chicago; Fermilab; Laboratori Nazionali di Frascati; Harvard University; University of Illinois; Johns Hopkins University; KEK, Tsukuba; Lawrence Berkeley Laboratory; University of Michigan; Osaka City University; University of Padova; University of Pennsylvania; University and Scuola Normale Superiore of Pisa; University of Pittsburgh, Purdue University; University of Rochester; Rockefeller University; Rutgers University; Texas A&M University; University of Tsukuba; Tufts University; University of Wisconsin. The collaboration will continue expanding.

OVERVIEW

The modifications and resources needed for CDF to address the physics accessible with higher Tevatron luminosity are summarized below.

1. Replace the gas calorimeters with scintilation tile calorimeters to accomodate the higher luminosity and shorter bunch spacing.
2. Move the muon toroids closer to the central detector and build new muon chambers and electronics. to increase muon coverage.
3. Upgrade the silicon vertex detector for operation at higher luminosity and shorter bunch spacing.
4. Upgrade front-end electronics, trigger and data acquisition system to allow efficient operation at 395 nsec bunch spacing.
5. Expand the bandwidth into and computing capacity of the Level 3 online event processing farm.
6. Make necessary improvements in existing detector subsystems.
7. Increase offline computing capacity to at least 2000 mips of CPU capacity and at least 0.3 TeraBytes of disk storage.
8. A substantial test beam run by early 1991 with large-scale prototypes of new detector systems.

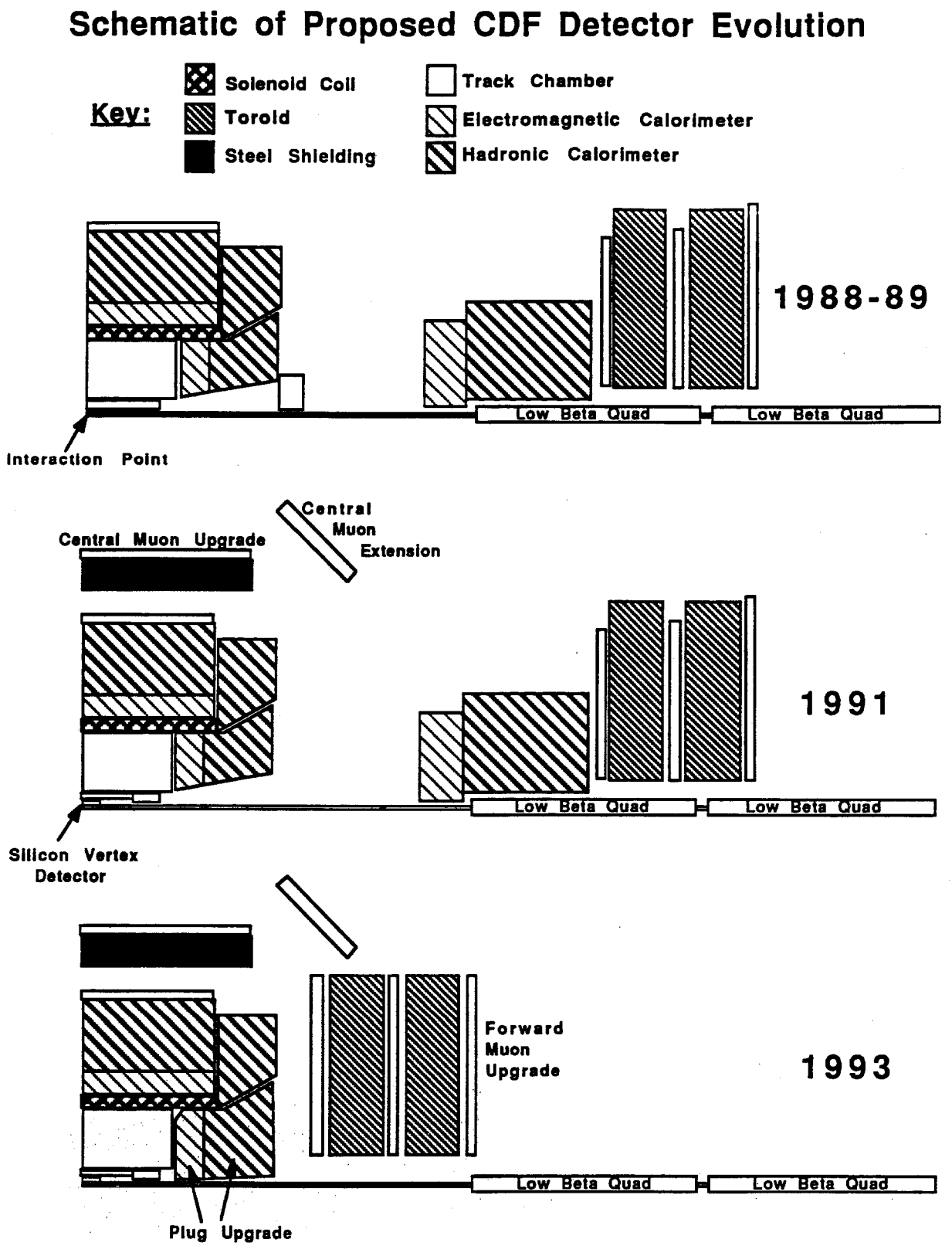

Figure 1-1: Schematic of Proposed CDF Detector Evolution

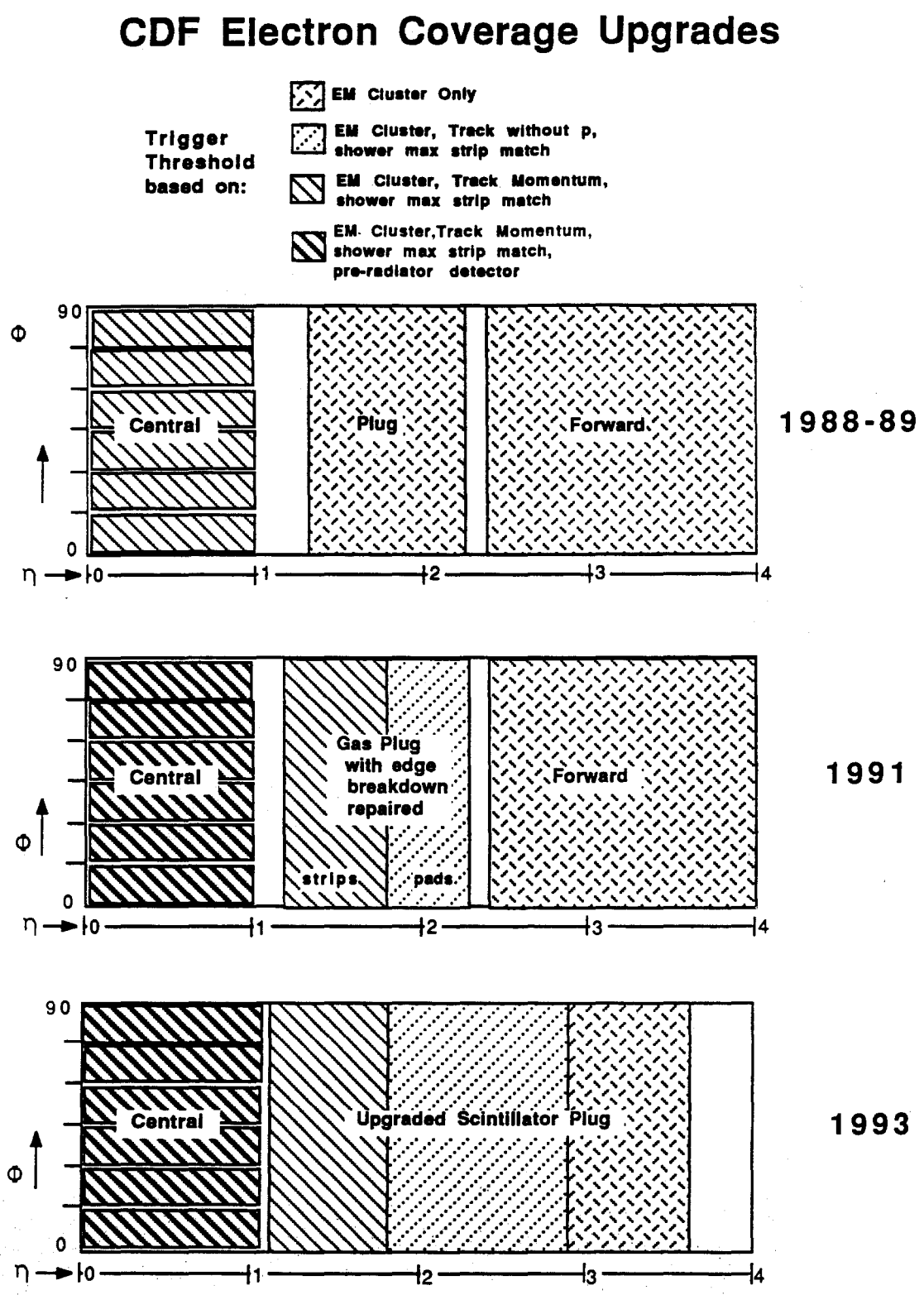

Figure 1-2: Evolution of $\eta - \phi$ coverage for electrons

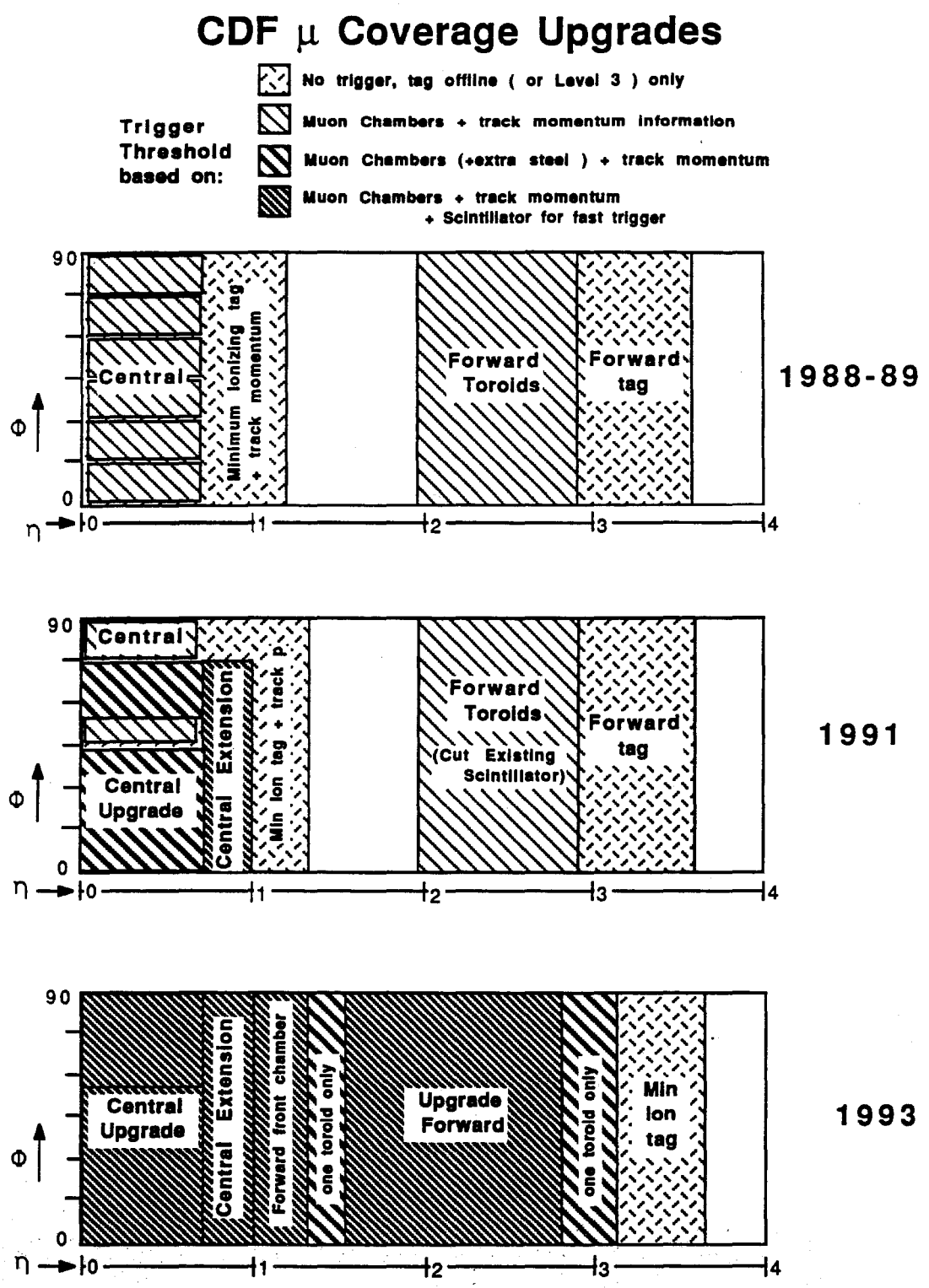

Figure 1-3: Evolution of $\eta - \phi$ coverage for muons

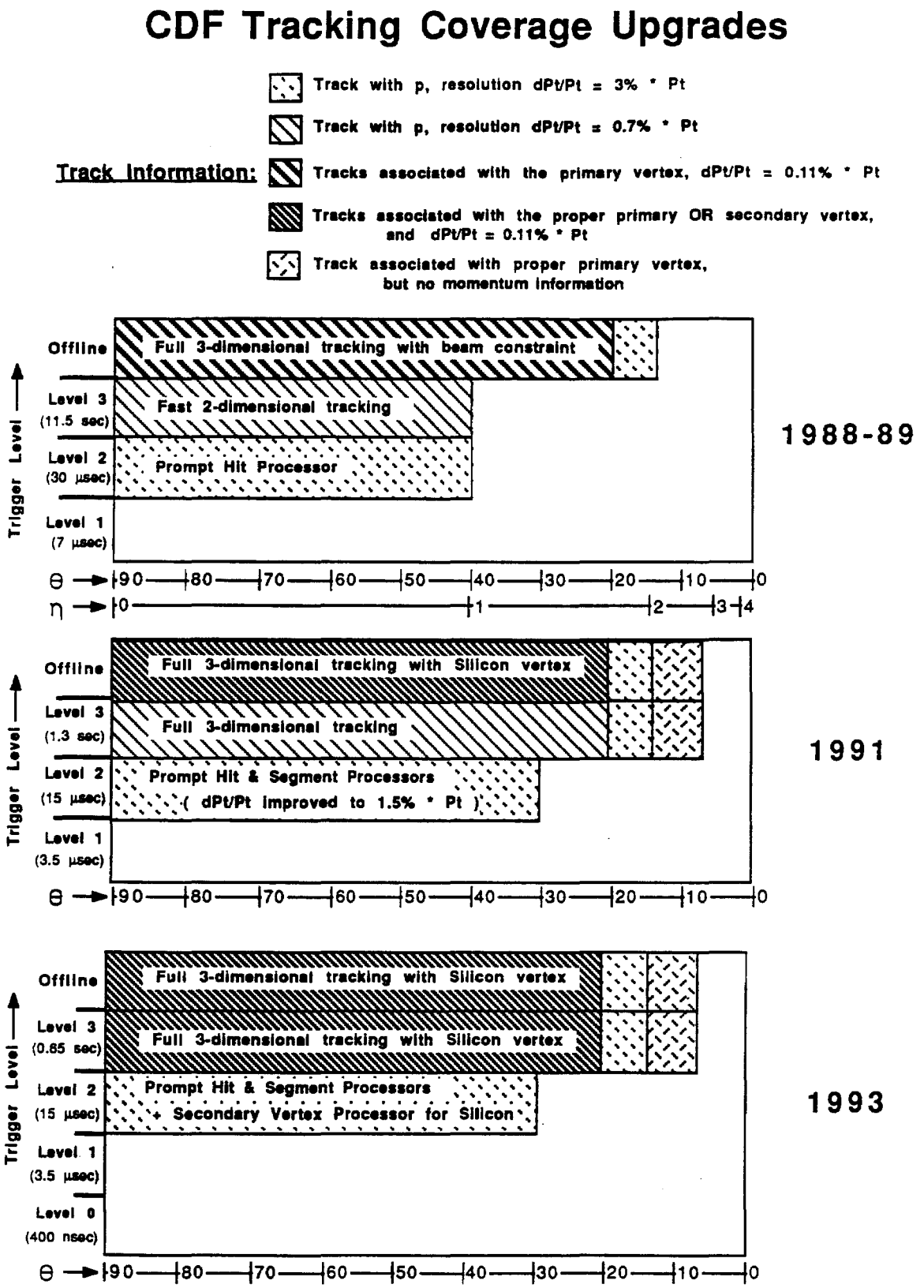

Figure 1-4: Evolution of tracking coverage for various trigger levels for various ranges of θ in the the 1988-89, 1991 and 1993 runs.

2 Physics Accomplishments

2.1 The 1987 Run

The operation of CDF during 1987 was intended as an engineering run, and it achieved its objectives of bringing into operation most of the major detection systems, the Level-1 trigger, and most of the data acquisition system. Operational procedures, calibration techniques and safety systems were refined as their strengths and weaknesses were observed under "battle conditions."

Approximately 25 nb^{-1} of integrated luminosity were accumulated and 250 tapes of data written. This data set allowed CDF to confront and solve most of the problems of analyzing these complex events: maintenance of large databases for calibrations and run conditions, development and tuning of Monte Carlo programs, and integration of data from a variety of complicated subsystems into a unified analysis.

A much more important product of the 1987 run was a rich yield of unique physics results from 1.8 TeV $p - \overline{p}$ collisions which are described in a number of Ph. D. theses and papers, both published and in preparation. These include:

1. Measurements of the transverse momentum distribution[28] (Fig. 2-1) of charged particles produced at $\sqrt{s} = 630$ and 1800 GeV. The average P_T increases more rapidly than $\log s$.

2. A measurement of the pseudorapidity distributions of charged particles produced at $\sqrt{s} = 630$ and 1800 GeV.[29] This data, combined with lower energy data, show a growth faster than $\log s$ at $\eta = 0$. (See Fig. 2-2.)

3. The inclusive jet cross section was measured. Jets were seen up to $p_T = 250$ GeV/c, higher transverse momentum than ever before observed.[30] The predictions of Quantum Chromodynamics (QCD) assuming pointlike partons were consistent with the distribution (Fig. 2-3). Fits to the distribution assuming non-pointlike partons placed a lower limit of 700 GeV on the compositeness parameter. This implies that quarks and gluons are pointlike down to distances of order 3×10^{-4} fermi.

4. The production and subsequent decay of $W^{\pm} \rightarrow e^{\pm}\nu$ in 1.8 TeV $\overline{p}p$ collisions was measured to be $\sigma \cdot B = 2.6 \pm 0.6 \pm 0.5$ nb, in good agreement with theory and extrapolation from lower energy data.[31]

5. A search for supersymmetric particles was performed. Assuming the simplest versions of SUSY models, it was established that the masses of squarks and gluinos, if they exist, must be greater than 75 GeV.[32]

6. The dijet angular distribution was measured, and it confirmed the predictions of QCD. This distribution also tested the pointlike parton hypothesis and placed a lower limit on the compositeness parameter of 330 GeV.[33]

7. A measurement of the transverse momentum distribution of K_s^0 mesons.[34] (See Fig. 2-4.)

8. A search was performed for heavy, stable charged particles.[35] It set cross section and mass limits in the context of specific models.

9. Identification of D^* states in jets produced at CDF.[36] Fig. 2-5 shows the observed signal for this state.

10. A measurement of the two-jet invariant mass spectrum.[37]

11. Measurement of the jet-broadening parameter, Q_T, as a function of jet-E_T.[38] This parameter is sensitive to the ratio of 3-parton to 2-parton final states, and is free of divergences which plague other global parameters. (See Fig. 2-6.)

12. Measurement of Two Jet Differential Cross Sections $d^3\sigma(\overline{p}p \rightarrow J_1 + J_2 + X)/dE_t d\eta_1 d\eta_2$ averaged over $\eta_1 \leq |0.6|$ is in agreement with QCD predictions.[39] (See Fig. 2-7.)

13. A study of jet fragmentation.[40] Figure 2-8 shows the distribution of charged particle fractional momentum, Z, within jets, summed over all jet energies. Studies of the Z-distribution as a function of di-jet invariant mass show that it becomes more steeply falling with increasing M(j-j) from 60 to 200 GeV/c^2 as expected from scale breaking in QCD.

Many of these analyses led to Ph.D. theses at the participating institutions. Among these are:

- Berkeley: Rob Harris, Brad Hubbard
- Chicago: George Redlinger, Y. Tsay, Rick Snider
- Harvard: Rick St. Denis, Dave Brown, Rob Carey
- Illinois: Dave Smith, Tom Westhusing
- Penn: Marshall Miller
- Pisa: Simone Dell'Agnello, Marco Incagli
- Purdue: Martin Schub, Aesook Byon, Steve Kuhlmann
- Rutgers: Brenna Flaugher
- Tsukuba: Yohei Morita, Maki Sekiguchi, Aki Yamashita, Masa Shibata
- Wisconsin: John Skarha

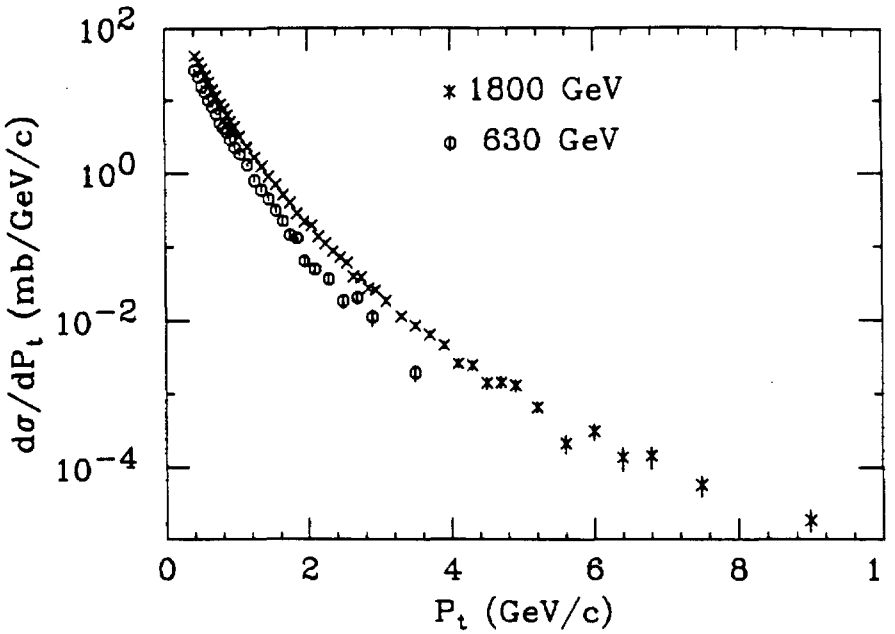

Figure 2-1: Inclusive charged particle cross section vs. P_T for rapidity $|y| < 1.0$ at $\bar{p}p$ energies of 630 and 1800 GeV.

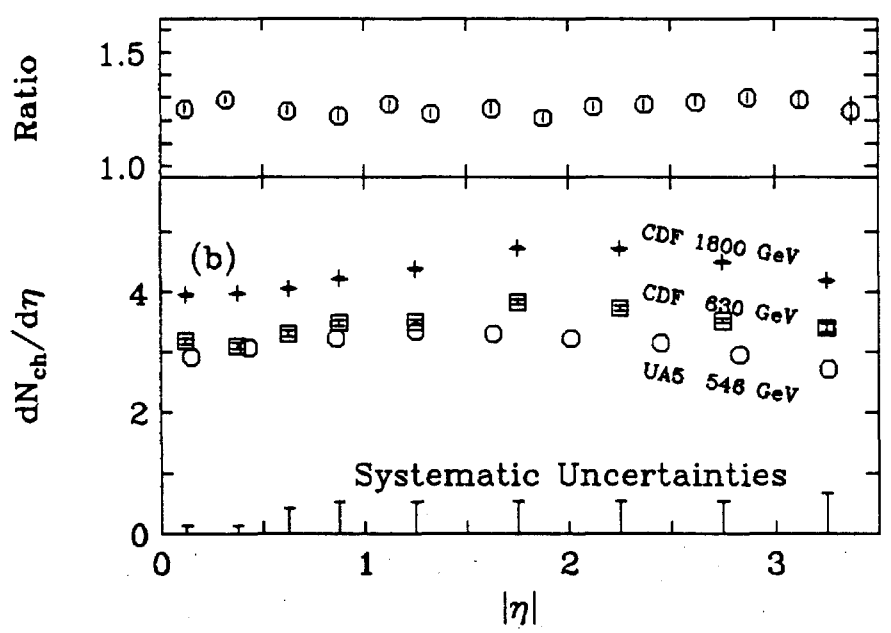

Figure 2-2: A plot of the charged-particle distribution, $dN_{ch}/d\eta$, at $\eta = 0$ measured by CDF and UA5[41,42,43]. The upper plot shows the ratio of the distribution at 1800 GeV to that at 630 GeV.

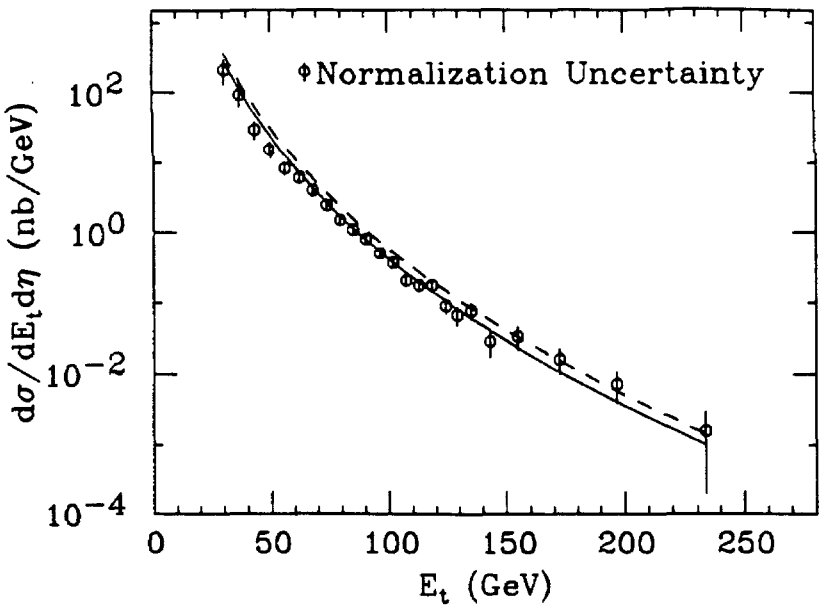

Figure 2-3: Inclusive jet cross section as a function of transverse energy, E_T at $\sqrt{s} = 1.8$ TeV compared to a range of QCD predictions described in Ref. 30. Error bars include statistical uncertainty and the E_T-dependent part of the systematic uncertainty. There is an overall normalization uncertainty of 34%.

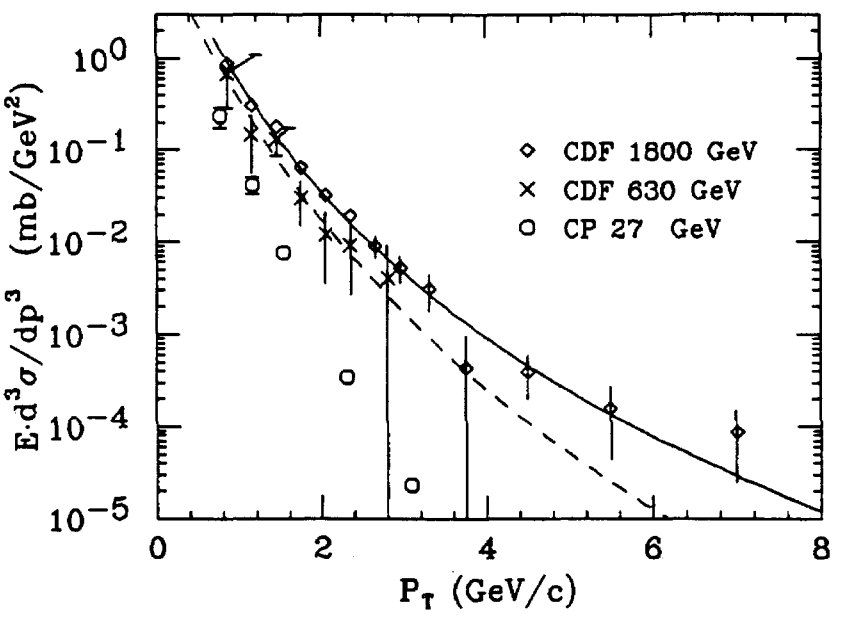

Figure 2-4: Inclusive K_s^0 Cross Section from CDF for rapidity $|y| < 1.0$ $\bar{p}p$ at $\sqrt{s} = 630$ and 1800 GeV. Also plotted are K production data from the Chicago-Princeton group,[44] pp at $\sqrt{s} = 27$ GeV. The dashed curve is a fit to data from UA5,[45] $\bar{p}p$ at $\sqrt{s} = 546$ GeV. The solid line represents a fit to the 1800 GeV data with a function of the form $Ap_0^n/(p_T + p_0)^n$ where p_0 is fixed at 1.3 GeV/c and $n = 7.7 \pm 0.2$.

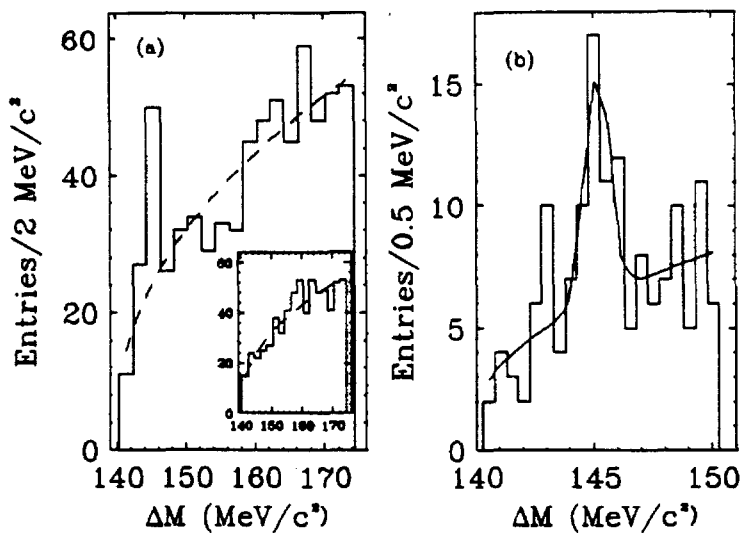

Figure 2-5: (a) The mass difference, $\Delta M \equiv M_{K\pi\pi} - M_{K\pi}$ after all cuts. The dashed line is a fit to the background. The inset shows the mass difference after all cuts for the wrong-sign mass combination, i.e. where one tries to form a D^{*+} with the combination $K^+\pi^-\pi^+$ instead of $K^-\pi^+\pi^+$. (b) The region of the peak in finer detail.

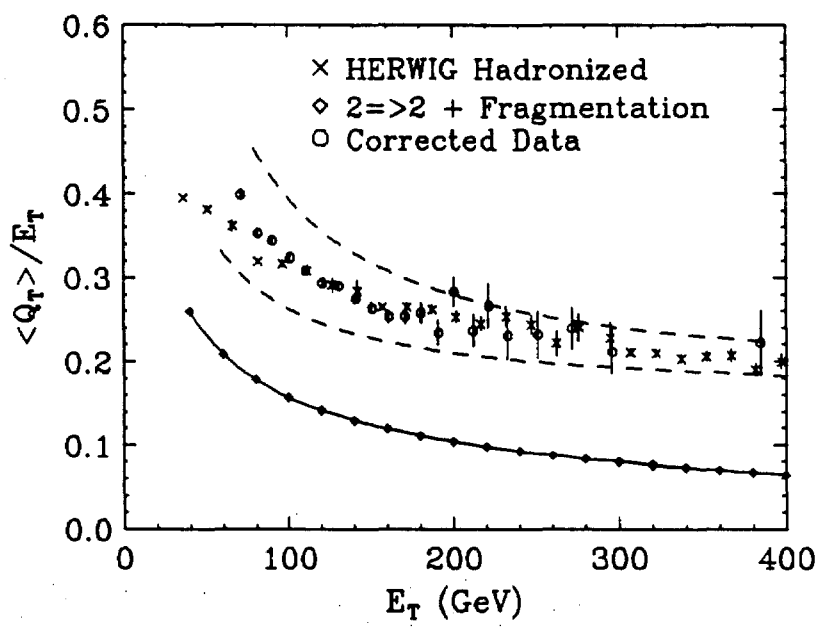

Figure 2-6: A plot of the ratio $< Q_T > / E_T$ vs. E_T in the range $|\eta| < 1.1$ compared with a high-order QCD calculation done with the Herwig Monte Carlo program. The dashed curves above and below the corrected data points show the systematic uncertainty limits. A fragmented $2 \rightarrow 2$ calculation was done to show how much of the broadening is due to soft processes without hard bremstrahlung. The solid curve is a spline fit joining these calculated points.

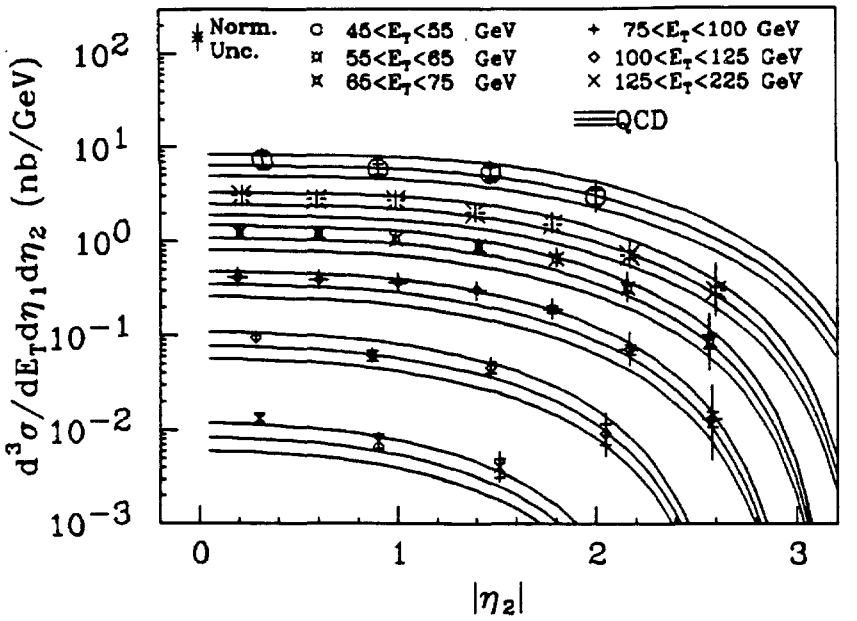

Figure 2-7: Two Jet Differential Cross Sections averaged over $\eta_1 \leq |0.6|$ compared with QCD predictions where η_1 (η_2) is the rapidity of the first (second) jet. The inner error bars are statistical, and the outer error bars include the statistical uncertainty and the E_T and η_2 dependent part of the systematic uncertainty. The $E_T - \eta_2$ independent normalization common to all points is $1.00^{+0.41}_{-0.30}$.

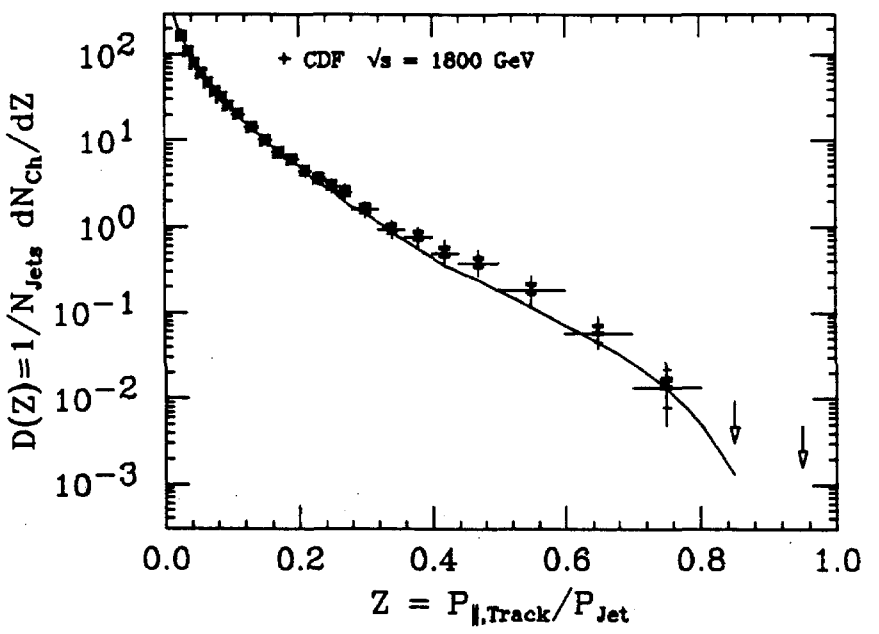

Figure 2-8: A plot of the charged fragmentation function, D(Z). The CDF data have statistical and systematic errors as indicated. The curve is a prediction of the HERWIG 3.2 Monte-Carlo program.

2.2 The 1988-89 Run

For the run beginning in June, 1988, all of the CDF components were fully operational. The forward calorimeters were fully instrumented. The far forward section was fully instrumented with new silicon detectors and drift chambers down to small angles to measure the total cross section. The Level-2 and Level-3 trigger systems were brought on line. Faster and more useful control room displays of events and detector performance were installed. Substantial improvements had been made to all aspects of operations based on the earlier running experience.

The primary emphasis of this run was physics, and major resources were devoted to offline analysis to enable it to keep up with the production of data. Approximately 4.4 pb^{-1} of integrated luminosity were written to 5000 magnetic tapes during the year-long run. The first-pass offline processing of the complete data set was finished within a month after the run ended, and the various physics groups began to work with the full data set. At this writing (October 9, 1990), the following physics topics are either published or nearing completion:

1. From samples of $Z^0 \rightarrow \mu^+\mu^-$ and $Z^0 \rightarrow e^+e^-$ the mass of the Z^0 has been measured to be $M(Z^0) = 90.9 \pm 0.3(stat. + syst.) \pm 0.2(scale)$ GeV.[46] (See Figs. 2-9 and 2-10.)

2. From samples of $W^\pm \rightarrow \mu^\pm\nu$ and $W^\pm \rightarrow e^\pm\nu$ the mass of the $W^\pm$ has been measured to be $M(W^\pm) = 79.91 \pm 0.39$. (See Figs. 2-11 and 2-12.) The value of $\sin^2\theta_W$ is thus determined to be 0.232 ± 0.008.[47,48]

3. We have searched for the top quark through the decay channel: $t\bar{t} \rightarrow e + jets$.[49] The existence of a standard-model top quark is excluded in the mass range 40 to 77 GeV/c^2 at the 95% confidence level. (Figure 2-13).

4. We have searched for the top quark or fourth-generation b quark (b′)through the decay channel: $t\bar{t} \rightarrow e\mu X$[50] (Figure 2-14). The existence of a standard-model top quark or b′ in the mass range 28 to 72 GeV/c^2 is excluded at the 95% confidence level.

5. Further analysis of other di-lepton signatures has been done, e.g. $t\bar{t} \rightarrow e^+e^-X$, $t\bar{t} \rightarrow \mu^+\mu^-X$, and $t\bar{t} \rightarrow e + \text{soft}\mu X$. A preliminary combined result of all di-lepton modes places a lower limit on the top mass of 89 GeV/c^2 at the 95% confidence level.

6. We have measured $R = [\sigma \cdot B(W \rightarrow e\nu)]/[\sigma \cdot B(Z \rightarrow ee)]$, ratio of the products of cross-section and branching-fractions, to be $R = 10.2 \pm 0.8(stat.) \pm 0.4(syst.)$.[51] Combining this with other measurements, we find the width of the $W^\pm$ to be $\Gamma(W) = (2.19 \pm 0.20)$ GeV.

7. From a measurement of the forward-backward asymmetry in the decay $Z^0 \rightarrow e^+e^-$, we have determined $\sin^2\theta_W = 0.232 \pm 0.016$. This result does not include corrections for radiative loops. (See Sec. 3.1.) (Preliminary result.)

8. We have put 95% confidence level lower limits on the masses of a heavy W or a heavy Z at 380 GeV and 400 GeV, respectively. (Preliminary result.)

9. We have searched for a light Higgs Boson in the process $Z^0 \rightarrow Z^0 + H^0$ with the H^0 decaying to two light charged particles (e^+e^-, $\mu^+\mu^-$, $\pi^+\pi^-$). At the 95% confidence level the existence of such a particle with standard model couplings is excluded in most of the mass range below 1 GeV/c^2.[52]

10. We have measured the transverse momentum distributions of the electro-weak gauge bosons (W, Z and photon[53]) (Figs. 2-15 and 2-16). (Preliminary result.)

11. We have measured the transverse momentum distribution of jets (Fig. 2-17) and the dijet mass spectrum (Fig. 2-18). Dijets with invariant masses up to about 1 TeV are observed. Analysis should allow tests of parton compositeness to an energy scale above 1 TeV. (Preliminary result.)

12. The angular distributions and fractional energy per jet have been measured in a high statistics three-jet sample and show good agreement with QCD. (See Fig. 2-19.) (Preliminary result.)

13. The search for SUSY particles has been extended, and no evidence for their existence is found at masses up to 150 GeV (110 GeV) for squarks (gluinos). (Preliminary result.)

14. We have measured production cross section times branching ratio for W and Z bosons to be $\sigma(W \rightarrow e\nu) = 2.19 \pm 0.04(stat.) \pm 0.21(syst.)nb$ and $\sigma(Z \rightarrow e^+e^-) = 0.209 \pm 0.013(stat.) \pm 0.017(syst.)nb$. See Fig. 2-20. (Preliminary result.)

15. Using the $J/\psi \rightarrow \mu^+\mu^-$ sample, a search for exclusive B meson decays has been performed. We have fully reconstructed the decays $B^- \rightarrow J/\psi K^-$ and $B^0 \rightarrow J/\psi K^{*0}$, $K^{*0} \rightarrow K^+\pi^-$ (as well as the charge conjugate modes), the number of observed B events in these channels is 35 $\pm$ 9. Figure 2-21 shows the sum of the J/ψ K and J/ψ K^{*0} invariant mass distributions with a fit overimposed. (Preliminary result.)

Many of these analyses are the subjects of Ph.D. theses, completed or in progress, by students at the participating institutions. Among these are:

- Brandeis: Milciades Contreras, Luc Demortier, Les Nakae
- Chicago: Aaron Roodman, Paul Derwent
- Harvard: E. Kearns, W. Trischuk, C. Jessop, J. Ng,
- Illinois: Phil Schlabach, Vic Scarpine, Peter Hurst, Hovhannes Keutelian, Ray Swartz, Chris Luchini, Dave Kardelis
- Berkeley: Brian Winer, Bob Drucker

- Penn: Dave Connor, John Walsh, Tim Rohaly
- Pisa: Giovanni Punzi, Sandra Leone
- Purdue: B. T. Huffman, J. I. Tonnison
- Rutgers: Ping Hu
- Texas A&M: Tim Hessing
- Tsukuba: Fumi Ukegawa, Toshi Mimashi, Shun-ichi Kanda, Satoru Ogawa, Mikio Takano, Mariko Ninomiya, Yoshi Seiya, Takashi Ino, Masa Yokoyama
- Wisconsin: Karen Byrum, Lee Markosky, Rich Markeloff, Jodi Lamoureux

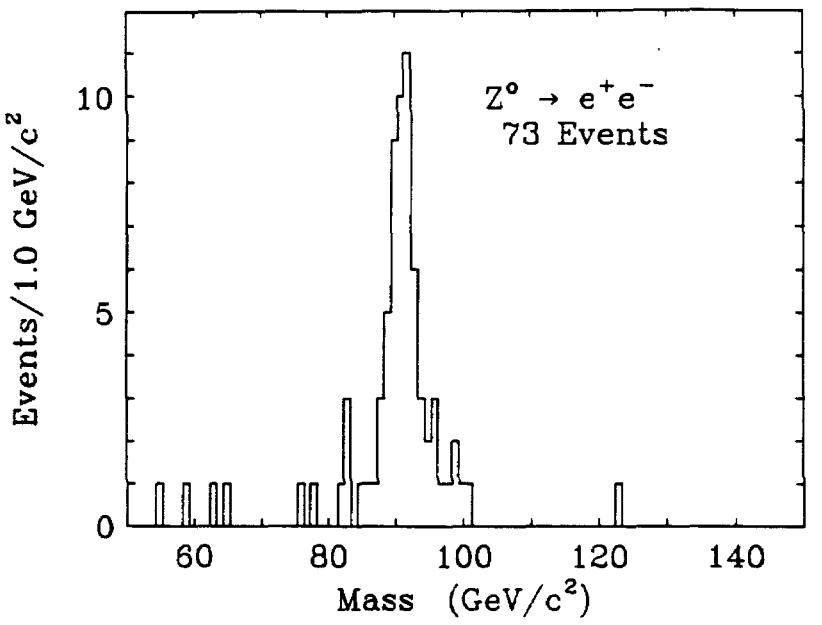

Figure 2-9: Calorimeter-based invariant mass plot for electron-positron events.

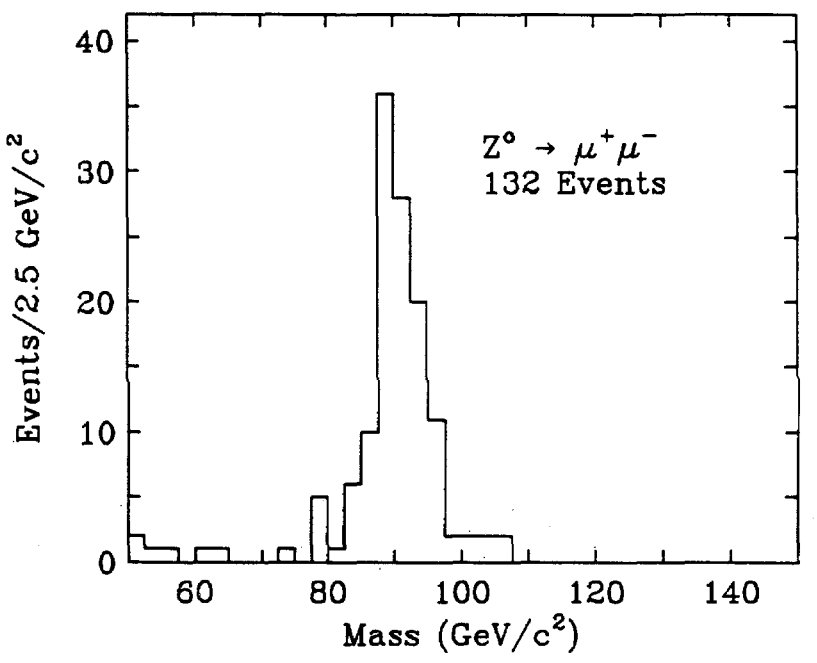

Figure 2-10: Invariant mass plot for $Z \rightarrow \mu^+\mu^-$ based on tracking data.

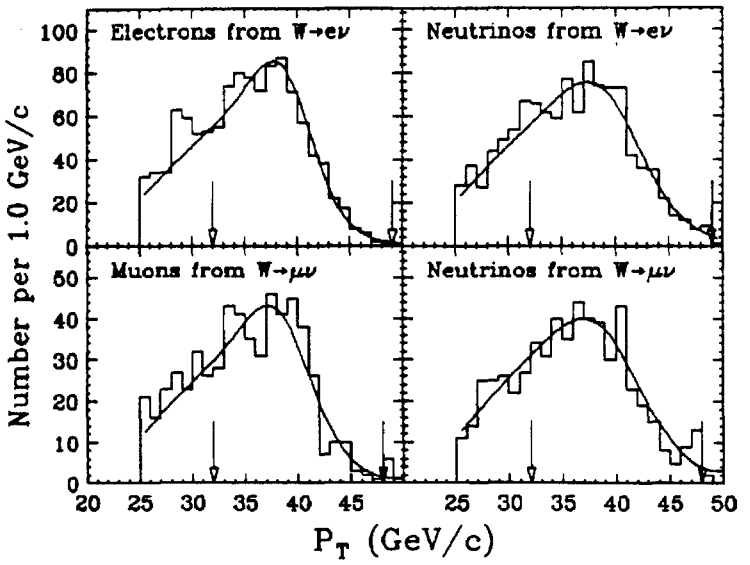

Figure 2-11: P_T distributions for charged leptons and corresponding neutrinos from $W^{\pm} \rightarrow \mu^{\pm}\nu$ candidates and $W^{\pm} \rightarrow e^{\pm}\nu$ candidates. The best fit to the data is indicated in each case. Arrows indicate the boundaries of the regions used in the fits.

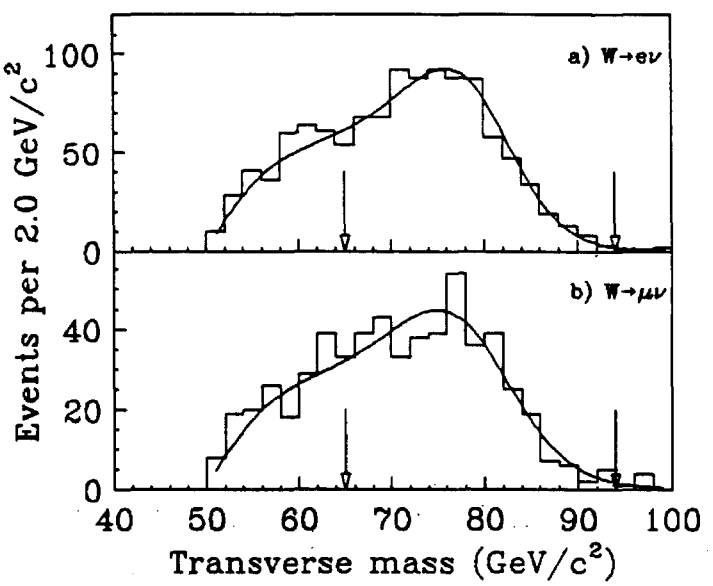

Figure 2-12: a) The transverse mass distributions for $W^{\pm} \rightarrow e^{\pm}\nu$ candidates. Overlaid is the best fit to the data. The range of transverse masses used in the fit is indicated by the vertical arrows. b) The transverse mass distribution for $W^{\pm} \rightarrow \mu^{\pm}\nu$ candidates.

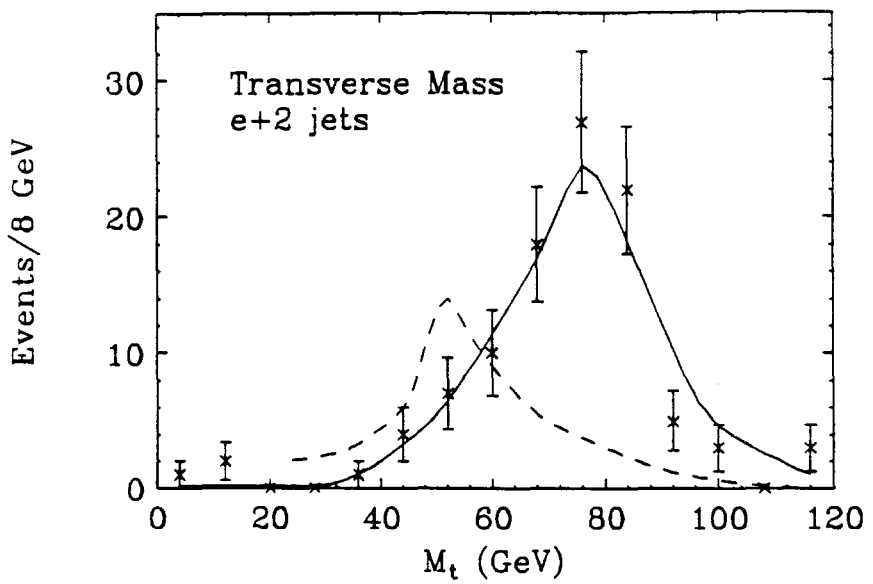

Figure 2-13: The transverse mass ($M_T^{e\nu}$) distrubutions for the $e^{\pm}$ + 2 jets data (points), W + 2 jets (solid curve), and $t\bar{t}$ production with $M_{top} = 70$ GeV/c^2 (dashed curve).

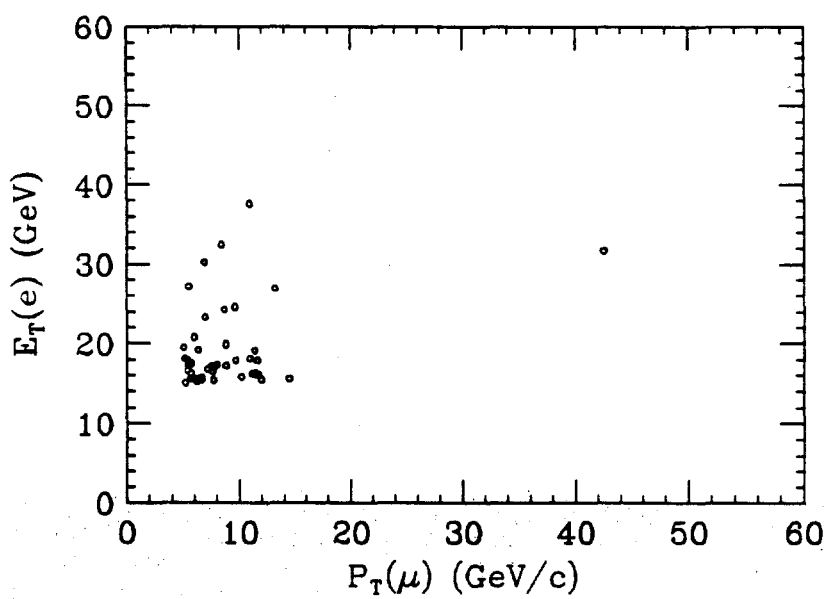

Figure 2-14: Electron transverse energy vs muon transverse momentum for the CDF data with an integrated luminosity of 4.4 pb^{-1}. Approximately seven events would be expected in the region $p_T(\mu) > 15$ GeV/c and $p_T(e) > 15$ GeV/c if the top quark mass is 70 GeV/c^2.

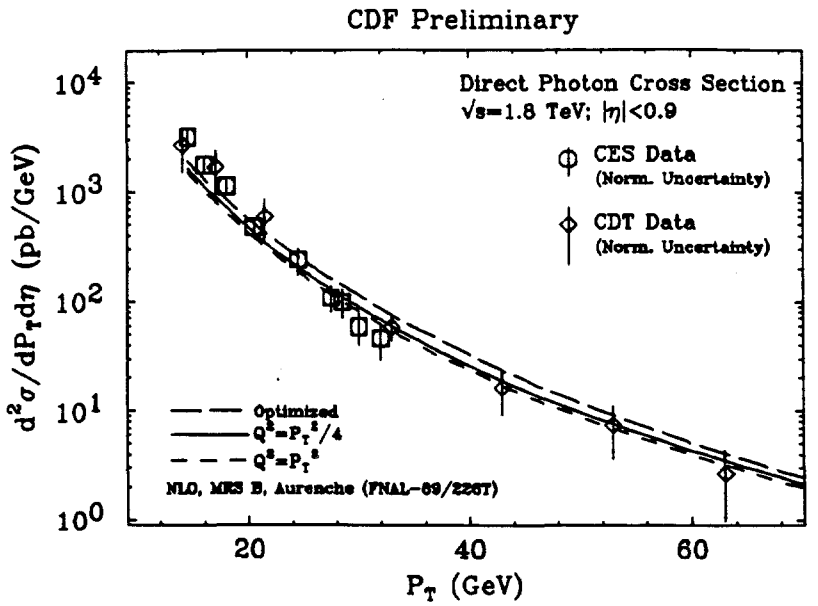

Figure 2-15: The P_T distribution for isolated photons.[53] Two different analyses were performed to eliminate isolated π^0's from the sample, one using the central strip chambers (CES) and the other using the central drift tubes (CDT). The theoretical curves are a QCD calculation.[54] Photon candidates exist up to considerably higher E_T than the points plotted here, but they are contaminated by π^0's. With the addition of the central pre-radiator in 1991, and the increased statistics expected in that run, we expect to measure the photon cross section to E_T of 200 GeV and beyond.

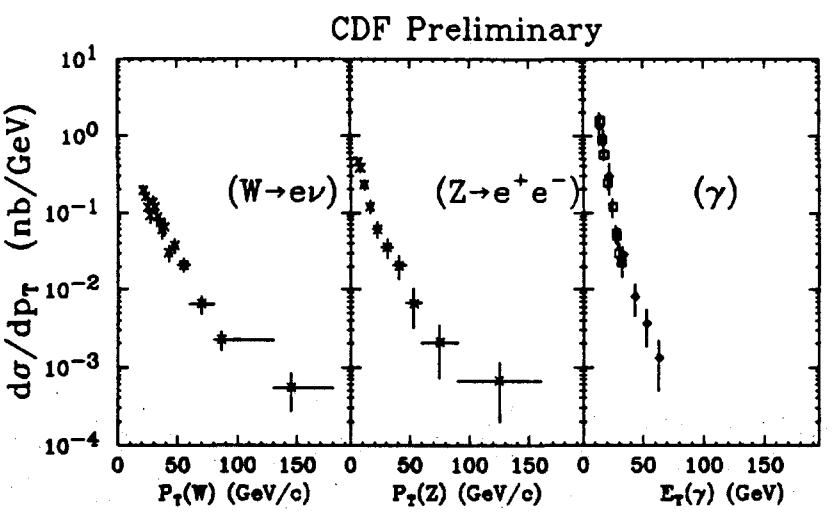

Figure 2-16: Transverse momentum distributions for $W^{\pm}$, Z^0 and γ in the psuedorapidity interval $|\eta| < 1.0$. The W and Z distributions have been divided by the branching fraction for the observed decay mode. The photon data are the experimental points from Fig. 2-15 multiplied by two units of pseudorapidity.

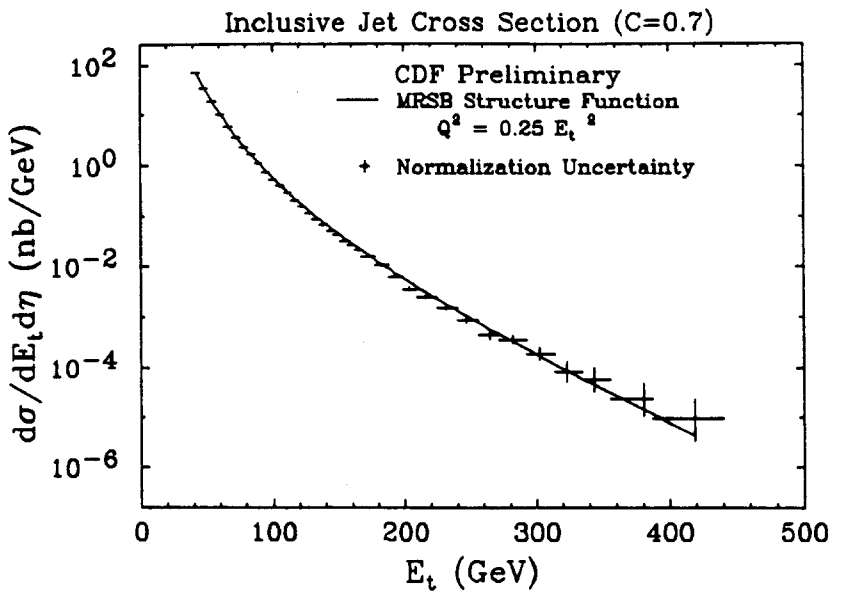

Figure 2-17: The transverse energy distribution for inclusive jet production. The curve is a QCD fit, with no compositeness term, using the MRSB structure function.

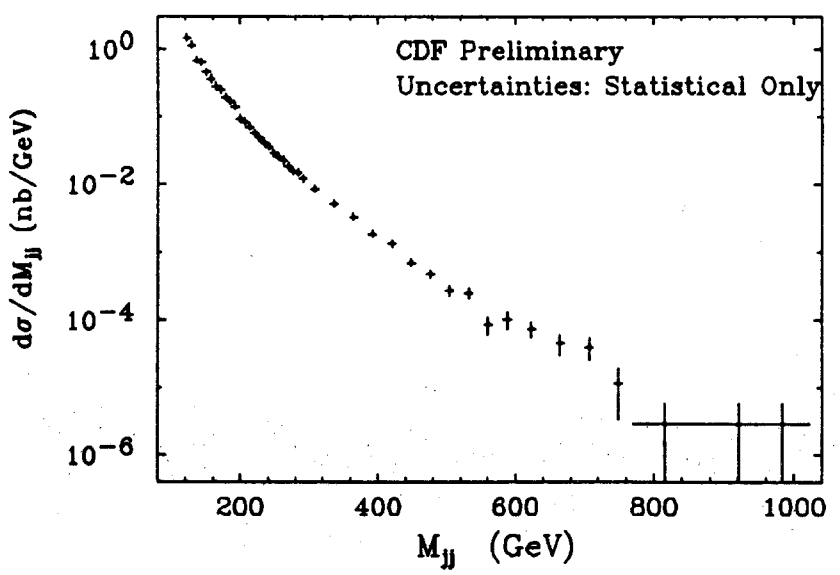

Figure 2-18: The dijet invariant mass spectrum.

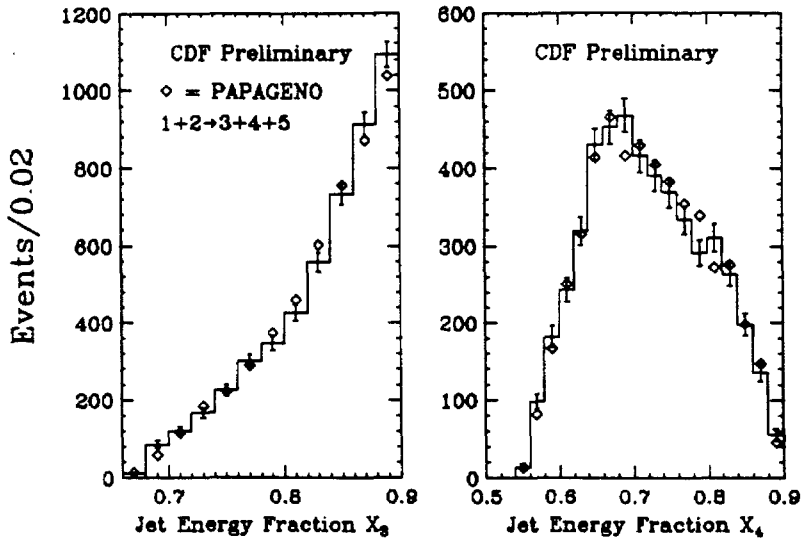

Figure 2-19: Three-jet final states are a measure of the parton processes $1 + 2 \rightarrow 3 + 4 + 5$ where the final state partons fragment into the observed jets. In the rest system, the jet energies are E_i ordered $E_3 > E_4 > E_5$. We define $x_i = 2E_i/M$ where $M = E_3 + E_4 + E_5$. The x_3 and x_4 Dalitz plot projections are plotted along with the QCD predictions.

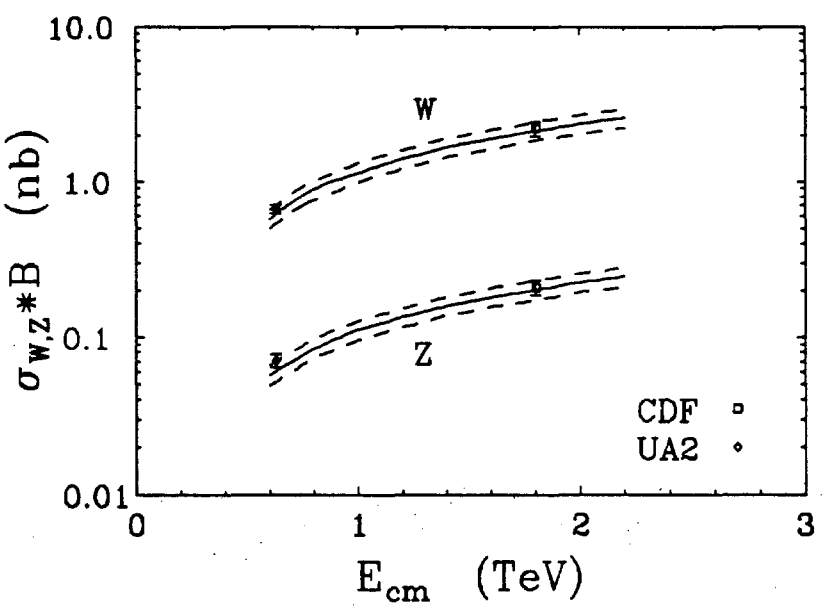

Figure 2-20: Production cross section times branching ratio for $W \rightarrow e\nu$ and $Z \rightarrow e^+e^-$. Results are shown from CDF,[55] and UA2.[56] The solid lines are theoretical predictions,[57] and the dashed lines represent the 1-σ theoretical uncertainties.

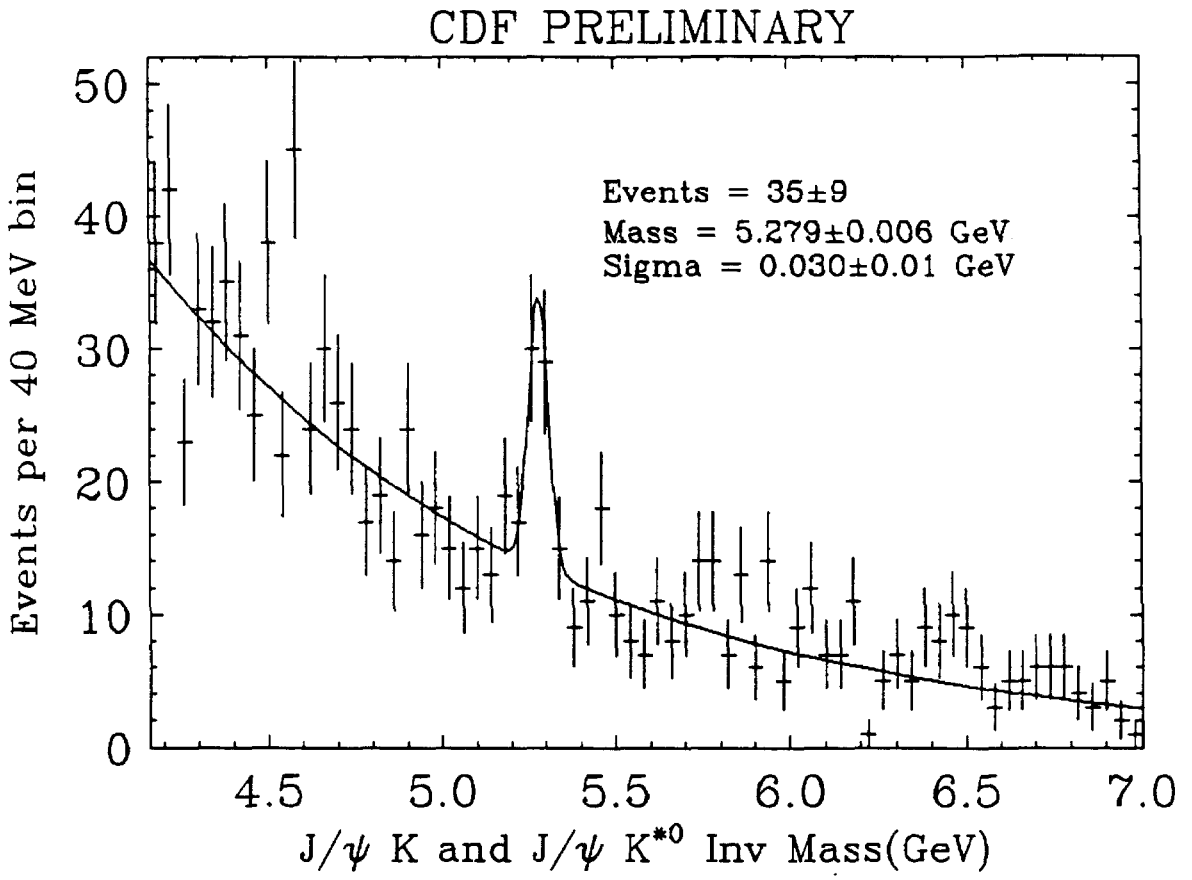

Figure 2-21: A histogram of events from the $J/\psi \rightarrow \mu^+\mu^-$ sample, which shows evidence for $B^- \rightarrow J/\psi K^-$ and $B^0 \rightarrow J/\psi K^{*0}$, $K^{*0} \rightarrow K^+\pi^-$ (and charge conjugate modes).

3 Planned Physics Program

3.1 Electro-Weak Physics

The minimal Standard Model (SM) of $SU(2) \times U(1)$, surprising in its elegant simplicity, has been extraordinarily successful in describing weak and electromagnetic phenomena over the full reach of experimental observation. The model, with the exception of the Higgs sector and the KM mixing angles, is completely determined by three input parameters. Two are known to very high precision, albeit at low energy and momentum transfers: the fine structure constant, α and the Fermi constant, G_F from muon decay. The third parameter enters through the weak bosons, W and Z^0. Until recently, the most precise measurements were of the electroweak mixing angle, $\sin^2\theta_W$ as determined from deep inelastic neutrino scattering experiments. With the model so fixed, all other parameters – the W and Z^0 masses in particular – are determined up to radiative corrections from loop diagrams associated with the gauge boson masses and running the input coupling constants to a common kinematic regime.

The picture has recently changed with the operation of the SLC and LEP e^+e^- colliders. The Z^0 mass has supplanted $\sin^2\theta_W$ as the most precisely known weak boson parameter, thus properly becoming input to the SM.

It is now the task of the Fermilab Collider to make improvements on precision measurements of the W mass, the W width and $\sin^2\theta_W$ to confront improved SM predictions that result from high precision LEP results. The Z^0 sector will continue to be the domain of electron-positron colliders. The precision measurements of the Z^0 parameters from LEP experiments have secondary benefits for W physics at Fermilab. They provide a calibration point to control some of the systematic uncertainties that have previously limited the precision of W measurements at hadron colliders, and also help to refine predictions for Z^0 production cross sections at the Tevatron - important for improvements in *e.g.* the W / Z^0 cross section ratio and W width measurements.

The proposed improvements in CDF lepton coverage result in significant improvements for both W and Z^0 physics. For example, the proposed upgrade for the muon system, extending the triggerable muon coverage out to $|\eta_\mu| < 2.8$, provides roughly a twofold increase in trigger acceptance for both $W \rightarrow \mu\,\nu$ and $Z^0 \rightarrow \mu^+\mu^-$ over that expected for the 1991 collider run. For electrons, the proposed improvements for enhanced coverage in the region $1.1 < |\eta_e| < 3.0$ for the 1993 run, in terms of hermeticity, triggerability, enhanced electron identification and background rejection in turn implies enhanced statistics and greater cleanliness for both $W \rightarrow e\nu$ and $Z^0 \rightarrow e^+e^-$ data samples.

We discuss the ramifications of the proposed improvements to the CDF lepton coverage on various electroweak physics topics - contrasting expectations for two scenarios, 50 pb^{-1} and 500 pb^{-1} of integrated luminosity to that of the present experimental situation (5 pb^{-1}), with particular attention given to those systematic effects which limit the precision of various measurements. In these discussions we have assumed that the Z^0 parameters are known from the LEP experiments to essentially infinite precision.

The W Boson Mass

Unlike the Z^0, the W invariant mass cannot be reconstructed from its leptonic decays since the neutrino is not detected. Rather, the tranverse components of the neutrino energy are inferred from the missing transverse energy ($\not{E}_T$) in the event. The transverse mass, M_T (the three-vector analog of the invariant mass) is used to extract the W mass. Unfortunately, the shape of the M_T distribution is influenced by a number of other effects such as the $\not{E}_T$ resolution, lepton energy/momentum resolution, lepton subtraction from the underlying event, the W width and also structure function uncertainties. Our estimates for the uncertainties are given in Tables 3-1 and 3-2 for the electron and muon W decay channels.

Category	$5\,pb^{-1}$	$50\,pb^{-1}$	$500\,pb^{-1}$
W Statistics	340	95	40
Energy Scale	310	90	40
Structure Functions	100	50	25?
Resolutions, $W\ P_t$	120	35	10
Electron Subtraction	170	35	10?
Background	50	20	10?
Fitting	50	30?	20?
Overall	520	155	70?

Table 3-1: Projected Uncertainties in the $W \rightarrow e\,\nu$ Mass Measurement

Category	$5\,pb^{-1}$	$50\,pb^{-1}$	$500\,pb^{-1}$
W Statistics	520	110	50
Energy Scale	160	50	20
Structure Functions	100	50	25?
Resolutions, $W\ P_t$	190	55	10
Muon Subtraction	205	60	10?
Background	50	20	10?
Fitting	50	30?	20?
Overall	625	160	65?

Table 3-2: Projected Uncertainties in the $W \rightarrow \mu\,\nu$ Mass Measurement

The uncertainty associated with each of these systematic effects is a product of the partial derivative of the fitted W mass with respect to the parameter of interest, times the uncertainty in the parameter itself. For example, consider the $\not{E}_T$ resolution:

$$\text{Systematic uncertainty on } M_T = \sigma_{M_T} = \frac{\partial(M_T)}{\partial(\sigma_{\not{E}_T})} \cdot \Delta(\sigma_{\not{E}_T}) \qquad (1)$$

The derivative $\partial(M_T)/\partial(\sigma_{\not{E}_T})$ is determined by Monte Carlo simulation. The uncertainty in the $\not{E}_T$ resolution, $\Delta(\sigma_{\not{E}_T})$ is extracted from the data. We have, perhaps optimistically,

assumed that enough computing power will be available so that the Monte Carlo part is never a limiting factor. The uncertainty in a parameter can be itself limited by statistics, as is the case for the $\not{E}_T$ example above. For such parameters, the uncertainty, though systematic, will scale like the square root of the integrated luminosity. Others, such as the proton structure function, may not. Combining the two W decay channels to obtain a single measurement of the W mass, and using the world-average Z^0 mass to set the mass scale, the overall uncertainty in the W mass for integrated luminosities to tape of 5, 50, and 500 pb^{-1} is estimated to be ± 450, ± 115, and $\pm$ 50 MeV/c^2, respectively.

In Fig. 3-1, we show the W mass (combined e and μ W decay channels) and uncertainties for the three scenarios as a function of the top quark mass, with the Higgs mass as a parameter. For illustration, we assume the central value of the W mass remains at its present value, 79.91 GeV/c^2, and the uncertainties scale according to Tables 3-1 and 3-2. The current situation (4.4 pb^{-1}) imposes rather crude constraints on the the top quark mass. However, for 50 and 500 pb^{-1} the top quark mass would be constrained to lie within a $\pm 25\, GeV/c^2$ and $\pm 15\, GeV/c^2$ mass range at the 1-sigma level, respectively for Higgs masses between $50 \leq M_H \leq 1000\, GeV/c^2$.

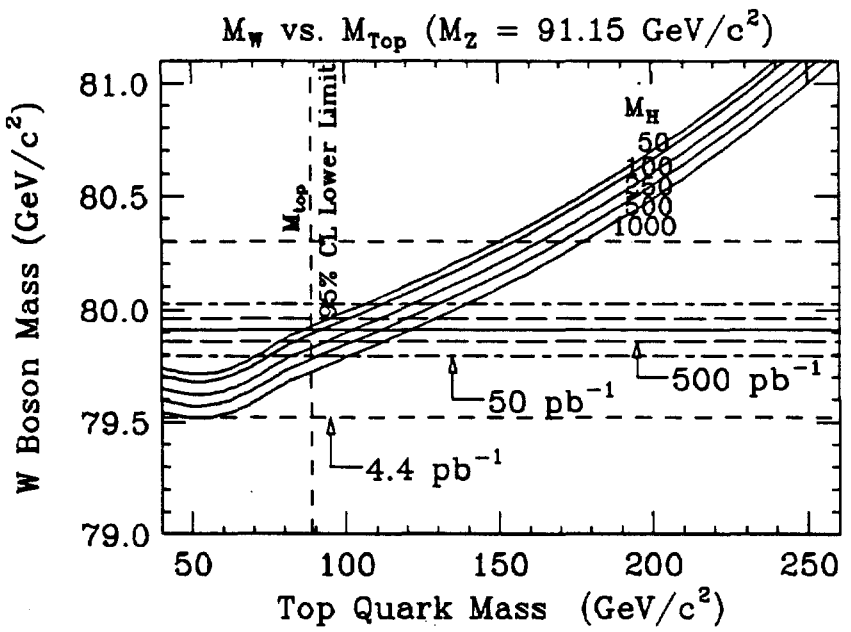

Figure 3-1: Constraints on M_{top} by measurements of M_W. Uncertainties are given for several values of integrated luminosity. Example given is for the current best measurement of M_W.

With 50 pb^{-1} of data, a direct search for the top quark should have a discovery limit of $M_{top} \sim 140\, GeV/c^2$ and thus would not be in conflict with the W mass constraints. With 500 pb^{-1} the top mass limits from the W mass are compressed slightly. However, the discovery limit for a direct top quark search in this latter scenario is much larger, exceeding

200 GeV/c^2.

Alternatively, the top quark may be found. Suppose the top quark mass were $\sim$ 120 GeV/c^2 and thus discoverable with 50 pb^{-1} of data. The measured rate alone is enough to constrain the top quark mass to $\sim$ 10%. In this scenario, improved knowledge of both the W mass and top quark mass may begin to give us a hint of the Higgs mass. With 500 pb^{-1} of data, the situation becomes even more interesting in this regard.

R, the Ratio of W to Z^0 Production and Leptonic Decay

The ratio R is the ratio of W / Z^0 production cross sections $\times$ leptonic decay branching ratios:

$$R = \frac{\sigma(\bar{p}p \rightarrow W\,X)\,B(W \rightarrow \ell\nu_\ell)}{\sigma(\bar{p}p \rightarrow Z^0\,X)\,B(Z^0 \rightarrow \ell\ell)} = \frac{\sigma(\bar{p}p \rightarrow W\,X)}{\sigma(\bar{p}p \rightarrow Z^0\,X)}\,\frac{\Gamma(W \rightarrow \ell\,\nu_\ell)}{\Gamma(Z^0 \rightarrow \ell\ell)}\,\frac{\Gamma(Z^0)}{\Gamma(W)}$$

The advantage of dealing with ratios is the cancellation of many systematic effects in both the experimental measurement and the theoretical calculations. The ratio of the total cross sections and the leptonic partial widths can be calculated to rather high precision. Moreover, recent precision measurements of the Z^0 width from SLC and LEP experiments rule out a fourth family of light neutrinos. Thus a precise measurement of R yields the total W decay width. The W width is sensitive to anything which can couple to the W and would be the only practical way to detect objects that so couple and then decay without a distinctive signature. We consider an example below.

We show the expected statistical and systematic uncertainties for R in Tables 3-3 and 3-4 for the W and Z^0 electron and muon decay channels. In contrast to the case for the W mass, the overall uncertainty in R is statistics-limited (by the total number of Z^0's) until the 500 pb^{-1} scenario. The W width should be determined to 1-2%.

Category	5 pb^{-1}	50 pb^{-1}	500 pb^{-1}
$Z^0 \rightarrow e^+e^-$ Statistics	300 events	4000 events	50,000 events
	6.0 %	1.6 %	0.5 %
W Backgrounds	0.7 %	0.5 %	0.3 %
Z^0 Backgrounds	1.5 $	1.0 %	0.5 %
Efficiencies	3.0 %	1.0 %	$\leq$ 0.5 %
Acceptances	2.0 %	1.0 %	0.5 %
S.M. Input Parameters	0.5 %	$\leq$ 0.4 %	$\leq$ 0.3 %
Overall	7.1 %	2.4 %	1.1 %

Table 3-3: Projected Uncertainties in the R_e Measurement

As noted above, the R ratio is an inclusive technique for searching for objects which couple to the W and Z^0 but have masses that are kinematically allowed for the W and forbidden for the Z^0. The top quark in the mass range 45 to 80 GeV/c^2 is a familiar

Category	$5\,\mathrm{pb}^{-1}$	$50\,\mathrm{pb}^{-1}$	$500\,\mathrm{pb}^{-1}$
$Z^0 \rightarrow \mu^+\mu^-$ Statistics	200 events	3500 events	45,000 events
	7.3 %	1.8 %	0.5 %
W Backgrounds	0.7 %	0.5 %	0.3 %
Z^0 Backgrounds	1.5 $	1.0 %	0.5 %
Efficiencies	3.0 %	1.0 %	$\leq$ 0.5 %
Acceptances	2.0 %	1.0 %	0.5 %
S.M. Input Parameters	0.5 %	$\leq$ 0.4 %	$\leq$ 0.3 %
Overall	8.3 %	2.6 %	1.1 %

Table 3-4: Projected Uncertainties in the R_μ Measurement

example. If the top decay were dominated by a charged Higgs and a b quark, $t \rightarrow H^+ + b$, direct observation of the top quark would be very difficult. Estimates of the W branching ratio into a top quark in this mass region range up to 16% which is easily observable in measurements of R.

Asymmetry in Leptonic Z^0 Decays: $\mathrm{Sin}^2\theta_W^{AFB}$

The angular distribution of leptonic Z^0 decays (where the decay angle $\hat{\theta}$ is defined as the angle between the positron and the proton in the Z^0 CM system) shows a forward-backward asymmetry due to interference between the vector and axial-vector components of the electroweak neutral current. The vector part is proportional to $(0.25 - \sin^2\theta_W^{AFB})$, so the asymmetry is a sensitive measure of the deviation of $\sin^2\theta_W^{AFB}$ from 0.25. Note that $\sin^2\theta_W^{AFB}$ is not the same as $\sin^2\theta_W^{MS}$, which is defined in terms of the W and Z^0 boson masses:

$$\sin^2\theta_W^{MS} \equiv 1 - (M_W/M_Z)^2$$

which is sensitive to radiative corrections associated with *e.g.* fermion loops involving top quarks. On the other hand, $\sin^2\theta_W^{AFB}$ is more closely related to intrinsic couplings as defined at the Z^0 pole. The relation between $\sin^2\theta_W^{MS}$ and $\sin^2\theta_W^{AFB}$ is given by:

$$\sin^2\theta_W^{MS} = \sin^2\theta_W^{AFB}/(1 - \Delta R')$$

where the radiative correction factor $\Delta R'$ is a function of the gauge coupling constants g and g' and decay constants f and $\bar{f}$ evaluated at the W and Z^0 mass scales. The current CDF data for the Z^0 forward-backward asymmetry are shown in Fig. 3-2. By definition, the asymmetry is the rate difference for the transformation $\cos\hat{\theta} \rightarrow -\cos\hat{\theta}$. This transformation is identical to the transformation $\ell^- \rightarrow \ell^+$. Therefore the detector acceptance will be symmetric in the angular distribution if it is charge symmetric. Electron (positron) identification is dominated by the calorimetric information, which cannot distinguish charge. For muons, the systematics of the CDF detector are such that it is very nearly charge independent. In short, the asymmetry measurement is remarkably free of systematic effects due to irregularities in

detector acceptance.

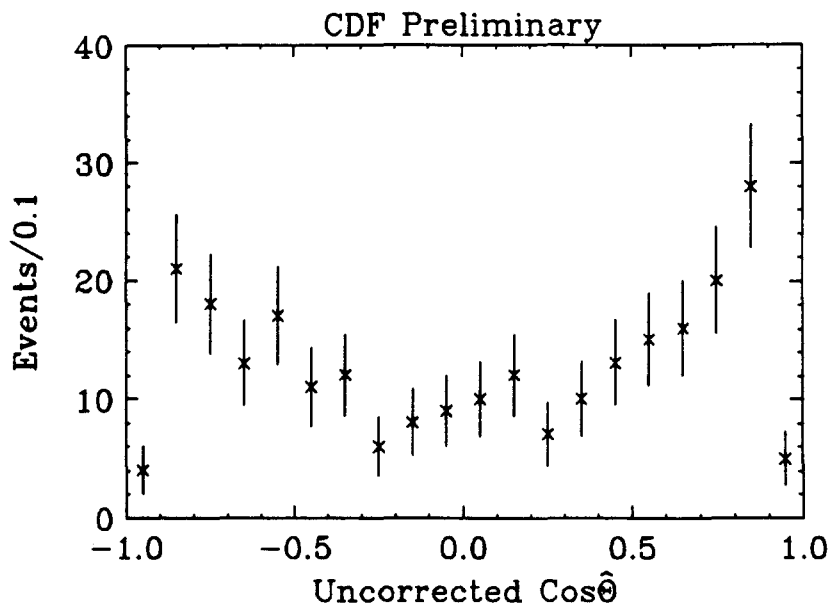

Figure 3-2: Forward-Backward Asymmetry in $Z \rightarrow e^+e^-$

We have examined the statistical and systematic uncertainties in our three standard scenarios and the results are shown in Tables 3-5 and 3-6. Notice that the overall uncertainty in $\sin^2\theta_W^{AFB}$ is statistics-limited until the total data set approaches 500 pb^{-1}. The dominant systematic uncertainty comes from imprecise knowledge of the structure functions. The systematic uncertainty in Tables 3-5 and 3-6 represents the extreme variations to a wide choice of structure function parameterizations. Our optimism that these variations will decrease in the future is based on the expectation that the structure functions will become better known from other measurements (see *e.g.* the following section).

Category	$5\,pb^{-1}$	$50\,pb^{-1}$	$500\,pb^{-1}$
$Z^0 \rightarrow e^+e^-$ Statistics	0.0160	0.0048	0.0016
Structure Functions	0.0020	0.0010	0.0010
Detector Efficiency	$\leq$ 0.0010	–	–
Overall	0.0160	0.0049	0.0019

Table 3-5: Projected Uncertainties in the $\mathrm{Sin}^2\theta_W^{AFB}$ $Z^0 \rightarrow e^+e^-$ Measurement

We show the combined e and μ results for the three scenarios and a comparison with the SM prediction in Fig. 3-3. Since the Z^0 forward-backward asymmetry essen-

Category	$5\,pb^{-1}$	$50\,pb^{-1}$	$500\,pb^{-1}$
$Z^0 \rightarrow \mu^+\mu^-$ Statistics	0.0260	0.0054	0.0016
Structure Functions	0.0020	0.0010	0.0010
Detector Efficiency	$\leq$ 0.0020	–	–
Overall	0.0260	0.0055	0.0019

Table 3-6: Projected Uncertainties in the $\mathrm{Sin}^2\theta_W^{AFB}$ $Z^0 \rightarrow \mu^+\mu^-$ Measurement

tially measures the ratio of the coupling constants g_A/g_V at the Z^0 pole, the result for $\sin^2\theta_W^{AFB}$ depends very weakly on the top quark mass. Therefore the measurement is a direct test of the SM alone. Also, since this process has a $q\bar{q}$ initial state, the asymmetry depends on the weak charges of the light quarks and is, thus, different from the lepton asymmetry measurements at LEP.

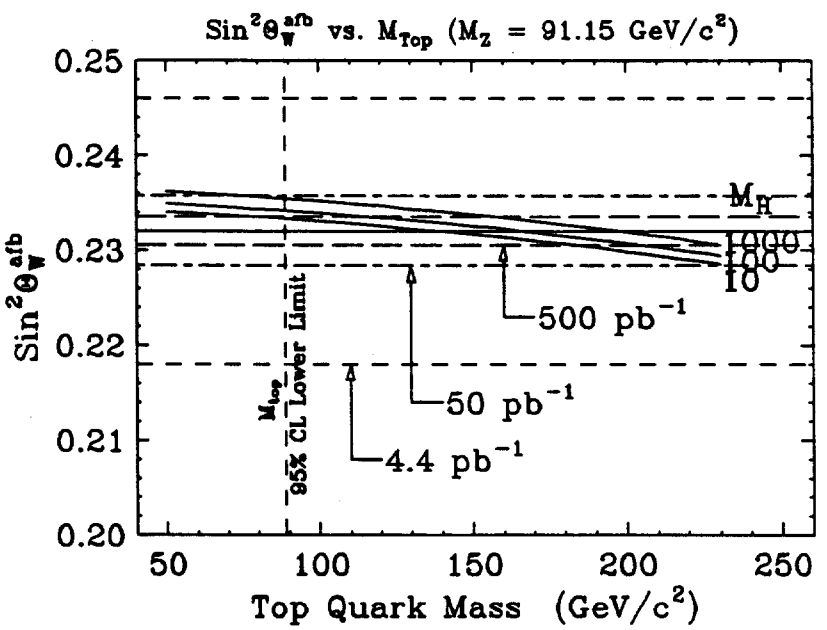

Figure 3-3: Predicted M_{top} dependence of $\sin^2\theta_W^{afb}$ from the combined results of forward-backward asymmetry measurements in $Z \rightarrow e^+e^-$ and $Z \rightarrow \mu^+\mu^-$. Uncertainties are given for several values of integrated luminosity. Example given is for current CDF measurement.

Charge Asymmetry in Leptonic W Decays

The charge asymmetry in leptonic W decays, *e.g.* $W \rightarrow e\nu$ and $W \rightarrow \mu\nu$ while interesting in its own right as a fundamental measurement of the V-A structure of the charged-current weak interactions, also yields important information on the ratio of d/u quarks at a $Q^2 \simeq M_W^2$. Along with other structure function information obtained at the Tevatron collider from QCD jet and direct-photon production, this information can be fed-back into other analyses such as the W mass and R measurements, in order to help reduce systematic uncertainties due to imperfectly known structure functions. At the present time, we use various sets of structure functions fit to parton distributions measured at much lower Q^2 values. These must be evolved to the W and Z^0 mass scales. With the present 4.4 pb^{-1} CDF has analyzed $W^{\pm} \rightarrow e^{\pm}\nu_e$ and $W^{\pm} \rightarrow \mu^{\pm}\nu_\mu$ events in the pseudo-rapidity ranges $|\eta_e| < 1.0$, and $|\eta_\mu| < 0.6$ respectively. Analysis in progress is extending the asymmetry measurements for $W^{\pm} \rightarrow e^{\pm}\nu_e$ into the range $1.0 < |\eta_e| < 1.7$. Sensitivities due to acceptance and different choices of structure functions are shown in Fig. 3-4. There are significant gains in structure function sensitivity with improved muon coverage.

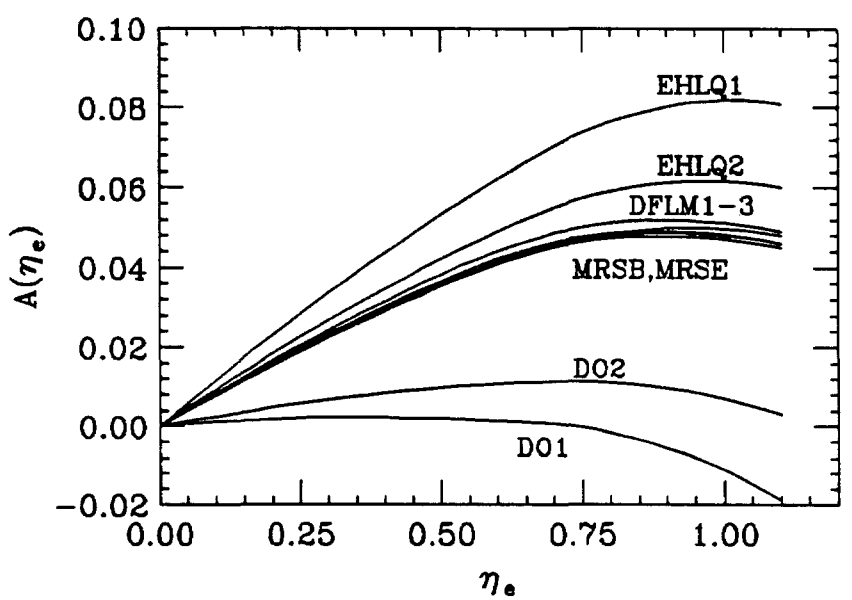

Figure 3-4: Charge Asymmetry in $W \rightarrow \ell\nu_\ell$

Search for Sequential Z' Bosons

Having considered several precision tests of the SM, we turn now to one possible extension of the model – sequential Z'. Sensitivity to a high mass Z' will be unique to Fermilab. We have investigated the prospects for detecting a high-mass Z' decaying into lepton pairs. Assuming SM couplings for the Z' width, the Z' branching ratios are the same as those of the Z^0. The calculations for the total and partial cross sections are given in Table 3-7 and shown in Fig. 3-5.

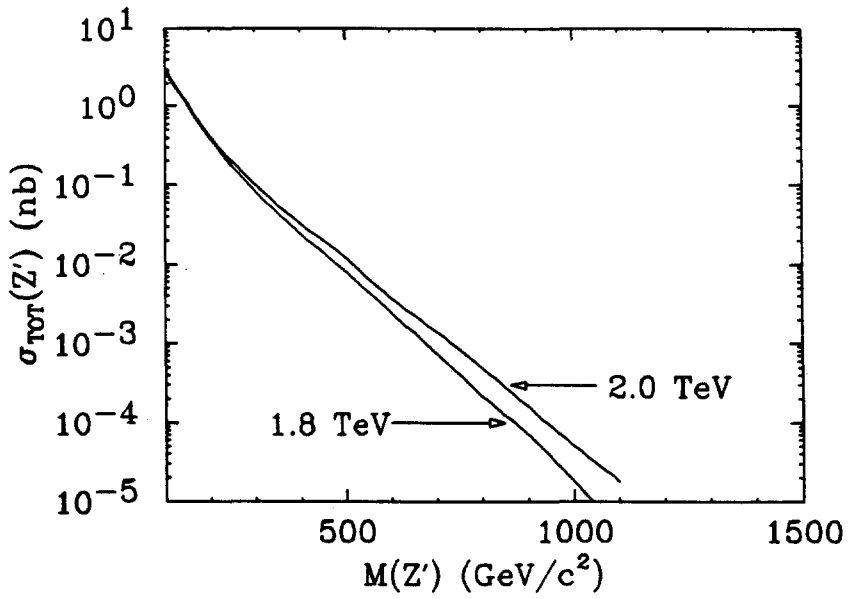

Figure 3-5: Total Cross Section for High-Mass Z' Production

Before translating the cross section into discovery limits, the mass resolution must be investigated to determine the signal-to-background ratio. The inherent signal-to-background (Z' versus Drell-Yan) is the same as that at the Z^0 according to our assumption of SM coupling constants. However, for muon pairs, the muon momentum resolution gets worse at much higher P_T. Some resolution degradation can be recouped at high P_T by using the constraint on the total E_T as measured by the calorimeters. For example, if the vector sum of the E_T in all calorimeter towers were zero (i.e., no $\not{E}_T$) then the two muon P_T 's in the event are constrained to balance within the calorimetric resolution. This constraint leads to a relative mass resolution which is better than 20%, even at a Z' mass of 500 GeV/c^2. This mass resolution is completely adequate for a Z' peak to stand out over the Drell-Yan background.

We show the calculated total cross section as a function of the Z' mass in Fig. 3-5. We estimate the discovery limits based on the production of 10 events of either Z' into an

Z' Mass (GeV/c^2)	500	750	1000
$\sigma_{Z'}$ (pb) $\bar{p}p$ $\sqrt{s} = 2.0\,TeV$	10	0.6	0.03
$\sigma_{Z'} \cdot BR(Z' \rightarrow \ell^+\ell^-)$ (pb)	0.33	0.02	0.001

Table 3-7: Z' Total and Partial Cross Sections

e-pair or Z' into a μ-pair. The discovery limit for 500 pb^{-1} at $\sqrt{s} = 2.0\,TeV$ is 750 GeV/c^2. The proposed upgrades to the muon coverage for CDF will also play a crucial role here, doubling the acceptance over that of the 1991 muon detection system. Improvements to the hermeticity, triggerability and background rejection of the electron coverage will also improve the sensitivity for the detection of Z' production and decay into e^+e^- pairs. If a Z' exists we can measure its electroweak structure by looking at the Z' asymmetry in the same way we do for the Z.

The expected rate for production of W' and subsequent decay to electron-neutrino or muon-neutrino is roughly ten times that for Z'at a given mass for the conditions in Fig. 3-5.

Search for Quark-Lepton Compositeness

The search for sequential Z' bosons requires a measurement of the Drell-Yan lepton pair continuum beyond the Z^0 pole. If quarks and leptons are composite objects with a compositeness scale Λ_{QL}, then the differential and integral $d\sigma/dM_{pair}$ distributions beyond the Z^0 pole will deviate from the D-Y predictions, with a dependence set by the contact interaction scale Λ_{QL}, as shown in Fig. 3-6 for different contact Λ_{QL}'s. Here again, the proposed upgrade, which doubles the (triggerable) muon coverage plays a crucial role. Improvements to the hermeticity, triggerability and background rejection of the electron coverage will also significantly improve the sensitivity for the detection of of high-mass e^+e^- pairs. The present CDF limits from di-electron data on a left-left pseudoscalar contact term in the interaction Lagrangian are:

$$\Lambda_{QL}(-) > 1.7\,TeV \text{ at 95 \% CL for } \eta = -1$$
$$\Lambda_{QL}(+) > 1.3\,TeV \text{ at 95 \% CL for } \eta = +1$$

These limits can be increased to more than 3.0 TeV for the upgraded CDF detector as proposed for the 1993 run, with 500 pb^{-1} integrated luminosity for both e and μ pair channels.

Detectability of Gauge Boson Pairs

The study of pair production of vector bosons probes the gauge structure of the SM since these processes are sensitive to tri-linear gauge couplings. For example, the process $\bar{p}p \rightarrow W + \gamma$ probes the magnetic moment of the W boson, for which the SM makes very definite predictions. In Wpair production, gauge theory predicts cancellation of diagrams to produce good behavior at high energies. The process $\bar{p}p \rightarrow Z^0 + \gamma$ is a good test of Z^0 boson

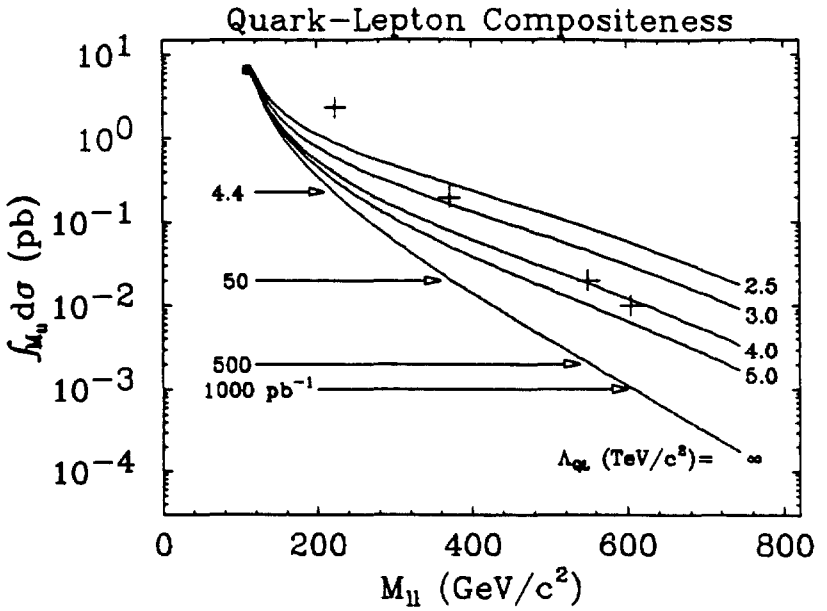

Figure 3-6: A plot of the integral of the di-leption cross section above a given di-lepton invariant mass for various assumptions about the compositeness scale parameter, Λ_{QL}. Limits on Quark-Lepton Compositeness from Drell-Yan Cross Section are indicated by the crosses. For each assumed value of the integrated luminosity, these show a contribution from the contact potential of ten events at a di-lepton mass where the pure Drell-Yan contribution is one event.

compositeness, since its cross section is enhanced by more than an order of magnitude in some composite models.

At the Tevatron, the SM predictions for the gauge boson pair production cross sections are not large. (See Table 3-8.) Based on preliminary results from the present run as well as on theoretical expectations, a search for heavy gauge-boson pairs with one of W or Z^0 decaying to hadrons will be obscured by background from single boson production in conjunction with QCD jets. In practice, such searches will likely be limited to the doubly-leptonic decay channels, with considerable reduction in rate. Furthermore, for W pair production, there are potential backgrounds from top pair production and decay if the top quark mass is within the mass range of $90 \leq M_{top} \leq 130\ GeV/c^2$. For these reasons, the predicted event yields for doubly-leptonic decays of $W\ W$, $W\ Z^0$ or $Z^0\ Z^0$ boson pairs are expected to be too low for detailed studies beyond rough cross section measurements. This will, however, provide good sensitivity to anomalous boson pair production, either a failure of the diagram cancellation in the Standard Model or the presence of di-boson resonances as predicted in some models. The outlook for $\bar{p}p \rightarrow W + \gamma$ or $\bar{p}p \rightarrow Z^0 + \gamma$ is much more favorable due to suppression of the event yield by only one factor of the W or Z^0 leptonic branching ratio. With an integrated luminosity of 500 pb^{-1} a test of the standard model

prediction of the W magnetic moment appears feasible, by studying the angular distribution of the $\gamma's$ in $\bar{p}p \rightarrow W + \gamma$. It also appears feasible with an integrated luminosity of 500 pb^{-1} to measure the cross section for $\bar{p}p \rightarrow Z^0 + \gamma$ to an accuracy of $\sim$ 6 %, and, if found in agreement with the SM prediction, to place constraints on composite models of W and Z^0 bosons. The gauge boson pair event yields are summarized in Table 3-8, summed over all e - μ final state combinations.

Gauge Boson Pair Process	Total Prod'n Cross Section (pb)	5 pb^{-1} Event Yield	50 pb^{-1} Event Yield	500 pb^{-1} Event Yield
$W\,W$	6.0	0.7	10	130
$W\,Z$	1.2	0.1	0.5	8.0
$Z\,Z$	0.7	0.0	0.1	0.2
$W\,\gamma$	10.0	5.6	75	990
$Z\,\gamma$	9.0	1.4	20	280

Table 3-8: Gauge Boson Pair Total Cross Sections. The W-W, W-Z and Z-Z entries are summed over all μ-e final state combinations. The $W\gamma$ and $Z\gamma$ yields assume that the photon passes an E_T cut of 10 GeV.

3.2 Top Quark Physics

A primary goal of CDF in the coming runs is to discover the top quark and to study its properties. The current CDF top search places a preliminary lower limit on the top quark mass (M_t) of 89 GeV at 95% confidence level.[49,50,58] Standard model calculations based on the world averages for various electroweak parameters indicate that M_t should be less than ~200 GeV.[59] This offers the Tevatron a unique window for top physics in the next decade. A t-quark search using the CDF detector will be sensitive enough to discover the standard model t-quark if it lies within this allowed mass interval with as little as 100 pb^{-1}, and with a data sample of 500 pb^{-1} will be able to do more detailed studies of its properties.

Figure 3-7 shows the $p\bar{p} \rightarrow t\bar{t}$ production cross section at $\sqrt{s}$= 1.8 TeV, as a function of M_t.[60,61] From the experience gained during the last run, the CDF collaboration

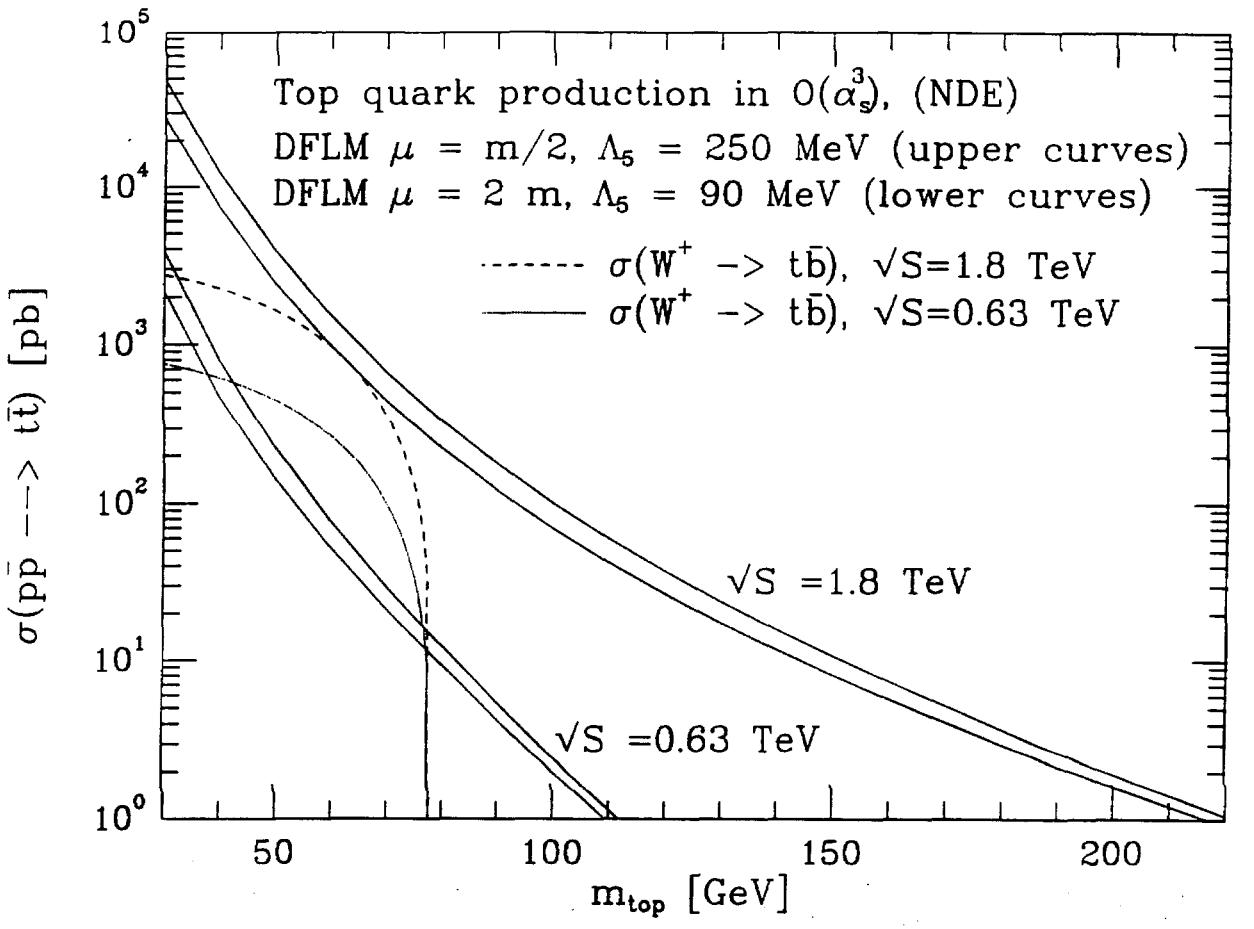

Figure 3-7: Production of $t\bar{t}$ as a function of top mass in $\bar{p}p$ collisions at 1.8 TeV.

is focusing its search on two specific decay topologies. The first is the dilepton channel, where each t-quark decays semileptonically, producing e + μ, e + e, or $\mu + \mu$, plus $\not{E}_T$ and two B's. The second channel is the electron or muon + jets mode, where only one of the t-quarks is required to decay semileptonically. Other potentially sensitive channels are being

investigated, such as multi-jet events with large $\not{E}_T$, with and without leptons such as τ's. Another tool in the search for top is B tagging in top events with an upgraded CDF. Finally, there is physics to be done with the top sample once the t-quark is discovered. These issues are discussed in the subsections which follow.

Dilepton Production

The 1988-89 CDF data taught us the importance of good lepton identification in the top search. The search for top in the e + μ channel will have as its dominant background production of two vector bosons, which has a cross section comparable to 160 GeV $t\bar{t}$ production.[49] The background from the process $p\bar{p} \rightarrow Z \rightarrow \tau^+\tau^-$ is potentially quite large but can be rejected by making cuts on the lepton acollinearity, energy and $\not{E}_T$. We therefore expect little or no background in the e + μ channel with cuts that are relatively efficient for $t\bar{t}$ up to $M_t \approx 160$ GeV.

The primary benefits of the CDF upgrade to the di-lepton search are in the increase in the solid angle coverage of the lepton identification systems. The completion of the muon systems will extend the triggerable muon coverage out to $|\eta| < 2.8$. Electron coverage in the region $1.1 < |\eta| < 3.0$ will also be enhanced by improving its hermeticity, triggerability, and background rejection. With these improvements, the increase in acceptance in the e + μ channel for 150 GeV $t\bar{t}$ events is calculated to be 45% over the CDF detector of the 1991 run. Figure 3-8 shows the expected rate of e + μ events from $t\bar{t}$ vs. M_t in the e + μ channel. Also shown is the expected rate for $t\bar{t}$ events with the additional requirement of two detected

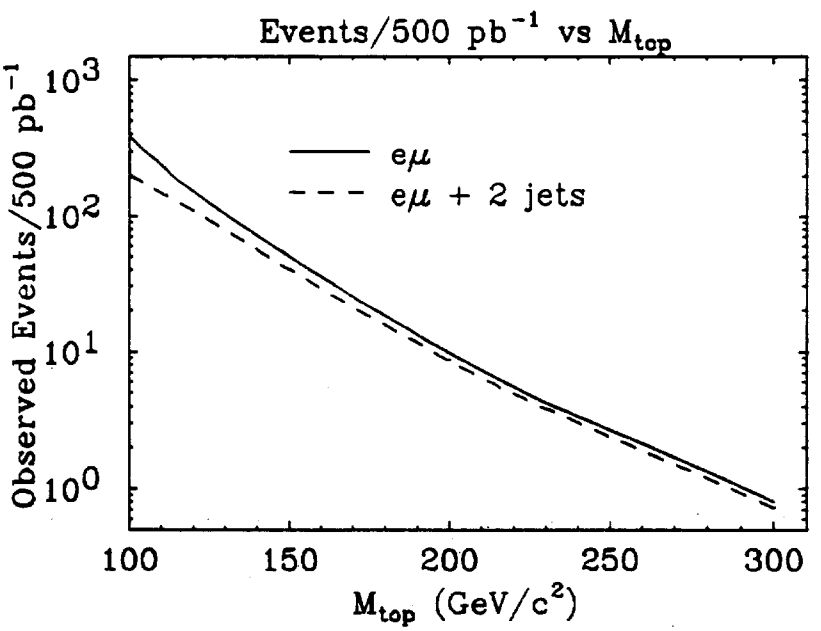

Figure 3-8: Expected number of observed $t\bar{t}$ events for $t\bar{t} \rightarrow e\mu$ as a function of top mass.

jets. This requirement rejects most of the divector boson background and keeps this channel relatively background free compared to the signal rates for top masses well above 200 GeV.

The other sources of backgrounds, such as Z's produced with additional jet activity, where the Z decays to two τ's, can be suppressed with cuts on the lepton-pair opening angle.

The dilepton channels resulting from the semileptonic decay of both heavy quarks into either electron or muon pairs have also been used in the current CDF top search and will be used in t-quark searches in the upcoming runs. The sum of these two channels has the same product branching ratio (2.5%) as the e + μ final state. The primary background in these channels comes from Z production and decay into lepton pairs. However such events are easily rejected with a cut on lepton pair masses consistent with the Z mass, and by requiring $\not{E}_T$ > 20 GeV to reject the remaining Drell Yan events We find that the addition of these two channels increases the acceptance for top by 65% over that which one gets from the e + μ channel alone. The proposed CDF upgrade will increase the $\mu - \mu$ (e-e) acceptance over that expected in the 1991 run for 150 GeV top by 100% (20%). Figure 3-9 is similar to Fig. 3-8 but for the e-e and $\mu - \mu$ rather than the e + μ channel. The dominant

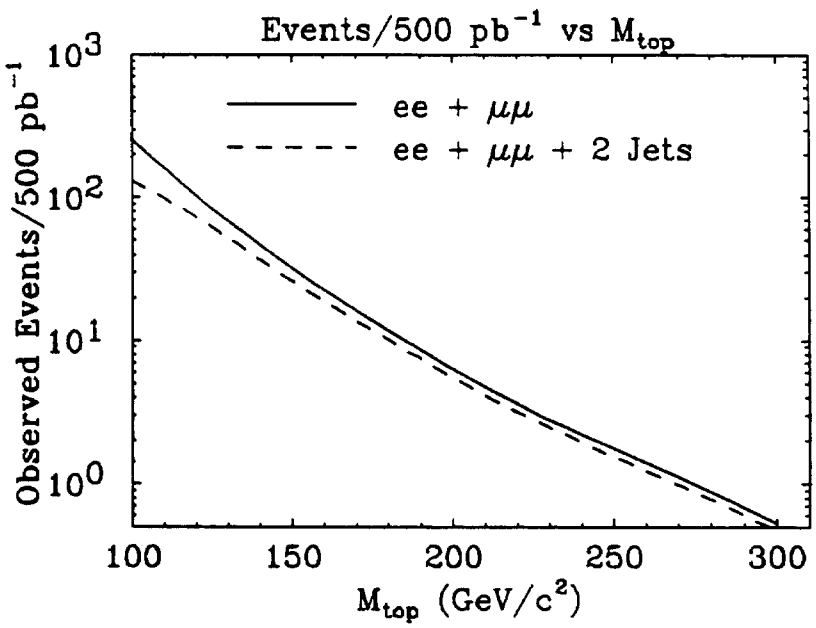

Figure 3-9: Expected number of observed events for $t\bar{t} \rightarrow e^+e^-$ and $t\bar{t} \rightarrow \mu^+\mu^-$ vs. M_{top}.

background in these channels is likely to be Drell Yan or mismeasured Z's with sizable Pt and mismeasured $\not{E}_T$. To suppress this background we can cut on $\not{E}_T$ significance (a measure of the magnitude of $\not{E}_T$ divided by the uncertainty in the observed $\not{E}_T$) and $\not{E}_T$ isolation (the absence of jets nearly co-linear with the direction of the $\not{E}_T$). The background rates in the e-e and $\mu - \mu$ modes is expected to be small compared to expected top signals for top searches up to 200 GeV.

We expect to be able to claim discovery of top with an excess of 10 events over small expected backgrounds in the e + μ sample and a comparable excess in the e-e and $\mu - \mu$ channels combined. With 500 pb^{-1}, this puts our discovery reach well in excess of M_t = 200 GeV. This ignores the search for top into lepton + jets, which will be equally sensitive to top when combined with b-tagging techniques.

The Lepton + Jets Channel

The CDF t-quark search also exploits the second $t\bar{t}$ decay topology where one quark decays semileptonically to yield an energetic electron or μ, a ν plus a b jet, and the other quark decays to three jets. This decay topology represents about 30% of the total t-quark rate, making it a factor of six more copious that the sum of the di-lepton channels. We are confident that QCD backgrounds generating fake lepton candidates and large $\not{E}_T$ will not be the primary source of background events. (Note the 1%-2% rate of such backgrounds in our inclusive W sample). However, there is a sizable background rate from W's produced with associated multijet activity (referred to as W+jets).

None the less, CDF has successfully used the e + jets mode to first rule out top below 77 GeV using a transverse mass analysis to subtract this background. We have subsequently used both the e +jets and the μ + jets samples to extend the sensitivity of the t-quark search by requiring, in addition, a leptonic b-quark tag. This analysis combined with the results of the di-lepton search have been used to increase the lower M_t limit to 89 GeV.[50] Reliable estimates of the size of the W+jets background to a heavier t-quark search are difficult to make due to the fact that the background results from higher-order QCD diagrams that in practice are difficult to calculate. However, with reasonable assumptions and using our existing W+jet data as a guide, we anticipate that this background can be handled even above $M_t = 200$ GeV.

The planned upgrade of lepton coverage will increase the acceptance for the μ + jets channel by 40% and e + jets by 10% for $M_t = 150$ GeV over that expected for the CDF detector in the 1991 run. We also expect better rejection of non-electron background in the range $1.1 < |\eta| < 3.0$ resulting from both the improvements in tracking and in the calorimeters in this region. Figure 3-10 shows the yield vs. M_t for an e + $\not{E}_T$ + 4-jet analysis, where the jet E_T thresholds have been varied to optimize signal-to-noise at each mass. For example, we expect about 550 detected events from a 150 GeV top in the combined e + 4-jets and μ + 4-jets channels for 500 pb^{-1} of data. In the currect CDF data sample, we observe no events passing this event selection, which implies, with 95% confidence, a lower limit on the expected signal-to-background ratio of about 1-to-1. There are additional kinematic variables, such as P_T of the W, which we can exploit to further reject W+jets and further enhance the signal-to-noise in this channel. However, we believe that the b tagging techniques discussed below will provide the cleanest way of separating top from the W+jets background while maintaining modest efficiency for top.

B Tagging With the Upgraded CDF Detector

We believe that regardless of the decay topology used to detect events resulting from t-quark production, the most convincing piece of evidence that we do see top decay is an enhanced rate of b-quarks in the final state above the rate expected from other sources. This implies that B meson tagging will have a crucial impact on CDF's ability to both detect t-quarks and study them. We have considered two ways of tagging b-quarks: tagging the low-energy lepton resulting from the semi-leptonic decay of the b-quark and the use of the SVX to tag

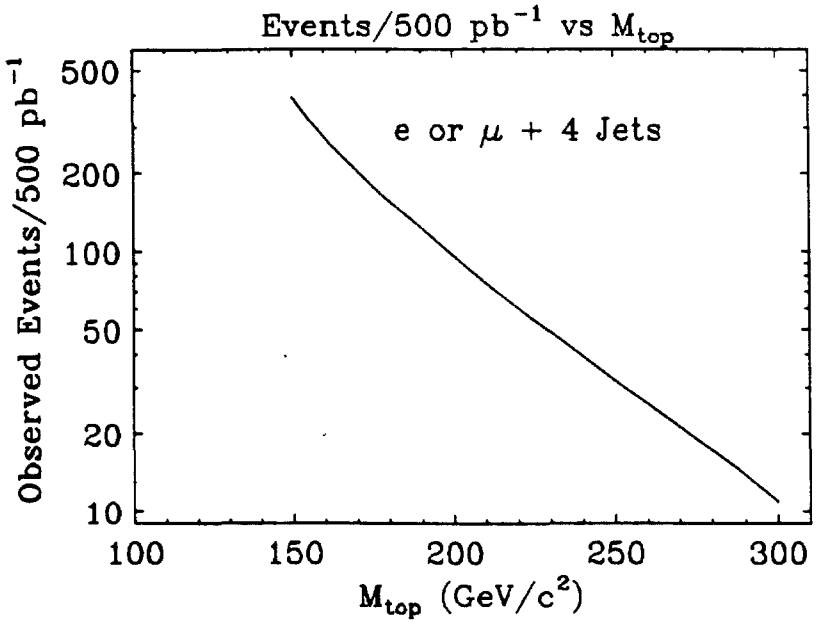

Figure 3-10: Expected number of observed events for $t\bar{t} \rightarrow$ lepton + four-or-more jets as a function of top mass.

secondary vertices resulting from the finite b-quark lifetime.

In the search for top with the current CDF data, we have tagged b-quark decays using the presence of a low energy muon. At least one such muon will be produced in 36% of $B\overline{B}$ pairs. The current CDF detector has an 12% efficiency for detecting these muons in $t\bar{t}$ events that are in our lepton + jet sample. The 1991 CDF upgrades to the central muon detector (CMU) and the addition of the central muon extension (CMX) will provide a substantial increase in the low energy muon detection because of the increase in muon system acceptance and the overall reduction in the rate of punch-through backgrounds allowing us to make looser cuts on the muon candidates. The proposed 1993 upgrade will further improve muon detection by increasing the solid angle covered by the forward muon toroid system (FMU). In addition, we are currently developing a low energy electron-finding algorithm that exploits the excellent performance of the central electromagnetic strip chambers.

In the proposed CDF upgrade, the B meson lepton-tagging efficiency will be further increased by the improvement in the electron identification in the plug region. We estimate an increase in B-tagging of 40% for muons and 20% for electrons over our projected capabilities in the 1991 run.

We believe that the silicon vertex chamber (SVX) will be the primary method by which b-quarks will be tagged in $t\bar{t}$ events. We have estimated the SVX tagging efficiency for b-quarks produced in the t-quark decays using the ISAJET Monte Carlo. The proposed B tag is based on the number of tracks in a jet that have large impact parameters relative to the primary vertex. We require that at least three tracks have impact parameter (with respect to the beam line) greater than three times the extrapolated impact parameter resolution.

Backgrounds to this tag from charm and accidentals are estimated to be about 5%.

The kinematics of t decay present a favorable situation for tagging. For example, approximately 65% of the b-quark jets in a $t\bar{t}$event with a M_t of 120 Gev are within $|\eta| < 1.0$. The mean P_T of the B jets is 30 GeV. Thus the majority of these jets will have relatively long B flight paths, will have the B meson daughters contained in the CTC tracking volume, and will have small impact parameter uncertainties from multiple Coulomb scattering. The complete CTC + SVX acceptance and efficiency for the 3 track tag is 29%. The probability of tagging at least one B jet in an event is 49%.

The B tagging efficiency vs. M_t is shown in Fig. 3-11. For $M_t >\sim 100$ GeV, the

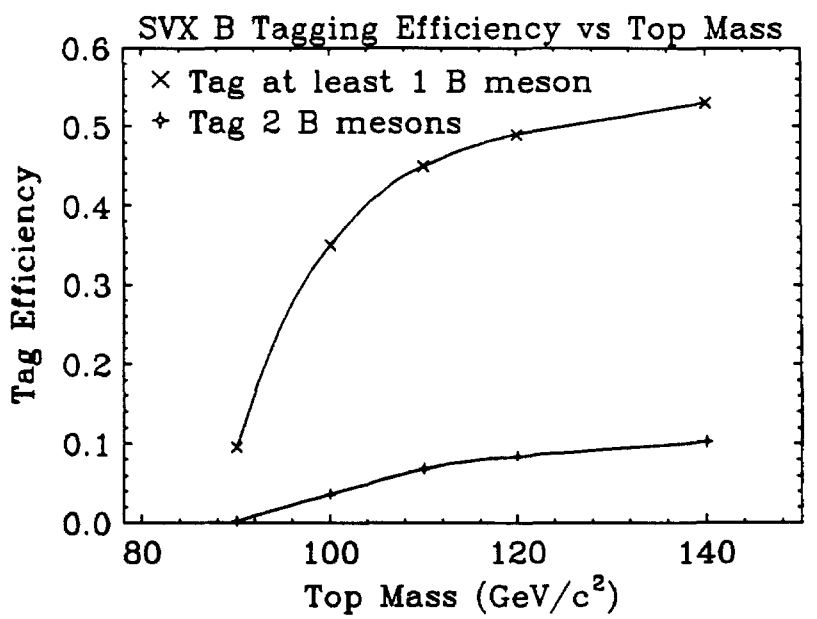

Figure 3-11: CDF Efficiency for Detecting $t\bar{t}$ through b tagging as a function of top mass.

SVX tagging rate is substantial. Note that our B tag requirement of three tracks with 3σ impact parameters is rather conservative. With more experience we hope to develop more efficient tags with equivalent background rejection. With 500 pb^{-1} of data, for example, we expect to use events containing a Z and significant jet activity as a control sample in order to develop tags that efficiently isolate the top signal from the quite similar W+jets background.

Using the leptonic and secondary vertex tags, we expect to tag a substantial fraction of the B's in both the dilepton and lepton + jets sample. A fully functioning SVX is a critical tool for this. It provides additional background rejection, with high efficiency for the top signal, which is needed to exploit the higher rate for top found in the lepton + jets channel.

Physics Opportunities with a Top Sample

The most important physical parameter of the t-quark is its mass. Assuming the Standard Model, the Electroweak parameters (most notably the W mass) vary with M_t as a result of

radiative corrections. A fairly precise measure of M_t is, therefore, one of the most important tests of the Standard Model available to us in the 1990's.

There are three ways CDF will attempt to measure M_t. The first is by the observed rate of top candidates. Since the cross section for top is falling rapidly (Fig. 3-7, and the theoretical uncertainty in this rate is not large ($\pm 30\%$), a measure of the top rate alone constrains M_t. For example, if M_t is 150 GeV, we expect to measure M_t to within 10-15 GeV using the rate of observed dilepton events.

The mass can also be extracted directly from the dilepton and lepton + jets top candidate sample. Baer et al.[62] suggest ways of determining M_t using the dilepton + 2 jet sample. They claim a measurement of M_t to within 10 GeV is possible using as few as 10 events, for M_t in the range of 150 GeV.

The lepton + jet sample seems to be the obvious place to try to reconstruct M_t, because one of the top decays does not involve a neutrino. It is complicated, however by combinatorics, initial-state radiation, and jet overlap. Here B tagging can help to reduce the combinatorics. Others have studied mass resolution in the lepton + jet events and find promising results.[63] A CDF study of our mass resolution in this channel is underway.

Beyond measuring M_t, it will be important to confirm that this quark decays according to the minimal standard model. Extensions of the standard model that include charged Higgs particles predict rather large changes in the relative rate of single and multi-lepton final states from a $t\bar{t}$ event. Observation of such unusual decay rates will therefore be suggestive of the presence of a charged Higgs.[64,65] If the top is heavier than the W, then the relative rate of $t \rightarrow bW$ is quite often comparable to the rate of $t \rightarrow h + b$. Figure 3-12 shows the branching ratio for $t \rightarrow bW$ for $M_t = 150$ GeV for a particular two-Higgs doublet model,[64] as a function of the Higgs mass and the ratio of Higgs doublet vacuum expectation values (often expressed as $\tan\beta$). Except for a narrow range of $\tan\beta$, where the standard model charged current decay is totally suppressed, it is resonable to expect to discover the top with a 500 pb^{-1} sample via its decay $t \rightarrow W + b$.

There are three measurements CDF can make with an upgraded detector which will rule out or discover a charged Higgs in a finite range of Higgs masses and $\tan\beta$. First, we can compare M_t as measured by rate with M_t measured directly from the kinematic features of the candidate events. A mass (as inferred from the rate) larger than that measured directly could be an indication that the t-quark has a significant non-charged current decay rate. If the t-quark decays to h^+b, the h^+ has two significant decay modes ($h^+ \rightarrow c\bar{s}$ and $h^+ \rightarrow \tau^+\nu$) whose relative rate is a function of $\tan\beta$. Significant decay rates into charged Higgs may therefore drastically change the rate of τ decays from top. We expect to be able to search for τ's in the inclusive lepton samples and look for top candidates where one top decays to e or μ and the other to τ. Drastic deviations from the Standard Model prediction of the number of τ's from top are predicted for certain Higgs masses and $\tan\beta$ values. The relative rate of dileptons and single lepton events is also sensitive to non-charged-current top decays. Significant departures from the Standard Model rate of 1/6 are possible if the t-quark decays via $t \rightarrow h^+b$. We also expect to be able to search for τ's in the multi-jet plus $\not{E}_T$ sample as a signature of $t \rightarrow h^+b$.

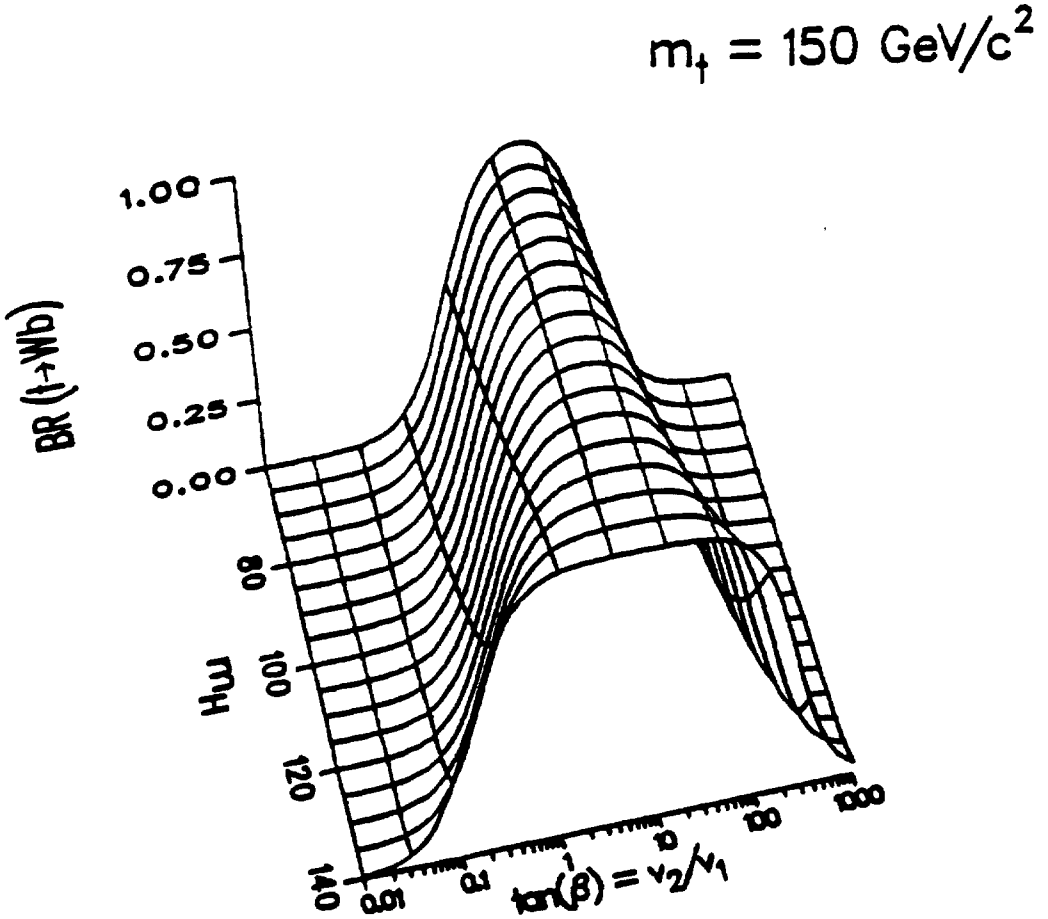

Figure 3-12: The branching ratio for $t \rightarrow W + b$ for $M_t = 150$ GeV for a particular two-Higgs doublet model,[64] as a function of the Higgs mass and the ratio of Higgs doublet vacuum expectation values ($\tan\beta$).

If M_t is roughly 150 GeV, and there exists a charged Higgs between the W mass and M_t, with 500 pb^{-1} of data CDF is likely to observe departures from the Standard Model predictions in the top sector.

In summary, the enhancement in lepton coverage produces a significant increase in the $\mu + jets$, $e + \mu$, and $\mu + \mu$ acceptances as well as in b tagging efficiency. This will provide a substantial improvement in our top quark prospects since top detection in a number of channels is required both for discovery and for the search for non Standard Model top decay.

830

3.3 QCD Physics

In the study of hadron collisions, QCD processes are, and will continue to be the baseline against which all new processes will be measured. The luminosity upgrades to the Tevatron, and specifically the main injector will extend the studies of QCD into a substantially higher energy regime where many new phenomena may be found. In addition, new calculations and improvements in the understanding of detector performance will increase the precision of the tests of QCD. To illustrate the reach in energy gained by the upgrade, the following processes will be discussed along with the discovery potential in each channel: a) jet cross section, b) direct photons, c) high P_t W's and Z's. High invariant mass Drell-Yan events were discussed in Sec. 3.1.

Jet Cross Section

The measurement of the inclusive jet cross section ($p\overline{p} \rightarrow$ Jet + X) is well defined to all orders of perturbation theory. Because of the large cross section, jet production explores the highest Q^2 available. For example, the highest dijet invariant masses seen at the Tevatron to date are about 1 TeV. Recently, the inclusive jet cross section has been calculated[66] to order α_s^3. This calculation greatly reduces the theoretical uncertainty associated with the variation in renormalization scale associated with α_s and with the evaluation of the parton distribution functions.

Figure 3-13 shows, as a function of jet E_t, the jet cross section measured by CDF, based on an integrated luminosity of 4.2 pb^{-1}. The most outstanding feature is the large range ($\approx$ 7 orders of magnitude) over which the cross section has been measured, and the highest transverse energy reached (420 GeV). The solid line, indicating the predictions of leading order QCD, appears to already provide a fairly good description of the data.

The new calculations to order α_s^3 have the additional feature that the jet cross section depends on the effective radius in the η-ϕ metric used for clustering. This is because at the theoretical level, gluon radiation can escape the jet clustering cone. This aspect of the calculation does not exist at leading order where only two partons are emitted in the final state. Figure 3-14 shows the variation in the jet cross section with cone radius at 100 GeV E_t, and compared to the predictions of Soper *et al.*[66] There is some expectation that the prediction would steepen with calculations performed at still higher orders.

The jet cross section can be used as a probe of effects which appear with large coupling strengths. The best known example is the effect of quark substructure on the shape of the jet E_t spectrum at the high end. If quarks were composed of smaller objects, a structure function for the quark would exist, which would modify the scattering at short distances. This effect can be parameterized by adding a contact term to the QCD Lagrangian with an effective distance scale defined by the parameter Λ_{comp}.[67] Figure 3-13 shows the effect of a Λ_{comp} of 950 GeV as a dashed line. This is the current best lower limit (95 % CL), derived from CDF data.

Figure 3-15 shows the ratio of the observed jet cross section to that predicted by

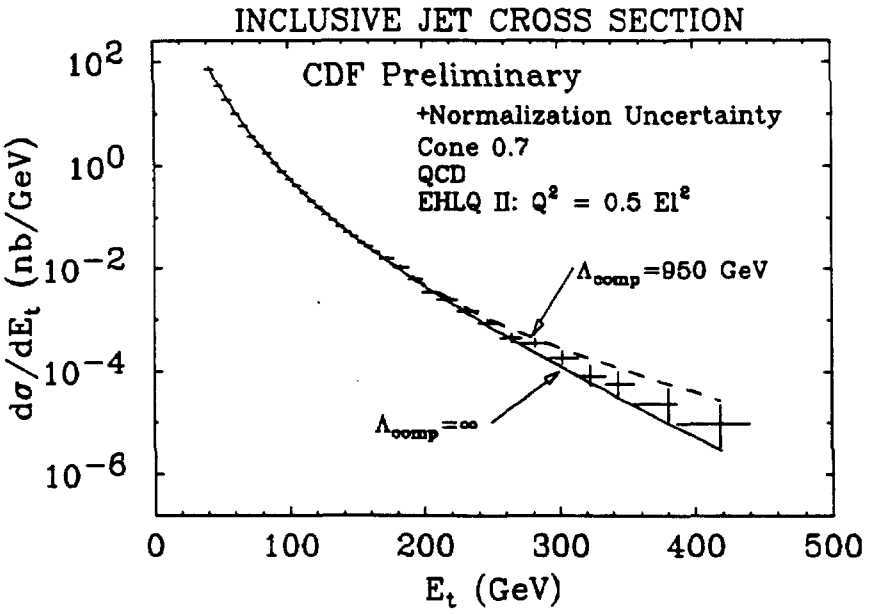

Figure 3-13: The inclusive jet cross section measured by the CDF detector. The solid line is the prediction of leading order QCD, where the curve has been normalized to the data in the region $70 \leq E_t \leq 200$ GeV. The dashed curve shows the effects on the cross section of compositeness with scale parameter of 950 GeV.

leading order QCD. In general, the agreement is quite good. At the high end there appears to be a small excess of events relative to QCD. This excess is of order 2.5-3.5 sigma (where we have used statistical errors only in evaluating the significance) and for now is a curiosity.

Figure 3-16 shows the theoretical prediction for the high energy end of the inclusive jet cross section, and the E_t reach for different amounts of integrated luminosity. The arrows indicate the potential reach in cross section for several values of integrated luminosity. From this, it can be shown that that the ultimate reach, e.g. from two runs of 500 pb^{-1} , will correspond to a Λ_{comp} of approximately 1.8 TeV. It is important to point out that in the event of no signal, this measurement plays a role in tying down the high x end of the parton distribution functions. For example, if an excess is eventually observed at the SSC, the results of a Tevatron measurement at high x should provide the basis for understanding whether the excess lies in the structure functions or in some new effective interaction.

The two-jet invariant mass spectrum is likewise sensitive to heavy objects produced with a strong coupling. In chiral color models[68], a massive octet of gluons is predicted which would lead to a broad resonance in the two-jet invariant mass spectrum above 150 GeV. This resonance, because of its strong coupling, would produce a sizable enhancement in the dijet mass spectrum above the QCD background. Figure 3-17 shows the two jet mass

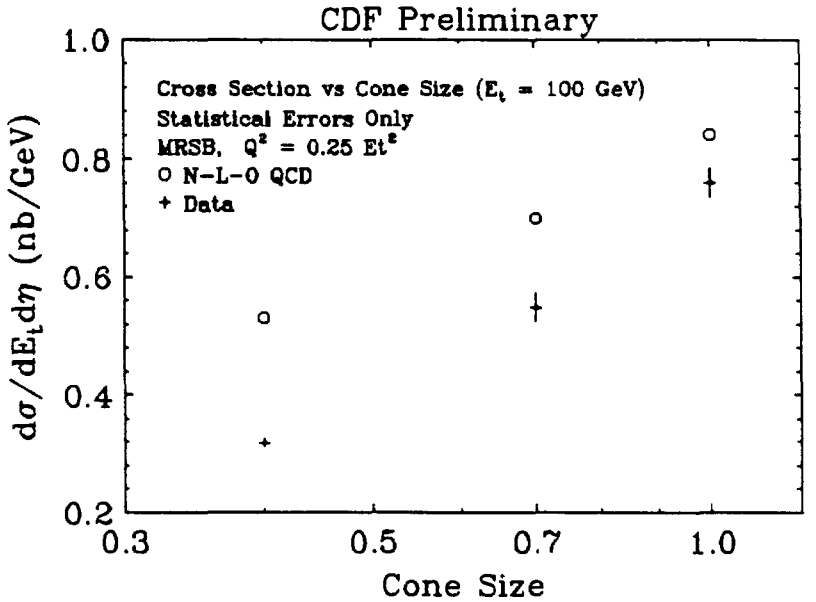

Figure 3-14: The variation in the jet cross section with the clustering cone radius at fixed transverse energy (100 GeV). The predictions are those of Soper *et al.*

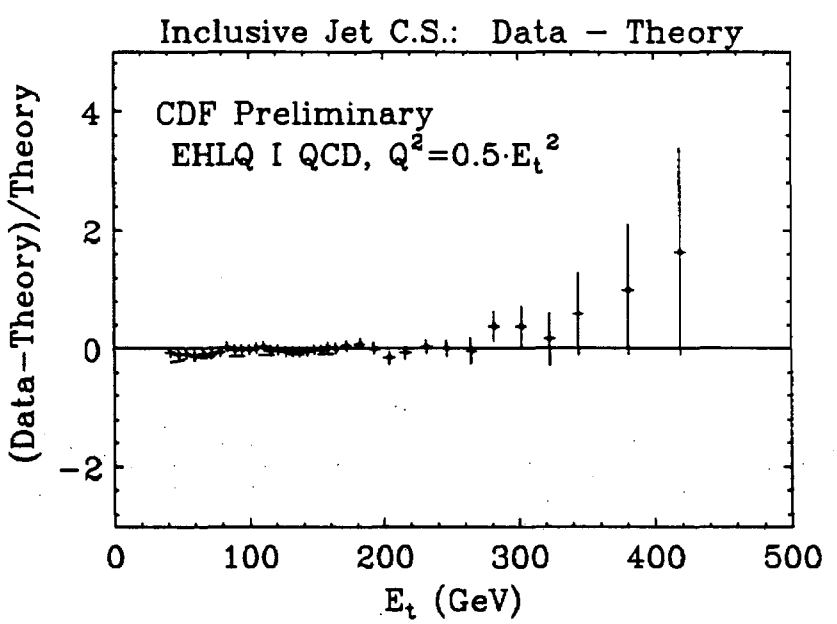

Figure 3-15: Jet cross section from CDF, plotted on a linear scale, and compared to leading order QCD.

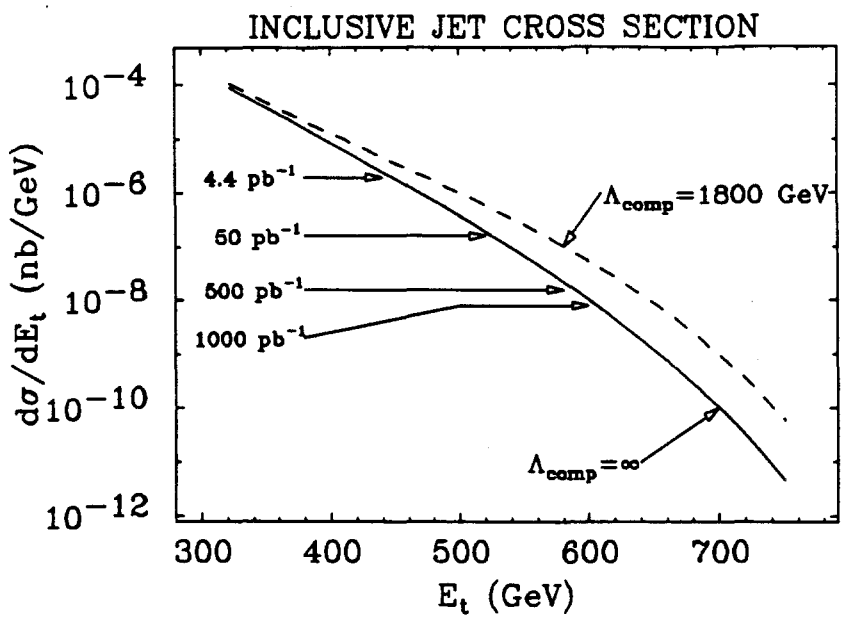

Figure 3-16: High energy end of the inclusive jet cross section. Arrows indicate the expected reach in jet E_t for different amounts of integrated luminosity.

spectrum from approximately 25 nb^{-1} of data. The leading order QCD predictions again provide a good description of the data, allowing the axigluon to be excluded in the mass range $120 \leq M_a \leq 210$ GeV for $\Gamma_A = .09 M_A$. The most current data set includes events with invariant masses in excess of 900 GeV, allowing a substantially higher sensitivity to such objects. For the eventual reach of the Tevatron luminosity, 1 fb^{-1} of data, the discovery limit for axigluons should extend well above 1 TeV. This is shown in Fig. 3-18 where the predicted signal is shown above a QCD background for different masses.

Direct Photons

As with jets, direct photons provide both a probe of QCD and a signature for interesting new physics processes. Figure 3-19 shows the highest E_t (300 GeV) direct photon candidate observed to date in the CDF detector. Direct photons in QCD probe the quark-gluon vertex, and are sensitive to the gluon structure function at low x. At high energies, they provide a good test of vector boson couplings (Wγ) and don't involve losing rate because of the branching fraction.

Figure 2-15 shows the most recent direct photon cross section from CDF. This is compared to a next-to-leading-order QCD calculation. In Fig. 3-20 the expected cross section is shown as an integral cross section above a fixed E_t. From this, it is apparent that the reach in E_t will be up to 300 GeV for this process.

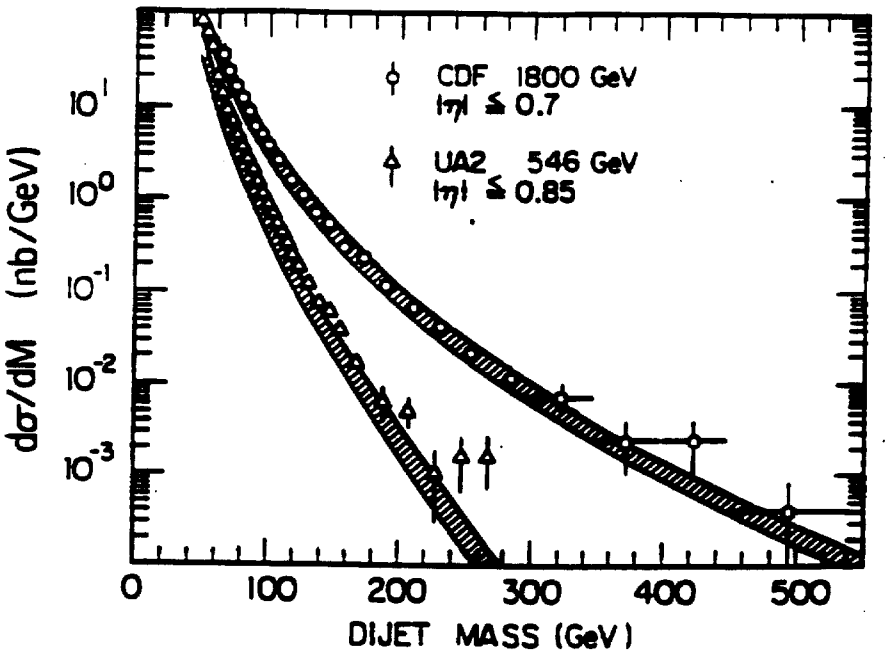

Figure 3-17: Two jet invariant mass spectrum from CDF data, along with a band representing the range of leading order QCD predictions. New CDF data exists, increasing the reach in invariant mass to above 900 GeV.

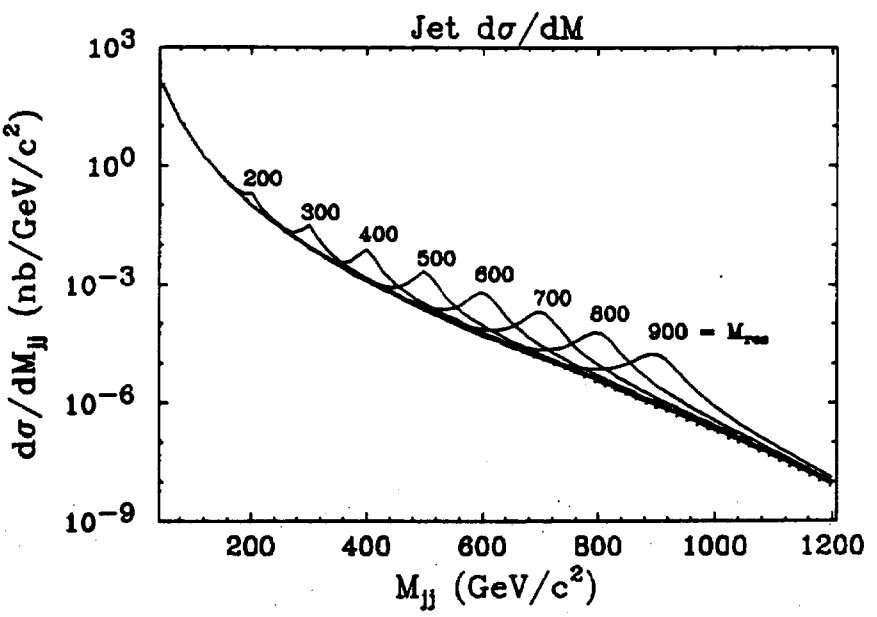

Figure 3-18: Expected cross section for the two jet invariant mass up to 1.2 TeV. Sensitivity to possible new strongly interacting particles would show up as resonances, with a sensitivity reaching 1 TeV.

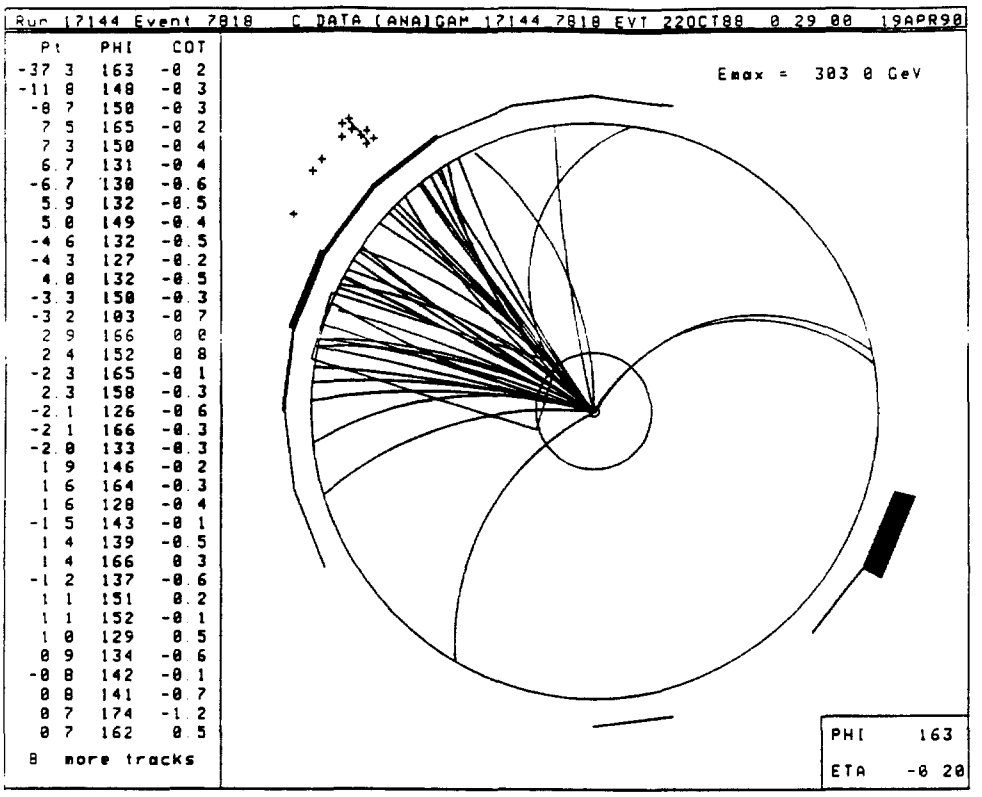

Figure 3-19: The highest E_t direct photon candidate observed in the CDF detector, having over 300 GeV transverse energy.

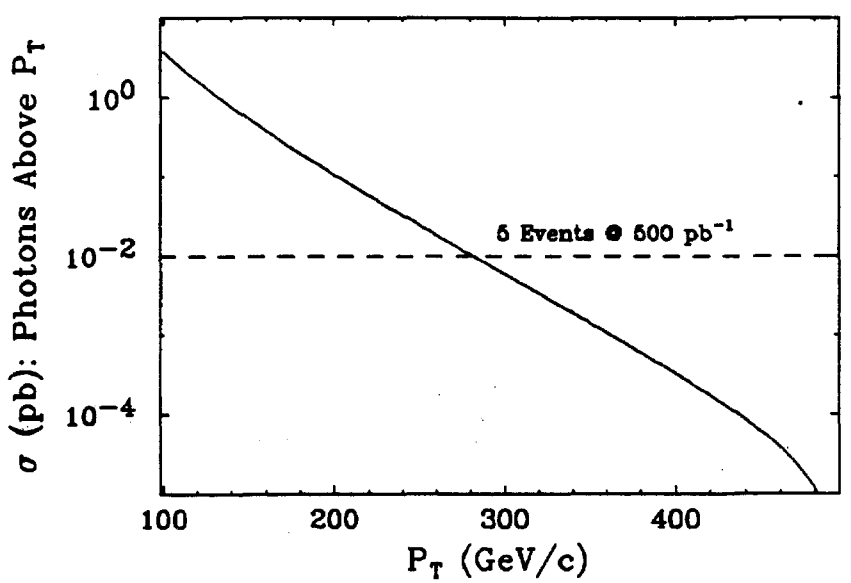

Figure 3-20: Integrated cross section for direct photons above a fixed E_t.

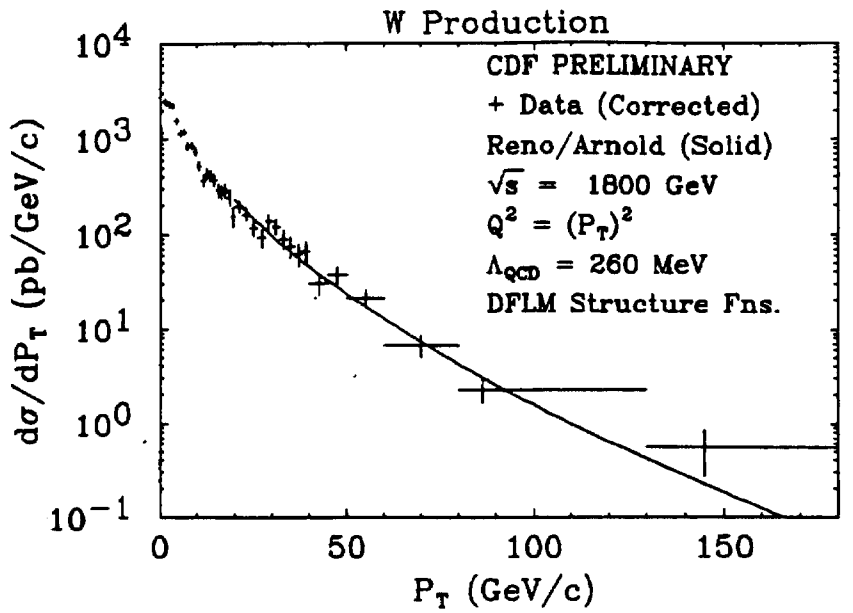

Figure 3-21: P_t distribution for W production from CDF compared to the order α_s^2 predictions of Arnold and Reno.

High E_t W and Z production

High P_t W and Z production are analogs to direct photon production, and form the background for other processes, such as heavy top. Other, non-standard processes, such as a techni-rho would appear as an enhancement in the P_t spectrum.[69] Recently, calculations have been performed at order α_s^2 for the P_t spectra of the W/Z.[70] These calculations reduce the theoretical uncertainty in the cross section. Figures 3-21 and 3-22 show these predictions for the cross section along with CDF data. Clearly there is a reasonable agreement between theory and experiment. With 1 fb^{-1}, the P_t reach for W's should allow a significant measurement out to 250 GeV.

Processes involving technicolor-type models could produce heavy particles decaying to W pairs. The exact nature of such couplings are not certain, but do provide some impetus to examine the potential discovery limits. From different scenarios, and depending on the coupling, it may be possible to detect techni-rho's with masses up to 250 GeV.

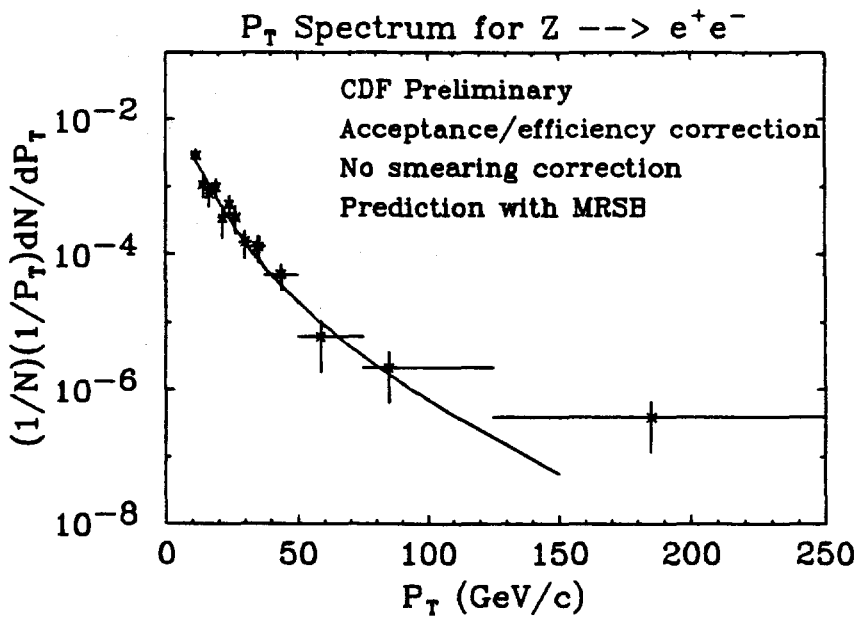

Figure 3-22: P_t distribution for Z production from CDF (points) compared to the order α_s^2 predictions (solid curve) of MRSB.[71]

3.4 B Physics

In this section we consider some of the possibilities for b quark related physics with CDF at very high luminosity (500 pb^{-1}). CDF has already shown important capabilities in this area with strong B signals from tracking data in the 1988-89 run as discussed below. These capabilities will be enhanced in 1991 with the use of the silicon vertex detector. The addition of a silicon vertex detector and the improved version in 1993 will allow us to resolve secondary verticies associated with b decays. For those decays in the fiducial region of the SVX, this will allow us to greatly reduce the backgrounds from non b events and combinatorics with tracks from the b-jet fragmentation. Vertex measurements will also allow us to measure the lifetimes of various B hadrons. It is essential that the SVX be upgraded to cope with the luminosity and shorter beam crossing interval expected in future runs. The Forward Muon upgrade will further increase the solid angle that can be used for b physics. This will be especially useful for conducting the b tagging studies that will need to be carried out before a measurement of CP violation could be performed in a Tevatron experiment. The detailed studies of b decays require a high statistics experiment. Thus the upgrade of the DAQ system is also an important part of this program.

At CDF, B particles are produced both as specific products of the decays of massive states, such as in the process $t \rightarrow Wb$ and as a component of the QCD continuum. Tagging B's as a way of tagging top is discussed elsewhere. At high luminosity, the large QCD production cross section will result in a very large sample of B's for exclusive studies, lifetime, and mixing measurements. This topic represents a promising area of research for CDF relating to b quark production and decay. We see B physics at CDF as an evolutionary program. It will rely upon the successful completion of a corresponding program at lower luminosity to be carried out during the 1991 run and the necessary enhancements to CDF's vertex and trigger systems for high luminosity use. In particular, investigating exclusive B decays will require enhancements to the trigger system which allow for the efficient processing and collection of a properly enriched data sample. Furthermore, the early experience gained in the use of secondary vertex identification during the 1991 run will be important for developing instrumentation techniques for use at higher luminosity. Below we will consider these topics in more detail.

Within the past few months, CDF has identified the largest sample yet of fully reconstructed B mesons in the decay channel $B \rightarrow \psi K$. See Fig. 2-21. We have also observed an inclusive electron P_T spectrum consistent with that expected from B decay. We see D*'s quite clearly (Fig. 2-5), and studies of other exclusive decays, such as $B \rightarrow \psi K_s^0$, are in progress. Another analysis in progress studies the production rate for B mesons at high P_T using the semileptonic decay modes: $B^{0,-} \rightarrow e^- \nu D^0 X$. The electron and the $D^0 \rightarrow K^- \pi^+$ decay are detected in b-jets. Figure 3-23 shows the $K^- \pi^+$ invariant mass spectrum for oppositely charged track combinations near high- P_T electron candidates. Figure 3-24 shows the invariant mass distribution for eD^0 obtained by subtracting the sidebands about the D^0 signal in Fig. 3-23 from the data centered on the peak. The subtracted distribution is confined to the region below the B-meson mass, as expected for the semi-leptonic final state.

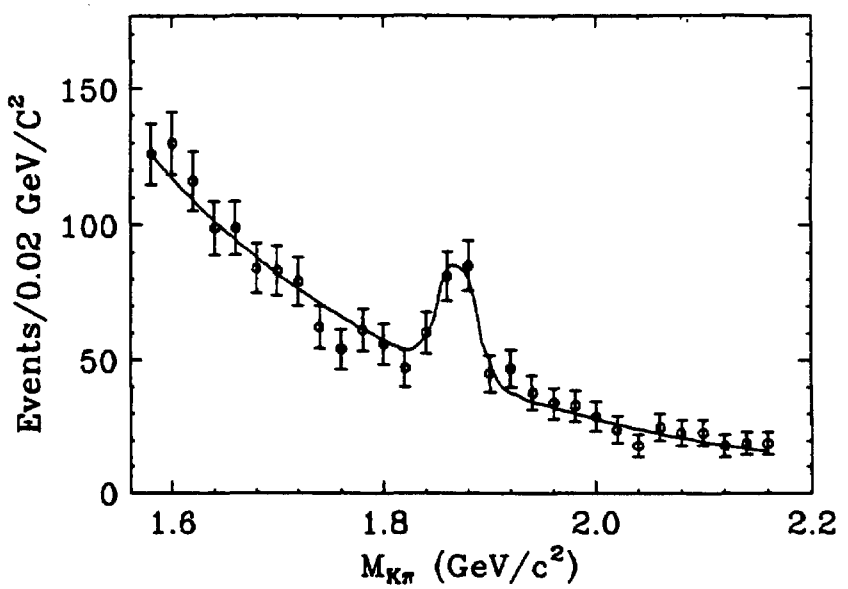

Figure 3-23: Invariant Mass Spectrum $K^-\pi^+$ ($K^+\pi^-$) combinations for hadron tracks near a high- P_T e^- (e^+).

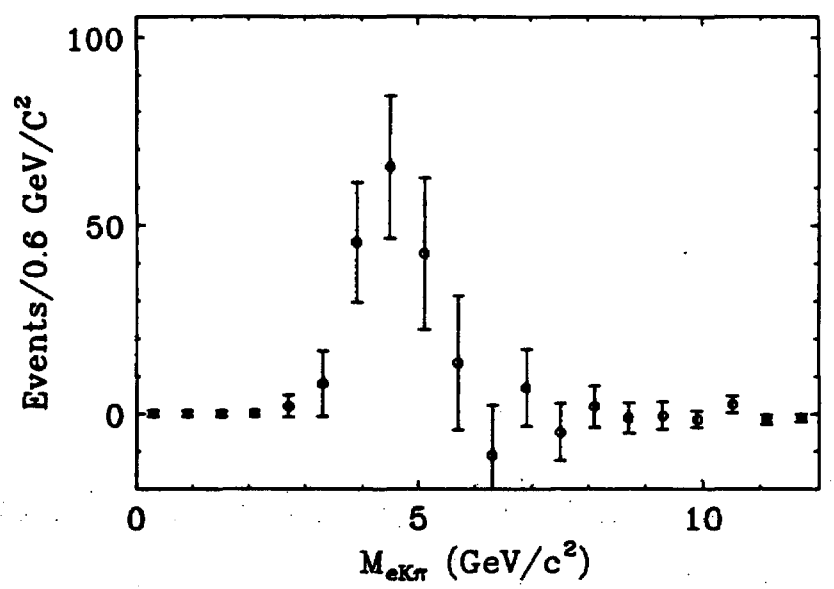

Figure 3-24: Invariant mass spectrum for $e^-K^-\pi^+$ ($e^+K^+\pi^-$) for combinations in the D^0 peak ($\pm 30 MeV/c^2$) shown in Fig. 3-23. Sidebands ($\pm 90 MeV/c^2$) in the $K\pi$ spectrum have been subtracted to reveal the e^-D^0 ($e^+\overline{D^0}$) contribution. The spectrum peaks below the B-meson mass due to the missing ν and additional pions in the B semileptonic decays.

Estimate of Data Sample Size

The ultimate scale of the event sample available for exclusive studies is set by the total cross section above some reasonable trigger threshold for the lepton. A conservative estimate can be based upon the inclusive lepton sample collected in the 1988-89 run of CDF. Improvements to the trigger such as an enhanced muon system coverage and online vertex or B topology triggers will allow us to lower these thresholds significantly, giving a much larger acceptance than in the past.

For a high statistics run, we envision a single lepton trigger as a means of tagging $b\bar{b}$ events. The second B in such events can be studied in an unbiased manner. In an inclusive single lepton sample, a typical analysis approach would be to look for the second B in an event tagged by a lepton with p_t below about 20 GeV/c. As a benchmark we use the inclusive lepton sample with the following cumulative assumptions:

1. $\sigma_{b\bar{b}}(p_{tB} > 10\ GeV/c) = 1.5\,\mu b$ for $|\eta| < 1.5$
2. Branching ratio into one or more electron = 0.24
3. Branching ratio into one or more muon = 0.24
4. Probability for one lepton $p_t > 7\ GeV/c = 0.2$
5. Reconstruction and triggering efficiency for electrons = 0.3
6. Reconstruction and triggering efficiency for muons = 0.7

The electron and muon effective efficiencies are then 0.014 and 0.033 respectively. Assuming an integrated luminosity of 500 pb^{-1} the samples include 1.1×10^7 and 2.5×10^7 electron and muon decay candidates respectively. This sample exceeds a reasonable event writing rate and must be reduced by specific triggering and filtering strategies, such as requiring a vertex tag or additional stiff tracks. Typical efficiencies for these could be in the range 0.05 to 0.3. CDF could, thus, be sensitive at the few event level to branching ratios as small as 10^{-6}. Enhancing the acceptance or further reducing single lepton p_t trigger thresholds will improve this significantly.

For the di-muon trigger, we plan to lower the muon pt threshold from 3 GeV to 2 GeV for the 1991 run. This should increase the triggerable $b \to \mu^+\mu^- X$ cross section by about a factor of 4. The central muon extension should also increase the cross section by a factor of 2. There are other possible enhancements to this trigger which could result in another factor of 4 increase, but for this section we will assume a total increase in triggered cross section of 10 over the current data set. Thus with 500 pb^{-1} we expect $\approx 10^6$ $b \to \psi X \to \mu^+\mu^- X$ events, with approximately 10% of that being taken in the '91 run. Given the number of observed $B \to \psi K$ and ψK^* events, we would expect to have $> 10^3$ events in each of these modes in '91 and $> 10^4$ with 500 pb^{-1}. Assuming that $Br(B_s \to \psi\phi) = Br(B_d \to \psi K^*)$ and that the cross section for B_s is $\approx 1/3 \leftrightarrow 1/2$ that for B_d, we expect to have a few hundred fully reconstructed B_s events in '91 and a few thousand with 500 pb^{-1}.

New b Hadrons

There are many species of b hadrons that could be found at CDF in the next few runs. Given the assumptions listed above, we expect that we have a handful of $B_s \to \psi\phi$ events in our current data sample. In '91 this sample should be a few hundred fully reconstructed events easily demonstrating the existence of the B_s and measuring its mass. The few thousand events expected with 500 pb^{-1} will enable us to perform precision measurements of its decay properties.

Bottom baryons should also be observed. The numbers will depend on what the branching ratio for the various baryons is into ψ's. If we make the following assumptions:

- that bottom baryons account for 10% of our $b \to \psi$ events,
- that 20% of the bottom baryons are Λ_b's,
- and that the exclusive decay $\Lambda_b \to \psi\Lambda$ accounts for 10% of the inclusive $\Lambda_b \to \psi X$ decays,

then we expect to see ≈ 30 events in '91 and a few hundred with 500 pb^{-1} .

The B_c is an interesting system from a QCD standpoint. It is composed of two heavy quarks so the non-relativistic quark model should work as it does for charmonium and the upsilon. The lifetime and decay modes of the B_c depend critically on the depth of the potential, since this will affect the relative fraction of b vs c decays. $B_c \to \psi X$ is a normal spectator decay, and should account for a large fraction of the B_c decays where the b quark decays. However, the cross section for B_c production at the tevatron is very uncertain. It has been estimated that B_c production accounts for 4% of all $b \to \psi$ events with $p_t > 5$ GeV at Tevatron energies.[72] This would predict that we would have $4 \times 10^4 \psi$'s from B_c in a 500 pb^{-1} run. If this estimate is correct, then we should have a very good chance of observing this state in the decay modes $B_c \to \psi\pi$, $\psi 3\pi$, ψD_s, and $\psi l\nu X$.

Lifetimes

Almost all physics done currently at e^+e^- machines is complicated by the fact that all measured quantities also involve some convolution of the semileptonic branching ratios of the B_d and B_u mesons (b_u and b_d) as well as the production fraction on the $\Upsilon(4S)$ (f_u and f_d). The observation of non-$B\overline{B}$ decays of the $\Upsilon(4S)$ also means that $f_u + f_d < 1.0$. Since $b_u/b_d = \tau_u/\tau_d$, the measurement of the lifetimes of individual B mesons will allow this source of uncertainty to be eliminated. Combinations of several measurements may then allow CLEO and ARGUS to measure f_u and f_d also.

The lifetime ratio is also interesting in its own right. The naive spectator model predicts that $\tau_u = \tau_d$. For charm mesons they are known to differ by a factor of 2. Explanations for this difference range from interference between specific two-body charm decays to a possibly large contribution from non-spectator decays. Comparison of the lifetimes $\tau_u : \tau_d : \tau_s$ for B mesons will allow these explanations to be further tested.

At present, the measurements of b lifetimes are all an average over the various species of b hadrons produced at the respective accelerators. With at least 10^3 fully reconstructed B_u and B_d mesons in the '91 run, we will make a precision measurement of τ_u and τ_d, to be further improved with 500 pb^{-1}. A first measurement of τ_s will be made in '91 with a precise measurement with 500 pb^{-1}. The lifetime of the bottom baryon Λ_b should also be measurable with 500 pb^{-1}, and maybe the lifetime of the B_c.

$b \to \psi X$

With 10^6 $b \to \psi X$ events, we should be able to do a fairly detailed study of this decay. Using the SVX we will be able to determine the number of charged particles associated with the ψ at the b decay vertex. We should be able to fully reconstruct $B_{u,d,s} \to \psi X$, where X is composed entirely of charged particles for all modes with branching fractions greater than 10^{-3}. We will also look for resonant structure in these decays. In particular we should be able to determine the various K^* components and fully map out the Dalitz plot in the $\psi K \pi$ channel. Also by measuring the decay angular distributions we will be able to determine the importance of the various partial waves in decays such as $B \to \psi K^*$. Currently, many B measurements cannot be turned into KM measurements because of model dependence in the answer (for example the $b \to u$ result has a factor of 2-3 uncertainty in V_{bu} due to differences between Isgur-Wise and Bauer-Stech). The addition of detailed information in the $b \to \psi$ channel will allow the models to be tested and tuned, and thus reduce such uncertainties.

By measuring the ratio $Br(B_s \to \psi + \phi)/Br(B_d \to \psi + K^*)$ we will be able to measure the important ratio $\sigma_{B_s}/\sigma_{B_d}$ using

$$\frac{\sigma_{B_s}}{\sigma_{B_d}} = \frac{N_s/eff_s}{N_d/eff_d}\frac{\tau_d}{\tau_s}\frac{\Gamma_d}{\Gamma_s},$$

where we rely on a theoretical calculation of the partial widths. The ratio of B_s to B_d cross sections is important to help interpret mixing results which, without this, are an unknown mixture of B_s and B_d mixing.

Semileptonic B Decays

We currently have about 70 D^0's associated with leptons. Although CLEO will have large samples of semileptonic B_d and B_u, there will be opportunity to do much in the semileptonic B_s sector. The possibility of using the SVX to get a 0C fit to extract specific final states of semileptonic B_s is being explored. We hope this improves our capability to study mixing beyond that expected for 1991, especially given a measure of the ratio of B_s to B_d cross sections.

Rare Decays

There are a few rare decays that CDF should be sensitive to with 500 pb^{-1}. The theoretical estimate for the decay $B \to \mu^+\mu^-$ is $Br(B^0 \to \mu^+\mu^-) \approx 10^8$. CDF already has a preliminary

limit on this decay of $< 3 \times 10^{-6}$. Although we are currently background limited, very little effort has gone into suppressing the background in this mode yet. Using the SVX and added muon steel installed for the 1991 run, it will be possible to greatly reduce the background. Then, with the increased data set, we should be able to push our sensitivity for this mode into the $10^{-7} \leftrightarrow 10^{-8}$ range. If we observe this decay and the related mode $B_s \rightarrow \mu^+\mu^-$, we can compare them to obtain a value for $|V_{td}|/|V_{ts}|$. This method of determining these important KM matrix elements is complementary to the measurement described below, which uses the time evolution of B_s mixing to measure the same quantity.

We will also look for the decay $b \rightarrow s\mu^+\mu^-$. This decay which proceeds via an electromagnetic penguin is important because the rate is a strong function of the top quark mass. The theoretical prediction for this channel is $BR(b \rightarrow s\mu^+\mu^-)/Br(b \rightarrow s\psi \rightarrow s\mu^+\mu^-) \approx 10^{-2}$. This implies that with 500 pb^{-1}, we will have written to tape around 10 times as many of these rare decays as we currently have $b \rightarrow \psi$ events, or roughly 10,000. A possibly large background to this decay is $b \rightarrow c\mu^-\overline{\nu} \rightarrow s\mu^+\mu^-\nu\overline{\nu}$, where we are not able to separate the b and c decay verticies in the SVX. However, in the exclusive decays $B \rightarrow K\mu^+\mu^-$, $K^*\mu^+\mu^-$, the backgrounds will not produce a peak at B mass.

We also plan to search for non-Standard Model decays, $B \rightarrow \mu e$ and $K\mu e$. Although the sensitivity we can obtain depends on the specifics of the triggers we decide to use for muon-electron events, we can expect that they will be roughly comparable to the limits from the di-muon trigger. Here again the SVX will be essential for reducing the background.

Mixing

In addition to a search for an excess of like-charged leptons in inclusive dilepton events, we plan to measure the time-evolution of mixing. The determination of the parameters which describe mixing in the B^0 system are of fundamental importance in constraining the elements of the Cabibbo-Kobayashi-Maskawa (CKM) matrix. The phenomenology of mixing in the B^0 system has been discussed by many authors[73]. The parameter which determines the oscillation probability is the ratio, $x = \frac{\Delta M}{\Gamma}$ where ΔM is the mass difference between the mass eigenstates and Γ is the average decay rate. The probability that a B^0 with mean lifetime, τ, created at $t = 0$, decays at t as a $\overline{B^0}$ is given by,

$$P(B^0 \rightarrow \overline{B^0}; t) = 0.5exp(-\Gamma t)(1 - cos(\frac{xt}{\tau})).$$

Evidence for mixing has been reported in the B_d system by ARGUS[74] and CLEO[75] with $x_d = 0.7$. Significantly higher frequency oscillations are expected in the B_s system due to the estimated ratio of matrix elements $|V_{ts}|/|V_{td}|$. For the B_s system x_s is expected to be greater than ~ 3. A measurement of x_s when combined with x_d from e^+e^- measurements will constrain the element $|V_{td}|$. A time integrated measurement of mixing will give no useful information on x_s or the CKM element $|V_{td}|$. For the B_s, where mixing is large, x_s can only be determined by measuring the time dependance of the oscillation. This is a very demanding measurement but would be an important result from a program of B physics at the Tevatron collider.

By using the vertex detector it may be possible to observe the time evolution of the $B^0 - \overline{B^0}$ system and thereby determine x_s experimentally. This measurement has been considered as the goal of a new experiment at the CERN collider[76] relying on the full reconstruction of 10^4 exclusive flavor tagged hadronic states. This approach is demanding and suffers because the fully reconstructed modes will be inefficient. As an alternative, an early study has been made to determine whether this measurement could be done with CDF by studying the decay vertex distributions of dilepton events. This "semi-inclusive" measurement relies on a considerably less sophisticated event reconstruction and trigger requirement than the CERN experiment.

In the dilepton decay vertex measurement, events of the type $p\overline{p} \rightarrow l^{\pm}l^{\pm}X$, where $ll = ee, e\mu, \mu\mu$, are used. The events are divided into two samples on an event by event basis depending upon whether the leptons are opposite sign or same sign. These leptons will be a combination of charged and neutral B decay products, mixed and non–mixed, as well as background. For each event, the ratio, $L_n = \frac{L_{decay}}{p_B}$, of the B decay length divided by the B momentum is entered for each B into the like- or unlike-sign distribution. The distributions are added and subtracted, bin by bin, to form a second set, SUM and $DIFF$. The former is just the decay distribution of all B's in the measurement, an average over the lifetimes of B_s, B_d, and charged B mesons. The latter contains a non–exponential component determined by B_s oscillations above a background due to the non–mixed parts. To factor this background out, the ratio $DIFF/SUM$ is formed.

These distributions are shown in Fig. 3-25 for $x_s = 5$. For these figures, $b\bar{b}$ events were generated with ISAJET, demanding a lepton $p_t > 10\ GeV/c$. They are not smeared by finite resolution on the decay distance or the B meson momentum. In practice, the B meson momentum determination is the major limitation on such a measurement. In Fig. 3-26 the same set of plots for L_n are shown where instead the B meson momentum is estimated as equal to the lepton momentum. This is a reasonable approach since most lepton triggers in CDF are biased towards B mesons which decay into relatively stiff leptons. Improvements will result if additional particles can be assigned to the B decay vertex, though at the expense of efficiency.

An estimate can be made of the integrated luminosity needed to attempt such a measurement. This estimate will be based again upon acceptances and efficiencies which apply to the previous runs of CDF (as listed above in the discussion of exclusive studies). and so are conservative. For this analysis a sample of dileptons with both vertices measured is required. In addition to the factors listed earlier we take also, the probability of both leptons having $p_t > 5\ GeV/c$ to be 0.1 and the lepton vertex reconstruction efficiency to be 0.3. Then the efficiencies for each channel will be, $\epsilon_{ee} = 1.2 \times 10^{-5}$, $\epsilon_{e\mu} = 2.7 \times 10^{-5}$, and $\epsilon_{\mu\mu} = 6.4 \times 10^{-5}$. The total efficiency is 1.0×10^{-4}, resulting in 150 events/pb^{-1} with both vertices measured. To resolve x_s to ± 2 units up to a value of ~ 10 we estimate that $\sim 10^4$ vertex measured pairs are needed. This implies that the integrated luminosity required approaches 70 pb^{-1}. With a data set based upon 500 pb^{-1} the mixing measurement can be done in significantly greater detail. It may be possible to reconstruct more of the tracks in the decay and thereby reduce the major smearing effect coming from the use of the lepton momentum as an estimate of the B momentum. Systematic effects and biases which will be

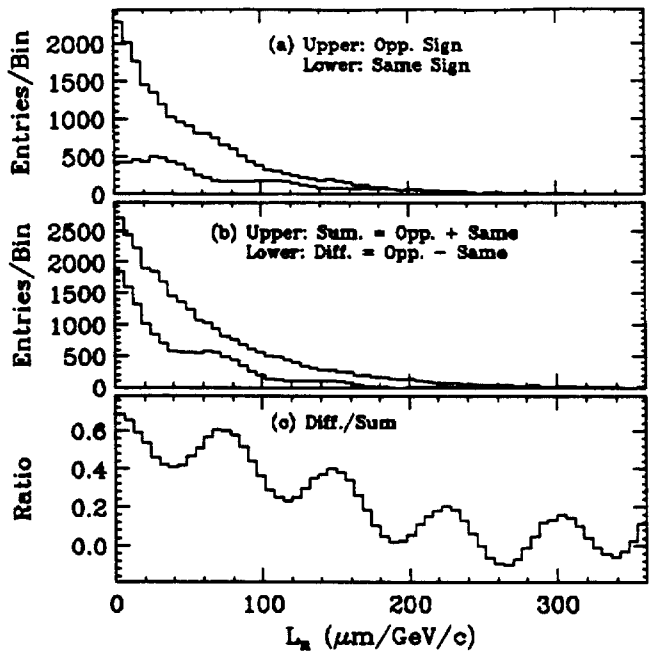

Figure 3-25: B^0 mixing with $x_s = 5$, distributions of L_n for (a) opposite (upper curve) and same (lower curve) sign events; (b) sum (upper curve) and difference (lower curve) of curves in (a); and (c) ratio of difference/sum.

important to understand in such a measurement can also be studied with more precision. A luminosity of 500 pb^{-1} represents a comfortable statistical margin for the measurement of mixing in the B system at CDF.

CP Violation / Feasibility Studies

In the 1991 run CDF expects to reconstruct ψK_s^0 with a cross section of $10pb$. With the possibility of very large datasets, a few fb^{-1}, provided by the TEVATRON before the year 2000, it seems within reach to collect in excess of 10,000 fully reconstructed ψK_s^0 decays. This would require us to maintain the dimuon trigger thresholds close to the 1991 levels. If one could obtain a b quark tagging efficiency of 10%, and if systematic errors do not dominate, one could observe a 3σ effect from a 15% asymmetry caused by CP violation.[77]

By 1993 CDF should have in excess of 10,000 fully reconstructed B's in various ψ channels. We propose to study tagging techniques, such as lepton and vertex tags. Systematic effects that could give a false asymmetry will also be studied. Observing CP violation in the B sector is clearly an important physics challenge for the late 1990's.

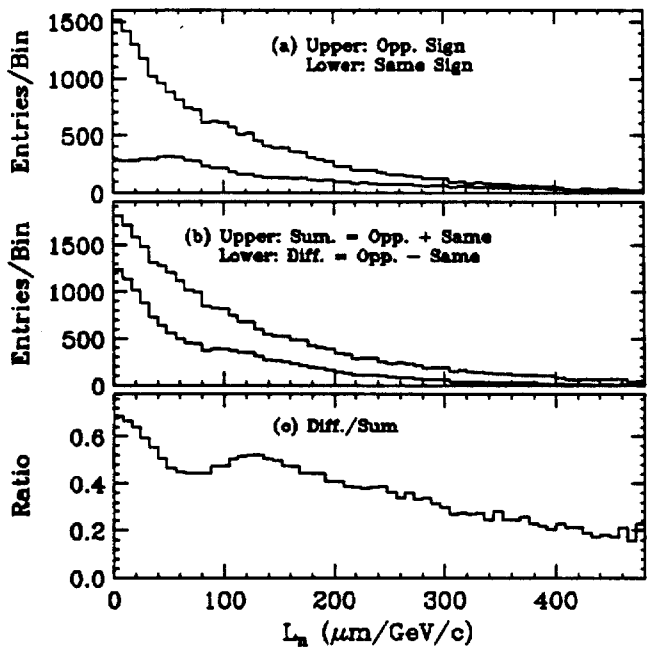

Figure 3-26: B^0 mixing with $x_s = 5$, distributions of L_n including effects of momentum smearing (~30%) resulting from the use of p_{lepton} as an estimate of p_B, for (a) opposite (upper curve) and same (lower curve) sign events; (b) sum (upper curve) and difference (lower curve) of curves in (a); and (c) ratio of difference/sum.

3.5 Exotic Physics

SUSY

$\not{E}_T$ is an important signature for SUSY physics. Searching for an excess of high $\not{E}_T$ events allows us to set limits on SUSY production. With 4.4 pb^{-1} data, we are sensitive to masses of about 150 GeV/c^2. Our sensitivity is limited not by production cross sections, but by how well we can estimate the standard model $\not{E}_T$ backgrounds. We use our CDF data set for this. For $\not{E}_T$ > 40 GeV, we have 98 events in our 4.4 pb^{-1} data set, which is consistent with the expected background of 92 $\pm$ 18 events. The uncertainty on the background is about 25%, and is dominated by the finite statistics of our W and Z data sets, which are used in the background estimation. With 100 pb^{-1} of data, we estimate that the background uncertainties will be less than 10%. This will allow us to probe supersymmetry to masses of larger than 220 GeV/c^2.

Leptoquarks

Leptoquarks are scalar, color triplet objects with lepton number. They are predicted in several theories like Technicolor or supersymmetry extensions. We are sensitive to two production mechanisms for Leptoquarks: Pair production, and Drell-Yan production of lepton+leptoquark. Leptoquarks are expected (if they exist) to conserve generation number. Then, pair production via gluon fusion will populate equally all three types of leptoquarks, while Drell-Yan production will generate almost exclusively first generation leptoquarks. Typical production cross sections for gluon fusion to form a leptoquark pair are: 1 nb (M = 40 GeV/c^2), 0.01 nb (M = 100 GeV/c^2), 1 pb (M = 160 GeV/c^2). For Drell-Yan production, cross sections are up to eight times larger, depending on the model.

Leptoquarks decaying into quark+neutrino generate $\not{E}_T$ signatures. An ongoing analysis of 4.4 pb^{-1} data indicates we will be sensitive to pair-produced leptoquarks with masses up to about 70 GeV/c^2. With 100 pb^{-1} , we will probe up to about 160 GeV/c^2.

For decays into quark+lepton, analysis of the Drell-Yan mode will be sensitive at higher levels, due to less background. (The main background is regular Drell-Yan lepton pairs.) A signal of 100 events should be visible above background. This means we will be sensitive to masses up to about 190 GeV/c^2 for this decay mode in 100 pb^{-1} data. Searches for second and third generation leptoquarks decaying into quark+lepton should be sensitive to about 160 GeV/c^2 with 100 pb^{-1} of data.

Charged Higgs

The top quark signal may be obscured if there is a charged Higgs particle at lower mass. Then the major decay mode of top could be $t \rightarrow bH^+ \rightarrow b\tau\nu$. This decay mode would not generate the electrons and muons used for conventional searches. However, depending on the mass of the top and charged higgs, $\not{E}_T$ searches can be sensitive to these decays. CDF's $\not{E}_T$ > 40 GeV observed cross section is about 25 pb, consistent with Standard Model expectations. The uncertainty on this expectation is about $\pm$6 pb. Therefore we are sensitive

to 15 pb of excess cross section. From Barger and Phillips, MAD/PH/484, we can see that this sensitivity to excess rates of large $\not{E}_T$ events can rule out the existence of top/higgs combinations of 50 GeV/c^2 $< M_t <$ 80 GeV/c^2 and 30 GeV/c^2 $< M_H <$ 70 GeV/c^2 for branching fraction of H into τ larger than 10%-20%. An analysis of the 4.4 pb^{-1} data set is ongoing. We expect a search for this mechanism will be sensitive to M_t = 140 GeV/c^2 in 100 pb^{-1} of data.

3.6 Rare Processes

There are some indications of "ZOO" events, which are defined as those where the expected rate in a given data run from known physics processes is very low - of order 1% probability or less. Interpretation of such events is a delicate matter. There are dangers in over- or under-interpreting their significance. Since there are many channels where such events could show up, it is not surprising that we have seen some. On the other hand, any one of these ZOO events might be the "tip of the iceberg", the first hint of new physics which might be confirmed with more statistics in future CDF runs. In this section, we describe briefly several of the classes of ZOO events found so far in the 1988-9 CDF data run, and speculate on the physics which might explain them *if they are not due to statistical fluctuations or detector inefficiencies.*

The first two items were uncovered in the study of high P_T distributions. The rest are individual ZOO events. Note that the "standard model probabilities" given below are estimates subject to a variety of uncertainties. One must be clever enough to base the estimate on the dominant process(es) leading to the observed topology. Such expectations could easily be wrong by factors of order 3-5.

Boson-Multijet Events

We observe two high P_T Z's: a $Z \rightarrow e^+e^-$ with $P_T = 213$ GeV/c recoiling against two jets with observed E_T of 136 GeV and 54 GeV; a candidate for $Z \rightarrow \nu^+\nu^-$ inferred from a corrected $\not{E}_T$ of ~230 GeV recoiling against four jets with observed E_T of 93 GeV, 90 GeV, 31 GeV and 10 GeV. These events seem well separated from the falling P_T spectrum of Z's.

In an attempt to understand if this is a significant signal, all high P_T W/Z→leptons candidates were examined to see if they are consistent with the expected P_T dependence. For those recoiling against a single jet, the P_T dependence appears to be consistent with expectation, as are those events with high transverse momentum for the W or Z boson (P_T^{boson}) recoiling against multijets with $P_T^{boson} < 100$ GeV/c.

There appear to be five anomalous high P_T^{boson} events recoiling against multijets with P_T^{boson} above 125 GeV/c. They are well separated from the steeply falling low P_T^{boson} (< 125 GeV/c) events. In addition to the two Z events mentioned above, there are two W+multijet candidates (one $W^\pm \rightarrow e^\pm\nu_e$ and one $W^\pm \rightarrow \mu^\pm\nu_\mu$). All four events have P_T^{boson} roughly 50 GeV/c higher than the highest P_T W/Z + single-jet event. Furthermore, all four events have a second jet with very high E_T (> 50 GeV). Three of the four have a third jet with E_T above 20 GeV. This is extremely unlikely (of order 0.1 or less of W/Z + single-jet rate) if one assumes these events to be normal QCD production of high P_T W/Z's. Thus, we only expect of order 0.05 such events in our data sample, while we see four events. The fifth candidate has three stiff jets ($E_T = 70$ GeV, $E_T = 50$ GeV and $E_T = 30$ GeV) and an electron with $E_T = 29$ GeV and corrected $\not{E}_T$ about 180 GeV.

The number of such events is surprising, considering either the boson + single-jet behavior or the behavior of the low- E_T part of the boson + multi-jet E_T spectrum.

High Pt Upsilon Candidates

Several candidates for low mass ($\sim$10 GeV/c^2) dileptons with P_T near 100 GeV/c were observed. The presence of only a single Υ at this high P_T would be unexpected, but unremarkable. However, the presence of several such events suggests that we should watch this in future runs for interesting physics.

Diphoton + multijet event

We have one unusual diphoton + jets event. The three leading 'partons' are in a "Mercedes" topology, consisting of a 225 GeV (corrected E_T) jet, a 197 GeV $E_T\,\gamma$, and a second 98 GeV $E_T\,\gamma$ (Note that we can not tell whether these photon candidates are γ's or π^0's; there are no tracks pointing to those "photons", thus implying a fragmentation-z of at least $\sim$0.95 if this is a π^0). There are also three softer jets of order 15-30 GeV. There is no significant $\not{E}_T$.

The (uncorrected) cluster summed E_T of this event is about 525 GeV. Only a few dozen events in the 1988-9 run have such large summed cluster E_T . The estimated probability of having two photons in an event with cluster summed E_T above 500 GeV is about 10^{-4}. We find only one single-γ + jet event with high summed E_T ($\sim$530 GeV). This has a more likely topology (photon directly opposite the jet in azimuth).

Trilepton - Jet event

We have one unusual e+μ+jet+soft-μ event - our only dilepton top candidate. The E_T 's of the four "partons" are: 40 GeV (μ #1), 32 GeV (e), 11 GeV (jet; corrected E_T about 20 GeV), and 7 GeV (μ #2, at rapidity near 2). Known physics processes (excluding top) would give a probability of order 0.01. Among them :

- We expect one Z into τ pairs with subsequent decay into e + μ for e and μ P_T threshold of 15 GeV/c; for threshold of 30 GeV/c, the probability is less than 0.01. The event is even less likely if we put in the probability of the jet and the second muon.
- We expect 0.15 W pairs decaying into e + μ. The P_T of the leptons are consistent with this hypothesis. However, if we take into account the jet and the second muon, the probability drops to $\sim$0.01.
- We expect 0.05 W+Z or W+Drell-Yan(mass>30 GeV/c^2). This could explain the second muon. The dimuon mass is near 50 GeV/c^2. Taking into account the 20 GeV jet would reduce the probability $\sim$0.01.
- In contrast, the electron and μ #1 P_T is consistent with coming from $t\bar{t}$ assuming a top mass above 90 GeV/c^2. If the top mass is above roughly 120 GeV/c^2, the b jets from $t \rightarrow b + W$ would have E_T of order 15-30 GeV; 22% of the events would have one b jet decaying via $b \rightarrow \mu + \nu + c$, which would have E_T (mu) about 5-10 GeV. Thus, this event is entirely consistent with $t\bar{t}$ and a top quark mass above $\sim$120 GeV/c^2. It is also consistent with the expected cross section. We would love to have higher integrated luminosity and a hundred of these.

Concluding Remarks

The exploration of the highest available energies is one of the foremost goals of the US High Energy Physics program. CDF has already detected jet events with a parton-parton center-of-mass energy close to a TeV in an sample of 4.4 pb^{-1} . We also observe small numbers of unusual events with very high center-of-mass energies. The limitations are statistical only. The detector resolves the events unambigously, such that each event carries a lot of weight. One needs, however, more than the handful of events we have now for discovery.

The Tevatron is unique, and will remain so for quite a long time, in being able to explore the energy region up to a TeV. There are likely to be big discoveries in this energy region, and with an improvement to two orders of magnitude larger than our present sample our physics reach is far beyond that available anywhere else. It is the discovery of something entirely new that is the big prize for Fermilab, and the Collider running at high luminosity is its best shot! We want to go for it with a detector able to accomodate and exploit these opportunities.

4 Hardware Upgrades

This section discusses our plans to upgrade CDF for the 1993 run. Figure 1-1(a) shows the detector as it was configured in the 1988-89 run. At this writing, construction is in progress to prepare CDF for the 1991 run. See Fig. 1-1(b). We will add a central muon extension (CMX) and a silicon vertex detector (SVX) to the system shown. The vertex time projection chamber (VTPC) will be replaced with a design better able to withstand the higher luminosity (VTX).

Figure 1-1(c) shows the detector as proposed for the 1993 run in comparison with the 1989 and planned 1991 configurations. A more detailed view of the 1993 version is given in Fig. 4-1. An overview of the strategy was presented in Sec. 1. This section discusses the upgrade in terms of each of the major subsystems. While all are discussed, the "big ticket" items in the proposal are: a new plug scintillation calorimeter to replace the gas calorimeters, a radiation-hardened replacement for SVX, improved muon coverage by moving the muon toroids closer to the central detector and major modifications to the data acquisition electronics. We also need substantially enhanced offline data analysis facilities and discuss them in this section. Cost estimates are given in Sec. 5 as a CDF budget request plus a separate request for offline computing resources.

Since much of the work and cost scales with the number of detector channels, we summarize in one place (Table 4-1) the number of readout channels associated with each system. For 1993, the front end electronics must be rebuilt for all Rabbit channels.

System		Rabbit Channels			LRS1879 Channels		
		1989	1991	1993	1989	1991	1993
CEM	Central EM ADC's	960	960	960			
CEG	Central EM ADC's (x16)	960	960	–			
CES	Central EM Strips	9216	9216	9216			
CET	Central EM TDC's			480			
CHA	Central Hadron ADC's	768	768	768			
CHG	Central Hadron ADC's (x16)	768	768	–			
CHT	Central Hadron TDC's	384	384	384			
WHA	End Wall Had. ADC's	768	768	768			
WHG	End Wall Had. ADC's (x16)	768	768	–			
WHT	End Wall Had. TDC's	288	288	288			
CCR	Central Crack Detectors	480	480	480			
CPR	Central Pre-Radiator	–	1536	1536			
CDT	Central Drift Tubes	3024	3024	3024			
CMU	Central Muon	3456	3456	3456			
CMUP	Central Muon Upgrade				–	864	950
CMEX	Central Muon Extension				–	1632	2208
PEM	Plug EM ADC's	6912	6912	–			
PES	Plug EM Strips	1488	1488	–			
PEA	Plug EM Anodes	272	272	–			
PHA	Plug Hadron ADC's	1728	1728	–			
PHW	Plug Hadron Wires	480	480	–			
FEM	Forward EM ADC's	5760	5760	–			
FEA	Forward EM Anodes	1200	1200	–			
FHA	Forward Hadron ADC's	2880	2880	–			
FHX	Forward Hadron Wires	1120	1120	–			
FMU	Forward Muon Wires				4608	4608	6000
FMS	Forward Muon Pads	2160	2160	–			
FMS	Forward Muon Scintillator	–	–	2160			
CTC	Central Tracking Drift Ch.				6180	6180	6180
VTPC	Vertex TPC Wires				3072	–	–
VTPC	Vertex TPC Pads (FADC's)				1500	–	–
VTX	Vertex Time Projection Ch.				–	8448	8448
FTC	Forward Tracking Radial Ch.				3024	–	–

(continued)

(continued)							
		Rabbit Channels			Fastbus Channels		
System		1989	1991	1993	1989	1991	1993
SVX	Silicon Vertex Detector				–	10000	–
SVX	Rad-Hard SVX				–	–	10000
	Plug Pre-Radiator ADC	–	–	736			
	Plug Pre-Radiator TDC	–	–	736			
	Plug Strip Chambers	–	–	9000			
PSEM	Plug Scintillator ADC's (EM)	–	–	2688			
	Plug Scintillator TDC's (EM)	–	–	1344			
PSHA	Plug Scintillator ADC's (Had)	–	–	912			
	Plug Scintillator TDC's (Had)	–	–	456			

Table 4-1: Number of readout channels for each of the CDF subsystem detectors for the 1988-89 run and as planned for 1991 and 1993. Note that the SVX does not use LRS 1879's. Instead it uses a Fastbus-based sequencer. The SVX chips do a sparse scan readout of 48,000 (150,000) channels for the 1991 (1993) run.

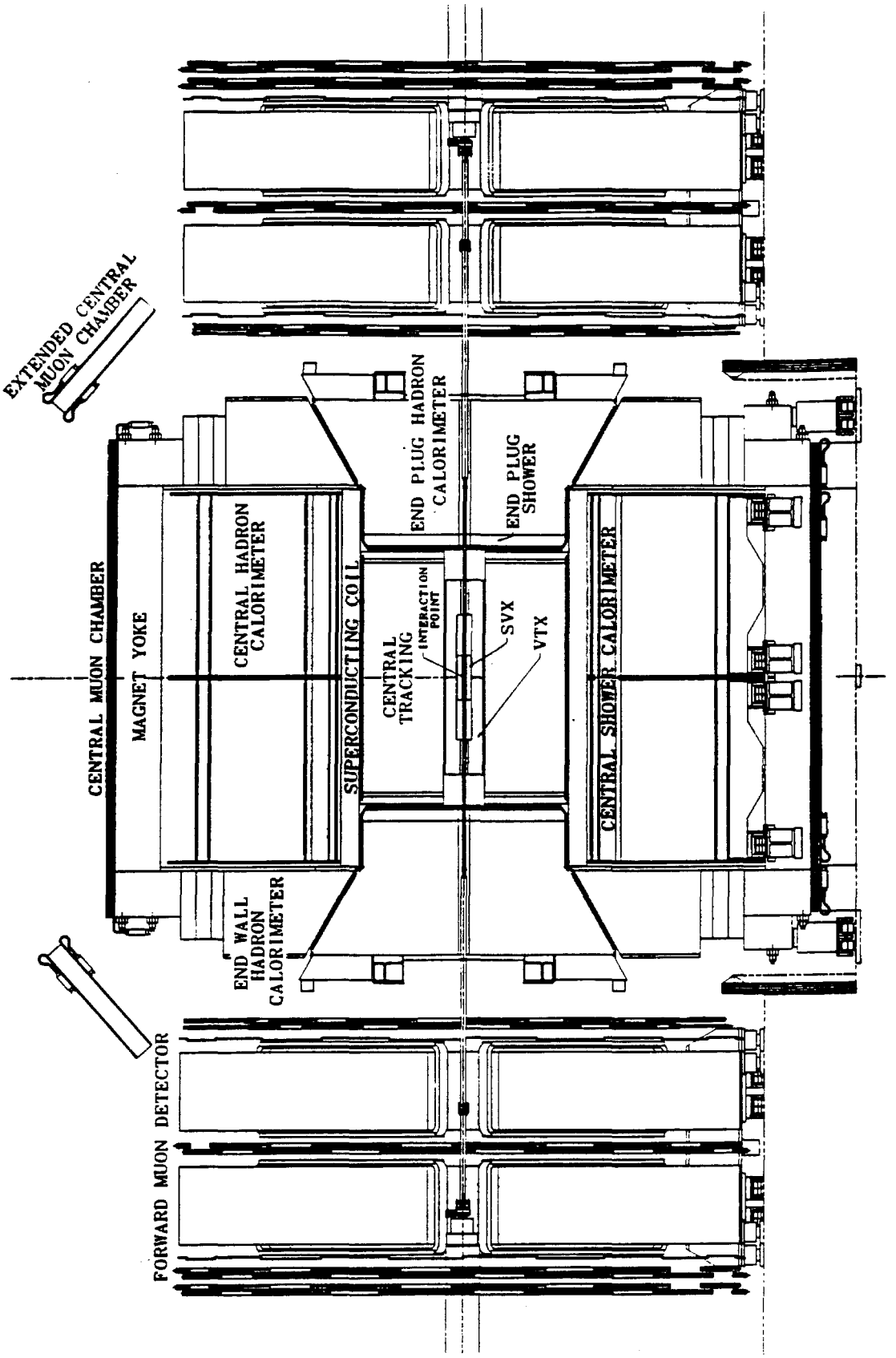

Figure 4-1: A view of the CDF detector for the 1993 run, showing relationships of the various subsystems with the new plug calorimeter and the relocated forward muon system.

4.1 Tevatron Upgrade

The Tevatron upgrade will occur in several phases.

- Separators are being installed in the ring to reduce the beam-beam interaction. Planned completion: 1991.
- The bunch structure will be changed from the present 6-bunch operation, with a 3.5 μsec interval between beam crossings, to 36-bunch operation with 395 nsec between crossings. Details of the bunch parameters are given in Table 4-2. Planned completion: 1993.
- A rapid-cycling Main Injector will replace the present Main Ring in all its functions. Planned completion: 1994.

These upgrades will benefit all parts of the Fermilab fixed target and collider programs and will provide a new 120 GeV slow spill at 2 μA for fixed target experiments.

Quantity	Value
Circumference	6.283185(3) km
Single-turn Period	20.9586 μ sec
Number of RF buckets	1113
	$= 3 \times 7 \times 53$
	$= 21 \times 53$
	$= 3 \times 371$
RF Period	18.831 nsec
RF frequency	53.105 MHz
36–Bunch Collider Operation	
Number of Groups of Populated Bunches	3
Populated Buckets per Group	12
Interval Between Populated Buckets	21 RF Periods
	= 395.4 nsec
Length of Populated Interval	11×21 RF Periods
	= 4350 nsec
Length of Empty Interval	140 RF Periods
	= 2636 nsec

Table 4-2: Tevatron Parameters Governing Timing of Bunch Crossings

The implications for CDF are considerable. Most important, the physics reach of the detector will be extended by the higher luminosity. This, however, does not come for free. Much of the present data acquisition system will have to be replaced in order to avoid an unacceptable increase in dead time due to the shorter bunch spacing. A Level-0 trigger

mounted directly on the detector must be designed and built. Shorter signal-collection times are an important consideration. Individual detector systems will have to survive in a much more intense radiation field, both in terms of tolerable instantaneous noise levels and long term damage.

4.2 Plug and Forward Calorimeters

Extensive R&D has been carried out by members of CDF to study the properties of various calorimeter technologies for use at angles below ~35°. This region is presently served by gas calorimeters in the plug (PEM, PHA) and forward (FEM, FHA) regions.

The increased Tevatron luminosity and 400ns bunch spacing in the 1993 run pose a number of serious technical problems for the gas calorimeters. R&D is taking place (bench tests and test-beam work) to understand how they can be kept operational for that run. Faster response times and lower noise levels can be achieved. However, the chamber high voltage will have to be reduced to prevent glow mode at very high luminosity and to reduce aging. This will result in some deterioration of the calorimeter energy resolution. Thus, the gas calorimeters will eventually have to be replaced if CDF is to operate successfully at the high luminosities planned for the upgraded Tevatron. The natural time for this replacement to occur is the 1993 run when the Tevatron bunch crossing interval drops to 395 nsec.

Work is in progress to develop scintillation plastic as the replacement for the gas detectors. Our R&D efforts initially followed two scintillator technologies: tiles and fibers. Prototypes of each were built and studied in the test beam. Based on these studies as well as implementation plans in the CDF detector, we have selected scintillating tiles with fiber readout for the upgrade. This would allow CDF the most flexiblity in carrying out its upgrade program, and would cause the least disturbance to the existing detector.

Vigorous R&D will continue in the next test beam cycle. A large prototype of the upgrade calorimeter will undergo extensive testing. We will also test prototype preamplifiers necessary to keep the gas calorimeters as a fallback option for the 1993 run.

4.2.1 Plug Scintillation Calorimeter

A key element in CDF's upgrade program is the replacement of the gas calorimeters in the plug ($38° < \theta < 10°$) and forward ($10° < \theta < 3°$) regions with a single scintillator-based plug calorimeter. Like the central calorimeter, it will consist of a lead/scintillator electromagnetic shower calorimeter followed by an iron/scintillator hadron calorimeter. As will be discussed below, this new device offers several advantages: tripling the density of the EM calorimeter improves the hermiticity of the CDF electron and jet acceptance; the finely segmentated position detector at EM shower maximum will allow a reduced trigger threshold for electrons and photons; calorimeter compensation (E/H $\simeq$ 1) improves jet resolution for better measurements of jet E_T 's and jet spectroscopy; removal of the forward calorimeters allows the muon toroids to be brought forward for increased muon coverage; the scintillator/phototube system offers improved uniformity and gain stability; and a reduction in the maintenance and calibration effort. Figures 4-2 and 4-3 show views of the detector in the present and proposed configurations.

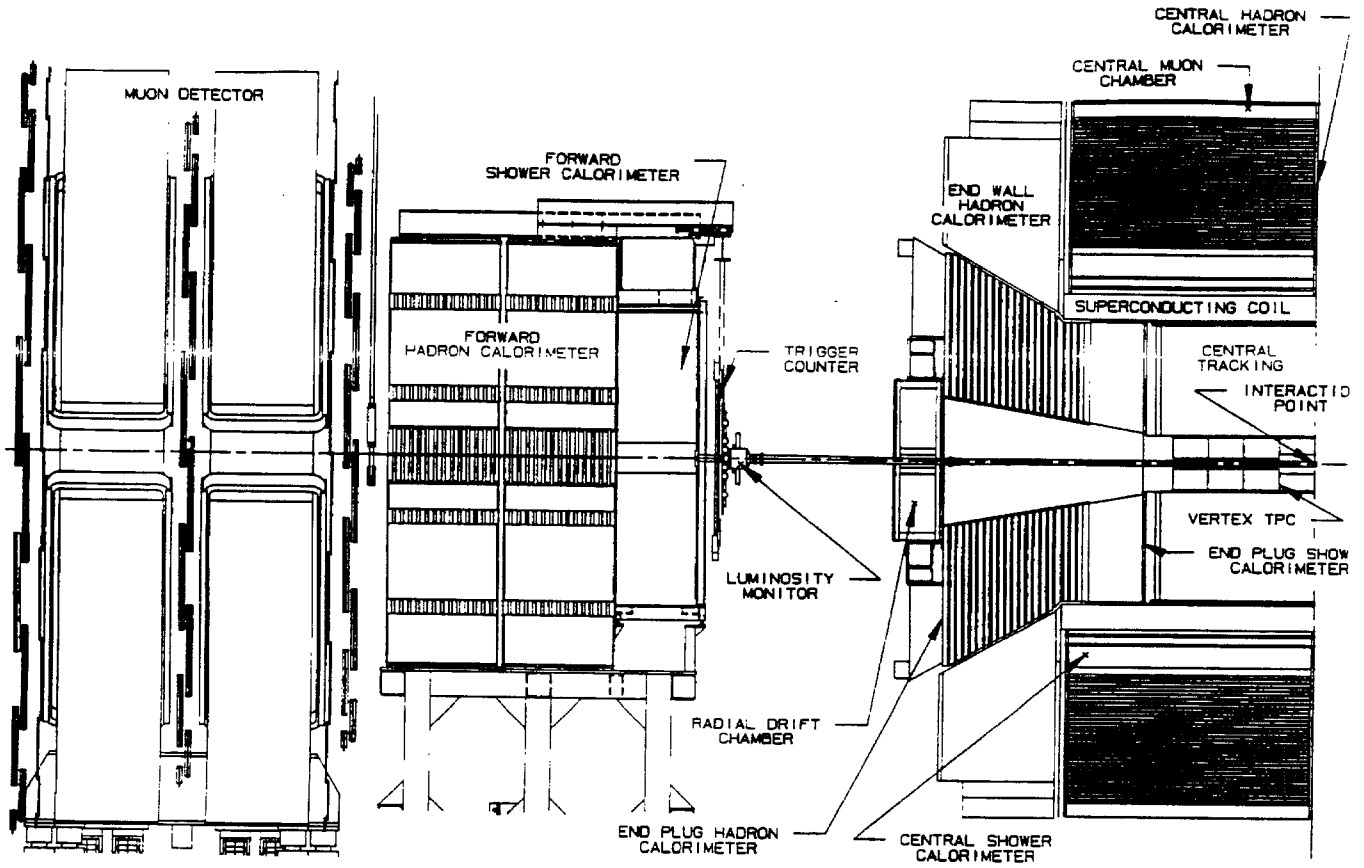

Figure 4-2: Side View of Existing CDF Detector

Tile Calorimeter Methods

The technology chosen for the hadron and EM calorimeters is a "tile" system constructed from scintillating plastic plates ("tiles") with wavelength-shifter optical fibers imbedded for readout. These tiles are assembled into planes of scintillator which replace the gas proportional chambers in the gaps between the existing absorbers. The projective towers are formed by the optical segmentation of the tiles within each scintillator plane. The clear optical readout fibers from each tile are led to phototubes outside of the calorimeter along the path currently taken by the electrical cables of the gas calorimeters. The "tile" technique has already been successfully employed in a full scale endplug calorimeter [BNL 814] as well as several smaller-scale calorimeters [UA1, D0, etc.].

The "tile" configuration makes it possible to preserve the existing steel structure of the plug hadron calorimeter. By preserving this structure we gain several benefits: The cost of the new calorimeter is reduced by about $400K, the cost of replacing the steel. Stainless steel and other non-ferromagnetic materials will be used for modifications to the absorber structure, so that the central magnetic field is unperturbed and no new field mapping is needed. Similarly, no new magnetic forces are induced on the solenoid. The mechanical

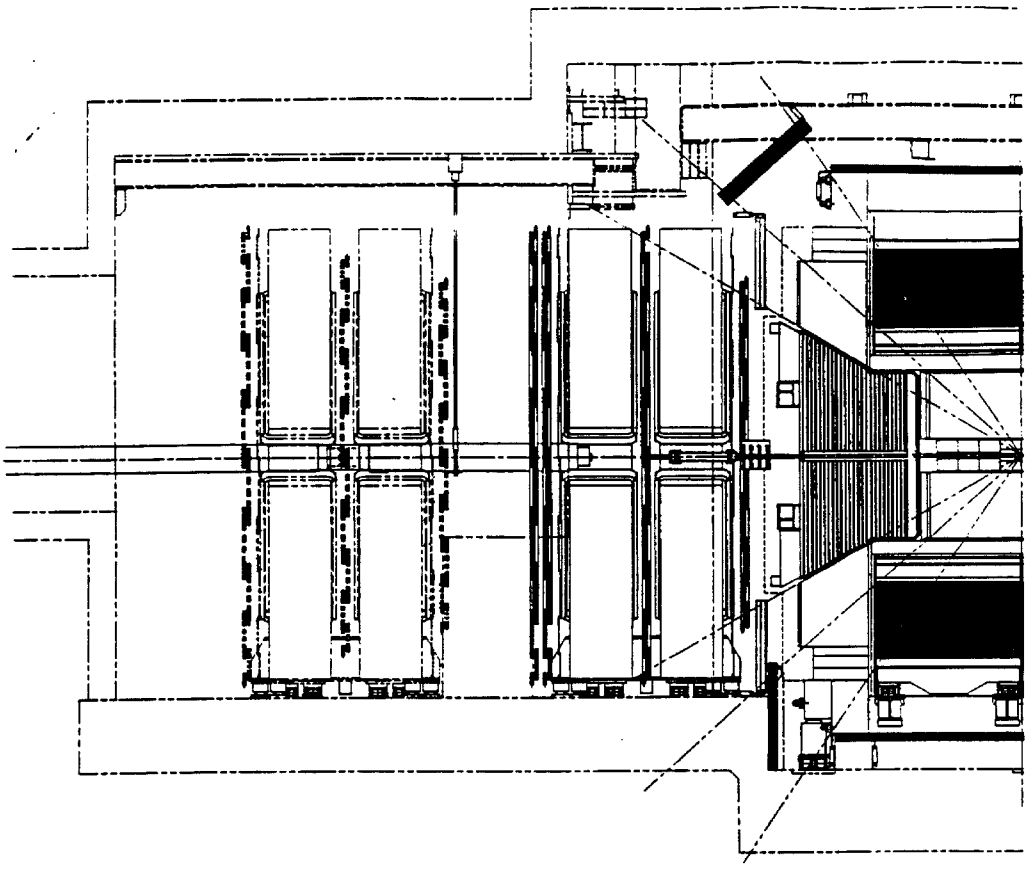

Figure 4-3: Side View of Upgraded CDF Detector. The plug calorimeter is now a single unit extending from 38° to 3°, and the muon toroids have been moved inwards. The density of the endplug EM calorimeter has been increased and the corner beveled to improve the hermeticity near the "37° crack"

and magnetic structure is essentially unchanged, so we can be assured of the mechanical integrity of the detector. In the case of the EM calorimeter the "tile" technique uses lead plates instead of iron as the EM absorber.

The technique of tile calorimetry has several pertinent features: The light yield of this configuration is high, several times larger than the conventional scintillator plate/wave-shifter bar strategy (for example CDF, UA1, UA2, or ZEUS). This high light yield ensures good EM energy resolution, and allows us to design a compensating calorimeter with either lead radiator or steel absorber. The small size and flexibility of the readout fibers allows us to retain the absorber structures which were originally designed for use with the gas proportional chambers. In addition, each tile can be made quite uniform, with an rms variation of light yield with position of about 1%. In contrast, there is up to 20% variation in a conventional plate/WLS bar device. The spatial uniformity of this technique provides benefits to both electron and jet physics.

Test Beam Prototypes

During the spring and summer we built several prototype calorimeters and exposed them to test beams at Fermilab. The prototypes built were a 3×3 tower EM calorimeter, a 1 tower EM calorimeter, and a 4×4-tower hadron calorimeter.

3×3-tower EM prototype

This device was used to explore tile construction techniques, energy resolution, and uniformity, in particular uniformity at tower boundaries. In addition, a position detector, described below, was installed into this calorimeter and its performance was evaluated. The tower size was $6 \times 6\text{cm}^2$ and was non-projective. The absorber was 1/4-inch lead plates. The total thickness of the device was 22 X_0.

The tiles for this EM prototype were made of 2.6-mm polystyrene scintillator (SCSN 81). Imbedded in the surface were 0.7-mm waveshifter fibers (Y7) for readout. For this prototype, the waveshifter fibers were not spliced to clear fibers, simply taken straight to the phototubes. The tile perimeters, grooves, and glue holes were all laser cut by a private vendor. The tiles were glued and the calorimeter assembled by summer students at Fermilab.

The 3×3-tower calorimeter was exposed to electron, pion and muon beams at the MT test beam. Energies of the beam particles were varied from 10 to 227 GeV. Cross calibration of the 9 phototubes was done by exposing the 9 towers to electrons, and adjusting the gain to equalize single tower response. The light yield was determined to be about 60 photoelectrons per GeV by fitting the low side of the minimum ionizing peak of muons to a Gaussian. The ratio of standard deviation to mean was used to determine the light yield. Figure 4-4 shows the measured energy resolution for electrons. Also shown in this figure is the resolution for a 1-tower EM prototype. This device is described below.

A position scan of the detector is shown in Fig. 4-5. Scans were made through the center of the prototype in the hortizontal and vertical planes. The beam spot was approximately 2.5 cm square. Particle impact positions were calculated using the beam drift chambers. The central tower lies between 3 and 9 cm in X, and between -2 and 4 cm in Y. We do not see any marked effect at the tower boundaries. From these measurements we conclude that the rms uniformity of the device is better than 2%.

One Tower EM Prototype

The one tower EM prototype was used to explore questions of resolution and light yield for tile calorimetry. Recall that the 3×3-tower calorimeter used 0.7-mm fibers and had a light yield of about 60 photoelectrons/GeV. We wanted to see the effects of using 1-mm fibers. The 1 tower protoype was built of $12 \times 12\text{cm}^2$ tiles, each 2.6-mm thick, with 1-mm diameter waveshifter fiber embedded in the surface. The waveshifter fibers were spliced to clear fibers, then read out by a phototube. The absorber was reconfigurable, either totally absent (to see a clean minimum-ionizing signal), 1/8-inch lead (40 samples), or 1/4-inch lead, (20 samples). The 40 tile "naked" stack was exposed to a pion beam to see the MIP signal. This signal is shown in Fig. 4-6. The very sharp rise of the lower edge of the MIP peak indicates that the device has a large amount of light. A fit to the signal with a Landau distribution with Poisson fluctuations from photostatistics yielded a average of 80 pe's per

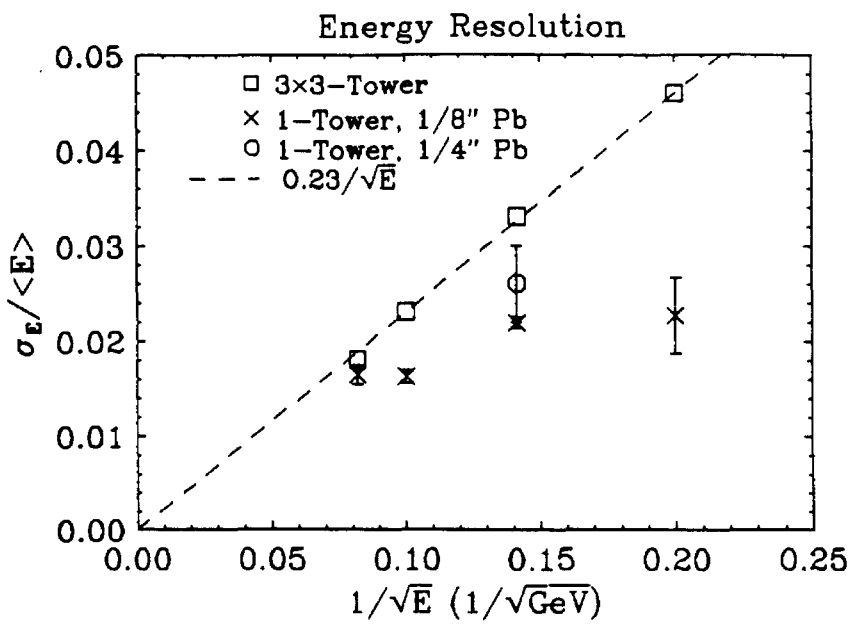

Figure 4-4: Energy Resolution of the 3 × 3-tower EM calorimeter with 0.7-mm fibers. The squares are measured energy resolutions for various energy electrons. The data for each energy were fit to Gaussians to yield the width, σ, and its uncertainty. The dashed line is a linear fit to these points constrained to pass through the origin. Also shown are the measured resolutions for the 1-tower EM prototype with 1-mm fibers and two sampling thicknesses. Although full shower containment was not possible with a single tower, significant improvement in resolution was achieved with the larger-diameter fiber.

MIP. This corresponds to about 280 pe/GeV in a calorimeter. We plan on 25 layers of sampling in the upgrade calorimeter. We thus expect approximately 130 pe/GeV, scaling this number to the number of tiles and the fiber readout length.

We also made an energy scan of this prototype. Results of energy resolution are shown in Fig. 4-4. With this single-tower prototype, full shower containment was not possible. However, the lower energy points in the figure show a marked improvement in resolution over the 3 × 3-tower prototype with the 0.7-mm fibers. Future prototypes with 1-mm fibers and more towers for full shower containment will be built and tested.

Hadron Calorimeter Prototype

We built a 4 × 4-tower hadron prototype with a tower size of 6 × 6 in^2. The device had twenty-four 2" iron absorber plates. This corresponds to the twenty 2" plates of existing plug iron plus four additional stainless plates to be installed for the upgrade. A preliminary energy resolution of σ = 9.7 GeV at 100 GeV was measured. We expect to attain about $80\%/\sqrt{E}$ resolution with this sampling thickness. A preliminary measurement of E/H, compensation, was also made. At 100 GeV, the ratio of electron to pion signals was found to be 1.16 .

The number of photoelectrons per GeV for the hadron calorimeter was determined

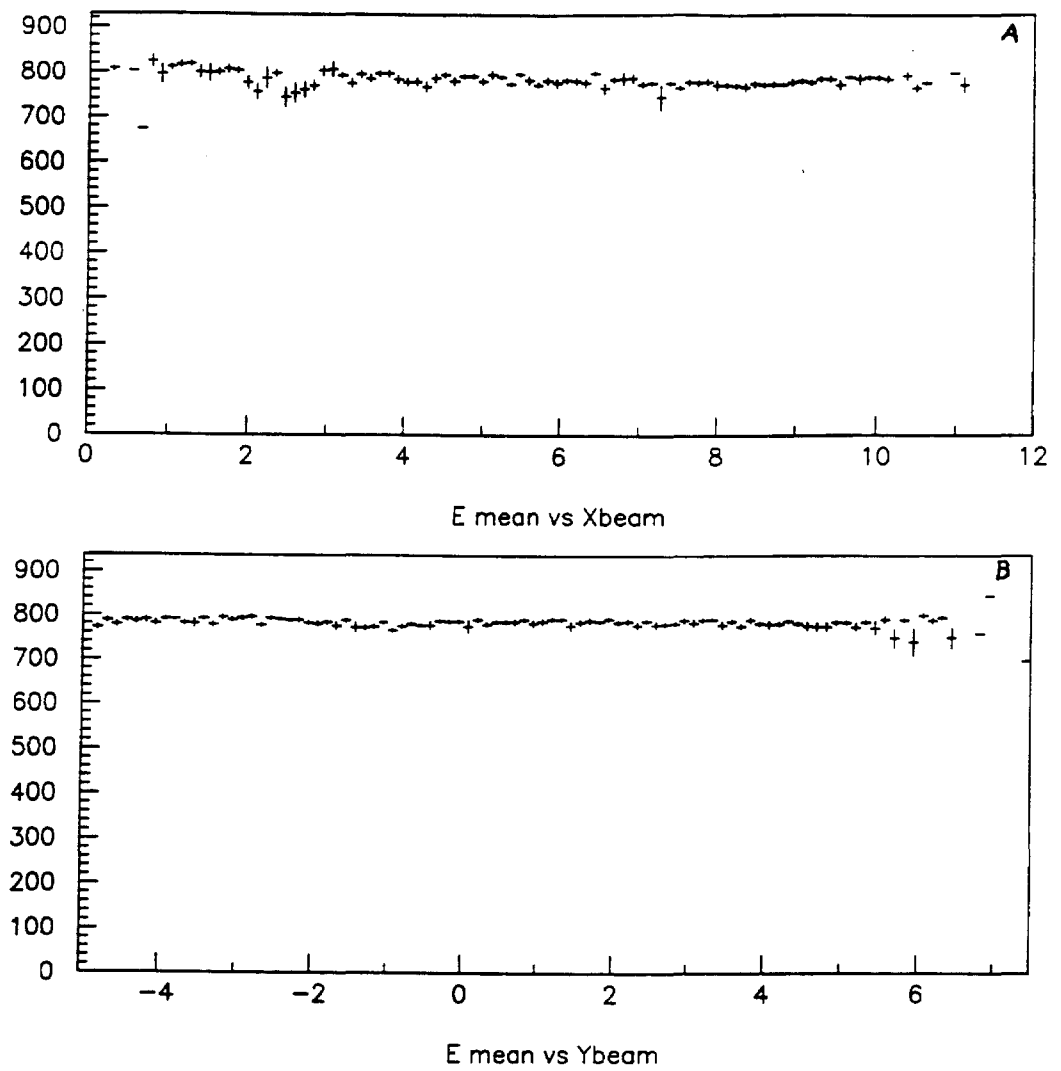

Figure 4-5: Plotted is the average response vs position of the incident particles. Fig. A shows results for a hortizontal scan. Fig. B. shows results for a vertical scan.

in a preliminary way from the ratio of the hadron tile response to the EM tile response. At this writing, we conservatively estimate it to be >100 pe/GeV. Further tests will determine this accurately.

In the process of constructing these prototypes, we built more than 1000 tiles. This corresponds to more than 1% of the final required number of tiles for the upgrade calorimeter. From this effort we learned a great deal about manufacturing techniques, uniformity of tile responses, and the labor involved in assembly.

New Calorimeter Geometry

The density of the new EM calorimeter is approximately three times that of the existing gas EM calorimeter. This eliminates one of the major hermeticity problems currently faced by CDF, the "37° Crack". This arises from electromagnetic showers in the range $35° < \theta <$

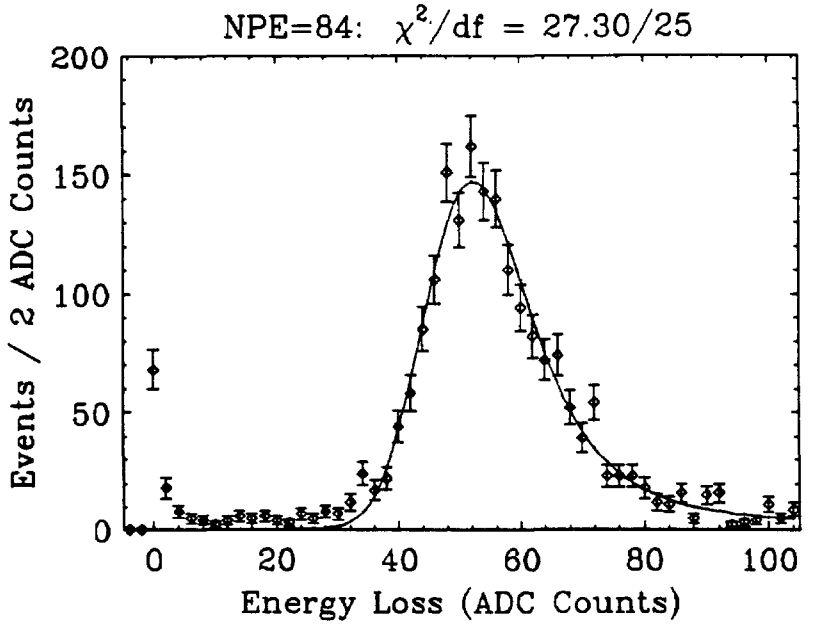

Figure 4-6: Pulse height distribution for pions passing through the 40 tile stack.

40°, which clip the corner of the endplug calorimeter and reach EM shower maximum inside the dead material of the solenoid. The situation is aggravated by the sizable structural elements located near the ends of the solenoid. The solution to this problem is twofold: Firstly, by increasing the density of the EM calorimeter we reduce the width of the "central-endplug transition region" in which EM showers can deposit significant energy in the solenoid. Secondly, by beveling the corner of the EM calorimeter, one can arrange for a sharp transition between the situation in which all of the EM energy is deposited in the endplug, or in the central EM calorimeters.

The higher density EM calorimeter will require less space in z (along the beam axis). In the free volume, we will add four 2" stainless steel absorber plates to the front of the hadron calorimeter. This provides additional active shielding in front of the 30° readout crack in the hadron calorimeter, in addition to the obvious benefits of better hadronic energy containment and reduced hadron punchthrough into the muon detectors. Additionally, to replace the forward gas calorimeters, it is necessary to insert a set of stainless steel absorber disks into the 10° hole in the plug hadron steel structure – the "miniplug".

The $\eta - \phi$ segmentation of the new plug calorimeter is shown in Fig. 4-7. In contrast to the old CDF plug and forward calorimeters, we choose not to maintain the constant segmentation in η which results in a very large fraction of channels at small angles. Instead, we maintain an approximately constant physical tower size. This has the effect of concentrating the channel count at smaller η, where high-P_T physics occurs and where the momentum analysis of the solenoid is available. Coverage of the very forward region $3 < \eta < 4$ is necessary primarily for missing E_T resolution. Monte Carlo studies indicate that the missing E_T resolution is not significantly degraded by this coarse-tower granularity in the very forward region. The number of towers is determined primarily by the requirement of

maintaining the 24-fold ϕ-segmentation of the trigger.

The hadron calorimeter tower size is somewhat coarser than the EM calorimeter tower size. This is reasonable due to the larger spatial extent of hadron showers. Integral numbers of EM towers, typically four, project into a single hadron tower. This alignment of boundaries simplifies the hadron/EM energy cut used in electron identification. Table 4-3 contains an overview of the properties of the upgrade calorimeter. Energy resolutions and light yields are based on results of our test beam studies.

	EM	HAD
Segmentation	$\sim$ 8 x 8 cm	$\sim$ 24 x 24 cm
Total Channels	2688	912
Energy Resolution	$21\%/\sqrt{E}$	$80\%/\sqrt{E}$
Light Yield (photons/GeV)	130	$\geq$100
Thickness	22 X_0, 1 λ_0	7 λ_0
Density	$0.6\rho_{Pb}$	$0.75\rho_{Fe}$
Unit Sampling Cell	2.5-mm Scint + 5-mm Pb	2.5-mm Scint + 2" Fe
Number of Samples	25	24
Expected E/H	1.05	1

Table 4-3: Overview of Proposed Calorimeter Upgrade. The EM (HAD) resolution is for a single electron (pion).

Mechanical Considerations

The mechanical design of the tile-based calorimeter is largely determined by the decision to retain the iron of the plug hadron calorimeter. Several significant modifications are required:

1. A stainless steel insert ("miniplug") closes the hole from 10° to 3° in the existing hadron plug. This consists of a series of 2" stainless steel disks which are welded into the center holes of the existing 2" iron plates. The axial forces on individual iron plates (which are currently taken up by a set of support bars on the interior of the 10° hole) are transferred to a stainless pipe at the interior of the stainless disk inserts.

2. Four additional 2" stainless plates are added to the front of the hadron calorimeter. This requires unbolting and replacement of the external support bars at the outer edges of the front of the hadron calorimeter, but no other changes to the structure of the device. These disks extend down to 3° and do not require "miniplug" inserts.

3. The increase in the weight of the plug from approximately 120 to 140 tons may require reinforcing the support arms. The support arms themselves are believed to be strong enough but their anchoring into the iron return yoke may need strengthening. This is under study.

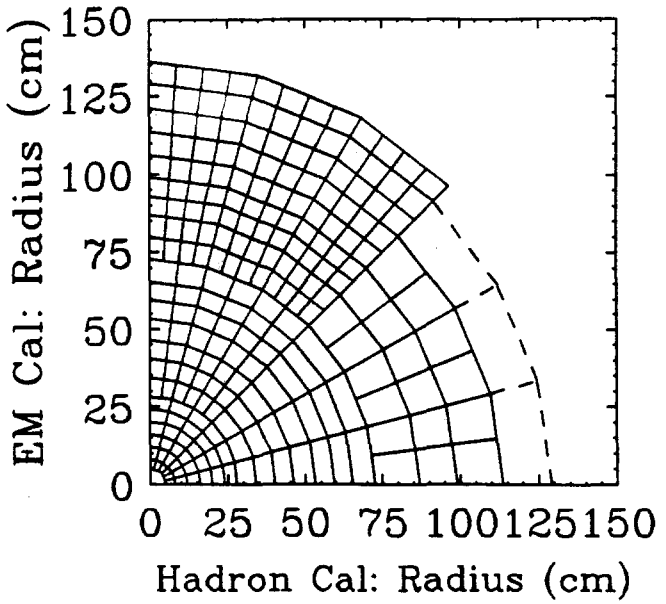

Figure 4-7: $\eta - \phi$ segmentation of the EM (top) and Hadron (bottom) Calorimeters. The electromagnetic section has 56x24 = 1344 towers, and the hadronic section has 19x24 = 456 towers, for a total of 1800 Photomultiplier tubes on each endplug. The outermost hadron segment (with 24-fold ϕ-symmetry) is actually part of the endwall hadron calorimeter.

4. The suspension of the lead plates in the plug EM calorimeter will be accomplished in a manner similar to the current PEM. The significant differences are i) the new higher-density EM calorimeter is about 25 cm deep instead of 60cm, which reduces the lever arms and the stresses on the structural members, ii) the lead sheets extend down to 3° instead of the current 10°, and iii) the outer 15cm of the corner is beveled at 38° for improved EM resolution near the "37° crack".

Phototubes and Electronics

The phototube ADC/TDC cards required for the system are essentially identical to those used in the central calorimeter. Slight modifications may be necessary on the trigger output signals on the PM ADC cards. These cards contain all necessary circuitry for calibrations involving charge injection, flasher systems, and source current monitoring. The software and calibration procedures associated with these cards will be taken from those used in the central calorimeters.

The specification and testing of photomultiplier tubes is straighforward. Numerous CDF collaborators have experience with PM tube test procedures. The small cross section of the readout fiber bundle (0.5 cm^2) makes 1" diameter phototubes a practical and economical choice. The small tube size simplifies the mechanics and magnetic shielding of the PM housings.

The phototube mounting and cabling system is as follows. Optical fibers from both the EM and Hadron calorimeters are led out the 30° crack along the path currently taken by the readout cables for the gas calorimeter. These are led to an array of 1800 phototubes and bases which are mounted along the 13m circumference of the back edge of the plug. We anticipate grouping the 1" PM tubes in mechanical modules containing 8-12 PMTs, so that the modules would be spaced at an average separation of 2-3" along this circumference. The axis of the PM tubes may be either parallel to the beam pipe, or radially away from it. In any case, the HV and signal cables are then routed to the readout crates and HV distribution racks currently used for the gas calorimeters. The minimum number of "Rabbit" readout crates required for the Phototube ADC's is: (1800 channels)/(12 channels/card)/(20 cards/crate) = 8 crates. Sixteen readout crates with power supplies already exist on each endplug. This leaves 8 crates at each end for the shower position detector and PM TDC electronics (if required).

Calibration System

The calibration system will be similar to that which has successfully maintained calibrations to 1% accuracy in the central calorimeter. It will make use of movable radioactive sources to measure the response of the scintillator, phototubes, and electronics. The chief design issues here are the number and locations of the imbedded sources, and their allowed motions. In the case of the hadron steel there is more than ample room for source motion over an entire plane of scintillator, since the scintillator tile assemblies are much thinner (3-4 mm) than the gas proportional chambers (15 mm) which they replace. In the case of the EM calorimeter the constraints on space and dead areas are more severe, and a suitable compromise must be worked out. This task is made easier by the fact that the region which one has to monitor carefully for the first signs of radiation damage is a relatively small volume near EM shower maximum and close to the beam pipe.

The required calibration fixtures will be prototyped in the ongoing test beam cycle, using the existing test beam fixturing and infrastructure.

EM Shower-Maximum Position Detector

A position detector is placed near EM shower maximum at a depth of about 5 radiation lengths in the EM calorimeter. This position detector, similar in function to the gas proportional "strip" chambers in the present CDF central EM calorimeter, will have a far greater granularity due to its construction from 2-mm scintillating fibers. A relatively modest cost is afforded by reading out the fibers by multi-anode photomultipliers. The present central strip chambers, even with anode wire spacing of 7 mm and cathode pad spacing (in the other dimension) of 18 mm, have proven invaluable for electron and photon identification in the central rapidity region. The increased granularity and higher physical density of the scintillating fiber position detector should make it an even more valuable tool for identifying electrons and single photons in the forward/backward directions, particularly since the tracking provides only limited knowledge of momentum in this region so that charged/neutral

pion overlap backgrounds are higher.

The performance of the position detector has been studied with an EGS simulation, using a double layer of 2-mm round fibers, where the second layer is offset by 1 mm from the first, at $5.1X_0$ in the electromagnetic calorimeter, taking into account air gaps, etc. The simulation shows that the particles which reach large distances from the core of the electromagnetic shower and degrade the position and 2γ separation ability of most devices, are of low energy. This can be seen in Fig. 4-8, which shows the pulse height distribution for five EGS events in 2-mm scintillating fibers. The fine granularity of the fibers allows one to ignore the fluctuations in the low-energy "wings" of the showers to improve the position resolution and two-photon discrimination. A very simple algorithm of taking the energy-weighted mean position from fibers having energy above various thresholds was used to make Fig. 4-9. From this figure, one can see that a position resolution of $500\mu m$ can be attained for electrons of 10GeV energy. More sophisticated algorithms which fit the shower profile to extract a position and a χ^2 ought to achieve even better position resolution, and can be used to investigate the power of the position detector to distinguish single photons from π^0's, and to distinguish electrons from jets. One can also anticipate improved electron identification near a jet, as in semileptonic b decays.

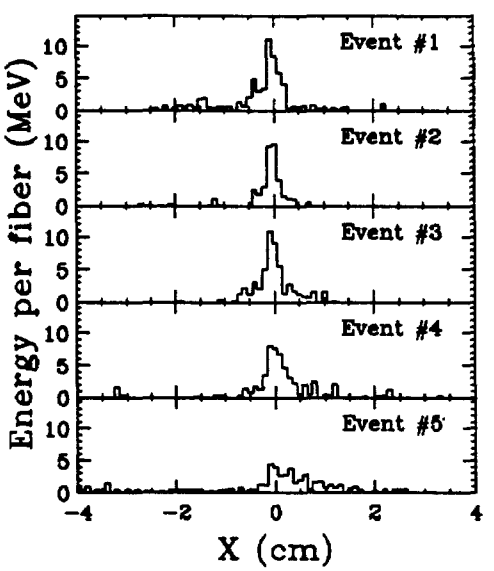

Figure 4-8: Energy deposition profiles in a double layer of 2-mm round fibers at $5.1X_0$ from 10 GeV EGS electron showers.

The problem of distinguishing single photons from π^0's can be thought of in the following manner. The separation between photons from π^0 decay at the shower maximum position detector is always greater than $50\text{cm}/E(\pi^0)$. The minimum separation occurs when the π^0 decays to two photons of equal energy. In this case, we expect to be able to recognize the two showers with the position detector if they are further apart than 5 mm with good efficiency (> 80%) for single photons. This allows us to reject π^0 backgrounds to single

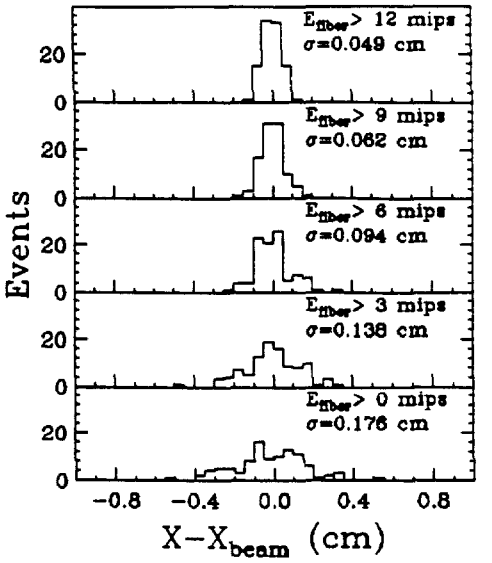

Figure 4-9: Deviations from true position using a double layer of 2-mm scintillating fibers, predicted by 10 GeV EGS electron showers. The algorithm used is simply to take the energy-weighted mean position of all fibers having energy above some threshold.

photon events up to energies of 100 GeV. Of course, when the π^0 decays to one photon of high energy and another of lower energy, the separation increases but the lower-energy shower is more difficult to recognize. This effect will need more Monte Carlo study.

One parameter which may be adjusted is the depth of the position detector in the EM calorimeter stack. By placing this device at least 5 radiation lengths deep, one achieves better energy linearity and resolution. This is useful for distinguishing the signals of high-energy electrons or photons from the ever-present background of low-energy "underlying event" particles. Good energy linearity should also aid in finding the second low-energy photon from asymmetric π^0 decay. Another advantage of placing the device fairly deep in the calorimeter stack is a much higher light yield, thus making it more immune to the effects of Čerenkov radiation from particles passing through the readout fibers brought out through the 30° crack. The only disadvantage is that the low-energy part of EM showers spread more as the depth is increased. We have found this to be a rather unimportant effect with a fine-grained detector which can directly "image" the low-energy wings of the EM showers.

The scintillating fibers from the position detector must be joined to clear fibers at the edge of the active region. This is done both to avoid "hot spots" (from particles which shower along the fibers in the crack) and to improve the overall light yield (since the attenuation length of clear fibers is much longer than that for scintillating fiber). The reliable mass-production of fiber joints is described in the section below titled "Scintillating Tile Fabrication." The clear fibers are then brought out to the back of the plug calorimeter, where they are coupled to position-sensitive phototubes. The "venetian blind" type of position-

sensitive phototubes has been developed just recently[78,79] and can now offer reasonable (on the order of $10/channel) cost per fiber with a reduced electronics channel count, at the expense of slight complication in the event reconstruction software. The Hamamatsu R4135 phototube, for example, uses 28 anode wires in one dimension and 8 anode strips in the other dimension to accommodate 224 fibers using 36 readout channels, and can be obtained for $3K/phototube.

A first prototype of a scintillating fiber position detector, consisting of two R4135 phototubes connected to 112 parallel scintillating fibers of 2-mm diameter, was recently tested in the CDF test beam. The device was placed at $5.5X_0$ deep within the 3-by-3 scintillating tile/waveshifter fiber EM calorimeter prototype. Analysis of test beam data shows that the nominal beam position (extrapolated 17m from the last beam drift chamber) agrees with the position in the fiber detector with an RMS deviation of 2 mm. This is shown in Fig. 4-10. The energy sharing between adjacent towers in the 3-by-3 calorimeter is also correlated with the mean position in the position detector. A study of this energy sharing indicates that the position measured by the position detector is accurate to better than 0.9 mm RMS.

The beam tests uncovered several important problems. Some of these, such as offsets due to DC-coupled preamps, and a grounding problem, were fixed during the tests. Another problem appears to be a non-linear photomultiplier behavior for large signals. This lead to showers which appear to have anomalously large widths. When the device was put at $2X_0$ depth in the EM calorimeter, where the number of photoelectrons is much smaller, these widths were observed to be smaller. Tests with a picosecond pulsed laser have since confirmed a non-linear PMT behavior. For the next round of prototype tests, this problem will be minimized by reducing the phototube voltage and using high-gain preamplifiers. Hamamatsu is aware of the non-linear behavior of the R4135 phototubes and is working to solve them with a modified design. An improved version of this tube should be available on the time scale of about one year.

There are two close-packed geometries for arrangement of the fibers over the area of the plug calorimeter which are interesting. The first of these, shown in Fig. 4-11, has fibers which run at constant pseudo-rapidity (concentric arrangement), crossed with fibers which run at approximately constant ϕ (radial orientation). This "η-ϕ" arrangement makes it easy to match position of an electron shower to a track from the CDF vertex time projection (VTX) chamber, which has good resolution in pseudorapidity; or to a short track in either the central tracking chamber (CTC) or the silicon vertex detector (SVX), which have good resolution in the ϕ direction.

The other "spiral" arrangement, shown in Fig. 4-12, is similar to that depicted in the SDC collaboration's letter of intent for use in the forward region scintillating fiber tracker for SSC application. In our case, it is necessary to use two sections to cover the full rapidity range. The outer section (50–135cm radius) covers the pseudorapidity 1.1–2.0, while the inner section (20–50cm radius) covers pseudorapidities 2.0–2.9. The principle of this arrangement is that every fiber within a section starts at the inner radius and runs to the outer radius. As the circumference of the outer radius is larger than that of the inner radius,

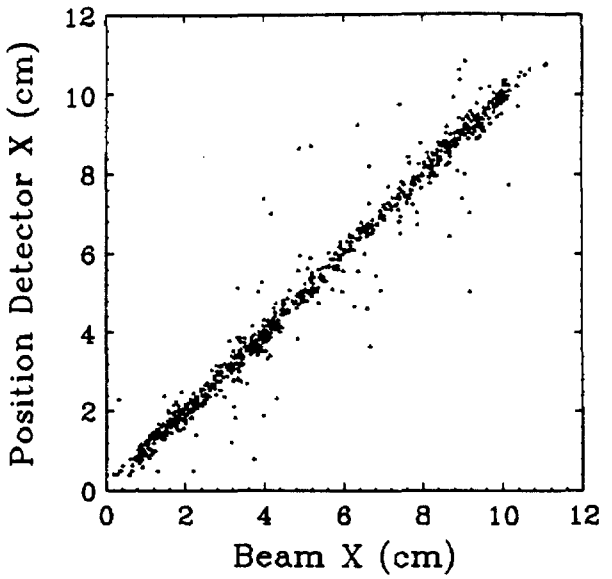

Figure 4-10: Reconstructed fiber detector position versus beam position: preliminary CDF test beam results.

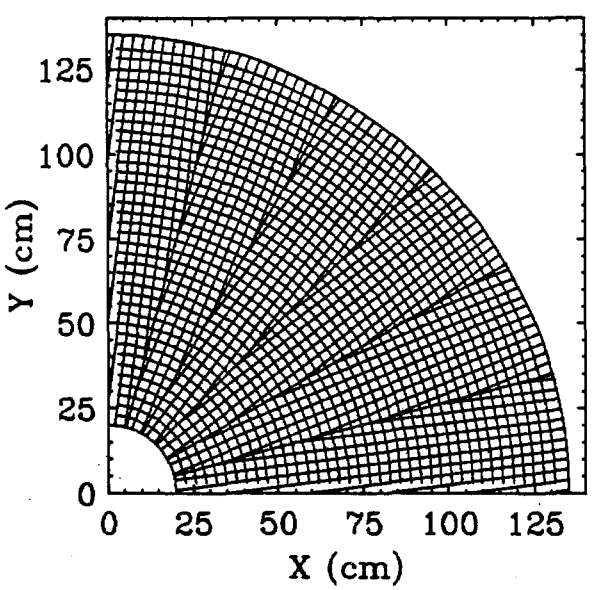

Figure 4-11: An $\eta - \phi$ arrangement of scintillating fibers for the shower-maximum position detector. The ϕ fibers are divided in 15° slices to match the segmentation of the CDF hardware trigger. The actual segmentation is 30 times finer than that shown.

the fibers must bend in order to subtend a constant fraction of the circumference. Such an arrangement has several advantages. The first is perfect ϕ symmetry, i.e., every fiber within a section has exactly the same length and shape. In the η-ϕ arrangement, there are many different lengths of fibers and there are 24 ϕ boundaries in each plug where shower shape reconstruction would be complicated. Another advantage of the spiral geometry is in how the fibers are brought out of the detector. At the outer radius, the fibers must make a right-angle bend in order to come back through the 30° crack of the detector to phototubes. In the "$\eta-\phi$" arrangement, there must be a dead space in which the fibers running at approximately constant ϕ can make this bend in the radial direction. In the spiral arrangement, this bend can be made mostly in the ϕ direction, thus requiring a much smaller dead space. Yet another advantage of the spiral arrangement is that the total number of fibers which have to be read out is reduced to 17,000 compared to 25,000 in the η-ϕ arrangement, whereas the granularity and spatial resolution of both designs are very similar. Since the phototubes are the highest-cost item in this device, reducing the number of fibers significantly lowers the overall cost.

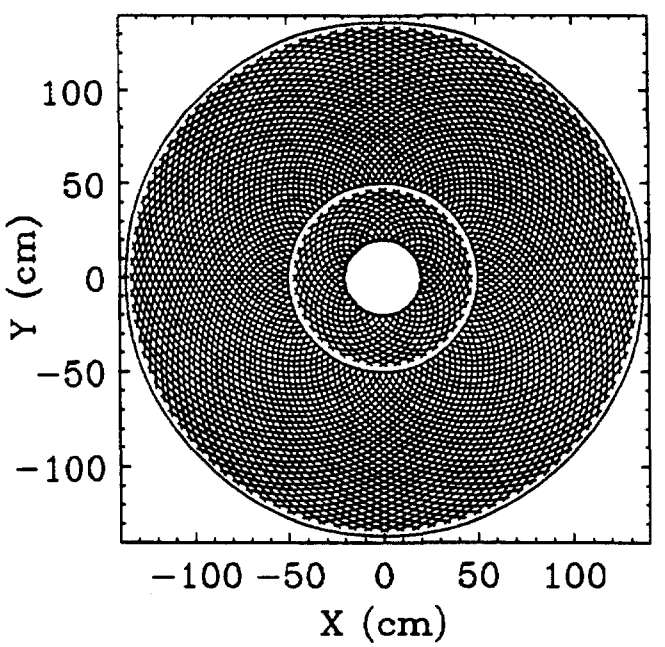

Figure 4-12: A spiral arrangement of scintillating fibers for the shower-maximum position detector. The actual segmentation is 30 times finer than that shown.

We tend to favor the spiral arrangement for its elegance and simplicity of construction; although if ease of track matching, say for triggering purposes, or if the mechanical support structure of the electromagnetic plug were to make it impossible, the first arrangement would be acceptable.

Trigger Upgrades

The trigger will benefit in several ways from the scintillator plug upgrade.

1. On the basis of our experience with the central calorimeter, we expect that neutron-induced noise spikes ("Texas Towers"), as well as low-level coherent noise pickup, will be absent in the new plug. This will allow us to lower the Missing E_T thresholds, as well as to remove several potentially problematic cuts (put in specificallly to reject gas noise) in the Level 2 trigger.

2. A low E_T plug electron trigger will be possible, using the additional information from the EM shower position detectors. The E_T threshold for plug electrons in the last run was not fully efficient even for W physics. The electron signature information available to the trigger will include: an isolated shower profile in the strip detectors at EM shower max, matching with an isolated EM cluster in the EM calorimeter, and with little hadronic energy in the hadron compartment(s) behind it. In addition, fine ϕ matching between the position detector and a (future) track processor in the plug region is possible.

3. The intrinsically fast response of the phototube signals will significantly relax the timing constraints on the Level 0 trigger. We note that this could be a make or break issue for the survival of the existing CTC track proccessors, which require a level 0 signal within ~800ns of the beam crossing.

Scintillating Tile Fabrication

The basic tile unit (fig. 4-13) is a keystone-shaped scintillator plate of typical dimensions 8×8 cm, the pad size of the tower. Each tile has a "U" shaped channel formed in it. A wavelength shifter fiber of diameter 1 mm is glued into this channel. This fiber collects the scintillator light produced in the tile. At the point that the fiber leaves the tile, it is spliced onto a clear optical readout fiber (of typical length 3m) which carries the light to the phototube.

The construction of a tile unit then consists of 3 principal operations: the manufacture of the tile; building the spliced fiber; and gluing the two pieces together. Quality control must be provided as needed at each stage of manufacture.

The tile pieces will be laser cut from plates of the bulk scintillator. This is a standard process prevously used by CDF, ZEUS, and others. Laser cutting provides the flexibility to produce the large number of individual tile designs needed for projective towers in a plug calorimeter, at reasonable cost. The "U" channel of size $1 \times 1\text{mm}^2$ will also be created, using the laser beam at a lower power. Prototypes obtained from Laser Services, Westford, MS (the firm which cut the ZEUS scintillator) were very successful, generating cuts and channels which are superior to those obtained by diamond fly-cutters. This technique of tile/groove fabrication was used for the constructed EM calorimeter prototypes.

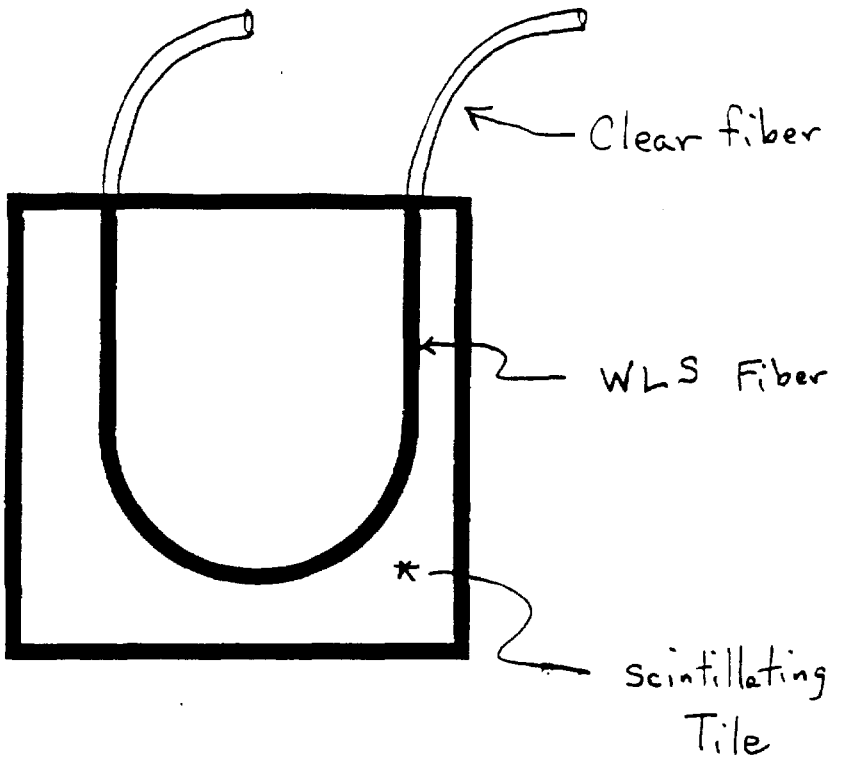

Figure 4-13: Scintillating tile with waveshifting optical fiber imbedded into it. The wavelength shifting fiber in the tile is spliced onto a clear optical fiber for readout.

After the tile pieces are formed, the edges of the tiles are painted with optical white paint. This enhances the light yield and uniformity of response, and prevents optical crosstalk from neighboring tiles.

The spliced fiber assemblies are constructed by heat-welding wavelength shifter fibers to clear fibers. The techique is as follows: First, squarely cut the ends of the fibers to be spliced. This can be done by hand with a razor blade, or in production with the fiber cutting machine such as the one built by M. Mishina and C. Lindenmeyer. (Since the ends of the fibers will be melted at the joint, the only important criterion is that the fiber cut be relatively square). Next, insert the ends of the fibers to be joined into a capillary tube which fits tightly about the fibers. Finally, briefy heat the tube to about 200 degrees F. At this point, the fibers have melted together and fused. As the joint cools, the welded fiber pulls away from the capillary tube due to its higher thermal coefficient of expansion, and can easily be removed from the tube. Initial studies indicate that splices made with this technique have optical transmissions of ~95%, with splice-to-splice variation of ~2%.

The fiber is then manually loaded into the U-channel. The tile is then clamped onto a smooth surface (mylar film) and degassed optical epoxy glue is injected into the region around the fiber through a laser drilled hole of 0.5-mm diameter through the back surface of tile at the apex of the "U".

During construction of our prototypes we measured the average light yield of the tiles by exposing them to a radioactive source and measureing the current produced by a

readout phototube. We found that the tiles were quite uniform, with a rms variation in average light yield of about 3%.

Tile Assembly into "Sectors"

The tile units are then assembled into 15° "sectors" before insertion between the absorber plates of the calorimeter. These "sectors" provide mechanical support and positioning of the tiles. The faces of each sector are covered with a wrapper/mask that optically isolates the tiles and corrects tile-to-tile nonuniformity in the manner used by ZEUS.

The entire sector assembly is then inserted into a computerized test fixture. Using a 25 millicurie Ru107 source with appropriate scintillator telescopes and/or MWPC's, one can obtain an accurate response map of a single tile in approximately 10 seconds. This response map is used to calculate the correction mask pattern, which is computer plotted onto a reflecting foil mask. Tiles that fall outside of selection criteria are discarded. The correction mask is applied to the entire assembly, and the final uniformity of the resulting sector is verified with the radioactive source. A production line for this procedure is being set up in the FNAL Scintillator Fabrication Facility (Lab 6).

Radiation Damage Issues

Radiation damage is an obvious worry for scintillator based calorimeters at high luminosity, especially at low polar angles. Substantial progress has been made in this area for the purposes of SSC calorimeters. The situation at CDF is better by a factor of more than 100, due to differences in beam energy, luminosity, total cross section and particle multiplicities.

Clearly, the new plug has to be able to survive several years of operation in $\mathcal{L} = 10^{32}/\mathrm{cm}^2/sec$ environment. At these luminosities the radiation dose is primarily due to beam-beam interactions and can be estimated fairly accurately. The maximum radiation dose is confined to a rather short region around the electromagnetic shower max, and will be of the order of 1 Mrad/year at $\theta = 5°$, and 10 Mrad/year at $\theta = 1.7°$. The radiation dose at a fixed distance from the interaction point has very strong angular dependence, $\sim \theta^{-3}$.

Our Japanese CDF collaborators, in conjunction with Kuraray Ltd. (formerly Kyowa Gas) have produced numerous samples of scintillating fiber, plate, and pellets containing new shifter dyes and compositions which are expected to exhibit significantly enhanced radiation hardness. These are undergoing testing here and in Japan, and are being incorporated in the calorimeter modules now being prepared for the test beam.

The primary effect of radiation damage to scintillator is the result of a substantial shortening of the attenuation length, due to damage of the bulk polymer. This effect is strongly dependent on the wavelength: the longer the wavelength, the smaller the effect. Thus we plan on using "green" scintillator tiles (Kyowa SCSN81 doped with Y7) for the tiles, which are more radiation resistant by virtue of the longer wavelength of the transmitted light. The waveshifting fiber will be doped with an orange dye (Kyowa O-2 or equivalent) which shifts the transmitted light further away from the spectral region in which radiation damage occurs. Multi-alkali photocathodes have reasonable quantum efficiency for these wavelengths.

Our prototypes tile assemblies using these materials yielded light levels corresponding to more than 200pe/GeV.

An elementary feature of the tile design which provides great radiation resistance is simply to keep the optical paths short, particularly for unshifted light in the regions of high radiation damage. Thus an attenuation length for unshifted light of 50cm (which would be problematic in the central EM calorimeter) would have very little effect for the 1-2cm optical paths inside the small tiles in the EM calorimeter near the beam pipe.

Prototypes, Milestones.

As described in the section on test beam results, we have built and evaluated several small prototypes. These serve as "existence proofs" of our ideas. They have also helped us sharpen up our estimates of manufactoring resources required to build the plug upgrade. (Note that we built more that 1000 tiles in our prototyping effort.)

We recognize that timely completion of this project requires rapid progress in engineering, prototyping, testing, and production. Consequently we are organizing the effort with an experienced project manager and project engineer. We will also identify people who will develop specific plans for triggering, calibration and monitoring, radiation damage studies, and mass production and quality control of the scintillators.

We are currently designing realistic prototype EM and hadron calorimeters that will be built this fall and exposed to test beams in the spring. These prototypes will have the correct projective geometry, segmentation, fiber routing and phototube placement. We will build them using techniques that are suitable for the full plug calorimeter construction (automated fiber splicing, gluing and painting jigs, "air frame" installation jigs, ...). Construction and evaluation of these prototypes will allow us to finalize our design of the plug upgrade.

In the late spring/early summer of 1991 we will place orders for the plastics, fibers, photoubes, and other required materials for the calorimeter upgrade. In parallel, we will bring on line a tile factory in Lab 6 and Lab 8 of Fermilab. Tiles will be laser cut on the Thermwood machine in Lab 8, and glued, painted, and assembled into chambers in lab 6.

After the end of the 1991-1992 collider run, the plug calorimeters will be removed from the CDF detector. The mechanical modifications required for the new plug calorimeter will be made in the B0 assembly pit. As earlier noted, these changes include strengthening the plug supports, adding 4 stainless steel plates to the plug iron, and welding in stainless inserts to cover the region below 10 degrees. When these modifications are complete, the hadron chambers will be brought over from Lab 6 and installed.

The EM calorimeters will be constructed at Lab 6. When they are completed, fall 1992, they will be taken to the CDF test beam for calibrations. Finally, in the spring of 1993, they will be moved to B0 and installed on the plugs.

Feature	Benefit
Scintillator based Calorimeter	Calibration stability. Fast time response. Energy resolution. Noise-free operation. Reduction in number of different types of electronics channels in detector.
Phototube Readout	Reliable, stable and fast trigger. Lower electron trigger threshold.
Single unit extending from 38° to 3°	Eliminates "10° crack". Eliminates the separate forward calorimeter. Muon toroids can move forward for improved muon coverage.
High-density EM section	Eliminates the 37° crack. Increases depth of hadron calorimeter.
Retain Existing Steel Structure	Cost. Minimize mechanical disturbances. No need to re-map field.
Tile Readout	Proven technology [BNL 814]. High light yield. Tower Geometry with Depth Segmentation.
Position detector at EM shower max.	Electron identification. π^0/γ separation. Photomultiplier noise spike rejection.

Table 4-4: Features and Benefits of Proposed Calorimeter Upgrade.

4.2.2 Gas Calorimeters

It is imperative that CDF always be ready to take data with a complete detector. We thus must be able to respond to unforseen technical difficulties that delay the construction of the upgrade calorimeters. During the 1990 test beam period we studied whether the gas calorimeters could operate under the conditions expected during the 1993 run ($1-2\times 10^{31}/cm^2/sec$ luminosity and 395-nsec bunch spacing). There was concern that the higher luminosity might cause the proportional chambers to go into glow mode. In addition the bunch separation would be smaller than the signal settling time during the last run.

We found that by placing a low input impedance buffer on each channel at the chamber, the effect of the large chamber capacitance can be greatly reduced. Within 400 nsec the fast component of the chamber signal (electron motion) is complete. Moreover it appears that with some amplification in the buffer, a satisfactory signal to noise ratio can be maintained when the chamber high voltage is lowered to be safely away from the glow

mode region.

Although we believe that the completed tile calorimeters coupled with full lepton coverage will provide improved physics performance, nevertheless if technical difficulties delay the completion of the upgrade, the gas calorimeters can be used as a backup for the expected 1993 beam conditions. To be prepared for this possibility, we need a buffer amplifier card that is tested and ready for production. We also must be able to use the amplifier/digitizer cards being built for the upgrade calorimeters. Consequently we are designing a buffer amplifier that can drive the phototube amplifier.

4.3 Central Drift Chamber

This section covers planned Central Tracking Chamber (CTC) modifications for data taking at higher luminosity in 1991 and 1993. Tests are in progress for these future runs. A detailed description of upgrade options and test results is given in Ref. 80. A summary is given here.

If the CTC is operated at the same gain as in the 1988-89 run, three problems occur at high luminosity: glow mode, field voltage sag, and aging. Space charge affects are not expected to be large in 1991 and 1993, and can be corrected for in software. To counter possible future glow-mode problems and to reduce aging, we plan to operate the CTC at reduced gas gain.

A new preamp for the CTC has been designed, built, and tested with a 10' long "prototype" with a single axial cell. The noise levels already measured will permit future operation of the CTC with a gas gain of 1/10 to 1/3 that used in 1989.

R&D is continuing on the preamp gain and filtering. With the resulting improvements in pulse rise and fall times and other planned improvements to the amplifier-shaper-discriminator circuits (ASD) the two-track resolution should be improved by a factor of two.

For the 1991 run we will install the new preamps and ASD's where they are most needed: in the inner three super layers. For the outer six super layers, we will keep the existing preamps but add pulse transformers to reduce noise. Additional high voltage lines will be connected to the center points of each axial field chain to reduce sag. For the 1993 run, this work will be extended to all superlayers.

It is difficult to predict the rate of aging beyond 1993. The integrated luminosity through the chamber is so small compared to that expected in the future that we have only a "point", but no "slope" from which to extrapolate. So far, no significant deterioration of performance has been observed. The reduction in gas gain is specifically intended to prevent or minimize deterioration in the future runs with much higher integrated luminosity. A bench test will be performed with the "prototype" chamber. However, given the ambiguity in interpreting such tests, we will have to be alert to these issues as the 1991 and 1993 runs proceed. If evidence for aging or other problems are encountered in the 1991 run, we will need to proceed with design and construction of a replacement chamber as quickly as possible.

4.4 Vertex Time Projection Chambers

VTPC Performance during the 88/89 Run

The VTPC operated reasonably well during the 88/89 collider run. Many modules experienced DC current leakage problems outside the active region, but this did not affect the tracking performance or cause the experiment to suffer significant dead time. The current leakage was kept under control by the addition of approximately 0.5% water to the argon ethane 50/50 gas mixture. Spatial distortions due to positive ions in the drift region at high luminosity were studied offline and for the most part corrected for in the analysis. These measurements and associated calculations indicate that the space charge distortions will make the VTPC inoperable at $\mathcal{L} > 3 \times 10^{30}$.

The spatial accuracy of the VTPC is approximately $\sigma = 400$ μm per hit at $\theta = 90°$ and degrades at smaller angles to about 950 μm at 25°. Using tracks which point within 1 cm of the z vertex position, it was found that a primary VTPC track points to the vertex with an accuracy of $\sigma = 2$ mm along the beam direction and that the interaction vertex is determined to an average accuracy of 0.5 mm. The fast VTPC vertex finding routine was updated to find multiple interactions in the same event. Due to secondaries, very low momentum particles, spirals, and possibly some residual distortions due to space charge, the routine can only reliably separate vertices spaced by about 5 cm.

VTX Upgrade in Progress

Due to positive ion distortions in the drift region, the VTPC will be essentially inoperable at $\mathcal{L} \sim 3 \times 10^{30}$, so it must be replaced for the next collider run. In addition, the structure must be rebuilt to allow space for the SVX. The new vertex chamber (VTX) will also drift electrons in the z direction, but the drift gap is smaller (4 cm versus 15 cm). Further, pads have been eliminated to reduce mass and power dissipation from the accompanying electronics. The smaller drift gap and higher drift field of the VTX reduces the positive ion distortions by almost two orders of magnitude, thereby allowing operation for at least the next two collider runs.

The 4-cm drift gap means that the VTX (using conventional gases) will be sensitive to two crossings in 36 bunch operation of the Tevatron. As in the case of the CTC, one can discriminate against tracks from an out-of-time crossing by demanding a link between cell (or module) boundaries. We will investigate faster gases (e.g., CF_4) which may allow the separation of crossings in 36 bunch operation.

The central VTX modules, including those to which the SVX is mounted, have 16 sense wires per octant (compared to 24 sense wires per octant in the entire VTPC). In all there are 18 modules with 16 sense wires per octant, and 10 modules on the ends with 24 sense wires per octant. The spatial accuracy of the VTX is $\sigma \sim 200\mu$m at 90°, about a factor of two better than the VTPC. However, the vertex resolution in the beam direction is likely to be comparable due to multiple scattering in the SVX. Fast vertex finding routines have been written for the VTX which take into account the shorter module spacing.

Alternate VTX modules are rotated by 11.3° in ϕ, so that VTX tracks can be matched to CTC r-ϕ segments in the plug region to better than the CTC's two-hit resolution ($\sim$ 2.5 mm). Because of the increased number of proportional chambers, VTX tracking in the forward region should be considerably better than the present VTPC forward tracking. The path integral in radiation lengths of the combined SVX and VTX is about 50% larger than that for the VTPC in the central region and is approximately the same as the VTPC in the plug region. Production of the chamber and associated electronics began in the fall of 1989 and will be completed in Spring, 1991.

4.5 Silicon Vertex Detectors

The importance of vertex reconstruction for top tagging has been emphasized in Sec. 3-3.2, and the profound potential for B physics with high luminosity at the Tevatron has been discussed in Sec. 3-3.4. CDF is currently building a Silicon Vertex Detector (SVX) to be installed for the 1991 run. The device, shown in Fig. 4-14, employs 4 layers of silicon microstrip

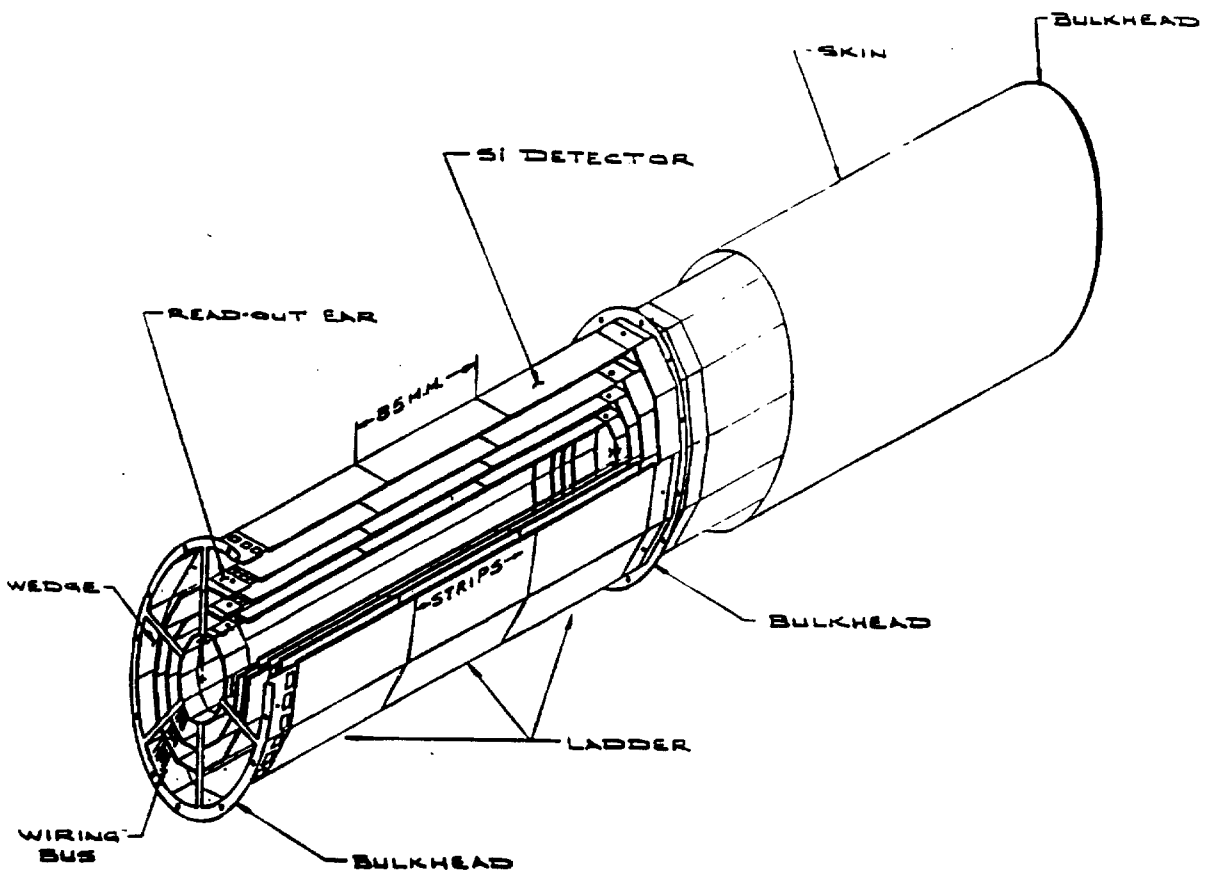

Figure 4-14: Drawing of the SVX detector.

detectors at radii between 3 and 8 cm from the beamline. Good geometric acceptance is achieved with respect to the long Tevatron bunch by implementing separate barrel arrays, 25 cm in length, on either side of the interaction point. The 25 cm barrel is acheived by a series connection of 3 microstrip detectors in length. The expected impact parameter resolution vs. track momentum is shown in Fig. 4-15; at high momentum, the resolution is 15 μ.

The 1991 version of the SVX is well into the construction phase. The device consists of 96 individual ladder modules as indicated in Fig. 4-14. At present 27 ladders

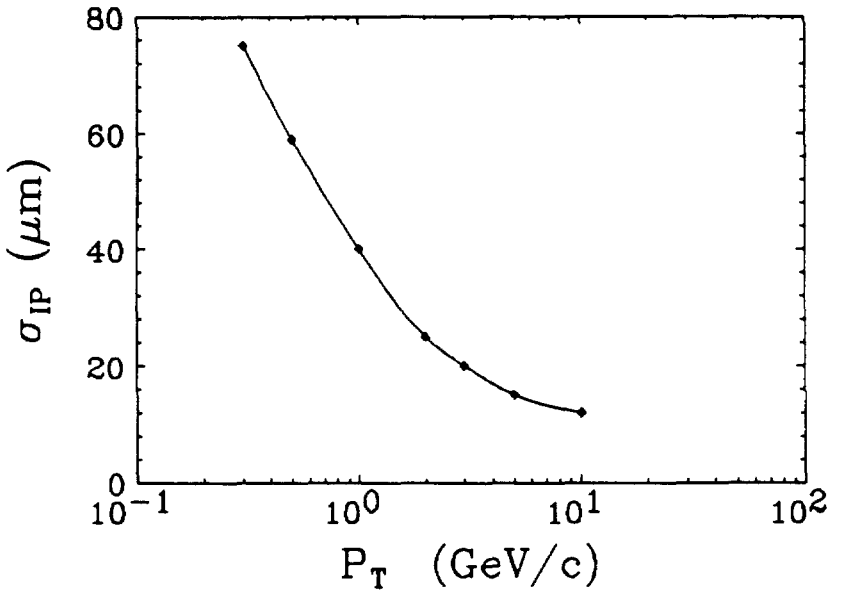

Figure 4-15: SVX extrapolated Impact Parameter Resolution vs. track P_T .

have been fabricated and of these, 25 are acceptable for use in the final array. For these good ladders, the rate of dead channels is less than 1.5% and the rate of noisy channels (usable but poor signal to noise) is less than 4%. Both these rates are seen to be improving through the production period as well. In addition, good consistency is observed among the ladders produced so far in various analog performance characteristics such as sparse readout thresholds and charge gains.

A complete four layer barrel segment, or "wedge", of the SVX was assembled and read out in the 1990 CDF test beam. A wealth of useful experience was gained in the construction and performance of the wedge. On the whole, the wedge proved to operate essentially as designed. Data sparsification in both positive and negative modes as well as the logic enabling nearest neighbor readout has been demonstrated to work. (See Fig. 4-16.) Preliminary measurements of the signal to noise and resolution are consistent with the design goals. Work is ongoing to analyze the abundance of data taken under a variety of triggers, readout schemes and detector conditions in order to further study the performance characteristics of the current design.

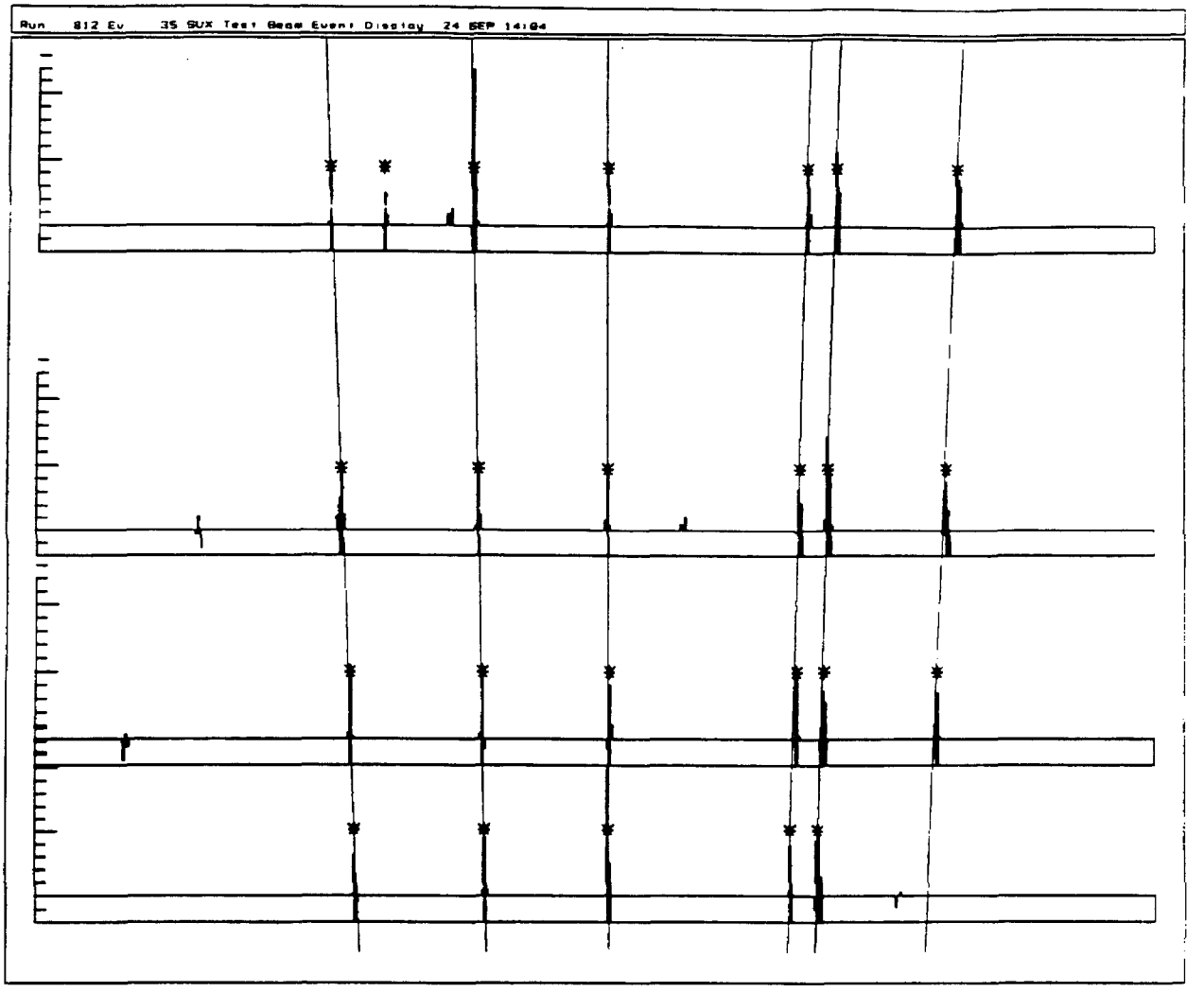

Figure 4-16: A typical test-beam event detected in a four-layer barrel segment or "wedge" of the SVX under construction for the 1991 run. A target placed upstream of the detector was used to create events with multiple tracks. The wedge was read out in negative sparse mode with neighbor logic enabled. A pedestal subtraction was performed offline. Each asterix indicates an identified hit cluster above threshold. In this event, with six tracks through four planes, there was one extra hit-cluster and one missing hit.

Essential Upgrades

The high luminosity and multibunch operation of the 1993 tevatron pose a new set of challenges to the SVX design.

1. Radiation damage to the readout chip will cause threshold shifts and increased noise before disabling the chip altogether. An appropriate rad hard VLSI technology must be used. Devices fabricated by United Technology Microelectronics Center (UTMC) using a rad hard CMOS process are currently being studied.

2. Radiation damage to the detectors will gradually increase strip leakage currents to hundreds of nA, saturating the readout chip preamplifiers in the present DC coupled arrangement. Several options currently being considered are an AC coupled hybrid connecting detectors to chips, AC coupled strip detectors, and methods of applying continuous feedback to the input preamplifier.

3. Finally, the 1.5 μsec settling time for the SVXD readout chip is clearly unsuitable for the planned 395 ns beam crossing interval. The challenge here is to reduce the signal pulse shaping time without sacrificing the signal to noise required for efficient pattern recognition and low occupancy in sparse readout.

Two general approachs are currently being pursued. One approach is to reduce the large (30 pf) detector capacitance by one third by reading out each silicon detector separately. This will make it substantially easier to achieve the required signal to noise ratio in terms of the input transistor area and power requirements. It has the additional advantage of improving the pattern recognition by adding a factor of three in segmentation. It will, however, require a significant rebuild of the mechanical support, cable connections, and cooling and can be expected to increase the amount of material in the detector. An alternative approach would be to press on the redesign of the readout chip to achieve an adequate signal to noise ratio with the present detector capacitance. This has the advantage of maintaining the current detector configuration, but can be expected to increase the power requirments. Furthermore, the noise figure attainable depends critically on the implimentation in a radiation hardened, CMOS technology.

Enhancements

While the response to the obvious technical challenges of 1993 are still being worked out, it is important to note that the 1991 run will be the first experience with a silicon vertex detector at a hadron collider. The requirements for the 1993 upgrade depend on the experience gained from this first run, as well as the physics goals for 1993. The physics goals and the vertexing requirements needed to achieve these goals must be evaluated and specified as soon as possible. It might be that the present geometry is adequate , and that the most appropriate upgrade is simply to replace the readout, maintaining the present detectors and superstructure, at minimal cost. Or we may decide that a much more elaborate upgrade is warranted.

For instance, a program of high sensitivity B physics would be greatly enhanced by the addition of a secondary vertex trigger. Such a device would have the bonus capability of tagging unexpected short-lived objects. Promising schemes with associative memories or neural networks are under development at Pisa, CERN, Michigan and FNAL, and we anticipate employing one for the 1993 run. Vertexing can be significantly improved by an inner layer closer to the interaction point. Simulation studies show a 30% increase in B tagging efficiency for an inner layer at a radius of 0.5 inches. This new Layer 0 would require a new set of silicon detectors, their associated readout hybrids and new cables, mechanical support for the new layer within the existing SVX superstructure, and a new 1 inch beryllium beam pipe. The new silicon detectors could employ the usual microstrip geometry with a smaller, 25 μm, pitch. An additional enhancement is to add segmentation in z in order to improve pattern recognition or perhaps to provide three dimensional vertexing. Two options being investigated are pixels or double sided detectors for the new inner and the outermost layer.

4.6 Muon Systems

The replacement of the CDF forward calorimeters by a compact plug design allows the toroid muon system to be moved closer to the interaction point, thereby closing a significant gap in the muon coverage. A new muon chamber/scintillator system will provide the neccessary increase in area and redundancy. The physics motivation and performance are discussed here .

Introduction

If the forward calorimeter is replaced by a compact detector inside the plug, the present 2-meter-thick toroid system may be moved 5 meters closer to the interaction point. The toroid system at the new location will provide a momentum measurement from 6° to 25°. The front and middle chambers extended to the full radius of the toroids will tag muons up to 41.5°. The proposed muon coverage is summarized in Table 4-5 and Fig. 4-17. Roughly

Muon Detector Subsystem	Angular Range (deg)	Rapidity Range	Trigger
Current FMU	3 - 7	2.8 - 3.6	not in 1989 trigger
	7 - 16	2.0 - 2.8	
CMU + CMX	41.5 - 90	0 - 1	
Moved up Toroid	6 - 25	1.5 - 2.8	track sees two toroids
	25- 30	1.3 - 1.5	track sees one toroid
	30- 41.5	1.0 - 1.3	track sees endwall only

Table 4-5: CDF Muon System Coverage

speaking, this proposal doubles the forward acceptance for many of the interesting muon production processes at CDF.

The momentum resolution of the toroid system in the new position ties on smoothly with the resolution obtainable in the central tracking chamber as shown in Fig. 4-18. Below 25°, the external toroid momentum resolution is multiple Coulomb scattering limited at 16%. In the range 25° to 30°, the single front toroid instrumented as decribed below is capable of a 30% momentum measurement at $P_T = 40$ GeV when the vertex constraint is applied. The region of overlap between the toroid and CTC measurements starts at about 14° where a muon from B0 crosses one superlayer. At 25°, a muon is observed in three superlayers of the CTC with a P_T resolution of 15% at $P_T = 40$ GeV. Thus the proposed detector configuration provides a muon momentum measurement over the entire angular range . Other advantages to the compact detector configuration include a reduction of decay in flight background below 10° by a factor of three and reduction in noise resulting from albedo from the quadrupoles.

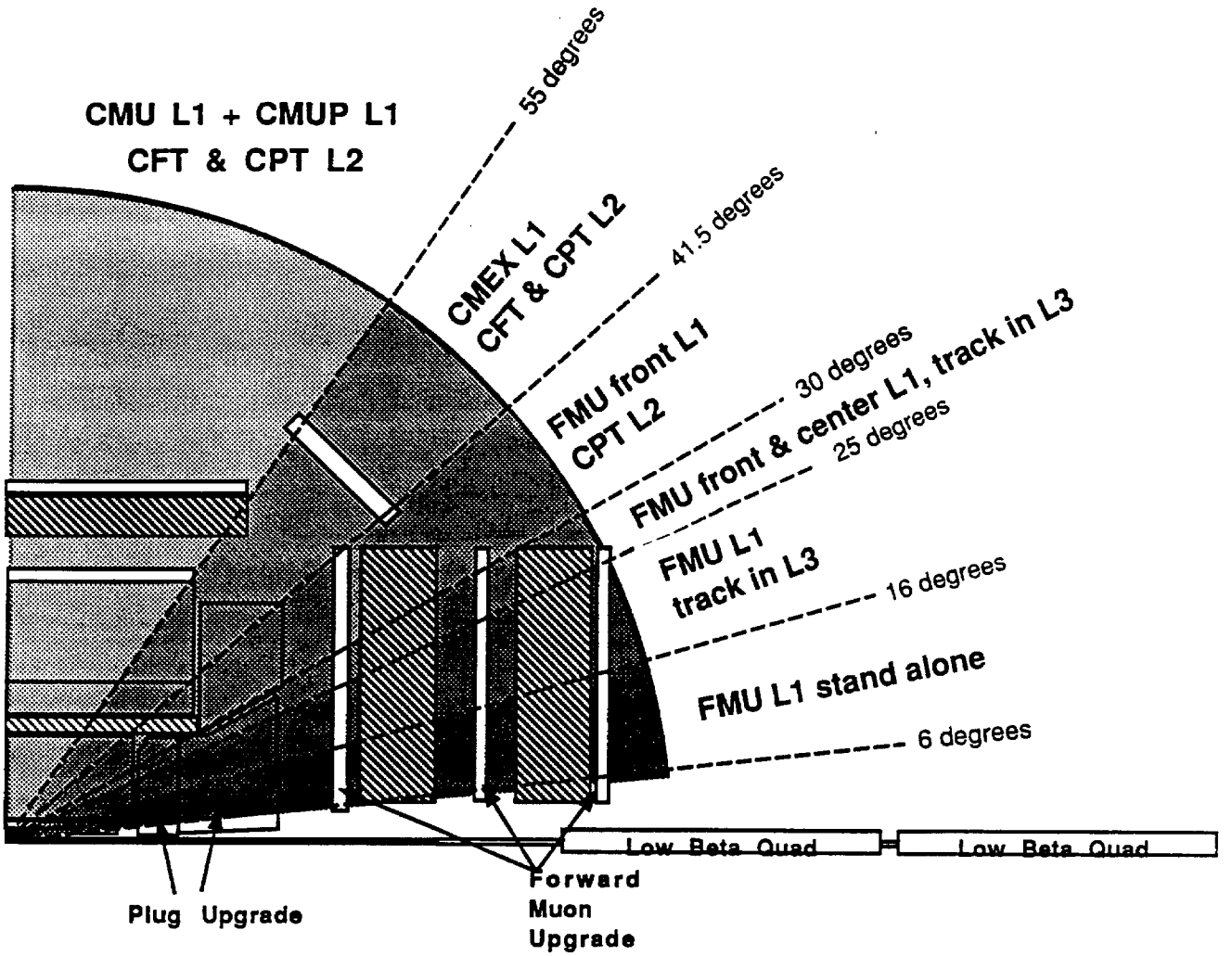

Figure 4-17: Intervals of polar coverage for the various muon systems. In each region the Level 1 (L1) and Level 2 (L2) triggering strategies are indicated. The abbreviations are as follows: CMU is the central muon system; CMUP is the central muon upgrade being installated for 1991; CMEX is the central muon extension also being installed for 1991; FMU is the forward muon system as proposed for the 1993 upgrade; CFT is a fast track recognition system (based on prompt drift chamber hits) which ran successfully in the 1988-89 run; CPT (Central Penn Tracker) is another tracking system (based on track segment finding in the drift chamber superlayers) which is planned for the 1991 run.

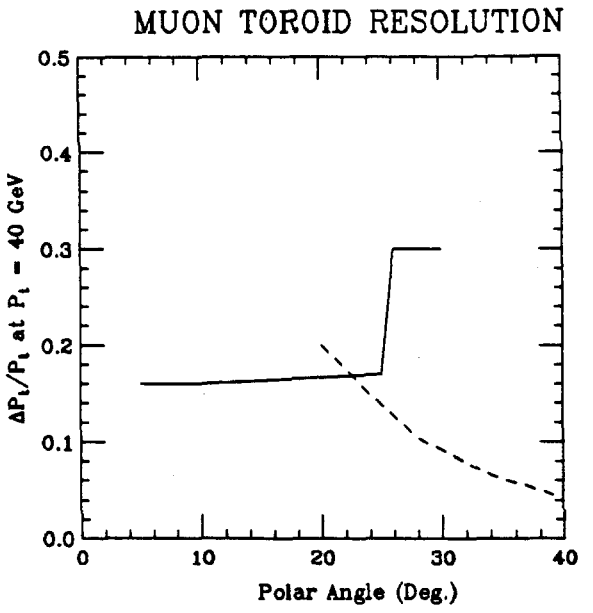

Figure 4-18: The momentum resolution $\Delta P/P$ as a function of polar angle. The solid line represents the resolution achieved from the toroid chambers alone. It has a step function at the point where tracks miss the last chamber. The dashed line gives the resolution which is obtained from the central drift chamber.

Muon Physics

Muons have played a key role in the most prominent analyses of the past run. The cleanest limits on the top quark come from the e-μ mode, and the $\mu - \mu$ and e or μ + jets + soft μ (from a B or C quark) contribute substantially to the overall limit. The one candidate we have for a top quark has two muons in it (one in the forward toroids). The high precision Z mass measurement used both e-e and $\mu - \mu$ modes, and the cross-check of having both modes was crucial. The important scale uncertainty of the calibration of the electromagnetic calorimeters was set by the mass scale of the ψ and Υ measured in the muon modes. The W mass measurement uses both the muon and electron modes, and similarly relies on the consistency of the two for understanding of the systematics of the two different lepton measurements. Searches for exclusive decays of the B meson rely on the muon modes, as well as measurements of the structure functions at very low x from Drell-Yan spectrum measurements in progress. Finally, inability to detect muons is a problem to all measurements that rely on missing $\not{E}_T$, as the P_T of unidentified muons is (largely) lost. In an experiment searching for rare new phenomena, detector hermiticity is very important. One does not want events which appear to be anomalous because $\geq$50 GeV/c of transverse momentum is carried off by a muon which is completely undetected.

The clearest goal of the collider is to discover or further limit the mass of the top quark. A $t\bar{t}$ system (produced by gluon fusion) is expected to decay to a pair of b quarks

and a pair of W's. The principal decay channels by which this process may be observed against the background from multijet systems produced by QCD processes include one or more leptons plus jets. The angular distribution of dimuons triggers from $t\bar{t}$events for various masses of the top is given in Table 4-6. Inclusion of the angular region covered by the toroid

	$Central - Central$	$Central - Forward$	$Forward - Forward$
$M_t = 100$	0.44	0.44	0.12
$M_t = 150$	0.48	0.42	0.10
$M_t = 200$	0.51	0.40	0.09

Regions:

41.5° - 138.5° "Central"

6°–41.5° & 138.5°–174° "Forward"

Table 4-6: Fraction of dimuon events of type central-central, central-forward, and forward-forward for $t\bar{t} \rightarrow \mu^+\mu^- + X$ events for various values of the top quark mass.

system in the new position increases the acceptance for single muon plus jet events by 40-50% for top quark masses between 100 and 200 GeV. The acceptance for dimuon events resulting from muon decays of both W's is increased by 95-125%. If a signal is found in single lepton or dilepton events, one may seek confirmation by tagging of the b's through their semileptonic cascade. The increase in acceptance for a muon resulting from a b decay is about 40%. Tagging of b jets through muons is expected to be important in the study of other processes including direct b production. The increased muon coverage will also benefit searches for exotic particles.

Toroids

The present system consists of a pair of one meter thick toroid magnets in both the forward and backward directions. Each toroid has an outer radius of 150" and inner radius of 18". The coils were operated with 1000 Amperes and the magnetic field varied between 1.6 and 2.0 Tesla. During the 1991 run, we intend to operate with 500 Amperes to save power with 0.1 Tesla less field. The magnet pair splits along the vertical centerline and each half may be rolled independantly. At the new location, the toroids would be positioned in front of the low beta quads. Opening the end-plugs of the detector requires that the toroid system be split apart a few feet and moved along the beam direction. It is necessary to split the toroids in order to clear the vertical support rods for the quadrupole focusing magnets. The fringe field of the magnets at the location of any proposed plug phototubes is readily shielded. It is expected that the chambers could be located as close as 4.6 meters from B0, limited by the plug support arms. The present position of the front chambers is 9.7 meters from B0.

Instrumentation Upgrade

We propose to replace the toroid muon detectors with a chamber/ scintillator system optimized for the new location . This replacement will provide finer segmentation in the scintillator trigger system, increased redundancy throughout the muon chamber tracking system for triggering and unambiguous momentum measurment, and extend the chamber area to provide a muon stub tagging capability in the endwall region. (The present system is described in Ref. 18).

We have taken the following requirements for the new design:

1. Operation with 36 bunches and $\times 50$ increase in luminosity,
2. Increased redundancy in tracking,
3. A multilevel trigger capable of a variable P_T threshold between 5 and 20 GeV.

The proposed design consists of three detector stations per end as in the present system. (See Fig. 4-19.) Each station contains a scintillation counter mosaic plane for trig-

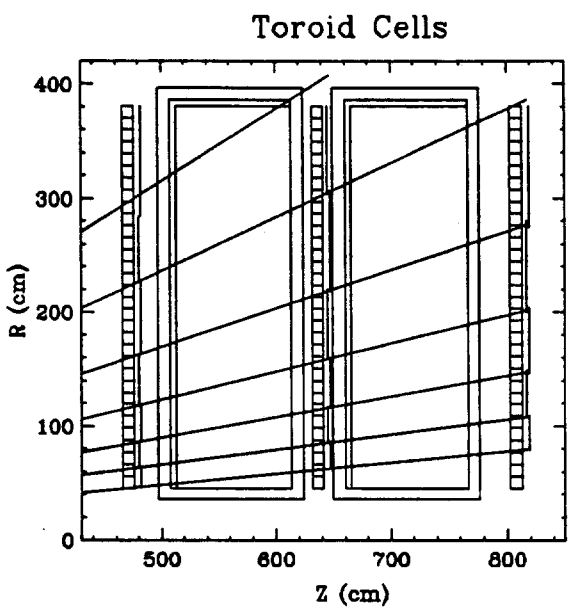

Figure 4-19: A diagram of the cell structure of the proposed modifications to the forward muon system. R is the radial distance from the beam axis. Z is the distance along the axis measured from the nominal beam crossing point - the detector center of symmetry. There are three detector stations per end as in the present system. Each contains a scintillation counter mosaic plane for triggering and for timing and azimuth measurement. Each also has a drift chamber containing four wire planes in an open cell geometry measuring drift time along the radial bend direction.

gering and timing and azimuth measurement, and a drift chamber containing four wire planes

in an open cell geometry measuring drift time along the radial bend direction. The scintillator provides a fast Level 0 trigger. The scintillator hit times will be recorded to determine the crossing number of a track. In most cases, this will resolve any ambiguities arising from chamber drift times longer than one crossing interval. The scintillator determines the track azimuth to 5°, supplanting the role of the pads in the present system. The chambers provide a muon stub at each measurement station, in contrast to the single hit pair of the present system, for improved noise rejection.

The scintillator segmentation is 5° in azimuth by about 0.3 in pseudorapidity requiring a total of 2592 channels. Three planes of scintillator rather than two are used to increase the redundancy. The segmentation corresponds exactly to the current pad segmentation and is 15 times finer than the current counter segmentation. During the 1989 run, the occupancy in two planes of 15° counters corresponded to about two counter pairs per minimum bias event. The large hit rate was ascribed to uncorrelated albedo particles from the quadrupoles. The increased segmentation is sufficient to reduce the accidental Level-0 trigger rate to several tens of kiloHertz at a luminosity of 5×10^{31}.

Two thirds of the plastic is in hand in the form of the present 15° paddles. A single 3/4" Hammamatsu phototube glued directly to each paddle without a light guide has high efficiency. In order to conserve space between the toroids, we are also exploring readout of the scintillator tiles with wavelength shifter fibers coupled to clear fibers which would run to multianode photomultiplier tubes on the outer radius. A coincidence of three projective counters defines a Level 0 trigger which imposes a very loose transverse momentum cut. As in the present system, a discriminator-base combination would be used and differential ECL logic signals shipped upstairs. These signals would be recorded in TDC's with 10 ns timing resolution thus determining the crossing and track azimuth.

The new drift chamber system doubles the number of hits per track compared to the present system by providing four radial position measurements per station with an assumed spatial resolution of 250 micron. Unlike the present system which has projective cells which increase in size with polar angle and distance from B0, the drift cells are identical in size reducing (by a factor of 36) complications in construction, high voltage distribution and monitoring, and reducing the overall channel count. All chambers extend to the full radius of the toroid. In particular, the front chambers provide a muon stub in the endwall region which may be matched to a CTC track.

As currently envisioned, the drift chambers are similar to the forward muon chambers of the ZEUS detector. Each chamber consists of an Aluminum U-channel wedge shaped frame containing 32 cells in the radial direction of 5.2 cm drift corresponding to a maximum drift time of approximately 1 microsecond in Ar-Ethane . Cells are separated by grounded foil cathode planes of low mass to minimize delta-ray production in the chamber while providing electrical and mechanical isolation. Each cell contains four slightly staggered sense wires in depth alternating with potential wires at positive high voltage and a set of field shaping electrodes. Conventional field shaping with wires or conducting strips may be used. We are also exploring the use of high resistance carbon loaded Kapton bonded to the front and back covers of the chambers for continuous field shaping.

The chambers may be constructed in overlapping octants or , as in the present system, in 15° azimuth sections with wire signals OR'ed over an octant . The number of wire channels is 6144 compared to 4608 in the current system. In the octant construction, alignment should be easier.

The number of wire planes and the open cell geometry are motivated by observations of muon track contamination in the present data. The observed probability of a delta ray or shower accompanying a muon in the present system is approximately 50%. This noise rate is reproduced by detailed GEANT simulation of the present toroids and chambers. The noise hits not only lead to possible ambiguity in the momentum reconstruction but complicate the trigger - a large trigger rate results from soft muons with accompanying delta ray hits which satisfy stiff track criteria. In order to impose a high P_T threshold which rejects such events without a multiplicity cut with its consequent 50% efficiency, the soft noise particles must be recognized and rejected on an event by event basis.

The sources and spectra of excess hits accompanying a muon signal have been studied by GEANT simulation. A 100 GeV muon exiting one meter of iron and measured with a chamber consisting of a 1 mm Al wall and 1 cm of Ar-Ethane is accompanied by one or more extra charged particles 20% of the time. This noise rate is a slowly varying function of the muon energy. Three quarters of such events contain only one or two electrons or positrons. The extra particles are produced in the last few mm of the steel or in the chamber wall with a broad angular distribution and typically several MeV of kinetic energy. Such particles are rather penetrating and can be scattered randomly by further chamber walls impeding track reconstruction. The r.m.s. projected angle of noise particles is about 25°. Even particles generated in the front chamber wall are expected to be typically separated from the muon track by several centimeters in the last plane and readily identified. While further simulation work is required, we expect to reduce the effective contamination rate to a few percent per station thereby increasing the effective track efficiency by a factor of two.

Trigger

Implementation of a high threshold trigger is complicated by the combination of the finite vertex distribution and the presence of multiple interactions - no single projective road accepts all stiff tracks and the possible vertices will not be available until L3 processing. Thus a high P_T trigger must make a measurement of sagitta not relying on projective geometry.

Representative bend angles and sagittas are given in Table 4-7. Segmentation at the level of 5 mm in radius is required at the trigger level.

The improved redundancy will be sufficent to allow the rejection of track segments at a station at wide angles to the muon direction. A complete trigger design has not been made but is expected to have the following elements:

- L0 provided by a scintillator coincidence,
- L1 consisting of separate pieces of information: a segment angle measurement for the

θ (deg)	P_T (GeV/c)	$\Delta(\theta)$ (mrad)	Sagitta (cm)
7	5	26	1.2
	10	13	0.61
	15	9	0.41
25	5	91	4.5
	10	46	2.2
	15	30	1.5

Table 4-7: Representative bend angles and sagittas in the toroid system.

fast tracking hardware with 10 ns (5 mm) resolution to provide a loose P_T cut below 25° and a muon tag in the front station between 25° and 41.5°,

- L2 high P_T trigger formed from the correlation of segments found at Level 1 between chamber stations.

The drift chamber signals are received upstairs in PSL FASTBUS TDC's and made available to the trigger via the auxillary connector. One possibility for trigger implementation is that each signal is sent to an eight bit shift register clocked at 10 megahertz. Each shift register bit corresponds to a 0.5 cm radial bin. For each station, the L0 result is used to address the corresponding range of wire data to three segment finding units each requiring three of 4 hits on a segment. By comparing to a prepared list of masks, each segment finder produces a list of segments containing segment position, angle, and quality information. A Level-1 trigger similar to the central muon stub trigger is also under consideration. Track segment information is fed to a track processing unit which performs a linear least squares fit determining track momentum and track quality information.

The inclusive muon trigger cross section estimated from present data leads to a rate of $\geq$1 Hz for a 15-GeV/c threshold at a luminosity of 5×10^{31} as shown in Table 4-8. Multiparton triggers would take advantage of lower threshold muon signals.

P_T threshold (GeV/c)	Cross section (cm^2)
5	6×10^{-32}
15	6×10^{-33}
20	2×10^{-33}

Table 4-8: Estimated trigger cross sections in the toroid system.

Mounts

Reproducible chamber alignment is extremely important to the momentum resolution above 100 GeV and nontrivial for a system of this size where straightthrus do not exist. To ease this problem we anticipate mounting the chambers directly on the toroids to reduce the number of degrees of freedom. The counter alignment is much less critical and we would suspend the counters from the existing movable chamber support system. It may be also possible to incorporate the scintillator onto the rear face of the chamber module.

Resolution

The expected momentum resolution as a function of momentum has been estimated, taking into account multiple Coulomb scattering correlations in an optimal fit as described in Ref. 81. In Fig. 4-20, the solid curves (a-d) show the resolution for muons below 25°. The two

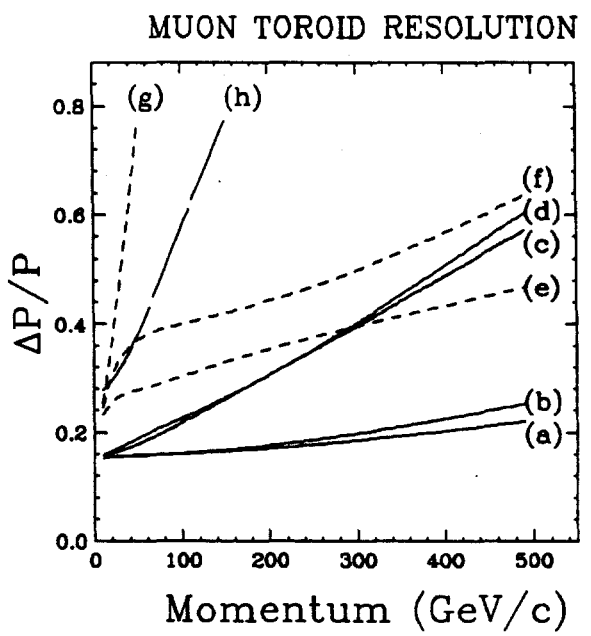

Figure 4-20: The expected momentum resolution as a function of momentum. The various curves are explained in the text.

lowest curves (a-b) show the resolution with and without the constraint of a vertex provided by the VTX chambers. With the assumed spatial resolution of 250 micron per wire, the resolution is multiple scattering limited for all momenta accessible to this experiment and the vertex constraint does not provide a significant improvement. The upper curves (c-d) show the resolution for 2-mm spatial resolution corresponding to a 1-mm alignment error. The actual resolution should lie between these sets of curves.

The dashed curves (e-h) show the resolution for muons between 25° and 30° which pass through only one toroid. In this angular region there is good CTC coverage for momentum measurment but a sign determination would be a useful check in matching tracks. The

short dash curves (e-g) assume 250 micron space point resolution. The uppermost curve (g) is the resolution of the entrance and exit angle measurments of the toroid chambers alone. The middle curve (f) shows the effect of including the vertex constraint. Above about 40 GeV, the multiple scattering in the plug calorimeter is sufficently small that the vertex and entrance point have sufficient lever arm to give a good entrance angle measurement with the middle toroid chamber providing an exit point measurement. The bottom curve (e) results if the polar angle measurement of the VTX chamber is included. The long dash curve (h) shows the case in which the vertex and VTX stub angle are included and the toroid chamber spatial resolution is degraded to 2 mm. In order to resolve the sign of 100 GeV muons in the toroid in this angular region, submillimeter alignment errors must be achieved .

4.7 Data Acquisition Electronics

Plans for a new data acquisition system for CDF began early in 1989 and settled into something like their present form at the Breckenridge workshop in August, 1989. A lengthier discussion of those plans can be found in Ref. 82. This section summarizes the broad features.

Design Guidelines

The principal constraints driving the design for an upgraded CDF data acquistion system (DAQ) are the increased luminosity and the modified bunch structure in the upgraded Tevatron. Further, we wish to enhance the strengths of the present system, and to eliminate its weaknesses. Below are listed the assumptions and global criteria and goals used in the design concept presented in this section.

1. Tevatron Luminosity $\mathcal{L} = 10^{32}/cm^2/sec.$

2. The bunch crossings will be spaced at 395 nsec intervals, with some larger gaps between groups of crossings.

3. The capacity to handle events to be digitized and sent to Level-3 will be > 100 Hz.

4. The dead time during system operation at 100 Hz will be $< 16\%$, with individual goals of 5% for Level-0 and Level-1, 5% for Level-2 trigger, and 6% for scanning.

   - This requires an on-detector Level-0 trigger and
   - a zero-dead-time pipeline at the front end.
   - Digitizing and transfer of data to buffers must be accomplished in 0.6 msec or less.
   - All subsequent parts of the DAQ system should have sufficient bandwidth and buffering to avoid any further dead time.

5. The system up time, i.e. time available for actual data collection as opposed to calibrations, startup and other non-data operations, will be $> 95\%$ of delivered usable beam.

6. Each calorimeter front-end amplifier card will have its own 16-bit ADC. There will be no digital traffic on these cards during conversion.

7. Transport through the DAQ will be data-driven, i.e. there will be no holdup in transmission when both data and an available transmission channel exist. This implies the following design guidelines:

   - parallel paths from each Rabbit crate or SSP to a FIFO data concentrator,
   - parallel paths (4 to 8) from the FIFO data concentrator to Level-3.
   - data flow should be driven by state registers, pre-loaded scan lists and pre-loaded destination address stacks wherever possible;

- control communication governing data flow should be limited to nearest neighbors wherever possible, and should be accomplished by direct connections rather than by system-wide broadcast messages;
- All channels will be digitized and sent to Level-3 for each event. Channel addresses will not be part of the data. The additional bandwidth required is more than offset by elimination of the delays involved in formation and downloading of scan lists for each event.
- Level-3 processors will be responsible for any *in situ* manipulation of data which is required. Such functions include sparsification, application of pedestal and gain corrections, calibration, re-formatting and YBOS bank formation.

8. Control functions and data flow will occur on separate paths in the DAQ during data acquisition. This restriction will not necessarily hold during run initialization.

9. The present capability to partition the system for calibration and debugging will be maintained.

10. The design must provide for calibration, monitoring, error reporting and diagnostic functions.

    - It must be possible to connect diagnostic tools, such as a PC, from the control room to the front-end cards.
    - The states of the front-end, FIFO data concentrator and Level-3 must be available continuously in one place for operators and for error-detecting programs.

11. The output event rate to tape must be increased to at least 10 Hz total capacity by providing parallel output streams.

12. The system should be expandable, i.e. there should be provision to add new detector subsystems and associated readout, more bandwidth to the data paths by additional parallel channels, and more computing power in the form of more and faster processors.

Overall System Description

Figure 4-21 gives an overall block diagram of the system. The two major subsystems of the detector, tracking and calorimeters, present somewhat different problems and are shown separately. The calorimeter front-end analog-to-digital converters (ADC) and associated electronics reside in the Rabbit crate system located on the detector. Time-to-digital converters (TDC) exist at present only for the central hadron calorimeter phototubes (CHA), but will be added for all phototube towers in the upgraded detector. TDC's for tracking are commercial Fastbus modules located outside the collision hall. In our design, data from these devices is moved in parallel over roughly 160 to 200 parallel cables (> 1 GB/sec total bandwidth) to FIFO buffers at the input of data concentrators Thus, extremely high bandwidth exists from the front end to the first multi-event buffer.

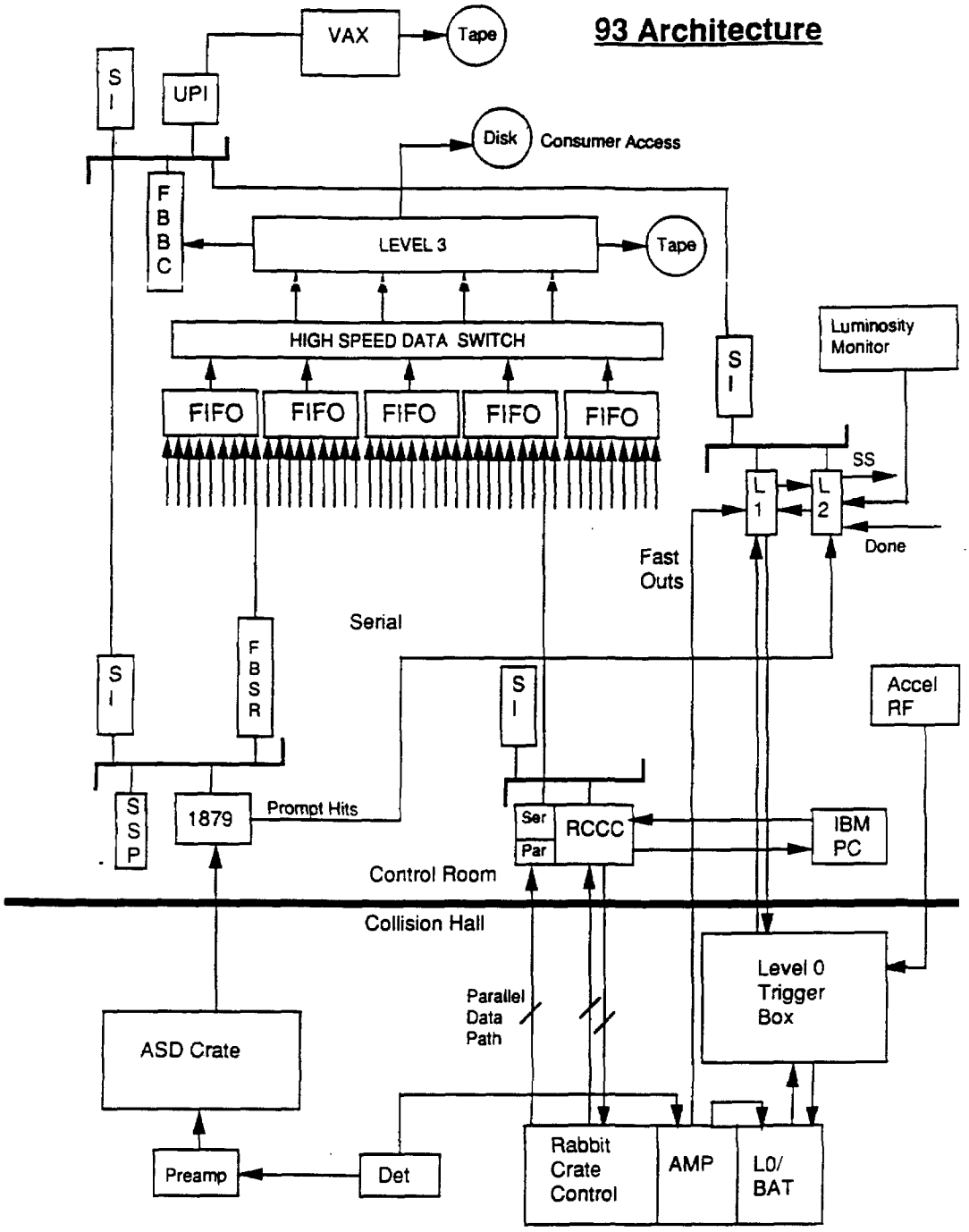

Figure 4-21: Block Diagram of the major components of the proposed CDF data acquisition system. Over 130 Rabbit crates contain the front-end electronics and ADC's for calorimeters. Data from the TDC modules (1879's) are collected in roughly 30 SSP modules in Fastbus. Data cables from each of the Rabbit crates and SSP's carry the data in parallel to the scanner/data-concentrator where all data from a single event are buffered and routed to a Level-3 processor, and, if the event is accepted by Level-3, to tape. The dedicated data paths are shown as groups of parallel lines. Separate dedicated paths exist for triggering and control.

The data concentrators gather data from a subset of the crates (Rabbit or Fastbus) serving the front end systems and concentrate them into a large fragment of the total data for a single event. We estimate six to eight such devices will be needed, depending on details of the technical design. Each communicates over a separate high bandwidth connection to a high-speed data switch which routes the event fragments to the proper buffer in the Level 3 farm.

The switch is not defined at present. At least three candidate designs have been proposed by technical groups at Fermilab. We are also investigating the applicability of commercial switching systems rated at the appropriate overall bandwidth.

All technologies under consideration have the feature that all cables to the Level-3 farm can be operating simultaneously. The Level-3 farm consists of an event-oriented multi-processor architecture with high-speed I/O and large CPU power. It is discussed at greater length in a later section.

The following sections deal with individual components of the system. Parts of it already exist in the present system and meet the criteria we have established. These will be retained.

Front End Calorimeter Electronics

The design guidelines above implied several changes in the characteristics of the present front end electronics. We expand that discussion here.

1. **A local Level-0 Trigger is required.**
   There is no longer enough time between crossings to send analog signals upstairs to make a trigger decision. A local Level-0 trigger must be provided on the front end that is capable of making a trigger decision every 395 nsec and that incurs no dead time until a Level-0 trigger is accepted.

2. **Zero-dead-time front-end pipelines are required.**
   Presently, with the exception of the LeCroy TDC's which can buffer one event, there is no buffering of events in the front end. Even with a local Level-0 trigger, it will take some time to process the event, and get a signal back to the front end gate control to stop the acquisition of signals. This implies that the front end will need pipelining or buffering to store events while Level-0 makes a decision.

3. **Increased readout speed is required.**
   As the interaction rate increases, the readout speed must be increased to keep the dead time below the 6% limit. At 100 Hz, the system must be capable of reading out an event from the front end in 0.6 msec. This limit is defined by the capabilities of the LeCroy TDC's which will be read out in parallel with other elements of the front end electronics.

4. **Optimize data flow path to Level-3.**
   The present data flow path is over the Fastbus network, where data transmission

requires bus arbitration in a network carrying other traffic. To reduce the data burden on the network, two time-consuming operations are performed on the critical path. The data are sparsified by the front-end scanners to reduce event size before transmission to the Event Builder. Subsequently, the Event Builder must unscramble the data before the event can be built. For better efficiency and speed, separate, highly-parallel data paths are to be provided for the front end to push data directly, with no processing to a "FIFO data concentrator" for routing into Level-3, bypassing the Fastbus network. Sparsification, pedestal and gain corrections, re-formatting and YBOS bank formation can be done in Level-3 which is highly buffered, highly parallel and easily expanded.

Interface to the Trigger System

One of the design criteria is to keep as much of the existing system intact as possible. Given the limitations of the present front end circuitry, it is clear that most of these boards must replaced. The trigger electronics, on the other hand, is fully developed and well integrated into the rest of the system. If we add a Level-0 trigger to provide a rejection factor of about 200, then Level-1 and Level-2 could continue to function as they do presently, 15 KHz into L1, 5 KHz into L2.

Retaining the trigger system implies keeping the analog-based fast out cables connected to it. This means that those detector systems that have fast outs in the present system will continue to have this circuitry on them in the upgraded system, including the cable connections to the Level-1 processors. The same characteristics which presently govern their operation will continue to apply.

RABBIT Electronics

The front end must provide some method of storing events locally, long enough for a Level-0 trigger decision to be made. That capability does not presently exist. Thus, all front end cards in the RABBIT system must be replaced. This includes approximately 2500 amplifier cards, 150 crate controllers, and 150 BAT gate generator modules. We plan to retain the RABBIT crates and 400 Hz power supplies.

The front end channels will need to have analog memory elements in order to provide time to make a Level-0 decision. The best estimate for the length of storage needed is 1.2 μsec, or three events deep at the 395-nsec cycle. This is based on the estimated decision time required in the Level-0 electronics and associated cable and propagation delays. It is proposed to use analog delay lines for the implementation. These devices have been around a long time, are well understood, and are relatively straight-forward to implement. Further, there are several existence proofs that a large system using analog delay lines can be built and operated to 14 bits of precision. A recent example of this technique is the liquid argon calorimeter electronics for E706 here at Fermilab, which has 10,000 channels. Delay elements of 1 or 1.5 μsec are feasible, with delay/risetime ratios in the range 6 to 10.

The analog delay line configuration is shown in Fig. 4-22. The device has a 395 nsec tap that is used to form the signal that is sent to the Level-0 trigger. The event continues

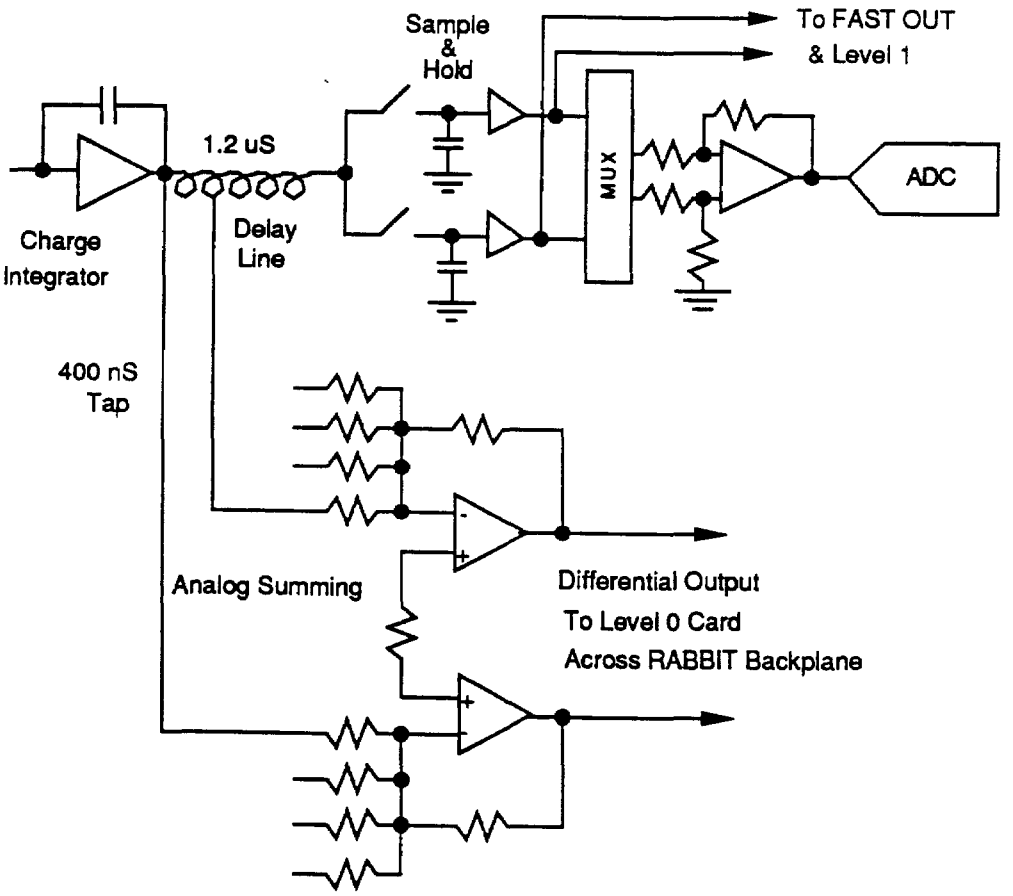

Figure 4-22: A circuit diagram of the basic elements of the proposed front-end electronics. Included are: pre-amp, 1.2 μsec delay line with a tap at 400 nsec for fast output to the Level-0 trigger, the before-after sample-and-hold circuitry gated by Level-0.

down the delay line, to emerge at the time that a Level-0 decision has been made for that event. Either the sample-and-hold switches are opened, thereby capturing the event, or they are left closed to wait for the next event.

Cost estimates are in the range $5.00 for a delay to risetime ratio of 6, to $15.00 for a ratio of 10, in quantity. Since it is not possible to purchase these devices off the shelf, an R&D effort needs to start early in the project to work with any interested, qualified vendors to ensure that the part will meet the specifications.

Other possibilities for the analog memory are the use of switched capacitors as an analog ring buffer or a linear pipelined array. Switched capacitor techniques are emerging as viable analog storage methods. However, they are typically realized in ASIC designs, which represent a substantial development project. Also, there are questions about the precision, calibration, and complexity of these schemes, given the need for continuous clocking and the fact that the capacitors are on the chip. For these reasons the switched capacitor schemes are not proposed as the primary implementation of analog storage elements on the front end.

Having provided a way to store events in analog form locally on the front end, circuitry must be provided to form a Level-0 trigger. The approach is to treat each RABBIT crate as a unit in which Level-0 trigger towers can be formed. This is accomplished by analog summing of the appropriate calorimeter channels to form a trigger channel. Thus, Level-0 looks for single trigger towers over one or more thresholds as a means for making a decision.

To form a Level-0 trigger we plan to send analog signals from all of the trigger channels in a crate to a special Level-0 receiver card located in the crate. These cards receive analog signals from the front end cards, each pair of which is dedicated to a single trigger tower formed on the front end cards. The analog signals are then input to comparators, where several thresholds may be applied. This scheme essentially incorporates much of the functionality of the present Level-1 trigger into Level-0. The ability to mask off individual trigger channels is provided for on this card. Also, it would be necessary to have an independent read out path that is separate from the normal data acquisition system, for checking the performance of the Level-0 circuitry.

Concerning the front end scanning, one of the specifications is to read out the detector in 0.5 msec to the precision that we presently have (16-bit ADC with 14 bits precision.) Given the present technology of ADC converters, it is difficult to achieve this goal without adding more ADCs to the crate, working in parallel. The proposal is to put an ADC on every front end card in the crate. The compact disk industry has created a huge market for 16-bit ADCs, driving the cost down far enough so that it is feasible to consider such a scheme. (Burr Brown presently has a 16-bit monolithic ADC which has 14 bits of precision and sells for under $50.00.)

With this scheme, every channel is digitized without doing any pedestal subtraction or data sparsification. These functions would be performed in Level-3. This has the advantage that pedestals are taken in the same way as data, thereby reducing errors associated with performing these functions differently. Also, this scheme has the potential of reducing the event building operation, since data are always sent to Level-3 with the same channel structure.

As an estimate for the time required to perform a readout operation, consider a typical crate with 20 cards with 32 channels on each card. The ADC mentioned above digitizes in 4 μsec, with 2 μsec additional time needed per conversion for settling. The time to digitize a 32 channel board is then 192 μsec. If all boards are digitizing in parallel, the digitization time is still 192 μsec. The parallel digitization will be done synchronously by a clock line across the RABBIT backplane, driven by the new gate generator module.

The digitized data from each channel are stored locally on each board. The memory of each card is read out sequentially after all of the digitizers are finished. The read operation is a 16-bit parallel data transfer across the RABBIT backplane, controlled by the new RABBIT crate controller which contains the scan list. This is attractive in that it minimizes the digital activity during the conversion process. If 16-bit words can be read out across the RABBIT backplane in 100 nsec, then for the above example it would take an additional 64 μsec to read out the 640 channels, for a total of 0.25 msec. Additional overhead is estimated to be approximately 0.25 msec, for a total of 0.5 msec.

The front end crate controllers push the data upstairs over a unidirectional, dedicated bus. It is desirable to make this a parallel bus, since the data push operation is simplified. Serial transfers tend to be more complicated than a parallel transfer, and require synchronization and clocking that are otherwise unnecessary.

The link to Level-3 would bypass the MXs and Fastbus. The data are pushed up the cable to a module that contains a FIFO from which it is routed to one of the parallel Level-3 nodes for pedestal subtraction, threshold testing, event building, and other processing. Note that this implies getting rid of the MXs, and shifting the distributed functionality of the combined EWE/MX/Fastbus system that we presently have to a central location in Level-3, where the processing power is expected to be capable of handling these operations with very little additional overhead.

The MXs are to be replaced by a module that interfaces between Fastbus and the RABBIT crate controller. The new function of this interface is primarily passive during data-taking, being active only to issue start scan messages and to receive the DONE signal back. It is used for downloading the scan lists at the beginning of the run, running diagnostics, and providing the readout path for the special trigger functions. It also acts as an interface between the RABBIT crate and a personal computer to perform other diagnostics.

In principle, the module that contains the FIFO that receives the digitized data from downstairs could be part of the system that interfaces between Fastbus and the RABBIT crate controller. This would make the packaging problem easier, and also enhances the ease of debugging crate problems. However, there must be no interference in the flow of data from the RABBIT crate controller into Level-3 by the Fastbus interface during data taking. Any monitoring of the data flow must be entirely passive at this point in the system, except to disable the data flow entirely.

Tracking Electronics

The LeCroy 1879 TDC's are used in the tracking systems in CDF, as well as the muon systems. The present plan calls for these detectors to be retained in the upgrade, albeit in a modified form. The electronic requirements will be similiar to the present configuration. The electronics consists of preamps on the chambers, Amplifier-Shaper-Discriminator (ASD) boards which receive the preamp signals, LeCroy 1879 TDC's, and the SSP scanners which read out the TDC's.

Some of the preamps and ASD cards for the CTC system will be changed for the run in 1991 as described elsewhere in this proposal. Concerns about running at the increased rate in 1993, i.e. saturation, rise and fall time response, and baseline shifts are being addressed in these modified designs. The VTPC will be replaced by the VTX for the 1991 run, so it will have new preamps to begin with. The new muon systems will also have new preamps, which are being designed to operate in the upgraded environment. The ASD cards which receive the preamp signals are satisfactory for operation in 1993.

The LeCroy 1879 TDC's presently take 0.6 msec to encode the hits from all 96 channels on a board. It then takes 250 nsec per data word read into the SSP. Each hit produces two data words, one for the leading edge and another for the trailing edge of the chamber pulse. The pulse width information is used offline to reject chamber afterpulses and other spurious hits. These pulses tend to be narrower than genuine hits. Presently, a typical event produces 2200 hits per SSP in the CTC. The total dead time is 1.7 msec, (0.6 msec for TDC encoding and overheads, and 1.1 msec to read the data from the TDC's.) Given that the upgraded accelerator runs in the 36-bunch mode, implying that the number of interactions per crossing is comparable to what it is now, it is anticipated that the number of hits per event will not dramatically increase. Thus, the system as presently operated misses the dead time goal of 0.5 msec by a factor of almost four.

There are several options available to make the Lecroy TDC's work in the upgraded system. One is to do away with the double reads of each hit channel. An unanswered question concerns what effect this will have in the off line analysis. Another option is to use the double buffer feature in the TDC's. The encoded data is stored in a separate buffer in the TDC so that it is possible to make the TDC live again immediately following completion of encoding. This presumes that the buffer can be read before another digitization occurs. There is also a question about noise sensitivity of the live TDC's to the digital traffic generated by the encoding process. Another possibility is to increase the number of SSP's to achieve the faster readout rate.

New Devices involved in Front End Electronics

- RC2 - Rabbit Crate Controller is the device which resides in the Rabbit Crate and provides control access to the front end cards. It controls the digitization of each channel and provides the parallel data path to the data concentrator.
- RC3 - Rabbit Crate Controller Controller resides upstairs and provides a read/write control path to the RC2 and the front end cards. Everything that is hardwired at the

crate level can also be controlled remotely from the RC3. In one option under consideration, the functions of this controller may be combined with that of the FIFO/Data Concentrator.

- FIFO/Data Concentrator. This is a key device in assembling data from Rabbit and Fastbus crates into large event fragments for transmission to Level 3. The number of lines coming into it will be of order 16 to 32 depending on details of available board real estate. Each incoming line is served by a FIFO buffer to store the data along with headers and trailers containing event ID and partition information. The data concentrator sequentially transfers the data for a single event from each FIFO to the output line along with routing information to direct it to the proper buffer in Level 3.

- Data Switch. As mentioned earlier, several options for this device exist. Our primary efforts at present are to define it so that details of the rest of the system can be designed.

- SSG - Start Scan Generator. This device has been specified, but is not yet designed. It controls the front-end readout.

Level-0 Trigger

The final Level-0 trigger logic collects the signals from the Level-0 cards in each front end crate and then makes the Level-0 decision. It will accept electrons, muons, jets and low threshold dileptons. Preliminary designs for the Level-0 trigger are described in CDF Note 1167.[83]

Level-1 and Level-2 Triggers

There is a strong desire to retain as much of the Level-1/Level-2 trigger system as possible. The requirements to do this are:

1. The signals from the detector must be made available in analog form and correspond to the $\eta - \phi$ mapping of 0.2 by 15°.

2. The tracking system must be able to provide a list of stiff tracks in a few μsec.

3. The muon systems must be able to provide a list of muons (η, ϕ, and momentum) within a few μsec.

4. The method of making decisions based on a list of items generated by the cluster finder must still be valid.

The trigger is designed around a detector geometry of 0.2 units in η by 15°. This mapping is repeated for electromagnetic and hadronic calorimeters. Also the muon and track hits are mapped into the same geometry. New detectors in CDF will generate trigger signals in the same organization.

The tracking system currently reconstructs stiff tracks in a few μsec. The tracks are used in the trigger system to identify muons by matching with the muon chamber hits and electrons by matching with electromagnetic calorimeter clusters. This ability will be exploited even more heavily in order to achieve improved rejection rates in the Level-2 trigger.

For electrons, we are already investigating matching either the wires from the strip chambers or the preradiators to tracks, as well as more sophisticated pattern recognition of electrons in the calorimeters. There is a large factor to be gained in the number of $B \rightarrow e$ inclusive decays we could accumulate. This is under intense investigation now. We are using our present data to develop the best strategy. We will use the 1991 run and its data as a testbed for these ideas.

The drift times in the muon chambers will be large compared to the Level-0 decision time. Scintillators will be added to the muon system in order to generate the Level-0 trigger. These signals will not have enough geometric resolution to be useful in Level-2, consequently there will be separate trigger signals generated for Level-2 which have position and momentum information. This will be used along with the tracking and calorimeter information in the Level-2 trigger to identify muons in various $\eta - \phi$ regions. Figures 1-3, 1-4 and 4-17 illustrate the strategies used in various ranges.

A factor of four speed improvement in the Level 2 processors from the 1988-1989 run is expected for the 1991 run. This will reduce the time associated with the Level-2 decision but does not increase the rejection factor. Additional rejection is required for the operation at luminosities of $\geq 5 \times 10^{31} cm^{-2} sec^{-1}$. Studies of additional algorithms which can be implemented are in progress. For example, beyond 1993 the electron algorithm could be improved if the strip chamber information from the EM calorimeters were available in the Level-2 trigger.

Luminosity Monitor

There are two components used in measuring the integrated luminosity: the live time and the instantaneous luminosity. The measure of live time will be kept in the Level-0 decision crate. In previous CDF runs the primary measure of luminosity has been the beam-beam counters. These will become less useful as the average number of events per crossing approaches 1, roughly 6×10^{30} for 6 bunches and 36×10^{30} for 36 bunches. These will be augmented by four counter telescopes, each with an effective cross section of 0.4 mb, one-hundred times smaller than that for the present system. The new monitors will be cross-calibrated with the BBC's at luminosities below $10^{30}/cm^2/sec$. The BBC's will still retain the ability to tag halo particles associated with the incoming beam.

Accelerator transducers can be used to calculate what the luminosity should be, using the individual bunch intensities, the β^*, and the beam profile from flying wires. The present accuracy is about 7%, and we believe that this can be improved.

4.8 Level 3 Trigger: Online Analysis and Event Filtering

Table 4-9 gives a list of operating parameters for the Level-3 micro-processor farm as it was configured for the 1988-89 run (see Fig. 4-23), along with those planned for subsequent runs. The 1988-89 version of Level-3, based on Fermilab's VME-resident ACP-I system, was rather well matched to the capacity of the DAQ system, trigger algorithms and output tape capacity during Spring, 1989. At that point, a rich set of programs used most of the available memory and CPU time in Level-3. For the 1991 run, both the event rate into Level-3 and the computing time per event are expected to increase to the point where 300 to 500 mips of CPU power will be required.

Quantity	1988-89	"1991"	"1993"
Event Rate (Hz)	~4	30	100
CPU-time/event (mips-sec/event)	9.2	15	≥30
Total mips needed	37	500	≥3000
Processor Type	68020	R-3000	R-?000 or ?
Processor Speed (mips)	0.8	15	50
# Processors	58	32	≥ 64
Total Capacity (mips)	46	480	≥ 3200
Real time/event (sec)	11.5	1	≥0.64
No. Branch Bus Cables	1	2	4
Event Size (MBytes)	0.15	0.25	≥0.3
Data Rate (MB/sec)	0.75	7.5	30

Table 4-9: Level-3 Parameters For Recent and Future Runs

To provide this, we have decided to replace ACP-I with RISC-based microprocessors, interfaced to VME, with at least 15 times the CPU power of ACP-I. This offers a natural growth path for subsequent runs in 1993 and beyond. Two options have been studied, both based on the MIPS Corp. R-3000 processor: ACP-II or Silicon Graphics. We have connected both to the DAQ network with interfaces to Fastbus and the Farm Steward μVAX. Data have been written to and read from memory with verification for periods of order 24 hours with no detected data errors. The data rates are consistent with rated bandwidths of the data channels, 10 MBytes/sec or above in both cases and more than sufficient for our needs. Details of directing and control of data flow all appear to be straightforward. Results to date indicate that, while either will work, the Silicon Graphics system is the better choice, and we assume that in subsequent discussion.

The Level-3 architecture planned for the 1991 run is shown in Figs. 4-24 and 4-25. There will be two event builders, each pushing data over a branch bus to half the Level-3 Farm. Control and communication with the DAQ supervisory process will continue to be

done by the Farm Steward. Data output will be to several streams:

- An express-line stream at about ~1 Hz through the VAX system and onto Exabyte 8500 8mm tape drives.
- A "solid-gold" subset of the above, top candidates and other highly interesting events, will be logged to disk and retained for several days for closer examination.
- A non-express-line stream at up to ~8 Hz onto four Exabyte 8500 8mm tape drives in parallel directly from Level 3, without event-by-event intervention from the VAX.

This is discussed at greater length in the following section dealing with RUN_CONTROL.

We plan to confront all the technical problems of Level-3 in time for solutions by the 1991 run so that the 1993 architecture (Fig. 4-26) will be an expansion of the 1991 architecture:

- Expand to four the number of branch bus cables into Level-3.
- Expand the number of processors in Level-3 to 64.
- Take advantage of any faster processors available at the time, e.g. the MIPS R4000 will soon be on the market and is rated at 50 MIPS.

A number of design issues are being worked on and seem to have viable solutions with the tools at hand:

1. Efficient polling can be accomplished by putting the present VME crate controllers (in slave mode) on the Silicon Graphics VME bus.
2. Expanded buffering can be handled in the Silicon Graphics memory with local buffer management.
3. Diagnostic programs have been re-written for the Silicon Graphics I/O and memory architecture and are being used in present tests.
4. The primitive operations needed for run startup, program loading, database access, etc., have been tested successfully. Plans are being made to integrate them into the Farm Steward and similar processes.
5. Test Stand simulation of the DAQ system message traffic with Level 3 should be re-written for Silicon Graphics by Summer, 1990.

At this writing, development of this new architecture for Level 3 is progressing amazingly well. We see no insurmountable problems for its timely implementation in a rather conservative design. A number of potential commercial developments have been discussed which would provide far more flexible and reliable operation at extremely high bandwidths in the future.

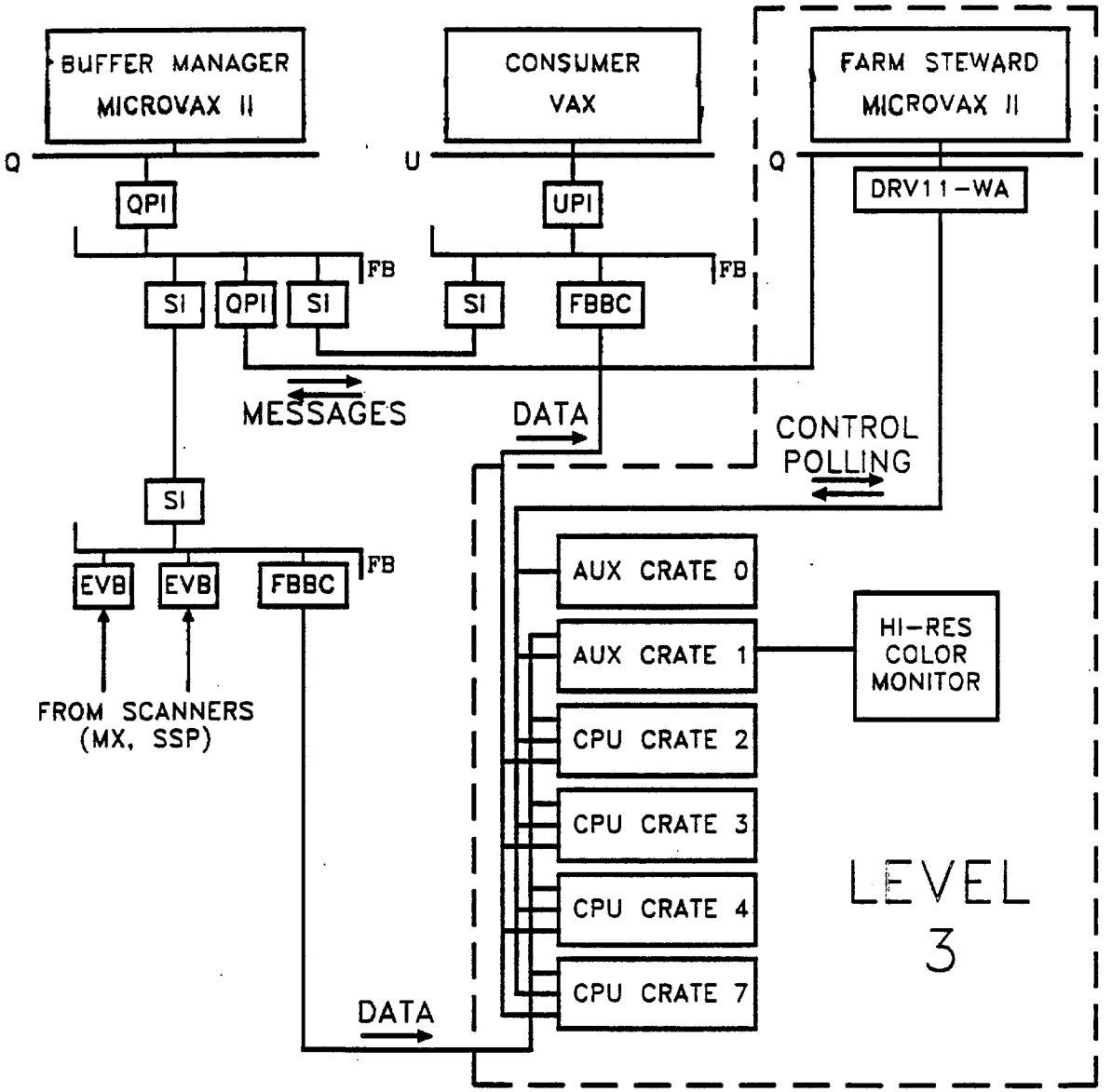

Figure 4-23: Relationship of the Level 3 VME crates to the DAQ system in the 1989 Run. Three branch bus lines provided high speed connections into VME crates for data input from the Event Builder (EVB), control, downloading and polling by the Farm Steward, and data output to the Buffer Multiplexer. The Farm Steward exchanged Fastbus messages with the Buffer Manager to direct the flow of event data to/from the individual nodes in the VME farm. It also sent messages to a specially equipped farm node which controlled a video monitor to display the farm status.

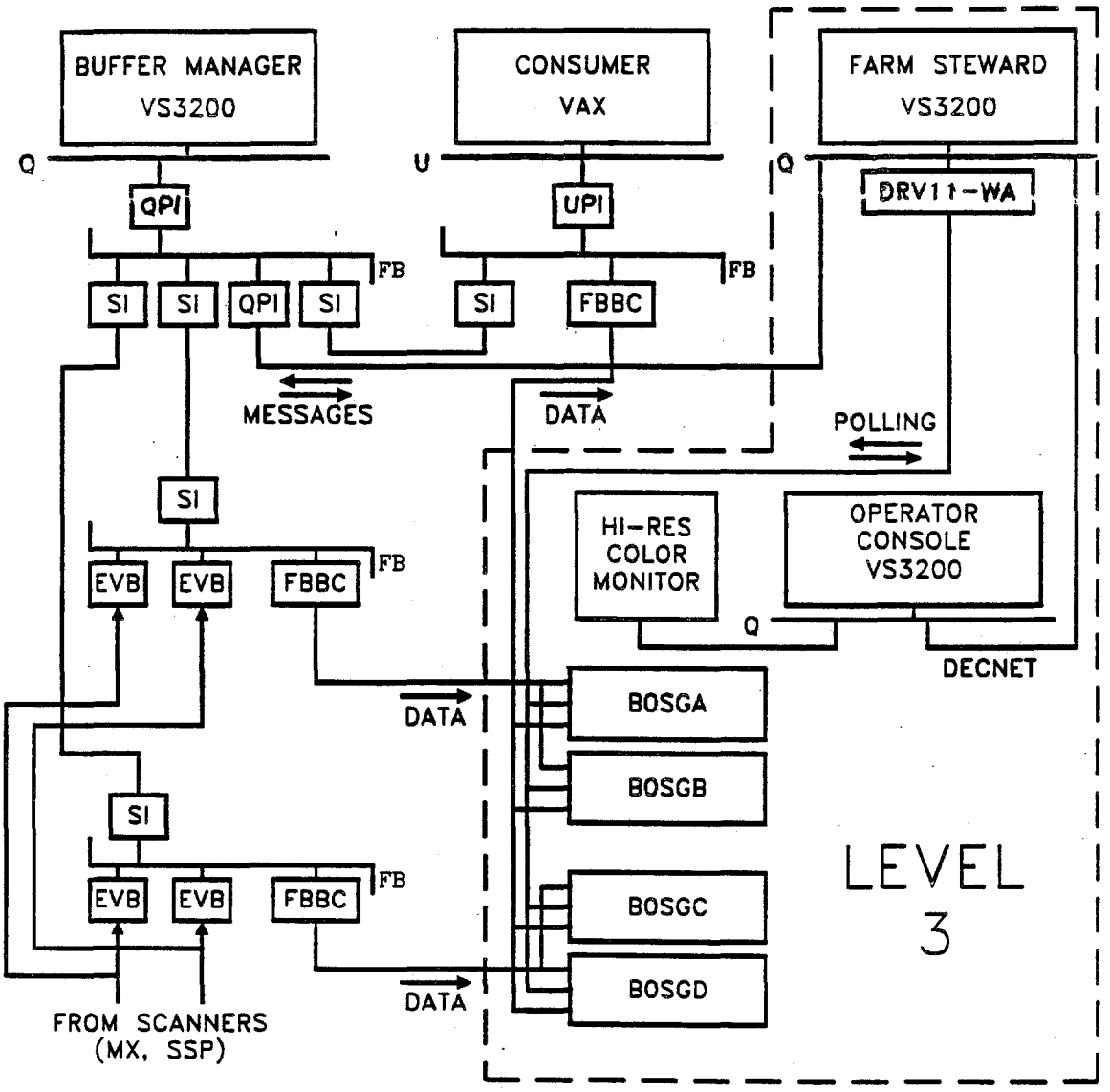

Figure 4-24: Relationship of the Level 3 VME crates to the DAQ system in the 1991 Run. The DAQ connections are similar to those in 1989 (Fig. 4-23) except that there are two Event Builders, each serving half the Level 3 farm over an independent branch bus. The main computing engines for Level 3 will be four Silicon Graphics boxes, each containing eight R3000 RISC processors benchmarked at about 15 MIPS. Ten VME slots for external I/O are provided in each box. Figure 4-25 shows details of the Silicon Graphics boxes and external connections.

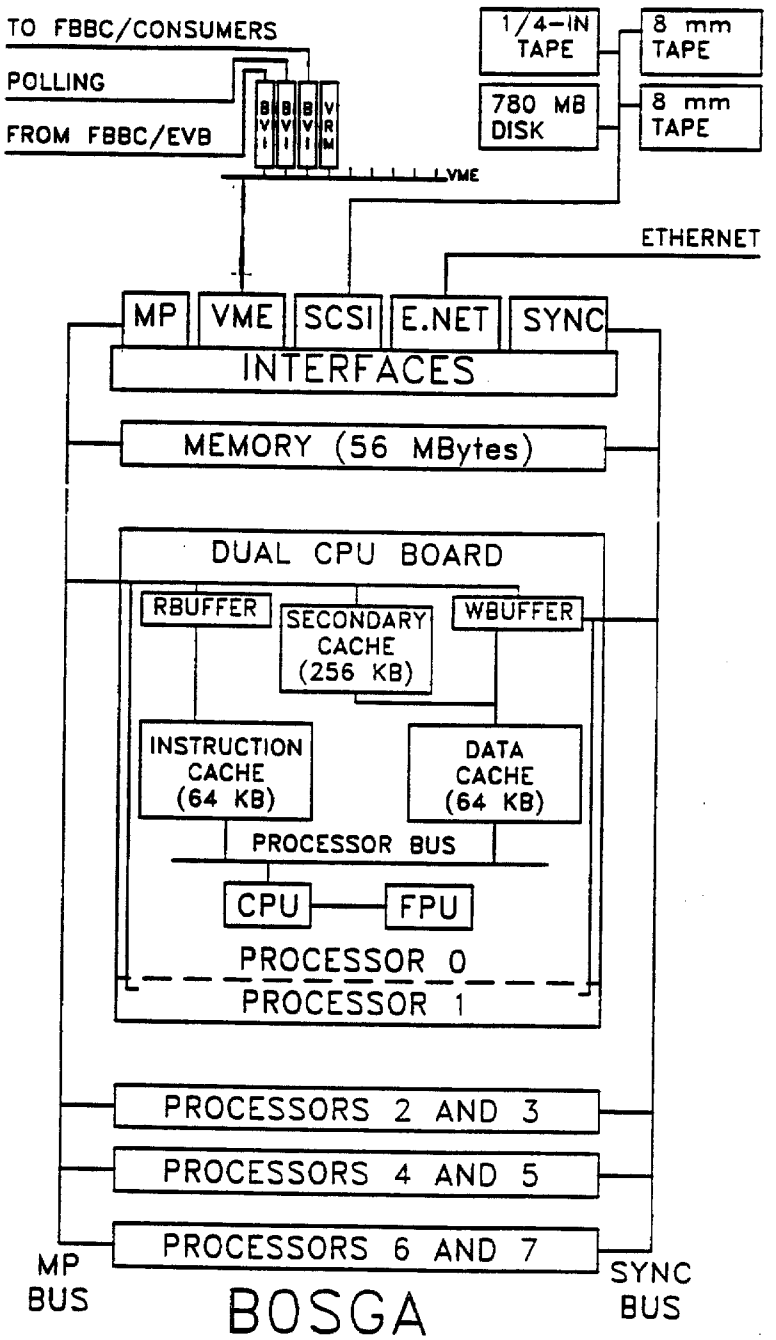

Figure 4-25: A diagram of one of four Level 3 Silicon Graphics boxes for the 1991 run. The VME connections for data I/O and control are similar to the 1989 run. The IO2 board is an interface between VME and the internal bus which maps VME addresses onto virtual memory. The box contains eight processors and 64 MBytes of shared memory, and has a UNIX operating system. The internal structure of one of the eight processors is shown. It has 64 KBytes of primary instruction cache and the same amount of primary data cache, plus 256 KBytes of secondary cache.

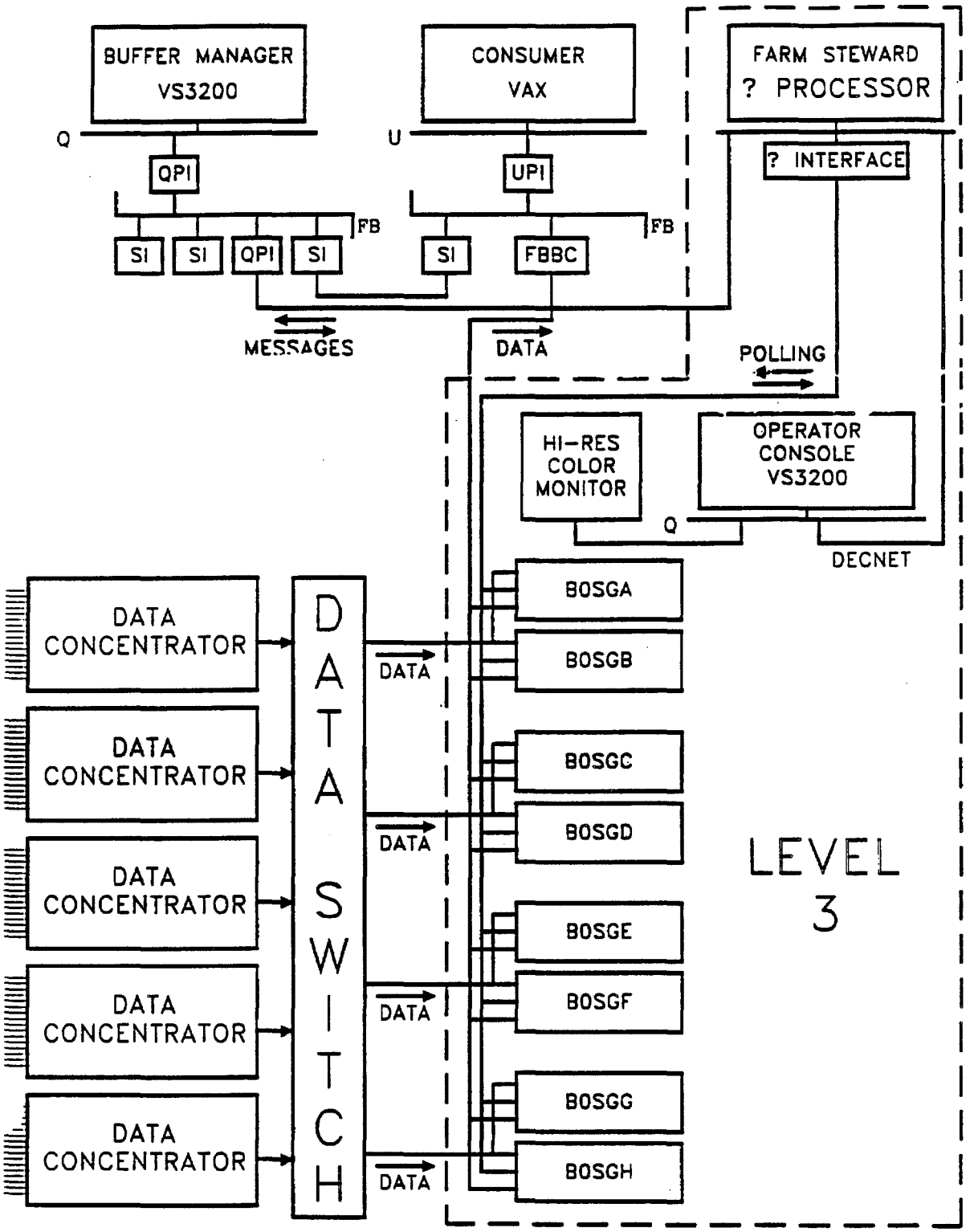

Figure 4-26: Relationship of the Level 3 to the DAQ system in the 1993 Run. The Silicon Graphics system for 1991 (Fig. 4-24) is expected to follow an appropriate growth path into 1993, with the number of boxes doubled and the R3000 CPU's (15 MIPS) replaced by R4000 (estimated at 50 MIPS). The number of branch bus connections from a high-speed switch in the DAQ should be four or eight depending on bandwidth of the technology selected.

4.9 Online Computing: RUN_CONTROL

In the CDF online system, VAX computers are used for high level control and monitoring functions. Such functions include hardware initialization and diagnostics for the trigger, Level 3 system, FASTBUS system and front end electronics; data logging, calibration, and processes that monitor the quality of the incoming data and from these data determine some global calibration parameters. The calibration data base is maintained on the CDF VAX cluster. The hardware voltage monitoring and high voltage control was also run from a VAX. Plans for this system are discussed elsewhere.

During the detector checkout phase, and during down times during the run, the detector is divided up into partitions operated in parallel for checkout and maintenance, each under the control of a separate VAX.

During normal data taking with the entire detector active, the control and monitoring functions are distributed among several of the nodes in this cluster. The existing computers used for these purposes include two VAX 750s, one VAX 785, three VAX 8350s, and several μVAX's. These provide multiple-user access to the DAQ and detector subsystems during tune-up at the beginning of the run, consumer processes during data collection, and redundancy in case one of the VAX's fails. In addition the cluster contains redundant HSC controllers and 8mm tape drives. Critical disks are shadowed.

For the next (1991) CDF run, we plan to retire the VAX 750's and begin migrating these higher level functions to μVAX workstations. Such workstations offer the advantage of greatly improved CPU performance at nominal cost, and an integrated graphics display station with a window based user interface. Some of the control and diagnostic programs will be modified to better take advantage of this capability.

For the 1993 run, at least some of the above functions such as data logging and some monitoring and calibration will be performed by the Level 3 system. However it is likely that some of these monitoring functions and most initialization and diagnostic functions will still be performed by the VAX's. It will still be important to support a number of checkout activities in parallel (and thus multiple detector "partitions") particularly given the large amount of new electronics to be debugged. For the 1993 run, we plan to complete migration of these functions to workstations, and retire the VAX 8350's.

The increased reliance on workstations will place greater demands on the performance and reliability of the boot nodes for those workstations. Thus, by the 1993 run we plan to upgrade the present μVAX 3500 server and also to provide redundancy for this function. In addition, large upgrades in disk storage capacity will be required.

For data logging in the 1988-89 run, CDF had a single output stream from Level 3 to processes running in the VAX system and onto 9-track magnetic tape. During the run as a test, Exabyte 8mm tape drives were added and recorded the same data redundantly with the 9-track drives. This exercise proved successful. In 1991 and subsequent runs, as discussed in the section on Level 3, the plan is to write to multiple data streams:

- An express-line stream at about $\sim$1 Hz through the VAX system and onto Exabyte 8500 8mm tape drives.

- A "solid-gold" subset of the above, top candidates and other highly interesting events, will be logged to disk and retained for several days for closer examination.
- A non-express-line stream at up to ~8 Hz onto four Exabyte 8500 8mm tape drives in parallel directly from Level 3, without event-by-event intervention from the VAX.

These drives are expected to be able to write data at 500 KB/sec, corresponding to approximately $\sim 5\pm \sim 2$ events per second per drive based on the expected event size.

At present, 8mm tape seems to be most cost effective recording medium with adequate bandwidth in terms of both drive and media cost. Other possibilities, such as 4mm DAT tape, 3480 tape cartridges, and optical disks are more expensive and/or cannot write data at a sufficiently high rate.

4.10 Offline Computing

Experience from the 1988/9 run

In the 1988/9 run CDF recorded 6-million events, representing 0.7 Terabytes of raw data. Event reconstruction took on average 250 million instructions per event and produced event records of about 200 KB. Subsequent compression, filtering, and analysis has required additional resources at Fermilab amounting to 150 MIPS of CPU and 50 GB of disc, including 40 distributed workstations, the latest of which consist of a Vaxstation 3100 (4.5 MIPS) plus one WREN V disc (0.6 GB), and an 8mm tape drive.

During the past run, CDF made substantial progress in dealing with large data sets, and making them accessible to a large international collaboration. Preliminary results based on highly selected subsamples of the data were presented in conferences during the running period. This experience gives a firm basis to understand and extrapolate our needs in the coming runs where we expect subtantial increases in the luminosity and number of exciting events. One major issue is having the offline system ready at the start of the collider run. Among other things, this requires having a robust development environment available to CDF in the periods between runs. Another major issue is fast and convenient access to large datasets for the large CDF collaboration. The available resources for the 1988/9 run were marginal at best. We will require substantial improvements particularly in fast access media and networking in order to deal with data from future runs.

Needs for the 1991/2 run

In the 1991/2 run the initial upgrade of the Level 3 trigger system will enable CDF to write out an "express-line" of chosen events at 1 Hz. There will be an additional 8 Hz of non-express-line events taken with lower thresholds and/or looser cuts for determination of backgrounds and efficiencies, and for more inclusive analyses. An estimate of our offline needs for the 1991/2 run is summarized in Table 5-11.

(A) Express-line event reconstruction and analysis :

Writing events at 1 Hz CDF will record up to 10-million raw express-line events (approx. 1.3 Terabytes) onto 8-mm tape during the 1991/2 run. The express-line sample alone could be twice the size of the entire 1988/89 data sample. Furthermore, we must plan to reconstruct and filter express-line events in essentially real time to enable the resources to be available after the run for processing sub-samples of the non-express-line data for background and efficiency calculations, for detailed Monte Carlo calculations, and for reprocessing of subsamples of express-line data when needed.

We will require the following resources to be able to analyse the 1991/2 data:

1. CPU for reconstructing events and producing DSTs from raw data: 500 MIPS.
   We estimate 500 million instructions per event in 1991/2, the increase with respect

to the reconstruction of events from the 1988/9 run coming partly from the increase in number of detector channels (and in particular the increased tracking capability of CDF) and partly from the increased complexity of the events (in particular the increased rate of multiple interactions).

2. 8 mm tapes for DST production: 500 double density double speed cassettes.
   If these are not available we will use single density cassettes, changing to double density when possible.

3. 8 mm robotic storage devices for DST's: 5 Robots.
   Each robot is assumed to store 100 double density tapes, and serve four 8mm tape drives. This will enable all DSTs to be spun within a 1 to 2 week period.

4. CPU for filtering DSTs and producing compressed data sets (microDSTs): 100 MIPS.

5. Mass storage for filtered DST events:
   This is a critical item and is addressed separately below.

6. Mass storage for compressed data sets : 100 GB of high speed disc and four 8 mm drives.
   Assumes an event compression factor of 10 in producing microDSTs. This will enable 50% of the express-line to be placed on disc and made available to the distributed CDF workstations at Fermilab. The compressed data sets will also be written to tape for distribution to the outside institutions.

7. 8 mm tape copying: 20 dedicated 8 mm drives.
   For duplication of microDST tapes and highly selected DST samples before distribution to the outside institutions.

8. Distributed workstations:
   The 40 CDF workstations currently at Fermilab will need to be maintained, upgraded, and replaced as they age, or as cheaper and better devices become available. We will need to supplement the present workstations with enhanced disc space (2 GB will be sufficient to store most highly selected working data samples) and dual 8 mm drives to reduce traffic to the central mass storage devices.

9. Analysis engine: 400 MIPS + 40 GB Disc
   Based on our present experience additional analysis needs after production require approximately 0.6 times the CPU needed for production.

10. High bandwidth networking:
    CDF will require high bandwidth links between the production and analysis CPU engines, the mass storage devices, and the 8 mm robotic tape drives. We will require FDDI networking as soon as it becomes available at Fermilab.

(B) Non-Express-Line data :

The upgraded level 3 trigger system will enable about 80-million non-express-line events to be written to tape during the 1991/2 run. These data will contain event sub-samples that will need to be analysed after the run to extract information about backgrounds and efficiencies. We plan to use the Level 3 and production CPU to reconstruct these data as needed. Processing the non-express-line data will require storage of at least 16-million additional DST event records, requiring 800 double density 8 mm cassettes and 8 robots each with four 8 mm drives.

Mass storage for filtered DST events

The accessibility of the very large DST data sample limits both the scope and rate of the present CDF analysis. In the future we will need to be able to store the bulk of the express-line DST events on a mass storage medium that can be accessed by the distributed CDF workstations at Fermilab, and by the main CDF analysis engine, via high bandwidth links. By the end of the 1991/2 run we would like to be able to store 50% of all the express-line DST events (1 Terabyte) on a medium that can be accessed by 40 CDF workstations with reasonable seek and read times. Since mass storage technology is improving rapidly with time we feel that it is too early to identify the best medium for the 1991/2 run. However as an example we consider in the following a solution based on 8 mm tapes stored in robotic devices.

We envisage filtering the DST data onto 8 mm tapes stored in 5 robotic devices, and sorted according to trigger type. Each robot would serve 50 double density cassettes, and four 8 mm drives.

Other technologies (for example optical discs) should also be considered before a final choice is made. We stress here that we consider making the bulk of the CDF express-line DST events accessable to the widest possible community within CDF to be a crucial goal.

Needs for the 1993/4 run

To store and access the 1993/4 data we will need additional 8 mm tapes and robots (if 8 mm tapes are the storage medium of choice) in quantites similar to those needed for the 1991/2 run. We will also require additional CPU power to cope with further increases in the number of detector channels and event complexity and more extensive Monte Carlo calculations of rarer processes.

Our estimates for the additional resources required in 1993/4 over and above those needed for 1991/2 data analyses are given in Table 5-12.

4.11 Miscellaneous Systems

Limits and Alarms

Limits and alarms will be substantially improved for the 1991 run. The exact plan for this is under discussion at this writing. One of the options is that the CDF experiment be fully integrated into the ACcelerator control system NETwork (ACNET). This is described at length in CDF Note 1112.[84].

Calibrations

Two important facets of the CDF DAQ system are the implementation of online calibrations and monitoring of the data flow. These tools are invaluable for maintaining the integrity of the output stream. Obviously, we will retain and improve the capabilities we already have, as well as add new tools to monitor the changes envisioned for the 1993 CDF DAQ upgrade.

The plans and budgets for individual detector upgrades and the DAQ upgrade provide for hardware features needed for calibration.

We have studied what revisions will be needed for calibration procedures and this is described at length in CDF Note 1150.[85].

5 Cost Projections

This section gives an estimate of the funds needed to accomplish the upgrades described in this proposal. It assumes continued support by Fermilab at the level currently supplied to the CDF Department and, therefore, does not include the yearly costs of simply running the experiment, e.g.

- $700K/year in general equipment,
- $4,675K/year CDF Department SWF,
- $300K/year operating R&D,
- $2,700K/year in operating M&S.

The incremental cost for the plug upgrade R&D is explicitly included Table 5-1. The costs of the various upgrades includes salaries for any new additional labor required.

Future upgrades for higher luminosity runs beyond the "1993" run are as yet unknown, and depend on still-developing plan for Tevatron upgrades, and on the results from this coming run, especially the status of the top quark search and progress in B physics.

5.1 Budget: Plug Calorimeter

A budget for the scintillator plug upgrade is presented below.

Plug Scintillation Calorimeter Costs

The costing scenario for the scintillator plug assumes the following:

- use of the existing plug iron assemblies,
- new lead for the Plug EM section,
- extending coverage down to 3°,
- add stainless steel re-entrant plates, and insert disks,
- 25 EM plates, 4.5-mm lead, 2.6-mm plastic,
- 24 hadron plates, 50-mm iron, 5-mm plastic.
- Scintillator cost: $200/m^2 (2.6-mm) (KYOWA SCSN 81)
- Scintillator cost: $300/m^2 (5.2-mm) (KYOWA SCSN 81)
- Shifter Fiber cost: $0.60/m, (KYOWA Y-7, 1.0-mm diam.)
- Clear Optical Fiber cost: $0.35/m.

The high voltage power is assumed to be $70 per channel. This estimate is based on a CAEN system using a Model A 119A Manual Controller, a Model CY 117A CAMAC Controller, 31 Model PS 35-100 Supplies and 69 Model SY 170 Dividers. Readout electronics are assumed to cost $52/channel. There are 3600 channels, and the budget provides for test stand, spares and empty channels on multi-channel electronic boards at system boundaries.

Item	Total Price ($1000)
EM towers	2,000
Hadron towers	1,265
Structure and Tooling	714
Phototubes, Mechanics, HV, cables	1,222
Shower Maximum Detector	364
Electronics	619
Test Equipment	100
Total Cost	6,284

Table 5-1: Tile Scintillator Plug Calorimeter Costs

5.2 Budget: Silicon Vertex Detector

Item	Total Price ($1000)
New Chip R&D, rad. hard production	300
New Hybrids, connectors, cables	150
New Silicon Detectors	830
Microbonds	150
Tooling	250
1-inch Be Pipe	100
New Fixtures and Supports	250
New DAQ Electronics	350
Subtotal	2,380

Table 5-2: Silicon Vertex Detector Costs.

5.3 Budget: Muon Detectors

Item	Number	Unit Price	Total ($1000)
CMEX/CMUP Completion			
Complete CMUP Coverage			153
CMUP Steel to close gaps			70
CMUP Cooling Upgrade			50
CMEX Chambers			140
Wire Chambers			
Chamber Planes	6		400
Additional TDC's	16	6,000	96
Chamber Mounts			50
Gain Monitor/HV Control			5
Cables			10
Labor			100
Projective Scintillators			
PMT/lightpipe/base	2448	220	539
Cut existing Scint.			15
Additional Scint. Sheet	48	850	41
Revise existing mounts			10
96-channel TDC's	34	5,000	170
Labor			50
Toroids			
Revise Toroid Support			25
Electronics: Calibration/Triggering			
Level 0 Projective Mosaic			35
Level 1 Angle Cuts			250
Wire pulsing			20
Scintillator Pulsing			20
Level 2 High P_T			75
Crates/Power			30
Additional Power Supplies			10
Additions to Gas System			5
Packing/Shipping			5
Subtotal			2,374

Table 5-3: Forward Muon Costs

5.4 Budget: Data Acquisition System

Electronics Hardware

The largest budget items in the DAQ system are those which scale as the number of channels. These include Rabbit cards and parts for the front-end pre-amp/delay-line/ADC, RC^3 cards, cables, etc. The channel count for 1991 systems which will be retained is 23,568. We allow an additional 20% for test stands, spares and logical division of channels into readout groups which leaves some boards only partially populated. The table below is based on this number. Additional electronics for new detectors are included in the individual budget estimates for those subsystems.

We assume that there will be 32 channels per card, i.e. a total of about 1000 Rabbit cards, including test beam and spares. The delay lines cost about $20 each, and each card will have a $200 ADC. The rest of the board will be similar to the existing system where we have experience with the costs for boards and components. The cost per board will be somewhat greater than that for the present boards because we must change from double-sided to multilayered. This also implies increased stuffing cost. Including delay lines and ADC's, we estimate $1500 per board. This works out to a subtotal of about $47/channel. Pro-rated costs for RC^3 cards and other parts of the system which scale roughly as channel count bring this up to $52/channel. This figure is used in the budget estimates for the various new detector subsystems.

The table below summarizes the estimated costs of all the new parts of the DAQ system up to the Fastbus to Branch Bus interface to Level 3. During production we will need to hire about 7 temporaries for between one and two years.

Item	Number	Unit Price	Total Price ($1000)
* Front End Cards for 28K channels	875	1,500	875
Tooling, test equipment, overhead			300
Temporary workers for 2 years			280
Other Rabbit System Cards			
* Rabbit Backplanes	80	750	60
* BAT	80	600	48
* Crate Controller (RC^2)	80	500	40
* Level 0 Interface Card	140	1,100	154
* System Interface Card (RC^3)	40	7,000	280
Fastbus Crates	4	15,000	60
Segment Interconnects	4	5,000	20
Display Modules	4	2,000	8
Tevatron Interface/Clock/Control			50
Interface to LeCroy 1879 Crates (FBSR)	33	10,000	330
Fastbus Crates	7	15,000	105
Segment Interconnects	7	5,000	35
Display Modules	7	2,000	14
Data Concentrator			
* FIFO Cards	10	5,000	50
FIFO Cards for test stand	5	5,000	25
Buffered FBBC Cards	20	5,000	100
High-Speed Switch			350
Subtotal			3,184

Note: Items marked * are used in per-channel cost estimate of $52 for the Rabbit system. This is used to scale additional Rabbit electronics costs in other tables.

Table 5-4: Data Acquisition Electronics Costs

Electronic Triggers

Item	Total Price ($1000)
Level 0 Trigger Crates and Cards	100
Level 0 Upstairs equipment	50
Level 1,2 Trigger	
CES/Pre-radiator	150
Cal. Pattern Recognition	150
Plug Electron Trig.	150
Processor Upgrades	50
Muon Trigger	100
Luminosity Monitor	50
Subtotal	1,150

Table 5-5: Level 1,2 Costs

Level 3 Trigger

The Level 3 budget is based on the assumption that the architecture planned for the 1991 CDF run can be expanded from four to eight Silicon Graphics 4D/220 servers, and that 50-MIPS CPU's will be available to replace the currently available 15-MIPS units. Further, it is assumed that each server will have expanded disk storage and tape drives.

Item	Number	Unit Price	Total Price ($1000)
CPU Power (MIPS)	3000	450	1,350
Disk Controllers and Drives (4 GB/box)	32	2900	93
Tape Controller and Two Drives per box	8	7000	56
High Bandwidth Links, Interfaces/Cable			80
Subtotal			1,579

Table 5-6: Level 3 Costs

5.5 Budget: Online Computing

Item	Number	Unit Price	Total Price ($1000)
Graphics Workstations	5	40	200
Program Development Workstations	10	20	200
File Server			150
Upgrade disk storage			100
Hardware Test Stands			300
Upgrade local network			100
General Program Development (Computer)			150
Subtotal			1,200

Table 5-7: Online Computing Costs

5.6 Budget: Miscellaneous

Item	Number	Unit Price	Total Price ($1000)
Central Tracking (CTC) Pre-Amps			98
Subtotal			98

Table 5-8: Costs for Miscellaneous Items

5.7 Budget Summary

The table below summarizes the total budget. A 20% project contingency is added.

System	Price ($1000)
PlugCalorimeter	6,284
SVX replacement	2,380
Forward Muon	2,374
DAQ Electronics	3,184
Level 1-2 Trigger	1,150
Level 3 and data logging	1,579
Online Computing (Run_Control)	1,200
Miscellaneous	98
Subtotal	18,249
Contingency (20%)	3,650
Total Estimate "1990 dollars"	21,899

Table 5-9: CDF Upgrade Budget Summary

5.8 Budget: Test Beam

These are the operating R&D costs for the plug upgrade prototype testing.

Item	Total Price ($1000)
Upgrade Wedge Fixture	85
Rabbit Crate	10
EM Test Calorimeter	56
Hadron Test Calorimeter	112
Sower Max Test Device	30
EM/HAD/PreRad Monitor Device	140
Total Cost	433

Table 5-10: Test Beam Costs

5.9 Budget: Offline Computing and Data Storage

The budget for CDF's offline computing needs is presented separately, so that it can be used as part of the laboratory's overall assessment of computing needs. A substantial part of the upgraded offline analysis capability must be present for the 1991 collider run, and the remainder for 1993. For this reason, two tables are presented.

A number of assumptions must be made in order to project the cost of computing.

- For a high-end Silicon Graphics system the cost per 15-MIPS CPU is $22,500 (or $1500/MIPS). We assume that the cost will be the same for a 50-MIPS CPU ($450/MIPS) for the upgrade.
- High Performance (HSC-acess) disk storage will cost about $9,500/GByte.
- Lower Performance (Ethernet-access) disk storage will cost about $2,900/GByte.

Item	Number	Unit Price	Total Price ($1000)
CPU Power (MIPS)	1000	450	450
8 mm Robots	19	30K	570
8 mm Tape Drives	96	3K	288
Disc Storage, high speed access (GByte)	140	9.5K	1,330
Controllers, links, etc.			330
Workstation Upgrades			
2 GB disks	40	6K	240
8 mm drives	40	2.5K	100
Subtotal			3,308
Contingency (20%)			662
Total Estimate "1990 dollars"			3,970

Table 5-11: Offline Computing Equipment Costs for the 1991 Run

Item	Number	Unit Price	Total Price ($1000)
CPU Power (MIPS)	1000	450	450
8 mm Robots	20	30K	600
8 mm Tape Drives	40	3K	120
Disc Storage, high speed access (GByte)	100	9.5K	950
Controllers, links, etc.			250
Workstation Upgrades	40	5K	200
Subtotal			2,570
Contingency (20%)			514
Total Estimate "1990 dollars"			3,084

Table 5-12: Offline Computing Equipment Costs for the 1993 Run

830 1/7/91

CDF/DOC/PUBLIC/1172 "Proposal for an Upgraded CDF Detector"

ERATUM

The following pages should replace Section 6 (pp. 156-159) in the Proposal.

MS/cip

Participating Institutions, Physicists, and Engineers

Argonne National Laboratory

Nodulman, L.	Blair, R.	Kuhlmann, S.
Proudfoot, J.	Wagner, R. G.	Wicklund, A.

Brandeis University

Blocker, C.	Behrends, S.	Bensinger, J.
Kirsch, L.	Students	

University of California at Los Angeles

Hauser, J.	Lammel, S.	Muller, J.
Students		

University of Chicago

Frisch, H. J.	Shochet, M.	Campagnari, C.
Contreras, M.	Eno, S.	Grosso-Pilcher, C.
Miller, M.	Sanders, H.	Sullivan, G.
Students		

Fermi National Accelerator Laboratory

Kephart, R.	Areti, V. H.	Atac, M.
Beretvas, A.	Berge, J. P.	Binkley, M.
Byon-Wagner, A.	Caner, A.	Carter, H.
Chadwick, K.	Cihangir, S.	Cooper, J.
Crane, D.	DeJongh, F.	Denby, B.
Drake, G.	Droege, T.	Elias, J.
Flaugher, B.	Foster, G. W.	Freeman, J.
Frei, D.	Fuess, T.	Geer, S.
Grimm, C	Grimson, J.	Hahn, S. R.
Harris, R.	Huth, J.	Hylen, J.
Jensen, H.	Johnson, R. P.	Joshi, U.
Jovanovic, D.	Kim, D. H.	Kovacs, E.
Lewis, J.	Limon, P.	Lukens, P.
Maeshima, K.	Marriner, J. P.	Mukherjee, A.
Nelson, C.	Newman-Holmes, C.	Para, A.
Park, S.	Papadimitriou, V.	Patrick, J.
Pawlack, J.	Plunkett, R.	Rauch, J.
Rodrigo, T.	Schmidt, E. E.	Segler, S.

Shaw, T.	Sphicas, P.	Stuermer, W.
Schurecht, K.	Theriot, D.	Tipton, P.
Tkaczyk, S.	Tollestrup, A.	Turner, K.
Vidal, R.	Wagner, R. L.	Wainer, N.
Yagil, A.	Yeh, G. P.	Yoh, J.
Yun, J. C.	*Ragan, K. J.	*Sinervo, P.

*Visitors

INFN - Frascati

Giromini, P.	Bertolucci, S.	Chiarelli, G.
Cordelli, M.	Miscetti, S.	Sansoni, A.

Harvard University

Brandenburg, G.	Feldman, G.	Franklin, M.
Konigsberg, J.	Oliver, J.	Sadowski, E.
Schlabach, P.	Students	

University of Illinois

Holloway, L.	Downing, R.	Errede, S.
Gauthier, A.	Karliner, I.	Liss, T.
Simaitis, V.	Students	

Johns Hopkins University

Barnett, B. A.	Matthews, J. A.	Skarha, J.
Snider, F.	Students	

KEK - Japan

Mishina, M.	Abe, F.	Fukui, Y.
Mikamo, S.		

Lawrence Berkeley Laboratory

Carithers, W.	Chinowsky, W.	Einsweiler, K.
Ely, R.	Galtieri, L.	Gold, M.
Haber, C.	Kadel, R.	Shapiro, M.
Students		

University of Michigan

Campbell, M. Amidei, D. Chapman, J.
Derwent, P. Wu, D. Zhang, S.
Students

Osaka City University

Takahashi, T. Teramoto, Y. Okusawa, T.
Yoshida, T.

University of Padova

Bisello, D. Bacchetta, N. Busetto, G.
Castro, A. Centro, S. Loreti, M.
Martinelli, R. Pescara, L. Wyss, J.

University of Pennsylvania

Williams, H. Gladney, L. Hollebeek, R.
Lockyer, N. Low, E. Students

INFN - Pisa

Bellettini, G. Bedeschi, F. Belforte, S.
Bolognesi, V. Cervelli, F. Dell'Agnello, S.
Dell'Orso, M. Galeotti, S. Giannetti, P.
Grassmann, H. Incagli, M. Leone, S.
Mangano, M. Mariotti, M. Menzione, A.
Paoletti, R. Giovanni, P. Punzi, G.
Raffaelli, F. Rimondi, F. Ristori, L.
Scribano, A. Smith, D. Spitaleri, C.
Stefanini, A. Turini, N. Wenzel, H.
Westhusing, T. Zanetti, A. M. Zetti, F.
Zucchelli, S. Students

University of Pittsburgh

Shepard, P. Engels, E. Students

Purdue University

Garfinkel, A. Barnes, V. Laasanen, A.
Shaw, M. Students

University of Rochester

Bodek, A. Auchincloss, P. Budd, H.
de Barbaro, P. Haelen, T. Olsen, S.
Sakumoto, W. Zheng, H. Students

Rockefeller University

Goulianos, K. Chapin, T. J. Giokaris, N.
White, S. Students

Rutgers University

Devlin, T. Buckley, E. Mueller, J.
Watts, T. Students

Texas A&M University

Webb, R. C. Bowcock, T. Kamon, T.
McIntyre, P. M. Students

University of Tsukuba

Kondo, K. Funayama, Y. Hara, K.
Kim, S. Miyashita, S. Morita, Y.
Nakano, I. Takikawa, K. Yasuoka, K.
Students

Tufts University

Sliwa, K. Students

University of Wisconsin

Pondrom, L. Bellinger, J. Carlsmith, D.
Handler, R. Wendt, C. Students

References

[1] Design Report for the Fermilab Collider Detector Facility (CDF), D. Ayres et al., Fermilab, August, 1981 (unpublished).

[2] The CDF Detector: An Overview, F. Abe et al., Nuclear Instruments and Methods, **A271**, 387 (1988).

[3] The CDF Central Electromagnetic Calorimeter, L. Balka et al., Nuclear Instruments and Methods, **A267**, 272 (1988).

[4] The CDF Vertex Time Projection Chamber System, F. Snider et al., Nuclear Instruments and Methods, **A268**, 75 (1988).

[5] Design and Construction of the CDF Central Tracking Chamber, F. Bedeschi et al., Nuclear Instruments and Methods, **A268**, 50 (1988).

[6] The Design and Construction of the CDF Central Drift Tube Array, S. Bhadra et al., Nuclear Instruments and Methods, **A268**, 92 (1988).

[7] Radial Wire Drift Chambers for CDF Forward Tracking, M. Atac et al., Nuclear Instruments and Methods, **A269**, 40 (1988).

[8] A Computer-Controlled Wire Tension Measurement System Used in the Fabrication of the CDF Central Drift Tube Array, S. Bhadra et al., Nuclear Instruments and Methods, **A269**, 33 (1988).

[9] The CDF Central and Endwall Hadron Calorimeter, S. Bertolucci et al., Nuclear Instruments and Methods, **A267**, 301 (1988).

[10] CDF End Plug Electromagnetic Calorimeter Using Conductive Plastic Proportional Tubes, Y. Fukui et al., Nuclear Instruments and Methods, **A267**, 280 (1988).

[11] An Electromagnetic Calorimeter for the Small Angle Regions of the Collider Detector at Fermilab, G. Brandenburg et al., Nuclear Instruments and Methods, **A267**, 257 (1988).

[12] The CDF Forward/Backward Hadron Calorimeter, S. Cihangir et al., Nuclear Instruments and Methods, **A267**, 249 (1988).

[13] Calibration Systems for the CDF Central Electromagnetic Calorimeter, S. R. Hahn et al., Nuclear Instruments and Methods, **A267**, 351 (1988).

[14] Response Maps of the CDF Central Electromagnetic Calorimeter with Electrons, K. Yasuoka et al., Nuclear Instruments and Methods, **A267**, 315 (1988).

[15] Cosmic Ray Test of the CDF Central Calorimeter, R. G. Wagner et al., Nuclear Instruments and Methods, **A267**, 330 (1988).

[16] Phototube Testing for CDF, T. Devlin et al., Nuclear Instruments and Methods, **A268**, 24 (1988).

[17] CDF Central Muon Detector, G. Ascoli et al., Nuclear Instruments and Methods, **A268**, 33 (1988).

[18] The CDF Forward Muon System, K. Byrum et al., Nuclear Instruments and Methods, **A268**, 46 (1988).

[19] A Leveling System for the CDF Central Muon Chambers, G. Ascoli et al., Nuclear Instruments and Methods, **A268**, 41 (1988).

[20] CDF Front End Electronics: The RABBIT System, G. Drake et al., Nuclear Instruments and Methods, **A269**, 68 (1988).

[21] FASTBUS Data Acquisition for CDF, E. Barsotti et al., Nuclear Instruments and Methods, **A269**, 82 (1988).

[22] A Two-Level Fastbus Based Trigger System for CDF, D. Amidei et al., Nuclear Instruments and Methods, **A269**, 51 (1988).

[23] CDF Central Muon Level-1 Trigger Electronics, G. Ascoli et al., Nuclear Instruments and Methods, **A269**, 63 (1988).

[24] A Fast Hardware Track-Finder for the CDF Central Tracking Chamber, G. W. Foster et al., Nuclear Instruments and Methods, **A269**, 93 (1988).

[25] Integration of the ACP Multiprocessor Farm with the CDF Fastbus Data Acquisition System, B. Flaugher et al., IEEE Transactions on Nuclear Science, **NS-34**, 865 (1987).

[26] Level 3 System at CDF, J. T. Carroll et al., Nuclear Instruments and Methods, **A263** 199 (1988).

[27] CDF Physics Goals and Upgrade Plans for the 1991 Run. Fermilab, CDF Note CDF/DOC/CDF/CDFR/1039, October, 1989, (unpublished).

[28] Transverse Momentum Distribution of Charged Particles Produced in $\bar{p}p$ Interactions at $\sqrt{s} = 630$ and 1800 GeV, F. Abe et al., Phys. Rev. Lett. **61**, 1819 (1988).

[29] Pseudorapidity Distributions of Charged Particles Produced in $\bar{p}p$ Collisions at $\sqrt{s} =$ 630 and 1800 GeV, F. Abe et al., Phys. Rev. **D41**, 2330 (1990).

[30] Measurement of the Inclusive Jet Cross Section in $\bar{p}p$ Collisions at $\sqrt{s} = 1.8$ TeV, F. Abe et al., Phys. Rev. Lett. **62**, 613 (1989).

[31] A Measurement of W Boson Production in 1.8 TeV $\bar{p}p$ Collisions, F. Abe et al., Phys. Rev. Lett. **62**, 1005 (1989).

[32] Limits on the Masses of Supersymmetric Particles from 1.8 TeV $p\overline{p}$ Collisions, F. Abe et al., Phys. Rev. Lett. **62**, 1825 (1989).

[33] Dijet Angular Distributions from $\overline{p}p$ Collisions at $\sqrt{s} = 1800$ GeV, F. Abe et al., Phys. Rev. Lett. **62**, 3020 (1989).

[34] K_s^0 Production in $\overline{p}p$ Interactions at $\sqrt{s} = 630$ and 1800 GeV, F. Abe et al., Physical Review **D40**, 3791 (1989).

[35] Search for Heavy Stable Charged Particles in 1.8-TeV $\overline{p}p$ Collisions at the Fermilab Collider, F. Abe et al., Phys. Rev. Lett. **63**, 1447 (1989).

[36] A Measurement of D^* Production in Jets from $\overline{p}p$ Collisions at $\sqrt{s} = 1.8$ TeV, F. Abe et al., Physical Review Letters **64**, 348 (1990).

[37] The Two-Jet Invariant Mass Distribution at $\sqrt{s} = 1.8$ TeV, F. Abe et al., Physical Review **D41**, 1722R (1990).

[38] Measurement of the Jet-Broadening Parameter, Q_T, in $\overline{p}p$ Collisions at $\sqrt{s} = 1.8$ TeV, F. Abe et al., (In preparation, to be submitted to Phys. Rev. D).

[39] Two Jet Differential Cross Sections in $\overline{p}p$ Collisions at $\sqrt{s} = 1.8$ TeV, F. Abe et al., Physical Review Letters **64**, 157 (1990).

[40] Jet Fragmentation Properties in $\overline{p}p$ Collisions at $\sqrt{s} = 1.8$ TeV, F. Abe et al., (submitted to Phys. Rev. Lett.).

[41] K. Alpgard et al., Phys. Lett. **115B**, 71 (1982).

[42] G. J. Alner et al., Z. Phys.**C40**, 81 (1986).

[43] G. J. Alner et al., Phys. Rep. **154**, 247 (1987).

[44] D. Antreasyan et al., Phys. Rev. **D19**, 764 (1978).

[45] G. J. Alner et al., Nucl. Phys. **B258**, 505 (1985).

[46] Measurement of the Mass and Width of the Z^0 Boson at the Fermilab Collider, F. Abe et al., Phys. Rev. Lett. **63**, 720 (1989).

[47] Measurement of the W Boson Mass, F. Abe et al., (Submitted to Phys. Rev. Letters.

[48] Measurement of the W Boson Mass in 1.8 TeV $\overline{p}p$ Collisions, F. Abe et al., (Submitted to Phys. Rev. D.

[49] A Search for the Top Quark in the Reaction $\overline{p}p \rightarrow$ Electron + Jets at $\sqrt{s} = 1.8$ TeV, F. Abe et al., Physical Review Letters **64**, 142 (1990).

[50] Search for New Heavy Quarks in Electro-Muon Events at the Fermilab Tevatron, F. Abe et al., Physical Review Letters **64**, 147 (1990).

[51] Measurement of the Ratio $\sigma(W \to e\nu)/\sigma(Z \to ee)$ in $\overline{p}p$ Collisions at $\sqrt{s} = 1.8$ TeV, F. Abe et al., Physical Review Letters **64**, 152 (1990).

[52] Search for a Light Higgs Boson at the Tevatron Proton-Antiproton Collider, by The CDF Collaboration, Physical Review **D41**, 1717R (1990).

[53] Recent Results on Direct Photons from CDF, The CDF Collaboration, presented by R. Harris at the Workshop on Hadron Structure Functions and Parton Distributions, Fermilab, April 26-28, 1990; FERMILAB-CONF-90/118-E, CDF Note 1210 (unpublished).

[54] P. Aurenche, R. Baier and M. Fontannaz, FERMILAB-PUB-89/226-T (1989).

[55] A Measurement of $\sigma(W \to e\nu)$ and $\sigma(Z^0 \to e^+e^-)$ in $\overline{p}p$ Collisions at $\sqrt{s} = 1.8$ TeV, F. Abe et al., (In preparation, to be submitted to Phys. Rev. D).

[56] J. Alitti, et al., CERN-EP/90-20, Feb. 1990, submitted to Z. Phys. C.

[57] K. Ellis, in Proceedings of the Eighth Topical Workshop on Proton-Antiproton Physics, Castiglione, Italy, September, 1989 (to be published).

[58] New Top Results From CDF, by J. Walsh, Seminar presented at FNAL, March, 1990.

[59] P. Langacker, Phys. Rev. Lett. **63**, 1920 (1989).

[60] P. Nason, S. Dawson and R. K. Ellis, Nucl. Phys. **B303**, 607 (1988).

[61] G. Altarelli et al., Nucl. Phys. **B308**, 724 (1988).

[62] 'Detecting Very Massive Top Quarks at the TEVATRON', H. Baer et al., University of Wisconsin Preprint MAD/PH/540, Madison, Wisconsin, January, 1990.

[63] Workshop on Top, Breckenridge, CO, August, 1989.

[64] S. L. Glashow and E.E. Jenkins, Phys. Lett. B196, 233 (1987).

[65] V. Barger and R. J. N. Phillips, Phys. Rev. D40, 2875 (1989).

[66] S. Ellis, Z. Kunszt and D. Soper, Phys. Rev. **D40** 2188 (1989); U. of Oregon Preprint OITS 436 (1990).

[67] E. Eichten, G. Kane and M. Peskin, Phys. Rev. Lett. **50**, 133 (1983).

[68] J. Bagger, C. Schmidt, S. King, Phys. Rev. **D37** 1188 (1988).

[69] E. Eichten and K. Lane, Phys. Lett. **222** 274 (1989).

[70] P. Arnold and M.H. Reno, FERMILAB-Pub-88/168 (1988).

[71] Martins, Roberts and Stirling, Z. Phys. **C42**, 277 (1989).

[72] V. V. Kiselev et al. Sov. J. Nucl. Phys. **49**, 682 (1989).

[73] I.I. Bigi in Proceedings of the Workshop on Linear Collider B Factories, UCLA 1987, G. Stork editor, World Scientific, Singapore.

[74] H. Albrecht et al., Phys. Lett. **192B**, 245 (1987).

[75] A. Jawahery, in Proceedings of the XXIV International Conference on High Energy Physics, Munich, editors: R. Kotthaus and J. Kuhn, Springer–Verlag Berlin, Heidelberg 1989.

[76] A. Brandt et al., Proposal to the CERN SPSC, CERN-SPSC/88-3 SPSC/ P238, January 1989.

[77] J. Rosner, Phys. Rev. **D42**, ??? (1990).

[78] "Proposal to upgrade FNAL-E731/E799 with a Scintillating Fiber Preshower Detector", K. Arisaka, et al., UCLA/HEP internal note.

[79] "Position-sensitive photomultiplier tube R4135-01", HAMAMATSU technical data, Feb. 1990.

[80] CTC Upgrade Plans for 1991 and 1993 by A. Mukherjee et al., CDF Note CDF/DOC/TRACKING/CDFR/1151, 1990.

[81] Forward Muon Resolution, by D. Carlsmith, CDF Note CDF/ANAL/MUON/CDFR/1111, 1989.

[82] An Upgraded CDF Data Acquisition System, by G. Drake et al. CDF Note CDF/DOC/CDF/CDFR/1147, 1990.

[83] Preliminary Design for the 1993 Level 0 Card and Level 0 Crate, by M. Miller et al., CDF Note CDF/DOC/TRIGGER/CDFR/1167, 1990.

[84] A Proposal to Convert CDF to ACNET, by R. Johnson, CDF/MEMO/ONLINE/CDFR/1112, Fermilab, January, 1990.

[85] Calibrations
of the Upgraded CDF, by S. Hahn, CDF Note CDF/DOC/ONLINE/PUBLIC/1150, 1990.

FERMILAB-PROPOSAL-0830-2 1993

FERMI NATIONAL ACCELERATOR LABORATORY
P.O. Box 500
Batavia, Illinois 60510

Collider Detector
Mail Station 318

January 13, 1993

Dr. John Peoples, Director
Fermilab

Dear John,

We are submitting a proposal to build a new silicon vertex detector (SVX II) that is capable of operating with the accelerator bunch spacing and luminosity expected in run II and beyond. As you know, neither the present device (SVX) nor its run Ib radiation hard replacement (SVX') can operate with 400 nsec. between bunches.

Our proposal presents the physics arguments for a system that is built in two stages. The first stage, a barrel silicon detector, will greatly enhance our high P_T and b physics capabilities. The second stage, a system of forward disk detectors, will be needed if CDF is to successfully attack the difficult but extremely important $B\bar{B}$ physics accessible with the Main Injector such as $B_s\bar{B}_s$ mixing and CP violation.

It is stage I, the barrel detector, for which we now seek approval. The mechanical and electrical designs are described in the proposal. The project cost and timetable are also presented. It is important that Lab approval not be deferred since we must commit resources now if we are to be ready for run II. We understand of course that the Lab will have a technical review of the project later in the design and R&D phase, before major funding is committed. We note that the proposed barrel detector is needed no matter which option we select for the forward tracking upgrade (stage II).

Sincerely,

Mel

Mel Shochet

Alvin

Alvin Tollestrup
for the CDF Collaboration

SVX II
Upgrade Proposal
and
Simulation Study

CDF Collaboration

January 12, 1993

Contents

1 Summary **4**

2 SVX Performance **7**

3 SVX and SVX II Design Comparison **13**

4 Tracking Simulation **16**

4.1 Model Geometries 16

4.2 Simulation Tools 20

4.3 Single Track Results 23

5 Physics Simulation **30**

5.1 Physics Motivation 30

5.2 Physics Benchmarks 34

5.3 Top Analysis 35

5.4 Impact on W and Z Physics 39

5.5 B Decays 41

5.6 B_s Mixing 54

5.7 CP Violation Studies 63

5.8 Summary of Simulation Studies 71

6 SVX II Mechanical Engineering and Design **73**

6.1 General description 73

6.2 Ladder Support Designs 77

6.3 Bulkhead structure 82

6.4 Hybrid Mechanical Considerations 86

6.5 Readout Cables and Routing 87

6.6 Prototyping/Testing 87

6.7 Support of SVX II within the VTX 88

7 Silicon Microstrip Detectors **90**

7.1 Description of the Detectors 90

7.2 Technical Issues Shaping the Design 91

7.3 Prototypes 96

8 Front-End Design **98**

8.1 Occupancy Study 98

8.2 LBL Chip Design 99

8.3 Fermilab Chip Design 100

9 Radiation Damage **106**

10 Data Acquisition System **108**

10.1 Direct Fiber Option 109

10.2 High-Density Interconnect Portcard Option 112

11 Triggers **116**

11.1 B Triggers 116

11.2 Secondary Vertex Trigger 117

12 Project Schedule, Cost and Manpower Needs **121**

1 Summary

The accumulated CDF data make it clear that high resolution vertex detection is a key tracking component in the CDF program of high p_T physics, specifically the top search, and b physics. The planned increase in the number of p and $\bar{p}$ bunches in the accelerator in 1996, and the resulting shorter bunch spacing (132 ns or 395 ns) requires a replacement for the SVX and SVX′ detectors. Based on the experience gained with the current SVX detector we are proposing SVX II Stage 1 which is capable of operating with the shorter bunch spacing and which extends the high p_T and b physics capabilities of the present vertex detector.

The SVX was installed at the beginning of the current Run Ia. It has been successfully commissioned and the data taken demonstrates that it is working reliably and well (see below). Based on performance of the SVX we have confidence that the SVX II upgrade can be constructed, and will substantially strengthen the physics capabilities of CDF. This proposal to build the SVX II Stage 1 detector must be regarded as an urgent priority for CDF for Run II to start in 1996.

This document constitutes a proposal to begin the construction of the barrel portion of an upgraded silicon vertex detector. This SVX II Stage 1 detector is needed by CDF in order to both maintain and extend its capability to pursue the high p_T top search and mass measurement which is both the collaboration's and the laboratory's highest priority. SVX II Stage 1 also provides a necessary step in the evolution of the physics capabilities of the CDF detector toward an ambitious b physics program for the latter half of the decade.

In summary the design goals for the the SVX II upgrade are:

1. Accommodate improvements to the accelerator which necessitate replacement of the SVX, specifically shorter inter-bunch spacing and higher radiation levels. This is required for Run II which is the first run with the reduced bunch spacing.
2. Improve performance for vertex detection in high p_T physics, in particular to tag b decay vertices in top events.
3. Enhance the b physics capabilities of the present detector.
4. Provide a detector and electronic readout capable of supporting a Level 2 vertex trigger processor.

<u>Features of the SVX II Stage 1 Barrel Detector</u>

A summary of the SVX II barrel detector for which we are seeking stage 1 approval is given below:

- A set of three barrels which approximately double the length of the present SVX. See Fig. 1(a) and (b).

- Double-sided detectors with 90 degree stereo. The proposed detectors with intermediate strips and 7-bit analog to digital conversion should attain a resolution of $\approx 10\mu m$ in r-ϕ and $\approx 25\mu m$ in r-z.

- A pipelined readout chip which will support operation at either 395 ns or 132 ns between beam crossings.

- High speed digitization and readout of the SVX II analog data in $<5\mu s$ in response to a level 1 trigger. The high speed of the readout is required in order to use the SVX II data in a level 2 vertex trigger processor.

- Support for a level 2 microvertex trigger processor (SVT). [1] This is a separate project which is being developed by the CDF collaboration. The ability to trigger on the impact parameters of reconstructed tracks will greatly extend the physics capabilities of the CDF detector.

- A new data acquisition system (DAQ) employing a highly parallel fibre optic readout and control utilizing low power optic drivers and receivers.

We expect the top physics program and other high p_T physics topics to be helped by increasing the length of the vertex detector in order to improve coverage of the luminous region in z at the interaction point. Doubling the length and adding z information will increase the b tag efficiency for top events by a factor of 1.6 to 2.0 depending on the top mass. In combination with an increase in luminosity, this increased efficiency gives a dramatic improvement to the overall physics capabilities of the detector.

The capability of using impact parameter information obtained from a vertex detector in the level 2 trigger to select events with secondary vertices will be of fundamental importance for any experimental program of b physics in a hadron collider environment. Having an impact parameter trigger implemented for SVX II will significantly increase the size of the b sample on tape. The experience gained in installing and running this trigger will help us to design more ambitious triggering systems in the future.

Upgrade Path

The SVX II barrel detector proposed here is the detector required to pursue the high p_T physics goals of the CDF collaboration once the collider begins operation with the shorter bunch spacing. It is also the first stage in a two stage upgrade path. The second stage would add forward disks to extend the η coverage out to approximately three. This additional η coverage is necessary for CDF to pursue b physics goals such as B_s mixing and CP violation studies with good flavor tagging capabilities.

This Stage 2 system greatly improves both the ability of the collaboration to pursue b physics and the solid angle coverage for several high p_T physics topics such as the measurement of the charge asymmetry for W production. We believe that our upgrade program will provide a powerful vertex detector with the large η acceptance required for flavor tagging in

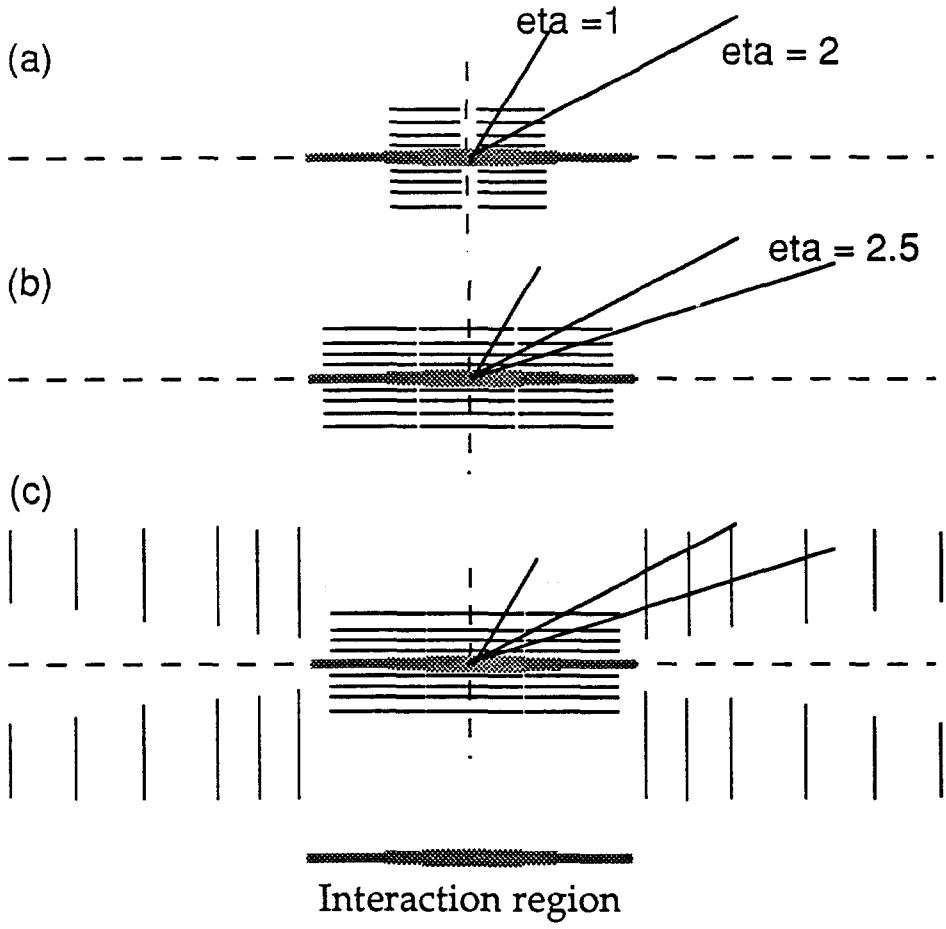

Figure 1: Schematic of the upgrade concept showing: (a) The present SVX. Barrel geometry with a total length of 51 cm. (b) SVX II Stage 1. Barrel geometry with a total length of 102 cm, still contained within the present VTX. (c) SVX II Stage 2. As (b) with the addition of disk detectors for forward tracking.

order to pursue a b physics program into the Main Injector era where measurements involving B mixing and CP violation studies will be important physics objectives. Figure 1 shows the present SVX layout and our SVX II Stage 1 and 2 concept. Stage 1 can be viewed as a detector for Run II in 1996, with Stage 2 an addition for the Main Injector running in the latter part of the decade. The proposal presented here covers the Stage 1 barrel portion of the SVX II upgrade.

Summary of Manpower, Schedule and Cost

Our initial estimate for the project cost in materials and services for the SVX II barrel detector is $3.8M, of which $360K will be spent on R&D in FY93, with the major purchases in FY94. With this funding, and with the level of manpower outlined in section 12 the detector will be ready for installation in January 1996. This requires that the design and R&D work be completed and that the final design decisions be made by early 1994. The

construction process, including the testing of delivered components and sub-assemblies is then expected to take one and a half to two years, based on our experience in building the SVX and SVX′ detectors, and assuming improved efficiency with additional assembly facilities.

This schedule is aggressive. It is essential that the project be funded, and the design and R&D be fully supported this year for SVX II to be ready for the operation with shorter bunch spacing in Run II.

Proposal Outline

Sections 2 and 3 of this document discuss the performance of the present SVX in Run Ia and compare the design of the present SVX and the proposed SVX II barrel detector. Section 4 discusses the Monte Carlo tools that were developed for the design of SVX II and gives results for the tracking studies carried out as part of the design process. Section 5 presents the physics motivation for the SVX II upgrade in detail and presents the results of the various high p_T and b physics benchmarks used to develop the SVX II design. Sections 6 through 11 of the proposal cover the various technical subsystems of the SVX II barrel detector. Section 6 discusses the mechanical engineering and design of the SVX II bulkheads, ladders and assembled barrels, and the cooling scheme. Section 7 covers the design and continuing R&D of the double-sided silicon strip detectors. Section 8 addresses the design of the electronics readout chip for SVX II which is a joint Fermilab/LBL project to provide a common chip for both CDF and D0, and section 9 outlines the radiation damage considerations that are critical in the design of the detector and electronics. Section 10 discusses the rest of the data acquisition system, and section 11 discusses triggering and in particular the level 2 trigger processor development. Finally section 12 discusses the cost, manpower and schedule for the Stage 1 SVX II project.

2 SVX Performance

The SVX detector has been installed in CDF and is currently taking data in Run Ia. The installation and commissioning has gone smoothly. In this section we summarize initial indications of SVX performance and potential.

During the spring and summer of 1991, the two SVX barrels were assembled at Fermilab. Optical survey information was used to measure the position of each silicon microstrip detector to 10 microns. First $\bar{p}p$ collisions were observed in the SVX in April, 1992, and as of mid-December CDF had collected 5 pb^{-1} of data with the SVX. Through the commissioning of the Tevatron and CDF, no serious damage, radiation or otherwise, has occurred to the detector. Greater than 98.7% of the 46,080 strips are functioning well. Included in the bad-strip count are 128 channels from the one SVX chip (out of a total of 360) that has failed. Fits to the Landau distribution of SVX hits show a signal-to-noise in routine CDF operations of about 9:1. Occupancies are typically 8% with 2% coming from physics, and

6% coming from noise fluctuations. Much of the noise contribution could be reduced with additional flexibility in setting the readout threshold levels. Nevertheless, the occupancy is still such that the SVX is a factor of three away from limiting the CDF DAQ readout time.

Tracks are reconstructed in the SVX by projecting found tracks in the central tracking chamber back into the SVX. We have compared the ratio of three-layer to four-layer SVX tracks in order to measure the individual layer hit efficiencies. They range from 97% to 99% with on-going improvements in the hit association and clustering algorithms being made to gain efficiency.

The addition of the SVX has made a noticeable improvement to the CDF momentum and mass resolution. For the $J/\psi \rightarrow \mu^+\mu^-$ data sample, the J/ψ mass width reduces by 35% from 26 MeV/c^2 (CTC only, no beam constraint) to 17 MeV/c^2 (CTC + SVX combined fit) when the SVX hits are included. This should help in the reconstruction of exclusive B meson final states and preliminary results are expected soon. Improvement in the W boson mass resolution is also anticipated.

Much care and attention was paid during the SVX design and construction to the use of low mass materials and components. The result was an $\sim$ 3% of a radiation length of material contribution (at normal incidence) to the CDF detector. Early studies indicate that the secondary particle and photon conversion backgrounds from this material are very low and present no problems to the data analysis.

Using the optical survey constants measured during the barrel construction, we observe a residual distribution with a sigma of 18 microns. When tracks are used to align the device in situ, allowing for only simple translations of the individual ladders, the residual distribution narrows to less than 14 microns. This is shown in Figure 2. Such a high quality alignment so early in the data-taking, when the asymptotic resolution is only 10 microns, is a nice reward for the effort spent in the careful design and construction of the SVX.

First indication of displaced vertices can be seen in the SVX event display of Figure 3. This event contains a clearly displaced J/ψ decay with associated tracks on one side and a second displaced vertex on the opposite side. The analysis of such events with bubble chamber-like clarity and micron scale precision will provide significant new physics results. Quantitative analysis of these events has already produced a preliminary measurement of the J/ψ 3D decay length distribution (Figure 4). A clear excess on the positive side is evident. After background subtraction using the side band distribution, a correction (derived from a Monte Carlo study) assuming the J/ψ is from a B decay. The resultant distribution agrees well with the average B lifetime. The decay length distribution in the signal region is also well fit to a sum of prompt J/ψ production and a reasonable fraction of J/ψ's from B decay. B tagging algorithms designed for the top search perform as expected on the J/ψ sample. Studies of jets, which should have a B contamination at the fraction of a % level, can be used as a control sample for the b tagging algorithms. First results indicate that the background rejection expected from Monte Carlo studies is attained in data.

Some effort has gone into using the SVX pulse height information for particle identi-

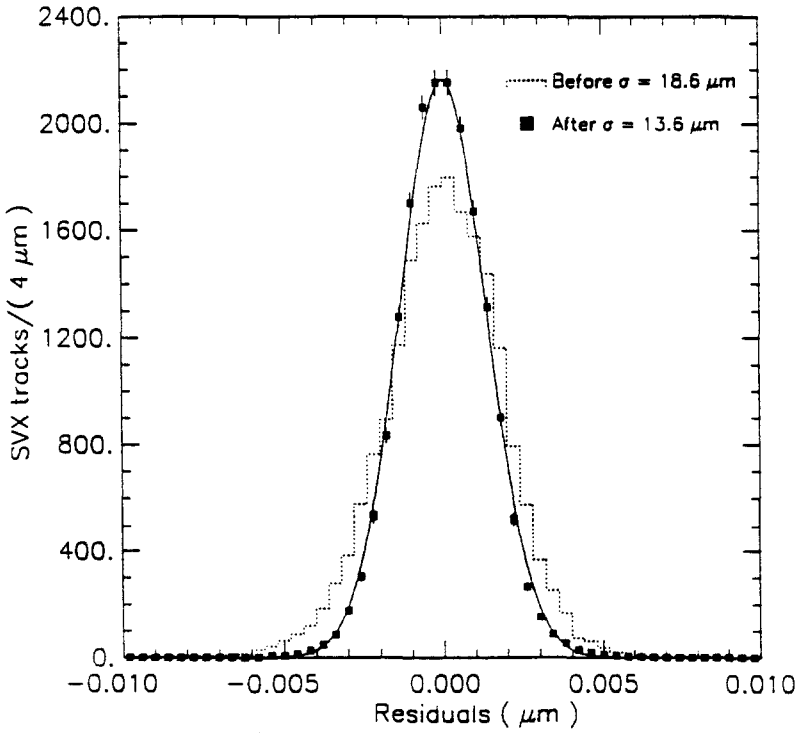

Figure 2: Residual distribution for hits associated with tracks before and after in situ track alignment.

fication. Figure 5 shows the smallest pulse height, from four-hit SVX tracks versus track momentum. Proton and kaon bands are clearly visible. This information may prove useful in B meson and baryon tagging and reconstruction.

To date, the radiation protection system for the SVX is functioning well. The accelerator division has been very cooperative in keeping the dose to the SVX at a minimum. So far no noticeable increase in SVX noise or leakage current, which would indicate radiation damage, has been observed. We estimate (with an uncertainty of about a factor of two) that the inner layer of the SVX has been exposed to about 2 Krads. The radiation dose will be carefully controlled and monitored throughout the CDF data-taking.

Overall, it can already be concluded that the SVX project has been successful. A silicon vertex detector can be installed and operated at the Fermilab Tevatron collider. It is with this understanding and experience that the design and construction of the SVX II detector can proceed with confidence.

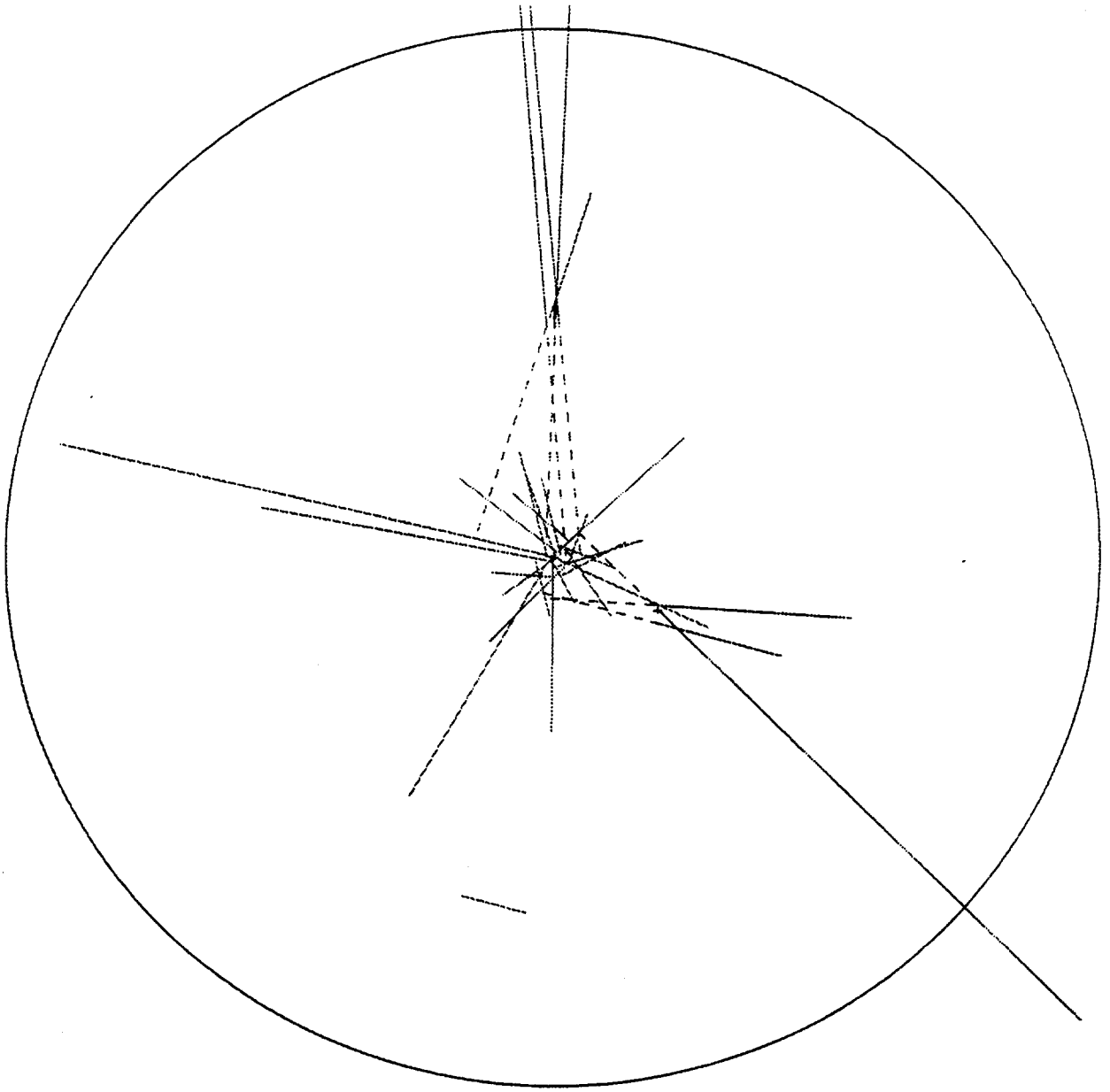

Figure 3: SVX display showing two displaced vertices in a $J/\psi \rightarrow \mu^+\mu^-$ event. The length of the tracks is proportional to their momenta and the J/ψ is in the displaced vertex at the 4 o'clock position.

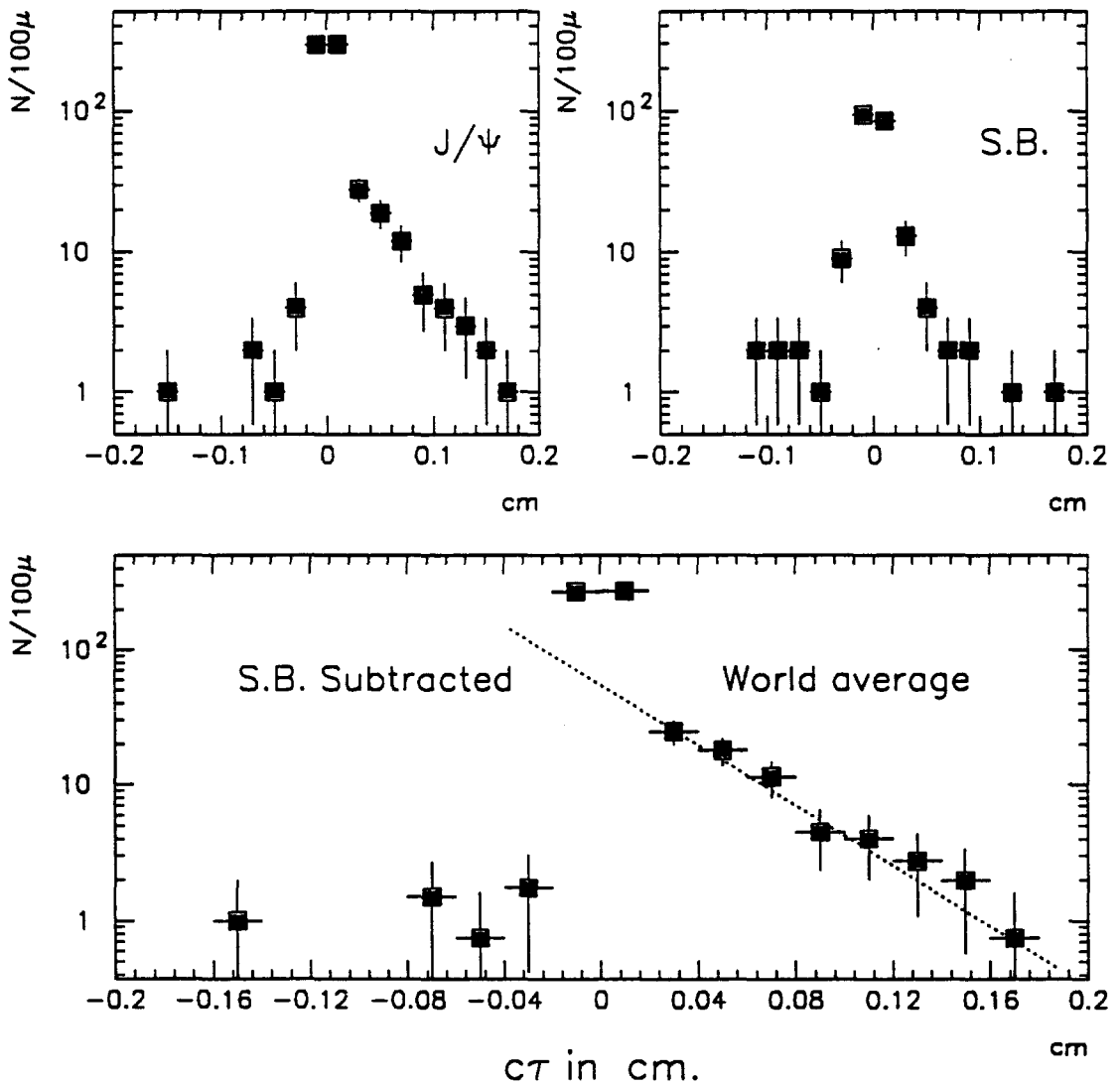

Figure 4: Preliminary CDF $J/\psi \rightarrow \mu^+\mu^-$ decay length distribution in the signal region (top left), the side band region (top right) and the background subtracted signal distribution, corrected by Monte Carlo calculation for the momentum ofthe missing decay particles (bottom).

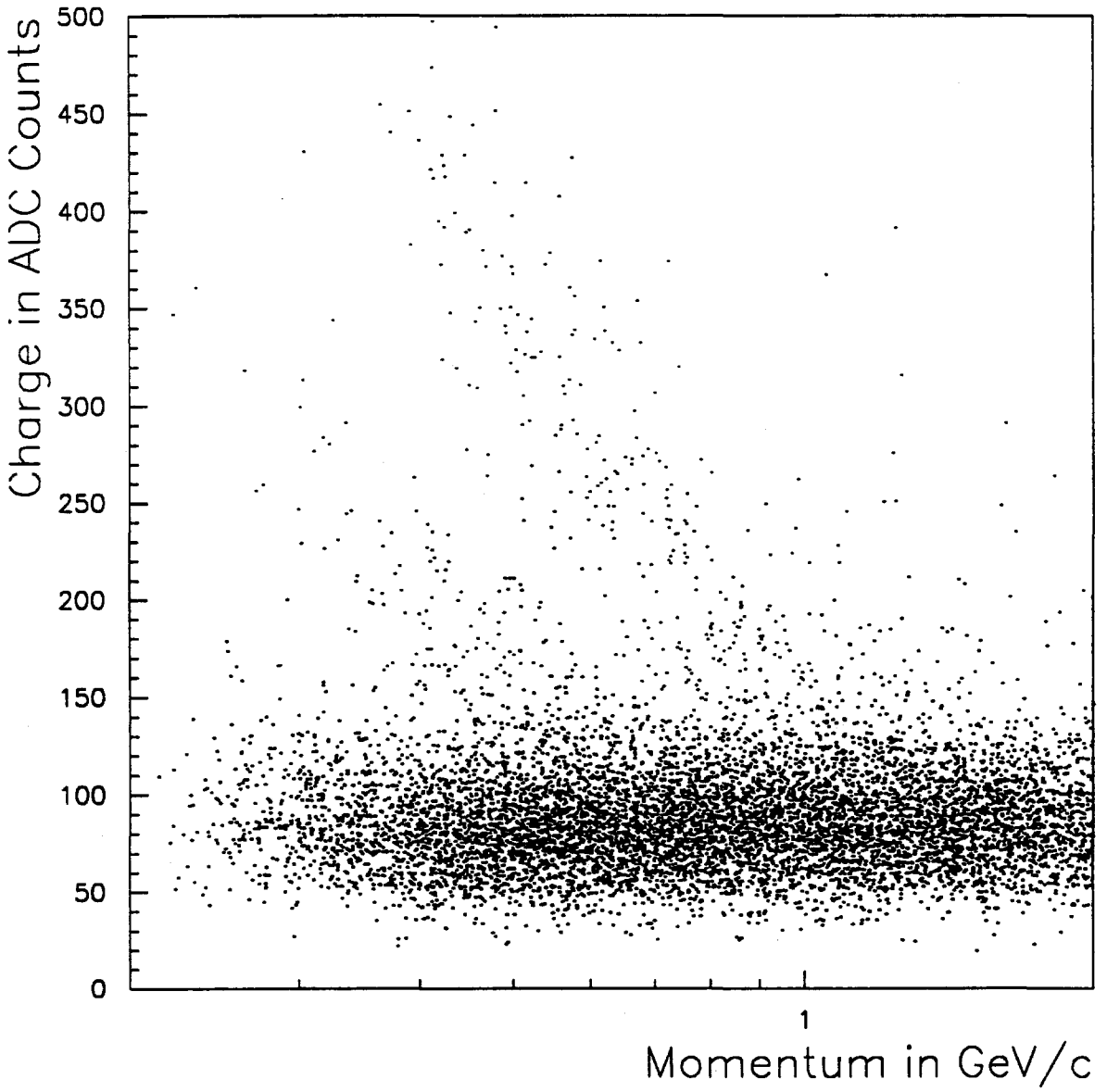

Figure 5: Smallest pulse height versus track momentum in the SVX, showing distinct proton and kaon bands.

3 SVX and SVX II Design Comparison

The two principal contributions to the improved performance of the SVX II Stage 1 barrel detector over the present SVX detector are the increased geometric coverage and the addition of z readout. Table 1 shows a comparison between the SVX and SVX II detector designs. We discuss below the reasons for choosing the SVX II detector parameters.

In order to better cover the CDF interaction region, and to extend the geometric acceptance to higher η, the length of the SVX II barrel detector has been significantly increased compared to the present SVX detector. The length of approximately 1 meter is well matched to the length of the CDF interaction region and the acceptance of the CDF outer tracking system. With the geometry of wedges described below and in Table 1, standard 4 inch diameter silicon wafers allow individual detectors of length 8.5 cm (as in SVX), and result in a total SVX II active length of 102 cm. The parameters in Table 1 assume this individual detector length. In order to optimize the detector yield and cost, we may choose a slightly shorter detector length. In particular, if the interaction region can be made shorter, the SVX II geometry can be better optimized to meet this change.

Unlike SVX, the SVX II barrels will use double-sided detectors to provide information for tracking and vertex finding in two views, r-ϕ and r-z. The amplifier chips will again be 128 channels wide with a pitch of 50 microns. In order to avoid the need for significant fan in/fan out of the detector read out to the electronics, this limits the ϕ readout pitch on the detectors to be approximately this size. We are also considering the use of detectors with an intermediate strip geometry for SVX II to obtain an improved position resolution over the present SVX readout pitch.

Experience using SVX in the present run has confirmed the advantages of having four layers per view for alignment, efficiency (redundancy) and pattern recognition in the high multiplicity hadron collider environment. The inner radius is given by the detector readout pitch and the requirement of an integral number of r-ϕ readout chips and is limited by the accelerator beampipe radius. We are proposing a new 1.0 inch diameter beryllium beampipe for SVX II, compared to the present 1.5 inch diameter pipe used with SVX, to obtain additional improvement in track impact parameter resolution. The outer radius is chosen to be compatible with the present VTX, and with this radius the detector position resolution is well matched to the outer tracking system track projection error. Larger radii would increase the channel count without a significant improvement in track finding efficiency and track parameter resolution.

For SVX II, the silicon microstrip detectors will be mounted onto ladder structures and arranged in twelve azimuthal sectors in each barrel. This is a similar geometry to that used for SVX. The 30° wedge geometry is well matched for detector widths (again quantized in integral number of chips) and to axial cabling schemes, and to the parallel processing used in the Silicon Vertex Tracker (SVT). The SVT will reconstruct tracks in individual detector wedges simultaneously to reduce processing time.

Detector Parameter	SVX	SVX II
Readout coordinates	r-ϕ	r-ϕ;r-z
Number of barrels	2	3
Number of layers per barrel	4	4
Number of wedges per barrel	12	12
Number of ladders	96	144
Ladder length	25.5 cm	34.0 cm
Combined barrel length	51 cm	102 cm
Layer geometry	3° tilt	staggered radii
First layer radius	2.989 cm	2.416 cm
r-ϕ readout pitch (4 layers)	60;60;60;55 μm	60;55;60;55 μm
r-z readout pitch (4 layers)	-	166;111;166;166 μm
Active length of readout channel (r-ϕ)	25.5 cm	17.0 cm
Number of r-ϕ readout chips/ladder (4 layers)	2;3;4;6	4;6;8;12
Number of r-z readout chips/ladder (4 layers)	-	4;6;8;8
Number of readout chips/wedge (r-ϕ;r-z)	15;-	30;26
Number of r-ϕ readout channels	46,080	138,240
Number of r-z readout channels	-	119,808

Table 1: Comparison of the geometrical layout and design parameters of the SVX and SVX II detectors.

In order to allow wedge-to-wedge alignment, adjacent detectors in a layer will overlap by several strips. A small overlap was achieved in SVX by tilting the detectors 3° from tangential. With double-sided detectors, the clearance restrictions for chips and wirebonds would require much larger tilt angles. This is particularly true for the innermost layer which is at a reduced radii compared to SVX. We are therefore considering the use of a staggered radii geometry with a separation of ~7 mm between neighboring ladders to allow greater overlap between wedges without mechanical interference.

In order to minimize the bulkhead support material, yet keep the length of silicon read out per electronics channel sufficiently small (and therefore reducing the amplifier input capacitance and noise), we have chosen a three barrel configuration. Each ladder is composed of four 8.5 cm detectors and is 34 cm in length. Pairs of detectors are wire-bonded together and read out at each end of the ladder, for both the r-ϕ and r-z readout. To minimize the inactive gaps between barrels, the readout electronics will be mounted on hybrids glued onto the detector surface. Only a small gap between barrels will be required for the bulkhead support, cabling, and cooling lines. Mounting the readout hybrids on the detector surface will noticeably reduce the gap between SVX II barrels and improve the geometric coverage compared to SVX.

Given the detector lengths and widths, and chip pitch, there are natural choices for the pitch for the z strips and these are shown in Table 1. We have simulated the detector performance with resolutions corresponding to pitches similar to the ones chosen and find it

to perform well for tracking and vertex-finding in the r-z plane.

SVX II will use an entirely new data aquisition system to operate with beam-crossing times as short as 132 nsec, and provide the digitized analog information in time for level 2 trigger formation. The use of analog information for the present SVX, to find the pulse-height weighted cluster centroid, provides a significant improvement in the resolution. In addition, for SVX II, the use of analog information in centroid finding provides good z resolution for tracks out to high incidence angles (high rapidity). The large number of channels and the need for fast readout speeds, have lead to a design with digitization on-board the front-end chip. Many of the features of this chip, for example the "nearest neighbor" readout scheme, and the desire for a readout threshold which can be set per chip, are based directly on our experience with the present detector. The data aquisition, and the control of the front-end chips will be highly parallel, to reduce the impact of a single component failure. To provide the necessary bandwidth with minimal material and low power consumption, SVX II will use optical fiber transmission from the detector to a VME based DAQ system and the SVT trigger processor. There has been significant R&D on optical readout for SSC experiments, and while this is a relatively new technology, the development appears timely for SVX II.

From our study of the design parameters chosen for the SVX and the experience gained in the SVX construction, we have found that a 4-layer barrel structure with a wedge geometry is a natural choice for SVX II. Several significant improvements will be made, however, when compared to the SVX detector. SVX II will have double the length, z readout, a smaller inner radius, a smaller inactive region between barrels, and a fast DAQ system with trigger capabilities. The staggered radii geometry will simplify the barrel construction and improve the wedge-to-wedge overlap for alignment. These improvements will make the SVX II detector an even more powerful vertex detector than the already successful SVX.

4 Tracking Simulation

4.1 Model Geometries

The geometric design of a vertex detector for CDF is strongly influenced by the long luminous region of the Tevatron. For this study we assume that the extent of the luminous region in z will remain unchanged from current operation (a gaussian with $\sigma_{z_v} = 30$ cm). In order to cover such an interaction region, one is naturally led to a barrel geometry. Considerations such as acceptance for high p_T leptons, and tagging of b jets from top (see section 5.3), and the desire to minimize the material preceeding the CTC in the central rapidity region lead naturally to the conclusion that the length of the barrel should be about $\pm 2\sigma_{Z_v}$. This length fits conveniently inside the present CDF VTX. The considerations that led to the choice of four layers of silicon in the barrel at the radii of the current SVX design remain valid: an inner radius as small as possible to achieve the best impact parameter resolution, given the constraints of the beam pipe diameter and the severe radiation environment; an outer radius as large as the VTX will allow; four layers to allow for redundancy in case of catastrophic loss of a large section of a barrel layer. As discussed below, the outer radius is sufficiently large compared to the inner radius to provide efficient pattern recognition.

There remain two critical design issues:

- measurement of the z coordinate in the barrel,
- tracking and vertexing at large η.

With a barrel of length 102 cm, the detector provides precision vertexing through 4 layers of silicon out to $|\eta| < 2.5$ for tracks originating from the center of the detector (detector η). Due to high track multiplicities, stand alone tracking (pattern recognition) in the SVX II barrel detector is expected to be difficult. For the current run, the tracking algorithm is based on finding a track in an outer tracker, which currently is the CTC. Figure 6 shows the pointing resolution in the azimuthal direction of the barrel detector as a function of the ratio of outer to inner barrel layer radii with the SVX. The corresponding CTC error is 0.6 mR. The choice of the current SVX design, with a ratio of 2.6 for the outer layer and inner layer radii, is seen to be nearly optimal and well matched to the CTC pointing resolution. At high luminosities, the increased track multiplicities make pattern recognition more difficult in the inner CTC superlayers. Changes in the front-end electronics for the CTC are expected to improve the two track resolution by about a factor of two and roughly compensate for the increased track density. Wire aging is not expected to be a problem up to an integrated luminosity of at least 1 fb^{-1}. In this study, we assume that the tracking performance of the CTC will not degrade at high luminosity. However, the CTC single track efficiency drops off sharply for tracks that traverse fewer than 4 super layers, corresponding to a detector η of 1.4. A set of radial disk tracking devices at fixed z from the edge of the barrel (55 cm) out to the CTC end plate (155 cm), with each disk extending out to a radius equal to the inner wall of the CTC (27 cm) is modelled to provide tracking capability at high

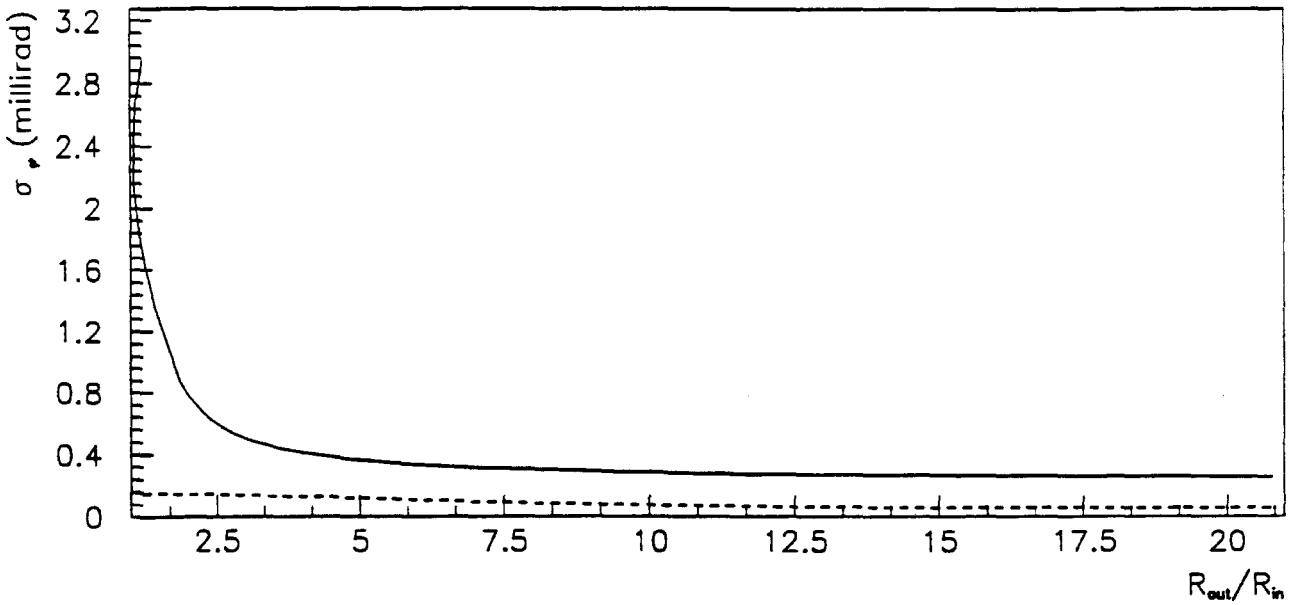

Figure 6: The solid curve is the error on the azimuthal pointing resolution (σ_ϕ) as a function of the ratio of barrel outer to inner radii (R_{out}/R_{in}) using only the SVX. The dashed curve is the same pointing error with the CTC resolution included.

rapidity $1.4 < |\eta| < 2.5$. Candidate technologies for these disks include silicon detectors and gas microstrip detectors. Other geometries, such as layers of axial straw tubes preceeding the CTC can be imagined. One aspect of this study was to first demonstrate the physics motivation for tracking at large rapidity, and for this purpose we take a set of radial disks as an example of how to achieve tracking in this region.

An important consideration in the SVX II design is how a z coordinate measurement can be achieved and how such a measurement supplements the tracking of the CTC. The measurement of the z coordinate in the SVX barrel will improve the single track z resolution by almost an order of magnitude. This will improve the tagging of leptons from heavy flavor decays as well as mass and vertex resolution.

To evaluate the capability of an elongated silicon barrel detector as well as the enhancements of z measurement in the barrel and additional disk devices, we examine five detector geometries:

G1 The present SVX geometry, with measurement of the ϕ-coordinate only. The active silicon covers a total length in z of 51 cm. There is a gap in the coverage at $z = 0$ to allow for support and cable access.

G2 A barrel geometry with 4 layers, similar to the present SVX, but with a total z coverage of 102 cm. This geometry again has measurement of the ϕ-coordinate only.

G3 Same as (G2) but with both ϕ and z information.

G4 Geometry (G2) with a forward tracking upgrade using 6 radial disks spaced in z from 55 to 155 cm and each extending out to 27 cm in radius. The spacing in z has been chosen to enhance the tracking coverage in the CTC plus disk system.

G5 Geometry (G3) with the same disk arrangement as (G4).

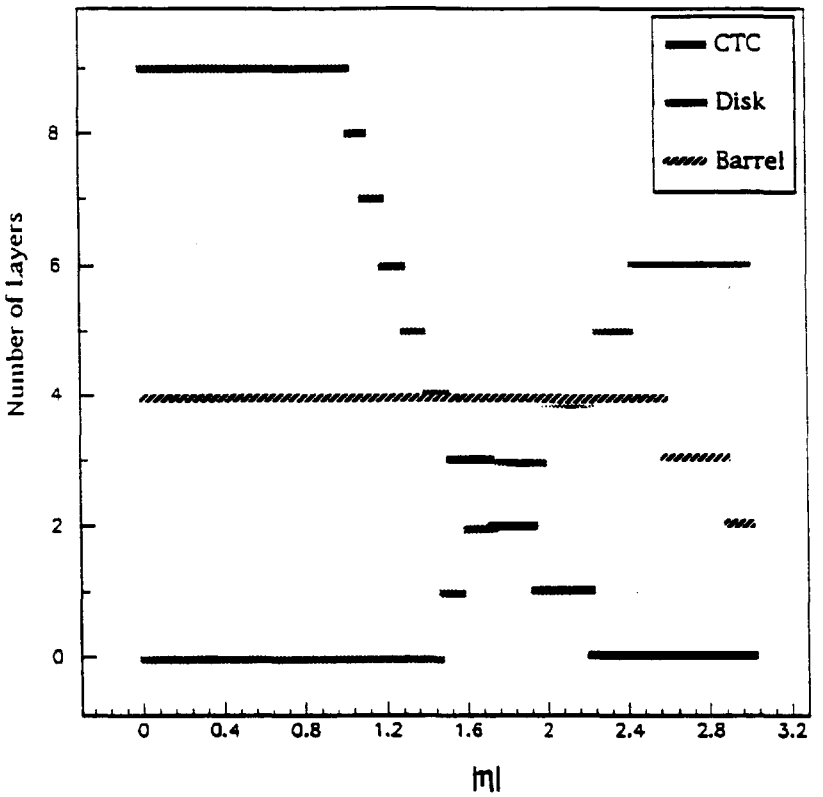

Figure 7: The number of detector elements (layers or superlayers) traversed by a high p_T particle originating at the detector origin vs η.

The acceptance of the CTC, SVX barrel, and radial disks is shown in Fig. 7, where the number of detector elements traversed by a high p_T particle originating at the detector origin is plotted as a function of rapidity. The geometric acceptance for geometries (G1) and (G2) is plotted as a function of rapidity in Fig. 8, where the tracks originate from an interaction point smeared in z with $\sigma_z = 30$ cm. The increase in acceptance for (G2) demonstrates the importance of covering the extended interaction region. The extension of the tracking to larger rapidity provided by a system of radial disks is demonstrated in Fig. 8 as well. The radial disk placement has not been optimized and involves consideration of the other detector elements in the endplug region.

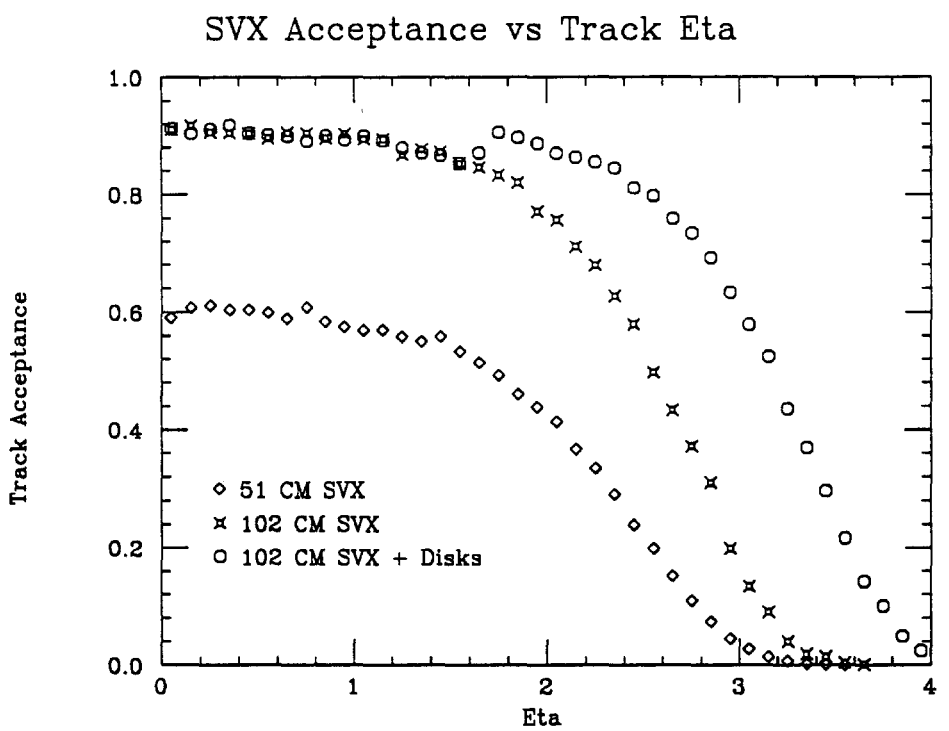

Figure 8: Geometric acceptance for geometries G1 (current SVX barrel length) , G2 and G3 the elongated barrel (2 × current SVX) , and G4 and G5 the elongated barrel plus disks. The acceptance of the CTC is not included.

4.2 Simulation Tools

Two fast simulation programs were developed to model the geometries G1-G5. The first is the CDF fast detector simulation, QFL, modified for an elongated barrel geometry with both ϕ and z measurements (G1-G3). The second, SVXSIM, is a very fast, easily modified, simulation developed specifically for this study and capable of incorporating the VTX z resolution and radial disks. These simulations share many features. They are based on a covariance matrix calculation technique [2]. As a consequence, any inefficiencies due to pattern recognition are modeled in an ad hoc fashion. In QFL, the CTC efficiency is 100% for tracks with $p_T > 200$ MeV/c traversing at least three CTC superlayers. For SVXSIM, the efficiency per CTC wire layer from the data is used to model an efficiency per superlayer. We require 4 of 12 axial and 3 of 6 stereo wires for a layer to be included in the fit. We then further require some minimum number of axial superlayers plus disks in order for a track to be found in the outer tracker. The absolute minimum is a point-slope measurement: at least one axial superlayer or two disks. More stringent requirements are investigated in the following section on single track results. The CTC error calculation includes efficiencies and resolutions per wire layer from the data. This is known to properly reproduce the CTC errors measured in the data [3]. The material in the barrel is equivalent to the total material in the current SVX plus VTX inner wall, equally distributed in each of the four cylindrical layers. The z measurement resolution is degraded as a function of the angle of incidence α into the silicon according to a parameterization interpolated from calculations done by Luth [4] (see Fig. 9). This parameterization includes the effects of strip pitch (100 μm), the thickness of the silicon layer (300 μm), and the readout signal/noise ratio (12:1). We have studied this resolution in detail, following the work of Luth [4], to determine the effect of strip layout and signal/noise for our design. The results of these studies are summarised in section 7.2 of this document. In SVXSIM the contribution of the VTX to the z resolution is modeled [5] as 16 measurements from a radius of 21 cm down to a radius of 11 cm each with a resolution of 200 μm/$\sin\theta$ (see impact parameter resolution plots in Fig. 10 labeled G1). The disks are idealized tracking elements providing 3D information with resolution comparable to the barrel detector. The r measurement is degraded with the angle of incidence of the track according to the z resolution parameterization given in Fig. 9. The geometry, resolution and material of the barrel and disk detectors are summarized in Tables 2 and 3.

These two simulations have been compared in detail to the CDF full detector simulation, CDFSIM, for G1. We have compared the calculated errors on all five track parameters as a function of p_T and η. The calculations from all three simulation programs are in good agreement. This checks the material model as well as the simulation algorithm. For example, the error on the impact parameter is calculated as 11 μm at high p_T and 44 μm at a p_T of 1 GeV/c. The agreement in our simulation tools is such that further discussion of geometries G1-G5 will be made without reference to the method of simulation.

Table 2: Summary of Barrel Detector Parameters.

Structural element /detector	radius (cm)	$\frac{1}{2}$ length (cm)	thickness[5] (cm)	thickness[5] (%X_0)	σ_ϕ (μm)	σ_z^1 (μm)
Beam pipe	2.60	—	—	0.16	—	—
VTX[2]	11.0-21.0	51.0	—	—	—	200.0
CTC[3]	27.6	155.0	0.10	3.00	—	—
SVX II[4]	3.0, 4.3, 5.7, 7.8	51.0	0.03	0.75	12.0	30

[1]At $\eta = 0$.
[2]16-wire modules.
[3]Inner wall.
[4]Layers 1 - 4.
[5]Thickness of one layer

Table 3: Summary of Radial Disk Parameters.

z (cm)	55.0, 62.5, 70.0, 102.5, 126.5, 150.0
Disk radius (cm)	27.0
thickness (%X_0)	0.75
thickness (cm)	0.03
σ_{ϕ_0} (μm)	15.0
σ_r (μm)[1]	30.0

[1]At $\eta = \infty$

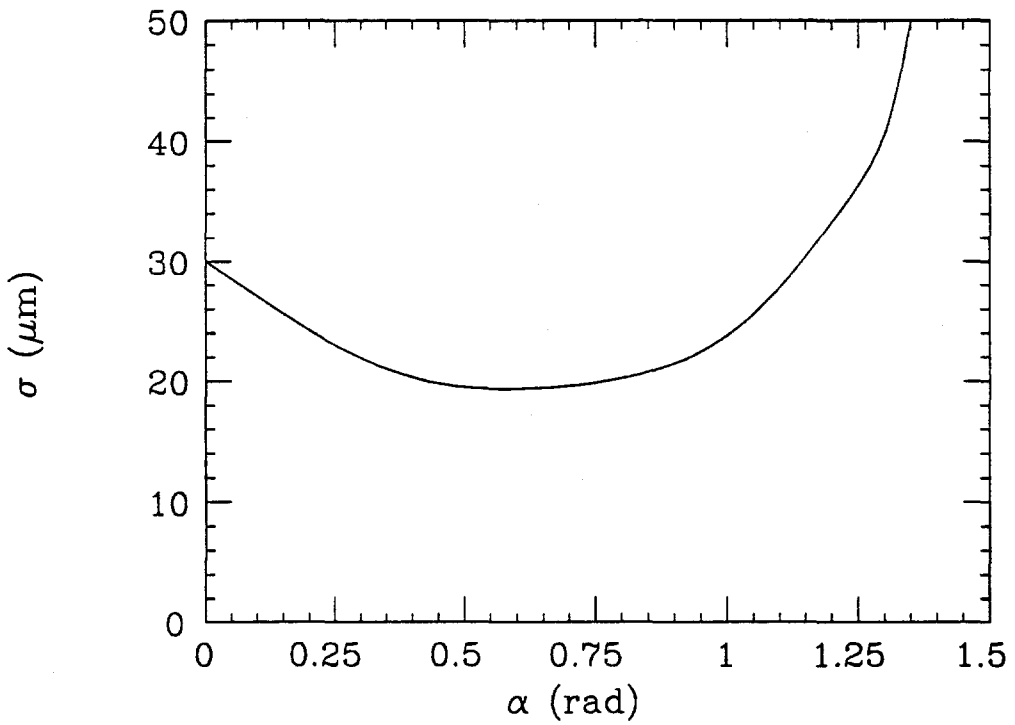

Figure 9: z resolution as a function of angle of incidence α. The parameterization is an interpolation for a thickness of 300 μm, S/N = 12, and pitch = 100 μm.

4.3 Single Track Results

In order to demonstrate the tracking capabilities of the different geometries, we examine the behavior of the transverse impact parameter error (σ_D), z impact parameter error (σ_z), and momentum resolution as a function of rapidity for track p_T of 1 GeV/c and 20 GeV/c. Figures 10, 11, and 12 compare these errors for the different geometries. These plots show the enhanced capability of the elongated barrel, of the elongated barrel with z resolution, and of the high η tracking provided by the disks. We note that the disks allow tracking out to $|\eta| \sim 3.0$. Because the precision of the tracking at large rapidity is limited by the large multiple Coulomb scattering in the barrel detector, the precision of the radial disks is not very significant. Their role is predominantly one of an outer tracking device allowing the track to be found in this region. This can be seen by comparing Tables 4 and 5, the latter being for a situation with the CTC and disk systems having an enlarged resolution. Table 5

Table 4: Errors on track parameters: nominal resolutions. Shown are the track parameter errors in the curvature, σ_C, the azimuthal angle, σ_{ϕ_0}, the transverse impact parameter, σ_D , the cotangent of the polar angle, σ_{cot} , and the z impact parameter, σ_{z_0}. The units are cm and radians.

p_T	η	$\sigma_C \times 10^6$	$\sigma_{\phi_0} \times 10^4$	$\sigma_D \times 10^2$	$\sigma_{cot} \times 10^3$	$\sigma_{z_0} \times 10^1$
1	0.	2.86	12.82	0.431	1.54	0.060
100	0.	1.24	1.43	0.097	0.38	0.027
1.	2.5	21.05	29.91	0.913	17.71	0.527
100	2.5	11.14	3.04	0.155	0.82	0.048

Table 5: Errors on track parameters with the CTC and disk resolution increased by a large factor (10^5).

p_T	η	$\sigma_C \times 10^6$	$\sigma_{\phi_0} \times 10^4$	$\sigma_D \times 10^2$	$\sigma_{cot} \times 10^3$	$\sigma_{z_0} \times 10^1$
1	0.	313.2	31.5	0.76	1.54	0.060
100	0.	228.0	25.1	0.63	0.40	0.028
1.	2.5	615.7	56.3	1.28	17.71	0.527
100	2.5	228.1	25.1	0.63	1.18	0.064

shows that the resolution in σ_{z_0} is almost unaffected by making the measuring errors in the outer tracker very large. In the case of σ_D there is some increase but it is due primarily to the increase in the curvature error caused by the loss of the outer tracker.

The amount of material traversed by a track as a function of rapidity is shown in Fig. 13 for the different geometries. Here we clearly see the predominance of the large path length in the barrel detector at large rapidity.

The utility of covering the elongated interaction region with the barrel detector was demonstrated in Fig. 8. When radial disks are included, geometries G4 and G5, the single track acceptance is > 80% for tracks produced anywhere along the interaction region out to

a track rapidity of ~ 2.5. For the disks, the relevant question is one of efficiency at large rapidity. Without doing a detailed simulation it is not possible to completely model the single track efficiency due to pattern recognition in the complete outer tracker of CTC plus disks. In order to evaluate what kind of efficiency can be achieved, we calculate the single track efficiency for tracks produced with a Gaussian distributed z position under different assumptions on the capability of the outer tracking system. We require some minimum number of CTC super layers (N_{ctc}) to be traversed by the track, or some minimum number of radial disks (N_{dsk}). Figure 14 shows the single track efficiency as a function of η for three cases: (1) $N_{ctc} > 2$ OR $N_{dsk} > 3$, (2) $N_{ctc} > 2$ OR $N_{dsk} > 4$, and (3) $N_{ctc} > 4$ OR $N_{dsk} > 3$. In each case the track was required to traverse at least two SVX barrel layers. These plots serve to emphasize the importance of the outer tracker performance for tracking at high rapidity. In this study we assume the efficiency as in case (1) of our model.

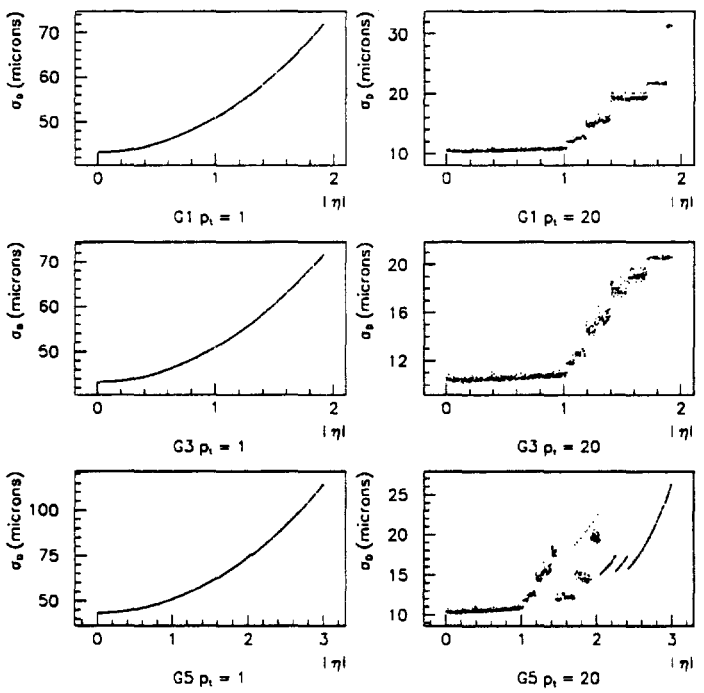

Figure 10: σ_D vs η for G1, G3 and G5 for tracks from $z = 0$. (Note horizontal scale change for G5 plot.)

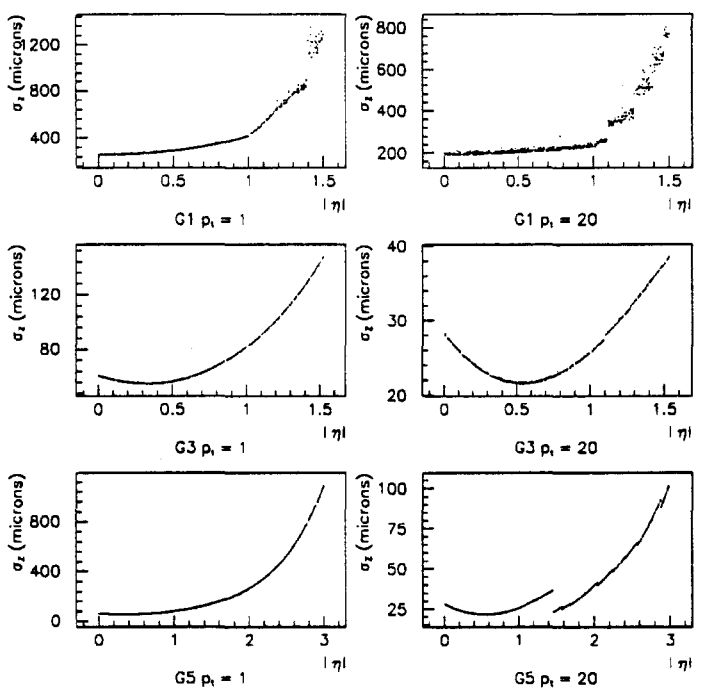

Figure 11: σ_z vs η for G1, G3 and G5 for tracks from $z = 0$. (Note horizontal scale change for G5 plot.)

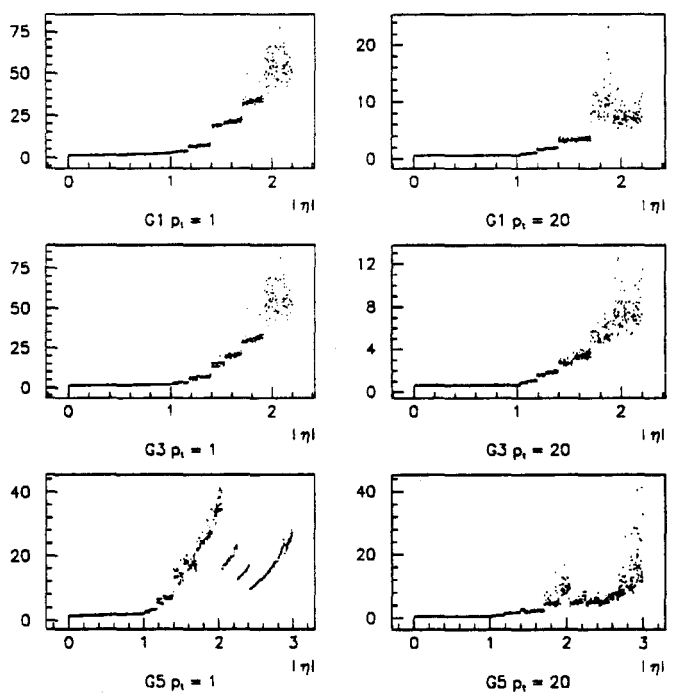

Figure 12: $\delta p_t/p_t^2/.001$ vs η for G1 G3 and G5 for tracks from $z = 0$. (Note horizontal scale change for G5 plot.)

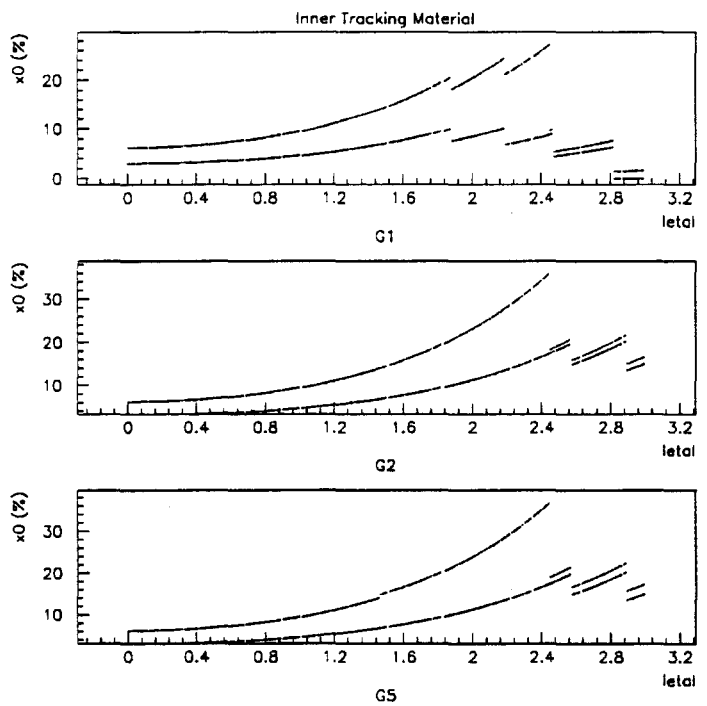

Figure 13: Material traversed vs η in G1, G2 and G5 from the SVX barrel (lower curve) and from all material preceeding the CTC (upper curve). The ordinate is in units of percent of a radiation length.

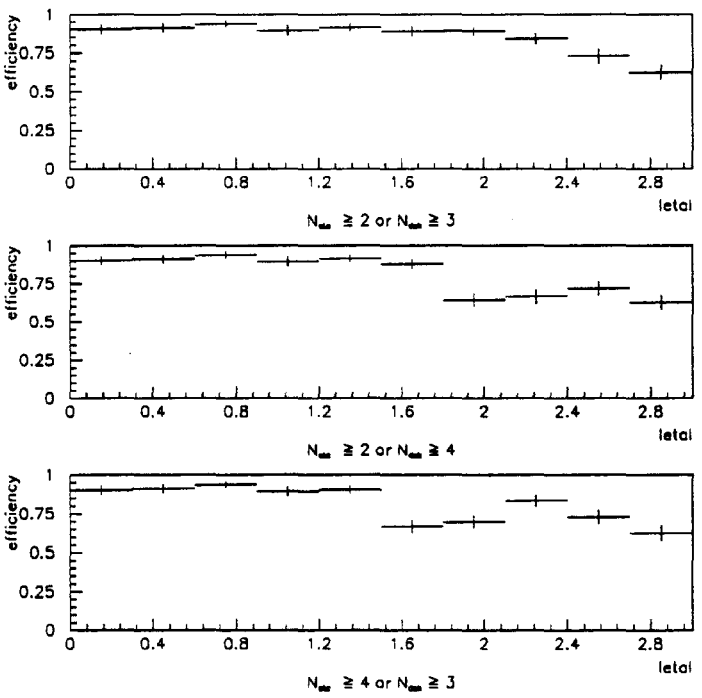

Figure 14: Single track efficiency vs η for three cases.

5 Physics Simulation

5.1 Physics Motivation

Top Physics

The discovery and subsequent study of the top quark are major goals for the collider program. Top production at the Tevatron is expected to be dominated by the production of $t\bar{t}$ pairs. In CDF, top events have been searched for with the following event signatures that require high p_T leptons plus neutrinos and jets: $t\bar{t} \rightarrow l - \nu - jets$ and $t\bar{t} \rightarrow 2l - \nu - jets$. The present lower bounds from CDF place $m_t > 91$ GeV/c^2 assuming Standard Model decay modes [6]. Within the Standard Model, electro-weak measurements limit $m_t < 200$ - 225 GeV/c^2 [7, 8]. If the top quark falls within this mass range, a top signal should be visible in both the $t\bar{t} \rightarrow l - \nu - jets$ channel and in the $t\bar{t} \rightarrow 2l$ channel with the luminosity expected this decade. The expected reconstructed event yields in CDF for the channels $e/\mu - \nu - jets$ and $e - \mu$ are given in Table 6 [8] for an integrated luminosity of 1 fb^{-1}.

Table 6: Expected reconstructed top event yields in CDF as upgraded for Run II with a 1 fb^{-1} run. The reconstruction requires $p_T(l) > 20$ Gev/c, $p_T(jet) > 15$ GeV/c, $|\eta_l| < 1$, $|\eta_{jet}| < 2$, and missing $E_t > 20$ GeV. Yields are given as a function of m_t. Yields for $t\bar{t} \rightarrow l$+4 jets events assume a b tag efficiency per event of 50%; for the e-μ channel there is no b tag requirement.

m_t (GeV/c^2)	e or μ + b jet + 3 jets	e - μ
120	1380	240
140	850	98
180	260	24
210	140	12
240	60	5

Top Discovery

The cleanest signal for top will be the observation of two high p_T leptons from the semileptonic decays of both the t and $\bar{t}$ quarks. The $t\bar{t} \rightarrow 2l$ channel has a background from the direct production of W^+W^- pairs that subsequently decay leptonically. This background exceeds the top signal for values of $m_t \geq 160$ GeV/c^2 as shown in Fig. 15 [8]. The W pair background can be controlled by adding the requirement of high p_T jets in the event, and/or by the requirement of a b tag in the event. The presence of a tagged B meson suppresses the W pair background and provides strong evidence for the top interpretation.

Because the branching fraction of $W \rightarrow e/\mu + \nu$ is 2/9, only 4/81 of the $t\bar{t}$ events decay

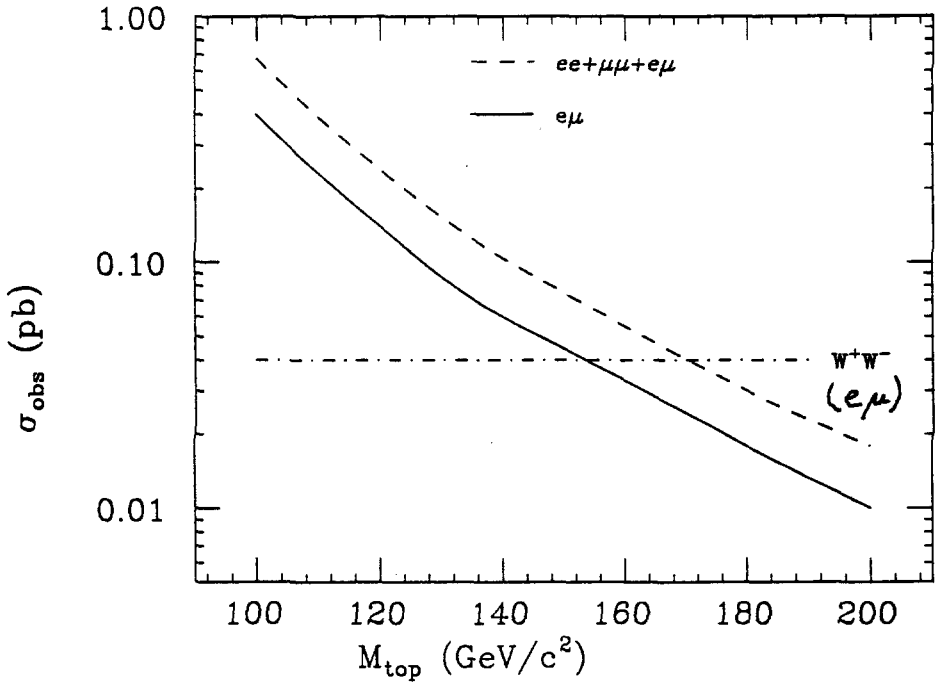

Figure 15: Cross section for high p_T dileptons from the direct production of W^+W^- pairs and from the production of $t\bar{t}$. The top production is shown as a function of the top mass: m_t. The cross sections include CDF detector efficiencies.

via the $2l$ channel. By comparison, the fraction of top events with one of the t quarks decaying semileptonically (the trigger e/μ) and the other hadronically is 24/81. The larger branching fraction for the $t\bar{t} \rightarrow l - \nu - jets$ channel is important to extend the top search to high masses. The $l - \nu - jets$ channel is needed both to search for anomalous top decays and for the measurement of the top mass. Backgrounds in this channel from $W+ \geq 3$jets are significant as shown in Fig. 16 [8, 9]. These backgrounds can be controlled by requiring ≥ 3 high p_T jets, (or ≥ 4 high p_T jets for large m_t), and by requiring a b tag.

Top Mass Measurement and Related Analyses

An excess of $2l$ and/or $l - \nu - jets$ events in CDF will provide evidence for top, and strong support for the discovery of top is the demonstration of the $t \rightarrow b$ decay. Standard Model studies, including the measurement of the branching fraction for $t \rightarrow W + b$ and the measurement of m_t, and searches for deviations from the Standard Model [10], require the largest possible data samples in both data channels: $t\bar{t} \rightarrow l - \nu - jets$ and $t\bar{t} \rightarrow 2l$.

One example of Standard Model tests is the comparison of the event rates for $t\bar{t} \rightarrow 2l$ and $t\bar{t} \rightarrow l - \nu + jets$. Deviations from the expected ratio of $2l$ to $l - \nu - jets$ events of 4/24 would signal new physics. For a b tag efficiency/event $>>1/6$, the estimated reconstructed event yields shown in Table 6 indicate that a $\sim 10\%$ statistical precision can be achieved for

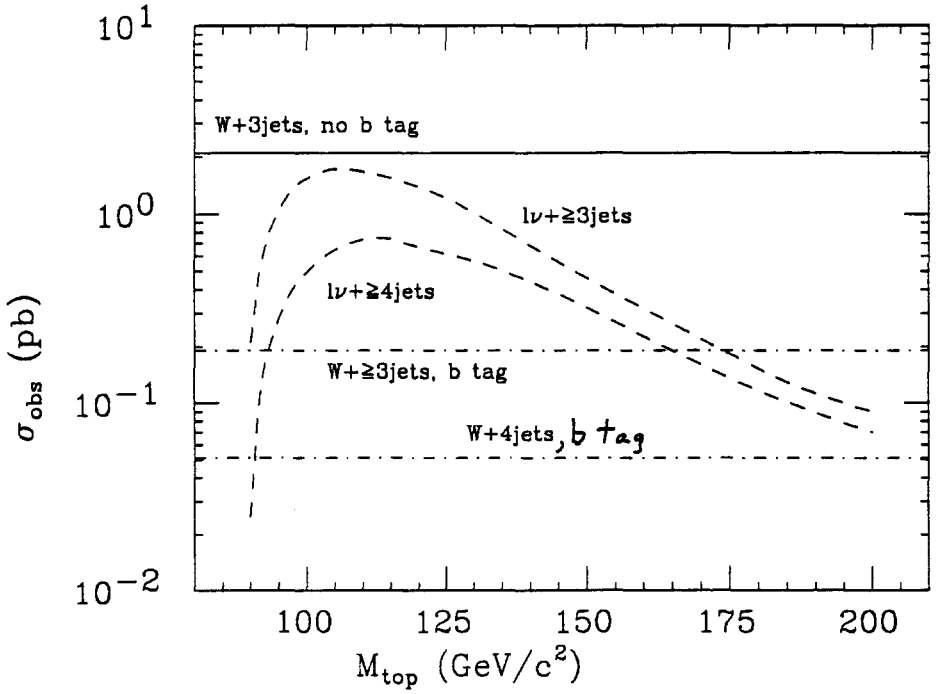

Figure 16: Cross section for $t\bar{t} \rightarrow l - \nu - jets$ as a function of top mass: m_t. The cross sections for $W + n$jets is shown without and with a b-tag. Jets and leptons were selected with (E_t, η_{max}) values ($\geq$ 15 GeV, 2.0) and ($\geq$ 20 GeV, 1.0) respectively.

this measurement for $m_t \leq 140$ GeV/c^2.

Simulation studies have been done to evaluate the measurement precision of m_t by CDF using the $l - \nu - jets$ channel. W bosons are reconstructed using 2-jet invariant mass combinations consistent with m_W and by constraining the $l-\nu$ mass to m_W. The precision on measuring m_t is limited to $\sim$ 5 GeV/c^2 from a combination of jet energy scale uncertainties, combinatoric backgrounds, and backgrounds from the underlying event [8]. The statistical precision is estimated to be $\sim$ 30 GeV/c^2 / $\sqrt{N_{ev}}$. Based on the numbers of events in Table 6 the statistical precision should not dominate the measurement of m_t unless the b tag efficiency is significantly less than 50%.

As noted above, b tagging is needed for the effective use of the $t\bar{t} \rightarrow l - \nu - jets$ events. b tagging in CDF relies on either a lepton tag (from the semileptonic decay of the b) or on the identification of a displaced decay vertex with the SVX. The lepton tagging efficiency per B is $\sim$ 10%. This almost meets the minimal requirements of the m_t and top branching fraction measurements. This efficiency is insufficient to extend the m_t measurement to the highest top masses or to effectively tag $> 1B$ per event as needed in searches for possible deviations from Standard Model decays of the top. With the SVX upgrade the tagging efficiency per B will be significantly increased. In the simulation section we present the results of a simulation of top decays to compare the b tag efficiency for the present SVX and for the proposed SVX

II upgrades.

B Physics

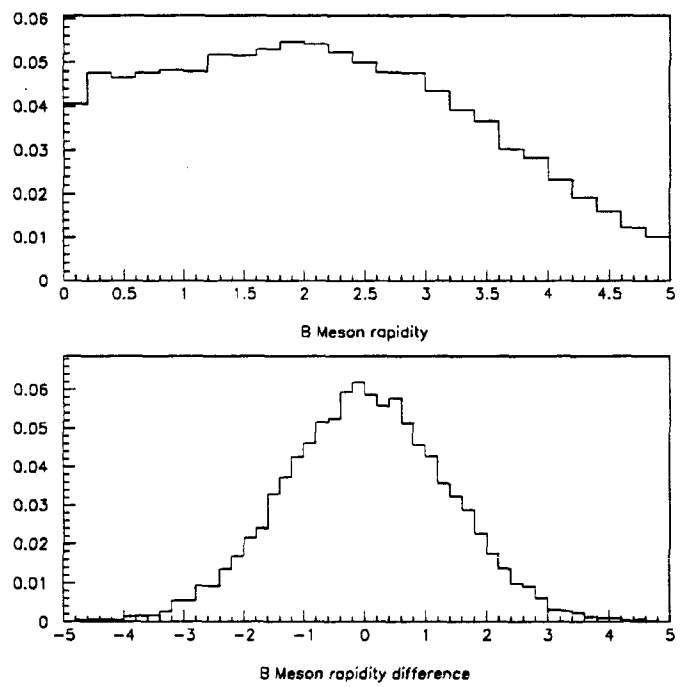

Figure 17: Rapidity distribution of B particles, and the difference in rapidity for the B and $\overline{B}$ (generated by ISAJET).

By mid-decade CDF will have reconstructed several thousand exclusive decays in ψK^+, ψK^* and other similar modes. A large fraction of these will have reconstructed secondary vertices using the SVX or SVX'. Several hundred $B_s \rightarrow \psi\phi$ decays, several tens of $\Lambda_b \rightarrow \psi\Lambda$, and a few tens of $B_c \rightarrow \psi\pi$ are expected in Run I. This is in addition to several million inclusive semileptonic B decays. These samples will allow cross section and $B\overline{B}$ correlation measurements, B spectroscopy and rare decay measurements, lifetime measurements to $< 5\%$ statistical error for B^+ and B^0, and studies of b flavor tagging. Substantial improvements to the above analysis are possible by increasing the acceptance for b flavor tagging, by providing three dimensional vertexing, and by implementing a level 2 secondary vertex trigger.

The kinematics for B's in $b\bar{b}$ events are very different from those in top events. The B's in $b\bar{b}$ events populate a broad distribution in rapidity. The rapidity correlation between the B and $\overline{B}$ is weak as shown in Fig. 17. In addition, the B's have a soft p_T distribution (see Fig. 18) with an average $p_T \sim 5$ GeV/c.

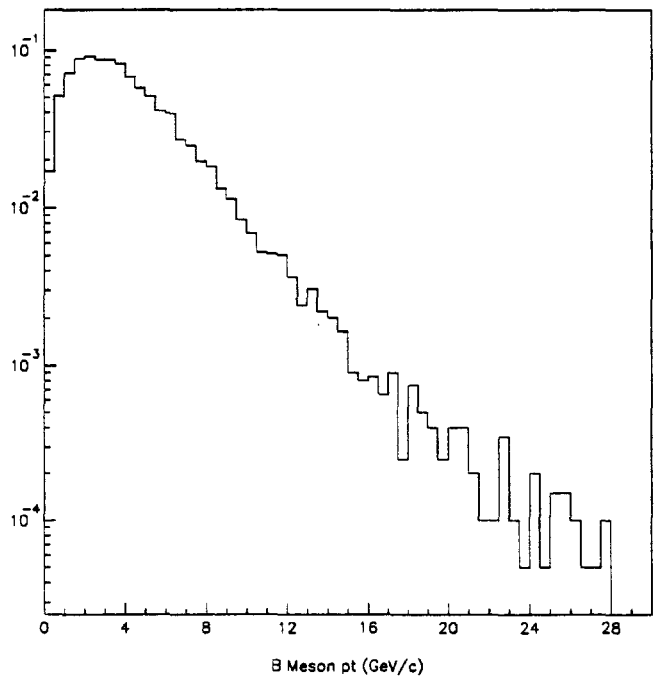

Figure 18: p_T distribution for B mesons (generated by ISAJET).

Important considerations for enhancing b physics in CDF include the following. The low p_T of the B daughter particles means that good position resolution at the vertex requires that the multiple scattering in the SVX II, and thus the material, be kept to a minimum. This requirement is also important in order to minimize photon conversion background to the inclusive electron trigger. The need to partially reconstruct both B particles for some physics topics implies that the detector should cover a large continuous rapidity range. With upgrades, CDF will have essentially continuous electron and muon coverage for $|\eta| < 3$. For the purposes of this document, we assume that CDF will have an effective tag for leptons (electrons and muons) for $p_T > 2$ GeV/c for $|\eta| < 3$. Maximizing the B signal to background for completely reconstructed decays requires good mass resolution over most of this rapidity range. Finally, while many CDF detector requirements for b physics and top physics differ, we will show that the need to provide vertex tracking over the extended interaction region at the Tevatron results in a conceptual design for SVX II that performs well for both b and top physics.

5.2 Physics Benchmarks

We use several physics measurements as benchmarks to evaluate the performance of the detector geometry options. These modes have been chosen both as generic measurements

for a vertex tracking device as well as being modes of physics interest. We have generated the following physics processes with ISAJET:

1. Top events with m_t = 130 GeV/c^2 and 200 GeV/c^2, with all decay modes for the t and $\bar{t}$. This sample is used to study the efficiency for tagging the b decay vertex in top events.

2. The background suppression for top events is studied using the m_t = 130 GeV/c^2 sample with the b lifetime set to zero, and using a sample of events with W+ 4 jets.

3. $t\bar{t}$ in the lepton + 4 jets decay mode are used to study the improvements in combinatoric background, and in the top mass determination.

4. Inclusive B decays, with all decay modes, and $B^0 \rightarrow \psi K_s^0$ and $B_s \rightarrow \phi\psi$ exclusive decays are used to study B reconstruction, geometric acceptance, and mass resolution.

5. The ψK_s^0 mode, with a lepton tag of the other B is used in CP violating asymmetry studies.

6. $B_s \rightarrow \ell\nu D_s; D_s \rightarrow \phi\pi$ semi-leptonic decays and exclusive $B_s \rightarrow D_s 3\pi; D_s \rightarrow \phi\pi$, both with a lepton tag on the away-side are used to study B_s mixing.

All these modes are used to evaluate the general performance of the different geometric models in terms of acceptance as well as mass and vertex resolution. The discovery of the top quark, and measurement of its properties is the highest priority of the CDF physics program. The B_s mixing and CP violating asymmetry studies are used as a relative measure of the ability of the detectors to reach the longer term b physics goals. The B_s measurement [11] requires both flavor tagging and precise vertex-momentum information to extract the time evolution of mixed B_s decays. The CP violating asymmetries require efficient lepton tagging and maximum acceptance.

5.3 Top Analysis

<u>b Tagging Efficiency</u>

b tagging for top decay was studied for top masses of 130 GeV/c^2 and 200 GeV/c^2. For each top mass 1000 $t\bar{t}$ events were generated for each of the three geometries, G1 thru G3, discussed in section 4.1. In addition the top sample at 130 GeV/c^2 was studied for the geometry G5. The p_T of each top quark was required to be greater than 5 GeV/c. The b tagging algorithm consisted of three cuts: (a) tracks are within a cone of radius R=0.4 in η-ϕ space centered on the generated B direction,[1] (b) tracks with impact parameter significance $\frac{D}{\sigma_D} > 3$, (c) tracks with $p_T > 1$ GeV/c. In the case of the double-sided geometries G3 and G5,

[1]We also studied the case of any three tracks within an η-ϕ cone of radius 0.4 of each other disregarding any information about the B direction (see the ϵ_3 column of Table 7.)

the impact parameter cut was replaced by a 3D displaced track cut $\sqrt{(D/\sigma_D)^2 + (Z/\sigma_Z)^2} \geq 3$. Any event with three or more tracks that passed all the cuts was taken as having a b tag.

Tracks from the 130 GeV/c^2 top data sample were used to study the effect of these cuts. The results are shown in Fig. 19 which plot the R, D/σ_D, and p_T distributions respectively for tracks originating from B decay or B decay daughters and for tracks with non-B decay origins. The G2 geometry was used for these plots. Before the cuts the ratio of the number of tracks from B decay to the number of tracks with a non-B decay origin is ≈ 0.1. The cumulative effect of the three cuts is to change this ratio to ≈ 50, a relative enhancement of signal to background of ≈ 500.

Table 7: b tagging efficiencies for $m_t = 130$ and 200 GeV/c^2. The efficiencies have a statistical uncertainty of 1.5%

$m_t = 130$GeV/c^2			
Model	$\epsilon_1(\%)$	$\epsilon_2(\%)$	$\epsilon_3(\%)$
G1	27	27	30
G2	46	44	50
G3	57	55	63
G4		45	
G5		59	
$m_t = 200$GeV/c^2			
Model	$\epsilon_1(\%)$	$\epsilon_2(\%)$	$\epsilon_3(\%)$
G1	41	41	45
G2	60	58	64
G3	68	66	73

The results for the b tagging efficiency are shown in Table 7. The three columns, labelled ϵ_1, ϵ_2, and ϵ_3 respectively, correspond to the tagging efficiencies under the following conditions: (ϵ_1) any track can be used provided it passes the three cuts, (ϵ_2) all three tracks must have a B decay origin, (ϵ_3) the same as (ϵ_1) but the Monte Carlo B direction is not used in making the R cut. The cone cut was made with respect to the Monte Carlo B direction in the case of ϵ_1 and ϵ_2. For the calculation of ϵ_3 any three tracks with R less than 0.4 of each other are accepted. Only ϵ_3 corresponds to the experimentally realistic situation. The small differences between the three cases are an indication of the effect of background tracks and of the uncertainty of not knowing the direction of the B.

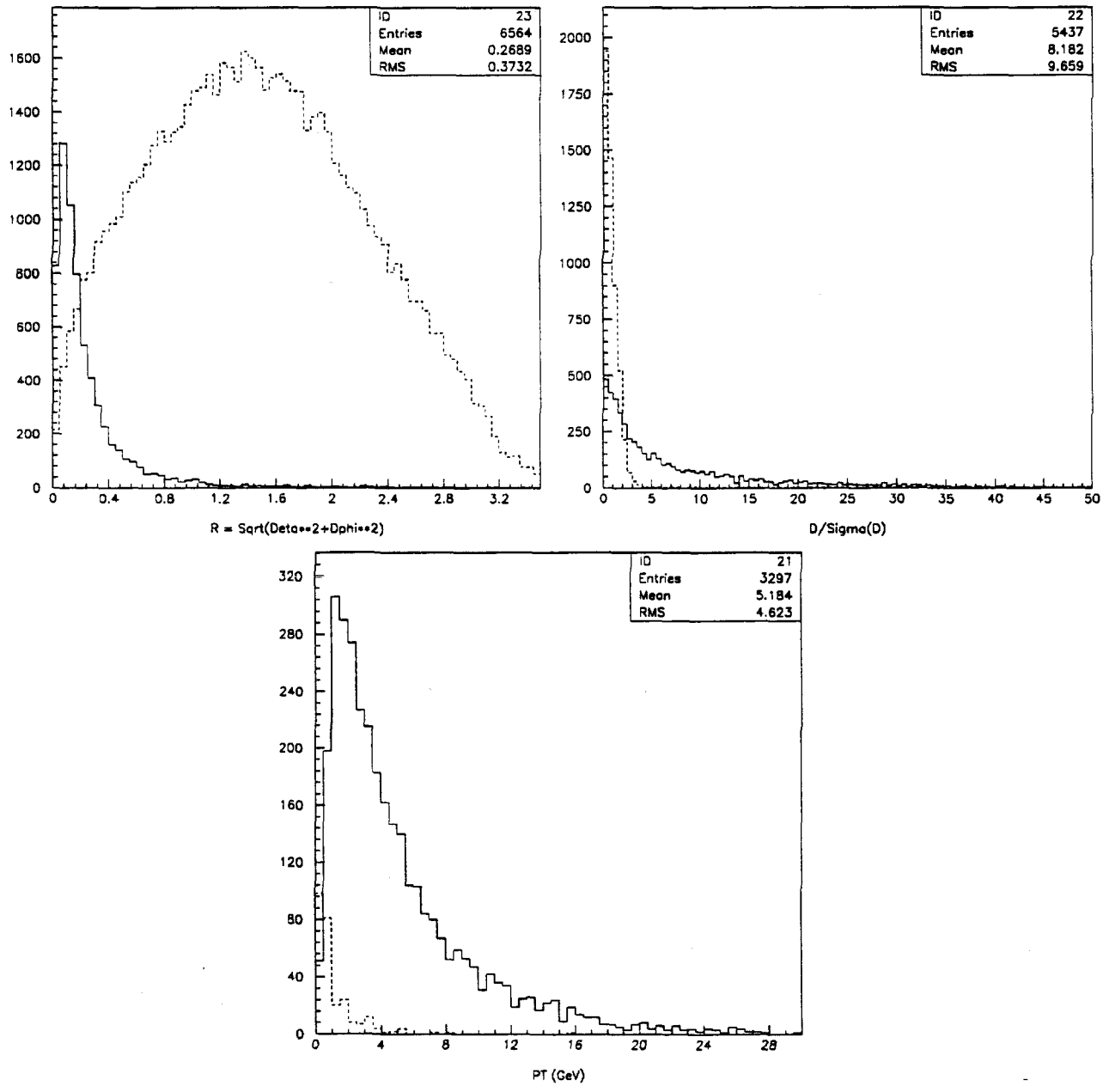

Figure 19: Shown are the distribution of ΔR with respect to the B direction, D/σ_D and p_T for tracks from B decay and B daughter decay (solid) and non-B decay (dashed).

We investigated the background by looking at the 130 GeV/c^2 top sample with the B lifetime (but not the charm lifetime) set to zero, and by studying a sample of $W+$ 4 jet events. With the B lifetime set to zero, 5% of the events are tagged due to the charm decay for model G1. For the $W+$ 4 jet sample the tagging efficiency is 0.2% but this is artificially low because there is no bottom or charm generated. To estimate the effect of this absence of b and c we considered the following. The minimum jet p_T is 8 GeV/c, and for a gluon jet an estimate of the gluon splitting into a $c\bar{c}$ pair is $\approx$ 3%[12]. If we assume 3 gluon jets per event, then 9% of the events have charm and we can expect to tag 5% of these or 0.45%. If we add the 0.45% to the 0.2%, then the background rejection factor is $\approx$ 150. Since 27% of the events produced a b tag originally, this gives an enhancement of signal to background of $\approx$ 40. These results are for 2D vertex information, and are very similar for the long barrel option G2. Depending on the analysis cuts used, we expect that even larger enhancement factors are possible with 3D vertex information.

For the models studied the biggest increase in b tagging efficiency comes from doubling the length. The effect of going to double-sided detectors is less dramatic. The increase depends on the top mass. For a top mass of 130 GeV/c^2 the b tagging efficiency increased by a factor of 1.6 in going from G1 to G2 and by a factor of 1.3 in going from G2 to G3. The corresponding factors for a top mass of 200 GeV/c^2 are 1.4 and 1.1 respectively, and this is to some extent due to the fact that the G1 efficiency is much higher for m_t = 200 GeV/c^2 than m_t = 130 GeV/c^2. It should be pointed out that we have not fully investigated all of the advantages of double-sided detectors. For example, in the case of 3D tracks it is possible to form vertices with two tracks which are true vertices, whereas, fake vertices are more of a problem with 2D tracks. This needs further investigation. Finally because of the central nature of top events, the addition of disks does not improve b tagging for top decay.

Top Mass Measurement

We have studied the impact of the SVX II design on the measurement of the top mass. The top mass can be obtained from the lepton (e or μ) plus jets channel. Because of its capability to tag one or both b jets from the produced $t\bar{t}$, the SVX II is a useful tool both in suppressing backgrounds from W plus jet events and in reducing combinatorial backgrounds. These combinatorial backgrounds, although reduced, still remain because one cannot identify with high probability which b jet is associated with the W decaying to lepton and neutrino. One can also consider to what extent the SVX II b tag will improve the mass resolution of the measurement.

We considered a sample of lepton plus 4 jet events corresponding to an integrated luminosity of one fb^{-1} and a top mass of 130 GeV/c^2. We applied the following cuts: (1) lepton $p_T > 15$ GeV/c and $|\eta| < 1.2$; (2) Missing $E_T > 15$ GeV; (3) two non-b jets have an invariant mass between 60 and 101 GeV/c^2, $E_T(j1) > 30$ GeV and $E_T(j2) > 10$ GeV; (4) b jet $E_T > 10$ GeV. Lepton plus 3 or more jets can also be considered but such a sample from pure $t\bar{t}$ events was only about 20% larger and gave no additional insight into the measurement.

We can form a top by combining the b jet with either the W decaying hadronically or

Table 8: Relative sample sizes for SVX and SVX II Stage 1 for lepton plus 4 jets for approximately 1 fb^{-1} and $m_t = 130$ GeV/c^2. The data in the two columns are from different Monte Carlo samples.

	SVX (G1)	SVX II (G3)
No b tag	1973	1936
One b tagged	524	945
Two b's tagged	56	129

the W decaying leptonically. We take the missing E_T as the neutrino p_T and obtain its z component by a W mass constraint of the lepton with the neutrino. In general there are two solutions. We considered both of them. Then the jets assigned as b jets are tried with each W. The non-b jets are required to pass the W-mass cut (cut (3) above). In order to reduce the combinatorial background, we select the combination with the minimum difference of the reconstructed top masses. Figure 20 shows the reconstructed invariant top mass from the lepton side of the event for the SVX II in three cases: Where the SVX II b tag is not used, where one of the jets has a b tag, and where two jets have a b tag. The sequence for the purely hadronic side is similar. The mass resolution remains approximately constant because the top mass resolution is determined by the jet energy resolution from calorimeters. The sequence indicates some decrease in the combinatorial effects. The number of events in each plot for both the SVX II case (Fig. 20) and the present SVX (not plotted) is shown in Table 8. The SVX II increases the single b tag efficiency by 80% and the double b tag efficiency by 130%. This will help determine the top mass with less data.

We noted that a background for a top mass measurement is W plus jet events. Without a b tag, the signal to background ratio is about 1:1 for $m_t = 130$GeV/c^2. With a single b tag, it improves to about 10:1. The double b tag should yield a cleaner signal. However, it would require a very large amount of data to make it useful. On the other hand, the $t\bar{t}$ cross section decreases rapidly as the top mass goes up. Therefore, in the case of a really heavy top, a double b tag would become much more important.

5.4 Impact on W and Z Physics

As demonstrated by the present SVX, the vertex detector improves the tracking resolution which will help the W and Z physics analysis. At present the transverse mass resolution is 4.6 GeV/c^2 for $W \rightarrow e\nu$ and 5.1 GeV/c^2 for $W \rightarrow \mu\nu$. The muon momentum resolution improves by 40% and as a consequence the $W \rightarrow \mu\nu$ transverse mass resolution will be 4.4 GeV/c^2, making it competitive with the $W \rightarrow e\nu$ channel. The improved tracking resolution will also help the Z p_T measurement.

The Stage 2 disk system will also extend the tracking coverage to the forward region, which is crucial for the W asymmetry measurement.

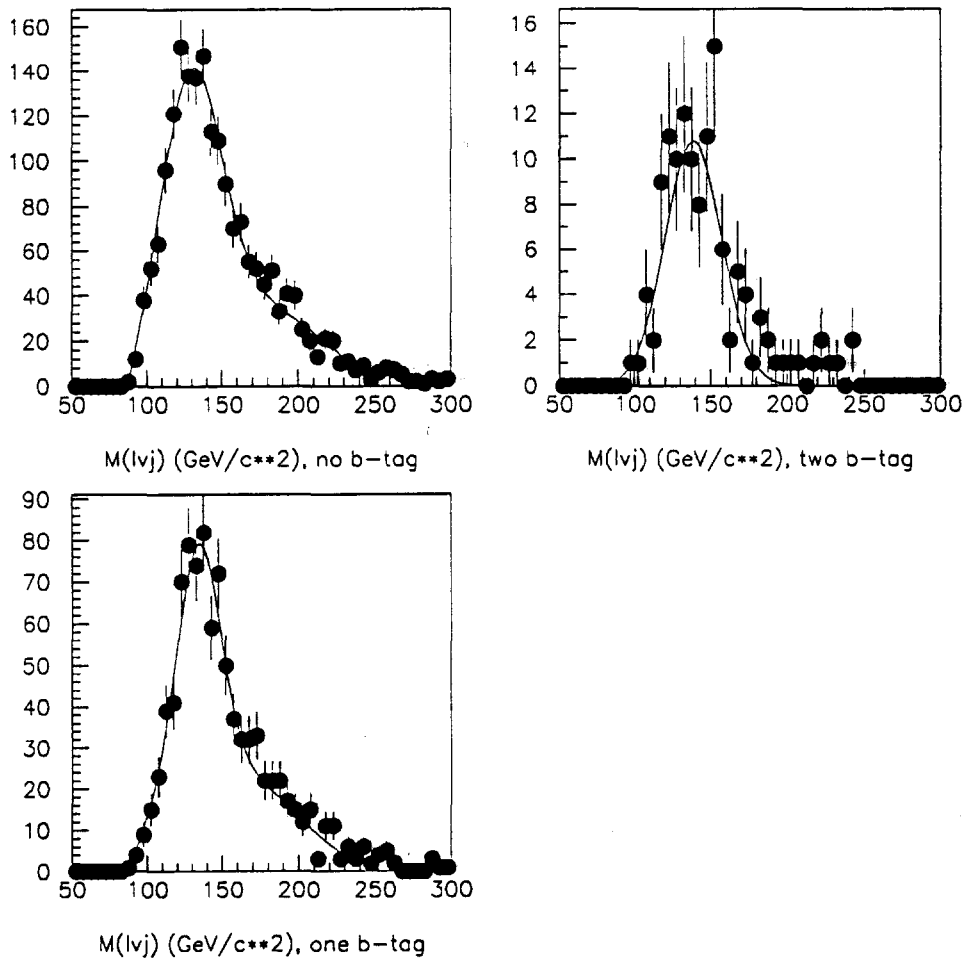

Figure 20: Reconstructed invariant top mass from the lepton side of the event for SVX II (G3) in three cases: Where the SVX II b tag is not used, where one of the jets has a b tag, and where two jets have a b tag.

The greatest improvement would be for the W' search. Without an SVX the current tracking on a high p_T muon is rather poor, making it not useful for the W' search. Figure 21 shows the transverse mass distributions from a 500 GeV/c^2 W' in the muon channel for different tracking resolutions. The first plot (upper left) is for CTC tracking only: $\sigma_p/p^2 = 0.002(\mathrm{GeV/c})^{-1}$. The upper right plot is for CTC plus a beam constraint: $\sigma_p/p^2 = 0.0011(\mathrm{GeV/c})^{-1}$. The lower 2 plots show what could be achieved with factors of 2 and 5 in the latter number. A factor of two is the least that can be expected from the SVX II. This might be the difference between a limit and a discovery.

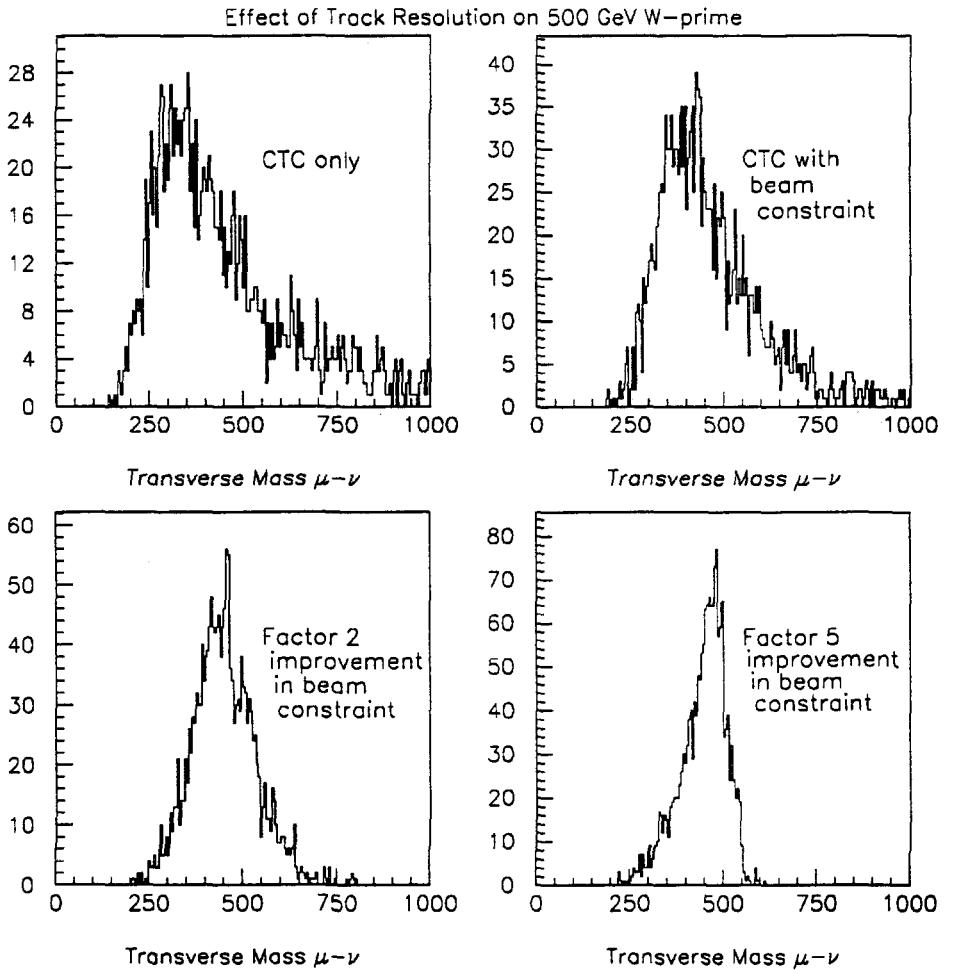

Figure 21: Transverse mass distributions from a 500 GeV/c^2 W' in the muon channel for different tracking resolutions.

5.5 B Decays

Studies were made to determine the mass and vertex reconstruction resolution and acceptance for representative B decay channels. These results are intended to indicate the acceptance and precision obtained with the geometries under consideration in a format as free as possible from constraints due to particular choices in the analysis technique.

Inclusive B Decays

In order to determine the improvement in geometrical acceptance for charged tracks from inclusive B decays for the SVX II detector, we have generated two samples of ISAJET inclusive $b\bar{b}$ production with $p_T(b) > 3$ GeV/c and $p_T(b) > 10$ GeV/c. The average B decay charged track multiplicity, including charged daughters from cascade charm decays, for these

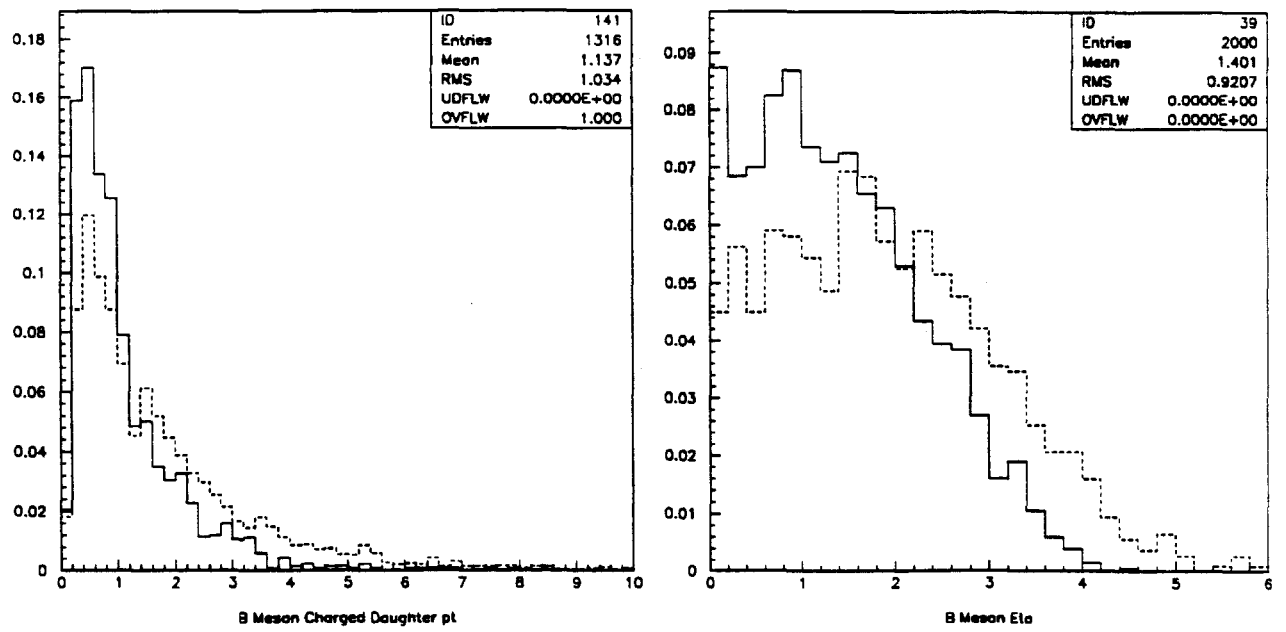

Figure 22: Shown are the B meson charged daughter p_T distributions (in GeV/c) and the B meson pseudorapidity distributions for the $p_T(b) > 3$ GeV/c (solid line) and $p_T(b) > 10$ GeV/c (dashed line) inclusive $b\bar{b}$ samples.

two samples was 4.6 tracks. The first sample gives the flatter pseudorapidity distribution and softer B meson track p_T that would be obtained for a non-triggered B while the latter is more suggestive for a triggered B meson. Figure 22 shows the B meson p_T and η distributions for the two samples. It is seen that the higher b quark p_T sample contains noticeably more centrally-produced and higher transverse momentum B mesons, as expected.

The geometrical acceptance for observing all charged tracks from a B meson was determined for the CTC, the SVX, and the SVX II Stage 1 and 2 detectors. For the CTC acceptance, the track was required to pass through the first two superlayers. For the SVX and SVX II Stage 1 detectors, the track must have been in the CTC acceptance and had at least 3 out of 4 hits in the silicon barrel. For the SVX Stage 2 detector, a disk tracking system with the inner three disks at $z = 55.0$, 62.5, and 70.0 cm and an outer radius of 27.0 cm was added to the Stage 1 double length barrel. For the case of a track missing the CTC or having less than 3 hits in the Stage 1 detector, it was checked if the track hit the first two layers of the barrel and fell within the acceptance of the inner three disks. If it did, the track was included in the Stage 2 detector acceptance. This combination of barrel and disk hits would allow the track to have useful vertexing information as well as a momentum or charge-sign determination.

Tables 9 and 10 show the geometrical acceptance for containing all charged daughters from B meson decay for the different detector elements. The first column describes the single B meson acceptance which is given as the fraction of B mesons which have all charged tracks in the detector acceptance. The second column gives the acceptance for all charged tracks

Table 9: Geometric acceptance for all charged tracks from a B meson for $p_T(b) > 3$ GeV/c.

Detector	Single B Accept.(%)	2nd B Accept.(%) given 1st B	Both B Accept.(%)
CTC	36	39	14
SVX	16	33	5.3
SVX II Stage 1 (G2 or G3)	28	34	9.5
SVX II Stage 2 (G4 or G5)	55	64	35

Table 10: Geometric acceptance for all charged tracks from a B meson for $p_T(b) > 10$ GeV/c.

Detector	Single B Accept.(%)	2nd B Accept.(%) given 1st B	Both B Accept.(%)
CTC	52	59	31
SVX	23	43	10
SVX II Stage 1	42	51	21
SVX II Stage 2	64	70	45

from the second B given that the first B was in the acceptance. The last column is just the product of the first two and gives the fraction of events which have all charged tracks from both B's contained.

Several conclusions can be drawn from the numbers in Tables 9 and 10:

1. A large increase in acceptance is seen for the double length barrel of the SVX II Stage 1 detector versus the present CDF SVX. The increase is $\approx 80\%$ for the single B acceptance and nearly 100% for both B's.

2. The double length barrel appears reasonably well-matched to the two superlayer acceptance of the CTC used here.

3. For $p_T(b) > 3$ GeV/c, the 9.5% two-B acceptance of the SVX II Stage 1 detector increases to 35% when the disk system is included. The disk system modeled here has not been optimized but this result indicates that a large increase in B acceptance can be obtained by improving the tracking capabilities in the forward rapidity region.

A second study of inclusive B acceptance was performed which required both B's to decay semileptonically with $p_T(l) > 2.5$ GeV/c. This was done for a $p_T(b) > 10$ GeV/c sample.

Table 11: Geometric acceptance for all charged tracks from a B meson for different pseudorapidity intervals of the dileptons for $p_T(l) > 2.5$ GeV/c and $p_T(b) > 10$ GeV/c.

Detector	$\|\eta(ll)\| < 1$, 21% of evts			$\|\eta(ll)\| < 2$, 61% of evts			$\|\eta(ll)\| < 3$, 92% of evts		
	1st$B$ (%)	2nd$B$ (%)	Both$B$ (%)	1st$B$ (%)	2nd$B$ (%)	Both$B$ (%)	1st$B$ (%)	2nd$B$ (%)	Both$B$ (%)
CTC	88	88	77	77	78	60	63	65	41
SVX	42	74	31	40	63	25	32	51	16
SVX II Stage 1	74	78	58	66	70	46	55	58	32
SVX II Stage 2	78	84	66	81	86	70	76	82	62

Table 12: Inclusive both B acceptance for different pseudorapidity intervals of the dileptons.

Detector	$\|\eta(ll)\| < 1$	$\|\eta(ll)\| < 2$	$\|\eta(ll)\| < 3$
	Both B (%)	Both B (%)	Both B (%)
CTC	16	37	38
SVX	6.5	15	15
SVX II Stage 1	12	28	29
SVX II Stage 2	14	43	57

The idea here was to look at the B meson acceptance as a function of the pseudorapidity of the two leptons which could have caused the event trigger. If daughter tracks from the B mesons were required in the event trigger, then it is more likely that the B meson and its other daughters were within the detector acceptance. Table 11 shows the same acceptance quantities as in Tables 9 and 10 above for different pseudorapidity ranges of the dileptons from the $B\bar{B}$ decay. The values given in this table have to be multiplied by the fraction of $B\bar{B}$ events generating dileptons in each of the three pseudorapidity ranges in order to obtain the inclusive B acceptance. This was done for the value for accepting both B's and the results are shown in Table 12. These acceptance values are significantly higher than in the study presented in Tables 9 and 10. For the dilepton $|\eta| < 2$ case, the two B acceptance for the SVX II Stage 1 detector increased from 21% for the fully inclusive sample to 28% for the dilepton sample. The SVX II Stage 2 detector both B acceptance also increased to 57% ($|\eta(ll)| < 3$) from 45% in the earlier study.

Finally, the inclusive B meson acceptance was studied for the case of only one of the B's decaying semileptonically with $p_T(l) > 2.5$ GeV/c and $p_T(b) > 10$ GeV/c. It is planned that a low p_T single lepton trigger will be used in conjunction with a secondary vertex trigger. For this reason, the average fraction of charged tracks from a B meson contained within each

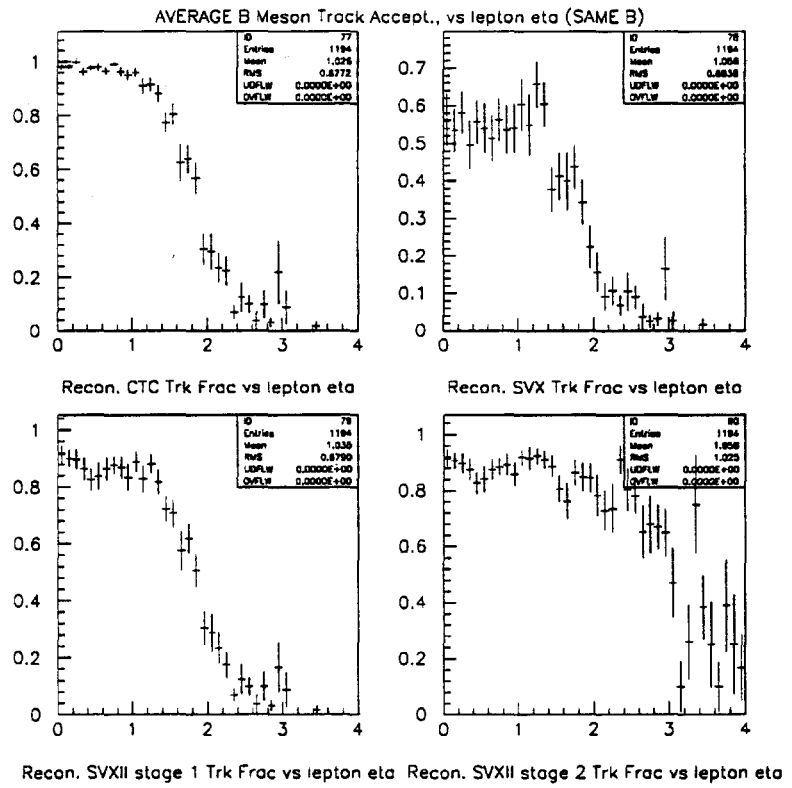

Figure 23: Average B meson charge track fraction for each detector as a function of the lepton (produced by that B) pseudorapidity.

detector acceptance was studied as a function on lepton pseudorapidity. This was done both for the B producing the lepton and also for the other B. Given a B meson average charged track multiplicity of 4.6, the mean number of tracks available to secondary vertex trigger could be estimated for the different detector acceptance and lepton η values. Figs. 23 and 24 show the average B meson charged track fraction contained in each of the detectors as a function of lepton η for the two cases of the lepton decaying from the same B and from the other B. We see that for the first case, the addition of the tracking coverage modeled by the disk system in the SVX II Stage 2 detector greatly increases the reconstructed charged track fraction in the lepton η range between 1.6 - 3.0. The fraction is greater than 75% out to $|\eta(l)| = 2$ and is still above 50% at a lepton η of 3. The reconstructed charged track fraction versus the lepton η from the other B is found to be relatively flat. This is expected from the uncorrelated nature of $B\bar{B}$ pair production.

It is seen from these studies that large increases in inclusive B acceptance can be obtained by doubling the length of the present SVX detector (SVX II Stage 1) and by the addition of tracking system (presented here as a disk system) to cover the rapidity region between $1.6 < |\eta| < 3.0$ (SVX II Stage 2). The addition of a suitable trigger, either a dilepton or single lepton + secondary vertex trigger, can also improve the acceptance and total yield of reconstructed and/or tagged $B\bar{B}$ events.

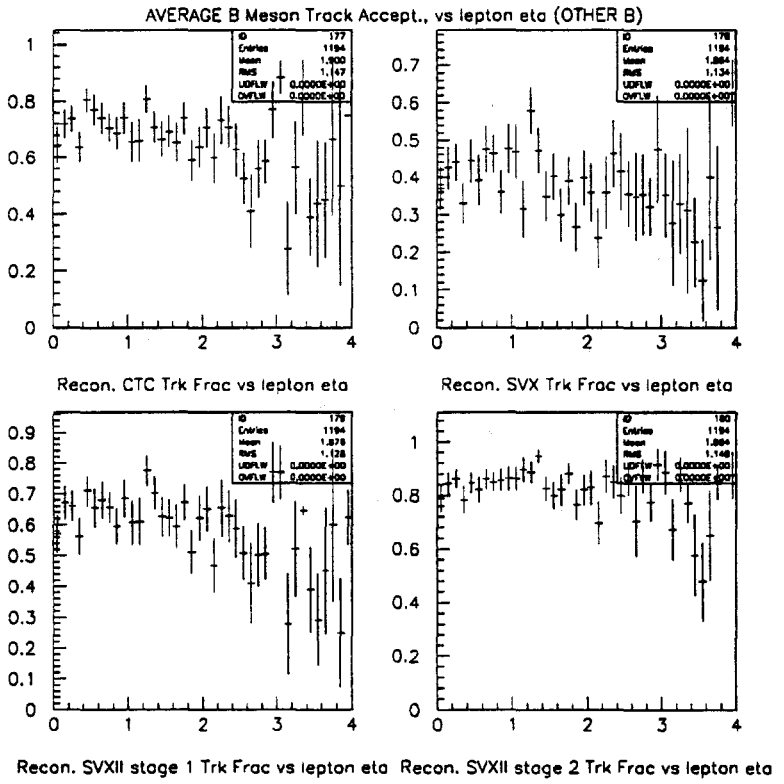

Figure 24: Average B meson charge track fraction for each detector as a function of the lepton (produced by the other B) pseudorapidity.

Exclusive B Decays

Invariant mass resolution was studied with a Monte Carlo data set of 450 $B\overline{B}$ events in which both B's decay to ψK_s^0. In this sample lifetimes of the long-lived particles were set to zero so that all decays occurred at the origin. Generated information was used to select the daughters of the ψ and K_s^0, and no requirements were placed on track p_T. To show the contribution of SVX II to the tracking system as a whole, the complete tracking system was used in the mass reconstruction. Consequently, tracks that were fit in the outer tracking system but which missed the SVX II were included. Fig. 25 shows the result; plotted is the reconstructed B invariant mass for geometries G1, G2, G3, and G5. Table 13 summarizes the obtainable widths for this channel with these geometries. The righthand column of Table 13 shows the percentage of the events within each geometry's acceptance which have a reconstructed B mass within 40 MeV/c^2 of the generated mass. The following features are evident:

1. Doubling the length of the barrel improves the mass resolution by 20%; adding barrel z readout improves it by another 10%. While the acceptance here is defined by the outer tracking, this improvement is due to a 38% reduction in the number of events whose resolution is degraded by having at least one track miss the silicon detector.

2. The addition of disks to the tracking system increases the geometric acceptance from 42% to 76% for the case considered.

3. Although the mass distribution for events reconstructed with G4 and G5 has evident tails, they are due to the significantly increased acceptance which the disks provide for low-p_T, high-η tracks, and the poorer resolution at high η.

Table 13: B mass resolution for 4-prong decay at the origin, for 5 geometries.

Model	σ_m (MeV/c^2)	Percentage of events with $\lvert m_B^{\rm recon} - m_B^{\rm gen}\rvert \leq 40$ MeV/c^2
G1	21 ± 1	31
G2	17 ± 1	35
G3	15 ± 1	36
G4	18 ± 1	53
G5	18 ± 1	53

The obtainable resolution is highly correlated with the $|\eta|$ of the track having maximum $|\eta|$. This can be seen in Fig. 26, a plot of the error on the reconstructed mass as a function of the maximum daughter $|\eta|$. In the range $0.0 < |\eta| < 2.0$, the mean error on the B mass increases from 5 to 40 MeV/c^2.

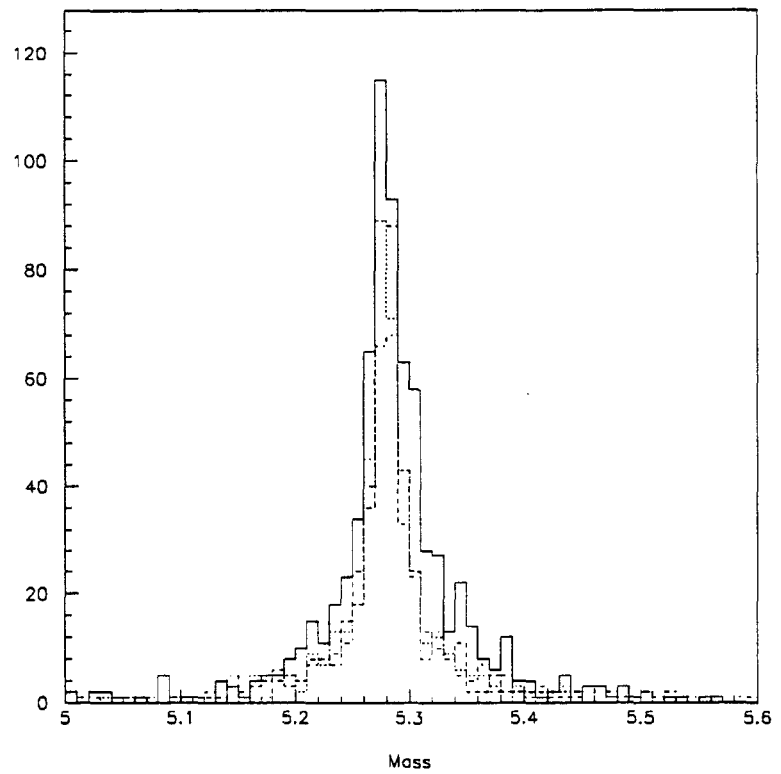

Figure 25: Reconstructed B^0 invariant mass for geometries G1(dot-dash), G2(dot), G3(dash), and G5(solid). Geometry G4 produces results which are statistically equivalent to those of G5, so it has been omitted in order to improve the figure's readability.

The decay mode $B_s \rightarrow D_s\pi\pi\pi$ with track $p_T > 350$ MeV/c is used to study the mass and vertex resolution for decays involving charm. The invariant mass distribution without vertex constraint is shown in Fig. 27 for geometry G2 and has a width of 18 MeV/c^2. The addition of a vertex constraint reduces the width by $\approx 30\%$ to 13 MeV/c^2. For geometry G3, the width is reduced to 10 MeV/c^2 for both the constrained and unconstrained vertex fits.

The study of vertex resolution includes modes with different multiplicity for both B decay through charm and direct B decay. The decay mode $B_s \rightarrow \psi\phi$ ($p_T(b) > 10$ GeV/c) with its single 4-prong vertex is an example of a direct B decay mode with possibly the best vertex resolution. Figure 28 shows a resolution of 53 microns for the tranverse decay length using geometry G1. Figure 29 shows the reconstructed transverse decay length divided by its error, i.e., the significance of the vertex separation. Figure 30 is an integral of this distribution, showing that a 5σ cut on the vertex separation is 65% efficient for this sample. Such a cut will reduce the background due to tracks from the primary vertex and retain a clean signal with good statistics.

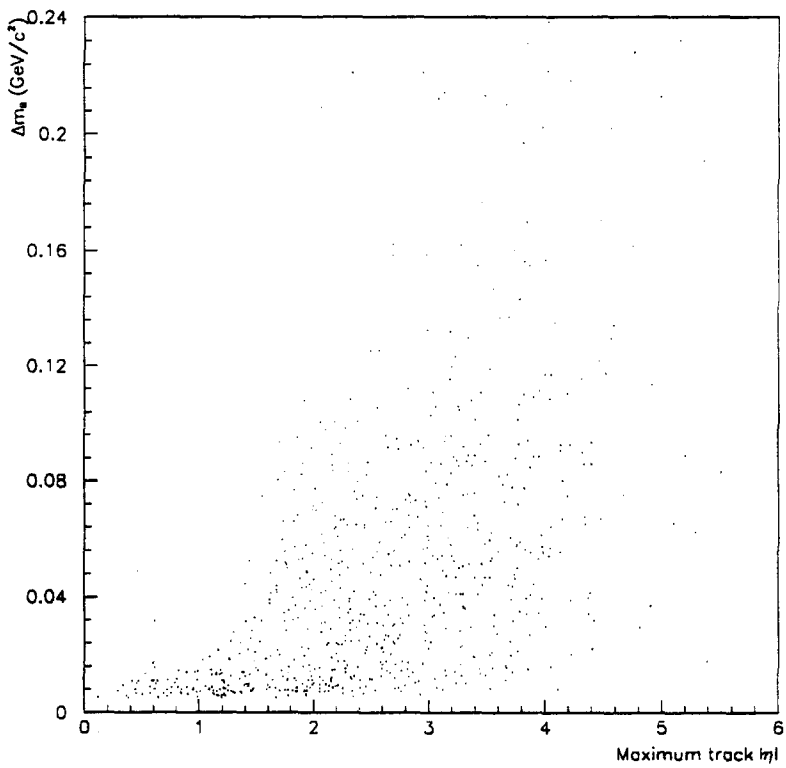

Figure 26: Error on the reconstructed mass as a function of the maximum daughter $|\eta|$.

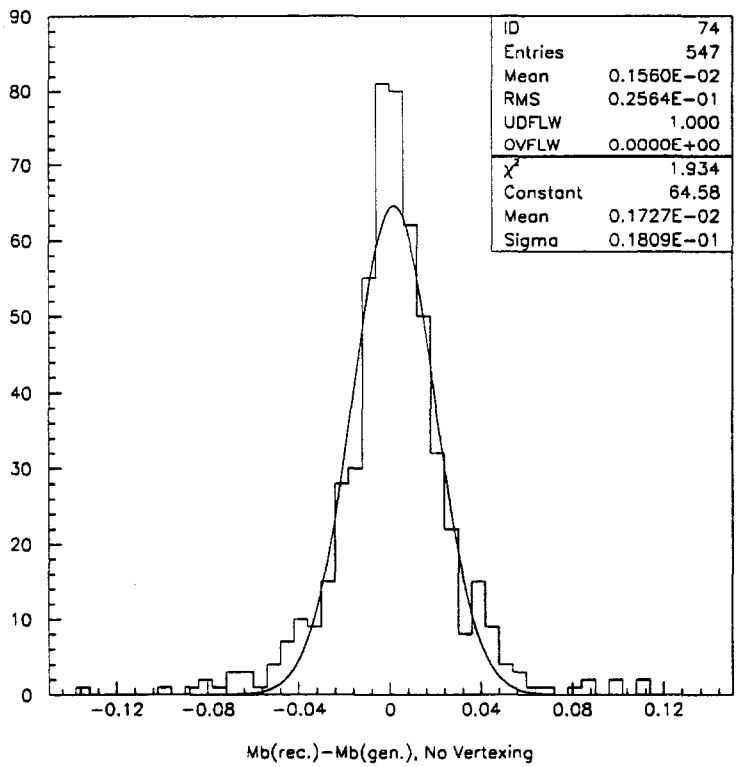

Figure 27: Mass distribution without vertex constraint for the decay mode $B_s \to D_s\pi\pi\pi$. Units are GeV/c^2.

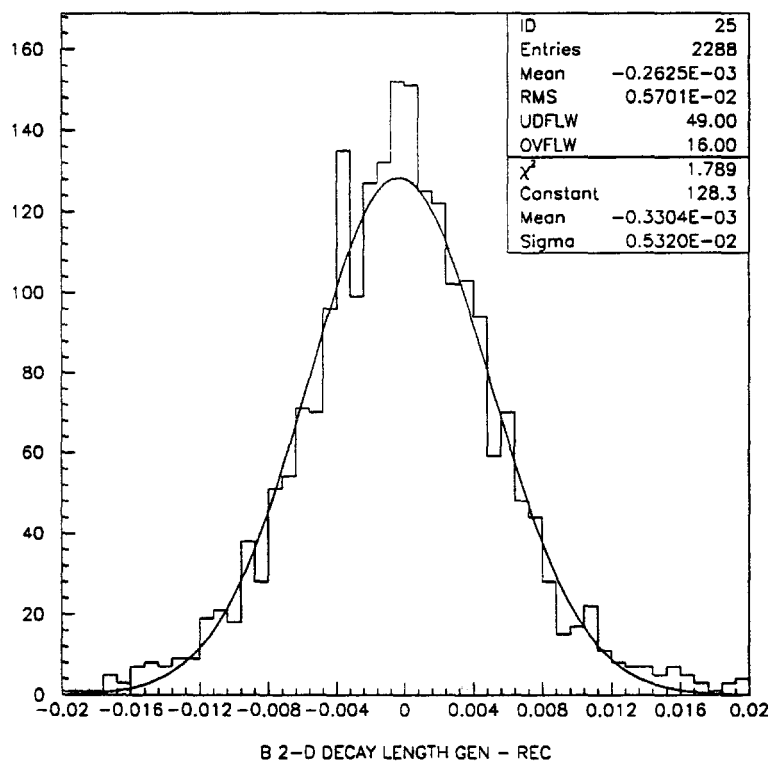

Figure 28: Transverse decay length resolution for the decay mode $B_s \to \psi\phi$ using geometry G1. The units are cm.

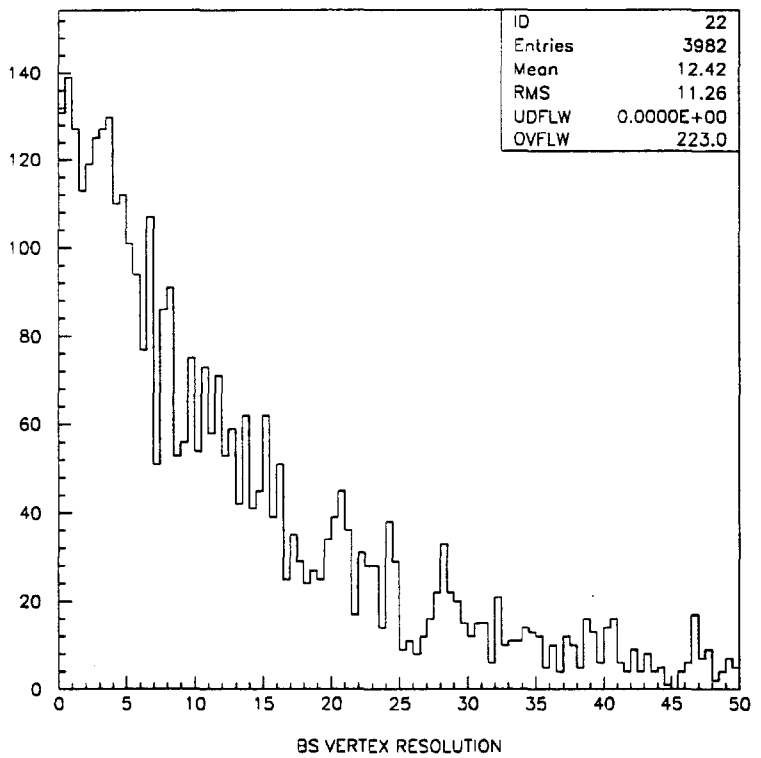

Figure 29: Transverse decay length significance for the decay mode $B_s \to \psi\phi$ using geometry G1.

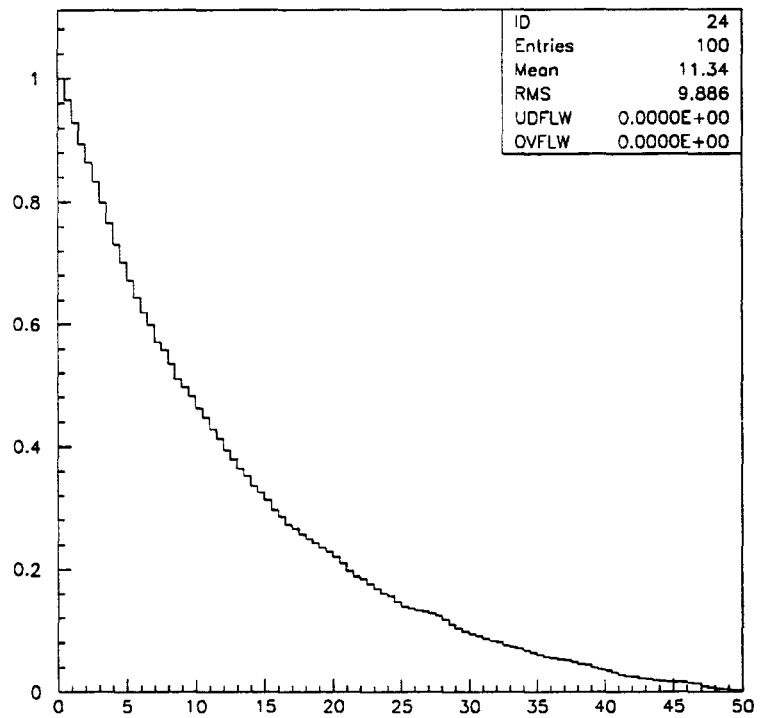

Figure 30: Integral transverse decay length significance (normalized) for the decay mode $B_s \rightarrow \psi\phi$ using geometry G1.

5.6 B_s Mixing

Introduction

The primary interest for measuring X_s is to determine the CKM matrix element $|V_{td}|$ through the relationship:

$$\frac{X_s}{X_d} = \frac{f_{B_s}^2 B_{B_s} \tau_{B_s}}{f_{B_d}^2 B_{B_d} \tau_{B_d}} \frac{|V_{ts}|^2}{|V_{td}|^2}, \tag{1}$$

where $f_{B_{s,d}}^2$, $B_{B_{s,d}}$, and $\tau_{B_{s,d}}$ are the decay constant, bag parameter, and lifetime of the B_s and B_d mesons respectively. Several common factors, including the dependence on the top quark mass, cancel in the ratio of X_s/X_d where we need only to know the quantity $f_{B_s}^2/f_{B_d}^2$ rather than $f_{B_s}^2$ and $f_{B_d}^2$ individually, for which there is much greater uncertainty [13]. Present estimates are that $f_{B_s}^2 = (1.6 \pm 0.4) f_{B_d}^2$ [14], $B_{B_s} \approx B_{B_d}$ [15], and $\tau_{B_s}/\tau_{B_d} \approx 1$ [16]. Thus, we can determine $|V_{td}|$ by measuring X_s and using the value of X_d from ARGUS [17] and CLEO [18] since $|V_{ts}|$ is constrained by unitarity to be approximately $|V_{cb}|$. $|V_{td}|$ is of course related to the CP violating phase in the CKM matrix, for which there is a great deal of interest. The unitary constraint of the CKM matrix provides only limited knowledge of $|V_{td}|$ and further improvement for a direct determination of $|V_{td}|$ requires the measurement of the top quark mass and knowledge of f_{B_d}.

The current estimate for the value of X_s has a broad range and is separated into two regions depending on the value of f_{B_d}. A value of f_{B_d} near 131 MeV is favored by many potential-model and QCD sum rule estimates while $f_{B_d} \approx 225$ MeV is suggested from lattice QCD calculations. Potential models give $f_{B_s}^2 \approx 1.6 f_{B_d}^2$ while the overall range for this quantity in various models appears to be between 1.2 to 2. The prediction for B_s mixing is:

$$X_s = (14 \pm 6)(f_{B_s}/200\text{MeV})^2. \tag{2}$$

if we assume $m_t = 140 \pm 40$ GeV/c^2 and $f_{B_s}^2 = (1.6 \pm 0.4) f_{B_d}^2$[19] where the error is dominated by the uncertainty on the mass of the top. This formula yields $X_s = 28 \pm 12$ and $X_s = 10 \pm 4$ for $f_{B_d} = 131$ MeV and $f_{B_d} = 225$ MeV respectively. In both cases X_s is large and a time integrated measurement of mixing will be saturated. Therefore, a measurement of the time evolution of the mixing oscillations is necessary.

Simulation Studies

To determine the B_s mixing parameter X_s, the decay length and momentum must be measured for a sample of flavor-tagged B_s mesons. These B_s mesons must be flavor-tagged at both production and decay in order to determine if they oscillated or not. Typically, the flavor of the B_s meson at production is tagged by the flavor of the other B meson at decay. The ability to tag the B_s at production requires good acceptance for the other B. This can lead to a mistagging dilution of the B_s sample if the other B is a B_d or B_s meson which oscillated. The B_s flavor at decay is obtained from its decay products. However, certain decay modes of the B_s are un-taggable, such as $B_s \to \psi\phi$, because the particle-antiparticle nature of the B_s cannot be determined from its daughter particles. We attempt here both

to simulate the performance of the SVX II upgrade and to identify the best way to perform the X_s measurement.

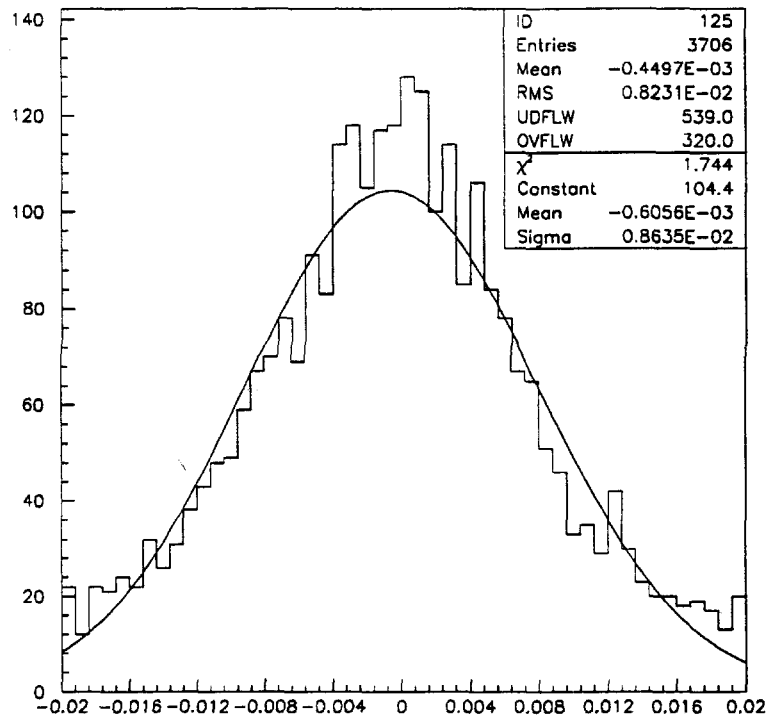

Figure 31: B_s transverse decay length error obtained by combining the ϕ and lepton in semileptonic B_s decay. The units are cm.

Two approaches are considered in determining the optimal decay mode of the B_s for this measurement. The most promising for lower luminosity is requiring the semileptonic decay of both the B_s and the other B:

$$B_s \rightarrow l\nu D_s, D_s \rightarrow \phi + X; B \rightarrow l\nu + X. \tag{3}$$

This has the advantage of being able to trigger on the two leptons at low p_T and thus forces the other B to be within the detector acceptance. For this high-rate decay mode, we initially search for the ϕ near the lepton and use it to tag the likely presence of a B_s. Depending on the p_T and multiplicity of the D_s decay, the ϕ direction could be combined with the lepton direction to yield a good measure of B_s transverse decay length. A sample of ISAJET events containing oscillating B_s mesons with $p_T(b) > 10$ GeV/c and $p_T(l) > 2.5$ GeV/c was used. Figure 31 shows that for this sample the resolution on the $\phi - l$ transverse decay length is 86 microns in geometry G1, which is almost identical to the result obtained if the D_s is fully reconstructed in the decay $D_s \rightarrow \phi\pi$. Any additional pions from the D_s decay that are associated with the ϕ vertex would also be included in order to fully or more completely reconstruct the D_s. The limiting factor for finding the proper time of the decay in a semileptonic B_s mode is the uncertainty in the B_s momentum since the B_s is only partially

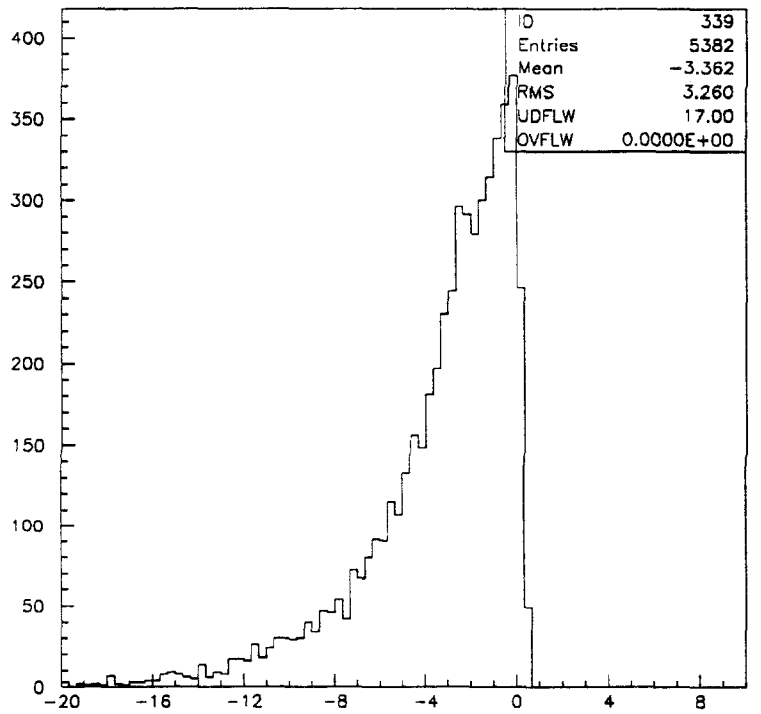

Figure 32: The difference in GeV/c between the B_s transverse momentum and the transverse momentum obtained by combining the D_s and lepton in semileptonic B_s decay.

reconstructed due to the missing neutrino or the lack of a fully reconstructed D_s. Figure 32 shows that on average the neutrino takes 3.4 GeV/c p_T in a semileptonic B_s decay. The missing p_T can be corrected using Monte Carlo simulation. Figure 33 shows the oscillation frequency plot for $X_s = 5.0$ with a perfect B_s tag and no cut on vertex separation. A clean oscillation structure is seen with $\approx$ 4000 events. A vertex cut will reduce the statistics at short lifetimes.

Using a calculation similar to that derived in Reference [20], we obtain the following estimate for the number of events, N, needed to observe a B_s oscillation signal at five standard deviation significance for a given value of X_s and proper time resolution σ_t:

$$N \simeq \frac{125}{6} X_s e^{\frac{4\pi}{X_s}} e^{\frac{(X_s^2-1)\sigma_t^2}{2}}, \tag{4}$$

where σ_t is in units of proper time. This expression includes the effect of signal dilution from mistagging due to B_d meson oscillation. From Monte Carlo studies, the proper time resolution for the semileptonic B_s decay mode is estimated to be in the range of 0.20 - 0.30 proper times. This is due to the relatively poor momentum resolution of the partially reconstructed B_s decay. Applying various kinematic cuts and using improved momentum estimators can reduce the uncertainty on the B_s momentum at some cost in reconstruction efficiency. The number of tagged and reconstructed events required is between 2000 and

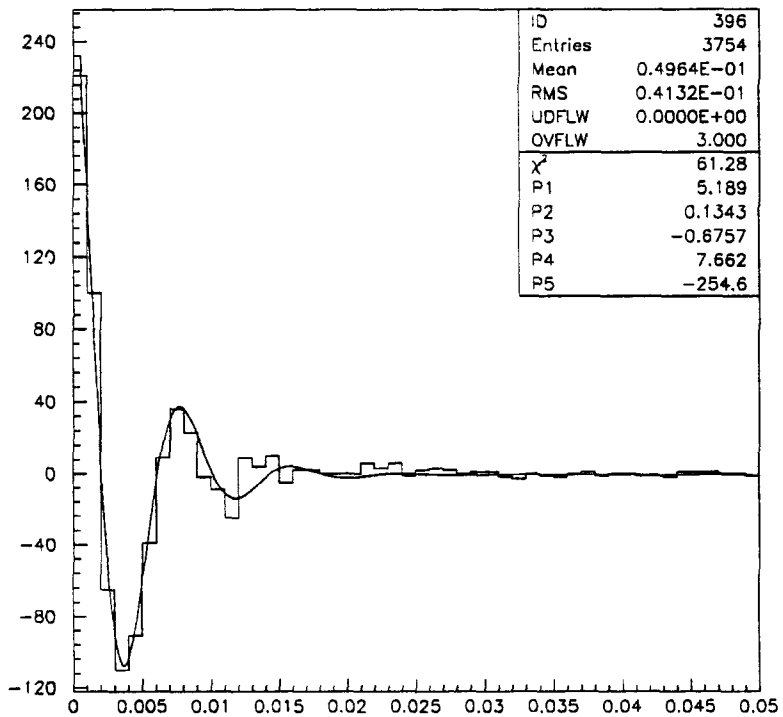

Figure 33: Oscillation plot for semileptonic B_s decay with $X_s = 5.0$. The units on the abscissa are cm/GeV/c.

5000 over the range of $4 < X_s < 7$ for the semileptonic B_s decay mode ($0.20 < \sigma_t < 0.30$).

The luminosity necessary to reach a given X_s value can be obtained by estimating the cross section for tagging and reconstructing a semileptonic B_s decay and using the above number of events necessary for a clear signal. This was done assuming a dimuon trigger with $p_T(\mu) > 2.5$ GeV/c and muon and charged particle coverage for $\mid \eta \mid < 2.0$. For the decay chain in Equation 3, we use $\mathrm{BR}(D_s \rightarrow \phi + X) = 0.10$ and assume a 15% B_s meson content of all B hadrons. Including a cut of 5σ on the significance of the $\phi - \mu$ vertex and allowing a 30% background rate for ϕ production from $B^{\pm}$ and B° decay, we obtain a cross section of 8.0 ± 4.0 pb for reconstructing and tagging a semileptonic B_s decay. Figure 34 shows the integrated luminosity necessary for measuring X_s between 4 and 7 for $0.20 < \sigma_t < 0.30$. The shape of the curves show that for small X_s values, the B_s decays before it oscillates so that more data is needed to make a measurement than for slightly larger X_s values. It is also seen that the amount of data needed is very dependent on the proper time resolution σ_t and that for $\sigma_t \geq 0.30$, the measurement becomes very difficult. The minimum luminosity required to establish X_s as different from zero by five standard deviations occurs at $X_s \approx 5$. For $\sigma_t = 0.25$ this corresponds to a luminosity 200-400 pb^{-1}.

Since it is anticipated that the semileptonic mode will have a limited X_s reach due to the momentum uncertainty in the partial reconstruction of the B_s decay, a simulation of a

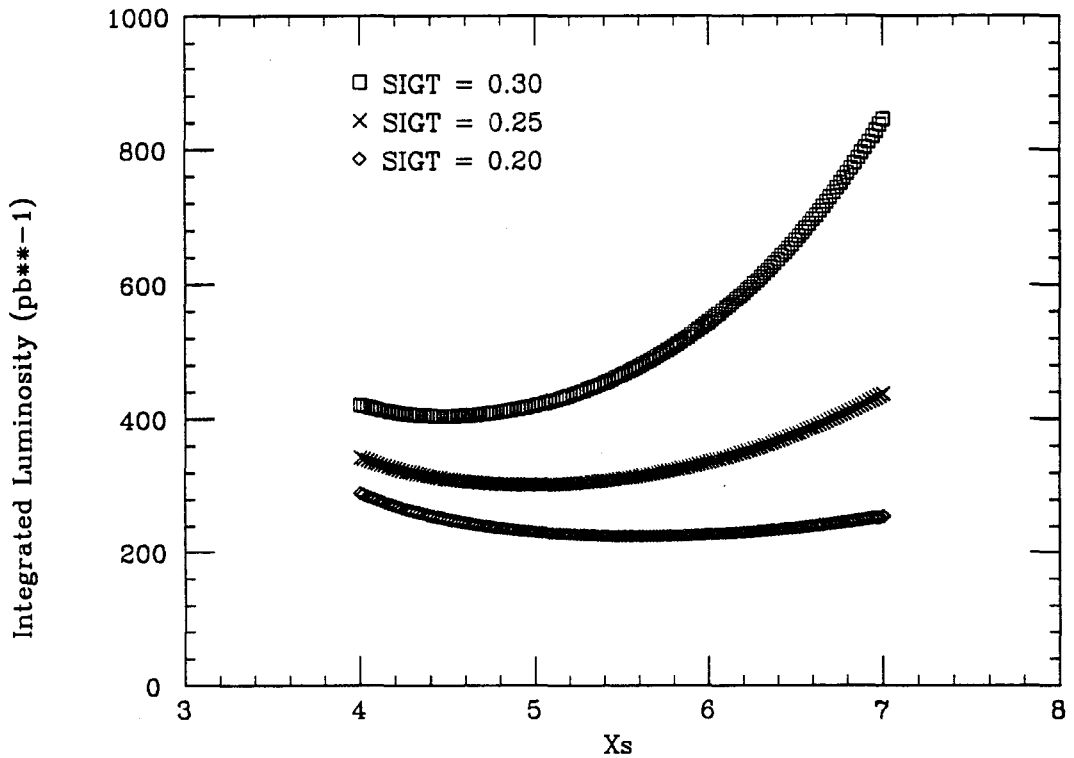

Figure 34: Estimated integrated luminosity necessary to measure X_s over the range $3 < X_s < 7$ for semileptonic B_s decay with $0.20 < \sigma_t < 0.30$.

fully reconstructable B_s decay was also studied. The disadvantages of this decay mode are that the event rate will be very small because all exclusive B_s decay modes have very small branching fractions and the reconstruction efficiency will also be lower.

As an example of an exclusive B_s decay mode, we studied $B_s \to D_s\pi\pi\pi$. The branching fraction of this mode is estimated to be 1.1%. The D_s has a 2.8% branching ratio decaying to $\phi\pi$, and half of the ϕ's will decay to K^+K^-. This kind of event will have three tracks from the B_s vertex and three tracks from D_s vertex. Since CDF does not have a secondary vertex trigger for this decay mode at this time, we have assumed that these events come from the inclusive lepton trigger, in which the lepton comes from the other B and also provides the flavor tagging.

We generated $b\bar{b}$ events from ISAJET, and selected those events with trigger B lepton $p_T > 5$ GeV/c and a B_s with the above decay mode. In order to be able to reconstruct the events, we also required all π's and K's to have $p_T > 0.35$ GeV. This decay can be reconstructed by looking for ϕ's with displaced vertices in the event, then reconstructing D_s with the tracks coming from the ϕ vertex, and finally reconstructing the B_s with tracks from the other 3-prong vertex.

Our current study was to find out what X_s range we can explore. The key in any X_s analysis is the resolution of the measured B decay time, which in turn is determined by

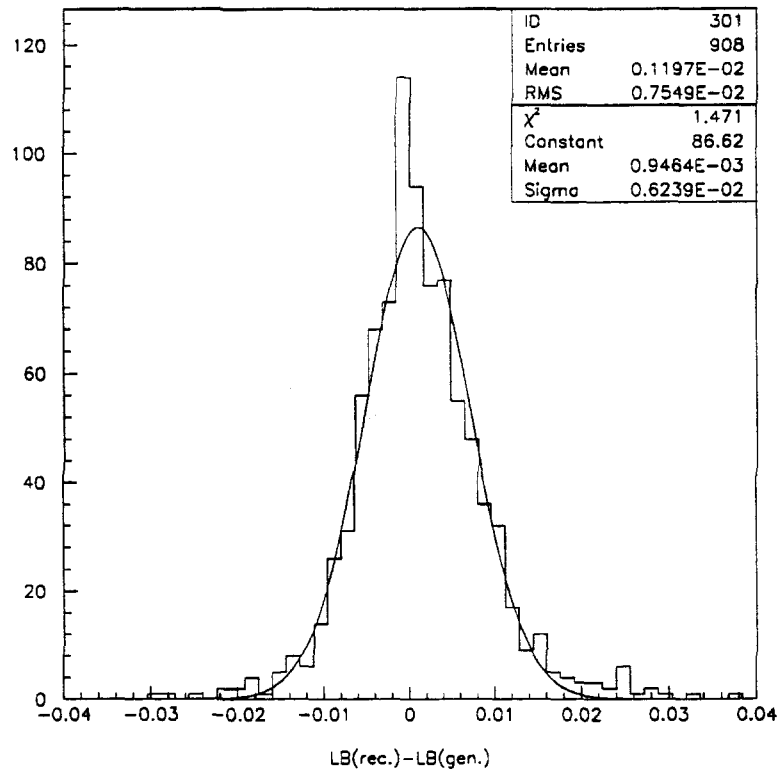

Figure 35: Resolution of the 3D B_s decay length for model G3 in cm.

the B vertex and B momentum resolution. The resolution of the decay length is shown in Fig. 35. For model G2, the momentum resolution is the same as for G3, but the 3D vertex resolution is of course much worse. However, if we project into the $r - \phi$ plane, the 2D vertex resolution shown in Fig. 36 is comparable as expected. The 2D and 3D resolutions in the proper time distribution are shown in Fig. 37. The 3D proper time resolution is about 20% better than the 2D resolution. To illustrate that the vertex resolution is adequate for measuring large X_s values, the reconstructed time-dependent oscillation plot with $X_s = 20$ for 2845 reconstructed and tagged B_s decays is shown in Fig. 38. No vertex separation cut is applied to this plot, but it shows that the vertex detector can resolve this frequency of oscillations.

To estimate the luminosity necessary to obtain such a sample of exclusive B_s meson decays, we assumed a single lepton trigger for both electrons and muons with $p_T > 4$ GeV/c. This lepton would be from the other B and its charge sign would tag the flavor of the B_s at production. Charged particle tracking and lepton triggering out to $|\eta| < 2.0$ was also required. The product branching ratio for $B_s \to D_s\pi\pi\pi, D_s \to \phi\pi, \phi \to KK$ was taken to be 2 x 10^{-4} and a proper time resolution of $\sigma_t = 0.10$ for this fully reconstructed B_s decay mode was determined from the simulation. Including the efficiency for reconstruction of the B_s and mistagging from B_d oscillations, it is estimated that at least 1 fb^{-1} of data would be needed to measure $X_s = 20$ with the SVX II detector.

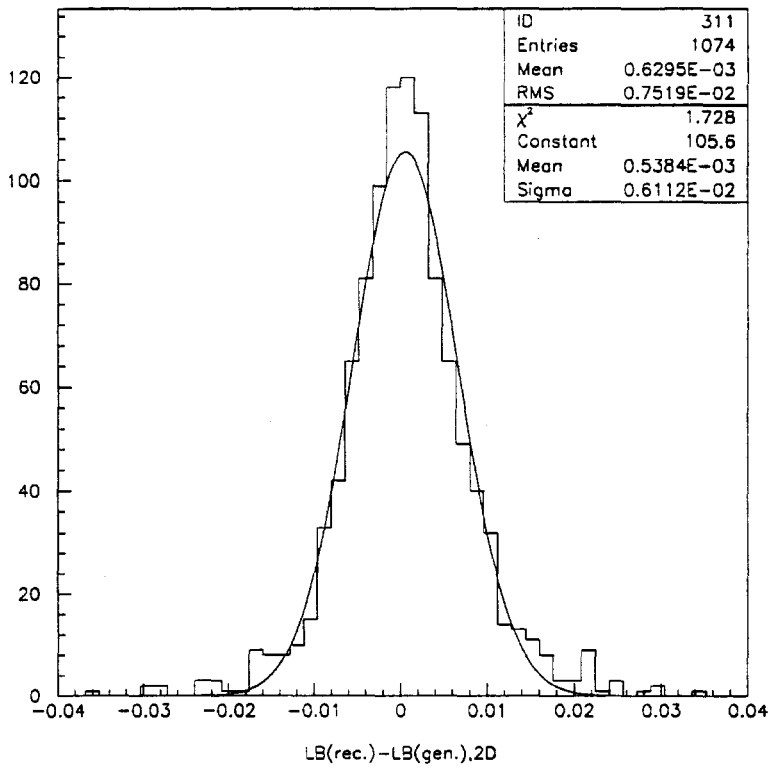

Figure 36: Resolution of the 2D B_s decay length for model G2 in cm.

These analyses do not include sources of mistagging semileptonic charm decay which will reduce the amplitude of the observed oscillations. For the fully reconstructed exclusive mode, background sources are expected to be very small. For the inclusive mode, the background (for example from the semileptonic B decays other than B_s into modes containing ϕ) could shift or skew the distribution in Fig. 38, but will not affect the frequency or the amplitude of the oscillations.

These studies are on-going and much use will be made of the present SVX data to determine better the reconstruction and tag efficiencies in the actual colliding beam environment. Improvements with the extended rapidity coverage of the disk system are also under investigation. Since this analysis requires tagging from the other B, we expect a significant improvement in acceptance when the disk system is added.

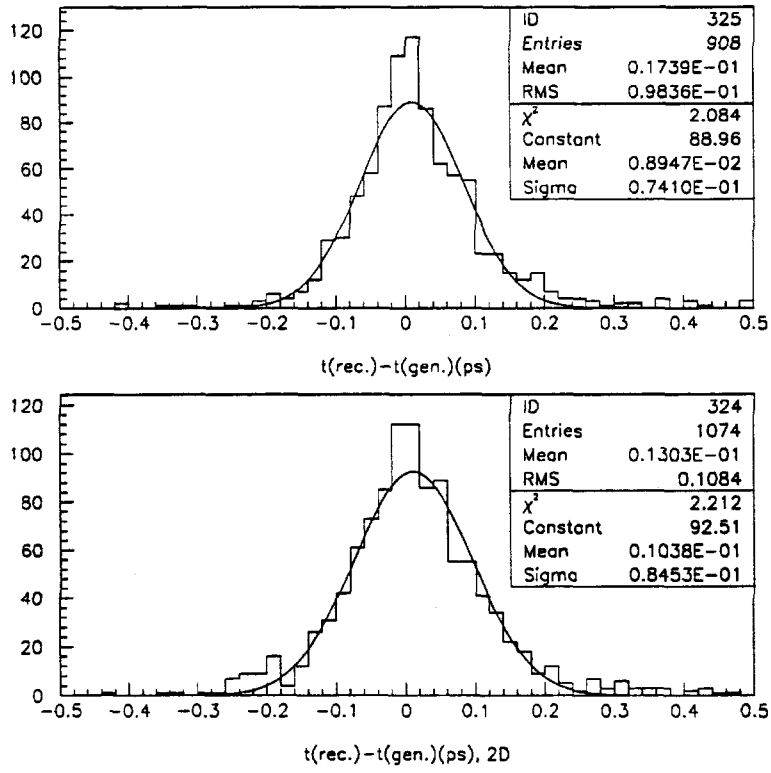

Figure 37: Reconstructed minus generated B_s decay time in picoseconds in 3D and 2D.

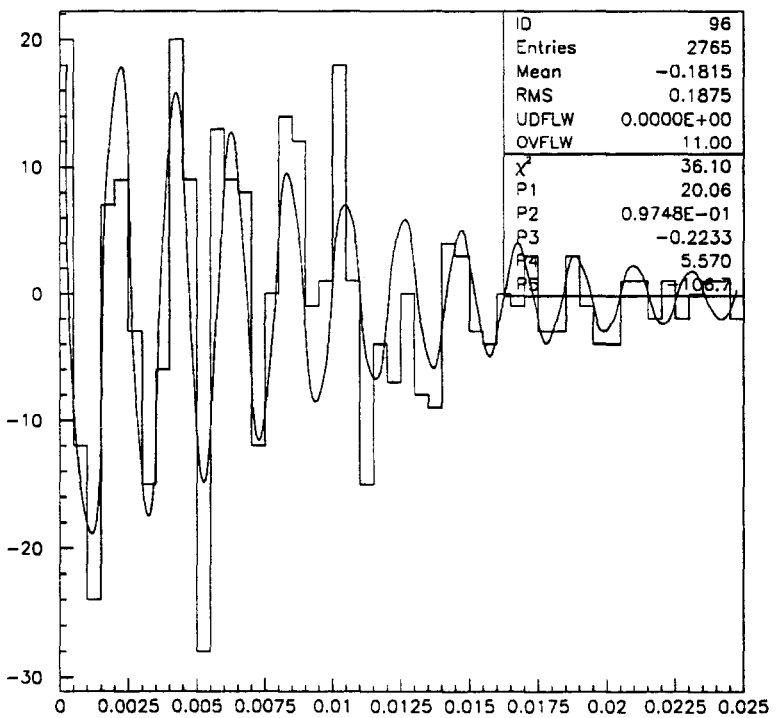

Figure 38: Oscillation plot for $B_s \to \pi\pi\pi D_s, D_s \to \phi\pi$ decay with $X_s = 20.0$. The units on the abscissa are cm/GeV/c.

5.7 CP Violation Studies

The measurement of CP violation in the B system would be a strong test of the standard model. At the Tevatron, CP violation in neutral B decays results in a net, time integrated asymmetry in the rate for $B(\bar{B})$ decays to CP eigenstates. Consequently, the measurement requires only the counting of the rates for B vs $\bar{B}$ decays. Even so, the measurement of such asymmetries presents an enormous experimental challenge. This is due to the statistics required, the small branching ratios involved, and the low p_T of the events. A key aspect of this challenge is the performance of the tracking detector, so it is important to examine the implications of our vertex detector design in this context. Our initial studies for the lepton tagged ψK_s mode indicate that there are substantial gains from both the z resolution with the double-sided barrels, and the high η acceptance of the disks, giving a factor of of four increase in sensitivity to CP violation in G5 over G1 (Table 14).

Table 14: SVX II relative tagging efficiency for the *b tag* example: $B \rightarrow e/\mu\, \nu X$, $B \rightarrow J/\psi K_s$ with $J/\psi \rightarrow \mu^+\mu^-$ for the different geometries G1 - G5. The SVX II tag requires an impact parameter significance $\delta/\sigma(\delta) > 3$ and $p_T > 2$ GeV/c for ≥ 3 leptons in the event. The tag efficiencies are normalized to G1. The errors are $\sim 10\%$.

SVX II Geometry	3 lepton tag efficiency
G1	1.0
G2	1.5
G3	2.4
G4	2.5
G5	4.1

<u>$B \rightarrow \psi K_s$ Mode</u>

The cleanest signal at a collider will likely be in the decay $B \rightarrow \psi\ K_s$, where the leptonic decay of the ψ provides a clear trigger. We wish to determine our sensitivity to CP violation as a function of luminosity. The analysis of the asymmetry is discussed in many references. [21] The statistical error on the CP violating parameter $\sin 2\beta$ is given by, [21]

$$\delta(\sin 2\beta) = 1/(\sqrt{N}D).$$

The factor N is the number of tagged, reconstructed events given by,

$$\mathcal{L}2\sigma\epsilon_{\psi K}\epsilon_{trig}\epsilon_{tag}\frac{S+B}{S}$$

and the factor D is a product of dilutions due to mixing of the B that decays to ψK_s, the

mixing of the tag, the mistag probability, and the background,

$$\frac{x_d}{1+x_d^2}(1-2\bar{\chi})(1-2w)\frac{S}{S+B}.$$

In these expressions,

$\mathcal{L}$	is the integrated luminosity
σ	is the total $b\bar{b}$ cross section
$\epsilon_{\psi K}$	is the total branching ratio and geometric acceptance for the decay $B \rightarrow \psi K_s \rightarrow \mu\mu\pi\pi$
S, B	are the signal and background
x_d	is the B_d mixing rate
$\bar{\chi}$	is the averaged B mixing probability
ϵ_{trig}	is the efficiency for triggering and reconstructing the trigger b
ϵ_{tag}	is the tagging efficiency for the second b
w	is the probability of mis-tagging the second b (excluding mixing)

The B_d mixing rate has been well measured at the $\Upsilon(4S)$ with the result, $x_d = 0.72 \pm 0.15$ [22]. The average B mixing probablility has been measured at CDF with the result $\bar{\chi} = 0.176 \pm .045$ and at LEP with the result $\bar{\chi} = 0.13 \pm .01$[23]. These numbers are very precisely known for the purpose of this measurement. Below, we estimate the b cross section and then investigate the remaining parameters which are dependent upon detector performance.

Cross Sections

CDF has measured the inclusive b cross section down to p_T=10.5 GeV/c from reconstructed B decays and, at higher p_T's from inclusive electrons [24]. Based on these measurements, we can extrapolate to lower p_T and higher rapidity and calculate the cross section for the exclusive ψ K_s decay mode.

We use ISAJET (version 6.43) to leading order to generate b events. In order to validate this method of extrapolation, we have compared the calculated cross sections as a function of quark p_T and rapidity y to the complete order α_s^3 calculation of Nason, Dawson, and Ellis (NDE) [25]. Figure 39 shows that the ISAJET p_T distribution agrees well with the NDE calculation, down to p_T's as low as 6 GeV/c. This is sufficiently low for calculating the cross section at the lowest thresholds for a ψ trigger. Figure 39 also shows a direct comparison of the shape of the b quark p_T distribution for b quark rapidity $|y| < 1$ from leading order ISAJET and NDE to the distribution measured with CDF data. The agreement in shape is good, although the low p_T behavior of the cross section is poorly constrained. In this way we normalize the ISJAET cross section to the CDF data in the following calculations.

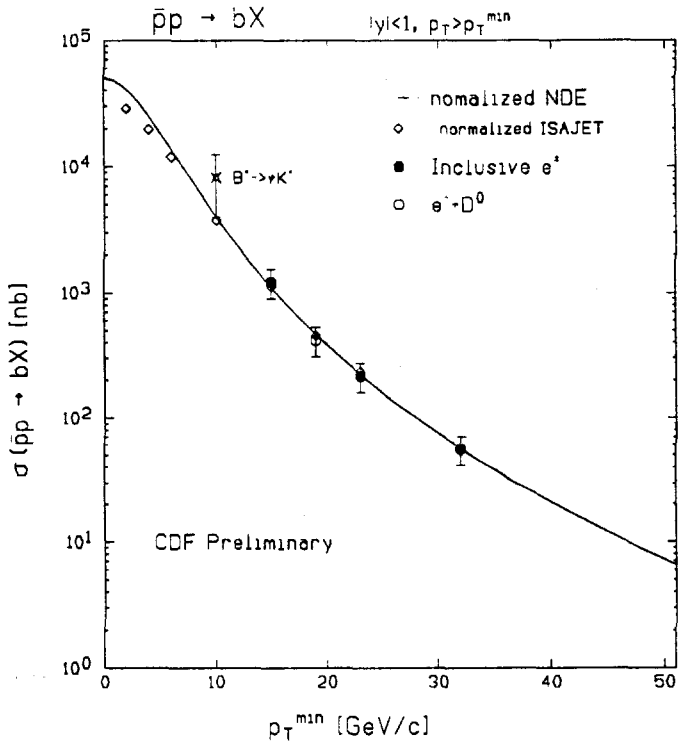

Figure 39: Comparison of the b cross section as a function of quark p_T between ISAJET, NDE, and CDF data. The theoretical calculations have been normalized to fit the data.

The leading order ISAJET cross section as a function of y is compared to NDE in Fig. 40. ISAJET compares well to the higher order calculation except perhaps at large rapidity ($y = 3$). There, ISAJET differs by as much as a factor of 1.75, although the theoretical uncertainties are large.

We have used ISAJET normalized to the CDF data to calculate the cross section for the process $b \to B \to \psi K_s \to \mu\mu\pi\pi$. The product of cross section, total branching ratio (1.34×10^{-5}), and acceptance ($\sigma\epsilon_{\psi K}$) for various acceptances is tabulated in Table 15. The muons were required to have $p_T > 2$ GeV/c and the pions $p_T > 1$ GeV/c, corresponding to realizable trigger thresholds. The cross sections include fragmentation and branching ratios. We see that the expected event rates in a high luminosity data set of the order 1 fb^{-1} are quite high. In addition, it is clear that high η tracking will significantly improve the statistics of the measurement, even given the possible over estimate of the cross section at high rapidity.

Tagging

The flavor (b quantum number) of the B that decays to ψ K_s, can be determined by the flavor of the other b in the event. As a flavor tag we consider the leading lepton (highest

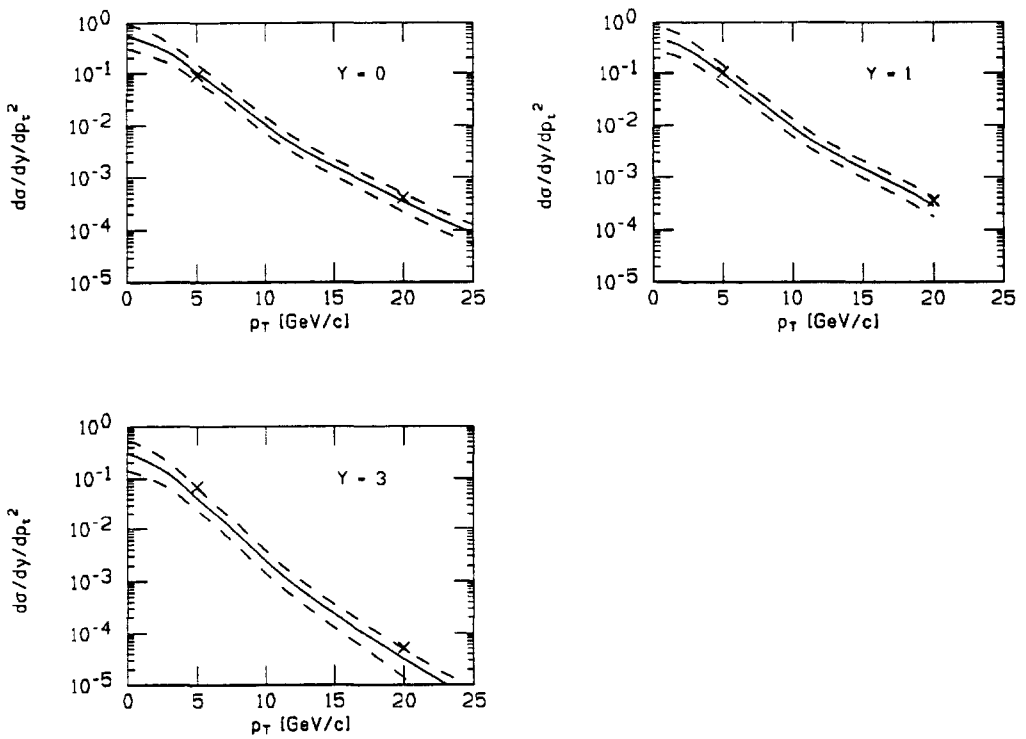

Figure 40: Comparison of the b cross section as a function of quark p_T between ISAJET(crosses) and NDE(line) for η = 0, 1 , and 3. The error bars indicate the size of the theoretical error.

p_T) opposite in azimuth to the trigger B. We then estimate the tag efficiency ϵ_{tag} and mistag probability w from a sample of ISAJET events generated in leading order. It is likely that ISAJET overestimates the strength of the correlations in p_T and azimuthal angle between the two b quarks. As an indication of the dependence of ϵ_{tag} and w on the p_T correlation, we plot in Fig. 41 the tag efficiency for the leading muon, and in Fig. 42 the corresponding mistag probability, with and without p_T cuts applied to the trigger B. The cuts are $p_T > 2$ Gev/c for each of the two muons and $p_T > 1$ Gev/c for the pions. These uncertainties in the Monte Carlo calculation underscore the importance of measuring the tagging efficiency and mistagging probability in the data now being taken with the current SVX.

The ISAJET calculation includes backgrounds from sequential (charm) leptonic decays. An additional background for a muon tag is pion/kaon decays in flight. We model this background in a simple way: we calculate the probability of decay inside of our tracking volume and consider this fraction to be detected as muons. We account for the kinematics of the decay simply by multiplying by an average momentum degredation of 80 %. No attempt is made to model the effects of the decay in flight on the track fitting. Since one might expect some reduction of decay in flight background using tracking information, this is a conservative background estimate. The resulting p_T distribution of the decay muon is very soft, and we expect that it has little effect on the tagging.

Table 15: The ψ K_s cross section as function of $|\eta|_{max}$. The cross section includes all branching ratios and kinematic acceptance for $p_T^\mu > 2$ and $p_T^\pi > 1$.

$\|\eta_\mu\|_{max}$	$\|\eta_\pi\|_{max}$	$\sigma\epsilon_{\psi K}$ pb
3.0	3.0	15.0
3.0	2.0	11.8
3.0	1.5	9.4
2.0	2.0	10.6
2.0	1.5	9.1
1.5	1.5	7.7

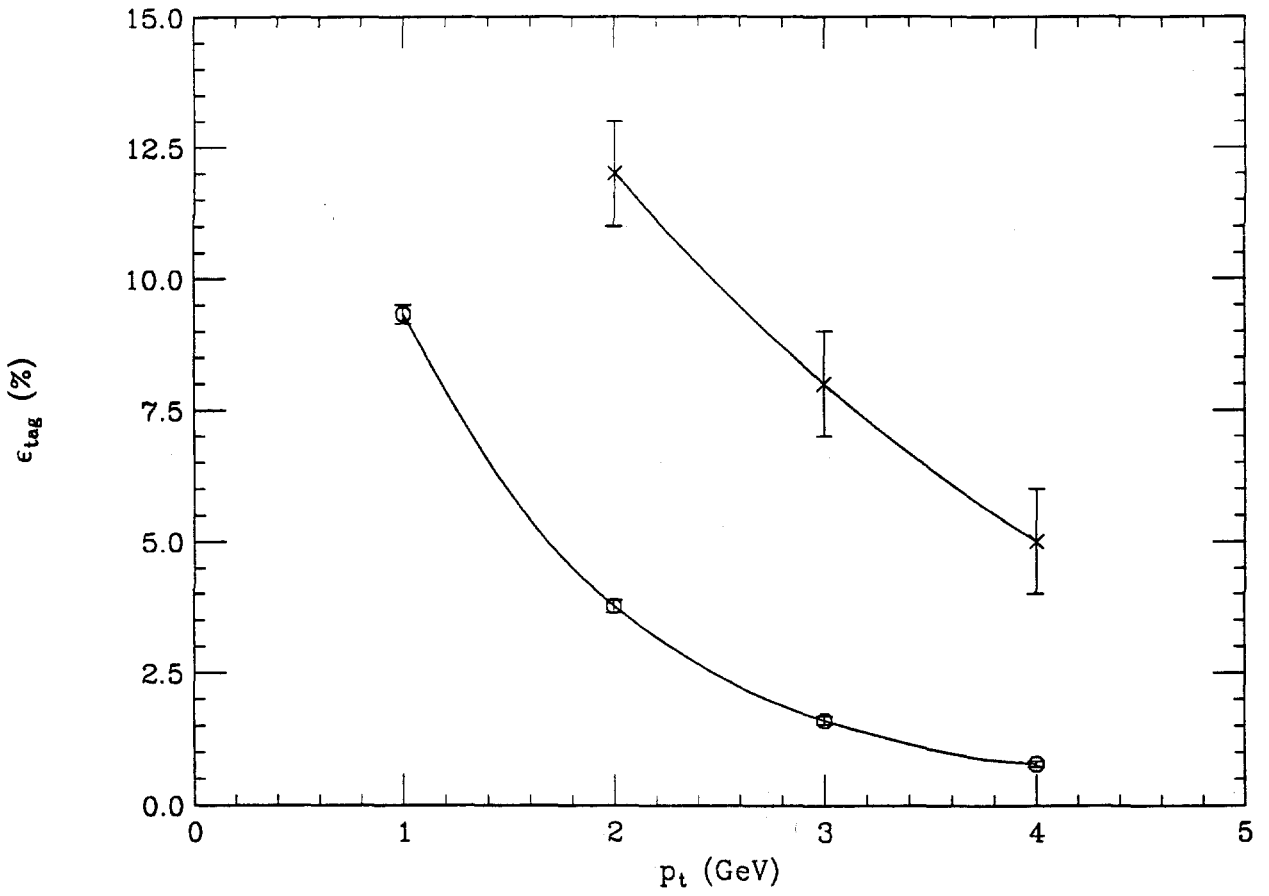

Figure 41: Flavor tag efficiency ϵ_{tag} in percent as a function of the minimum p_T of the muon from b decays. In the upper curve p_T cuts are applied to the trigger B as described in the text. No such cuts are applied in the lower curve.

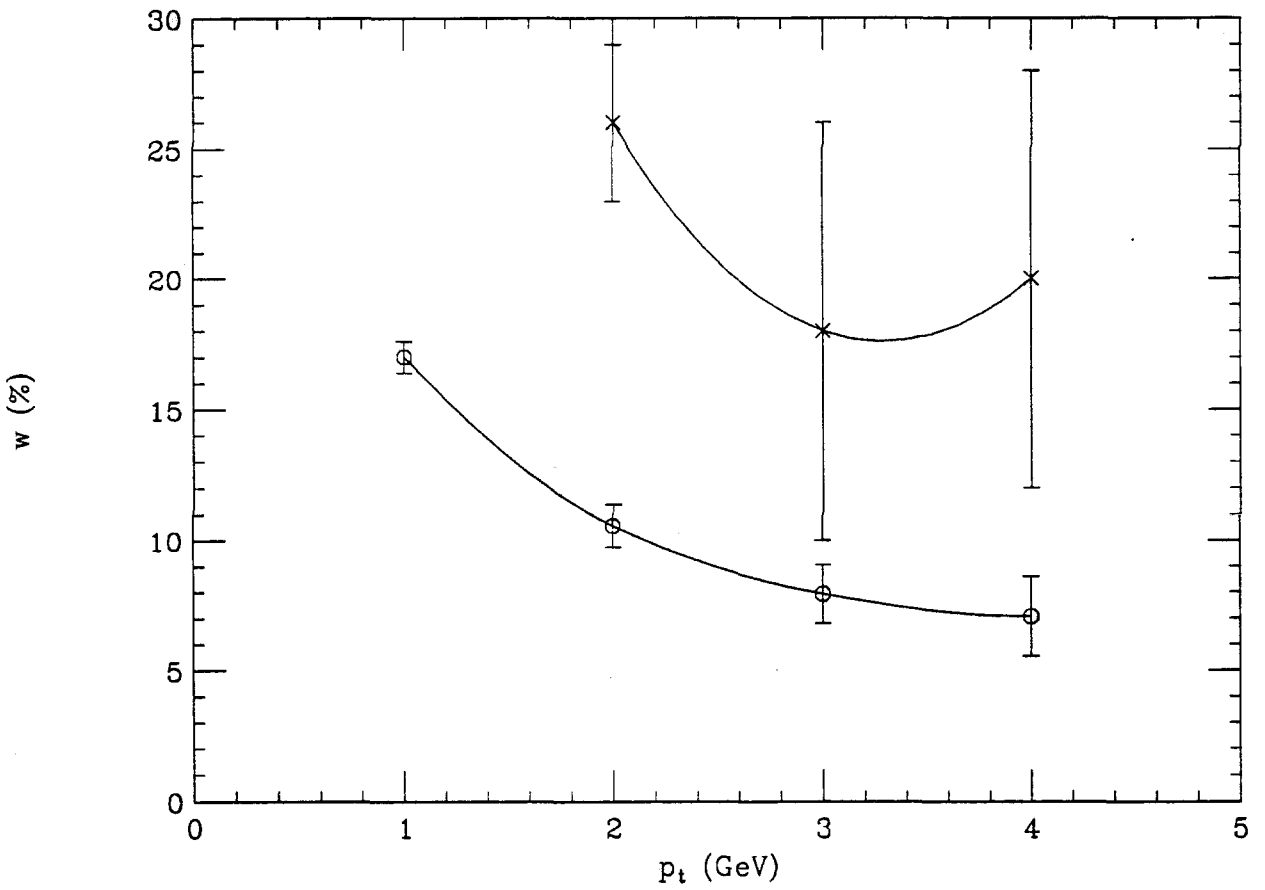

Figure 42: Flavor mistag probability w in percent as a function of the minimum p_T of the muon from b decays. In the upper curve p_T cuts are applied to the trigger B as described in the text. No such cuts are applied in the lower curve.

Sensitivity

We now combine the above results to yield an estimate of the error on the CP violating parameter ($\delta(\sin 2\beta)$). The two remaining parameters we estimate from the CDF measurement of the exclusive reconstruction of $B \rightarrow \psi K^{\pm}$ [24]. In this analysis, the ratio of signal to background was 3/1. With the vertex detector we expect a greatly improved signal to background, and so it is reasonable to expect $S/(S+B) \approx 1$ Including improvements expected in the trigger, we estimate $\epsilon_{trig} = 0.35$. The factors leading to the error on the parameter $\delta(\sin 2\beta)$ are summarized in Table 16. We find for a muon with p_T=2 GeV/c,

$$\delta(\sin 2\beta) = 0.18 \text{ for } \mathcal{L} = 1 \text{ fb}^{-1}.$$

Table 16: Summary of factors contributing to $\delta(\sin 2\beta)$.

$\mathcal{L}$	1000 pb^{-1}
$2\ \sigma\epsilon_{\psi K}$	2(15) pb
$(S+B)/S$	1
ϵ_{trig}	0.35
ϵ_{tag}	.04
N	420
$S/(S+B)$	1
$x_d/(1+x_d^2)$	0.47
$1-2\bar{\chi}$	0.74
$1-2w$	0.78
D	0.27

So far we have only considered a dimuon trigger and a muon tag. Efficient, low p_T electron identification can be achieved by effective use of CDF's high position resolution electromagnetic shower maximum detector. In addition, it is expected that precision tracking information from the vertex detector will help distinguish prompt electrons in B decays from backgrounds such as conversions. Furthermore, the planned inclusion of the shower maximum detector in the trigger will allow for an electron psi sample of comparable statistics to the muon sample. Thus, an improvement in the statistics by roughly a factor of four (triggering plus tagging) can reasonably be expected, corresponding to a reduction in the error on $\delta(\sin 2\beta)$ by a factor of two. Finally, we are exploring the possibilities for particle identification and pion-kaon separation to p_T's of $\sim$ 2.5 GeV/c.

$B \rightarrow \pi\pi$ Mode

In order to fully test the standard model mechanism for CP violation, it is desirable to search for CP violation in other decay modes that independently constrain the model.

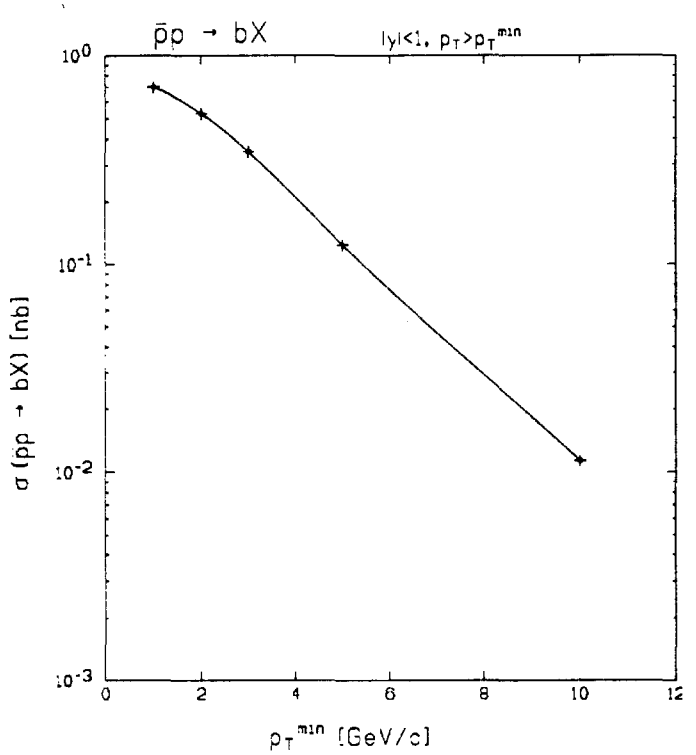

Figure 43: Cross section of $B \to \pi\pi$ as a function of the di-pion p_T threshold. A branching ratio of 1.2×10^{-5} is included. Since the $\bar{b}$ can also decay to $\pi\pi$, a factor of 2 should be used to obtain the total number of $\pi\pi$ events per unit luminosity. A smooth curve has been drawn through the calculated points.

Another such mode is the flavor changing neutral current decay $B \to \pi\pi$ whose branching ratio is expected to be about 2×10^{-5}.[26] It should be noted that this branching ratio is comparable to the product of branching ratios in $B \to \psi K_s \to \mu\mu\pi\pi$ which is 1.34×10^{-5}. Consequently, an equally powerful measurement is conceivable.

Here, one of the principal challenges is triggering. Figure 43 shows the cross section for $B \to \pi\pi$ as a function of the dipion p_T threshold including the branching ratio. Studies have shown that a dipion trigger with threshold of 2 GeV/c can be built with a trigger efficiency of $\approx 6\%$. We see that the cross section is not too steeply falling and one expects the statistics to be enhanced as the trigger efficiency improves with higher p_T. If we assume conservatively a trigger efficiency of 6% we estimate 60,000 $B \to \pi\pi$ events in a 1 fb^{-1} data set. These events can then be tagged via the semi-leptonic decay of the other B. Other challenges for this decay mode include flavor tagging and the separation of signal from combinatoric and πK background in identifying the trigger B.

5.8 Summary of Simulation Studies

These simulation studies illustrate just some of the improvements to be gained by doubling the barrel length over the present SVX, using double-sided silicon detectors, and by adding the disks or equivalent forward tracking. It is expected that additional benefits in background rejection, and in the use of 2-track vertices will be realized with the 3D vertex information. Our conclusion is that SVX II Stage 1 should be a barrel geometry, about one meter in length, with double sided silicon detectors employing 90° stereo. An upgrade path (Stage 2) would add forward disks capable of standalone tracking, either using silicon detectors or possibly another technology such as gas microstrips.

The benefit of extending the barrel length is seen in all the physics considered. The improvements due to the disk tracking have less effect on top but benefit b physics, and this is especially the case when "away-side" tagging is required because extended η coverage is essential.

In Summary:

1. Extending the barrel length by a factor 2 increases the number of top events tagged by a b vertex of three or more tracks by of order 50%, and making the barrels double-sided provides an additional factor of 1.1 to 1.3. In addition the double-sided readout will allow 2-track vertices to be used as a tag.

2. The rejection of $W+$ jets events in a top search gives a factor 40 improvement in signal to background using 2D vertexing over no vertex information. The improvement can be even larger for 3D vertexing.

3. The improved capability for identifying the b vertices provides a significant reduction in the jet-combinatorial backgrounds in studying top decays.

4. The improved momentum resolution achieved with the SVX makes the muon channel in W decay competitive with the electron channel for the W mass measurement. In addition in the W' search the improvement in the muon momentum resolution may be the difference between a discovery and a limit. The Stage 2 disk upgrade is needed for the W asymmetry measurement.

5. A large increase in B acceptance is achieved by doubling the barrel length, and a further increase of comparable size is achieved by adding disks for forward tracking. For single B decays the combined increase is about a factor of 3 over the present SVX. For accepting all the tracks from both B's the combined increase is a factor of 5.

6. Requiring a 3σ impact parameter cut on all three leptons, the acceptance for the lepton tagged ψK_s sample increases by 50% when the length of the present SVX is doubled, and the addition of the disks gives a further 70% increase. For these impact parameter cuts, a double-sided detector gains an additional 60% in acceptance.

7. The mass resolution improves with the addition of SVX information, with a 3D measurement providing a further improvement over 2D. The mass resolution begins to degrade with track pseudorapidity above $|\eta| = 1.5$.

8. The vertex resolution of the barrel system allows the efficient isolation of B decay vertices and the detailed measurement of the B decay distribution, even for modes including cascade decays through charm.

9. Our initial estimates of the capability of SVX II to measure B_s mixing and CP violation show that CDF will be able to provide significant results for these challenging measurements.

In conclusion the long barrel double-sided SVX II Stage 1 detector will be a powerful tool for the exploration of high p_T physics, and for extending the b physics capabilities. The evolution toward a more comprehensive b physics program will be accomplished in part by the addition of forward tracking in Stage 2.

6 SVX II Mechanical Engineering and Design

6.1 General description

The SVX II detector will be arranged in three identical barrel modules mounted symmetrically with respect to the interaction point (Figure 44). Each barrel will cover a region approximately 34 cm long in z, and will consist of four radial layers of detector ladders. Each ladder will consist of four silicon detectors mounted together into a single mechanical unit, and wirebonded electrically in pairs which are read out at each end of the ladder.

The ladder support structure will maintain detector-to-detector alignment to within ± 5 microns in the r-ϕ direction and provide sufficient stiffness and thermal stability to eliminate gravitational and thermal mechanical bowing. The maximum amount of intrinsic bow in the ladder support structure after construction will be kept to less than 50 microns and be measured to an accuracy of $\pm$ 10 microns. A tight tolerance on the radial uncertainty of the detectors is important for the orthogonal stereo angle double-sided detectors used in SVX II, since for tracks at large incident angles, there is a strong coupling between the radial and z position uncertainties. The z position uncertainty in the placement of the detectors during the ladder construction process will also be $\pm$ 10 microns. All of the ladder designs we are pursuing will be able to achieve these tolerances.

The ladders will be arranged in wedges in a 12-sided geometry. Each wedge will span slightly more than 30 degrees, and in the present design the wedges are staggered in radius with respect to each other in order to provide a small amount of overlap. This is shown in Figure 45. This staggered radius geometry will simplify the barrel construction and will allow additional overlap between neighboring wedges compared to the SVX and SVX′ detectors. The optimum mechanical length of the individual silicon detectors is still being explored. With four detectors of 8.5 cm length in each barrel, the total SVX II detector length will be 1.020 meters. The SVX II barrel geometry is shown in Figure 46.

In SVX, laser-drilled holes in the hybrid circuit boards at each end of the ladder were used to define a reference line to which the silicon detectors were aligned with a 5 micron accuracy. The same approach will be taken with SVX II, except that the reference feature will be masked onto the hybrid, and the hybrid will be mounted on the silicon surface. This design will achieve less dead space between the neighboring barrels than in SVX. The SVX dead space between barrels was 4 cm whereas the goal for SVX II (including space for readout cables) will be 1.5 cm or less.

Overall construction tolerances for SVX II will be similar to those achieved in the construction of SVX. A flex test of a layer 1 ladder from SVX revealed an equivalent "specific stiffness" of the composite (see Table 17), and a theoretical center deflection of 12 microns. The SVX II ladder design is 8.5 cm longer than SVX and the ladders may need to be somewhat stiffer, but the 50 micron bow limit should be achievable with either of the two ladder designs being considered below.

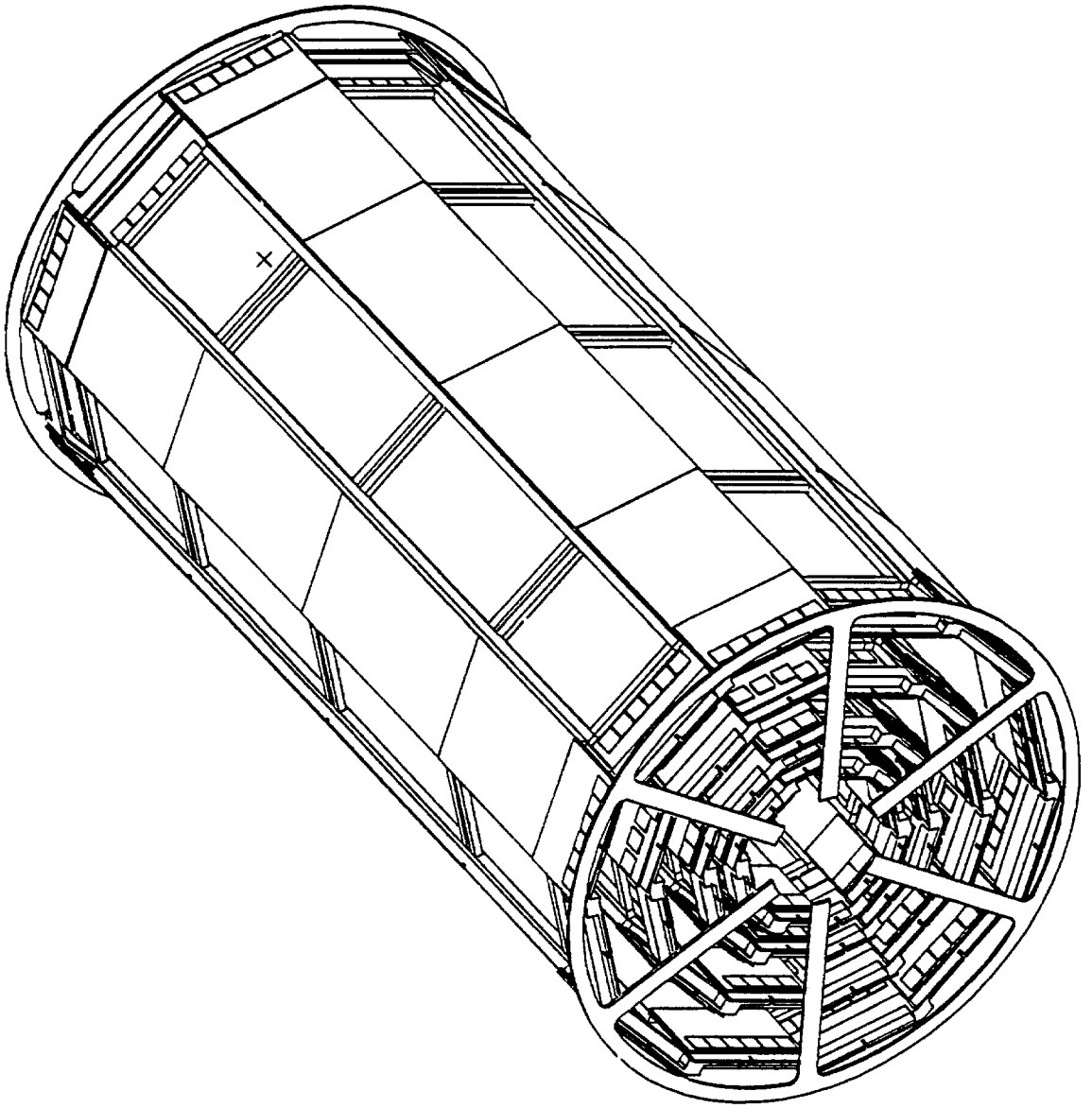

Figure 44: The CDF SVX II detector.

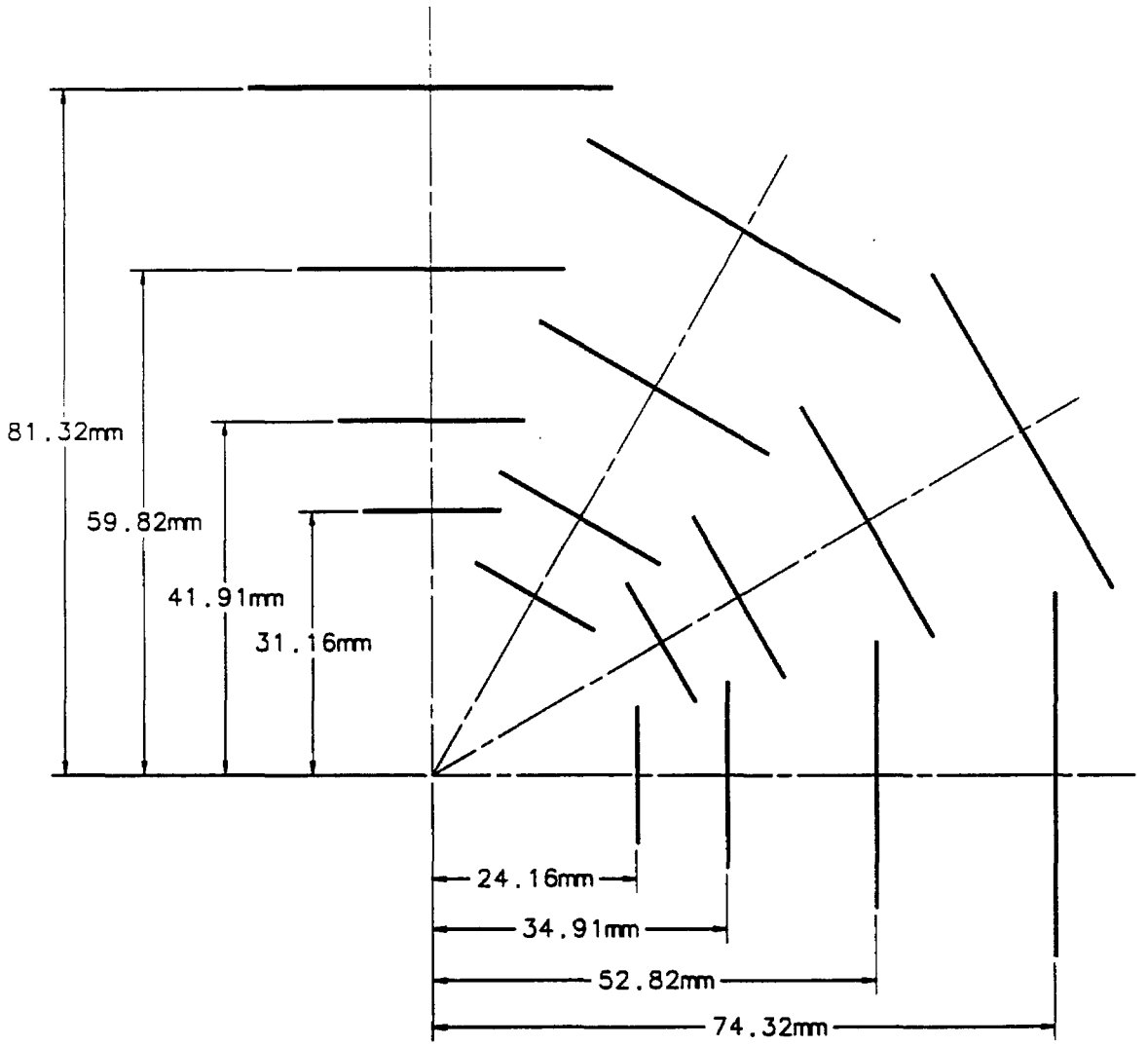

Figure 45: The staggered radius geometry in one quadrant of the SVX II detector.

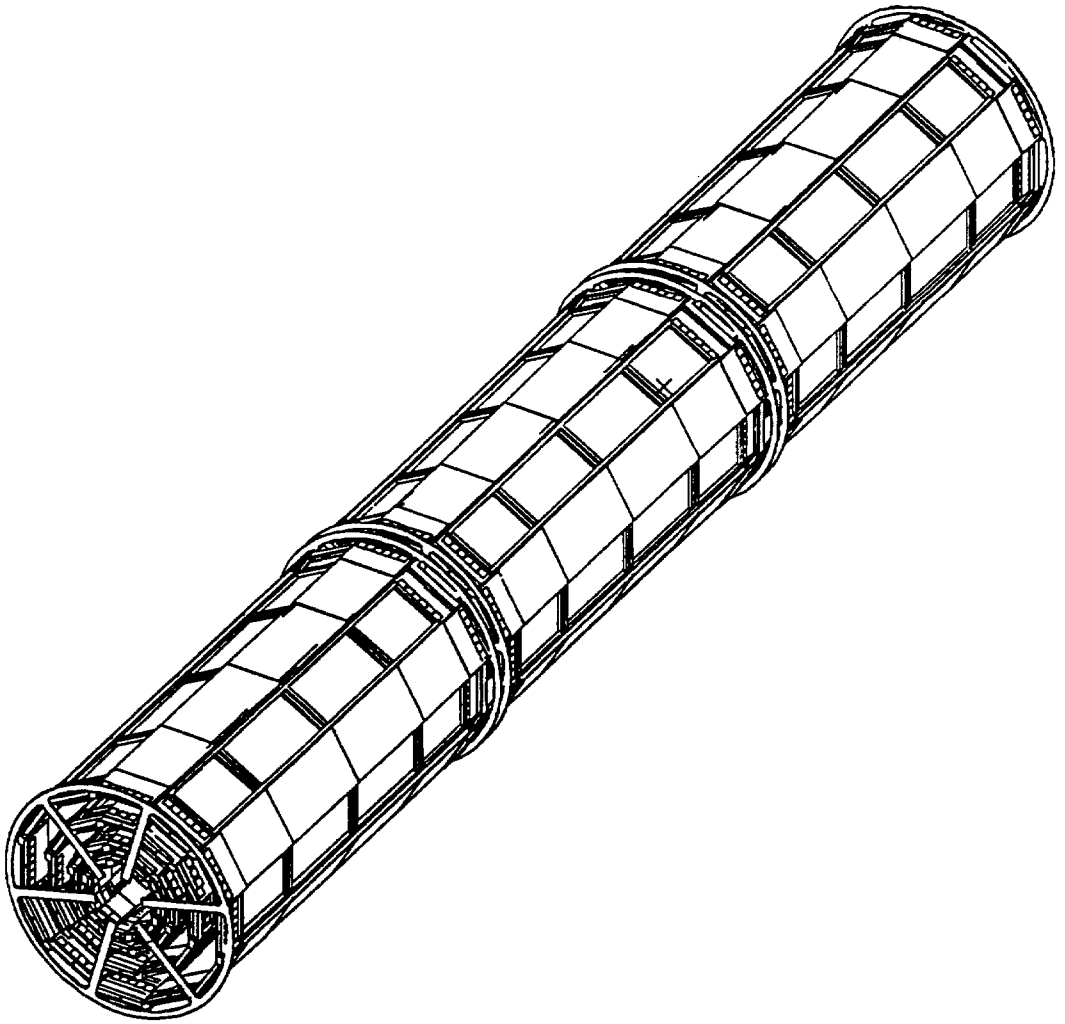

Figure 46: SVX II barrel geometry.

Quantity	Tolerance
detector thickness	± 10 micron
detector-to-detector alignment	5
maximum bow	50
uncertainty in bow	10
uncertainty in z location	10
ladder/detector twist	25
bulkhead precision	15
barrel to barrel	200
SVX II to CTC	200

Table 17: Construction and Alignment Tolerances for SVX II

The main challenge for the choice and arrangement of materials for the internal structure of SVX II is the need to achieve good mechanical and thermal stability in the location and alignment of the silicon detectors while using an absolute minimum amount of material. The design requirements are similar to those of the SVX, however the power generated by the front-end electronics will be greater for each ladder because of the additional channels read out from the double-sided detectors. The radiation dose expected during the detector lifetime (up to 1 Mrad) is also much higher than was the case for SVX and SVX′. This high radiation dose will have implications for the choice of detector electronics and structural materials. Finally, due to the exposed nature of the wirebonds on each side of the double-sided detector ladders, it will be necessary to provide a safe and reliable method of constructing, testing, mounting, and dismounting the ladders with minimal handling.

In the following sections we will describe our plan to proceed from the experience gained in the SVX mechanical design and construction to a design appropriate for SVX II, including all of the above considerations.

6.2 Ladder Support Designs

As described before, the silicon detectors are attached together and supported by a low-mass structural support. This support serves not only to combine the four silicon detectors together into a ladder structure, but also to hold the silicon flat by helping to remove any local bowing produced in the detectors during processing. The two support designs presently receiving serious consideration are:

1. Single-piece edge rails, as used in the Los Alamos design for the SDC silicon tracker;
2. Rohacell/Carbon Fiber Reinforced Plastic (CFRP) composite ladders, as used in the SVX and SVX′.

In both designs we have the option to edge bond the silicon detectors together at their ends in order to join them during assembly into a single mechanical unit. This edge bonding might provide sufficient strength to the detectors to perform the wirebonding prior to attaching the ladder support structure. This is not absolutely necessary in all assembly scenarios, however. The epoxy edge bond, if used, would help to provide stiffness at the joint for the wirebonding and would allow the wafer assembly to be moved after wirebonding and before attachment of the support structure.

Given the two sided wirebonding requirements of the SVX II, the alternative to edge bonding the silicon is to support the detectors on a vacuum fixture for the first side wirebonding, then affix the ladder support structure and wirebond the other side. We have found experimentally during the assembly process for SVX that with careful attention to the process used in gluing together the ladders, much of the residual bowing that may be present in a particular silicon detector can be taken out during the ladder construction. Consequently, careful attention to this step will be required. The final fabrication method will be determined by performing the appropriate tests with the wirebonder to become more familiar with its capabilities and detector support requirements.

In the SVX construction, the silicon load was transferred through the ladder to the readout hybrid and then to the bulkhead. At no point was the silicon part of the load bearing structure. For the SVX II, however, with the double sided detectors and associated front-end electronics, the silicon and hybrids become an integral part of the support mechanism due to the fact that the hybrids are mounted directly on the silicon. Extensive modeling and testing will be conducted to ensure that this will not induce excessive stresses in the silicon.

Edge Rail Design

The edge rail design consists of a rectangular CFRP piece being bonded to the side edges of the silicon detectors during the ladder construction (Figure 47). The stiffness of the ladder depends on the cube of the height of this rail, which for the materials we are considering, will lead to an edge rail height of several millimeters. This design must accomodate such relatively large rails between silicon layers without interference and with sufficient mounting clearance.

The rails will most likely be attached after the wirebonding is performed on both sides. As described above, either edge bonding or the appropriate fixturing will be required to achieve the double sided wirebonding since it is unlikely the wirebonder head could get close enough to the silicon edge to bond the outer pads with the rails already attached. Prototyping work has begun to determine the feasibility of edge bonding the silicon detectors together. A vacuum chuck has been built and attempts are underway to perform these edge bonds. The first effort will be to learn how to successfully epoxy edge bond the detectors and then to measure the reliability and strength of the bonds under mechanical and thermal loads as well as after radiation exposure.

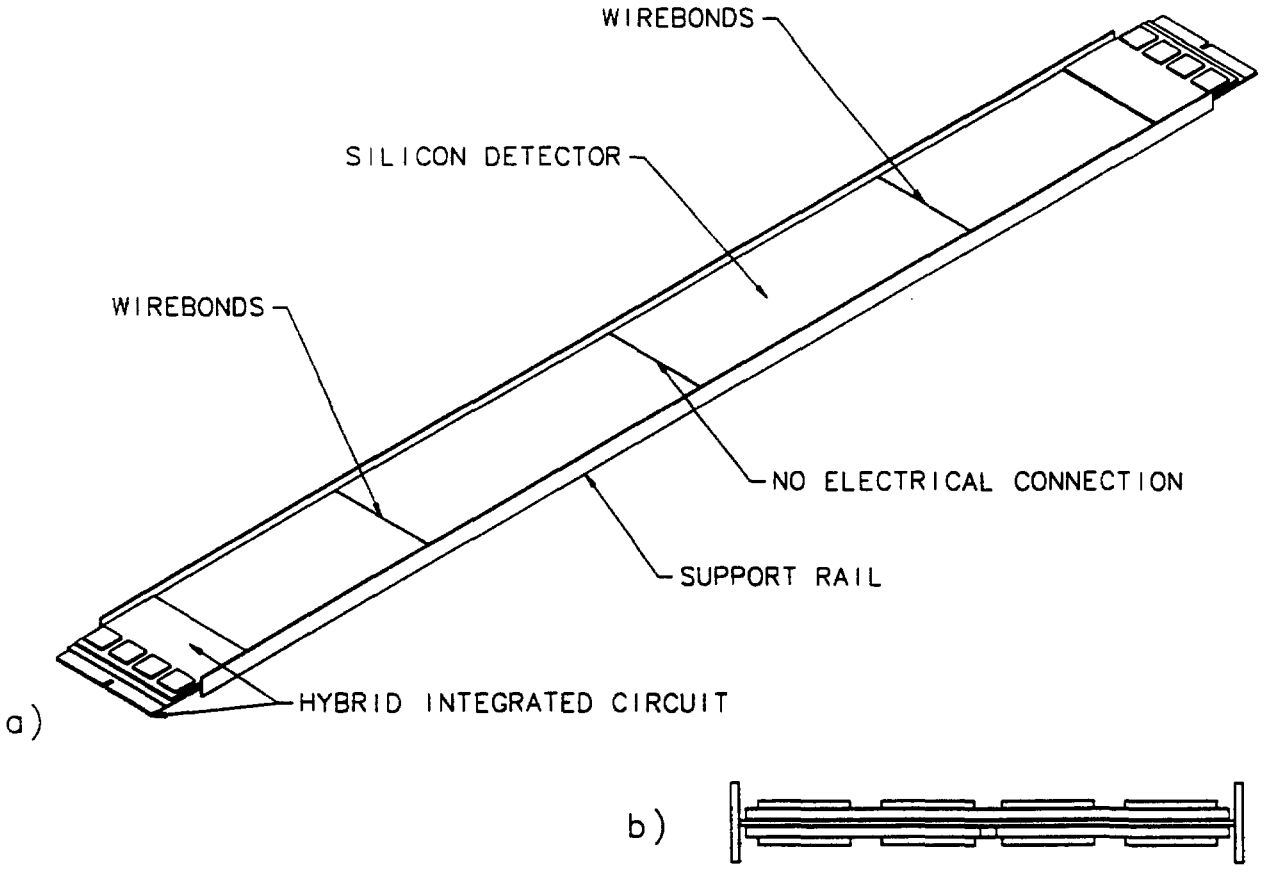

Figure 47: (a) Schematic and (b) cross-sectional views of the SVX II edge rail ladder design.

A second vacuum chuck will be built to hold the edge rails and enable gluing the silicon to them while maintaining a 90 degree angle. These rails will be mechanically tested for adherence to the above mentioned specifications. In addition, the experience of the Los Alamos group in developing the edge rail ladder design for the SDC silicon tracker will be used extensive in evaluating its usefulness for the SVX II detector.

Composite Ladder Design

The composite SVX-style ladder (Figure 48) is the second support option being considered. The materials to produce this ladder are the same as used in SVX, but the design is slightly different. The CFRP would need to be recessed to enable cutting away portions of the Rohacell to provide clearance for the wirebonding. The ladder would stop short of the end of the structure and, as in the rail design, the silicon/hybrid would carry the load to the bulkhead.

This support, if mounted only on one side of the silicon, would be mechanically asymmetrical, i.e. not the same on the top and bottom of the silicon itself. This could lead to thermal distortions if the operating temperature is different than that of the fabrication temperature, a condition which could well occur. In order to avoid this condition, the ladders could be built of materials whose composite coefficient of thermal expansion (CTE) is matched to that of the silicon. This was done reasonably successfully in SVX.

Alternatively, the support could be designed to be lighter weight and mounted on both sides of the silicon. One side of the ladders would be affixed to the silicon immediately after the wirebonding stage for the first side. The ladder would then be flipped, and with proper fixturing, the second side would be wirebonded. Prior to constructing full-scale prototyping fixtures, an analytical approach to composite structures is being developed to assist in determining the most suitable ladder composite structures. The analytical calculations are being verified by flex testing different combinations of composite cross-sections.

Materials

A list has been compiled (see Table 18) giving properties of interest for several candidate materials for the ladder structure. The specific stiffness has been determined, where possible, by flex testing the material at Fermilab. The ladder material must have a high specific stiffness and the appropriate geometry to achieve the above stated construction and alignment tolerances.

The SVX ladder was a composite structure made of carbon fiber and polyimide foam which exhibited an equivalent specific stiffness and flexural modulus of elasticity given in Table 18. Due to the increased length of the ladders in SVX II, investigation of variations on this design are being pursued.

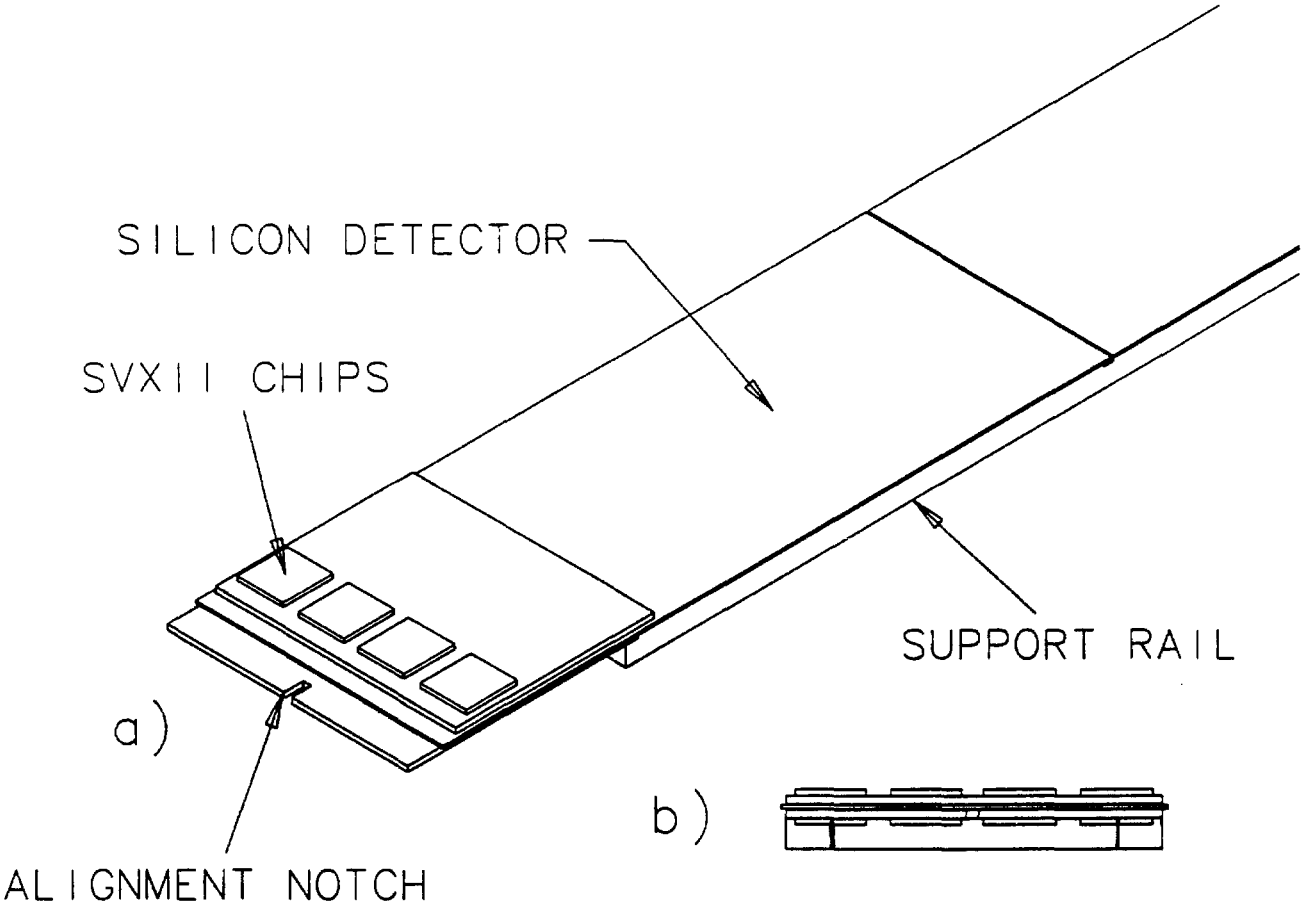

Figure 48: (a) Close-up and (b) cross-sectional views of the SVX II composite ladder design.

Table 18: Material Properties

Materials	Specific Stiff. (10^7 cm)	Radiation length (cm)	CTE (ppm $\frac{1}{°C}$)	Thermal cond.($\frac{W}{m\ °C}$)	Flexural Mod. (10^9 Pa)	Dens ($\frac{kg}{m^3}$)
SVX rails	49.7	208	?	?	10.4	213
Beryllium	160	35.4	11.6	180	290	1840
B/Epoxy 5521	97	21.6	4.5	?	190	2000
Silicon	57.4	9.37	2.6	129	131	2330
CFRP	60-180	28	≈ 0	4.9	100-300	1600
Aluminum	25.4	8.89	23.6	168	68.9	2700

Studies are underway as described below to investigate the performance of this design as a function of the choice of composite materials, dimensions, and placement in order to meet the increased stiffness requirements for SVX II.

The ladder material must not only have a long radiation length, but must remain stable in a high radiation environment. The selected ladder material will be thoroughly tested for mechanical stability under such conditions.

Compatibility with the surrounding environment will be thoroughly checked. Various epoxies and bonding agents will be used in the construction of SVX II. These materials will be checked for outgassing and purity to ensure compatibility with the silicon detectors and front-end electronics.

Thermal stability must be assured for our design as well. Materials with a low linear coefficient of expansion near that of silicon can be used in the rail supports in order to reduce thermal stresses in the silicon. The addition of a thin insulating layer between the silicon and the hybrid and good thermal contact between the hybrid and the bulkhead will channel the heat from the front-end electronics away from the silicon and into the cooling system.

6.3 Bulkhead structure

The bulkhead structure has to mechanically support the ladders, provide a suitable and stable structure for ladder alignment, and act as the cooling interface for the front-end electronics. The best material for such support is beryllium because it is light weight, has a high radiation length, and can be machined to tight tolerances.

In the SVX design, each bulkhead was machined from a single piece of beryllium stock, which was stress-relieved several times by annealing during the machining process in order to achieve the best possible results. Precisions on the order of 12 microns or less deviation from the ideal were typically achieved. This is well within the requirements for SVX II.

The basic design of the SVX bulkhead was an array of radial spokes which supported and connected the circumferential support ledges for the four silicon layers. An aluminum cooling tube was glued to the beryllium bulkhead for each layer. In order to improve the thermal contact between the cooling channel and the electronics for SVX II, we are instead considering a number of designs which have cooling channels machined directly into the material of the bulkhead. An example of such a design is shown in Figure 49. The channels in each bulkhead would be fed by small tubes on the reverse side, and closed at their front surfaces by cap rings which would be brazed on, sealed, and tested. This avoids having to glue a channel of different material into the bulkhead, thus minimizing thermal stress and improving thermal contact. Because the cooling load per detector will be approximately double that in SVX, this is an important consideration. Further details on cooling needs are discussed below.

Alignment reference features will also be incorporated into the cooling channel support members in the bulkhead for use during the ladder installation and alignment survey. In order to achieve the best possible accuracy, these will be arranged so that all of the precise machining can be done on one face of the bulkhead only, after removal of non-crucial material from the reverse face in preparation for this step.

SVX II Heat Load

Table 19 gives the expected heat load for the SVX II. At 2 mW per channel, the expected power generated by the front-end electronics is 256 mW per chip. To introduce a factor of safety into the cooling design and to account for other elements on the hybrid, we have used a larger number of 400 mW per chip. The heat load for SVX II is reported in Table 19.

The cooling will be provided with water pumped through tubes (aluminum or beryllium) in direct thermal contact with the electronics. Complete thermal analyses and modeling are being performed.

The chip power density (1.1 Watt/cm^2) is high enough to be of concern, but within the domain of water cooling schemes. Water in the laminar flow region in a cooling channel of modest dimensions will provide enough heat transfer to cool the electronics and maintain the alignment of the structure. The anticipated heat load of 270 Watts per barrel can be removed while maintaining a temperature rise of $\leq 1\ ^\circ C$ within the water coolant by a flow rate of 64 grams/second. To keep the flow in the laminar region, the minimum cooling channel dimensions for this flow rate are on the order of a few square millimeters. Careful selection and routing of flow channels will enable minimization of the channel dimensions. For instance, layer number 4 has 36% of the total heat load. By splitting the flow into two

Table 19: SVX II Thermal Load per Barrel

Layer #	r-ϕ chips per ladder end	r-z chips per ladder end	Total load per ladder end (W)	Total per layer (W)
1	2	2	1.6	38.4
2	3	3	2.4	57.6
3	4	4	3.2	76.8
4	6	4	4.0	96.0
Total power per barrel				270 Watts

branches, a rectangular channel of 1 mm by 5 mm would provide both sufficient heat transfer surface area and a sufficient hydraulic diameter. Further thermal analysis will be performed to optimize the location and dimensions of the bulkhead members and cooling channel from the point of view of the total mass inventory.

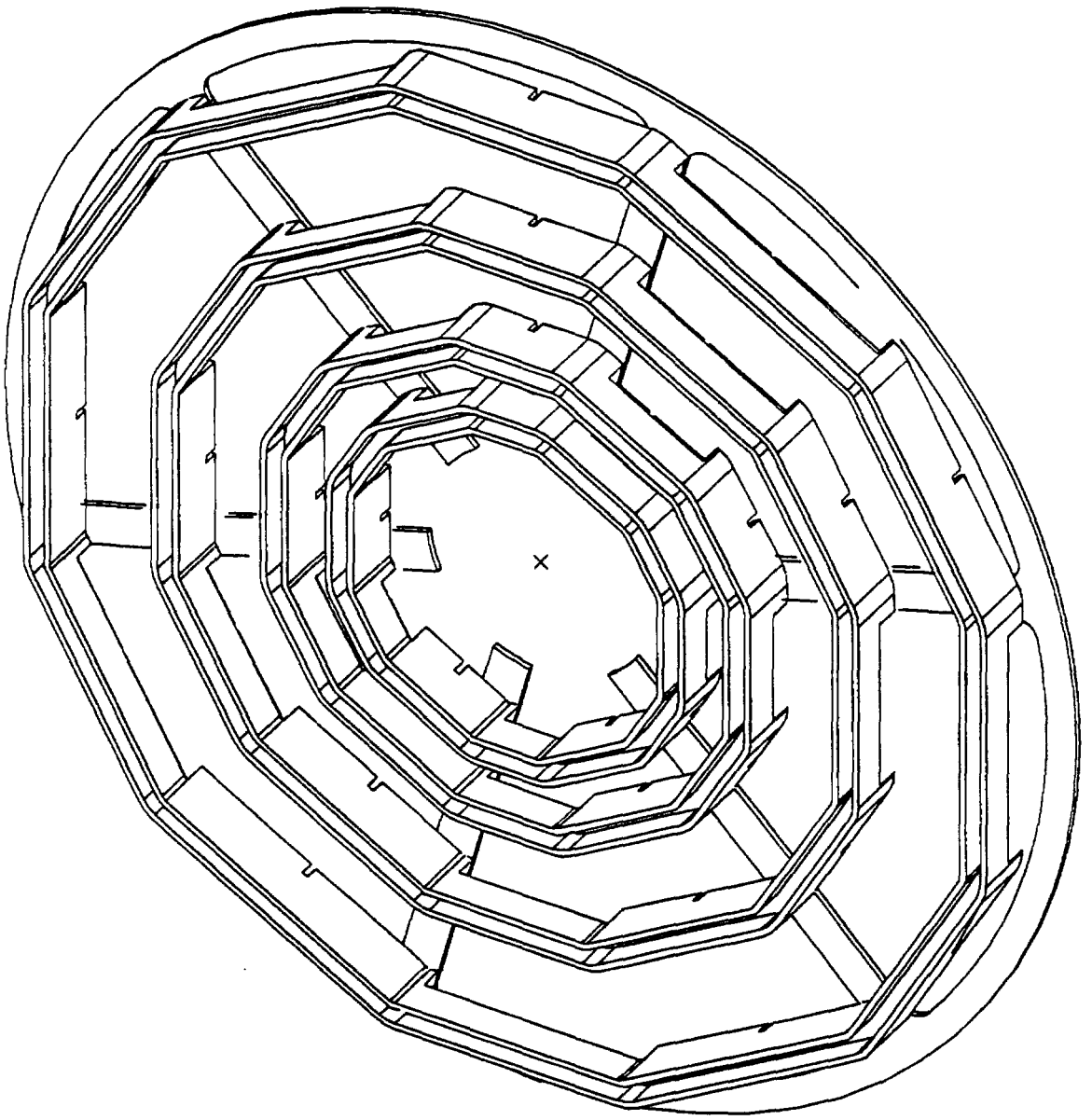

Figure 49: SVX II bulkhead design, showing the cooling channel integrated into the ladder mounting ledges before the cap rings and feed tubes are attached.

6.4 Hybrid Mechanical Considerations

Each front-end readout package will consist of a mechanically-supporting, thermally-conductive dielectric substrate with an electrically conductive pattern, two or more active SVX II readout chips, and several passive surface mount capacitors to provide bypassing and power filtering. The complete package with active and passive components attached is referred to as a Hybrid Integrated Circuit (HIC).

Each end of a ladder will have two such HICs mounted directly to the top and bottom surfaces of the silicon. Since the readout density on each of the four barrel layers is approximately the same for each layer, more SVX ICs are needed on the outer layer ladders. However, the hybrid design is very likely to be the same (or very similar) on each side, r-ϕ or r-z, of the silicon detectors for each layer. Thus only four (or at most eight) variations of a similar hybrid design are required. For any of the possible substrate options for these hybrid circuits, thermal contact with the cooling channels is an important design issue.

Hybrid Substrate Options

There are a number of packaging and interconnection variations that will provide solutions for the SVX II readout needs. Three packaging proposals and two interconnection schemes are being considered: (1) Thick Film, similar to that used in the SVX and SVX′, (2) Laminated Composite, and (3) Thin Film technology.

The thick film substrate designs used in SVX and SVX′ had approximately 15 layers of fired conductive and dielectric material. The packaging density involved 150 micron paths on a 300 micron pitch. To provide signal isolation and crosstalk reduction, signal routing was placed under the IC device sites within the substrate.

An alternative laminate packaging option uses a multilayer kapton film as both substrate and readout cable. Here, all connective metallization is patterned on kapton polyimide film, and this film is laminated onto a thermally conductive substrate whose primary function is to provide for mechanical and thermal support. An obvious advantage of this packaging is the absence of a connector between the hybrid and the subsequent readout cable. The kapton laminate film can be designed to be thinner where the ICs are placed in order to improve thermal performance. Alternatively, windows could be made in the kapton at the IC sites so that the ICs can be mounted directly on a supporting thermally conductive substrate. The kapton routing density that can presently be achieved is 125 micron paths on 250 micron pitch.

The third packaging option is for a multilayer polymer thin film design that would take advantage of photolithographic pattern generation to provide for high density, high performance connection of the active and passive components on the hybrid circuit. Current practical technologies can achieve a routing density of 75 microns on 150 micron pitch. This would be approximately four times the density of the present thick-film design. A hybrid

circuit appopriate to the SVX II could thus be achieved in approximately four to six layers. Current limits on this technology are approaching this number of layers.

6.5 Readout Cables and Routing

Connection between the electronics and the external data acquisition system was achieved in the SVX via laminated copper/kapton cables. These 23-line cables interconnect the hybrids on a parallel bus structure with additional driver cards for the readout. A similar system could be used in the SVX II. In this case, either the thick or thin film hybrid designs will require an appropriate scheme for connecting to the readout cables.

An alternative readout scheme also being pursued uses an optical interface between the hybrid circuits and the driver card. The current view is that each readout chip will have a serial output through a locally mounted LED optical transmitter, with one serial optical data link for each of its ICs plus two optical clock and trigger function receivers per hybrid.

Routing of the optical cables could be somewhat simpler than for the all-copper/kapton design since there would be only one serial optical output per chip. This optical line could be routed directly between the readout IC and the driver card (if any), or to an optical/analog interface. Both designs are proceeding at this time.

6.6 Prototyping/Testing

Several aspects of the engineering of the mechanical system as described above are beyond the initial conceptual stage and are already being subjected to tests in the laboratory to refine features of the design. These are described below.

Si Edge Bonding

As mentioned previously, we are pursuing the edge bonding of silicon detectors. A vacuum fixture has been built to hold two detectors while a heater is suspended above the bond to cure the epoxy. If successful, edge bonding the detectors could provide a means of temporarily holding them together for wirebonding.

Once the edge bonding technique has been perfected and is repeatable, we will aluminize some silicon test pieces near their edges in order to be wirebonded. These metallized surfaces will act as the pads and provide us with a surface to microbond. If the temperatures attained during the edge bonding are excessive to the point of damaging the metallized surface, we may learn this important fact prior to edge bonding actual silicon detectors.

Ultimately the goal is to derive a method of fabricating the ladders to be used in SVX II. Silicon edge bonding could provide a temporary structure, allowing wirebonding on one or both sides prior to affixing support rails.

Edge Rail Prototyping

The edge rails are constructed of carbon fiber reinforced plastic. A fixture will be built to hold the rail while the silicon is bonded to it. These prototypes will be flex tested to determine how they conform with theory, and provide useful information in the design iteration process.

Whether the silicon will require to be first edge bonded has yet to be addressed. It may be possible, with the proper fixturing, to perform the wirebonding while the silicon is held only in a vacuum fixture. The support rails would be attached after the wirebonding is completed. The other option is to determine if it is feasible to wirebond after the rails have been attached to the silicon by studying the operating characteristics of the wirebonder head.

Composite Structure

Several prototype composite rail supports based on the SVX ladder are also being pursued. Fixturing has been fabricated to produce three styles of composite structures. These will be flex tested to determine the CFRP modulus. This process should provide sufficient information to design a new ladder which will meet the stringent requirements of the SVX II.

The final ladder design will, to a great extent, be determined from the results of the prototype testing. In addition to the flexural strength of the structure, the fixturing and handling of the ladder during the fabrication process are important.

By building the centroid of the support structure at the same location as that of the silicon, thermally induced bending moments (in theory) can be made to be less important. If it is not possible to build a symmetrical cross section, the CTE of the support ladders must be near that of the silicon to minimize thermal stresses. Regardless of the support design, stresses in the silicon will be reduced by attempting to match the CTE of the support with that of silicon.

Materials chosen for the ladder will require radiation testing. The materials will be irradiated and tested for changes in their mechanical properties.

6.7 Support of SVX II within the VTX

Since the SVX II will consist of three mechanical barrel units instead of the present two, it will be necessary to split the VTX along a different boundaries than the present center gap at $z = 0$. Our present plan is to assemble the VTX in three sections, with the SVX II residing primarily in the central section of the VTX. Two options have been identified which meet the requirements for support of the cable pathways and cooling lines and still provide sensible

methods for installation and removal. These will be pursued with appropriate engineering support within CDF so that a decision between them can be reached.

The first method calls for separation of the VTX into asymmetric pieces, one of which will hold just one module of the SVX II, and the other holding the remaining two. In order to permit cables to be dressed properly to the outside, the larger of the VTX modules would be itself split into two sections, with a temporary gap at the extreme end of the SVX modules. These two sections would be assembled together prior to installation into the experiment.

The second method would place all three SVX II barrel modules together as one unit mounted into a central section of the VTX which would be just long enough to carry that unit. This would be more attractive from an installation and maintenance point of view, but would involve extended sections of SVX II and VTX cables which would have to be supported (at least temporarily) by external means during installation and removal of the remaining VTX end sections.

The design for both of these options is proceeding, with a decision to be made within the next year.

7 Silicon Microstrip Detectors

7.1 Description of the Detectors

The barrel of the SVX II will be constructed from double-sided detectors made with high resistivity n-type bulk silicon of thickness 300 μm. The exact dimensions of these rectangular devices depend upon the barrel layer in which they are located, but a typical device has an active area which is between 10 and 20 cm^2. The electrical specifications will be guided by research being carried out by the DELPHI and CLEO collaborations and by our experience working with prototype detectors.

The $r - \phi$ measurement will be made with the p-side. On that side, charge will be collected by longitudinal strips with 25 μm pitch. The 5 μm-wide implant strips will be capacitively coupled to each other, and alternate ones will be read out. The strips will be coupled to the readout by a thin (typically 0.2 μm) layer of silicon dioxide and an aluminum electrode. To minimize the capacitance of the side, the aluminum strip will be as narrow as possible while guaranteeing electrical continuity and while maintaining sufficient capacitance to the implant strips. Polysilicon resistors will be used for biasing because of their radiation resistance.

The z measurement will be made by transverse strips on the n-side. As with the p-side, the strips will be AC-coupled to the readout, the biasing will be polysilicon, and the implant and aluminum strip widths will be minimized.

The SVX II mechanical design will be simplified by reading out both sides of the detector at the same edge. We plan to use the "double metal" technique, in which each n-side transverse aluminum strip (the "first metal") is coupled by an aluminum via through a relatively thick insulator to a longitudinal metal strip (the "second metal") which lies on the detector surface. In an alternative to the double metal technology, signals from the transverse strips can be routed to the readout chips with an adhesive Kapton foil bearing copper laminated strips.

The details of the design of the ohmic side strongly affect that side's capacitance. In the case of the double metal technology, the ways to minimize the capacitance are by reducing the second metal's linewidth (and hence the overlap area with the strips of the first metal) and by maximizing the amount of dielectric between the two metals. At present the material with the best dielectric properties (in particular, radiation resistance) is polyimide.

The presence of positive charge at the Si-SiO_2 interface makes it necessary to isolate the strips on the n-side. This is because the positive charge attracts electrons in the bulk to the interface, where they spread out under the influence of the positive voltage on the n^+-strips, effectively short circuiting the strips. Manufacturers use two methods for isolating the n-implants—field plates and p-implants. We are presently investigating the capacitance, radiation hardness, and ease of operation of both in order to choose between them.

Two readout pitches–111 μm and 166 μm–result naturally from the use on this side of 85

mm-long detectors and an integer number of readout chips (with 128 channels per chip). In the preferred design, Layers 1, 3, and 4 will have 166 μm n-side pitch, and Layer 2 will have 111 μm n-side pitch, with all channels being read out. We will also investigate detectors with the pitch of the implants at half the values listed above, but with alternate channels read out. The use of 90° stereo strips with these pitches on a rectangular detector naturally results in the assignment of multiple sense strips to the same metal strip. The multiplexing ambiguities can lead to reconstruction of unphysical tracks known as ghost tracks. The detector pitch and dimensions are being selected so that the ghost tracks are identifiable with the aid of the pointing resolution of the outer tracking.

7.2 Technical Issues Shaping the Design

The parameters of the SVX II detector which have the greatest impact on its physics capabilities are its acceptance and position resolution. In turn the position resolution is related to the detector signal-to-noise ratio. The acceptance of the proposed geometry of the SVX II has been discussed elsewhere in this document. Extensive work is underway to simulate and measure the resolution and capacitance of silicon devices similar to the one whose properties are outlined above. This work is described below.

Z Resolution

It has been shown earlier that good resolution in z can impact the SVX II physics capabilities. In particular, simulations have indicated that the following can be expected upon replacement of a G2 geometry detector by a G3 geometry detector (with z resolution varying between 20 and 50 μm over the range in angles 0–1.35 radians with respect to the normal):

1. The efficiency for B tagging of top improves from 50% to 63% (for $m_{\rm top} = 130$ GeV/c^2) and from 64% to 73% (for $m_{\rm top} = 200$ GeV/c^2).

2. The relative tagging efficiency for events containing two B's, where one decays via $B \rightarrow e \,/\, \mu\, \nu\, X$ and the other decays via $B \rightarrow J/\psi\, K^0_s(J/\psi \rightarrow \mu^+\mu^-)$, improves by 60% for an impact parameter significance cut of 3σ and a p_T cut of 2 GeV/c on all three leptons.

These estimates were made following Ref. [4]. The values used in the SVX II simulations are shown in Figure 9. We have continued this study [4] to the cases of strip pitch, readout strip pitch, and large track angles of interest to SVX II [27].

The software package is based on code written by V. Luth [4] to simulate the response of a 300 μm-thick detector to charged tracks which traverse it at angles of incidence between 0.0 and 1.4 radians from the normal. Strip pitches of 73, 111, and 166 μm, and strip pitches of

73/2, 111/2, and 166/2 μm but with readout pitches of 73, 111, and 166 μm are considered. Results are shown for signal-to-noise ratios of 12 and 18 to 1. In the simulation, tracks are thrown for each angle of incidence under consideration such that a width in the center of the detector of one readout pitch is evenly illuminated.

Each track is propagated through the detector by slicing the detector horizontally into several virtual layers, typically 10 per 100 μm of silicon traversed, and depositing charge in each according to a Landau distribution with an average of 80 e^-/hole pairs per μm. As this charge is drifted through the detector, it responds to effects of diffusion, applied bias voltage, and magnetic fields. The charge is then collected on the strips. Gaussian random noise is added to the strips. To simulate detectors with both readout and non-readout strips, the diffusion pitch is halved, and the charge collected on the strips which are not read out is shared equally by the adjacent readout strips.

Three types of readout are considered: analog, in which all strips above a given threshold are read out and pulse height information is stored; digital, which is similar to analog without the preservation of pulse height; and nearest neighbor logic, which is similar to analog but which in addition requires readout of subthreshold strips neighboring those which pass the threshold cut. The preservation of analog information permits charge division, thereby improving z resolution on oblique tracks in detectors with intermediate (non-readout) strips.

Three clustering algorithms are considered. In analog clustering, channels are compared sequentially with a threshold. A cluster begins with the first channel encountered which exceeds the threshold and ends when a channel is encountered which does not exceed the threshold. Digital clustering uses the analog clustering algorithm with digital readout of the SVX II data. Finally, in predictive clustering we use the knowledge of angle of incidence, α, to predict the number of strips in a cluster. This could be obtained from extrapolation of a VTX track, for example. For our simulations the number of strips in the predictive method is required to be at least 3. Clusters are then identified by maximizing the summed pulse height in a "window" of this width and requiring that the sum of the pulse heights within the window must pass a threshold cut.

The centroids of the tracks in N-channel clusters are calculated according to several weighting schemes [27]. The algorithm that is least sensitive to the track angle, α, is a variant of the weighted mean, that we call central averaging:

$$\langle z \rangle = \frac{z_1 \mathrm{PH}_1 + z_N \mathrm{PH}_N + (\sum_{i=2}^{N-1} z_i) \times \langle \mathrm{PH} \rangle_{\mathrm{inner}}}{\sum_{i=1}^{N} \mathrm{PH}_i},$$

where PH_i is the pulse height on the ith strip and the average pulse height for the central strips:

$$\langle \mathrm{PH} \rangle_{\mathrm{inner}} = \frac{\sum_{j=2}^{N-1} \mathrm{PH}_j}{N-2}.$$

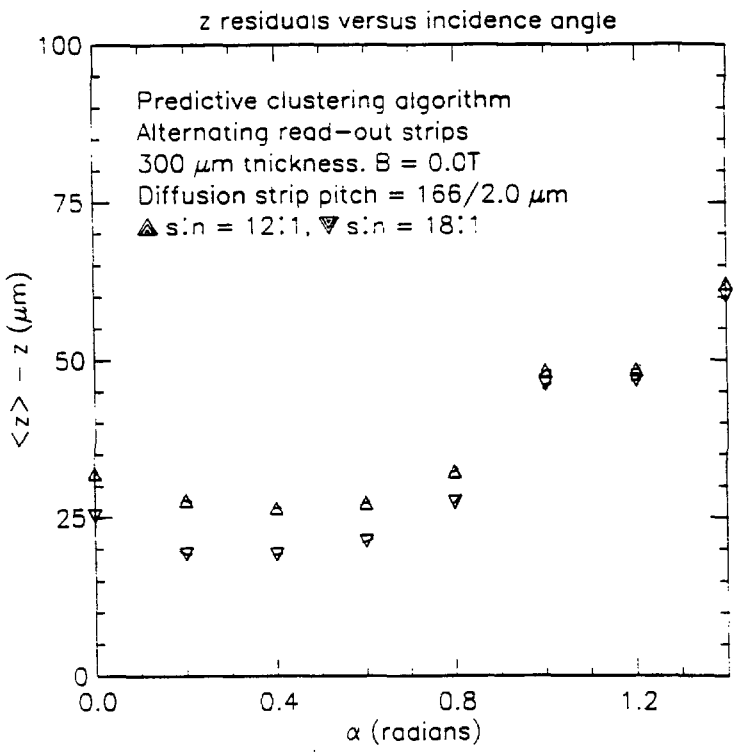

Figure 50: Expected z resolution using the predictive clustering algorithm and central averaging for the proposed SVX II double sided detectors. The scatter reflects the statisticaal error in the study.

The $i = 2$ to $i = N - 1$ terms reduce sensitivity to Landau fluctuations which dominate the resolution at large values of the track angle.

Our studies suggest that the following is one attractive choice for optimizing the detector resolution. Choose a 166/2.0 μm diffusion strip pitch and read out alternate diffusion strips only. (The interleaved strips are biased and capacitively coupled to the readout strips, but are otherwise ignored.) Keep only channels that pass a 25% *minimum-ionizing pulse height* cut, with the proviso that readout channels adjacent to those passing this cut are kept. Record the pulse height information. Predict the size of a "window" of strips, based upon an estimate of the incidence angle of the track, and position the window where it subtends the maximum pulse height. Calculate the centroid of the window using a pulse height weighted average where the average pulse height is used to weight the inner strips. The resolution obtainable with these parameters is shown in Fig. 50.

This result predicts somewhat increased z resolution from that shown in Fig. 9.

Capacitance

The detector parameters which determine the signal-to-noise ratio of the charge collection are the leakage current and the capacitance to ground of the strips. The work on the prototype amplifiers indicates that in order to achieve a signal-to-noise ratio of 12:1, the capacitance of the strips must be less than 30 pf. We wish to identify the electrical features which are the primary contributors to the capacitance in order both to extrapolate to our final design and to modify the design as necessary to achieve our required signal-to-noise ratio.

The following estimates are based on measurements of existing devices at Santa Cruz [28] and at LEP by the DELPHI group and on calculations by Ikeda *et al.*[29] The result is that, while the p-side capacitance is understood, the n-side capacitance remains difficult to estimate. We will test prototype structures to decide on the final technology.

One of the major uncertainties is the effect of ionizing radiation on the capacitance due to the build-up of fixed charge in the oxide. The calculations of Ikeda *et al.* show that there is a significant increase in the capacitance as the fixed charge at the oxide-silicon interface increases from 10^{10} to 10^{12} holes/cm^2. In unhardened MOS devices, charge densities of 10^{12} holes/cm^2 are typical of doses of 1 megarad, but this number is very dependent upon the type of oxide. Preliminary results from Santa Cruz indicate that this is not a significant problem on the p-side. This is reasonable, since the holes are the primary source of the problem, and they drift away from the interface on the p-side. The holes drift toward the interface on the n-side, however. Until we have experimental data, we will ignore the effect on the p-side but use the calculations of Ikeda *et al.* to include it on the n-side.

The results summarized here are estimates for an n-type bulk with a resistivity of about 5000 ohm-cm, a thickness of 300 μm, and implants which are capacitively coupled to the readout system. As an example consider a Layer 4 ladder. It is read out by six chips on each side and is 17 cm long, 3.84 cm wide and has 768 and 1700 strips on the p- and n-sides respectively. The pitch (p) of the strips is 50 microns on the p-side (ϕ) and 110 microns on the n-side (z).

The capacitance to ground of the p-implant on the cathode side of the detector depends primarily on the ratio of the metal width to the pitch (w/p) when p $\ll$ the thickness (t). C. Levier at UC Santa Cruz [28] has measured a set of Hamamatsu detectors with a 50 μm pitch and a variety of widths. The results have been fit to a straight line

$$C_I(\mathrm{pf/cm}) = 0.6 + 1.7 \cdot (\frac{\mathrm{w}}{\mathrm{p}})$$

Using this model, the capacitance of the p strips of the standard prototype with $w/p = 0.1$ is 0.93 pf/cm or 16 pf for a 17 cm detector.

This number agrees well with the calculations of Ikeda *et al.*,[29] who have calculated values for 5 μm wide strips on a 50 μm pitch using PISCES IIB with and without the intermediate floating strip. Their result is important because it shows how to scale the capacitance for the presence of a floating strip and for a variation in the fixed charge. They find that the change in the capacitance due to a floating strip is not large. In the Santa Cruz

paper it appears to be an increase of about 10% - 20%. It seems likely that this increase is primarily due to the fraction of the gap which has been shorted out by the electrode, i.e., an effective increase in w/p. The change may be greater for wider implants.

We feel that we will be able to exceed our target for signal/noise on the p-side. There is much less experience with n-side devices. Although we can learn from the experience of other groups, we will order prototype devices to make our own measurements. The DELPHI group at LEP is the first group to try the double metal scheme. Although the capacitance of the first prototypes delivered to DELPHI was so high that they were unusable, a substantial R&D project with suppliers has now resulted in usable devices (although the devices have yet to be delivered). Our ladder is larger than theirs, however, and it behooves us to take all steps to minimize the capacitance.

On the n-side, the effective source capacitance of one readout channel is a network with 3 types of elements:

1. Junction capacitance to the p-side, C_J,
2. Interstrip capacitance of the n strips, C_I,
3. 1st metal to 2nd metal overlap capacitance, C_m.

The first two components are similar to the p-side effects. On the n-side the interstrip capacitance depends upon (1) the mechanism used to isolate the n strips, (2) the total length of strip grouped to one readout channel, (3) the ratio of the width of the strip to the pitch, and (4) the fixed charge at the oxide-silicon interface. The latter is important because it tends to enrich the surface with majority carriers and reduce the resistance between strips. It is the major reason that some mechanism must be used to isolate the strips, and it is the reason why a sophisticated program like PISCES IIB must be used to calculate the charge distributions.

The Ikeda *et al.* calculations indicate that the interstrip capacitance is 30% larger for the p-channel isolation than it is for the field effect isolation, and that the p-channel devices are much more sensitive to the fixed charge. On the other hand, Micron Semiconductor has had good performance with p-channel isolation devices produced for OPAL. We are ordering prototypes of both isolation schemes for evaluation.

To obtain a budget for the metal-to-metal overlap capacitance, we first estimate the junction and interstrip components. The junction capacitance per unit area is the same as the junction capacitance on the p-side, and since the same area is being subdivided into the same number of readout channels, it has the same value, $C_J = 0.16 \cdot L(\text{cm})$ pf. This gives 2.72 pf for $L = 17$ cm. Our standard prototype uses field effect isolation for the n-strips. The measurements from the DELPHI prototypes are consistent with a value of 1.1pf/cm for our geometry. The total interstrip capacitance depends on the ratio of number of strips on the n-side to number on the p-side, the length of n strips and the capacitance per unit

length,

$$C_I = \frac{1700}{768} \cdot 3.84\text{cm} \cdot 1.10 = 9.35\text{pf}$$

This is smaller than the value on the p-side because the pitch is much larger. According to Ikeda *et al.*, we would expect a 30% larger number for p channel isolation. The sum of these numbers, 12pf, leaves a maximum of 18pf for the overlap capacitance. If the 12pf increases to 18pf due to radiation, the overlap capacitance must be less than 12pf to keep the total under 30pf.

The VTT devices tested by DELPHI had overlap regions between the strips of the "first metal" and the strips of the "second metal" of 5 μm by 18 μm separated by 1 μm of silicon dioxide with an ε_o of 4. If we treat the region like a parallel plate capacitor it results in C_m = 3.2 ff. (This can be reduced with thicker insulator and by using an insulation with small dielectric constant.) The total overlap capacitance is :

$$C_M = (N_n + N_p) \cdot C_m = 7.9\text{pf}$$

When DELPHI used this model they found that the estimate was small by a factor of three. No explanation for this factor of three is presently available, so to be conservative we wish to allow for this same effect. While 8 pf is usable, 24 pf will exceed the budget. This number can be reduced by using a thicker oxide.

Clearly the uncertainties are large and must be resolved by measurements. It seems likely that we can achieve an adequate signal/noise on both the n- and p-sides. The most important variable is the thickness of the oxide. We have asked the manufacturers to make devices with 2 microns of silicon oxide and up to 5 microns of polyimide. In the meantime we are measuring devices obtained from DELPHI.

7.3 Prototypes

Vendor Options

Double-sided silicon microstrip detectors are being planned or installed at nearly every major storage ring and collider experiment operating today, including OPAL, ALEPH, DELPHI, L3, and CLEO. As a result, there are at least 3 vendors (Hamamatsu, SI, and Micron) with experience in meeting the technological challenges that these devices pose.

We have made contact with the vendors and have been apprised of their production capabilities. Orders for prototypes will be placed with two of the three. Both vendors will be asked to make a mask which will provide 2 full-length Layer 1 detectors and 2 half-length Layer 2 detectors. The four detectors will have all the n- and p-side combinations of strip

pitch that interest us. Using these we can determine the pitches that are optimal for the production detectors with minimum investment in prototype masks.

Both of the Layer 1 and one of the Layer 2 detectors will have 50 μm pitch on the p-side. The remaining Layer 2 detector will have 25 μm pitch on its p-side, so that operation with intermediate sense strips which are not read out can be studied. Both of the Layer 2 detectors will have 111 μm pitch on their n-sides. Each of the Layer 1 detectors will have a different pitch on its n-side–83 and 166 μm. The other parameters of these prototypes will be as described in the first paragraph of this section.

Evaluation

A test bench has been set up for studies of the properties of these prototypes. The detectors will be mounted on custom-designed boards for operation with readout chips. The test facility includes an SRS/SDA system to operate the chips and digitize the data. The detectors will be exposed to beta-radiation provided by a Sr-90 source. A scintillator will provide the trigger, and there is an option for cutting on the beta energy and varying the impact angle of the radiation. Measurements will be made of the front-back charge correlation, n-side interstrip resistance, signal/noise for the p- and n-sides as a function of track angle, and cluster size and pulse height distributions. Capacitance measurements such as those which are already underway will be carried out as well. Following exposure to a gamma source the detectors will be re-examined for noise increase due to trapped charge in the oxide.

8 Front-End Design

In this section, we describe the current status of design and prototyping efforts for the front-end readout chips for SVX II. The goals for this effort are to produce a suitably radiation-hard chip with low noise and adequate gain bandwidth which can be used with the 132 ns bunch spacings expected in the late part of the decade with the Tevatron.

At present the design of the readout chip for SVX II has reached the prototype stage at both LBL and Fermilab. It is expected that the final chip will be a collaborative effort between the two groups. There is a memorandum of understanding which has been negotiated between the two laboratories and detailed discussions are currently in progress to define the exact activities of the two groups. Physicists from both CDF and D0 are responsible for agreeing on the detailed specifications of the readout chip. Below we summarize the present status of the design work by both groups. We begin with a brief summary of what is known about the expected occupancy in the SVX II detector based on the present SVX experience and from a Monte Carlo study.

8.1 Occupancy Study

We studied the expected occupancy for the proposed SVX II using the ISAJET Monte Carlo and a simple geometrical model. To check that this method would yield reliable results, we first used a similar model for the present SVX and compared the occupancy predicted by the Monte Carlo with that observed in our current data set. A "nearest neighbor" readout method as used for the real data sample was modelled for both the SVX and SVX II Monte Carlo samples. In this method, all hit channels over threshold are read out, along with the nearest physically adjacent channels. For the Monte Carlo samples, channels were considered to have been hit if they contained charge deposition greater than or equal to 0.15 times that expected for a minimum ionizing particle.

For the current SVX, the occupancy was determined by the combination of noise signals and true charged tracks. We refer to the occupancy due to true charged tracks as the "physics" occupancy. In the real data, when we demanded that there be at least one fully reconstructed track in the SVX, we observed a total occupancy of $\sim 6.7\%$. The occupancy observed when there were no tracks reconstructed in the SVX, on the other hand, was $\sim 5.7\%$. One can see that the physics occupancy is of order 1%, and that the total occupancy in the present SVX is dominated by noise signals.

To study Monte Carlo events in a physically interesting sample, we used an ISAJET model of $t\bar{t}$ production. Since the multiplicity of this Monte Carlo sample is approximately 3 times larger than the data sample used above, we expect a physics occupancy for the present SVX about 3 times larger also. In fact we observed in the model an occupancy of 2.6%, which is consistent with this expectation.

For the SVX II design, there are two features which will affect the occupancy. First,

the detector will be about a factor of two longer, which means that it will be sensitive to a larger number of charged tracks per event. This effect would tend to increase the observed occupancy. Second, however, there are 3 barrels rather than the present two, and each barrel will be subdivided electrically into two regions. This increases the number of read out regions to 6, which would tend to lower the occupancy by a greater factor. Using the same ISAJET $t\bar{t}$ Monte Carlo sample, we in fact observed an occupancy of only 1.3% overall with the SVX II geometry.

A breakdown of the expected occupancies for SVX II as determined from this study is shown in Table 20. Significant variations exist across the barrels, and across the layers of each barrel. As expected, the greatest occupancy will be for the center barrel at its innermost layer. Since the readout takes place on a wedge-by-wedge basis according to the present plan, layer-dependent variations will be less important to the front-end and DAQ system design than the overall numbers shown in the first column of the table. These estimates are for occupancy in the ϕ readout. For the z readout the physics occupancy will be higher due to the larger cluster size for angled tracks.

Table 20: Simulated SVX II occupancy broken down by barrel and layer.

Barrel	Overall Occupancy	Layer 0	Layer 1	Layer 2	Layer 3
±1	2.0%	3.7%	2.5%	1.9%	1.2%
±2	1.2%	2.2%	1.5%	1.1%	0.7%
±3	0.8%	1.5%	1.0%	0.7%	0.5%

8.2 LBL Chip Design

The LBL design for the SVX II readout chip will be fabricated in the UTMC radiation hardened 1.2 micron process. The principal features of the SVX II chip compared with the original SVX chip are as follows:

- Faster analog signal path - settling within 130 ns for the upgraded Tevatron.
- Continuous time analog signal path (no reset cycle necessary).
- Double sample capability (AC coupled detectors presumed).
- An analog pipeline of programmable depth (16 deep for up to 2 us of delay @ 130 ns).
- Only a single clock during acquisition (CMOS or balanced positive ECL).
- On-chip analog to digital conversion.
- Digitally programmable threshold for sparse readout.

- Complete digitization and readout option (no sparse).
- Faster all-digital sparse readout (>20 MHz).

For the LBL design prototype chips containing all of the critical function blocks of the SVX II chip have been designed and tested or are presently in fabrication (HP 1.2 micron). These include:

- A preamp prototype chip containing several variations, all with continuous time reset.
- A 16 deep analog pipeline prototype chip with double sample readout capability.
- A complete parallel analog to digital conversion sub-block prototype chip.
- A super-fast sparsifying readout prototype chip using a novel asynchronous method.

The preamp prototype chip has returned from fabrication. A summary of early test results is given in Table 21 below.

Table 21: Test results for a preliminary version of the LBL SVX II chip.

Source Cap.	Feedback	10-90% Rise	Gain	Noise
33pF	100fF	72 ns	11.5 mV/fC	2700 e
33pF	30fF	138 ns	35 mV/fC	1600 e
10pF	30fF	77 ns	31 mV/fC	1000 e

These measurements were taken at a supply voltage of 5 V, and a power consumption per channel of 1 mW. The figure for input noise is an approximation for a double sample with a period of 132 ns. More detailed measurements are in progress.

8.3 Fermilab Chip Design

The study of an advanced readout chip (ARC) for silicon strip detectors has also been continuing for some time at Fermilab. The work has included design and fabrication of numerous test chips containing subcircuits for a complete 128 channel readout device. The device being developed is designed to match the Fermilab colliding beam characteristics with beam crossing intervals between and 132 ns and 400 ns. The main features of the ARC are as follows:

- Operation at a high interaction rate.
- Low noise, power, and mass.

- Operation with double sided detectors.
- Pipelined storage for a level 1 trigger.
- On board, highly parallel and rapid digitization.
- Data sparsification.

The front-end design being pursued at Fermilab uses a high speed switched capacitor integrator and amplifier which is resettable within the constraints of the beam structure. A switched capacitor approach was used instead of a real time front-end to avoid problems associated with the tail of the signal pulse from earlier interactions affecting subsequent buckets. The design has an analog storage cell pipeline for each channel to provide the necessary buffer for the CDF level 1 trigger. After a level 1 trigger there is a separate low power ADC for each channel. This approach permits the use of a digitally set common threshold for data sparsification.

The chip does not overlap data acquisition and readout cycles, thereby avoiding digitization noise during data acquisition. Resetting the front end amplifier is done only during the long interval between super groups, not after each beam crossing, The design is being developed in two parts: (1) the integrator and amplifier design, and (2) the analog storage, ADC and data sparsification.

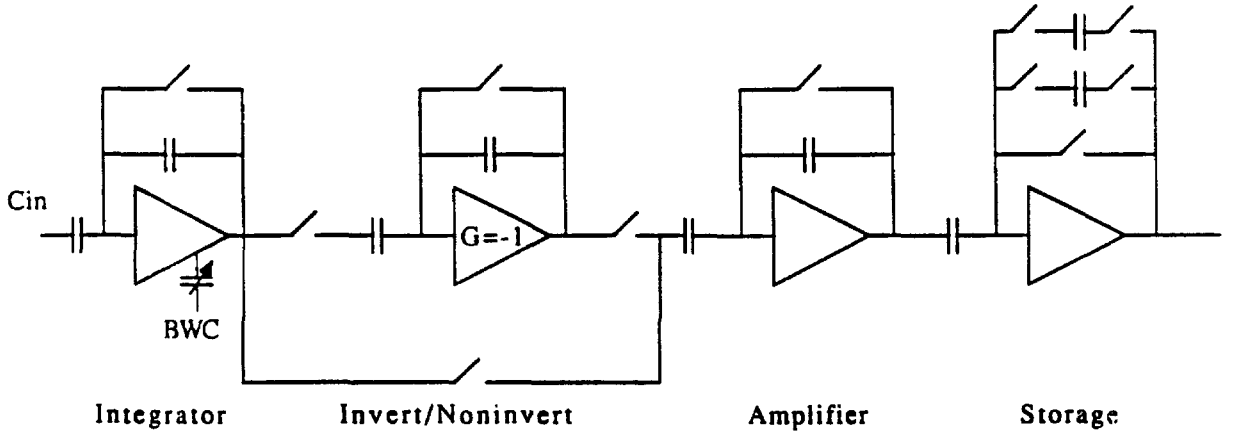

High Speed Switched Capacitor Front End block Diagram

Figure 51: Schematic of the SVX II front-end analog section.

A schematic of the most recent version of the front end integrator, amplifier and storage system is shown in Fig. 51. The integrator has a programmable gain bandwidth so that the signal to noise and risetime can be tuned to the beam crossing interval of either 132, 200

or 400 ns. This feature can also be used to tune individual chips to compensate for process variations in response time. The integrator is followed by an inverter so that the chip can be used with a bidirectional input. This is necessary for double sided detectors, since the signals from the two sides have opposite polarities. This prototype version had only a few storage cells.

The production version will require at least 16 cells, and preferably 24. The front-end power is approximately one milliwatt/channel. Because the integrator will only be reset during the intervals between super groups, the front-end integrator has a large dynamic range of ±400 fC. However, the amplifier preceeding the storage section is reset between every beam crossing, so that an appropriate double-correlated sample reflecting only the charge integrated for the desired beam crossing is stored in the successive analog storage cells.

Risetime measured at storage output for different switch combinations (BW settings) with: Cin = 10pf Qin = 10 fc.

	BW setting					
Trace	S1	S2	S3	S4	0-99%	10-90%
Top	0	0	1	0	108 ns	56ns
Center	1	0	0	1	182 ns	86ns
Lower	1	1	1	1	270 ns	128ns

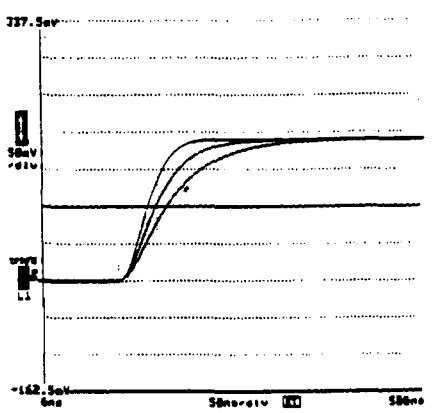

Figure 52: Risetime measured at the storage output for different integrator bandwidth settings with C_{in} =10 pf and Q_{in} =10 fC.

The risetime responses of the chip for input capacitances of 10 and 30 pf are shown in Figs. 52 and 53, respectively. Integrator/amplifier performance measurements for the various risetime and input capacitance settings are shown in Tables 22 and 23. All of these results are based on tested implementations in a 2 micron CMOS process through MOSIS.

Both prototype analog storage chips and ADC's have been produced and tested. They have now been combined into a single test prototype consisting of 8 parallel channels of analog pipeline four cells deep followed by an offset compensated comparator and ADC. A

Risetime measured at storage output for different switch combinations (BW settings) with: Cin = 30pf Qin = 10 fc.

Trace	BW setting S1	S2	S3	S4	0-99%	10-90%
Top	0	0	0	0	115 ns	61ns
Center	0	1	0	0	184 ns	88ns
Lower	0	1	1	0	294 ns	137ns

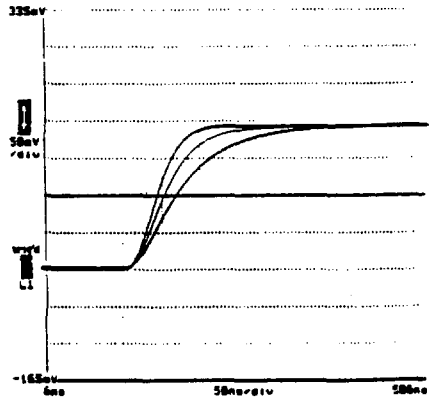

Figure 53: Risetime measured at the storage output for different integrator bandwidth settings with C_{in} =30 pf and Q_{in} =10 fC.

Table 22: Integrator plus amplifier performance for an input capacitance of 10 pf.

Integrator + Amplifier Performance

Cin	T sample	Pol	10-90%	Gain	Pattern	Noise
10p	400ns	+	129ns	19.0mv/fc	DCS	960e
10	200	+	86	18.8	DCS	1080e
10	150	+	56	18.9	DCS	1210e
10	400	-	132	18.3	DCS	1030
10	200	-	93	18.1	DCS	1130
10	150	-	64	18.3	DCS	1220
10	150	-	64	18.3	MDCS	1530

Table 23: Integrator plus amplifier performance for an input capacitance of 30 pf.

Integrator + Amplifier Performance

Cin	T sample	Pol	10-90%	Gain	Pattern	Noise
30p	400ns	+	137ns	19.1mv/fc	DCS	1720e
30	200	+	88	19.1	DCS	2050e
30	150	+	61	19.2	DCS	2220e
30	400	-	146	18.4	DCS	1730
30	200	-	95	18.3	DCS	1950
30	150	-	69	18.3	DCS	2180
30	150	-	69	18.3	MDCS	2330

Power (Integrator + Inverter + Amplifier)	1.17mw/ch
Integrator range	+ or - 300 fc
Linear output range	30 fc*

* Has been improved.

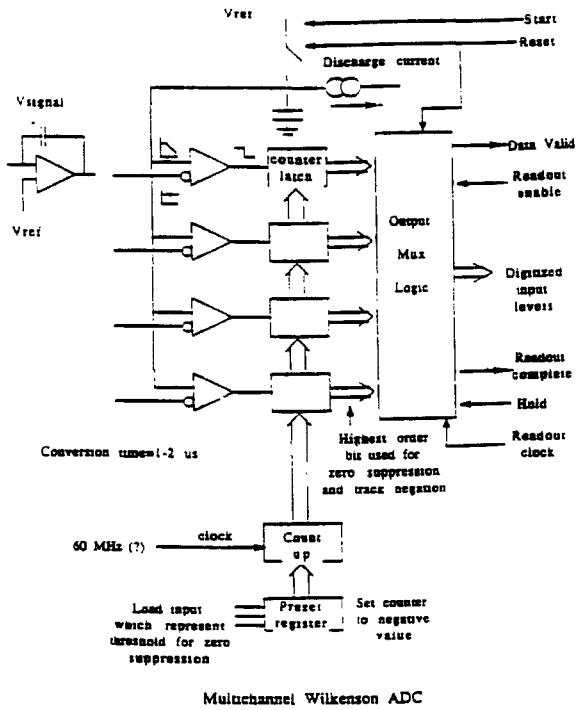

Figure 54: Schematic of the multichannel Wilkenson ADC to be used in the SVX II chip.

schematic of the ADC is shown in Fig. 54. The multi-channel ADC allows for the simultaneous digitization of many channels. A digitally applied threshold voltage is used for data sparsification. We plan for a 7-bit ADC with a digitization speed of $\leq 1.5\mu s$.

The initial test results on the analog storage/ADC performance are very encouraging. Variations in offset and gain for every cell of every channel on an eight channel device were checked. Maximum offset variation between cells on any given channel is less than 1.5 mV or 0.15 of the least significant bit (LSB). Maximum offset variation between any cells on two different channels is 4.0 mV or 0.4 LSB. Since the variation in offsets between all 24 cells is 4 mV or less, it is estimated that 4 mV is equal to $\pm 2\sigma$, which means that the RMS offset variation is about 1 mV or 0.1 LSB. The maximum gain difference between cells on a given channel was found to be 0.4 % or 0.4 LSB. The maximum gain difference between channels was found to be 0.5 % or 0.5 LSB. The cell and channel gain differences suggests that capacitors of the chip are matched to better than 0.5 %. The maximum gain variation between cells on two different channels is 0.8 % or 0.8 LSB.

The linearity of the combined analog storage and ADC was also very good. The maximum error over the seven bit range was found to be $\pm$ 3 mV or $\pm$ 0.3 LSB. It is interesting to note that placing the ADC converter on the chip with the integrator circuit should reduce the inherent gain variation due to integrator capacitor variations caused by process variations. Normally gain variations between runs of 20 % can be expected. Because of the capacitor matching measurements previously presented, effective gain variations could be reduced to

about 0.5 %.

9 Radiation Damage

The luminosity of the Main Injector presents serious requirements for the radiation hardness of the detectors, the electronics, and the materials used in the design. All components and materials in the final design will be tested for radiation damage at doses above those expected.

The design luminosity for the Main Injector is 5 to 6 $\times 10^{31}$ $cm^{-2} \cdot s^{-1}$ giving 600 pb^{-1} for a data run of 10^7 seconds at full luminosity. Our plan is to design for a total integrated luminosity of 2 fb^{-1}. Based on studies and experience with SVX we estimate that this corresponds to a dose of 1.0 Mrad at the inner radius of the detector, and 0.2 Mrad at the outer radius. This agrees to within a factor of two with the estimates of Ellison [30] of 0.25 Krad/pb^{-1} at 2cm from the beam. These doses correspond to a particle flux of 4×10^{13} particles/cm^2/fb^{-1}.

The components at greatest risk are the electronics and the silicon strip detectors.

Electronics

The front-end data acquisition ASIC must be manufactured in a radiation hard process. We plan to use the same UTMC foundry used to manufacture the SVXH chip. The major problems generated by radiation damage in MOS circuitry are due to threshold shifts and increased noise in the analog signals. The SVXH chip was tested at Berkeley up to 2 Mrads with a Co60 source. The threshold shifts were less than 0.1 volts and the noise increased by less than 20%. These measurements are in agreement with those on a previous version and we feel confident that the new electronics will be hard enough to last through a 2 fb^{-1} exposure.

Silicon Strip Detectors

Detectors suffer damage from both ionizing radiation and nuclear reactions. The ionizing radiation generates charge and traps in the surface in much the same way that it does in MOS circuitry. This affects the surface leakage currents and increases the capacitance between the strips. Studies by a Hammamatsu-Nagoya collaboration [31] and by U.C.Santa Cruz [32] with Hammamatsu detectors show that the effect of ionizing radiation on the p-side can be reduced by minimizing the ratio of strip width to strip pitch (w/p). They find a 30% increase in the capacitance after a dose of 500Krad for w/p=0.4 but the increase extrapolates to zero at w/p=0.2. On the other hand measurements by Masciocchi *et. al.* [33] on an unbiased detector which was a prototype in the *RD20* program for *LHC* show a uniform increase of about 30% after 1MRad. These disagreements indicate that we must carefully evaluate the products of each vendor.

There is less information about the n-side and the effects of radiation depend upon the type of isolation used. U.C.Santa Cruz has measured devices with p-implant isolation [32] and find that both the capacitance and the change of capacitance with a dose of 2MRad is minimized by using wide implants. Their best result was with a 24 micron p-implant and a 50 micron pitch which showed no measurable increase in the capacitance after a dose of 2MRad. However the capacitance was 1.6 pf/cm, substantially larger than that on the p-side. There is no published data for double sided devices using field effect isolation on the ohmic side but calculations by Ikeda [29] indicate that, if the oxide is 'rad-soft', the interstrip capacitance may increase by 50% at doses of about 1 Mrad. This would have a significant effect on the signal to noise ratio and needs to be verified experimentally.

Nuclear interactions are a potentially more serious problem. They cause both increased leakage current and, eventually, type inversion. There have been many studies of the increase of leakage current as a function of neutron dose but it is difficult to know how to translate these numbers to the collider enviroment. The increase in leakage current has been measured by CDF to be 0.14 na/Krad/cm for doses up to 15Krad and, again, this agrees to within a factor of two with the estimates of Ellison [30] based on the damage coefficients measured at Los Almos [32]. Since the CDF measurement was made on the beam pipe of the Tevatron collider, it has the right mixture of particles. If this effect is linear, it implies the leakage currents will increase to 2.4 microamperes at a dose of 1 Mrad. Assuming an integration time of 132ns, the shot noise will be $\sim$ 1,100 electrons. This will begin to compete with the Nyquist noise associated with the detector but should be tolerable.

10 Data Acquisition System

The SVX II DAQ is designed to be compatible with the upgraded CDF trigger and DAQ planned for Run II [34], and to be capable of working with eventual higher-speed upgrades which could be proposed. For Run II, the trigger system is intended to handle up to 5kHz of level 1 accepts into the level 2 trigger. Since the SVX II is designed to digitize and readout in response to a level 1 accept in $\leq 5\ \mu$s, it is compatible with this requirement. The high speed of the SVX II readout is also required for compatibility with a level 2 displaced-track trigger processor (SVT) discussed in the next section.

Two options are under study for the data acquisition system for the SVX II Stage 1 detector. Both options make extensive use of fiber optics to reduce electromagnetic interference and to speed the readout of the data for use by the level 2 trigger processor. The intention is to develop a DAQ including the front-end chip which is common as far as possible to both CDF and D0.

The first option, which we call the "direct fiber" option, is designed to replace as much as possible of the present SVX port-card system. The digitized sparse data from each 128 channel front-end chip would be read out serially on a single dedicated optical fiber connected directly to a low power LED driver. These drivers would be located either on the detector ladder hybrids immediately adjacent to the front-end ICs, or at the periphery of the detector bulkheads. The system would be highly parallel in that a separate data return optic driver and fiber would be provided for each front end IC. Fourteen bits of information would be transferred serially over each data return fiber: 7 bits for the channel address and 7 bits for the ADC. The bits in this design are clocked off the chip at a rate of 53 MHz using the accelerator clock. Trigger and control signals would be transferred over a single fiber connected to clusters of chips (4-10) also located at either the ladder hybrids or at the periphery of the detector bulkheads. The trigger and control signals as well as the data return fibers are self clocking using a technique known as pulse width modulation (see below).

The second option, called the "HDI-portcard" option, follows the portcard system of the present SVX but replaces the cables from the portcard to the trigger room with parallel high-speed optical links. Each portcard would control all 28 front-end ICs in a single wedge, so there would be a total of 72 port cards in the system. A high-density copper interconnect (HDI) between the portcard and the local cluster of ICs would permit the local cluster to return data at a rate of 7 bits of channel address and 7 bits of data every 18 ns, for a total 53 MHz rate. The sparse data from each chip in the cluster would be presented to the interconnect bus sequentially. At the portcard, the 14 parallel bits of address and data would be sent over a set of 8 low power optical fibers at a 106 MHz rate to the trigger room. In the other direction, trigger, clock, and control information would be sent to each portcard using two fibers, one for trigger and control and one for clock. The port-card would decode this serial information and send it on to the front-end ICs over the hybrid interconnect.

The principal differences between these two options are in the interface with the front end ICs. The rest of the DAQ system is largely common to both approaches. Below we

discuss the two different front end interfaces separately.

10.1 Direct Fiber Option

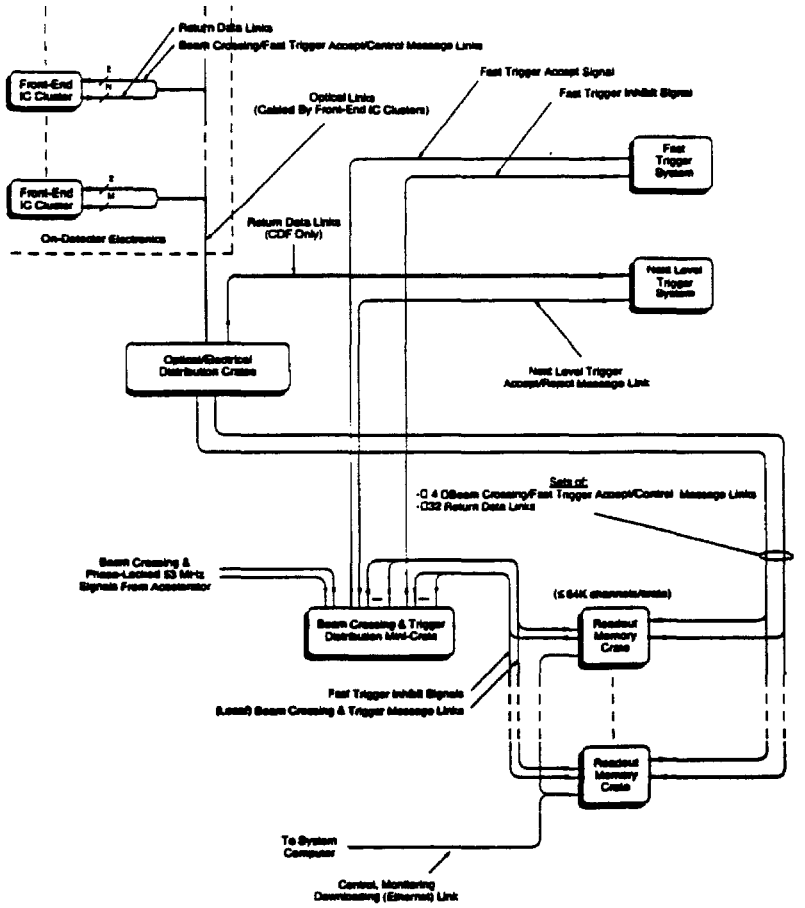

CDF & D0 Silicon Strip Upgrade
IC Cluster, Serial Readout Implementation
System Block Diagram
Version 3.0

Figure 55: Single front-end low-power optics readout implementation.

The system block diagram for the implementation of this option is shown in Fig. 55. Major blocks in this figure will be briefly described below.

Front-End IC Clusters

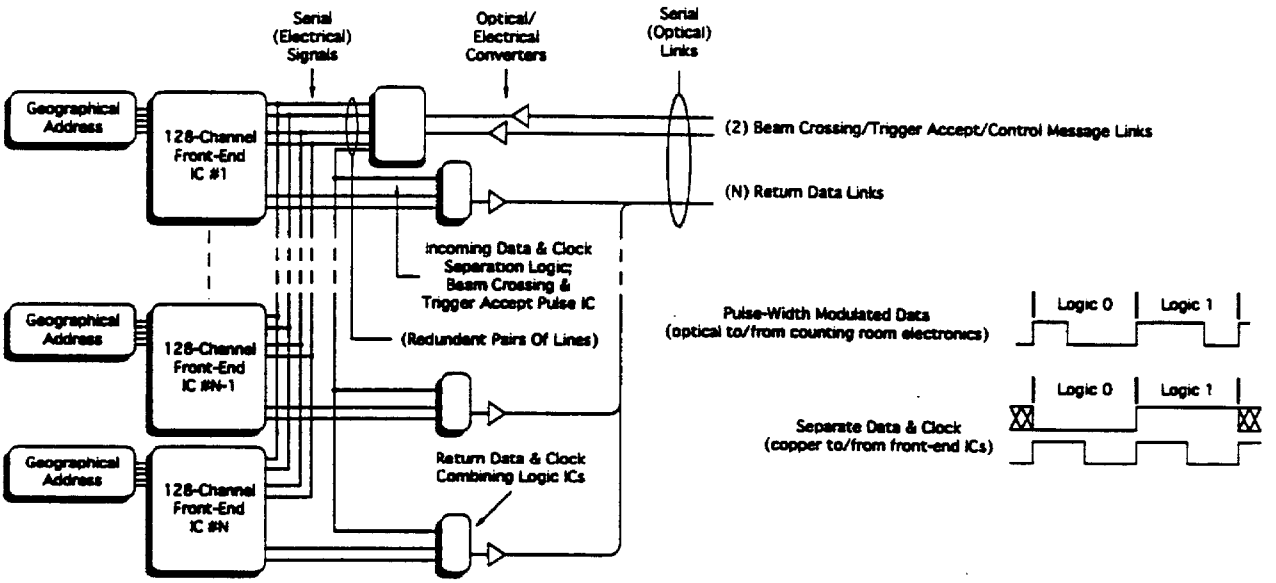

Figure 56: Low-power optics interface to IC cluster with N ICs.

Front-end IC clusters are logical groups of 128-channel silicon strip ICs, optical to electrical and electrical to optical converters, and minimal other logic needed to control, monitor, download the ICs as well as read data from the ICs. For each of the 72 wedges there are a total of 15 ϕ-data 128-channel ICs and 13 z-data ICs. This topology leads to either two, four or eight clusters per wedge. For example, in the four cluster per wedge configuration corresponding to one cluster per layer, the first (outer) cluster has 6 ϕ and 4 z ICs, the second cluster has 4 ϕ and 4 z ICs, the third cluster has 3 ϕ and 3 z ICs, and the fourth (inner) cluster has 2 ϕ and 2 z ICs.

The first or top IC cluster and the second or lower IC cluster shown in Fig. 55 contain N and M 128-channel ICs respectively. The pair of fast trigger accept/control lines entering each IC cluster are each used both to send fast trigger accept signals from level 1 and to download data and control information to the ICs. One of these lines is used for redundancy, in case of component failure in the first line. The N–IC cluster has N return data lines, one per 128-channel IC and the M–IC cluster has M return data lines, again one per IC. A schematic of the optical links to an N-channel cluster is shown in Fig. 56.

Figure 57 illustrates one method for encoding the various messages including beam crossings and performing simultaneous resets to all 128-channel front-end ICs within a cluster. Front-end ICs are responsible for decoding beam crossing messages, fast trigger accept messages and command messages. Although 16 bits of data are shown, data can vary in size with each command. The front-end IC must also decode one or two broadcast addresses as

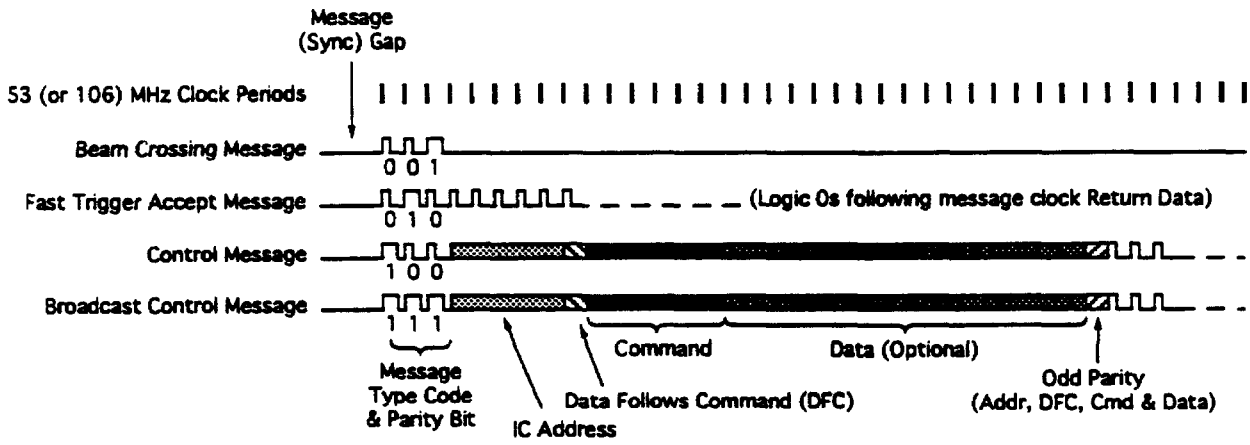

Figure 57: Message encoding

well as its own address.

In the data-taking (analog acquisition) mode, signals are present on the the fast trigger accept/control links when beam crossing messages are received. Signals are also present during the time between the receipt of fast trigger accept messages and a time shortly after the level 2 accept/reject message. These signals are always transmitted during the time that the front-end circuits are in the non-data-taking mode. This eliminates digital noise from incoming signals in the analog portions of the front-end chips.

Optical/Electrical Distribution Chassis

The optical/electrical distribution chassis serve the purpose of providing an easily-maintained, modular location to house the optical links which connect the front-end ICs to counting-house electronics. All conversions of links from differential copper to optical and optical to differential copper are performed in these chassis. Fast trigger accept/control signals to the front-end IC clusters are duplicated as necessary in these chassis. In the CDF system, these chassis also fan out return data links to the SVT and other portions of the level 2 trigger system.

Fast Trigger System (Level 1)

The silicon strip readout electronics interface to the level 1 trigger by accepting (and if necessary inhibiting) fast trigger accept messages. Fast trigger accept messages are fanned

out to readout memory crates via the Beam crossing & Trigger distribution crate. When any readout memory module is nearly full, it asserts a local fast trigger inhibit signal, which is passed through the system. Care must be taken to insure that the readout memory module asserting its local fast trigger inhibit signal has enough memory to continue taking data until triggers are actually inhibited, and that no further data are being transmitted to the module.

Level 2

A similar control system is used in level 2. Messages are used to either read out event data stored in readout memory modules (accepts) or to clear out event data memory from rejected events (rejects). In the CDF system, ϕ data are transmitted to the level 2 trigger system.

Readout Memory Crates

The readout memory crates house modules which are used to hold event fragment data from the 128-channel silicon-strip detector ICs. These modules are also used to transmit fast trigger accept and control messages. In addition to the readout memory modules, these crates each house a module used to accept or inhibit fast trigger signals from the level 1 system. The readout memory crates also contain a VME-bus CPU module used to interface the crates with the rest of the data acquisition system.

10.2 High-Density Interconnect Portcard Option

This is the second option which is being investigated for the SVX II DAQ. Since it has many features in common with the system described above, we only describe the features which are different. Figure 58 shows the block diagram for this option.

Interface To 128-Channel Front-End ICs

Figure 59 illustrates the interface between the port card and front-end 128-channel IC cluster. This interface is divided into two physical media: the port card readout bus, and the High Density Interconnect (HDI) bus. The HDI has yet to be designed in detail.

The bus interface between the ICs and the port card implements the following signals: bidirectional data bus, read/write signal, protocol handshake signals, beam crossing clock, digital readout clock, fast trigger signal, etc. The ICs handled by a port card are divided in clusters as determined by the silicon planes. It is anticipated that buffering will be required to isolate the capacitive loading provided by a cluster of ICs (assuming that the driving capacitive of the front-end ICs is limited).

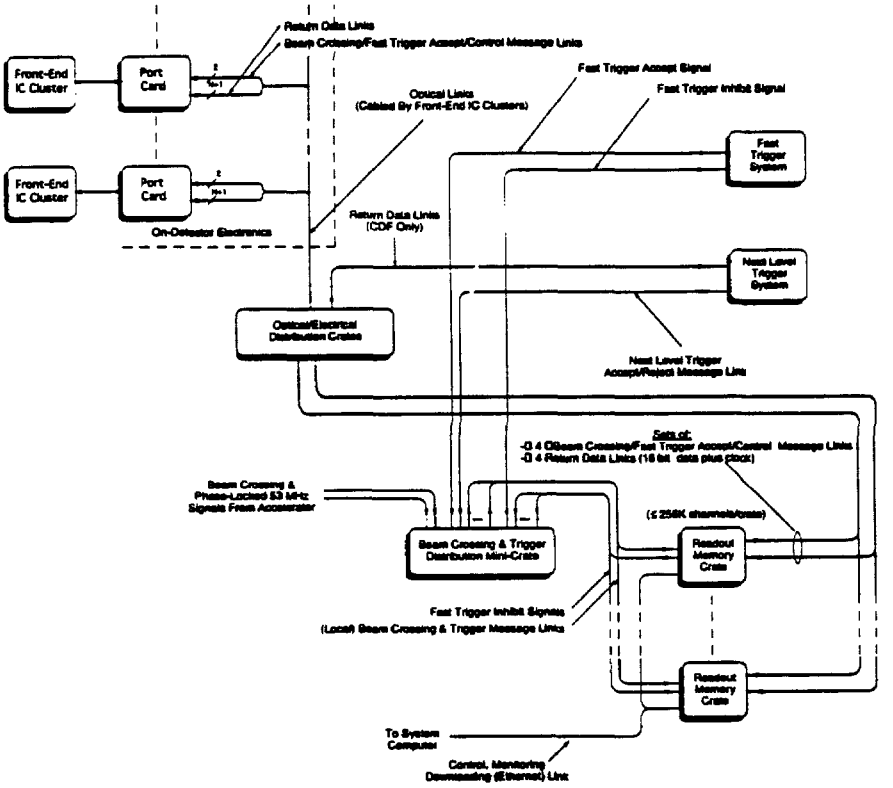

CDF & DO Silicon Strip Upgrade
IC Cluster, Port Card Readout Implementation
System Block Diagram
September 25, 1992

Figure 58: CDF Upgrade Port Card Implementation

There are two scenarios that need to be addressed. In the first case, buffering is performed at the hybrid and a single readout port card bus (cable) is used. This scheme requires the implementation of separate buffer enable signals, or that decoding be implemented at the hybrid. The second case moves the buffers to the port card, but multiple cables have to be implemented. For this description we will use the second option with two cables.

High-Density Interconnect Readout Bus

The HDI holds a number of front-end ICs which are wire bonded to the silicon strips and to the HDI bus and connected to the port card readout bus. The signals mentioned in the previous section are implemented on the HDI. In addition the HDI provides power, ground and geographical addressing for the front-end ICs. The number of geographical addresses

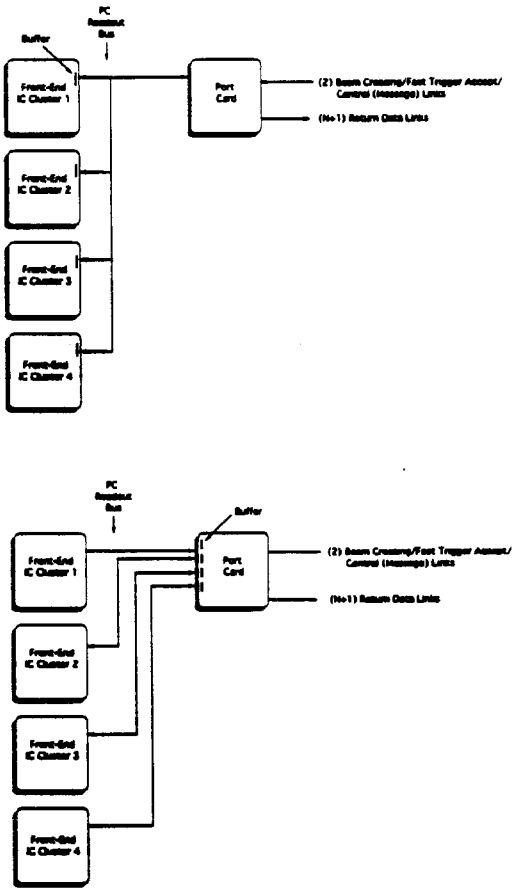

Figure 59: Port Card and Front-End IC Interface

will depend on the clustering and buffering implemented, for the system considered it will be between 3 and 4 lines.

Port Card

The port card is a centralized controller that handles a cluster of front-end ICs under the command of the readout system. This device implements two bidirectional ports, one to communicate with the readout system and the other to communicate with the front-end ICs. Note that the port card provides the protocol conversion between the readout system and the front-end ICs. The port card uses the fast trigger/control link to receive control, fast trigger and beam crossing messages. The control messages are intended for initialization of the front-end ICs. The beam crossing messages are used to generate the accelerator beam crossing signal given the 53 MHz accelerator clock.

During the initialization phase the port card receives commands from the system to

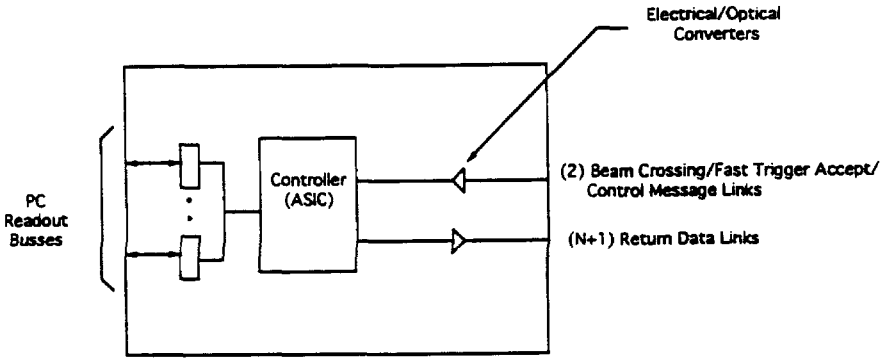

Figure 60: Port Card Block Diagram

control and download the front-end ICs. During data acquisition it receives trigger and beam crossing messages. Upon the arrival of a fast trigger message the controller requests the digitization of an event and when digitization is completed it reads out the digitized data and transmits simultaneously to the readout system. Note that for CDF the controller on the port card should be programmable to the level that the user can specify the readout order of the front-end ICs, allowing the implementation of a priority scheme. The implementation presented here assumes that the return data link is made of eight 106 Mbit/sec links (i.e. 106 Mbytes/sec). Figure 60 shows a block diagram of the port card.

Port Card Communication Ports

The port card implements two unidirectional communication ports to form a duplex communication scheme with the readout memory module. Both of the ports are synchronous to the 53 MHz system clock. The first port is the incoming data which is implemented in one serial data line. Messages received by the port card are encoded serially on this line using the protocol shown in Fig. 57.

The outgoing data port is one byte wide to support the readout rates imposed by the Next Level Trigger System. For this application the digitized data and channel ID uses 14 bits. Then the channel information is transmitted in two consecutive transfers with the two upper bits used to specify the data being transmitted.

11 Triggers

11.1 B Triggers

The inclusive b cross section at the Tevatron collider is $\sim 60\mu$b resulting in the production of $\sim 6 \times 10^{10}$ B's in a 1 fb^{-1} run. Although this cross section is large, an important goal of the Tevatron physics program is to search for B physics processes that represent only a tiny fraction of the total B yield. Triggering must select B candidates from the $\sim$ 1000 times larger total inelastic trigger cross section for CDF, while maintaining a high efficiency for the most interesting B events. CDF B triggers will typically require combinations of high p_T leptons and in some cases evidence for a separated vertex in the event. The trigger thresholds discussed here are somewhat speculative, but appropriate in light of the rate of improvement in DAQ and trigger technology.

At this time the exact capabilities and details of these upgrades, especially for muons, remain to be defined. At the trigger level the p_T threshold limitation is set by the desire to limit the Level 1 + Level 2 deadtime to $\leq 5\%$. In the absence of Level 1/Level 2 pipelines, a Level 2 decision time of 10 μsec limits the Level 1 accept rate to $\leq$ 5 KHz. Even with this restriction, trigger studies indicate that it should be possible for CDF to run a Level 1 dimuon trigger with $p_T(\mu)$ thresholds of $\sim$ 2 GeV and Level 1 dielectron trigger with $p_T(e)$ thresholds of $\sim$ 3 GeV at luminosities of 5×10^{31} cm^{-2}sec^{-1}. Level 1 single lepton trigger thresholds should be possible with $p_T(e/\mu)$ of $\sim$ 7 GeV, and with the inclusion of Level 1/Level 2 pipelines Level 1 single lepton thresholds could possibly be reduced to $p_T(e/\mu)$ of $\sim$ 4 GeV.

The CDF trigger options will provide efficient triggers for a large number of important B physics studies including rare B decays (for example $B \to l^+l^-$ and $B \to l^+l^-s$), production of B_c (studied through decays including: $B_c \to J/\psi\pi^+$, $B_c \to J/\psi l^+\nu$, $B_c \to J/\psi D_s$ [with $J/\psi \to l^+l^-$]), as well as all studies requiring a B tag (for example $b\bar{b} \to (B \to l\nu X)(B_s)$ and $b\bar{b} \to (B \to l\nu X)(B_d \to J/\psi K_s)$). The 2 GeV dimuon trigger has an efficiency of 15-20% for $B \to J/\psi$ decays, and future secondary vertex triggers for 2-body B decays (for example $B^0 \to \pi^+\pi^-$) are estimated to have an efficiency of $\sim$ 6%. The single lepton trigger, with $p_T \geq 4$ GeV, is estimated to have a B efficiency of $\sim$ 0.5%; this includes the 0.22 branching fraction of $b \to e/\mu$. With these efficiencies, CDF will obtain substantial B physics data samples from a 1 fb^{-1} run. As an example, the number of triggered and reconstructed events expected for the production of B_c in the channel $B_c \to J/\psi(\to \mu^+\mu^-)\pi^+$ is $\sim$ 500 assuming B_c production is $\sim 10^{-3}$ of the b cross section, and the $B_c \to J/\psi(\to \mu^+\mu^-)\pi^+$ branching fraction of $\sim 10^{-4}$.

For non-J/ψ modes, triggers based on secondary vertices will be increasingly important. The capability of using impact parameter information obtained from the vertex detector at the trigger level will be of fundamental importance for any experimental program centered on b physics in a hadron collider environment. Some of the decay channels that are interesting for the study of CP violation will be virtually undetectable at the Tevatron without an

impact parameter trigger (e.g. $B \rightarrow \pi\pi$). Other interesting decay modes (e.g. $B \rightarrow \psi K_s$) can be selected by the requirement of one or two leptons in the final state but will also benefit from an impact parameter trigger in terms of a better rejection factor against background and higher statistics on tape.

11.2 Secondary Vertex Trigger

The Silicon Vertex Tracker (SVT) is a secondary vertex trigger processor based on associative memories under development by the Pisa group in CDF. [1] It is designed to reconstruct tracks in the Silicon Vertex Detector (SVX) and Central Tracking Chamber (CTC) with enough speed and accuracy to be used at trigger level 2 to select events containing secondary vertices from b decay. Simulations have shown that the proposed tracker is effective and the performance is adequate for operating with CDF at luminosities up to 5×10^{31}. Prototypes of critical hardware components have been successfully tested and we are now ready to begin construction of a system that will be operational during Collider Run II.

The typical use of SVT will be in coincidence with some other L2 trigger. For example we would ask for a single muon above some Pt threshold and an impact parameter d significantly different from zero. The impact parameter cut will improve the rejection factor against background and will therefore allow us to lower the Pt threshold and improve the efficiency while keeping the L2 rate at an acceptable level.

To estimate the trigger efficiency for the process $b \rightarrow \mu + X$ we used an ISAJET event sample where b quarks were generated with no p_T threshold (fully inclusive sample). The muon trigger rates as a function of p_T threshold were obtained from CDF note 1467. The probability of getting a fake impact parameter was obtained from a simulation of the SVT algorithm applied to an event sample generated by ISAJET and assuming a 5% occupancy in the SVX generated by noise. The results are summarized in Table 24 for an 80 nb cross section. Comparing the b signal cross sections for an impact parameter cut at the trigger level to that for an offline cut, we see that the SVT provides a gain of an order of magnitude.

The primary challenges for an impact parameter trigger are fast pattern recognition in high multiplicity events and high accuracy track fitting. The strategy we choose to follow to tackle this problem is based on the combined use of the Associative Memory (AM) technique together with a farm of Digital Signal Processors (DSPs) [35].

The overall architecture of SVT is shown in Figure 61. Digitization is performed in parallel for all channels (front-end chips include one ADC per strip. Sparsified digital data are sent to Hit Finders over 72 parallel lines (24 lines per barrel). The task of Hit Finders is to find pulse height clusters and compute the coordinate of the centroid of each cluster. Hit coordinates from Hit Finders and tracks from the CTC track finder, are fed both into the Associative Memory and Event Buffer. The task of the Associative Memory is to perform the first stage of the pattern recognition process: it reconstructs tracks with a limited spatial resolution, using 250 μm bins in SVX layers. These coarse resolution track candidates are

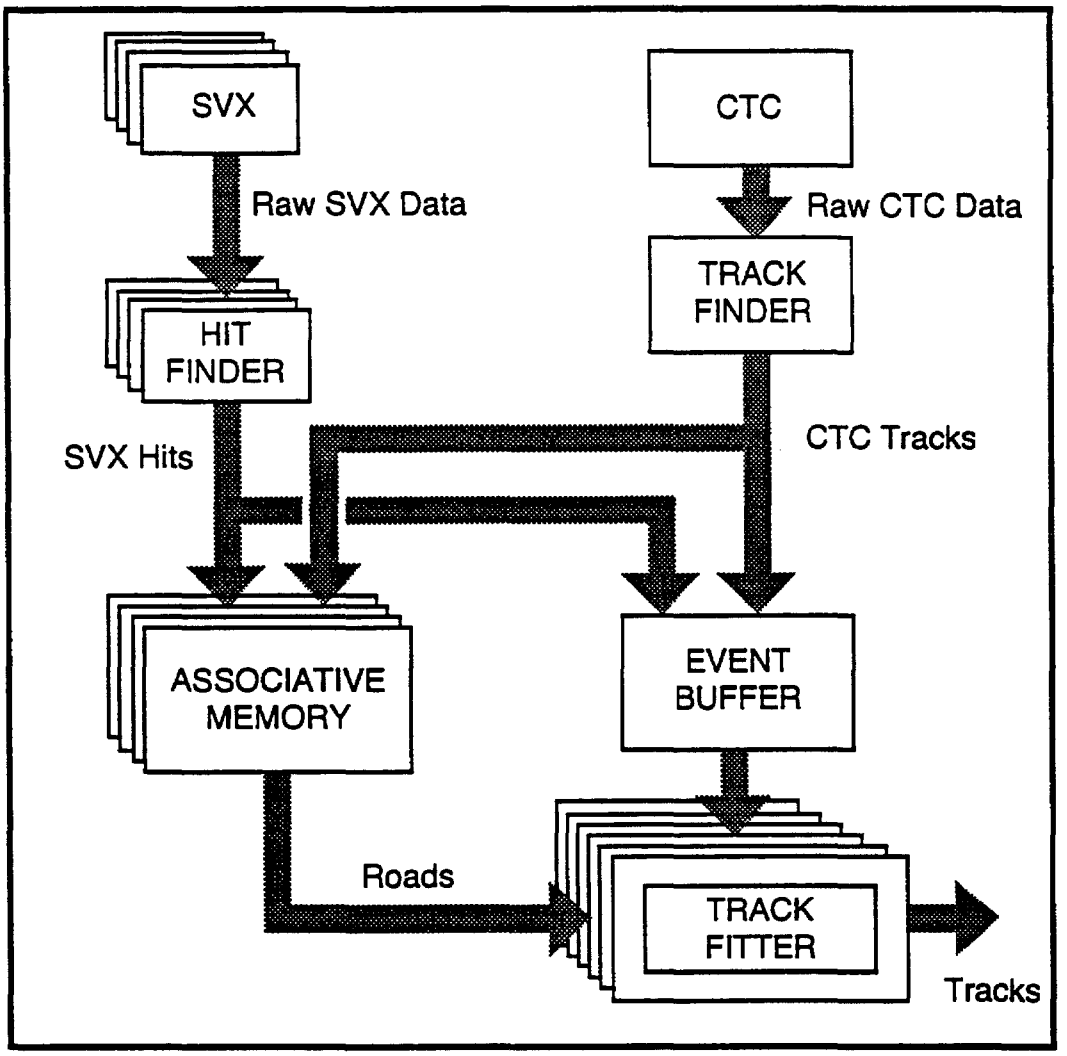

Figure 61: Conceptual design of the silicon vertex tracker (SVT). It is designed to reconstruct tracks in the Silicon Vertex Detector (SVX) and Central Tracking Chamber (CTC) with enough speed and accuracy to be used at trigger level 2 to select events containing secondary vertices from b decay.

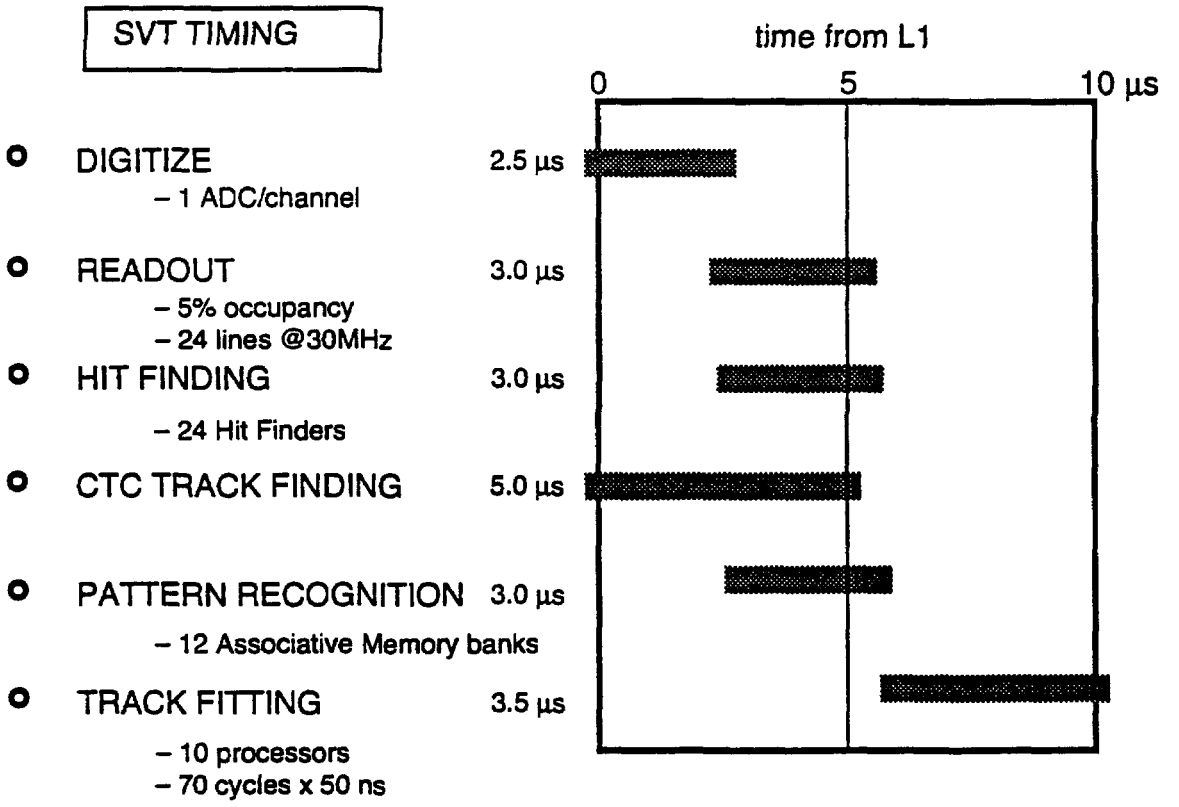

Figure 62: The overall timing of SVT for the average event.

Table 24: The first row shows the cross sections for a muon with p_T greater than 3 GeV/c and impact parameter greater than 100 um. The second row shows the cross sections for a muon with p_T greater than 6 GeV and no impact parameter information. The third row shows the cross sections we are left with if we take the cross section in the second row (without SVT) and apply an "offline" cut of 100 μm on the impact parameter of the muon. The first column (All) is the cross section for signal plus background. The second column ($b \rightarrow \mu X$) is the cross section for signal only.

	All	$b \rightarrow \mu + X$
SVT: $p_T > 3$ GeV, D> 100μm	80 nb	75 nb
no SVT: $p_T > 6$ GeV	80 nb	21 nb
no SVT: $p_T > 6$ GeV, D> 100μm offline	10 nb	6 nb

named roads, and are transmitted from the Associative Memory to a farm of processors (Track Fitters) where the track finding process is refined up to the full spatial resolution of SVX ($\sim$ 15 μm). Each processor in the farm receives one road from the Associative Memory, retrieves full resolution hits from the Event Memory and reconstructs one or more tracks within that road. All the processors in the farm do their work in parallel, each processor on a different road. The number of processors is large enough so that each processor has only one road to solve in the majority of events. Every time a processor finds a track it performs a geometrical fit and computes track parameters (impact parameter, momentum, ϕ). The expected accuracy of the track parameters from the SVT is:

$$\sigma_D = 35\mu\text{m} \ @ \ p_T = 2 \text{ GeV/c}$$

$$\sigma_\phi = 1 \text{ mrad} \ @ \ p_T = 2 \text{ GeV/c}$$

$$\sigma_{p_t} = 0.3\% \ p_T \ (\text{GeV/c})$$

Figure 62 shows the overall timing of SVT for the average event. Time is counted in microseconds from Level 1 Accept and is shown at the top. As can be seen from this diagram, SVT operation is finished in 10μs . Readout, Hit Finding and Associative Memory feeding overlap in time because they are pipelined.

12 Project Schedule, Cost and Manpower Needs

The schedule for the SVX II project is shown in Fig. 63. The design and R&D work will continue through 1993 on each subsystem , with final design decisions being made early in 1994. The construction process, including testing of delivered components and sub-assemblies is expected to take one and a half to two years. This schedule is based on our experience in building the SVX and SVX′ detectors. While SVX II is a significantly larger device with more readout channels and a more complex design, we believe that we can gain in efficiency from our experience, and that with adequate resources the detector can be ready for installation in January 1996. The level of M&S (materials and services) funding, and the manpower requirements are estimated in Table 25 and Fig. 64.

Detectors

We will continue to test the existing detector designs using double-metal readout (DELPHI detectors are already in hand) and kapton-metal readout (using detectors of Opal's design), and to compare the measurement of these detectors to our calculations of detector capacitance for different strip layouts. We will pursue our own prototype detectors with two different manufacturers, and study the capacitance, leakage current, resolution performace, and finally radiation hardness of these prototypes. Initial resolution studies will use a radioactive source or laser, but more complete measurements may require a test beam run.

A final decision on the strip design will be made in fall 1993, and the production detectors ordered early in FY94.

Mechanical–Ladders, Electrical Bonding, and Bulkheads

We are presently pursuing different materials and styles for ladder construction. The mechanical and thermal properties of our initial prototype designs are presently being measured. We expect to pursue two or three designs for some time before a final decision. We are studying alternative schemes for the electrical connection between detectors and between the detectors and the readout chips, including wire-bonding, flip-chip and tab bonding. The initial test structures will provide experience wire-bonding the double-sided ladders.

Candidate materials for the bulkhead include carbon fiber composites and beryllium. The bulkhead design will incorporate the cooling channels in the structure. Test structures will be built for cooling tests, incorporating realistic heat loads.

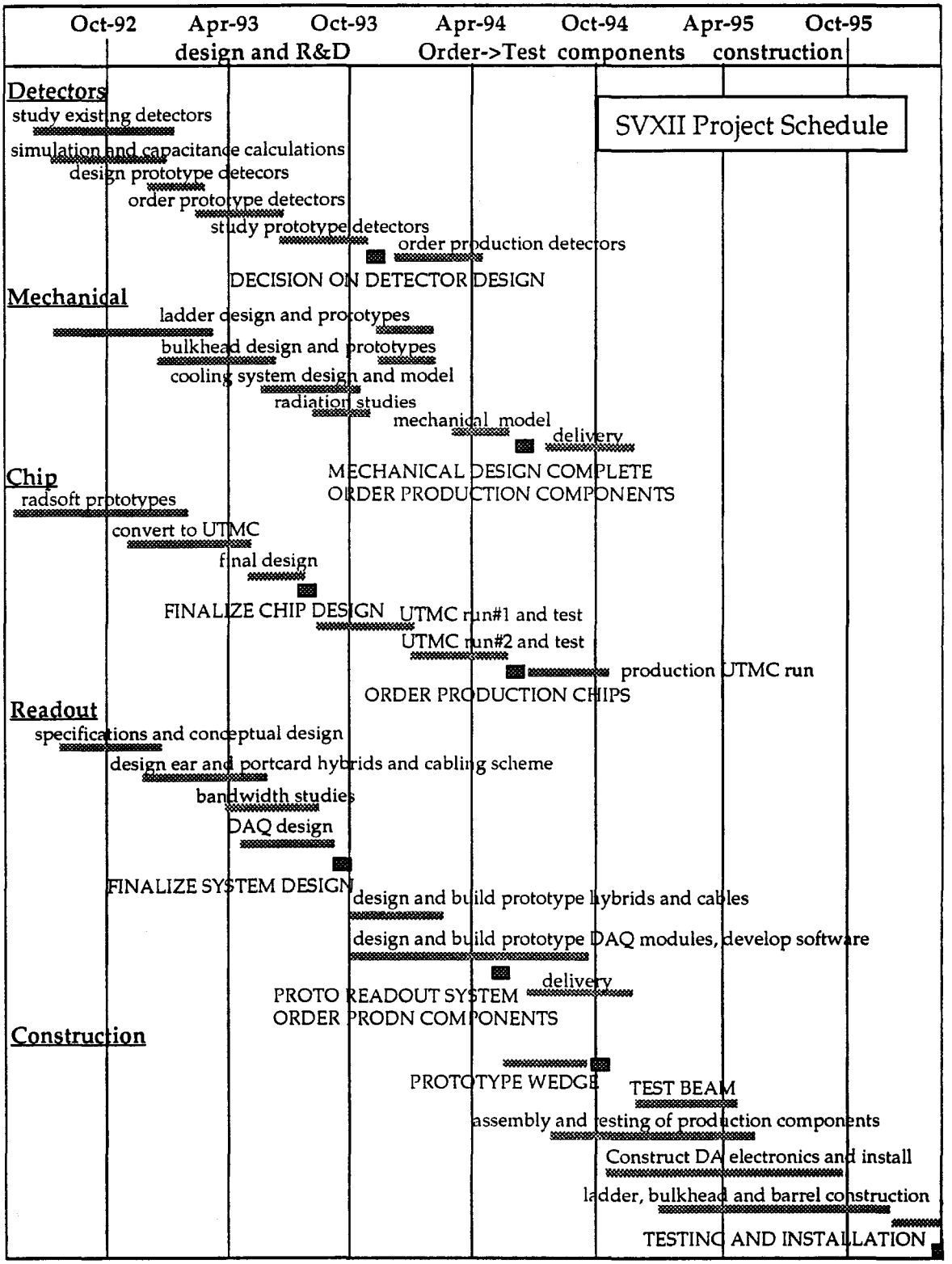

Figure 63: Schedule for the SVX II Stage 1 Project

The strength, thermal properties, and radiation hardness of all the materials to be used in the final design will be measured.

Table 25: M&S Cost Estimate for SVX II barrels

Fiscal Year	FY93	FY94	FY95	FY96
Dominant M&S Type	R&D	EQ	EQ	EQ
Detectors	170	1500	0	0
Ladders: structural and electrical	45	150	0	0
Bulkheads	30	150	0	0
Beam pipe	0	0	200	0
Chips	0	100	0	0
Hybrid/ear on the ladder	20	250	0	0
Hybrid/portcard - readout branch	15	100	0	0
DAQ System	40	630	0	0
Power Supplies	20	160	0	0
Cables/optical fibers	20	80	0	0
Fixtures	0	50	50	0
Total per FY	360	3170	250	0
Total				3780

Chip

Design and testing of prototype components - the front-end amplifier, analog pipeline and ADC - will continue at LBL and FNAL. Complete chips will then be fabricated in non-rad-hard technology and characterised. The design will be converted to a rad-hard process, and further developed if necessary. The schedule shown allows for three runs of the rad-hard process in total. While the initial runs may require some modifications before the final production, it is hoped that they will be suitable for use in constructing working prototype ladders.

Readout-hybrids, Cables, and DAQ

We are designing the front-end electronics on hybrids which are bonded onto the detector surface. The packaging of the detectors, the electronics, the on-board hybrid and the bulkhead and cooling channel is then rather complex and will require significant engineering. We expect to make several simple test structures before building realistic models. We will use live detectors and realistic heat loads (but probably using the present SVX chips) to build prototypes before committing to a final design.

There will be a readout cable branch per wedge, running at 53 MHz. We are investigating

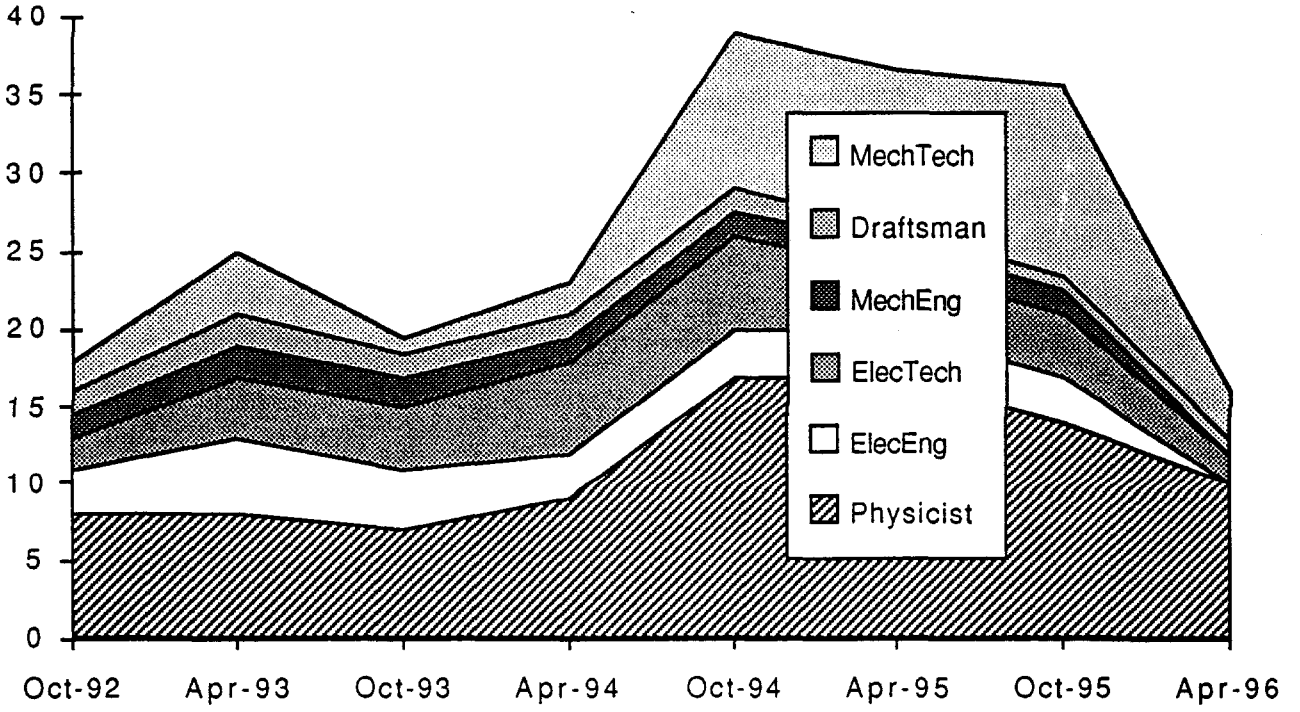

Figure 64: Mechanical technician, mechanical engineer, electronics technician, electronics engineer, and physicist full-time-equivalents needed.

the use of optical connections, and both optical and metal cabling schemes will be pursued initially. We will construct a realistic model of our design, to confirm the bandwidth and electrical properties of the bus, and again, all materials will be tested for susceptibility to radiation damage.

The data will be readout directly into memory in VME for both the SVT and the DAQ. Prototype VME boards will be built, initially to test the bandwidth performance of the system, and then to provide a prototype readout. The control of the front-end chips will also be via VME boards.

Construction

As the production components arrive, each will be tested and packaged into substructures; detectors, hybrids, ladder and bulkhead pieces, and branch cables. Hybrids and detectors will then be assembled on a ladder frame and electrically bonded, and the final ladders fully tested. The ladders will then be assembled onto the barrels. This is essentially the construction process used for SVX and for SVX′. Our estimate of the time and resources needed for this construction is scaled from this experience.

Funding and Manpower

As the design progresses a detailed cost estimate will be made. our initial estimate for the total cost for materials and services is $3.8M. A breakdown by fiscal year is shown in Table 25. The FY93 funding is for R&D leading to the final design. Most of the materials for the construction are purchased in FY94, although it is likely that some of these costs can be deferred to FY95. The silicon detectors themselves account for a large fraction of the cost. The figure used at present is based on preliminary discussions with vendors.

We estimate the work force needed to design and construct the SVX II barrels and their readout in Fig. 64, and again, the estimate is based on our experience with SVX and SVX′.

With these resources, the SVX II Stage 1 detector can be ready for installation in January 1996, and will significantly extend the physics capabilities of CDF for Run II and beyond.

References

[1] G. Punzi and L. Ristori, "SVT: The Silicon Vertex Tracker", Version 3.4, CDF 1872, December, 1992.

[2] F. Bedeschi, CDF 371, 1985 and references contained therein.

[3] R. Hughes, *et. al.*, CDF 1626, 1991.

[4] V. Luth, *Spatial Resolution of Silicon Detectors: A Monte Carlo Study*, SLAC Report (1991)

[5] M. Binkley, private communication.

[6] F. Abe et al. Phys. Rev. Lett. **68**, 447 (1992).

[7] D. Kennedy and P. Langacker, Phys. Rev. **D44**, 1591(1991).

[8] J. Huth, Proc. of Particles and Fields '91, 151 (1991); Presentation to HEPAP Subpanel, Feb 28, 1992.

[9] F. Berends et al. Fermilab-Pub-90/213-T (1990).

[10] G.L. Kane, *Top Quark Physics*, UM-TH-91-32 (1991).

[11] See for example, M. Gold, C. Haber, P. Tipton, *b Physics with Existing Colliders*, Physics at Existing Colliders, D. Green and H. Lubbati, editors, World Scientific, New Jersey, 1990.

[12] A. H. Mueller and J. Nason, Phys. Lett 157B, 226 (1985).

[13] M. S. Witherell, *Heavy Quark Physics and the CKM Matrix*, preprint UCSB-HEP-91-06, 1991 SLAC Summer Institute, August, 1991.

[14] J. L. Rosner, *The CKM Matrix and B Physics*, preprint EFI-92-02, Workshop on *b* Physics, Edinburgh, Scotland, December 9, 1991, submitted to J. Phys. G.

[15] H. Schröder, $B\bar{B}$ *Mixing*, preprint DESY 91-139, to be published in "B Decays", edited by S. Stone, World Scientific, Singapore.

[16] W. Venus, "Results and Perspectives in Particle Physics", La Thuile, Aosta Valley, March, 1992.

[17] H. Albrecht et al. (ARGUS collaboration), Phys. Lett. 197B, 452 (1987)

[18] M. Artuso et al. (CLEO collaboration), Phys. Rev. Lett. 62, 2233 (1989)

[19] J. Rosner, Presentation to HEPAP subpanel, Fermilab, February 27, 1992.

[20] N. S. Lockyer et al. *Proposal for a B-Physics Experiment at TEV I: The μBCD*, October 1990, unpublished.

[21] *b Physics at CDF*, June 4, 1991, CDF Collaboration.

[22] ARGUS Collaboration, DESY 92-050, March 1992

[23] Reported by Cassel, DPF, Fermilab, November 1992.

[24] F. Abe et al, Phys. Rev. Lett. 68 (1992) 3404.

[25] P. Nason, S. Dawson, K. Ellis, Nucl. Phys. B327 (1989) p. 49. This comparison is meant to validate our extrapolation, not to test ISAJET. A thorough comparison of ISAJET to NDE, where next to leading order corrections are done in ISAJET, can be found in D. Kuebel, *et al*, Phys. Rev. D, 43 (1991) p. 767.

[26] M. Bauer, B. Stech, and M. Wirbel, Z. Phys. C, 34, 103 (1987). This value for the branching ratio assumes $|V_{ub}/V_{cb}| = 0.1$. Recent results from CLEO II give a somewhat lower value, although there remains considerable model dependence. (see P. Drell, XXVI International Conference on High Energy Physics, Dallas, August, 1992.)

[27] M. Frautschi, CDF 1842, 1992.

[28] Nicolo Cartiglia, "Facts about Silicon Detectors", U.C.S.C. transparancies

[29] H.Ikeda, M.Tanaka, and S.Okuno, NIM A 313 (1992) 31–36

[30] J.A.Ellison, *Radiation Levels in D0 and Effects on Silicon Detectors,*, D0 Note 1155, July 12,1991.

[31] K. Yamamoto *et. al., Interstrip Capacitance of the Double Sided Slilicon Strip Detector*, presented to the IEEE meeting in Orlando, Fla, Oct., 1992. (preprint available)

[32] E. Barberis *et. al., Measurement of Interstrip and Coupling Capacitances of Silicon Microstrip Detectors*, presented to the the IEEE meeting in Orlando, Fla, Oct., 1992. (preprint available)

[33] S. Masciocchi (INFN Milano), A.Peisert (INFN Padova), C. Ronqvist (SEFT Helsinki), D.Vite and R.Wheadon (Imperial coll), *Capacitance Measurements on Silicon Microstrip Detectors*, presented to the IEEE meeting in Orlando, Fla, Oct., 1992. (preprint available)

[34] Ed Barsotti, Hector Gonzalez and Carl Swoboda, *D0 and CDF Silicon Strip Upgrade Project–Preliminary Conceptual Design–Electronics Implementation and Cost and Schedule Details*, Computing Division/PPI-123, December 31, 1992.

[35] M.Dell'Orso, L.Ristori "VLSI Structures for Track Finding" Nuclear Instruments and Methods A278 (1989) 436-440. S.R.Amendolia, F.Bedeschi, G.Bellettini, S.Galeotti, A.Lusiani, A.Menzione, F.Morsani, D.Passuello, L.Ristori. "Study of a Fast Trigger System on Beauty Events at Fixed Target and Colliders" Nuclear Instruments and Methods A289 (1990) 539-542. S.R.Amendolia, S.Galeotti, F.Morsani, D.Passuello, L.Ristori and N.Turini "The AMCHIP: A VLSI Associative Memory for Track Finding" Nuclear Instruments and Methods A315 (1992) 446-448.

FERMILAB-PROPOSAL-0830-3

1995

A Time-of-Flight System for CDF

The CDF Collaboration

Abstract

This proposal describes the physics motivation and technical design of a time-of-flight system that identifies low momentum kaons. The system is proposed as an upgrade for Run-II and beyond. The addition of this time-of-flight system will significantly improve the B physics capability of the CDF detector.

Contents

1 Executive Summary **4**

2 Introduction **5**

3 Physics Goals and Performance Requirements **6**
- 3.1 $\bar{B} \to e^- DX, D \to K^{\pm} X'$ 6
- 3.2 B_s Mixing 8
- 3.3 K Spectrum from $B \to J/\psi K^{*0}$ 10
- 3.4 $D^0 \to K^- \pi^+ \pi^+ \pi^-$ 10
- 3.5 $B^0 \to \pi^+ \pi^-$ 13

4 Scintillator TOF system in the CDT location **13**

5 Separation of $\pi/K/p$ **19**

6 Choice of Scintillator and PMT **19**

7 Readout Electronics **22**
- 7.1 Preamplifier 23
- 7.2 Time Measurement 23
- 7.3 Charge Measurement 25
- 7.4 System Organization 25
- 7.5 Electronics Cost Estimate 28

8 Trigger Considerations **30**

9 Cosmic Ray Tests of a Prototype TOF Counter **30**

10 Tests of a Prototype TOF counter with a N_2 laser **38**

11 Counter Occupancy **42**
- 11.1 Same-side 42
- 11.2 Opposite Side 43
- 11.3 Random J/ψ Events 43
- 11.4 Occupancy in Run-II 43

12 Determination of t_0 and an Algorithm for Kaon Tagging **46**

13 Track Z Uncertainty at 1.4 Meters **47**

14 Expected Time Resolution for the Final TOF System **50**

15 Other Potential Uses for the TOF System **55**

16 Cost estimate and Schedule **55**

17 Conclusions **56**

18 Acknowledgments **56**

19 Appendix A: Detector Choices **59**

20 Appendix B: Magnetic Field tests of PMTs **61**

1 Executive Summary

We propose to add a Time-of-Flight(TOF) system to CDF that will allow the tagging of soft kaons and protons. Such an addition will significantly improve a broad spectrum of B physics capabilities for CDF. The proposed TOF system will have a resolution near 100 ps and will be capable of identifying kaons from pions by their flight time difference with at least 2 σ separation up to kaon momenta of 1.6 GeV/c. This capability is well matched to the soft kaon momentum spectrum from B decay and will be useful for reconstructing many exclusive charm and bottom decay modes, such as $B_s \rightarrow D_s\pi$, where $D_s \rightarrow \phi\pi$ and $\phi \rightarrow K^+K^-$. In addition, the efficiency for reconstruction of semi-leptonic decays of B mesons such as $B \rightarrow D^0(D^*)l\nu$, where $D^0 \rightarrow K\pi$ should be improved. Kaon identification will also enable CDF to self-tag B_s mesons which is useful for B_s-mixing measurements. Background rejection for rare B decay studies such as $B_s \rightarrow D_s^+K^-$ will be improved. Finally, the prospect exists for CDF to observe CP violation in the decay $B \rightarrow J/\psi K_S$ during Run-II. We view the addition of the TOF system as part of an overall upgrade to improve the CDF detector for the study of B physics. The TOF detector envisioned would reside just inside the CDF coil and outside the central tracking chamber in the location presently occupied by the Central Drift Tubes. Such a system represents a moderate upgrade project that is compatible with most existing CDF equipment and consistent with our long term upgrade plans. Tests of full sized prototype TOF counters for the proposed system indicate that a practical TOF system for CDF can be built quickly and will operate with resolutions approaching 100 ps. The system could be installed for Run-II and will cost about $1 M.

2 Introduction

A time-of-flight (TOF) system capable of tagging charged kaons in the momentum range 0.6 to a few GeV/c would nicely complement the existing CDF dE/dx system and would add substantially to the physics capability of the CDF detector. The CDF detector currently has the capability to tag charged kaons produced centrally and tracked in the central tracking chamber (CTC) with momenta from 300-600 MeV/c with separations $> 2\sigma$ using dE/dx [1]. Above 600 MeV/c the dE/dx from pions and kaons becomes sufficiently similar that the 10% resolution of the dE/dx system is insufficient to separate them. (At 1.1 GeV/c the dE/dx for a pion and kaon are identical. Above about 2.5 GeV/c the dE/dx for pions and kaons again separate because of the relativistic rise, but the separation is never greater than $\sim 1\ \sigma$ for our system.) In contrast, most of the kaons from B decay at the Tevatron are produced at momenta above 600 MeV/c but at less than a few GeV/c. As we will show, a large fraction of these kaons can be identified with a TOF system.

We have explored the improvements in CDF's B physics program for Run-II and beyond that would result from the addition of an expanded particle ID system. We examined a number of possible technologies for such a system. These are discussed in Appendix A. From this study we conclude that the most practical detector for tagging kaons in CDF in the range of interest is a time-of-flight (TOF) system located where the Central Drift Tube(CDT) system presently resides. This system takes advantage of "available" space and would use a well proven technology. A TOF system located at the current CDT radius with 100 ps resolution could tag kaons from pions up to momenta 1.6 GeV/c with better than 2 σ separation. Other technologies such as Cerenkov Ring Imaging Detectors hold promise to extend the momentum range of particle identification in future upgrades. However, significant technical barriers exist that must be overcome before such devices are available for the high luminosity environment of the Tevatron Collider. In addition, such systems would require much more time, money, and effort than the proposed TOF system.

This proposal is organized in the following way: In section 2 we outline some of the physics goals of the proposed particle ID system. Section 3 describes the required performance necessary to achieve those goals. Section 4 describes the geometry and hardware of the proposed TOF system and section 5 how well it should work at separating $\pi/K/p$. Sections 6-10 justify the hardware choices made, and describe results of cosmic ray tests of prototype TOF counters. Sections 11-15 describe the tagging algorithm and how well we think the system will perform including addressing questions of expected time resolution and occupancy. Finally, in sections 16-17 we present a cost estimate, schedule, and conclude. Two appendices provide supporting detail.

3 Physics Goals and Performance Requirements

The physics capability of the CDF detector will be enhanced with the addition of a TOF system. The following list contains examples of physics topics that will be improved or made possible by the addition of a TOF system:

- Reconstruction and study of exclusive states such as $B_s \to J/\psi\phi$ with $\phi \to K^+K^-$, $B^+ \to J/\psi K^+$, $\Lambda_b \to J/\psi\Lambda$ with $\Lambda \to p\pi^-$, etc.
- Reconstruction of decay modes useful for mixing such as $B_s \to D_s\pi$ where D_s decays to $K^+K^-\pi^+$ or $K^+K^-\pi^+\pi^-\pi^-$ and self tagging of the B_s.
- Rare B decay studies such as $B_s \to D_s^+K^-$, and $B_d \to D_s^-K^+$ produced by exchange graphs, penguin graphs from modes such as $B_s \to \phi K_S$ and $B_s \to \phi\phi$ and annihilation graphs from modes such as $J/\psi D_s^+$, where $D_s \to KK\pi$.
- CP violation studies where the kaon is used as a tag of the flavor of the 'other' B and where the 'other' B is tagged using lepton plus charm decays, and where the charm decays to $D \to K\pi$, $D \to K\pi\pi\pi$, $D^* \to K\pi\pi$.

Next we present some typical kaon momentum distributions either predicted by Monte Carlo or observed in Run-Ia data for some of the processes mentioned above. In several cases we show data distributions that indicate how particle ID can improve signal to background.

The kaon momentum spectra from several of the B decays mentioned in the previous section can be used to set the performance requirements for a CDF particle identification system. The low momentum end of the particle identification requirements are determined by the soft momentum spectrum in the rapidity range $|\eta| < 1$ of the $K^\pm$ from the decay of a typical B-meson. To estimate the typical momentum of the kaons of interest we studied B decays from the HERWIG Monte Carlo. In these studies, to simulate trigger effects, one B was forced to decay to $D^*e\nu$, while the 'other' B decayed freely. We further impose requirements that the trigger electron must have $|\eta| < 1$ and $P_t > 3$ GeV/c. Figure 1 shows the $K^\pm$ momentum distribution from the 'other' B-meson. As can be seen the Monte Carlo models predicts that most of the kaons have momentum well above the 600 MeV/c capability of CDF's present dE/dx system. Only 15% have momenta less than 600 MeV/c and large enough so that they could be tagged by the dE/dx system. However, a system capable of detecting kaons up to 1.6 GeV/c could tag an additional 46% of the spectrum. Table 1 shows the fraction of kaons that could be tagged for various momentum ranges of interest.

3.1 $\bar{B} \to e^-DX, D \to K^\pm X'$

Another application of the particle identification using the proposed TOF system is to help reconstruct the charm particles in semileptonic B hadron decays. CDF

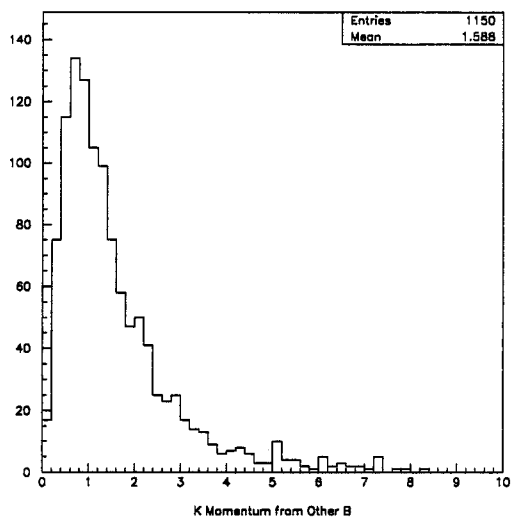

Figure 1: Momentum spectrum for $K^{\pm}$ from B-decay from the HERWIG Monte Carlo program. One B was forced to decay to $D^{*}e\nu$, the 'other' B decayed freely. We imposed trigger requirements that the electron must have $|\eta| < 1$ and $P_t > 3$ GeV/c and examine kaons from the "other" B. Kaons are required to be in the rapidity range of the proposed TOF system,$|\eta| < 1$. A TOF system capable of detecting kaons up to 1.6 GeV/c could tag 55% of the spectrum.

has measured the B meson cross section versus P_T and the lifetime of the $B^0/B^{\pm}$ mesons using an inclusive lepton sample. A similar analysis has yielded the B_s meson lifetime from CDF data. Decay products of charm particles often include charged kaons. Separating kaons from other particle species is useful in reducing combinatorial background. We know that precision tracking with a silicon microvertex detector is also useful in reducing combinatorial backgrounds through precise determination of decay vertices and application of decay length cuts. However, in the measurement of lifetimes, we would like to minimize the use of such cuts to avoid systematic biases. For such analyses particle identification is an ideal tool for the suppression of combinatorial backgrounds.

Figure 2 shows the transverse momentum spectra of the charged kaons produced in semileptonic B decays. The BGENERATOR Monte Carlo [2] was used for the generation of the b-quarks according to the momentum spectrum of the next-to-leading order calculation by Nason, Dawson and Ellis [3], and the CLEO Monte Carlo program was used for the weak decays of B and charm hadrons. The top two plots show the kaon spectra when an electron of transverse momentum 7 GeV/c or above is required. This is similar to our present trigger threshold. We have plotted the two charge correlations (e^-K^- and e^-K^+) separately. We see greater rates from e^-K^- combinations as expected. Both modes have similar kaon momenta. To reduce background, we currently apply a transverse momentum cut of 1.5 GeV/c on the track assigned to the kaon. Particle identification would allow a lower momentum cut and thus permit a higher reconstruction efficiency. The bottom two plots show the corresponding kaon transverse momentum spectra when the electron trigger threshold is lowered to 3 GeV. This may be feasible for Run-II given the expected improvements in DAQ and trigger system for that run. In this case the kaon momentum spectra are even softer, with the majority of kaons below 2 GeV/c.

3.2 B_s Mixing

Another area of interest is the study of B_s mixing with exclusive decays such as $B_s \to D_s n\pi$, where $D_s \to \phi\pi$ and $\phi \to K^+K^-$. We have used the HERWIG Monte Carlo with the CLEO decay table to estimate the kaon momenta from this process. For this study we required that the 'other' B-meson decay semi-leptonically and satisfy lepton $P_t > 3$ GeV/c. The kaon momentum in the rapidity range $|\eta| < 1$ is shown in Figure 3. A TOF system capable of tagging kaons up to 1.6 GeV/c will tag 58% of the spectrum. In addition, self tagging of the B_s meson may be possible using fragmentation kaons from the primary production vertex. To estimate the momentum spectrum of these kaons, B_s mesons were generated with Pythia, and were required to have $|\eta| < 1$ and $P_t > 5.0$ GeV/c. We select the K–B_s mass combinations below 6.5 GeV/c^2. The momentum spectrum for these kaons is shown in Figure 4. The solid line shows the spectrum for "right sign" kaons while the dotted line is the momentum spectrum for those with the "wrong sign". We estimate that 72% of the "right sign"

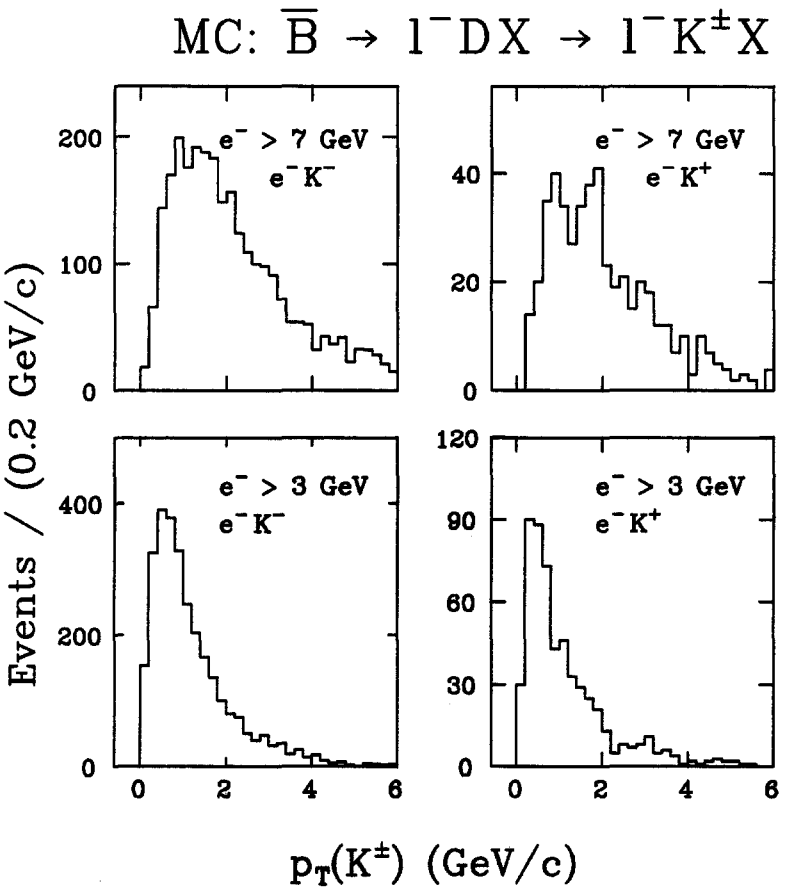

Figure 2: Transverse momentum spectra of charged kaons from charm particles in semi-leptonic B decays $\bar{B} \to e^- \bar{\nu} DX$. Two different electron thresholds are considered.

kaons are below 1.6 GeV/c.

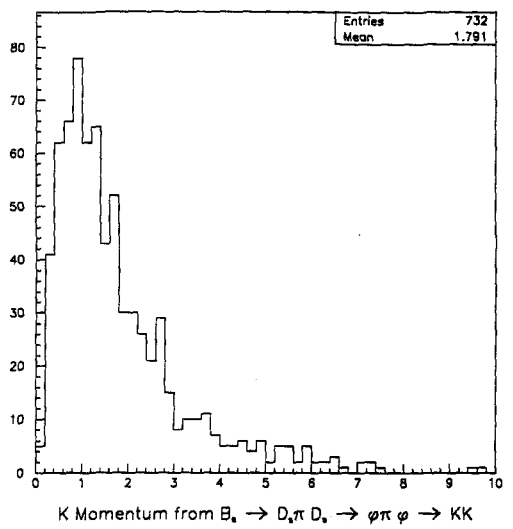

Figure 3: Kaon momentum spectrum from HERWIG Monte Carlo for $B_s \to D_s\pi$, where $D_s \to \phi\pi$ and $\phi \to K^+K^-$ in the rapidity range $|\eta| < 1$. A TOF system capable of tagging kaons up to 1.6 GeV/c will tag 58% of the spectrum.

3.3 K Spectrum from $B \to J/\psi K^{*0}$

An important B decay mode for lifetime measurements, polarization, tagging and CP violation studies is the decay $B \to J/\psi K^{*0}, K^{*0} \to K^{\pm}\pi^{\pm}$. The K momentum spectrum from this decay using 19 pb^{-1} of data from Run-Ia is shown in Fig. 5. To reduce background in the $J/\psi K^*$ mass spectrum, several cuts were required. The most significant of these were the requirement that $P_T(B) > 6$ GeV/c and $P_T(K^*) > 2$ GeV/c. With kaon identification using the proposed TOF system, the latter cut could be substantially relaxed improving the efficiency for detecting the lower P_T part of the spectrum.

3.4 $D^0 \to K^-\pi^+\pi^+\pi^-$

CDF has reconstructed the charm meson decay $D^0 \to K^-\pi^+\pi^+\pi^-$ using data from the inclusive electron and muon samples from Run-Ia. The number of events is seen in the peak in Fig. 6 is roughly 1000 with a nearly equal amount of background. The large background is due to the severe combinatoric problem with this decay mode. By reducing the combinatoric background the proposed TOF system is expected to improve the signal-to-noise by at least a factor of four providing another large sample of events with which we can study B lifetimes.

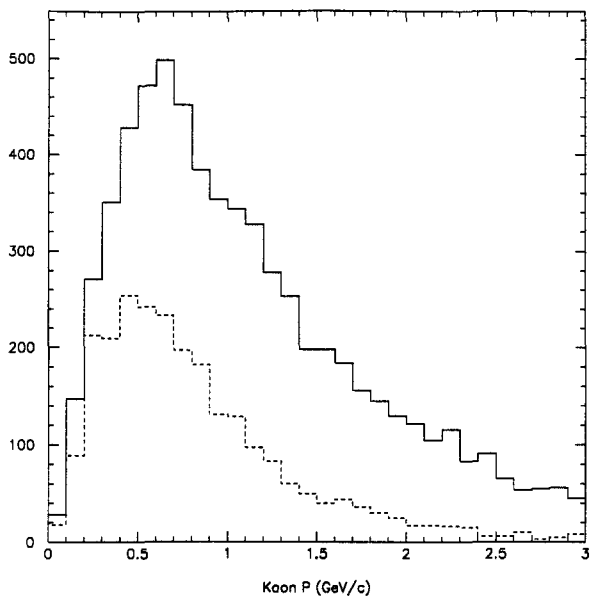

Figure 4: Momentum spectrum from PYTHIA Monte Carlo for self-tag kaons from the primary production vertex. Only kaons with K - B_s mass combinations below 6.5 GeV/c^2 and with $|\eta| < 1$ are included. The solid line shows the spectrum for "right sign" kaons while the dotted line is the momentum spectrum for those with the "wrong sign". We estimate that 72% of the "right sign" kaons are below 1.6 GeV/c.

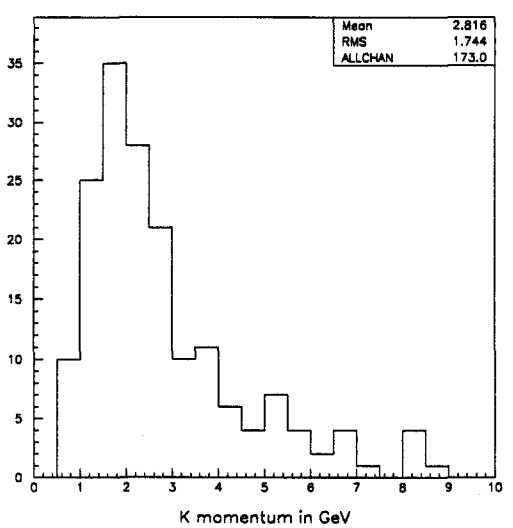

Figure 5: K momentum spectrum from $B \rightarrow J/\psi K^*$ decay.

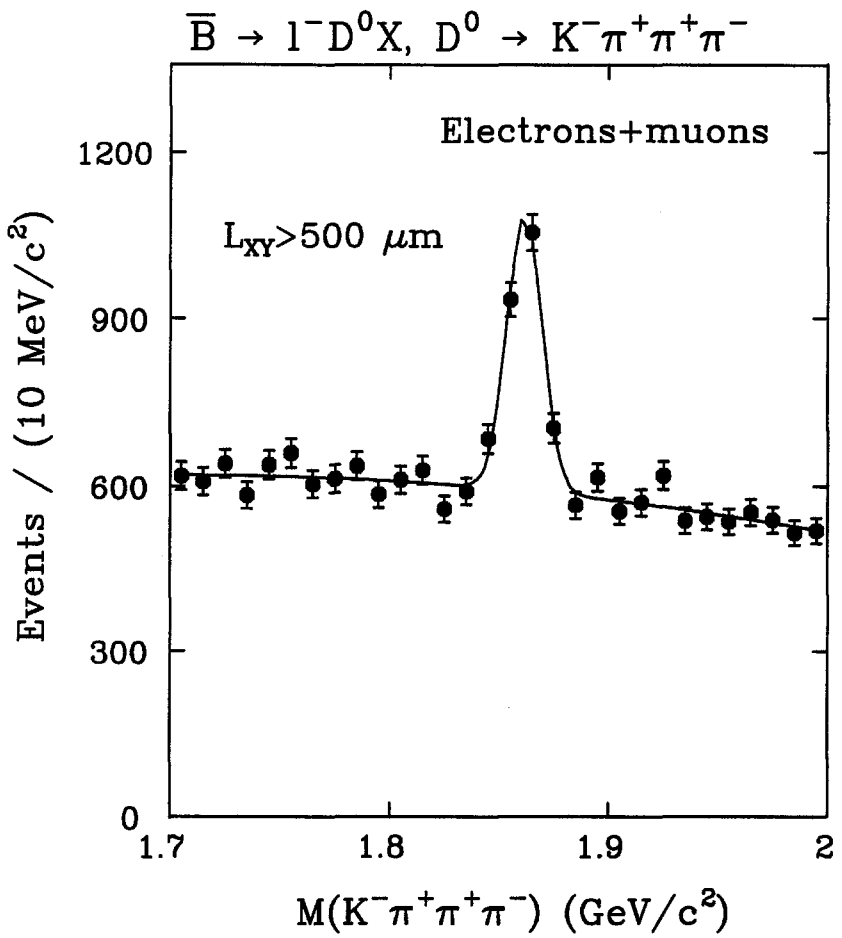

Figure 6: Mass spectrum of $D^0 \to K^-\pi^+\pi^+\pi^-$. The TOF will reduce the large combinatoric background observed in the figure.

3.5 $B^0 \rightarrow \pi^+\pi^-$

The high momentum end of the particle ID requirements for B physics is determined by the spectra of the two-body decay modes, such as $B^0 \rightarrow \pi^+\pi^-$ and the background process $B^0 \rightarrow K^+\pi^-$. A TOF system will not be an effective tool to separate such decay modes. Nevertheless, to illustrate how high in momentum the optimal particle ID system would tag kaons, Figure 7 [4] shows the mass distribution for the combination of $B_d \rightarrow \pi^+\pi^-$, $B_d \rightarrow K^\pm\pi^\mp$, $B_s \rightarrow K^\pm\pi^\mp$ and $B_s \rightarrow K^\pm K^\mp$ assuming all K's to be π's. The solid histogram is the combination and the dashed histograms show the four separate components. The CDF mass resolution is not sufficient to separate the different background sources in $B_d \rightarrow \pi^+\pi^-$. Furthermore, the $B \rightarrow K^+K^-$ mode lies directly under the B_d peak. As Figure 8 indicates, the momenta from two-body decay modes are substantially higher than decays from multi-body modes. From this we conclude that eventually it would be desirable to build a particle identification system capable of tagging kaons up to or above 5 GeV/c. However, such a system is non-trivial. It would require a sophisticated ring imaging detector or new technology. In either case long development times and lots of money will be required to make it work in the Tevatron collider environment. In the mean time, it appears that a TOF system is an attractive and practical alternative for a broad range of other B physics studies. However, as all the figures in this section indicate, we should strive to design such a system so that it will separate kaons from pions at the highest possible momenta.

Table 1: Fraction of kaons from B-decay versus momentum range.

Momentum Range	Fraction of Kaons HERWIG
0.0 - 0.2	1.6%
0.2 - 0.6	15.3%
0.6 - 1.6	45.8%
1.6 - 2.0	10.3%
2.0 - 4.0	19.1%
> 4.0	7.9%

4 Scintillator TOF system in the CDT location

From the considerations described in Appendix A we concluded that the most practical detector choice for tagging kaons from B's is a TOF system located where the

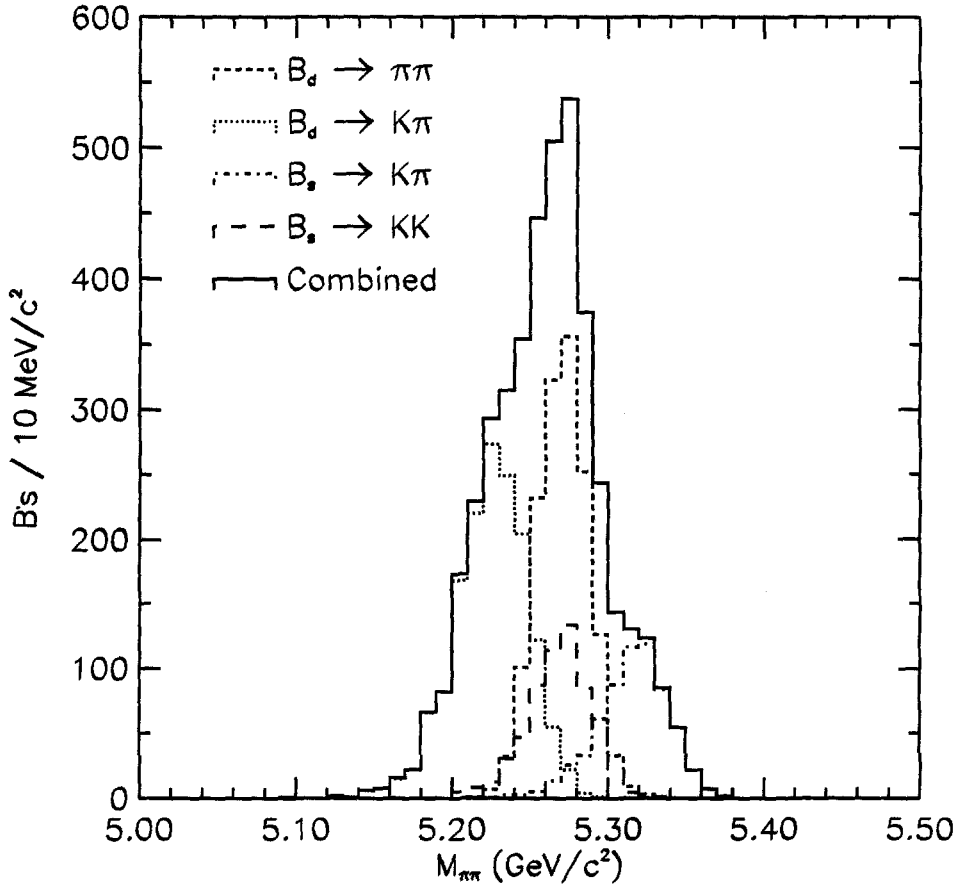

Figure 7: Mass distribution for the combination of $B_d \to \pi^+\pi^-$, $B_d \to K^\pm\pi^\mp$, $B_s \to K^\pm\pi^\mp$ and $B_s \to K^\pm K^\mp$ assuming all K's to be π's. The solid histogram is the combination and the dashed histograms show the four separate components.

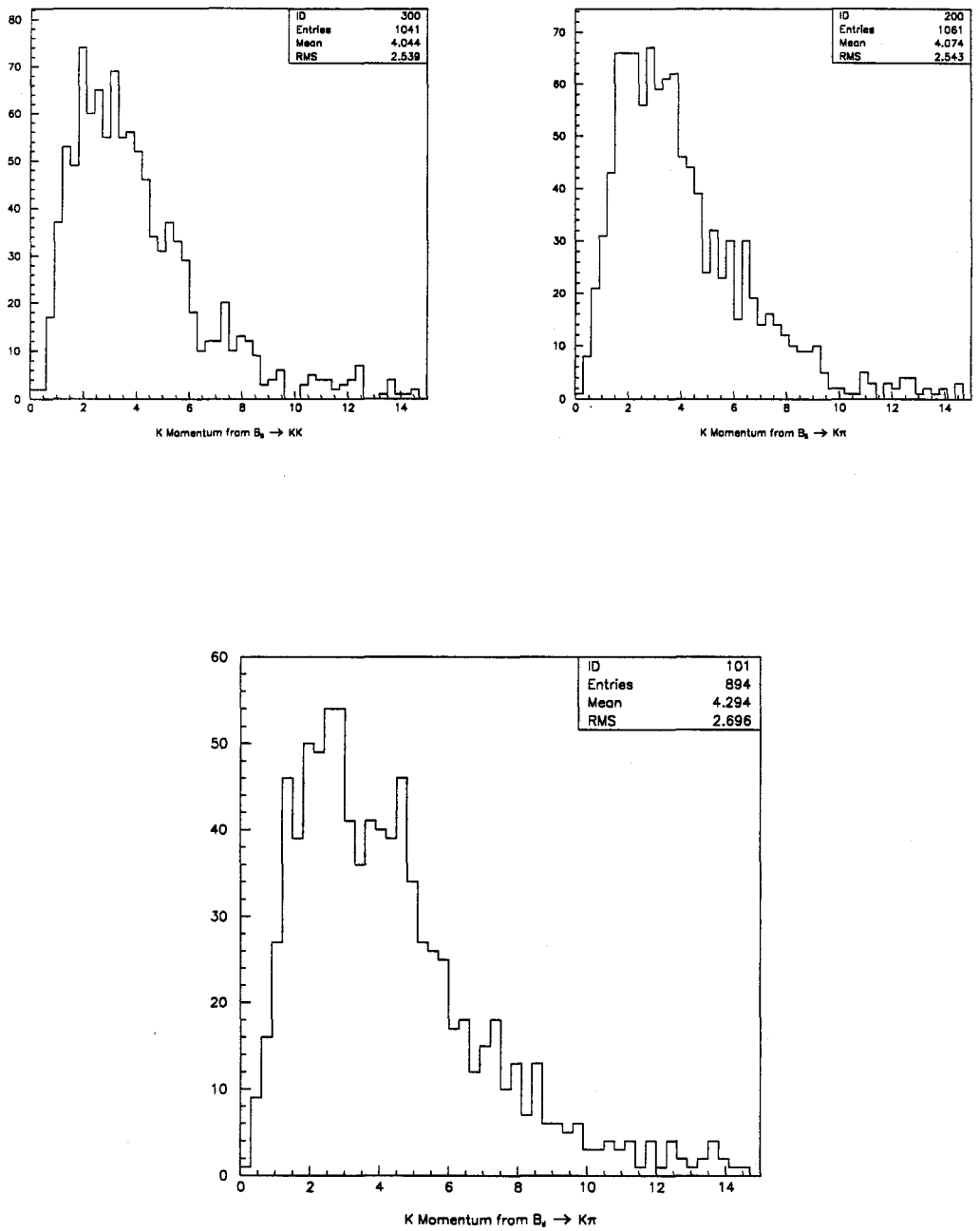

Figure 8: Momentum distribution for the kaons from $B_s \to K^{\pm}K^{\mp}$, $B_s \to K^{\pm}\pi^{\mp}$ and $B_d \to K^{\pm}\pi^{\mp}$, using the HERWIG Monte Carlo Generator. A RICH system or equivalent will be necessary to identify a significant fraction of these modes

Central Drift Tube(CDT) system presently resides. Time-of-flight systems have been successfully employed for particle identification in a number of different collider detectors, for example Mark-II and CLEO. The CLEO TOF system is the existing detector which most closely resembles what we propose for CDF. The current CLEO TOF system employs 64 counters at a radius of about 1 meter. The counters are 10 cm wide and 5 cm thick in the radial direction. Their length is 2.8 meters which is very close to the length of TOF counter that could be attached to the 3.2 meter length of the CTC outer-can in CDF. They achieve a time resolution of $\sigma \sim 155$ ps. The CLEO TOF system employs long light guides so that the PMT's are located in a field free region. H. Yamamoto from CLEO reported at the Snowmass 93 Workshop that the timing resolution is limited by photostatistics and that the CLEO TOF optics are such that less than half of the light makes it to the PMT on each end of the counter. Nevertheless, they achieve a 2σ π/K separation up to 1.1 GeV/c. In comparing this system with CDF we note that even with similar time resolution, the CDT location would provide better π/K separation than the CLEO system because of the 40% larger radius. We are also encouraged by the recent results from KEK B-factory TOF tests [7] which indicate a system with counter lengths and thickness similar to that planned for CDF could reach intrinsic resolutions of 75 ps using PMT's capable of operating in the 1.5 T magnetic field.

The CDT system consists of a set of drift tubes located just outside the CTC occupying the space from R = 1.380 to 1.420 m radius. The system resides just inside the 1/4 " aluminum inner wall of the CDF superconducting coil which has an inner radius of 1.428 m. The system was originally intended to measure the Z position of tracks emerging from the CTC using charge division. Improvements in the stereo reconstruction capability of the CTC provides equivalent information such that the system could be removed without significant effect on the CDF tracking capabilities. Moreover, the present CDT system operates in limited streamer mode and it is unlikely that this mode of operation is compatible with the higher luminosities expected for Run-II. (switching to proportional mode would mean much poorer Z resolution) On the other hand, if the CDT were removed then more than 4 cm of usable radial space at a mean radius of 1.401 meters from the beam line over the 3.2 m length of the CTC becomes available. We propose inserting a TOF system in this space and using bars of scintillator approximately 4.0 $\times$ 4.0 cm in cross section and shorter in length than the CTC outer support-can such that the PMT's would fit in the 3.2 m length. Such a system would consist of a total of 216 TOF counters with PMT's on each end. Figure 9 is a side view of the CDF detector and Figure 10 is an axial view showing schematically the proposed TOF system. Figure 11 shows how the counters fit in the available radial space and Figure 12 shows one TOF counter. A PMT and base of minimal size and axial length would be attached to both ends of the scintillator bar. The choice of scintillator and PMT is discussed in detail in later sections. We note that one other useful function of the CDT is to provide a cosmic ray trigger. A TOF system in the same location would also provide this function.

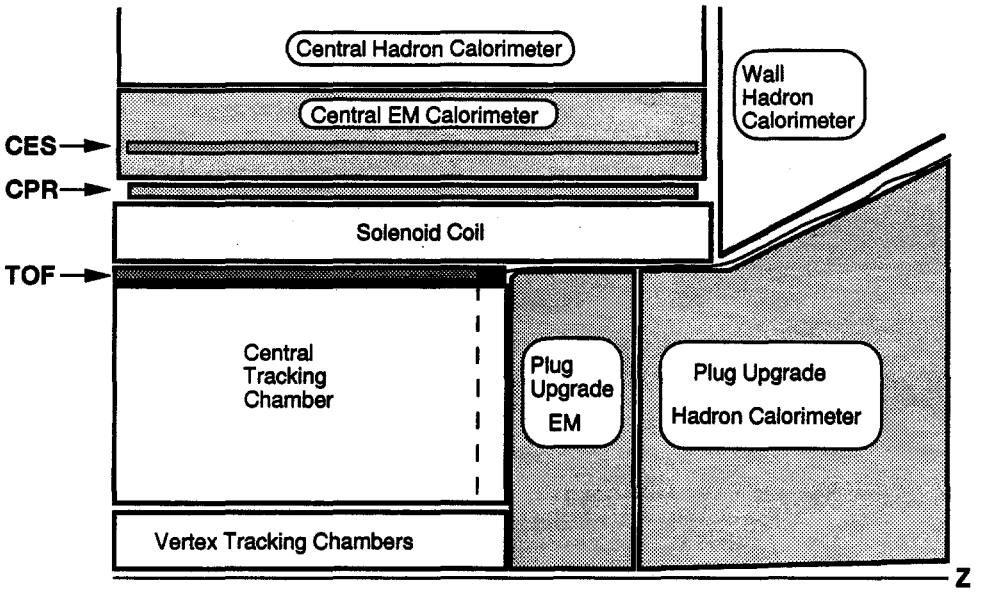

Figure 9: Side view of CDF Detector inside coil with TOF system

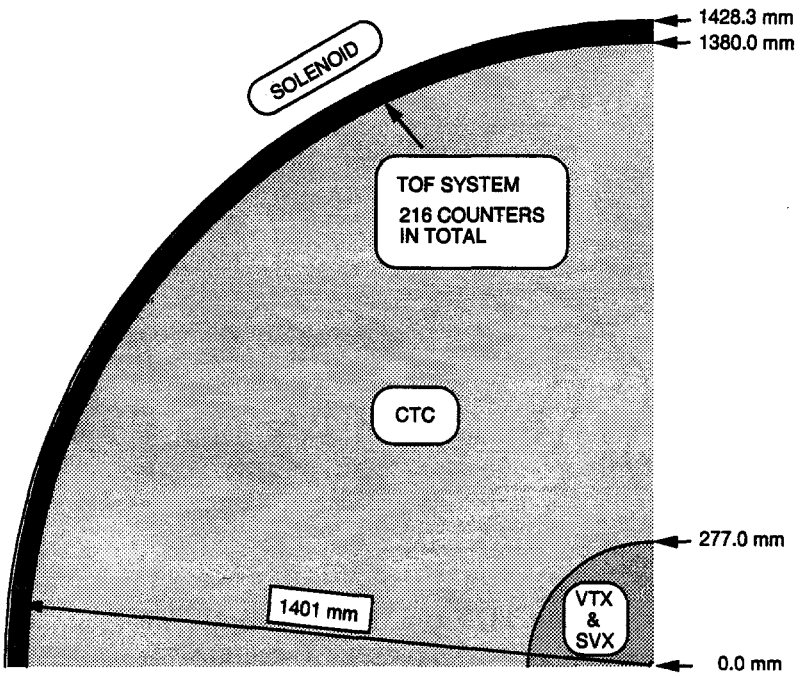

Figure 10: End view of CDF Detector inside coil with TOF system in CDT location.

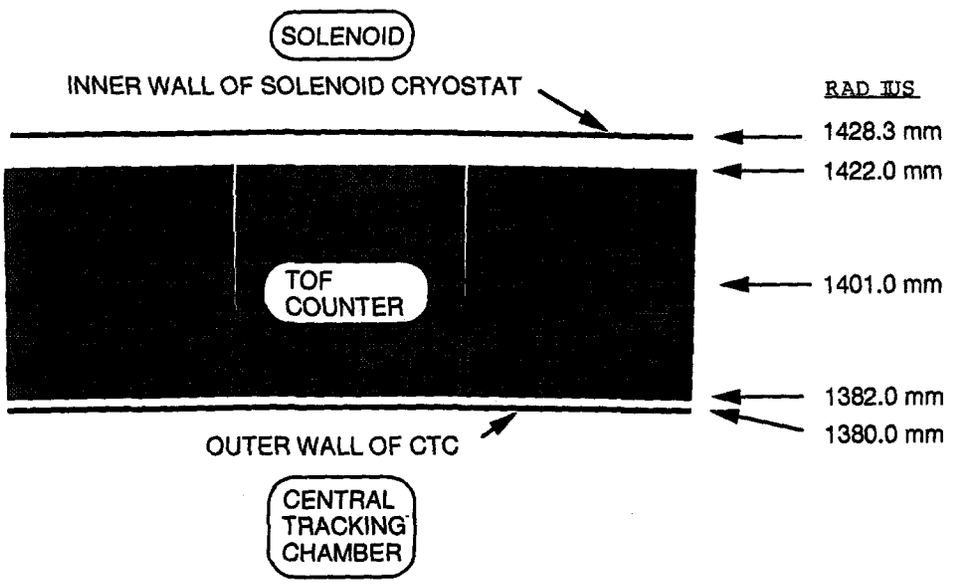

Figure 11: End view of TOF system in CDT location showing available radial space.

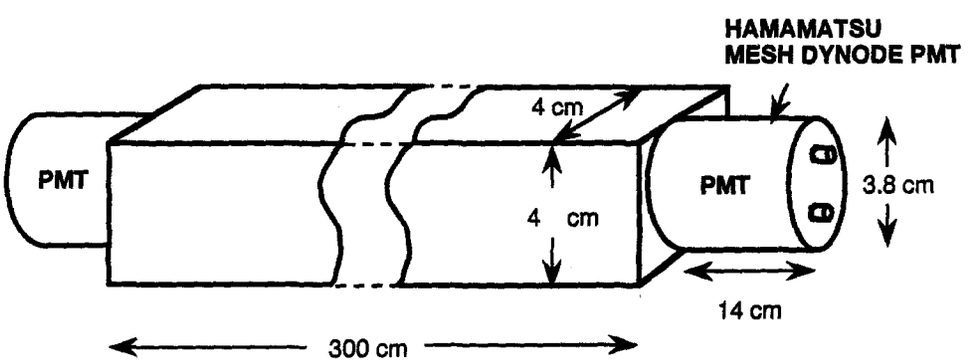

Figure 12: One of the TOF counters with PMT's

5 Separation of $\pi/K/p$

It is of interest to state how well $\pi/K/p$ can be separated using a time-of-flight measurement. The difference in the flight time between a π and K is given by

$$\Delta t = \frac{s}{pc}\left[\sqrt{m_K^2 + p^2} - \sqrt{m_\pi^2 + p^2}\right] \tag{1}$$

where s is the path length traveled and p is the momentum of the charged particle. This equation can be rewritten in as

$$\Delta t = \frac{s}{pc}\frac{m_K^2 - m_\pi^2}{\sqrt{m_K^2 + p^2} + \sqrt{m_\pi^2 + p^2}} \tag{2}$$

Figure 13 shows the flight time difference of π from K as a function of momentum. For this figure we have assumed the TOF system is in the location of the CDT system, and we neglect track curvature. A system capable of 100 ps resolution gives 2σ separation of pions from kaons up to 1.6 GeV/c and pions from protons up to 3.2 GeV/c. We also note that kaons and protons have 2σ flight time separations for momenta up to 2.7 GeV/c. Finally, we note that in the 1.4 T field of the solenoid a charged particle must have a minimum momentum of 0.3 GeV/c to reach the CDT location.

6 Choice of Scintillator and PMT

For long counters such as those envisioned, the principle effects that limit the time resolution are:

- Photostatistics combined with the intrinsic rise time of the light pulse from the scintillator and the transit time spread (*tts*) of the PMT for individual photoelectrons.
- Attenuation of the photons due to the bulk absorption length in the scintillator or due to losses as the photons reflect from the polished optical surfaces of the bar.
- Time dispersion due to variations in the optical path as photons travel to the PMTs.

Time dispersion due to variations in the optical path is proportional to the square root of the propagation distance[8]. Therefore it is advantageous to locate the PMT as close to the end of the scintillator active area as possible. This combined with the CDF geometry (*i.e.* the CDT location) means that the PMT must operate inside the solenoid 1.4 T magnetic field. As a result, the types of PMT available are quite limited. The only possible PMT choices seem to be:

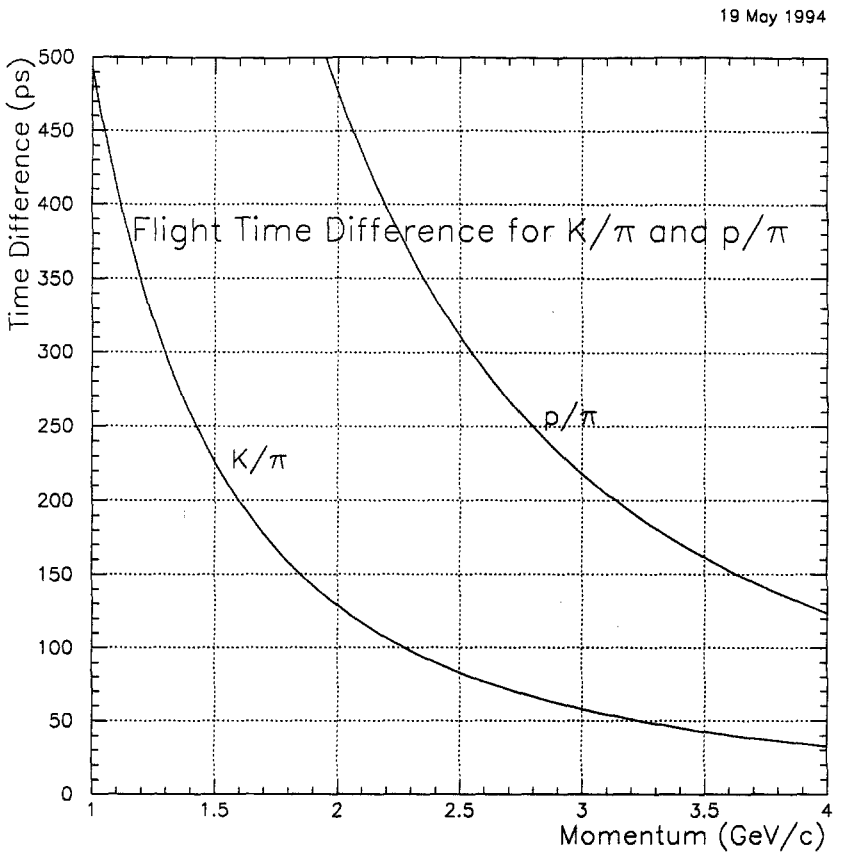

Figure 13: Flight time difference at a radius of 1.4 m (CDT location) versus momentum for π/K and π/p.

1. proximity focused fine mesh dynode,
2. microchannel plate,
3. silicon target PMT's.

The PMT should have a small *tts*, a good spectral match to the scintillator and high quantum efficiency. Small physical size and reasonable cost are additional requirements.

Fine mesh dynode PMT's like the R2490 from Hamamatsu are known to operate with reduced but stable gains in a magnetic field of 1.4 T. These tubes have reasonable transit time spreads (*tts*) (400 ps), and exhibit timing resolutions below 100 ps for signals with 160 photoelectrons in magnetic fields of 1.4 T[9]. Microchannel plate photomultipliers such as the Hamamatsu R2809U have excellent *tts* spreads

(under 40 ps) and also operate in high magnetic fields. However, although the R2809U is similar in physical size to the R2490-05 fine mesh tube it has only one quarter the photocathode area (18 mm diameter). Thus the loss in photostatistics would imply the timing performance improvement would be only one half that indicated by the relative *tts* of the tubes (but still very good). However, this expected performance was not realized in recent tests[9] in a magnetic field. With 160 photoelectrons the R2490 and R2809U actually had comparable performance. The biggest problem with microchannel plate tubes is that they are currently more than a factor of 5 more expensive than fine mesh dynode tubes. This makes them prohibitively expensive for a large TOF system. Finally, our investigations found that silicon target PMT's are not yet really commercially available. We do have one sample (a DEP PP0350B) which was developed as part of the CERN-LAA PROJECT. We plan to test this tube in a magnetic field in the near future. This tube was measured [10] to have good linearity, uniformity, and to work with large axial magnetic fields. However, the measured rise time is 13.8 ns and measured time resolution with 200 p.e. was unacceptable at 650 ps. It appears that silicon target PMT's are not a option for a near term TOF upgrade. As a result, we have focused our prototype studies on fine mesh dynode tubes. Fortunately Hamamatsu recently announced commercial availability of the R5946, a 1.5" version of the R2490-05 2" tube. This tube is small enough to fit in the space available in the CDT location. The performance of the R5946 in a magnetic field is expected to be similar to the R2490. Nevertheless, we feel it is important to measure the timing performance of the actual tube we intend to use. Appendix B describes a test magnet we constructed to perform such tests and shows our first measurements of gain reduction vs magnetic field for the R5946. The results are in good agreement with the curves provided by the manufacturer and indicate a gain reduction of 300 at a field of 1.4 T. We plan detailed timing performance tests of several versions of the R5946 with this apparatus in the near future.

The scintillator material for the TOF system must have short decay times, long attenuation length, and good spectral match to the PMT. Two likely candidates are Bicron BC408 or BC404. According to the Bicron sales catalog BC408 has a bulk attenuation length of 380 cm and a decay constant of 2.1 ns and thus would be suitable for 3 m long TOF counters. BC404 is attractive because its decay constant is 1.7 ns. However, standard BC404 has a 170 cm attenuation length and so would be a poor choice for 300 cm long counters. Recently Bicron announced a new version of BC404 with bulk attenuation lengths comparable to BC408. We have evaluated both of these materials and report the results later in this paper. The surface treatment of the bars of scintillator is also important. Good results have been obtained using both standard polishing and diamond fly-cutting techniques. In practice good quality control will be important for a big system. The thickness of the bar is determined by the desire to make it as thick as possible so as to get the maximum amount of light and yet fit in the CDT location. We chose to make them 4.0 cm thick, similar to the 3.9 cm thick CDT, in order to insure that they will fit (total space available with 0

clearance is 4.8 cm). The counter width is controlled by occupancy considerations (more on this later) and the desire for good optical area match to the photocathode. Both considerations argue for many bars. Cost and the physical area available for PMT's argue for a smaller number of bars. We have chosen 216 bars as a reasonable compromise. However, issues of counter occupancy cause us to consider dividing the counters at Z = 0 to reduce the occupancy at very high luminosity. Additional studies are still in progress. With either choice the bars would be 40 mm thick and 40 mm wide giving an area of 1600 mm^2. The photocathode diameter of the R5946 is 27 mm which means if we mount the tubes directly onto the end of the bar, we will capture only 37.7% of the light produced in the bar. Since the timing performance is limited by photostatistics (more on this later) we have studied adding optical concentrators to the ends of the TOF counters before the PMT and we are working with Hamamatsu to try to increase the photocathode area of tubes that will fit in the available space.

Finally, we have considered whether a solid bar of scintillator is the optimal choice. It has been suggested that an array of scintillating fibers might give better resolution because of the smaller time dispersion. Fibers have small capture angles and the core-cladding reflectivity can be significantly higher than the 0.97-0.98 typically achieved with polished plastic surfaces. As a result, one recent study [11] found that the attenuation length of such a scintillating fiber bundle could be improved from 0.7 meters to 1.8 meters for the same scintillator material using this technique. The fibers need not be small in diameter. Indeed for the study of Kuhlen *et al.*, they chose 1 mm diameter fibers and concluded they were too small for optimal performance. One problem with such a technique is that the small fiber capture angle reduces the amount of light that is transmitted initially into the fiber. In practice since the performance of our system appears to be photostatistics limited for a solid bar, reducing the amount of light by a large amount to lower the dispersion due to path length differences does not seem appropriate. Using light concentrators on a solid bar we believe that we can accept a larger fraction of the small angle light (ie photons with minimal dispersion) and achieve better performance. Thus we conclude a solid bar of scintillator is the best choice.

Extrapolating from the performance of other similar systems, we believe TOF counters made of solid bars of scintillator and read out with fine mesh PMTs and suitable electronics can have time resolutions approaching 100 ps if sufficient light collection can be achieved.

7 Readout Electronics

Immersing the PMT in a 1.4 T magnetic field results in a gain reduction of about 300 relative to the zero field case. As our baseline design (Figure 14) we assume that each PMT signal will be amplified ten to thirty times by a preamp/shaper at the tube base then sent to a TOF Front End Card (TFEC) located in VME crates on the endwall of the detector. In the TFEC the signal will pass through a buffer amp and then be

split into two signals for timing and pulse height measurement. Time is measured using a Constant Fraction Discriminator (CFD) feeding an analog Time to Amplitude Converter (TAC) for high precision and charge is measured using a conventional pulse shaping circuit feeding a fast sample and hold. Both time and charge measurements are stored as digital results in a small pipelined memory awaiting the results of the first level trigger. The time digitizations would be available immediately to feed into the trigger decision. A final decision on the system organization will need additional input from the collaboration.

7.1 Preamplifier

The preamplifier, shown in Figure 15, is a classic common base configuration chosen for its excellent noise, linearity, and dynamic range characteristics. Two emitter followers (NPN and PNP) buffer the voltage amplified signal from the collector of the input NPN device and provide low impedance to drive the base of the shaper/driver output transistor. Passive components in the emitter of the PNP output transistor set the gain and cancel the dominant pole of the preamp.

This simple, DC coupled design, without high frequency feedback should offer excellent stability and robustness. Values shown in the figure match those in the hand wired prototype used to calibrate the PMT gain in the 1.5T magnetic field test described in Appendix B. The measured gain (into a 50Ω load) was 0.5 mV per fC and the equivalent noise charge (input) was 3,000 electrons. With nearly four Volts of full scale output, this circuit should provide faithful PMT readout either in or out of the magnetic field. Pulse response of the prototype amplifier used in the LED pulser test for magnetic field attenuation measurements is shown in Figure 16.

7.2 Time Measurement

The timing signals will go into a constant fraction discriminator (or possibly a two discriminator system with high/low thresholds). The discriminated signal will then be used in conjunction with a precision crossing timing signal to generate a pulse of width equal to the time difference from discriminator to crossing as shown in Figure 17. The TAC is enabled during this time and a controlled current is withdrawn from the timing capacitor C. By using one of the newer high speed (50 ns cycle) relatively inexpensive ($10) ADCs such as the 10 bit AD876, it should be possible to complete a measurement cycle and reset the TAC ready for a next hit all within a single beam crossing period of 132ns. Using a 10 bit ADC such as the AD876 and a time range 5-35 ns corresponds to 35 ps per LSB. Figure 18 shows the approximate time sequence involved in this process. The stability of the the crossing clock timing signal relative to the beam crossing is not very important since t_0 will be determined event by event. The only important requirement on this signal is on the stability of the relative crate to crate and card to card timing. We imagine that a TOF specific clock distribution

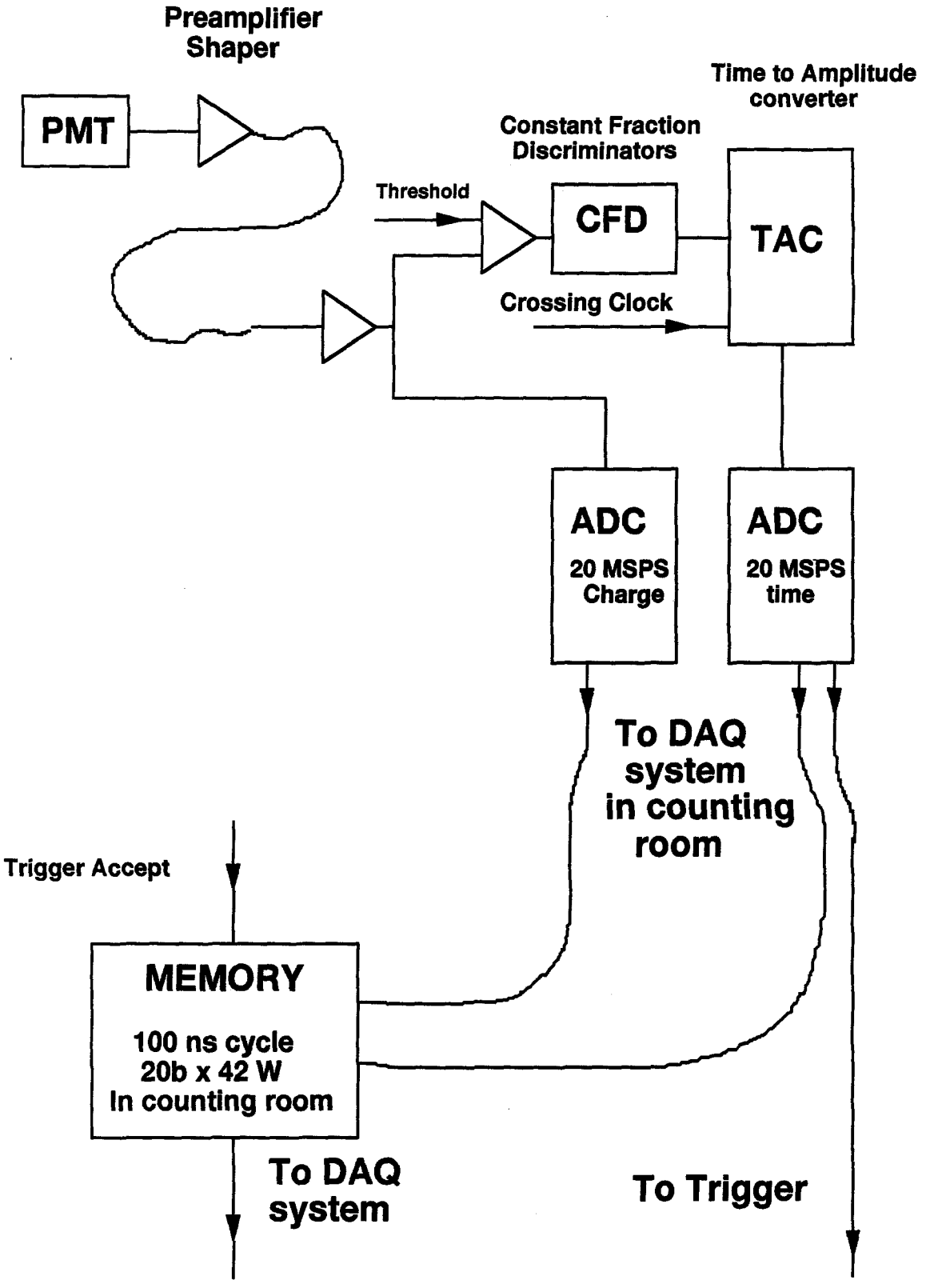

Figure 14: Block diagram of the TOF electronics system.

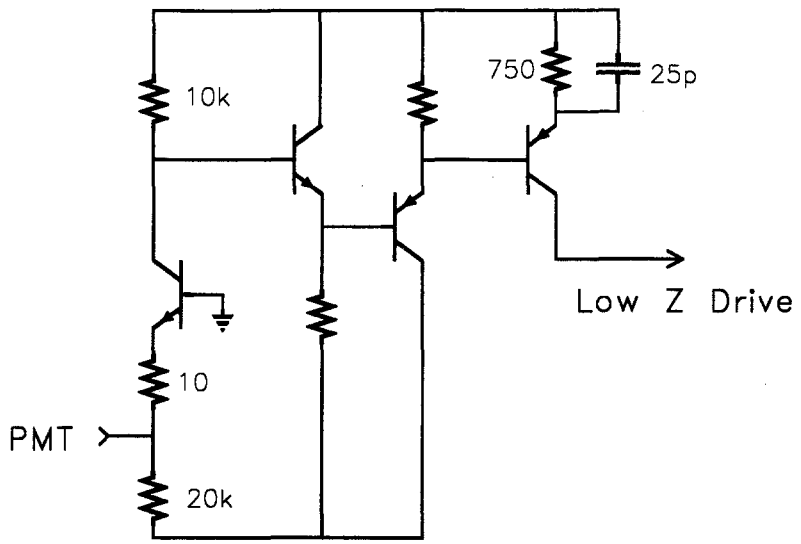

Figure 15: Schematic of TOF preamp front end. The gain is approximately 0.5 mV per fC of input. The noise is about 3,000 electrons.

system will be required to insure less than 30 ps RMS relative jitter for this signal.

7.3 Charge Measurement

The charge measurement is straight forward. Its purpose is provide information for discriminator time walk (ie proportional to pulse amplitude) corrections. Ten bit resolution should be more than adequate and is chosen for reasons of hardware symmetry.

7.4 System Organization

As noted above, the baseline design is to have preamplifiers/shapers/drivers in the PMT bases. We believe that this is necessary in order to maintain suitable noise immunity. This design places some active elements in a region with limited access and will require a very conservative design in order to ensure a high reliability. The TFEC cards will be mounted in endwall crates. The 216 scintillator bars will have 216 PMTs per end and thus there will be 54 PMTs per endwall crate. While it is probable that we could fit the electronics on a single card, the difficulty of bringing in 54 coaxial cables (even miniature ones) into a single card (and twice as many out) will probably force us to use at least two TEC cards (27 + spares? channels per card) per crate. The counting room cards (digitizers and memories) would be of similar density for the same reason. The cable plant between PMTs and TFECs is relatively modest, but given the premium on space in this region we will use miniature coaxial cable, HV twisted pair, and miniature preamp power supply cable for a total cross section of

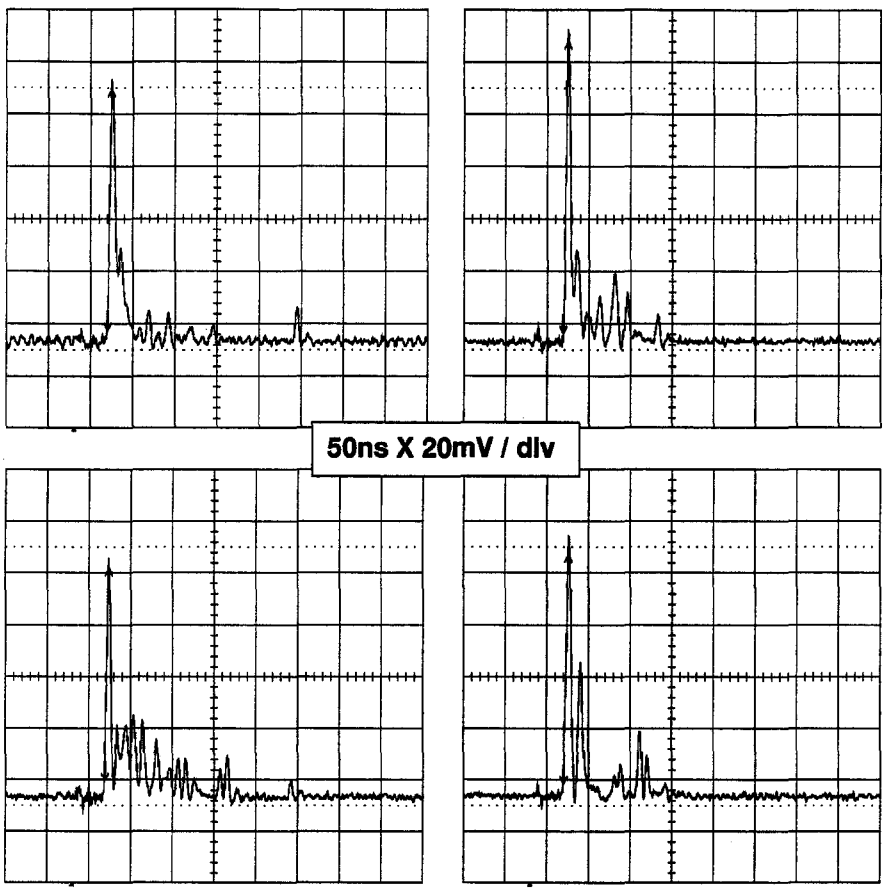

Figure 16: Sample PMT pulses at the shaper/line driver outputs of the prototype preamp/shaper. The PMT is operating at 1200 V in the earth's field. Time between cursors in all cases is 5.5 ns+/-.25 ns. This risetime is dominated by the LED emission process - impulse response risetime is of order 3 ns. Clusters of late photo-electrons from the LED source can be seen straggling in after the peak.

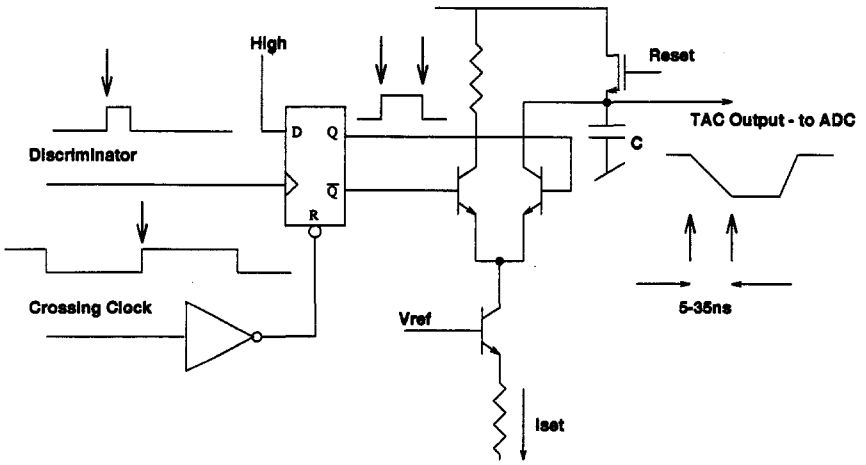

Figure 17: Width Generator schematic.

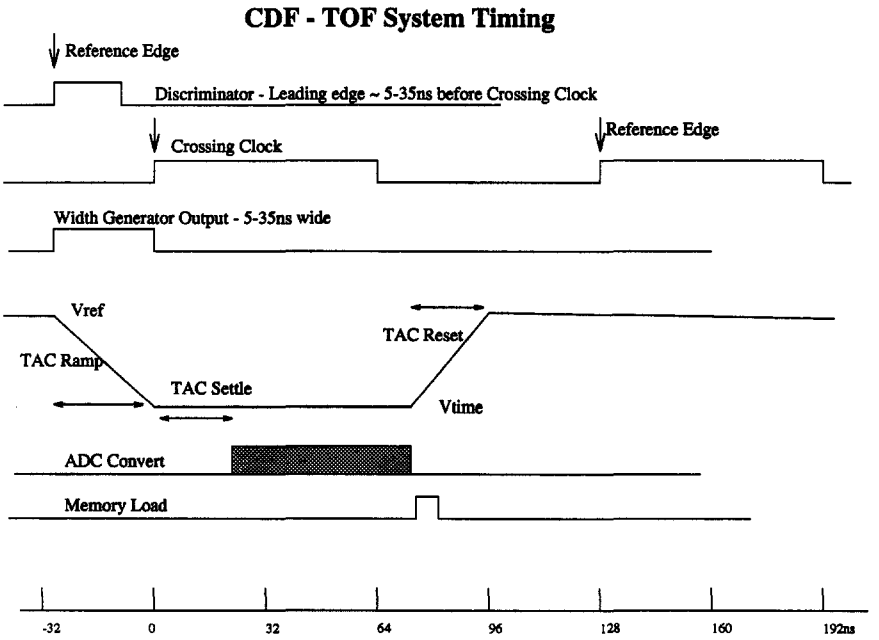

Figure 18: Timing diagram of the TOF measurement process from discriminator to memory write. Note that there is a guaranteed minimum pulse width of about 5 ns for any legitimate hit in order to avoid the non linear TAC response region near zero time.

less than 3 mm^2 per PMT. Depending upon the final mechanical arrangement, it may also be possible to bus the HV and LV power and thus save some space. The analog cables from the TFECs to the counting room need to be of a more normal size in order to avoid significant attenuation and dispersion over this much longer cable run. Thus we must budget for 864 RG58 class cables traveling from the endwall crates to the counting room. The actual position and organization of the digitizing/memory cards in the control room will be determined by trigger considerations and can not yet be sensibly settled.

7.5 Electronics Cost Estimate

A preliminary cost estimate has been made on the basis of the present block diagrams. This cost estimate assumes 216 x 2 PMTs (432) total and 27+ channels per TFEC or CHMB (Counting House Memory Board). To this we have added a bit over 10% spares to get 480 PMT bases and 20 boards of each type. Costs for electronics engineering are not included since we assume this engineering will be provided by the University of Pennsylvania.

Cost Estimate - TOF Electronics 3/20/95

PMT Base & Preamp	per PMT	per board	Totals	Basis
Volt Divider Parts	$4.50			Eng. Est.
Preamp/Shape Parts	$5.50			Eng. Est.
PC Tooling		$2,500.00	$2,500	Eng. Est.
PC Prototype		$1,500.00	$1,500	Eng. Est.
PC Board (Kapton)	$10.00			Eng. Est.
Assy/Test	$5.00			Eng. Est.
LV power			$1,200	$25/Watt
Total	$25.00		$12,000	
On Det. TFEC Digitizer Card				
Discriminator (CFD)	$16.00		$7,680	Parts
TAC Width Gen	$9.00		$4,320	Eng. Est.
ADCs	$30.00		$14,400	Parts
Buffers / Drivers	$5.50		$2,640	Parts
Interface Parts		$100.00	$2,000	Est.
PC Prototype		$2,500.00	$2,500	Eng. Est.
PC Tooling		$3,500.00	$3,500	Eng. Est.
PC Board		$250.00	$5,000	Eng. Est.
Assy/Test		$250.00	$5,000	Eng. Est.
Misc.			$10,000	Eng. Est.
Counting House Memory Board (CHMB)				
Receivers	$5.50		$2,640	Parts
Memory	$25.00		$12,000	Parts
Interface Parts		$125.00	$2,500	Est.
PC Prototype		$3,000.00	$3,000	Eng. Est.
PC Tooling		$3,500.00	$3,500	Eng. Est.
PC Board		$300.00	$6,000	Eng. Est.
Assy/Test		$250.00	$5,000	Eng. Est.
Crate/Power Supply			$20,000	Eng. Est.
Cables				
PMT Signal to TFEC	$30.00		$14,400	1$/ft.
PMT HV	$15.00		$7,200	0.50$/ft.
P/A LV	$7.50		$3,600	0.25$/ft.
TFEC to CHMB (2 cables)	$125.00		$60,000	0.25$/ft.
ADC to Trigger		$60.00	$1,200	$2/ft.
Totals			$195,280	

8 Trigger Considerations

It is desirable that simple algorithms make the kaon tag available to the trigger at Level 3. This TOF information would be used in association with CTC reconstructed tracks, especially those associated with secondary vertices. In practice this technique would have to associate tracks with a primary vertex position, determine the time of the event (t_0) from the prompt tracks and compute the TOF for each particle including those from secondary vertices using the global t_0, their momenta, and path length as measured in the CTC. Knowing the momentum and the TOF one can estimate the particle mass. Another simple technique might be to find the relative times of particles associated with a secondary vertex of a b-jet. Here the overall calibration is not an issue, just the relative times of arrival of the various particles and their momenta. It may be possible to combine such measurements with information from new trigger hardware such as the new CDF track processor (XFT) and secondary vertex processor (SFT) to obtain tagged kaon information from a secondary vertex at Level 2. Detailed studies are required to understand what new physics CDF would gain from such a trigger.

9 Cosmic Ray Tests of a Prototype TOF Counter

To optimize the performance of TOF counters of the geometry we plan to use in the CDT location we have begun testing prototype counters at Fermilab. The first three prototype counters are 40 × 40 mm in cross section and approximately 300 cm long. The scintillator for two counters was Bicron BC408, for the other Bicron BC404, all were cut and polished at the factory. The counters were wrapped in foil and black paper. We first tested both the BC404 and the BC408 with R2490-05 Hamamatsu PMT glued on each end. This tube is a 2" diameter version of a fine mesh dynode tube similar to that which we plan to use in the final system. Its performance both in and out of a magnetic field has been well studied and documented[9]. The photocathode diameter of the R2490 is 38 mm which means that it accepted 70% of the light produced in the bar. We also tested the BC408 bar with two Hamamatsu R5946 PMT's. This tube is 1.5 inches in diameter with a 27 mm diameter photocathode and is small enough to be used in the CDT location. Finally, we tested one BC408 bar with CPC light concentrators (more on this later) and two Hamamatsu R5946 PMT's. The test setup is shown schematically in Figure 19. Cosmic ray trigger counters above and below the TOF counter were mounted on a movable track so they could be positioned along the length of the TOF counter. For most of the results discussed here the top trigger counter used a 40 × 20 × 50 mm piece of BC408 scintillator and was equipped with an RCA8575. The scintillator was oriented with the 20 mm dimension along the length of the 3 m counter and the PMT was horizontal. The lower trigger counter used a 40 × 40 × 50 mm piece of BC408 scintillator read out with a Hamamatsu R2490-05 PMT. The bottom counter was oriented such that the

50 mm dimension and the PMT were vertical. The anode signals from all four PMTs were split with a resistive divider. One split signal was connected to an Ortec model 934 constant fraction discriminator, the other to a LeCroy 2248 CAMAC ADC. The signals from the constant fraction discriminator were passed through 64 ns of delay and then were connected to the stop inputs of a LeCroy 2228A CAMAC TDC (50 ps least count). The coincidence of the trigger counters provided the common start to the 2228A. The relative timing of the trigger counters was adjusted so that the counter with the R2490-05 always determined the timing of the coincidence. Figure 20 shows a typical pulse height distribution from one of the PMT's from a cosmic ray run with 4000 triggers. A run with this many triggers takes about 20 hours. The top two plots corresponds to the two trigger counters, ADC C2 the bottom and ADC 1 the top. Clear minimum ionizing peaks are observable. The bottom two plots show pulse height distributions for PMT's on the 3 m counter, the left tube (ADCL) and the right tube (TDCR). Again, minimum ionizing peaks are apparent. To measure the resolution we use only those events in which the ADC values are within the minimum ionizing peaks. For this run, we required "MIP" cuts of 400 < ADC C1 < 800, 400 < ADC C2 < 800, 100 < ADCR < 400 and 90< ADCL < 390 counts.

To determine the best scheme for measuring the arrival time of particles at the TOF array we have tried several methods of combining the measured times from the PMT's on each end. A typical set of time distributions for the left and right PMTs of the 3 m counter are shown in Figure 21 after "MIP" cuts. For this run the top trigger counter was placed at the middle of the 3 m BC404/R2490 counter. We observe similar time values from the two PMT's as expected. The RMS widths of the distributions are 3.2 and 2.8 counts, respectively. A TDC count corresponds to 50 ps so the time resolution of an individual PMT is about 150 ps. The bottom left plot of Figure 21 shows the distribution if we use the average times of the left and right PMT's. The RMS width is now 2.3 counts or 115 ps. The improvement over single tube measurements is presumably due to both the improved photoelectron statistics from both tubes and because averaging the left and right times reduces time smearing due to variations in the position of the cosmic ray as it passed through the the trigger counters.

When the time measurement is limited by the photoelectron statistics, we expect that the time resolution (σ_t) is related to the pulse height (ADC) in the PMT by $\sigma_t \propto 1/\sqrt{ADC}$. By weighting each time measurement by the pulse height in that PMT we should be able to minimize the width of the resulting combined time distribution. The bottom right plot of Figure 21 shows the distribution of the average of the times measured by the PMT's on each end of the 3 m counter weighted by their pulse heights. The RMS width is 2.4 counts, which is nearly identical to that of the simple average. This is not unexpected for a run with the trigger counters at the middle of the 3 m counter because two tubes have almost the same pulse heights at this location. We note however that this technique does improve the resolution over the simple average when the cosmics pass through locations away from the middle

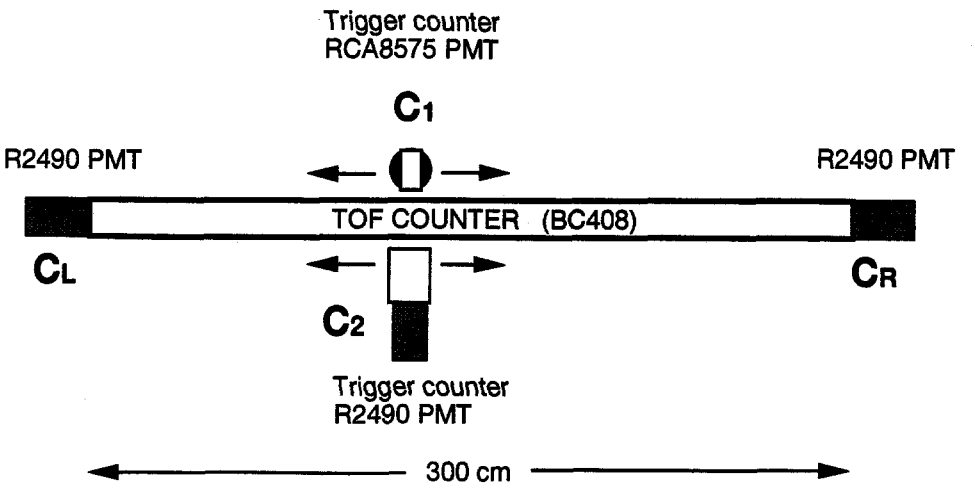

Figure 19: Prototype TOF counter and cosmic ray test setup

of the counter. Superimposed in the plot is the result of a Gaussian fit, which gives an RMS width of 2.4 counts (120 ps). Figure 22, and Figure 23 show these time resolutions measured at several locations along 3 m counters fabricated from BC408 and BC404 respectively and instrumented with R2490 PMT's. Figure 24 is a similar plot for the same BC408 bar but instrumented with the smaller R5946 tube. For these figures we used data taken with a small top trigger counter 20 × 40 × 50 mm to minimize trigger counter width effects. We observe that the difference between the trigger counter time and the pulse height weighted average time of the two PMTs exhibits a time resolution of less than 110 ps nearly independent of the position of the trigger counters for both the BC408 and BC404 bars readout with R2490 PMTS. We find no significant difference in performance between BC404 and BC408. The resolution of the BC408 bar instrumented with the R5946 is about 135 ps. In this case we expect the R5946 results to be worse than the results with the R2490 since this tube has a smaller photocathode and collects only about half as much light as the R2490. The fact that the resolution with the R5946 is not $\sqrt{2}$ worse than the R2490 indicates that other significant factors in our test setup other than photostatistics contribute to measured resolution.

Figure 25 is a plot of the difference in arrival time ($t_{diff} = t_{left} - t_{right}$) between PMT signals measured on each end of the BC408/R2490 counter versus the location of the trigger counter. From the slope of this distribution we can measure the effective propagation velocity of scintillation light from cosmic rays as it propagates down the length of the counter. The effective velocity is very close to 15 cm/ns. Figure 26 plots the pulse height (minimum ionizing peak position) of each PMT of the 3 m counter as a function of the location of the trigger counter along the bar. The measured points are nearly straight on the semi-logarithmic scale indicating an exponential decrease

22/09/94 16.09

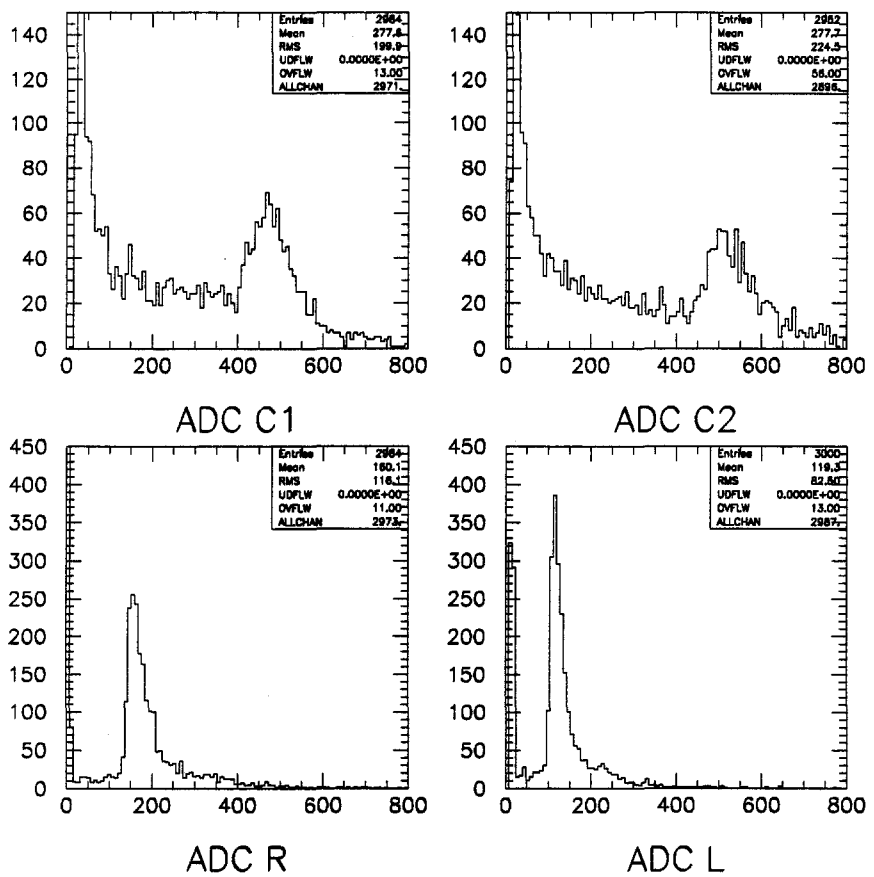

Figure 20: Typical PMT pulse height distribution from a cosmic ray run with 4000 triggers. The top two plots corresponds to the trigger counters, ADC C2 the bottom one and ADC C1 the top one. The bottom two plots show pulse height distributions for PMT's on the 3 m counter, the left tube (ADCL) and the right tube (ADCR). Minimum ionizing peaks are apparent.

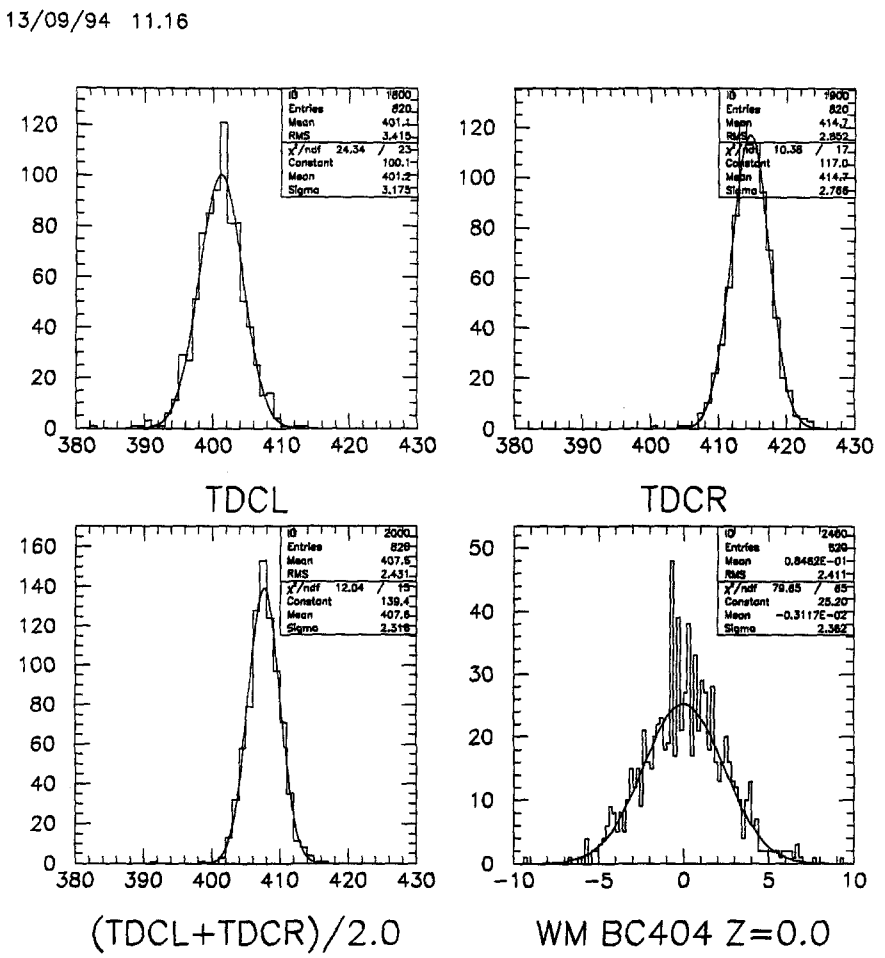

Figure 21: Time distributions for the a) Left PMT b) Right PMT c) sum of the times from both PMTs and d) Weighted average time using both PMTs. Data is from the 3 m long BC404 prototype counter. Tubes are R2490-05, readout via a constant fraction discriminator, and LRS 2228A 50 ps least count TDC

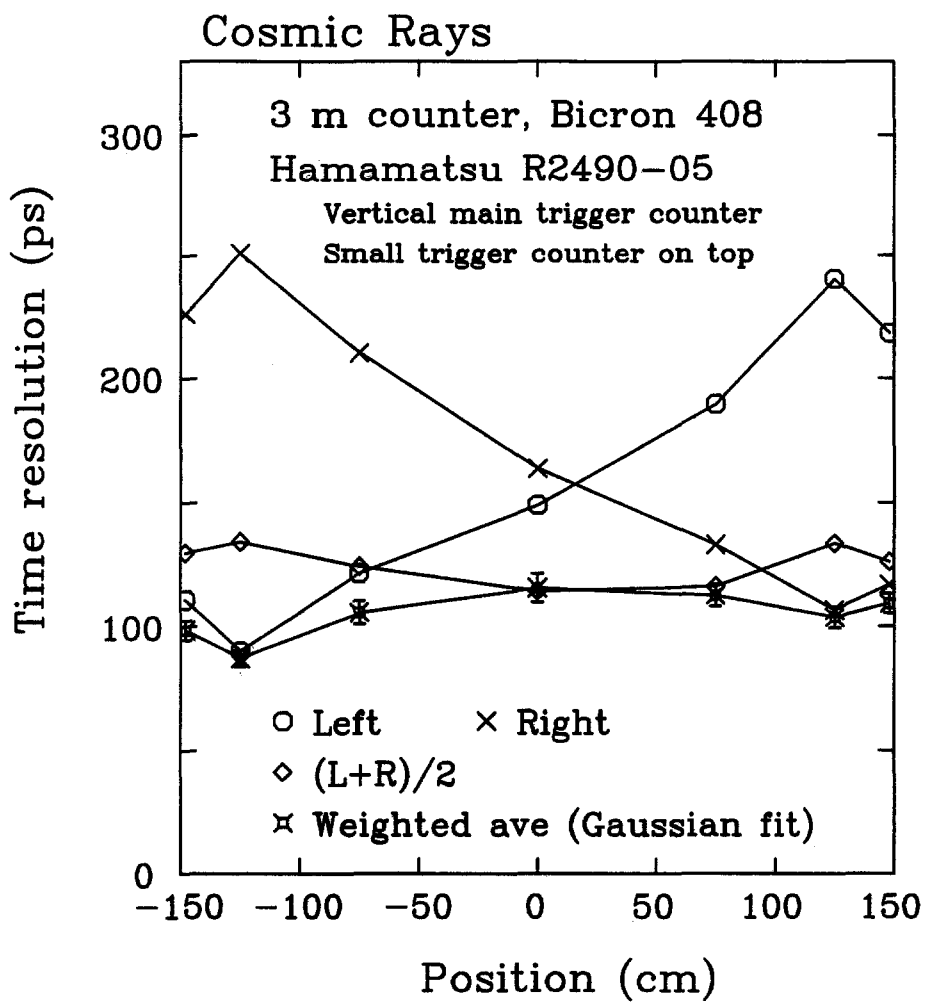

Figure 22: Time resolutions measured at several locations along the 3 m counter. Scintillator is BC408. Phototubes are Hamamatsu R2490.

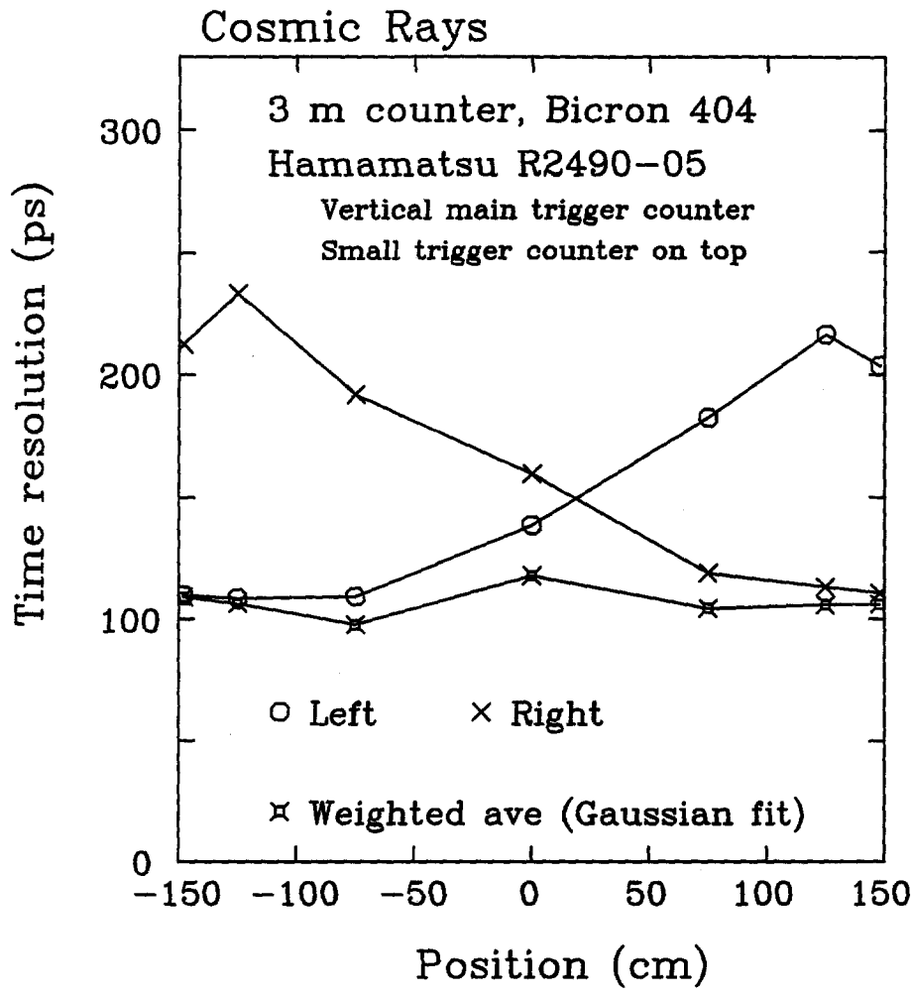

Figure 23: Time resolutions measured at several locations along the 3 m counter. Scintillator is BC404. Phototubes are Hamamatsu R2490.

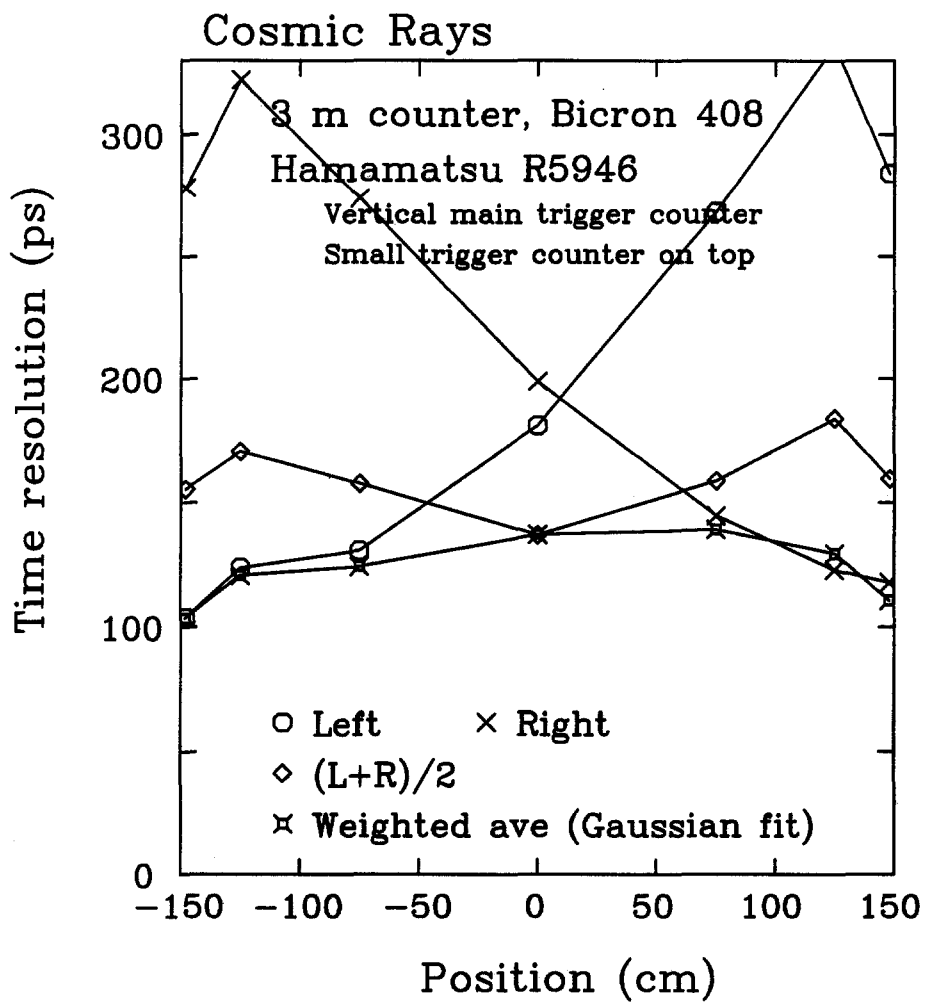

Figure 24: Time resolutions measured at several locations along the 3 m counter. Scintillator is BC408. Phototubes are Hamamatsu R5946.

in pulse height with increasing distance from the PMT. Using three points in the middle, the effective attenuation length of light in the 3 m bar is about 225 cm.

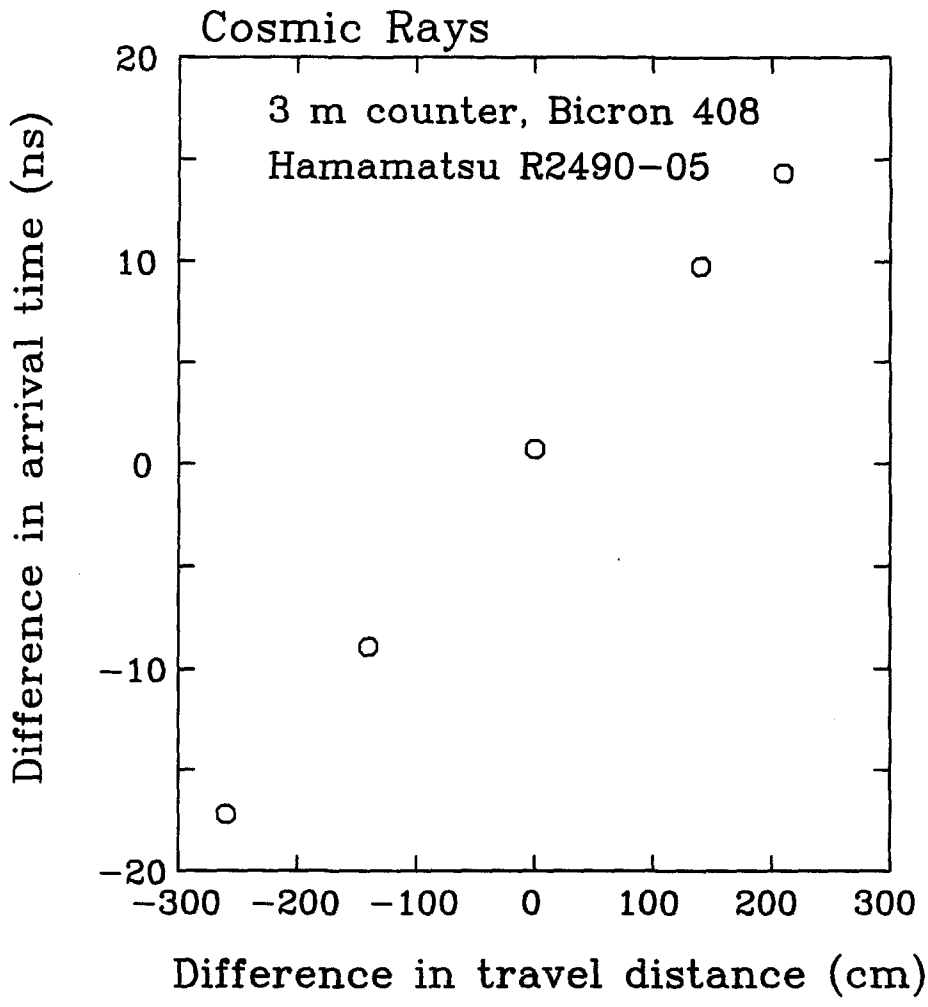

Figure 25: Time difference between PMT's measured at several locations with cosmic rays along the 3 m counter. The slope represents the effective propagation velocity. We find $V_{eff} = 15$ cm/ns.

10 Tests of a Prototype TOF counter with a N_2 laser

To understand to what extent photostatistics limit the prototype TOF counter performance we have done several tests with a N_2 Laser. The laser emits subnanosecond pulses at a wavelength of 430 nm. We connected the laser output via a quartz fiber to 5 ports on the 3 m test counter and to a port on the R2490 trigger counter. The

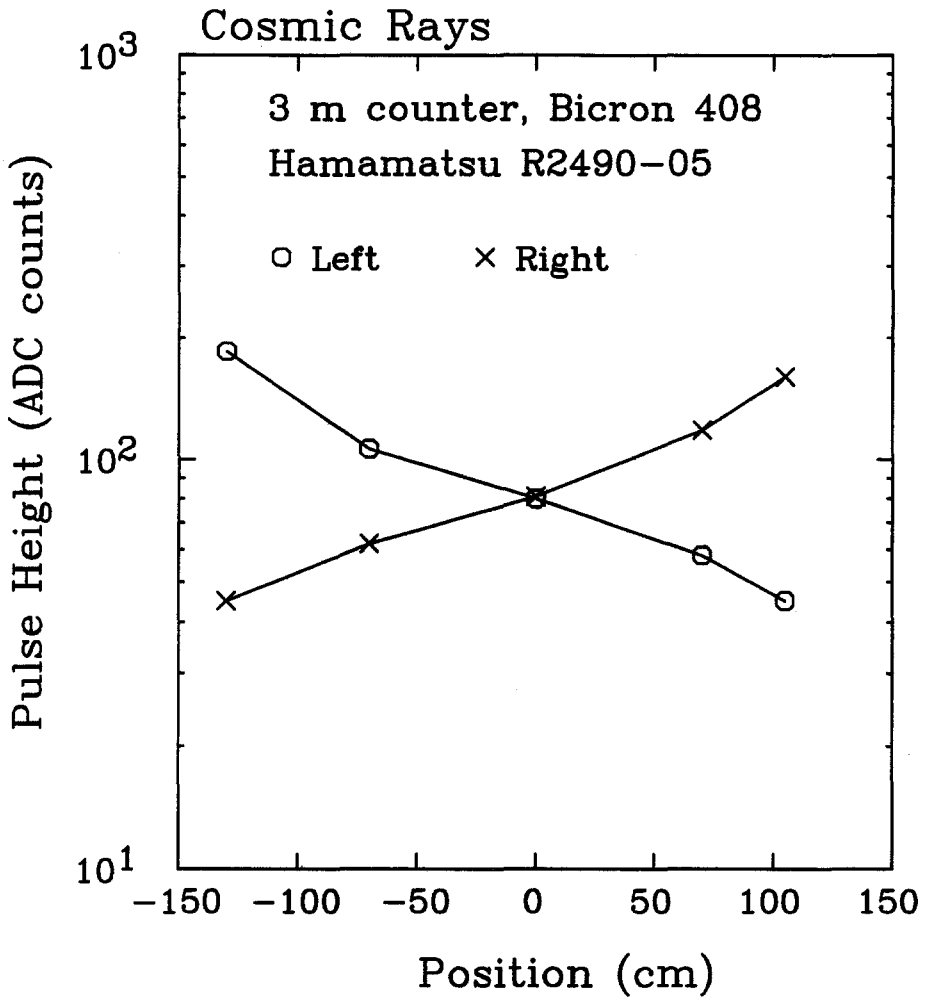

Figure 26: Pulse height (minimum ionizing peak position) of each PMT of the 3 m counter at several locations along the 3 m counter. From this we determine the effective attenuation length of the counter to be 225 cm.

ports are located in the center, near each end, and at the 2 quarter points of the 3 m counter so we can study Z dependent effects. We have varied the amount of light with an attenuator to simulate various pulse heights. The trigger counter pulse height is held constant at about 4 times minimum ionizing. We then study the time resolution of the long counter versus the amount of light observed. Figure 27 shows a plot of the RMS time resolution of the difference in times observed by the trigger counter and the BC408/R2490 3 m counter for the same laser pulse versus the amount of light injected into the center of the 3 m counter. The resolution varies approximately inversely as the square root of the pulse height, suggesting the resolution is dominated by photostatistics.

Figure 28 shows the difference in arrival time of light at the two PMT's of the 3 m long test counter for laser light injected at the 5 ports. The measured propagation velocity agrees well with what was measured with cosmic rays.

Finally, in Figure 29 the pulse height ratio for the two PMT's of the 3 m counter is shown for laser light injected into the center 3 ports. A fit to this distribution gives a measured effective attenuation length of 225 cm in good agreement with that obtained from cosmic rays. To understand this measured attenuation length we modeled the TOF bar with the ray tracing program (GUIDE7 from CERNLIB). Inputting a bulk attenuation length of 380 cm, the index of refraction of the scintillator, and our TOF counter geometry we obtained an effective attenuation length for the counter of 230 cm which is in very good agreement with the measured numbers.

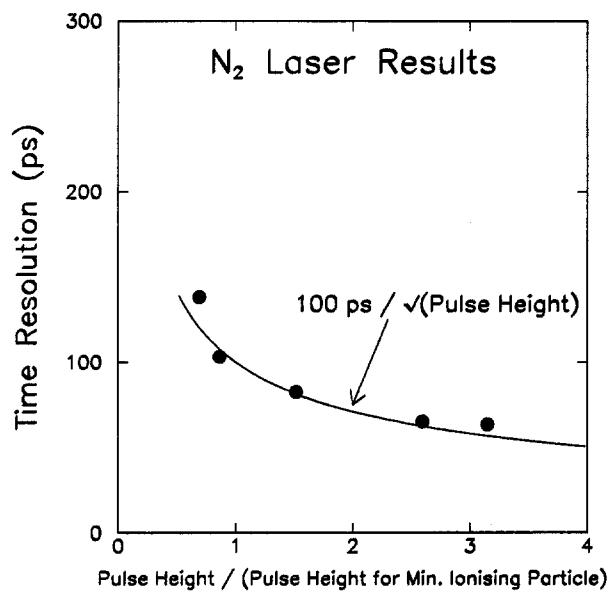

Figure 27: Dependence of Time resolution on amount of laser light. A value of 1 on the ordinate corresponds roughly to the amount of light observed by a R2490 equipped bar for a minimum ionizing particle that passes through the end of the bar near the PMT.

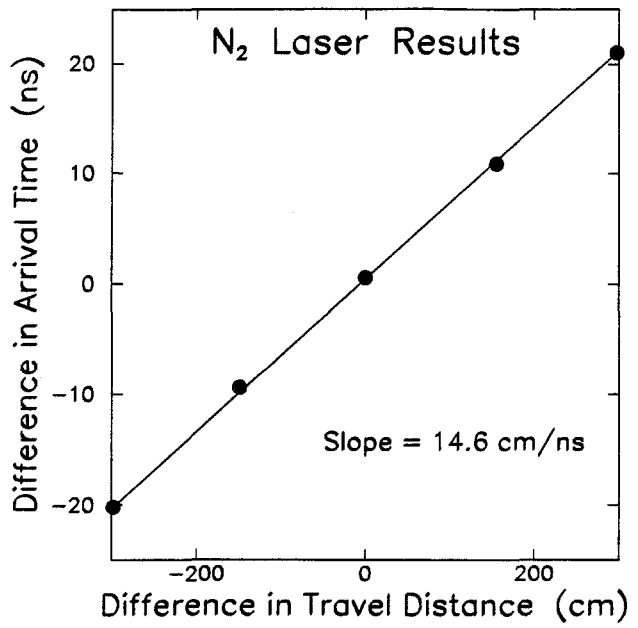

Figure 28: Propagation velocity down the 3m counter measured with N_2 laser.

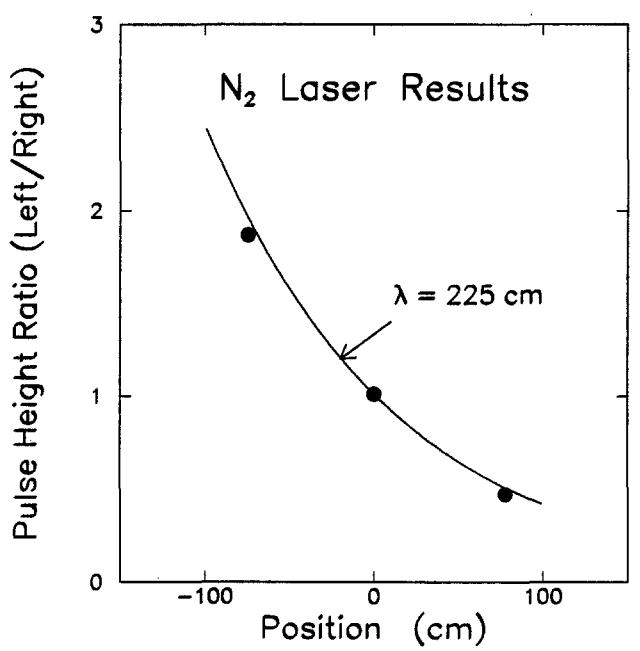

Figure 29: Effective attenuation length of 3m counter measured with laser light

11 Counter Occupancy

To estimate the occupancy of the TOF counters for Run-II we began by looking at the occupancy in typical data events from Run-Ia. We have studied three different scenarios. The first was whether the charged K in $B \to J/\psi K^{\pm}$ decay was associated with another track nearby that would contaminate the TOF measurement on the kaon. The second case involved a study of the opposite side of the $B \to J/\psi K$ events in order to simulate tagging of the kaon from the "other" B for mixing and CP violation studies. The third study involved a large statistical sample of J/ψ events. This sample is a mixture of B and non-B events and characterizes typical B events in the CDF tracking chambers. For this sample we determine the average occupancy over the whole TOF array. The results all give a consistent picture which we discuss later. We then add estimates for additional occupancy due to unreconstructed track, neutrals, and multiple interactions to estimate the TOF occupancy under Run-II conditions.

11.1 Same-side

We estimate the occupancy of the TOF counter array using real data events. We used a sample of $B \to J/\psi K^{\pm}, J/\psi \to \mu^+\mu^-$ events from Run-Ia. Using the measured direction and momentum of the kaons in these events we extrapolate the kaon track to the TOF location and ask how often any other reconstructed track in the event is within ± 2 cm, *i.e.* half the counter width, of the extrapolated track. We include the tracks from the $J/\psi \to \mu^+\mu^-$. With 4 cm wide counters (216 in all) we find that in about 15% of the events, the kaon identification might be confused by the presence of another hit in the same counter. We have studied the occupancy with other choices of TOF counter widths and a summary of results is given in Table 2.

Table 2: Occupancy vs segmentation in $B \to J/\psi K^{\pm}$ events. Column labeled "No extra hits" refers to the percentage of events in which no other charged track was found in the same TOF counter as the $K^{\pm}$. The column label "average occupancy" is the average number of tracks found in the same TOF counter as the $K^{\pm}$.

No. of TOF ctrs.	No extra hits	average occupancy
64	55%	.55
128	76%	0.27
256	87%	0.13
512	94%	0.06

11.2 Opposite Side

Because of the low multiplicity associated with the $J/\psi \rightarrow \mu^+\mu^-$ decay the occupancy estimated in the previous section might be low compared to a more"average" B decay. As a result we have estimated the occupancy in the time-of-flight counters in the region of the "other" B in such events. We studied a sample of 400 $B^\pm \rightarrow \psi K^\pm$ events with an estimated 75 % purity as shown in Figure 30. The "away-side" occupancy was estimated by finding the highest transverse- momentum particle that is at least 135 degrees away in azimuth from the $B^\pm \rightarrow \psi K^\pm$. In addition, this track is required to be inconsistent with coming from the primary event vertex. We treat this track as if it is the kaon from the decay of the "other" b. We find these tracks typically would have hit either one or two TOF counters. If another particle in the event would also have registered a hit in the same counter or counters, the event was considered damaged. Otherwise, the event was considered clean. We found the events in this sample were $(83 \pm 5)\%$ clean. A separate consideration is whether any counter struck by the high momentum particle was clean. For this case, the events are $(87 \pm 5)\%$ clean.

11.3 Random J/ψ Events

Next we have studied a sample of random $J/\psi \rightarrow \mu^+\mu^-$ events in the CDF data as an estimator of occupancy. Shown in the top of Figure 31 is the average number of counters hit per event. With very loose selection criteria and taking into account the curvature of the tracks we find a mean of about 23 counters struck. Shown in the middle of the figure is the number of counters on average that have more than one track striking the counter. We find a mean of 3.5 counters per event. The ratio is shown in the bottom figure and is a measure of the average occupancy in this type of event, which we find to be about 13%.

11.4 Occupancy in Run-II

There are additional sources of hits in the counters not included in the studies described so far. The studies described above are based upon reconstructed CTC tracks. By scanning event display pictures, we estimate the tracking finding program misses about 0.5 tracks per event that originate somewhere near the primary vertex and appear to strike the TOF counter location. In addition we observe events with unreconstructed tracks originating far from the primary that loop through the location of the proposed TOF array. (e.g. backscatter from the coil/calorimeters) Fortunately these are relatively rare. We also observe evidence for neutrons in the CTC, and estimate an additional 0.5 hits per event from this source. Next, since these events contain about 20 photons on average and the scintillator of the TOF array corresponds to about 10% of a radiation length, we can expect another 2 TOF counter hits due to conversions. Including these effects we expect an average occupancy of

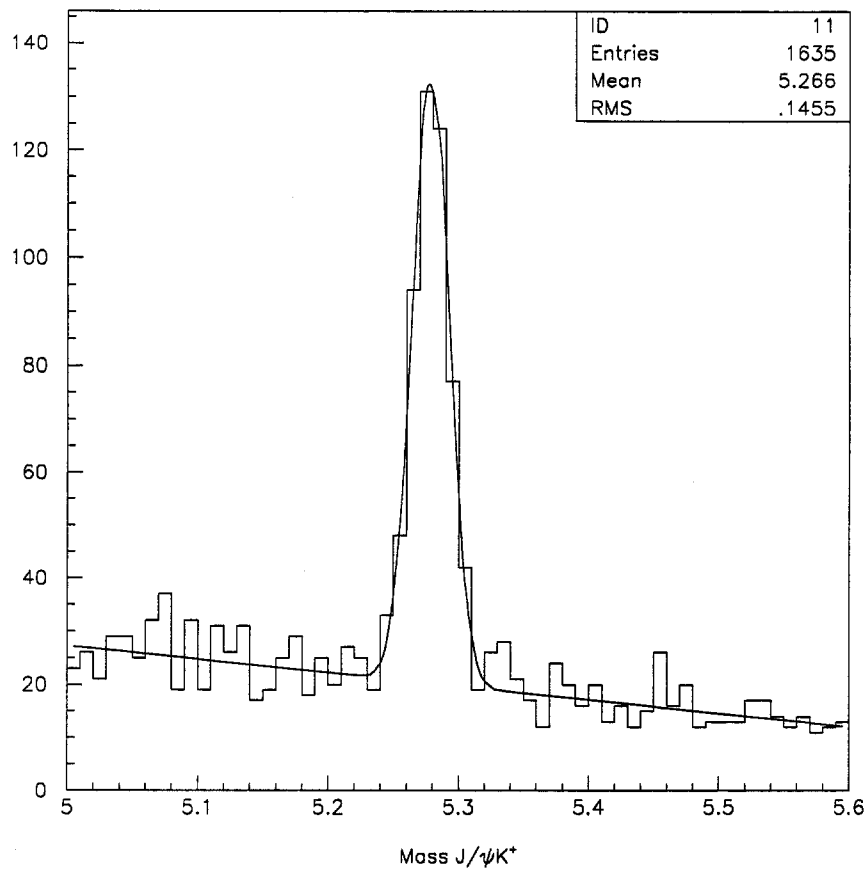

Figure 30: Sample of $B \to J/\psi K^{\pm}, J/\psi \to \mu^+\mu^-$ events.

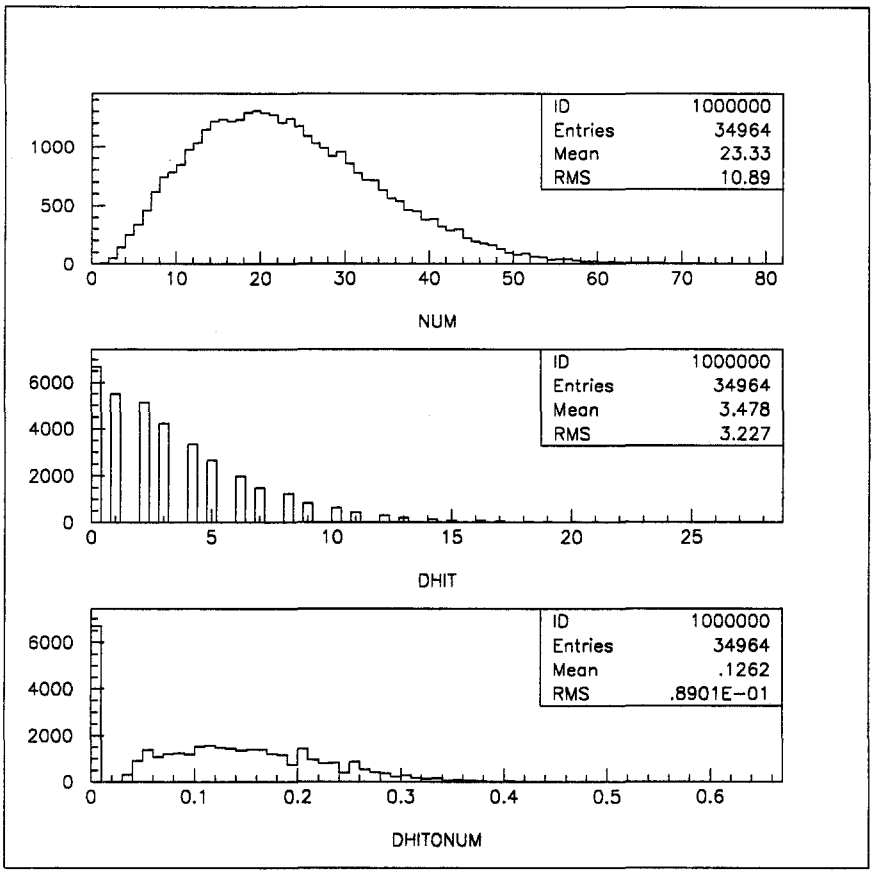

Figure 31: The top figure shows the average number of counters struck by a charged track in random J/ψ events. The middle figure shows the number of counters that have been struck by more than one track per event. The bottom plot shows the ratio. The observed mean indicates an occupancy of about 13% in this type of event.

16% at luminosities corresponding to those typical of Run-Ia. Next we note that the additional minimum bias interactions expected in each crossing for Run-II will further increase the occupancy in the TOF. We have estimated this contribution by overlaying minimum bias events on the random J/ψ event sample. When combined with the various studies described above these results using CDF data lead us to expect an occupancy approaching 35% at a luminosity of 1×10^{32} cm^{-2}s^{-1} with a crossing time of 396 ns and an occupancy of about 30% at a luminosity of 2×10^{32} with a crossing time of 132 ns.

Next we note that in many cases TOF counters with multiple hits will still yield useful particle ID information. As an example, if a single counter is hit in the middle by both a high momentum and a low momentum particle, we will correctly measure the arrival time of the high momentum particle. Similarly, if two particles of equal momentum strike the same counter at different Z values, we will make an arrival time measurement of each but with only one PMT. In this case the time resolution will be degraded but typically by less than 35%. Thus we conclude that from an occupancy standpoint, the counter width of 4 cm we chose on the basis of photon collection is a reasonable choice. Making the counters narrower in ϕ would not reduce the occupancy linearly since low momentum particles enter the array at angles such that they often pass through more than one counter. Dividing the counters in two at Z = 0 is a possibility since it would nearly half the occupancy. In addition, the time resolution for shorter counters would improve somewhat extending the momentum range. However such a change would lose about 10% of the coverage of the array by placing phototubes at Z = 0 and would nearly double the cost of the system. Dividing the counters at Z = 0 and using a single tube is another option but that would mean that we could no longer determine the Z position with the TOF counter. Our study of these issues is still in progress. In any case we find that the kaon tag efficiency should remain high at the occupancies in b-events we expect for Run-II.

12 Determination of t_0 and an Algorithm for Kaon Tagging

Because of the finite bunch length of the Tevatron, the Z vertex location alone is insufficient to determine the time of the collision (t_0) to the required precision (*i.e.* small compared to 100 ps). We plan to determine t_0 event-by-event using the tracks that reach the TOF system and that have been reconstructed in the CTC. A particle moving in a uniform magnetic field follows a helical path described by

$$p \cos \lambda = 0.3 B \rho \tag{3}$$

where $p \cos \lambda = P_T$ the transverse momentum of the particle in GeV/c, $\lambda = \arctan(Z/R)$ is the dip angle, B is the magnetic field in Tesla, and ρ is the radius of curvature in

meters. One can show that the path length (s) traversed by the particle as it travels out to a radius (R) is

$$s = \sqrt{\left[2\rho \arcsin\left[\frac{R}{2\rho}\right]\right]^2 + [R\tan\lambda]^2} \tag{4}$$

If one uses this path length and assumes the particle is a pion, then one can compute the flight time, subtract that from the time measured in the TOF and get an estimate of the collision time $t_0^i(Z)$ for each track that passes through the TOF counter array. This is given by

$$t_0^i(Z) = t_{TOF}^i(Z) - \frac{s}{\beta c} \tag{5}$$

where $t_0^i(Z)$ is the t_0 measured by the ith particle and the Z indicates time has been corrected for the propagation delay down the counter which is a function of the Z of the impact point of the particle at the TOF array.

The particle velocity is given by

$$\beta = \frac{P}{\sqrt{P^2 + M_\pi^2}} = \frac{P_T}{\cos\lambda\sqrt{(P_T/\cos\lambda)^2 + M_\pi^2}} \tag{6}$$

We expect a peak at a common t_0 from tracks which were correctly assigned the pion mass. Cutting at about $\pm 2\sigma$ on the resulting peak and calculating the resulting average yields t_0. Figure 32 shows number of tracks that reached the location of the proposed TOF system in $B \rightarrow J/\psi K^\pm, J/\psi \rightarrow \mu^+\mu^-$ data. In this case we have applied minimum P_T, track quality, and impact parameter cuts to assure a clean sample of tracks. The mean number of tracks passing these cuts is 13.8 / event. Assuming an individual counter time resolution σ_t^i of 125 ps, and using an the average number of tracks from Figure 32 of 13.8 tracks per event results in a t_0 determined to a precision of about $\sigma_{t0} = 125/\sqrt{13.8} = 34$ ps. Tracks with measured t_0^i differing by more than 2 σ_{t0} would be treated as non-pion candidates. In particular, one would compute t_0 for those tracks assuming the kaon mass and determine if with that assumption the t_0^i now agreed with the event t_0 within, e.g. $\pm 2\sigma$. If this condition were satisfied then the track would be assigned the kaon mass and its t_0^i would be included in the computation of the overall event t_0. The process is continued until each track is assigned a most probable mass or declared unusable. We plan to test this algorithm via Monte Carlo in the near future.

13 Track Z Uncertainty at 1.4 Meters

A determination of the flight time in CDF will require an accurate measurement of Z position of the charged track at the point where it enters the scintillator bar. The uncertainty on the Z measurement will result in a smearing of the flight time, hence

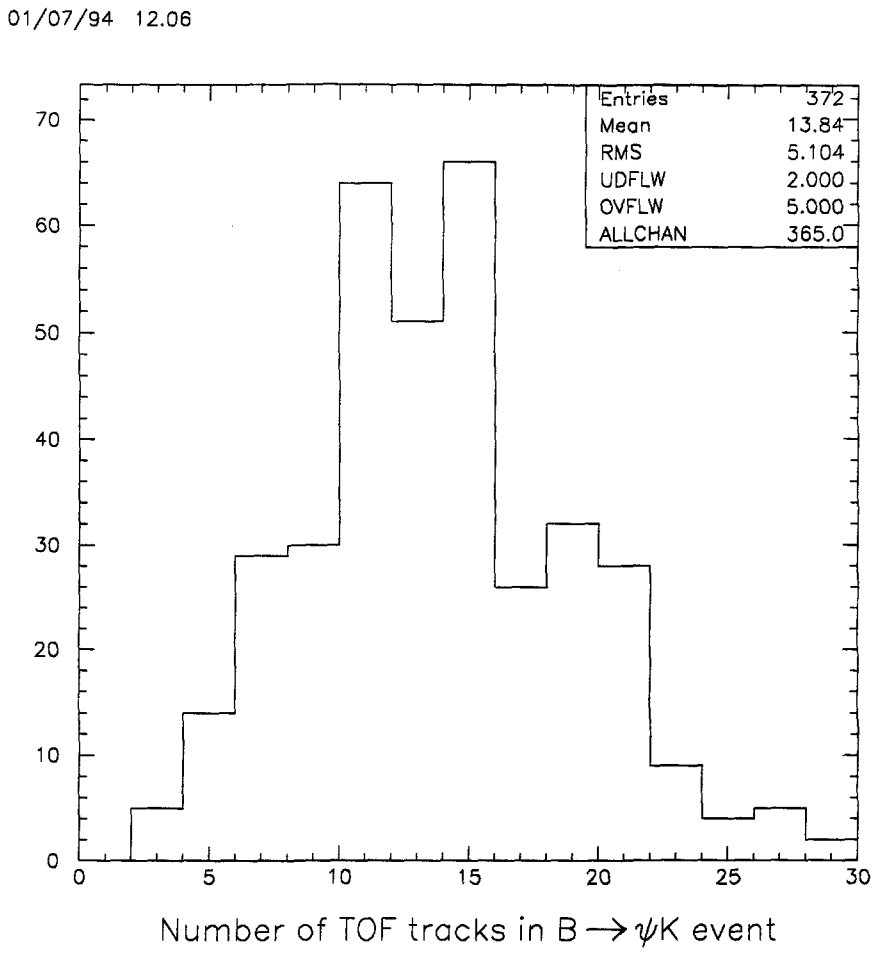

Figure 32: Number of tracks reaching TOF system in $B \to J/\psi K^{\pm}, J/\psi \to \mu^+\mu^-$ events.

reducing the system performance. In principle the Z position where a charged track crosses a bar can be obtained from the time difference between the arrival of the light pulse at each PMT. This only works if the counter has a single hit. In addition, the resolution in this case is only about $\Delta Z = (.125 \text{ ns})\sqrt{2}(15 \text{ cm/ns}) = 2.65$ cm. A better measure of the Z position can be obtained from the CTC track information. We have written a routine that extrapolates the $Z0$ track parameter to the 1.4 meter radius of the TOF system and correctly propagates the errors. The typical Z uncertainty is shown in Figure 33, and is about 0.5 cm. The shape of the distribution is peaked around 0.5 cm, but a small but long tail exists and continues beyond the end of the plot. This plot indicates we should probably require agreement between the TOF counter Z and the Z determined by the CTC track. In addition we should add a term $\sigma_{\Delta Z} = 33$ ps in quadrature into the expected time resolution in B0 to take into account uncertainties in the flight time due to the uncertainty in Z position of the particle as it passed through the TOF counter.

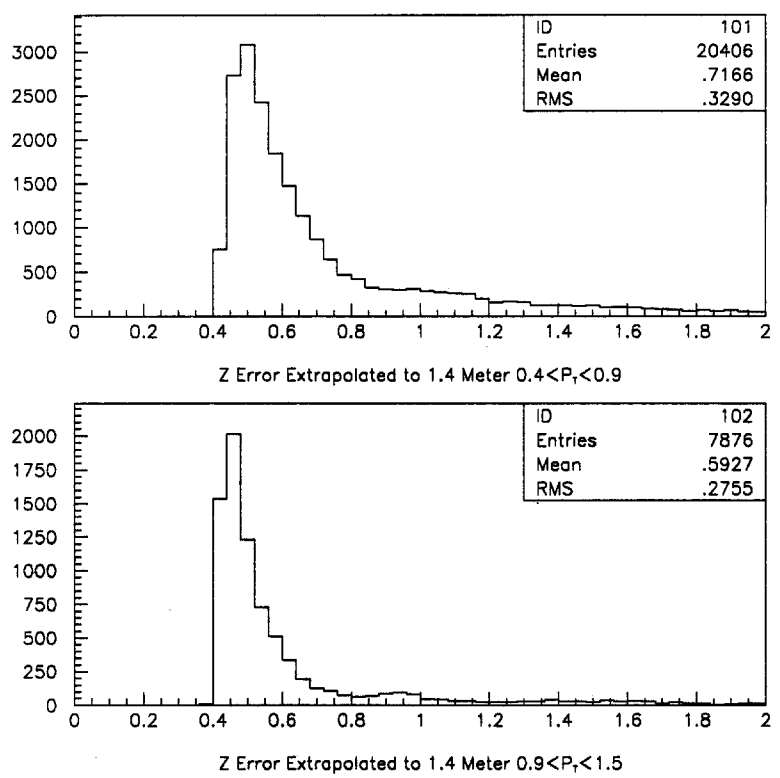

Figure 33: The $Z0$ uncertainty extrapolated to 1.4 meters for two different track P_T ranges.

14 Expected Time Resolution for the Final TOF System

The lowest set of points in Figure 22 show the resolution of the time difference between the pulse height weighted average of the 2 PMTs on the BC408/R2490 3m counter and the trigger counter time. The resolution is about 110 ps and is nearly independent of where the particle passes through the counter. Similarly Figure 24 shows a plot of the same quantity for the same BC408 bar but instrumented with R5946 PMTs. In this case the resolution is about 135 ps near the middle of the bar and improves somewhat near the ends. Using these resolutions, the measured trigger counter resolution, the estimated contribution due to the finite width of the trigger counter, and the expected t_0 accuracy in the actual experiment we can estimate the resolution the final system should attain.

The pulse height weighted time difference plotted in Figure 22 is

$$\Delta t = \frac{A_L t_L + A_R t_R}{A_L + A_R} - t_{C2} \tag{7}$$

where A_L and A_R are the pulse heights of the Left and Right PMT as measured with the ADC's, t_L and t_R are the times measured in the TDC's for the Left and Right Counter and t_{C2} is the time measured in the trigger counter C2. From this formula we can write down an expression that includes the various contributions to the observed resolution.

$$\sigma_t^2 = \frac{A_L^2}{(A_L + A_R)^2}(\sigma_L^2 + \sigma_{TDC}^2) + \frac{A_R^2}{(A_L + A_R)^2}(\sigma_R^2 + \sigma_{TDC}^2) + \sigma_{C2}^2 + \sigma_{width}^2 \tag{8}$$

where σ_L , σ_R and σ_{C2} are the expected time resolutions of the Left, Right, and trigger (C2) due to photostatistics and the transit time spread of the tube. In what follows we assume that the tubes have identical performance ($\sigma_L = \sigma_R$) and that the intrinsic resolution due to photostatistics scale as $\sqrt{A}$ where A is the pulse height. If we define σ_{PS} to be the expected time resolution when the particle passes through the center of the 3 m counter with observed pulse height A_C then $\sigma_L = \sqrt{A_C/A_L} \times \sigma_{PS}$ and $\sigma_R = \sqrt{A_C/A_R} \times \sigma_{PS}$. Similarly, σ_{TDC} is the RMS measurement error due to nonlinearity from the LRS 2228 TDC. We also note that this term does not contribute to the trigger counter time resolution since the trigger counter C2 was used to provide the common start for the TDC. The term σ_{width} term is included to take into account the time smearing due to the finite width of the trigger counter. For this case the trigger counter width was 2 cm, using the measured propagation velocity in the 3 m counter of 15 cm/ns corresponds to $\sigma_{width} = 38.5$ ps. Rewriting the above equation in terms of σ_{PS} we get:

$$\sigma_t^2 = \frac{A_C}{A_L + A_R}\sigma_{PS}^2 + \frac{A_L^2 + A_R^2}{(A_L + A_R)^2}\sigma_{TDC}^2 + \sigma_{C2}^2 + \sigma_{width}^2 \tag{9}$$

To get a feeling for the contribution due to photostatistics we can examine the case where the particle passes near the center of the counter so that $A_L = A_R = A_C$. Again, as mentioned above, we assume that all tubes have equivalent performance for the same number of observed photons then this equation simplifies to:

$$\sigma_t^2 = (1/2)\sigma_{PS}^2 + (1/2)\sigma_{TDC}^2 + \sigma_{C2}^2 + \sigma_{width}^2 \tag{10}$$

or

$$\sigma_t^2 = (1/2)\sigma_{PS}^2 + \sigma_X^2 \tag{11}$$

where now we use the symbol σ_X represent all contributions to the resolution except photostatistics. We have measured σ_t for two cases, the BC408 bar instrumented with R2490 tubes and with R5946 tubes. With the assumptions mentioned above, the two measurements should only differ because the R5946 collects less light than the R2490, then we can use that information to estimate the contribution to the resolution from photostatistics and from "everything else". In particular we expect the resolution component due to photostatistics and *tts* to scale like the square root of the number of photons collected and therefore like the square root of the photocathode area.

Using $\sigma_t = 110$ ps for the R2490 case and $\sigma_t = 135$ ps for the R5946 gives us the following two equations:

$$110^2 = (1/2)\sigma_{PS_2490}^2 + \sigma_X^2 \tag{12}$$

and

$$135^2 = (1/2)\sigma_{PS_5946}^2 + \sigma_X^2 = (1/2)(area\ ratio)\sigma_{PS_2490}^2 + \sigma_X^2 \tag{13}$$

The R5946 has a 27 mm diameter photocathode compared to the 38 mm photocathode of the R2490 so the area ratio is $(38^2/27^2) = 1.98$.

Solving these equations yields $\sigma_{PS_2490} = 112$ ps and $\sigma_{PS_5946} = \sqrt{1.98} \times \sigma_{PS_2490} = 158$ ps. Solving for "everything else" gives $\sigma_X = 76$ ps.

This number is in good agreement with our estimate of σ_X based upon adding each measured or estimate contribution to σ_X in quadrature. Namely we expect

$$\sigma_X^2 = (1/2)\sigma_{TDC}^2 + \sigma_{C2}^2 + \sigma_{width}^2 \tag{14}$$

To measure the trigger counter resolution we have performed the following test. We fabricated two identical trigger counters and arranged them as show in Figure 34. Each trigger counter had a 40 × 40 × 50 mm piece of BC408 glued to an R2490-05 tube. The relative timing of the counters was arranged so the bottom counter

determined the coincidence time. The coincidence provided the START signal for TDC. Figure 35 is a plot of the arrival time measured with the 2228A TDC for the top counter when both counters were required to have pulse heights in the minimum ionizing peak. A gaussian fit gives $\sigma_{meas} = 1.7$ counts = 85 ps. The contributions to this measured resolution are expected to be given by $\sigma^2_{meas} = \sigma_1^2 + \sigma_2^2 + \sigma^2_{TDC}$, where σ_1 and σ_2 are the contributions from photostatistics from trigger counter 1 and 2 respectively. Assuming $\sigma_1 = \sigma_2$, and using the measured value of $\sigma_{TDC} = 17.7$ ps gives $\sigma_1 = \sigma_2 = 59$ ps.

Using $\sigma_{TDC} = 17.7$ ps, $\sigma_{C2} = 59$ ps, and $\sigma_{width} = 38$ ps gives $\sigma_X = 71$ ps in good agreement with the value estimated above from Figure 22 and Figure 24.

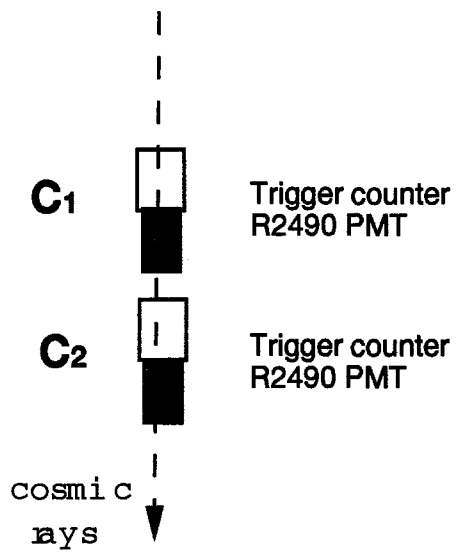

Figure 34: Setup for trigger counter resolution

Finally, we can estimate the resolution we expect for the final system in B0. In this case, assuming we use the R5946 and make no improvements in the light collection efficiency beyond what was obtained in the prototype counter then we expect:

$$\sigma_t^2 = (1/2)\sigma^2_{PS_5946} + (1/2)\sigma^2_{TDC} + \sigma^2_{to} + \sigma^2_{\Delta Z} \tag{15}$$

or

$$\sigma_t^2 = (1/2)158^2 + (1/2)17.7^2 + 34^2 + 33^2 = 122^2 \tag{16}$$

Thus assuming we make no improvements beyond the performance obtained in the prototype, then we expect $\sigma_t = 122$ ps using R5946 PMT from the final system in B0 assuming that charged tracks passed through in the middle of a TOF counter.

Since the amount of light observed by a phototube depends exponentially on the Z distance of the PMT from the track, we can substitute in equation 9 $A_L =$

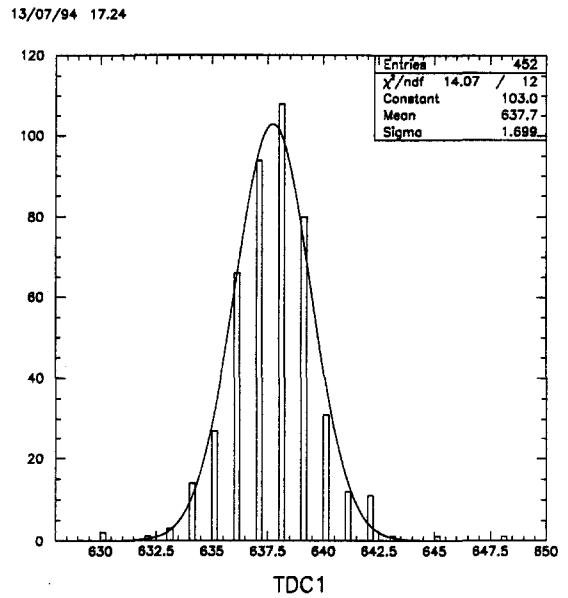

Figure 35: Trigger counter resolution. The width of 1.7 counts corresponds to 85 ps.

$A_C \times e^{-Z/\lambda_{eff}}$ and $A_R = A_C \times e^{+Z/\lambda_{eff}}$, where λ_{eff} is the effective attenuation length (225 cm) (see Figure 26) and Z is a distance from the center of the TOF counter in unit of cm. Then equation 18 becomes:

$$\sigma_t^2 = \frac{1}{e^{Z/\lambda_{eff}} + e^{-Z/\lambda_{eff}}}\sigma_{PS}^2 + \frac{e^{2Z/\lambda_{eff}} + e^{-2Z/\lambda_{eff}}}{(e^{Z/\lambda_{eff}} + e^{-Z/\lambda_{eff}})^2}\sigma_{TDC}^2 + \sigma_{C2}^2 + \sigma_{width}^2 \qquad (17)$$

or

$$\sigma_t^2 = \frac{1}{2\cosh(Z/\lambda_{eff})}\sigma_{PS}^2 + (1/2)(1 + \tanh^2(Z/\lambda_{eff}))\sigma_{TDC}^2 + \sigma_{C2}^2 + \sigma_{width}^2 \qquad (18)$$

Figure 36 shows the expected resolution vs Z position calculated from this formula for the R5946 (solid line) and for the R2490 (dashed line). As can be seen, the expected time resolution for a TOF system based upon the R5946 is always below 122 ps. A TOF counter system with the same light collection efficiency as the R2490 could achieve a resolution in B0 of $\sigma_t < 93$ ps. We are working on schemes to improve the light collection efficiency of the 1.5 inch tube. With Hamamatsu, we are developing rectangular 1.5 inch PMT's with larger photocathodes This should fit in the available space and capture 43% of the light vs 37% for the R5946. Similarly, by using the GUIDE7 optical ray tracing program described above we have designed refractive Circular Parabolic Concentrators[6] as light focusing systems to focus more of the useful light on the photocathode of the 1.5 inch tubes. The idea is to collect more of the small angle "early" photons at the expense of photons that arrive later in

time. We have fabricated concentrators optimized to collect light that arrives in the first 5 ns. The concentrators are 5 cm long and made from machined and polished Lucite. With these concentrators we can collect nearly as many early photons on the R5946 photocathode as are collected by the R2490. Timing measurements with a 3 m bar using cosmic rays are in progress. Preliminary results indicate a time resolution with the R5946 and CPC concentrator that is nearly as good as obtained with the R2490. Finally, we note that in the final system the time resolution may degrade slightly when the tube is operated in a magnetic field[7]. However a time resolution below 125 ps and perhaps as good as 100 ps resolution may be achievable.

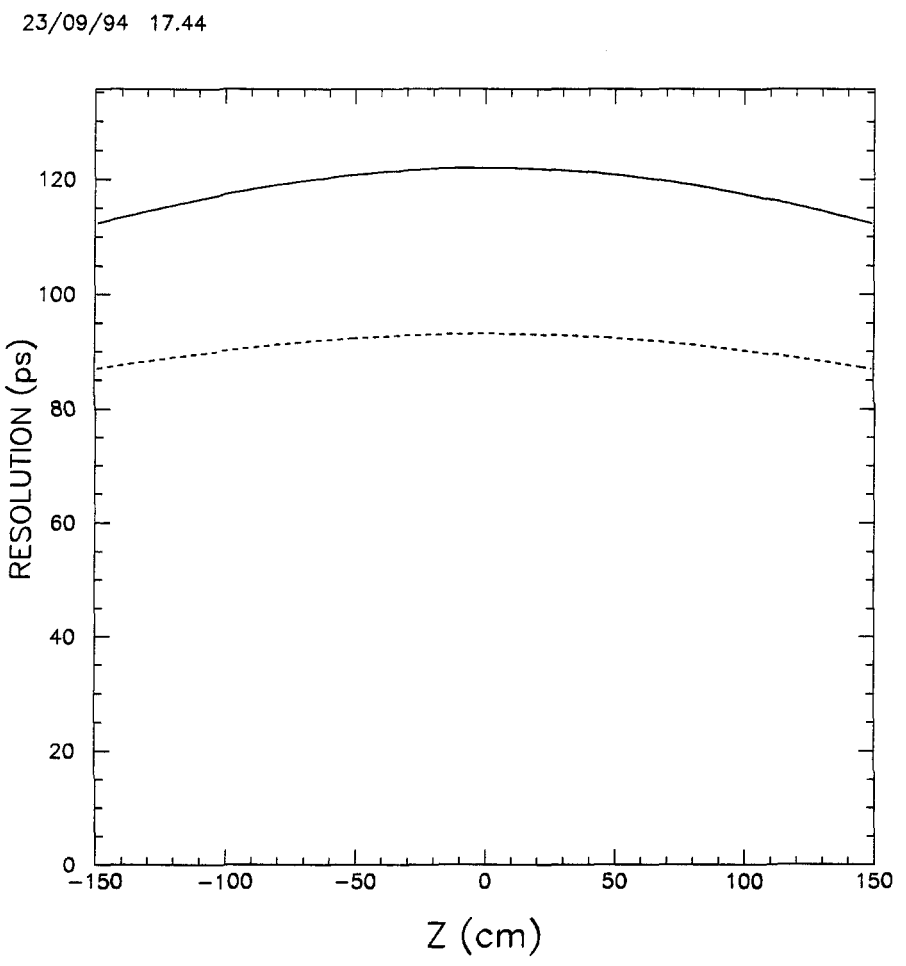

Figure 36: Expected resolution vs Z position for TOF system in B0. Solid line is for TOF counter equipped with R5946 and dashed line is for TOF counter with same light collection as R2490 tube.

15 Other Potential Uses for the TOF System

The TOF counter array has other potential uses besides $\pi/K/p$ identification. We have not explored any of these options in detail, but merely point out the possibilities.

- Since it is a large array of counters surrounding the CTC with good timing capability it could be used to reject cosmic ray muons.
- It should be quite useful for making a cosmic ray trigger.
- One could search for long lived heavy objects including those that would interact in the EM calorimeter.
- Since we intend to measure pulse height, it could also serve as a preradiator in front of the coil.
- Since it should have relatively low occupancy and it covers 1.5 units of rapidity, it might well serve as a luminosity monitor.
- Since it is very fast, and can measure both ϕ and Z, it might be useful when combined with track processor and calorimetry information as part of a level 1 or level 2 "mass" trigger.

16 Cost estimate and Schedule

We present a overall cost estimate for the proposed system. The results are summarized in Table 3. The overall cost is about $\$10^6$.

Our near-term schedule includes the following:

- Optimize light collection in 3 m counter using CPC light concentrators with R5946 1.5" tubes.
- Characterize timing properties of the R5946 at 1.5 T.
- Test 3 m counter with one PMT in 1.5 T field.
- Construct prototype electronics and test performance.
- Install 10 counter test system in CDT location during summer shutdown. Readout via Lecroy TDC and ADC.
- Determine timing performance and occupancy of TOF during collider operation in Fall 95.
- Complete and install TOF system for RUN-II.

17 Conclusions

We propose to add a Time-of-Flight(TOF) system to CDF that will allow the tagging of soft kaons and protons. Such an addition will significantly improve a broad spectrum of B physics capabilities for CDF. The proposed TOF system will have a resolution near 100 ps and will be capable of identifying kaons from pions by their flight time difference with at least 2 σ separation up to kaon momenta of 1.6 GeV/c. We propose to install the TOF system in the current CDT position.

We have built and tested prototype TOF counters. Preliminary results indicate the required counter timing performance is achievable. We have performed a design study and a rough cost estimate and conclude that a design that has 216 azimuthal segments with a fine mesh dynode PMT on each end is practical and appropriate. We estimate the entire TOF system will cost about $1 million and could be ready for Run-II.

18 Acknowledgments

We would like to thank Jim Welch for his work in fabricating the TOF prototype test setup and Ken Gray for preparing the counters. In addition we thank Walt Kononenko for his help in purchasing the tubes and scintillator. We also thank Bob Wands for his help with the ANSYS magnetic field calculations and Harry Carter, Stan Orr, Don Carpenter, and their technicians for their help in fabricating and installing the test magnet.

Table 3: Estimates of cost of the central TOF system.

Item	# req.	cost each ($)	Total cost (k$)
PMT	450	1300	585.0
Scintillator	225		120.0
PMT Base and Preamp	480	35.8	17.2
TFEC cards (27chan/card)	20	2850	57.0
CHMB cards	20	1730	34.6
CHMB Crate/Power Supply	1	20000	20.0
Cables			86.4
HV (Gamma supply)	1	5000	5.0
PISA box or equiv.	432	20	8.6
EDIA/mounts, etc.	1		100.0
Project Cost			1033.8

References

[1] H. Keutelian, et al., CDF/DOC/TRACKING/CDFR/2223, also see collaboration meeting talk by H Keutelian, April 15,1994.

[2] P. Sphicas, CDF/DOC/BOTTOM/CDFR/2655.

[3] P. Nason, S. Dawson and R. K. Ellis, Nucl. Phys. **B327**, 49 (1989).

[4] J. Lewis, J. Mueller, J. Spalding, and P. Wilson, *A Feasibility Study of Measuring the Angle α with CDF*, B-Physics Snowmass Workshop Proceedings (1993).

[5] CLEO II upgrade proposal.

[6] For a detailed treatment of the design of optical concentrators see High Collection Non-Imaging Optics, W.T. Welford, R.Winston, TS514.W45 (1989).

[7] H. Kichimi, *TOF Counter Design for KEK B-Factory*, KEK Proceedings June 1993. Also, N. Tamura, *B-Factory TOF Counter*, KEK B-Workshop, Nov.17-20.

[8] W.B. Atwood, Lecture at Slac Summer Institute, 1980, p. 287.

[9] H. Kichimi, et. al. *Timing characteristics of a Micro-channel Plate and Fine Mesh Photomultiplier tubes in a 1 T field*, Nuclear Instruments and Methods A325 (1993)451

[10] H Arnaudon et al. CERN-LAA/HC93-16, CERN-PPE/93-101

[11] M.Kuhlen et al. NIM A301(1991)223.

19 Appendix A: Detector Choices

Ideally, a detector chosen for kaon identification should be fast enough so that information on the tag could be available for the trigger. Optical readout of a TOF system by a photomultiplier tube (PMT) meets this requirement as would the similar readout of a threshold Čerenkov detector. Threshold Čerenkov detectors have the advantage that they are simple, but for the momentum range of interest, 0.6 to 4.0 GeV/c, the required index of refraction of the radiator is problematic. Threshold Čerenkov detectors were considered for the CLEO upgrade[5]. The authors of the CLEO report concluded that for the momentum range of interest to CDF, refractive indices in the range 1.008 to 1.06 with corresponding pion thresholds of 1.1 and 0.4 GeV/c respectively are needed. Two different radiators are needed to cover the momentum range of interest; silicon Aerogel for n >1.02 and high pressure (20 atm) gas for n < 1.02. In the CDT or CPR locations neither choice looks attractive because the geometry of either location limits the thickness of radiator that could be employed, thus reducing the amount of light available. For example, if one assumes 5 cm of radial space is available for the radiator at the CPR location and a high pressure gas radiator with n = 1.008 is used, then a 90% light collection efficiency and a PMT with 27% quantum efficiency detects only 3 photoelectrons from a 1.5 GeV/c pion. In practice, the geometry would make removing the light from such a radiator difficult and the actual number of detected photoelectrons would be less. Finally, it should be noted that the kaon tag from such a device corresponds to the absence of a hit for a track with momentum above pion threshold. Thus false tags arise from inefficiencies. Thus, we conclude that such devices could work in the momentum range of interest, but in practice, they would be difficult to make work in either the CDT or CPR locations because of the limited radial space available.

We investigated Correlated Čerenkov Timing (CCT) detectors suggested by M. Selens (U. of Illinois) and proposed for the CLEO upgrade. These devices would attempt to identify a particle by measuring the change in the effective length of a quartz bar at the Čerenkov angle of the particle emitting the light. At fixed momenta π's and K's emit Čerenkov light at different angles resulting in a difference in arrival time of the light at the ends of a long quartz bar. The effect goes in the same direction as the change of flight time due to the difference in the velocity of the two particles and is therefore additive. The authors of the CLEO upgrade document claim to be able to separate pions from kaons up to about 3.5 GeV/c if sufficient photons can be detected. However, beyond the obvious expense of high quality quartz, there are other potential drawbacks. A Monte Carlo written to study the CLEO CCT upgrade indicates that as the particle's dip angle increases to near 45° the detector performance deteriorates such that it is no better than that of a conventional TOF system. The technique looks potentially interesting as a way to extend the momentum range of standard TOF systems for CDF but extensive Monte Carlo simulation and test beam work with prototypes would be required before one could consider proposing it for

CDF.

A system Like the DIRC proposed for the BaBar detector at SLAC looks potentially attractive, but the geometry of the CDF magnet and end plug calorimetry would have to undergo major modifications before such a system could be installed. In addition such a system would be at least one order of magnitude more expensive than the TOF system we propose. We note however that its momentum reach would substantially exceed that of a TOF system and that its PMT readout makes it attractive for high luminosity machines like the Tevatron. It is a definite candidate for a longer term particle ID upgrade.

Finally, RICH detectors with liquid radiators have been suggested as a possible detector for particle ID, but given the problems of operating a RICH in the high rate environment, the high cost, complexity, long development time, and the space constraints of the existing CDF detector, this is not an option for a short term upgrade. RICH, threshold Čerenkov detectors, CCT, DIRC, and other devices should and will be studied as candidates for longer term particle ID upgrades to CDF. Such upgrades will benefit from the experience gained with a TOF system in Run-II and a TOF system may well be a part of the final solution.

20 Appendix B: Magnetic Field tests of PMTs

The geometry of the magnet is shown in Figure 37. The test magnet is a conventional water cooled solenoid.

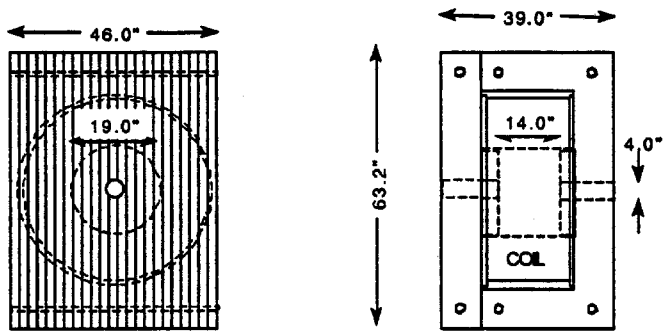

Figure 37: Schematic of TOF test magnet. The magnet has a useful bore of 19 inches. The pole tip to pole tip distance is 14 inches. There is a 4 inch diameter hole through the magnet for testing long counters. The magnet produces a field of 1.5 T at 1034 amps.

The gain and timing performance of fine mesh Photomultipliers similar to those we intend to use have been studied in magnetic fields.[9]. However, these studies were done mostly with fields of 1 - 1.2 Tesla. We believe it is important to study the performance of the actual tubes we intend to use (ie the Hamamatsu R5946) at the field in which we intend to use them. With this goal in mind we have constructed a test solenoid which we are using to measure the gain and timing performance of the R5946 tubes. The magnet was constructed at minimal cost using surplus steel plate and an existing water cooled copper coil. The solenoid has a useful bore of 19 inches. The pole tip to pole tip distance is 14 inches. There is a 4 inch diameter hole through the magnet for testing long counters. The design of the magnet iron was done with the ANSYS finite element program. For this design the magnet was assumed to be symmetric about the midplane of the coil and the iron was assumed to be axial symmetric. The iron/coil model used for the field calculations is shown in Figure 38. Contours of constant B field magnitude as calculated by ANSYS for the TOF test magnet are shown in Figure 39. The region plotted extends from 0 to 13 cm in radius relative to the axis of the solenoid and 0 to 10 cm along the axis of the solenoid. From the figure we see that the field should be uniform to $\pm 1\%$ over

this volume. Figure 40 shows a similar plot for the component of B along the axis of the solenoid. Finally Figure 41 and Figure 42 show the calculated distribution of B_Z along the axis of the solenoid.

The magnet construction is complete and the magnet is installed in the MS7 service building at Fermilab. In mid March 1995 we successfully powered the magnet. The magnet performed as designed. Figure 43 shows the measured magnetic field along the axis of the solenoid. For this figure measurements were taken at a current of 925 amps by moving a portable hall probe that measures the Z component of magnetic field along the R = 0 axis of the solenoid. Figure 44 shows similar results but over a more limited Z range and at various excitation currents. As can be seen the field is quite uniform and agrees well with the shape predicted by ANSYS. Figure 45 shows the measured magnetic field at center the TOF test solenoid vs excitation current. The test magnet produces fields as large as those in the CDF superconducting solenoid where the proposed TOF system will be installed. This will allow us to test the performance of TOF counters in the actual magnetic field conditions of operation. The magnet produces a central field of 1.5 T at 1034 amps. A current of 964 amps reproduces the normal operating field (1.4 T) of the CDF superconducting solenoid.

We began phototube testing with this magnet in mid March of 1995. Figure 46 shows the gain of a Hamamatsu 5946 vs magnetic field value. For this test the field was aligned along the axis of the PMT in the same way as it will be in the CDF solenoid. A gain reduction of 500 was observed at a magnetic field of 1.5 T. The shape and absolute value of the gain reduction at lower field values agree well with the curves provided by the manufacturer. The change in gain at the 1.4 T operating field of the TOF system is 300. Although the change in gain large, it is expected to be quite stable. Our near term plans include measurement of the gain stability, measurement of the timing resolution of small counters vs B field (to measure the change in transit time spread of the PMTs vs B), and timing measurement with full sized counters using cosmic rays. In the last test we will operate full sized counters with one tube immersed in the 1.4 T field of the test solenoid.

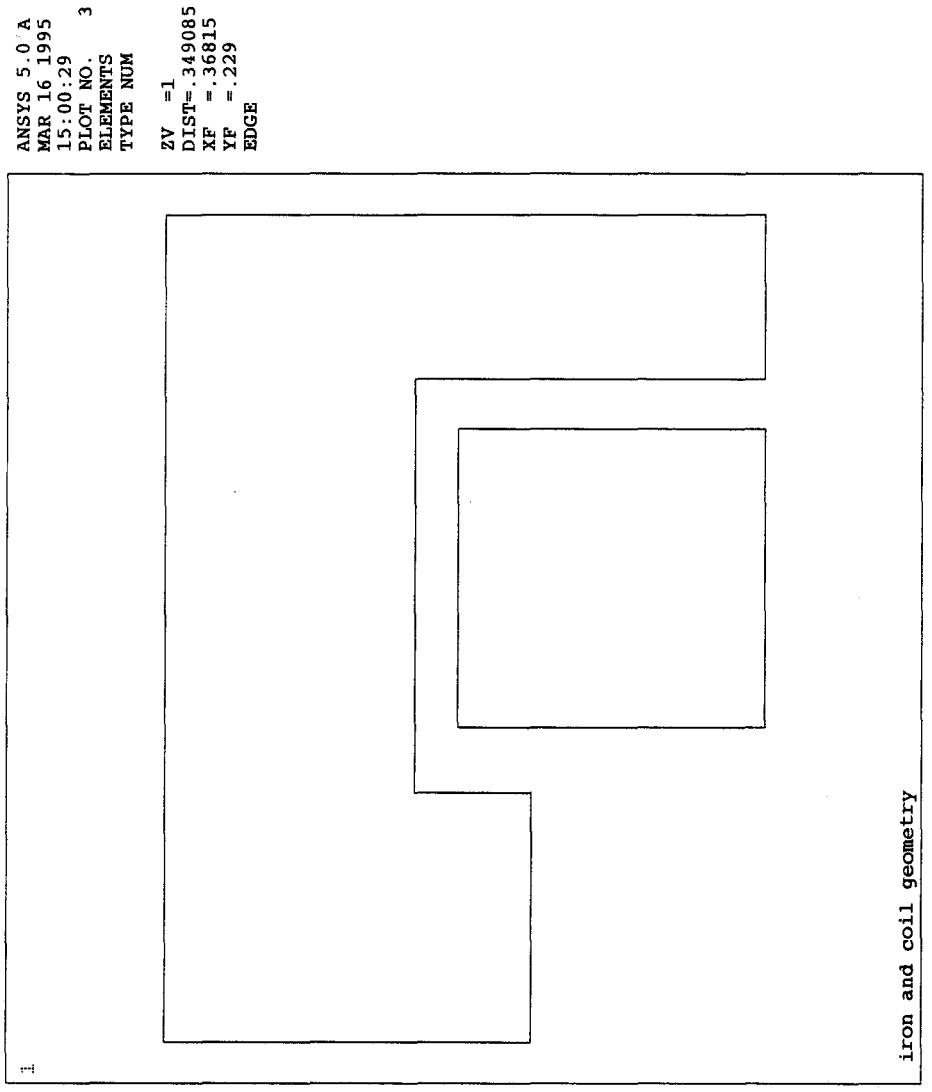

Figure 38: Geometry used in ANSYS field calculations for TOF test magnet. The axis of the solenoid is horizontal and corresponds to the bottom edge of the frame of the figure. Axial symmetry about this axis is assumed. Symmetry around the coil mid plane is assumed. The square region corresponds to the coil and the other region the iron return yoke. The rightmost edge of these regions is the plane of symmetry. The magnet has a pole tip that is 18.9 inches in diameter.The pole tip to pole tip distance is 14 inches. There is a 4 inch diameter hole through the magnet for testing long counters.

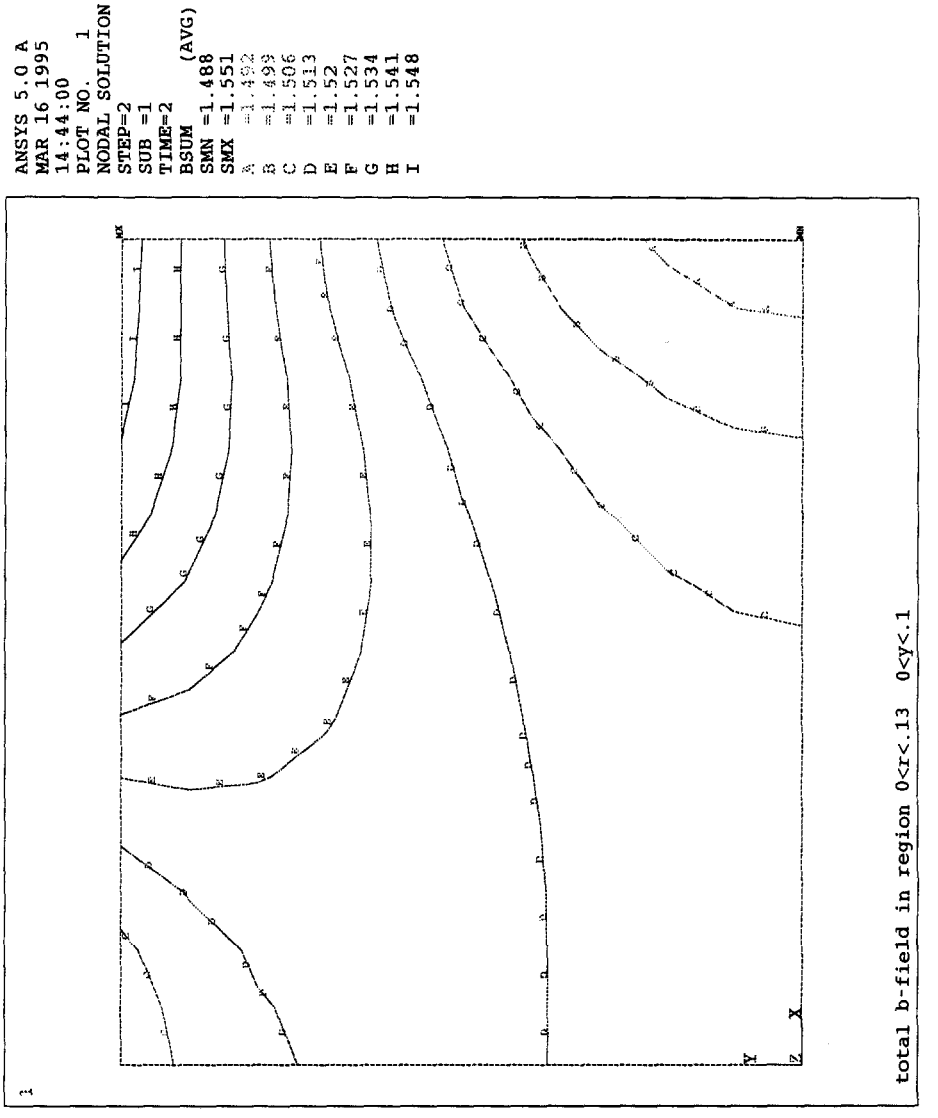

Figure 39: Contours of constant B field magnitude as calculated by ANSYS for the TOF test magnet. The vertical axis extends from 0 to 13 cm in radius relative to the axis of the solenoid(labeled x axis in this figure) and horizontal axis extends from 0 to 10 cm along the axis of the solenoid.(labeled y axis in this figure)

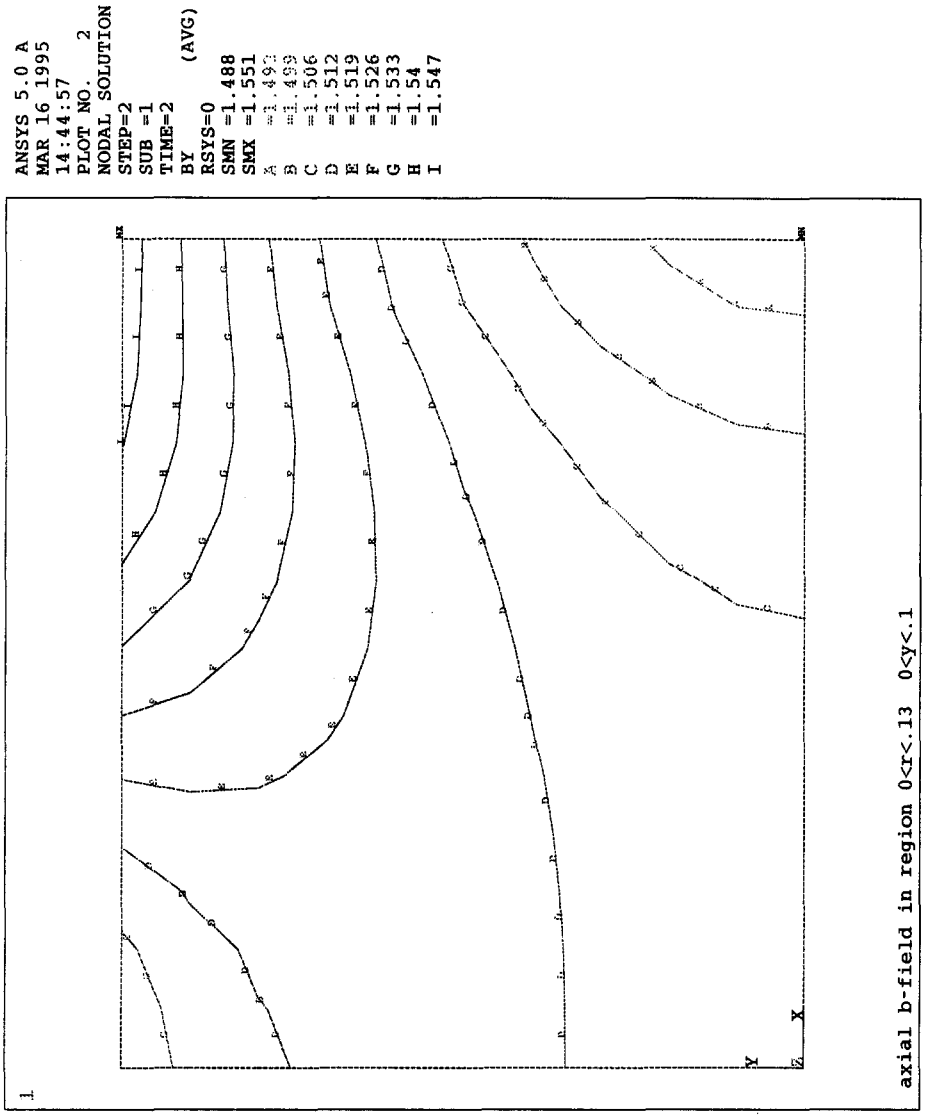

Figure 40: Contours of constant B_Z, the component of field along the axis of the solenoid as calculated by ANSYS for the TOF test magnet. The region plotted extends from 0 to 13 cm in radius relative to the axis of the solenoid(labeled x axis in this figure) and 0 to 10 cm along the axis of the solenoid.(labeled y axis in this figure)

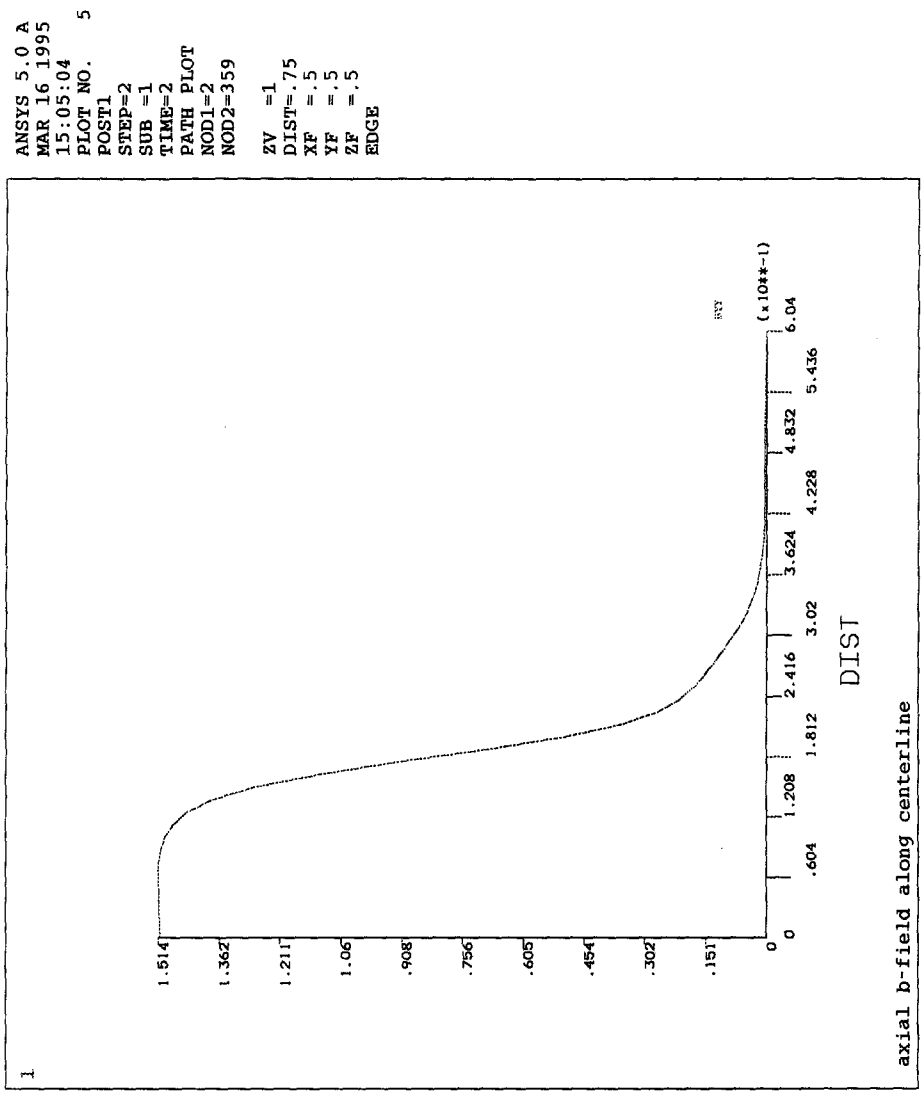

Figure 41: B_Z, the component of field along the axis of the solenoid vs Z distance (units =meters x 0.1) from center of solenoid as calculated by ANSYS for the TOF test magnet.

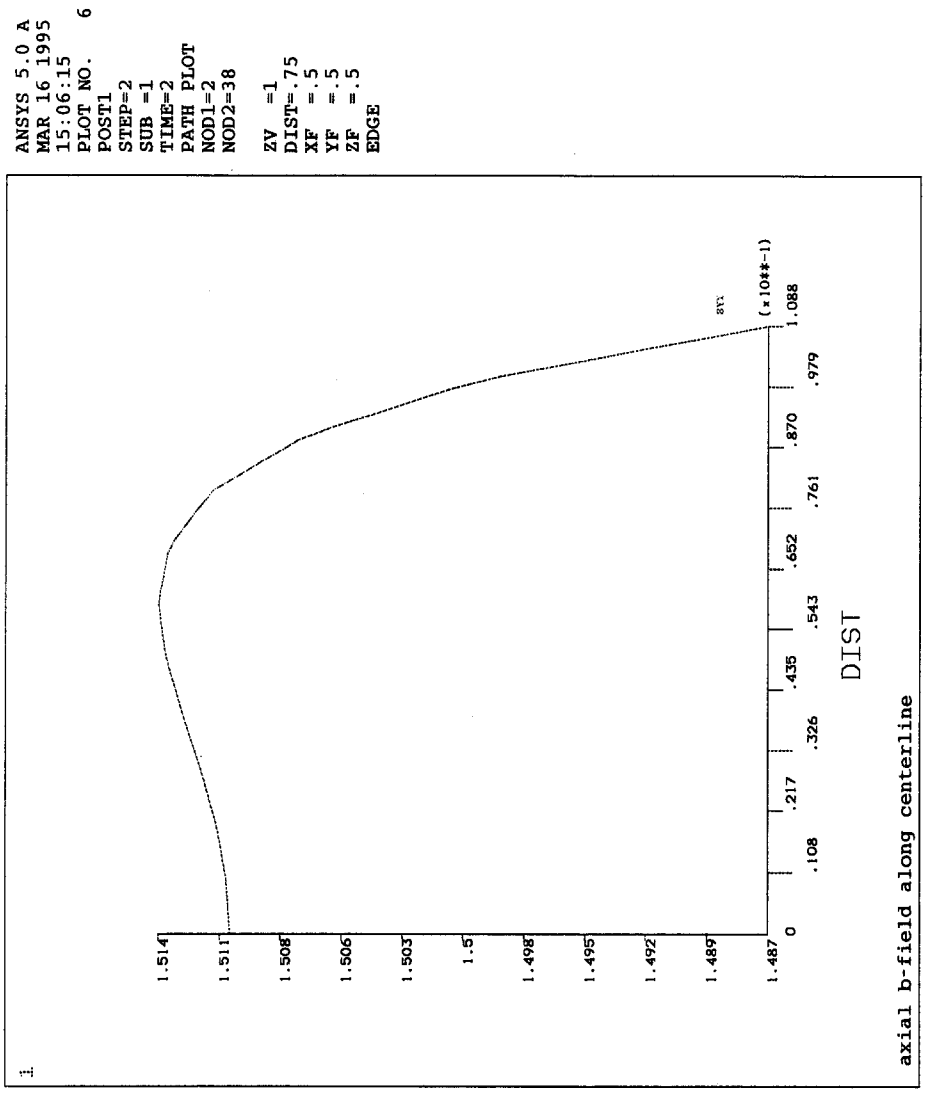

Figure 42: B_Z, the component of field along the axis of the solenoid vs Z distance (units = meters x 0.1) from center of solenoid as calculated by ANSYS for the TOF test magnet.

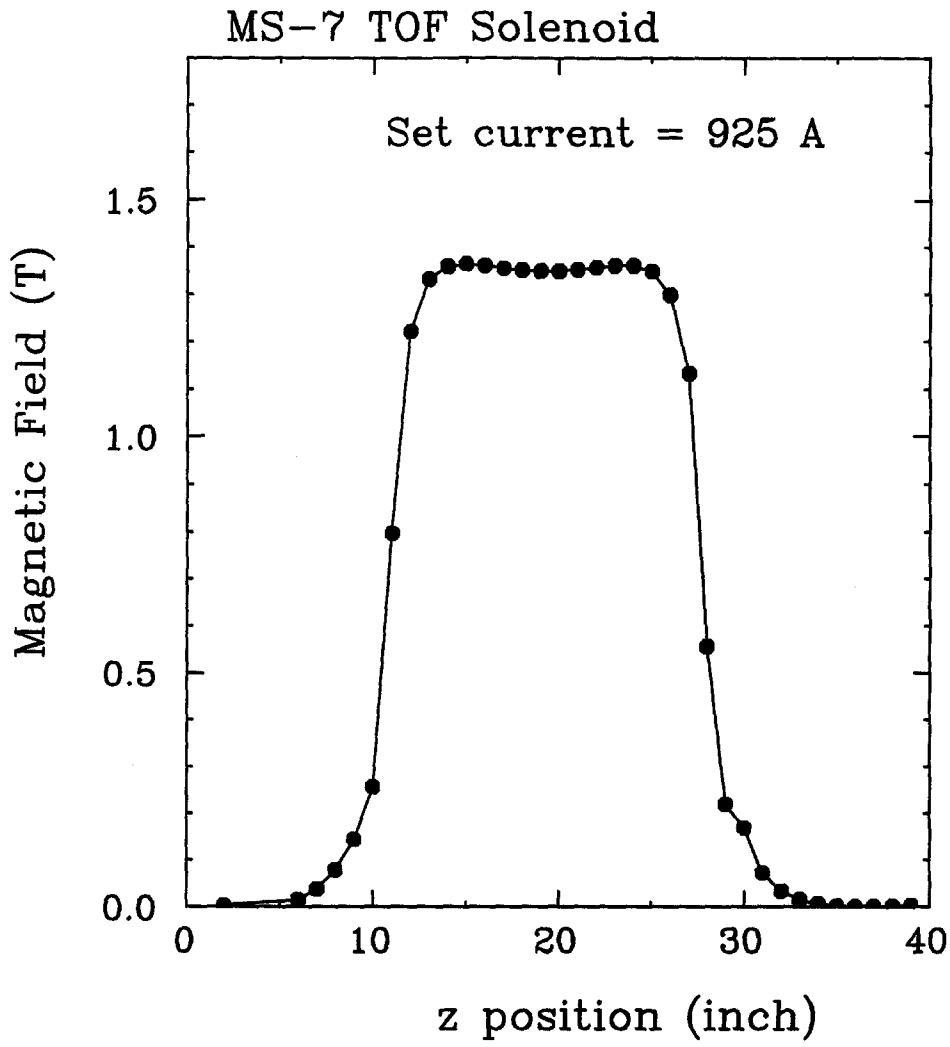

Figure 43: Measured magnetic field along the axis of the solenoid for the TOF test magnet. Measurements were taken at a current of 925 amps by moving a portable hall probe that measures the Z component of magnetic field along the R = 0 axis of the solenoid.

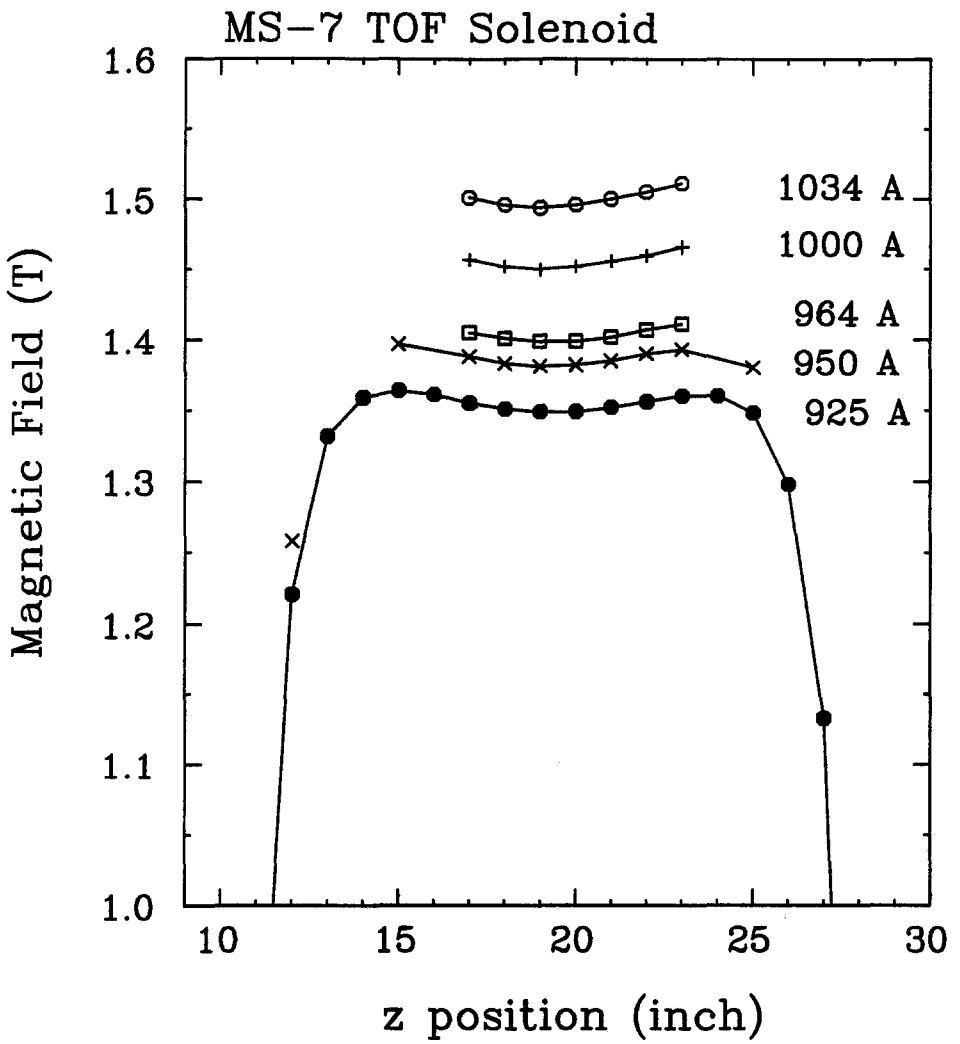

Figure 44: Measured magnetic field along the axis of the solenoid for the TOF test magnet. Measurements were taken at various excitation currents by moving a portable hall probe that measures the Z component of magnetic field along the R = 0 axis of the solenoid. A current of 964 amps produces a field of 1.4 Tesla. This is the same as the central field of the CDF superconducting solenoid.

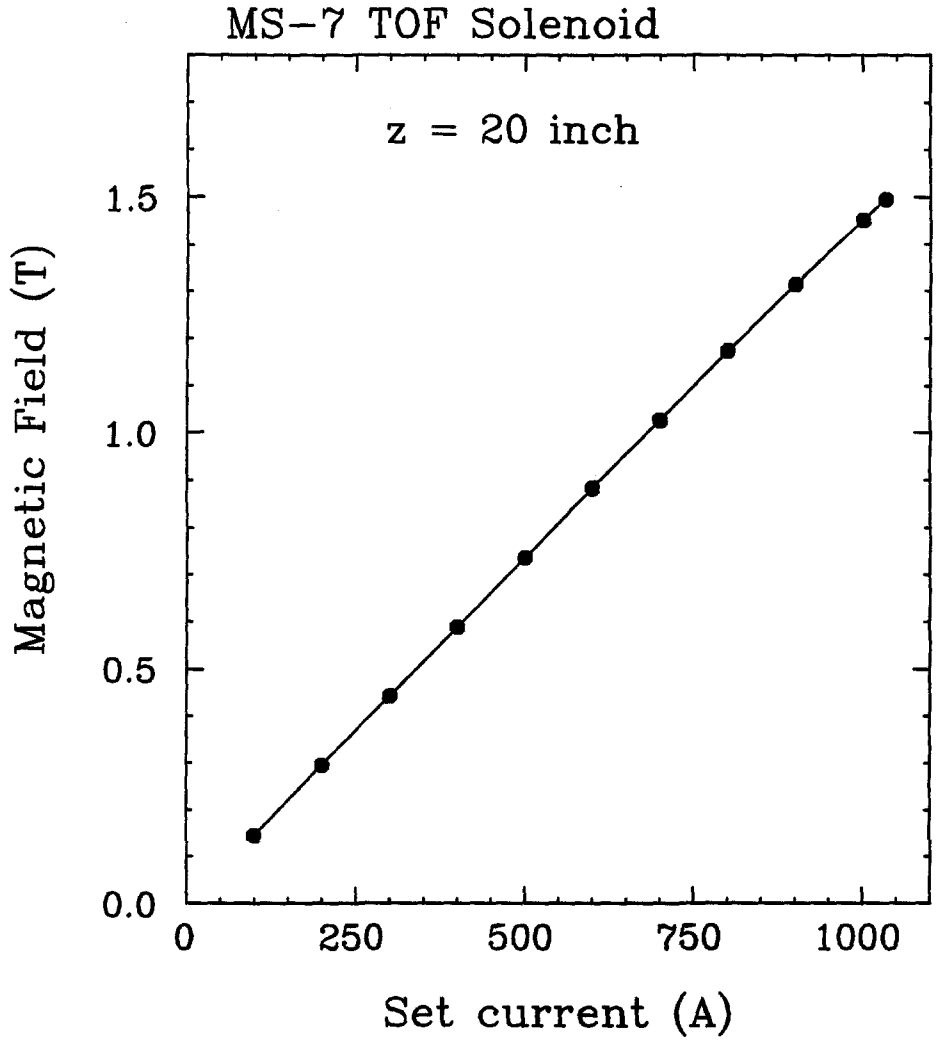

Figure 45: Measured Central magnetic field at center the TOF test solenoid vs excitation current. The test magnet produces fields as large as those in the CDF superconducting solenoid where the proposed TOF system will be installed. This allows us to test the performance of TOF counters in the actual magnetic field conditions of operation.

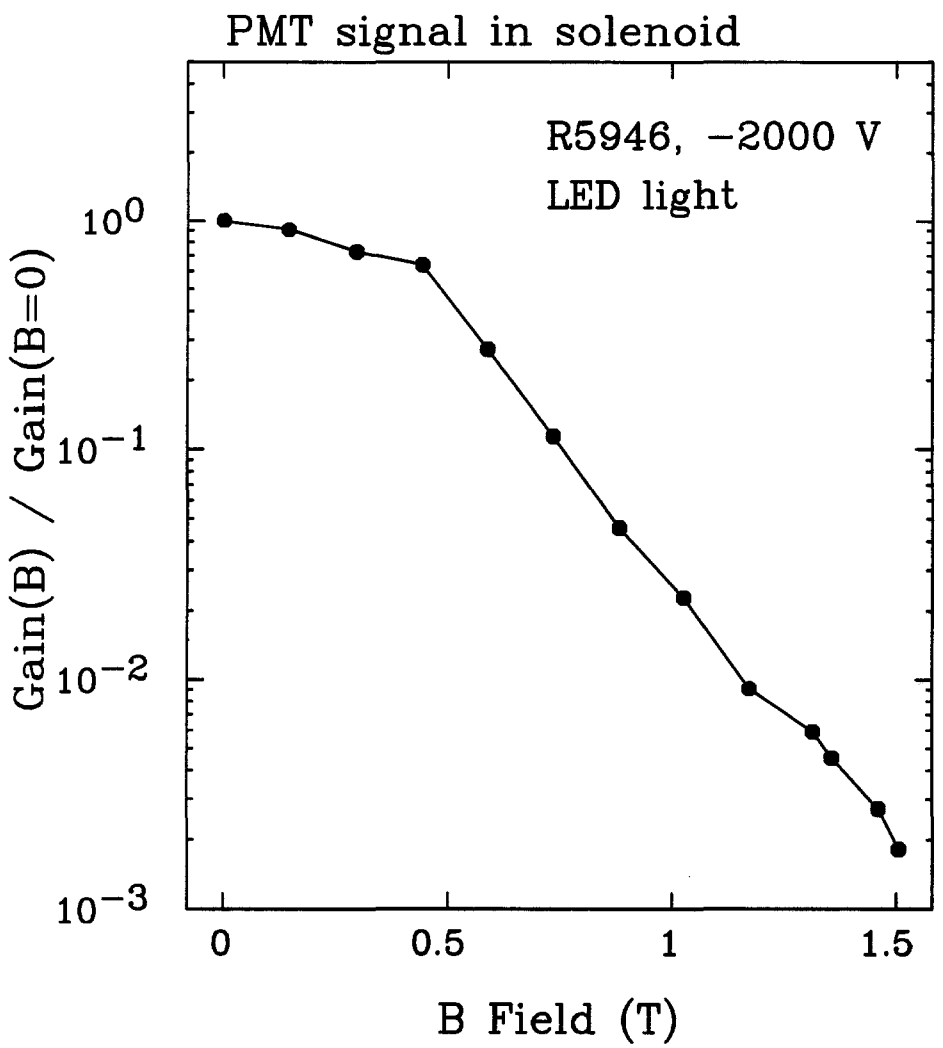

Figure 46: Measured gain of the R5946 vs magnetic field. The tube was oriented with the B field parallel to its longitudinal axis. We observe a gain reduction of 300 at the nominal 1.4 T operating field of the TOF array.

FERMILAB-PROPOSAL-0830-4 1995

CDF/DOC/TRACKING/PUBLIC/3079
Version 1.0
March 26, 1995

Proposal for Run II Tracking System Upgrades for CDF

The CDF Collaboration

Abstract

Experience has shown that having an excellent tracking system as part of the CDF detector is necessary for almost all physics analysis. The Central Tracking Chamber (CTC), designed for L = $10^{30} cm^{-2} sec^{-1}$ and in use since 1987, is still performing well at current luminosities, approaching L = $2x10^{31}$. For the expected run II luminosities of 10^{32} and above, the CTC performance will no longer be adequate, however, as will be documented in the first part of this proposal.

The proposed tracking upgrades form a two-step solution to this tracking problem. The first step, to be ready for the beginning of run II, consists of the replacement of the current VTX chambers with a new scintillating fiber tracker together with the addition of a fifth layer to the already-approved four-layer SVXII detector. The total estimated cost of this upgrade is $6.6M (FY1995 $, no contingency). The second step, to be ready for installation two years later, consists of a replacement of the CTC with a new tracker in the same volume. We are currently pursuing two different designs, a straw tracker (based on R&D done for the SDC) and a CTC-like chamber with 1 *cm* maximum drift distance (instead of 4 *cm*). The estimated cost is in the range $10M - $14M (FY 1995 $, no contingency). We expect to submit a conceptual design report for the CTC replacement in about a year.

CDF/DOC/TRACKING/PUBLIC/3079
Version 1.0
March 26, 1995

Proposal for Run II Tracking System Upgrades for CDF

The CDF Collaboration

Abstract

Experience has shown that having an excellent tracking system as part of the CDF detector is necessary for almost all physics analysis. The Central Tracking Chamber (CTC), designed for L = $10^{30} cm^{-2} sec^{-1}$ and in use since 1987, is still performing well at current luminosities, approaching L = $2x10^{31}$. For the expected run II luminosities of 10^{32} and above, the CTC performance will no longer be adequate, however, as will be documented in the first part of this proposal.

The proposed tracking upgrades form a two-step solution to this tracking problem. The first step, to be ready for the beginning of run II, consists of the replacement of the current VTX chambers with a new scintillating fiber tracker together with the addition of a fifth layer to the already-approved four-layer SVXII detector. The total estimated cost of this upgrade is $6.6M (FY1995 $, no contingency). The second step, to be ready for installation two years later, consists of a replacement of the CTC with a new tracker in the same volume. We are currently pursuing two different designs, a straw tracker (based on R&D done for the SDC) and a CTC-like chamber with 1 *cm* maximum drift distance (instead of 4 *cm*). The estimated cost is in the range $10M - $14M (FY 1995 $, no contingency). We expect to submit a conceptual design report for the CTC replacement in about a year.

Contents

1 Introduction **3**

2 CDF in Run II *without* a tracking upgrade **5**

2.1 CTC occupancy 5

2.2 Top event tagging 9

2.3 K_s^0 in J/ψ events 11

2.4 Summary of tracking loss *without* an upgrade 13

3 Fiber subsystem addition and expansion of SVX for Run IIa **14**

3.1 The fiber subsystem 14

3.2 The SVX II subsystem 20

3.3 CTC + fiber system performance 23

3.4 SVX II performance 28

3.5 SVX II + fiber system performance 29

4 CTC replacement in Run IIb **31**

4.1 Straw chamber 31

4.2 CTC style chamber 34

4.3 CTC replacement schedule 35

5 Cost summary **36**

1 Introduction

Highly efficient, high resolution tracking is at the heart of practically every physics analysis done with the CDF detector at the Tevatron. However, as the Tevatron luminosity increases over the next decade, the CDF tracking system will be inundated by ever higher occupancy, coming from additional events which occur within less than the detector live time of the events of interest. Higher granularity is needed to be able to reconstruct tracks from the interesting physics events in the face of these higher backgrounds.

Year	Design Luminosity	Bunch Spacing	CDF Tracking Upgrade
present	0.2 x $10^{32} cm^{-2} sec^{-1}$	3493 ns	
1999 (Run IIa)	$10^{32} cm^{-2} sec^{-1}$	396 ns	Fiber insert 5 layer SVX II
2001 (Run IIb)	2 x $10^{32} cm^{-2} sec^{-1}$	132 ns	CTC replacement

Table 1: Proposed Tracking Upgrade Schedule

We propose a phased upgrade of the tracking system, matching the expected increases in Tevatron luminosity. Without such upgrades, the tracking efficiency for reconstructing an isolated lepton will drop by 10% at L=$10^{32} cm^{-2} sec^{-1}$. The probability of reconstructing the K_s in a $B_d \rightarrow J/\psi K_s$ event will drop by 55%. The efficiency for tagging Top events using secondary vertexing with the SVX will drop by 35%.

The inner layers of the CDF Central Tracking Chamber (CTC) which are closest to the beam line are naturally the first to suffer from luminosity increases. We propose to replace their function by inserting a scintillating fiber tracker within the inner bore of the CTC. The fiber tracker will go in the space currently occupied by the VTX, as shown in Figure 1. The outer layers of the CTC plus the fiber system then form an efficient tracking system, which can handle luminosities up to $10^{32} cm^{-2} sec^{-1}$.

We propose to also expand the currently planned 4 layer Silicon Vertex Detector upgrade (SVX II) to a 5 layer system. The 4 layer system was designed with double-sided readout, having an axial readout and a 90° stereo readout for each layer. Matching the track segments found in the r-ϕ view with the segments in the r-z view was entirely dependent on the CTC tracking in that scheme. With 5 layers, we plan to have 3 layers of 90 degree stereo (which provide high

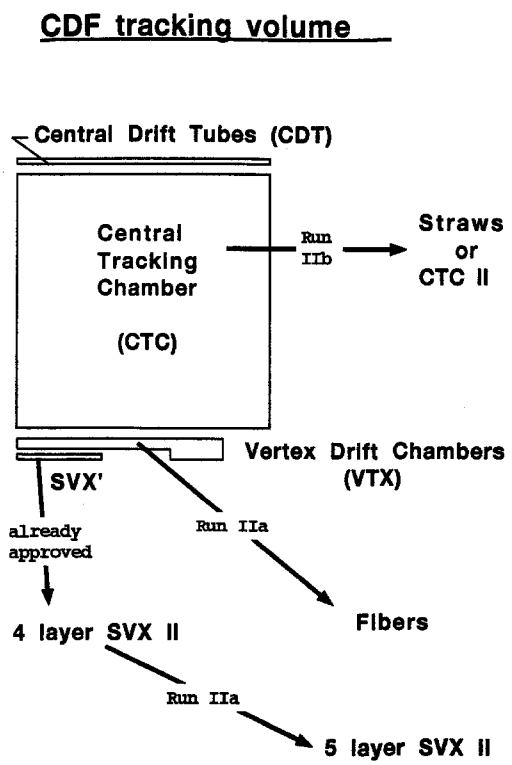

Figure 1: Sketch of the current CDF tracking system, with upgrade paths labeled.

precision tracking in the r-z view as before), and two layers of small angle stereo (which provide view matching between the axial view and the r-z view). The SVXII small angle stereo points provide much more precise hits than the CTC extrapolated road, and thus much more robust 3-D tracking.

The combination of the fiber tracker and upgraded SVX II then provides the added benefit of tracking for primary tracks over a much larger pseudo-rapidity range ($|\eta| < 2$) than can be covered by the outer layers of the CTC ($|\eta| < 1$)[1].

As the luminosity increases beyond $10^{32} cm^{-2} sec^{-1}$, even the outer layers of the CTC have occupancy problems. By L= $2\text{x}10^{32} cm^{-2} sec^{-1}$, the CTC track reconstruction efficiency is severly reduced even with the fiber upgrade. Hence for

[1] The CTC currently provides tracking to larger rapidity, however the efficiency for those tracks decreases very rapidly with increasing luminosity. This is because there are fewer hits for large rapidity tracks to begin with, and those hits are in more heavily occupied inner layers.

the latter part of Run II, we propose replacing the CTC with a gas-based tracker matched to the higher luminosity and shorter bunch spacing. Two technologies are under consideration: a chamber similar to the current CTC, but with a shorter drift time which is smaller than the 132 ns bunch spacing expected for the later half of Run II, or a straw tube chamber similar to that proposed for the SDC experiment at the SSC. We expect to submit a conceptual design report for the CTC replacement chamber next year. The CTC replacement, in conjunction with the fiber and SVX upgrades, will constitute an excellent tracking system at the higher luminosity now expected in Run IIb.

2 CDF in Run II *without* a tracking upgrade

A significant effort has been made to understand how the current CDF tracking system would operate under Run II conditions. Aging tests conducted with radioactive sources on a prototype CTC chamber showed no degradation of pulse height, with dose equivalent to an integrated luminosity of 1 fb^{-1} for the innermost layers[2]. With some work, positive ion distortions and voltage sags on wires can be kept manageable. The major problem uncovered is the expected high occupancy of the CTC. This has been studied largely with raw data mixing techniques, without resorting to Monte Carlo. This section demonstrates the deterioration in performance expected, and thus motivates the upgrade proposal.

2.1 CTC occupancy

The CTC is a drift chamber with multihit electronics that records both the leading edge of a hit and the pulse width. It contains 84 wire layers, grouped in 9 superlayers, 4 of which are oriented at a 3° stereo angle. Figure 2 shows an event display. Note that each track segment appears twice, because of the drift chamber left-right ambiguity, and that in the side-bar blow-up, one can see both the leading edge and the pulse width of each hit plotted. Note that even in this low luminosity event, the inner layers are heavily populated with hits.

Figure 3a shows estimates of the increase in Tevatron luminosity as a function of time. If the current bunch crossing frequency were retained as the luminosity increases, the entire tracking system would be swamped by hits from

[2] As this is being written, indications of wire aging in the CTC are being seen. The cause and possible solutions are currently under investigation. It is too early to say whether this fact will require an earlier CTC replacement date.

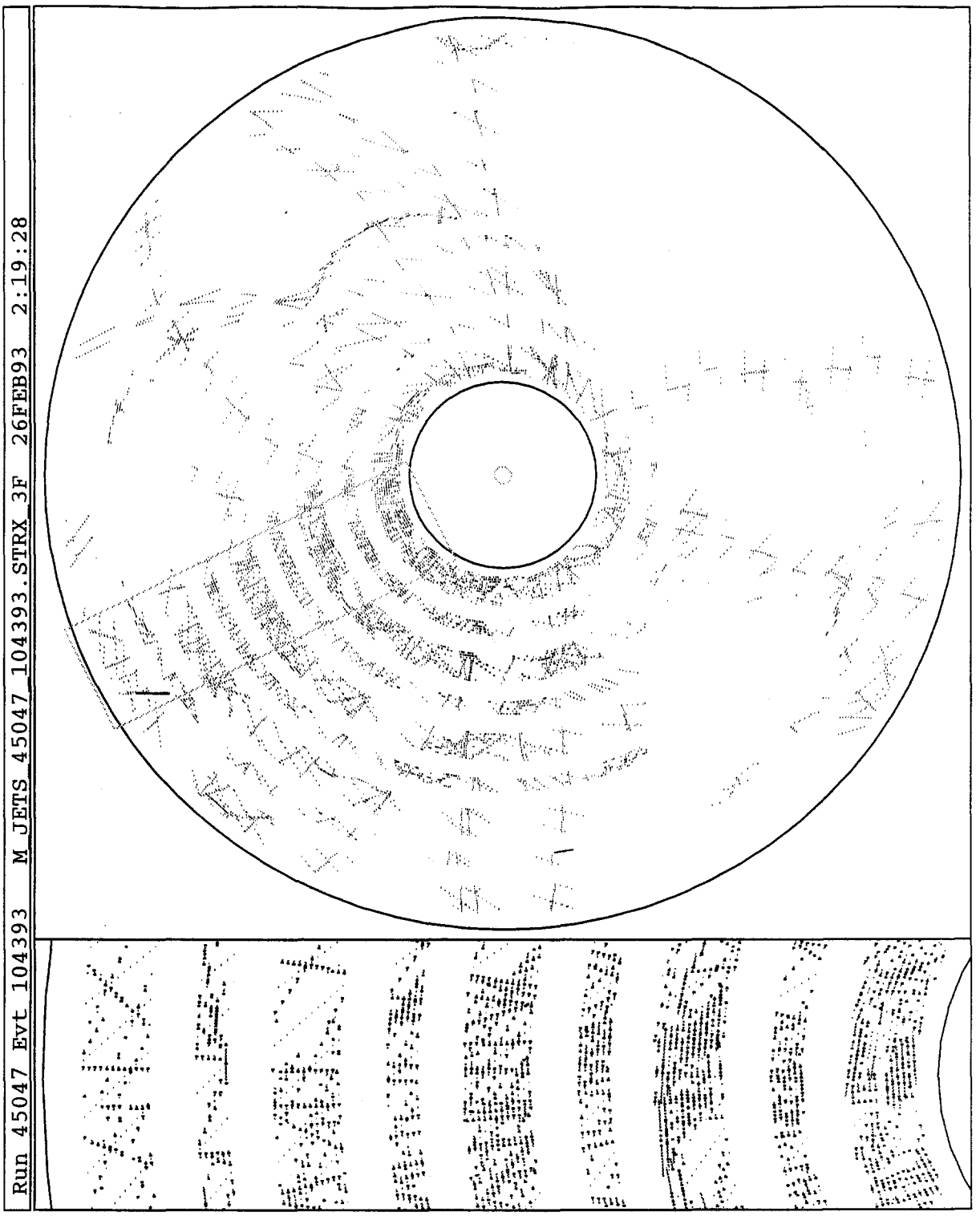

Figure 2: Event display showing hits in the CTC. This is a top event candidate from Run Ia.

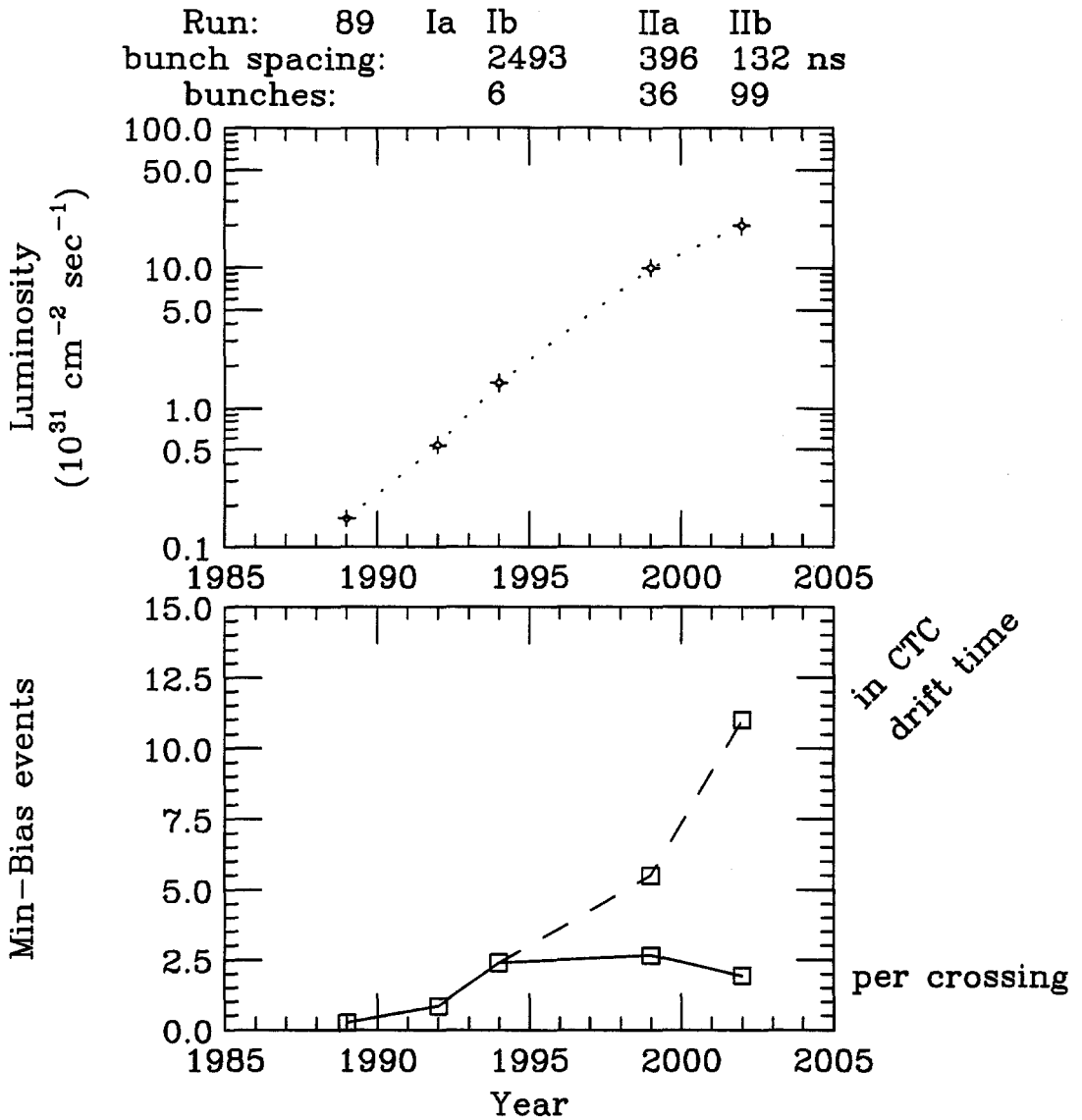

Figure 3: a) Instantaneous luminosity at the beginning of good stores, showing the improvements with Tevatron upgrades over time. b) Number of Minimum Bias events at the given luminosity, shown per crossing and also in the CTC drift time. The number of minimum bias events per crossing is held relatively constant by increasing the number of bunches with increasing luminosity, but the CTC does not benefit from this because of its long drift time.

extra minimum bias interactions happening in the same crossing. Figure 3b shows that by increasing the number of bunches, one can keep the number of minimum bias interactions in each crossing to around three, a manageable number. As the time between bunches is decreased to 396 ns, and then to 132 ns, the SVX II detector is still able to resolve the bunch crossings. However, the maximum drift time in the CTC is around 750 ns, so that an event in the CTC at high luminosity contains hits from several out-of-time bunch crossings. Elimination of these out-of-time hits is the motivation for building a CTC replacement with a maximum drift time of $\leq$ 100 ns.

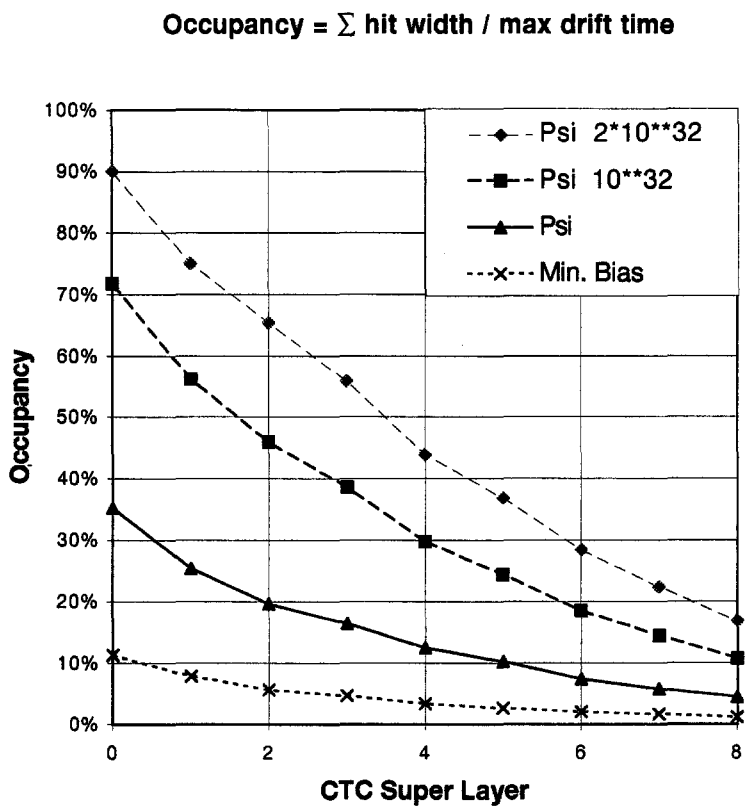

Figure 4: Occupancy of CTC wires as a function of layer, where occupancy is defined as the fraction of live time that the wire spends above threshold, i.e. the sum of the pulse widths over the live time. This is shown for Minimum Bias event and J/ψ events at low luminosity, and also for J/ψ events at higher luminosity showing the effect of multiple minimum bias event pile-up.

The fact that the pulse width is available in the data allows the simulation

of high luminosity events by mixing low luminosity events. The appropriate number of minimum bias events are combined with interesting physics events, merging hits when they overlap. Using this technique, Figure 4 shows how the CTC occupancy will increase with luminosity for $J/\psi \rightarrow \mu^+\mu^-$ events. Clearly the inner layers will be practically useless at high luminosity. How well the outer layers will work is a detailed pattern recognition and resolution question, which we examine below in some interesting physics channels.

2.2 Top event tagging

The most important class of physics events in CDF currently are the $\bar{t}t$ events tagged with the SVX [1]. $\bar{t}t$ events are rich in b quarks, which hadronize to B hadrons. The B hadrons can be identified by their finite decay length using the precision SVX vertex detector. However, the SVX is not a standalone device - it needs the pattern recognition and momentum resolution provided by the CTC.

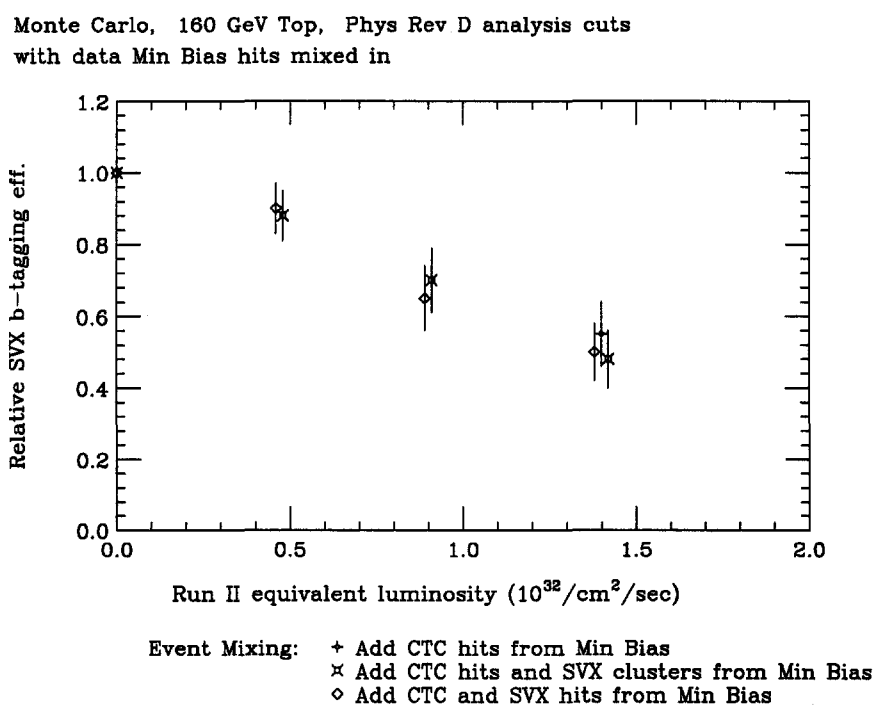

Figure 5: Relative SVX-tagging efficiency of top events, projected to Run II luminosities by mixing in minimum bias events from real data.

Figure 5 indicates how the relative rate of top event tagging will deteriorate

at higher luminosity in Run II. This is the result of mixing minimum bias events from real data with Monte Carlo top events. As seen in the plot, about a third of the secondary vertex tagging power is lost at a luminosity of $10^{32} cm^{-2} sec^{-1}$. ($10^{32} cm^{-2} sec^{-1}$ corresponds to nearly six extra minimum bias events in the CTC drift time). Also note that including or not including the SVX hits from the extra minimum bias events has little effect; the problem is in the CTC track reconstruction.

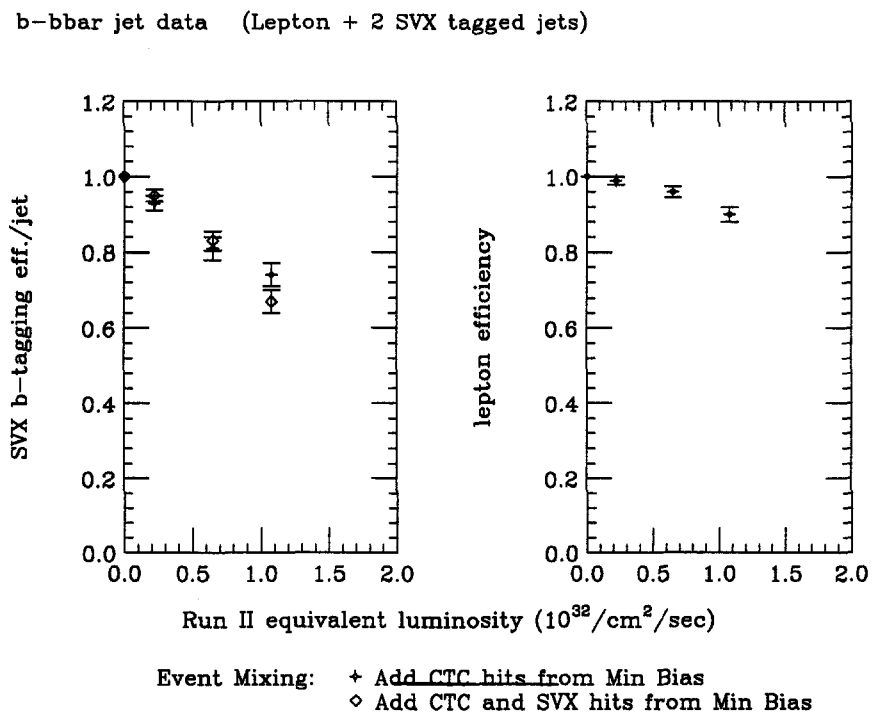

Figure 6: Relative SVX b-jet tagging efficiency, and lepton reconstruction efficiency, projected to Run II luminosities. The luminosity projection is done using mixing of low luminosity data events; no Monte Carlo is involved.

The same effect of relative secondary-vertex b-tagging deterioration can be measured in our current data set, by using our $\bar{b}b$ jet data sample. An extremely clean sample of $\bar{b}b$ events is first selected by finding jet events which are triple tagged; a lepton and two jets which are each secondary vertex-tagged are required. The relative efficiency of tagging these events as minimum bias events are mixed in is plotted in Figure 6. The drop in tagging efficiency seen agrees very well with that in the top Monte Carlo study, confirming that the CDF top

studies will be severely impacted unless a tracking upgrade is undertaken.

2.3 K_s^0 in J/ψ events

There are several reasons to look at the efficiency for finding $K_s^0 \to \pi^+\pi^-$ in J/ψ events as a measure of CTC performance. A measurement of CP violation using $B_d \to J/\psi K_s^0$ is one of the major B physics goals of CDF for Run II [2]. The large impact parameter of the pions to the primary vertex provides a challenge to the pattern recognition. Also we can compare the results of the event mixing analysis for K_s^0 reconstruction efficiency with a direct measurement of the CTC performance as a function of instantaneous luminosity in the current data set.

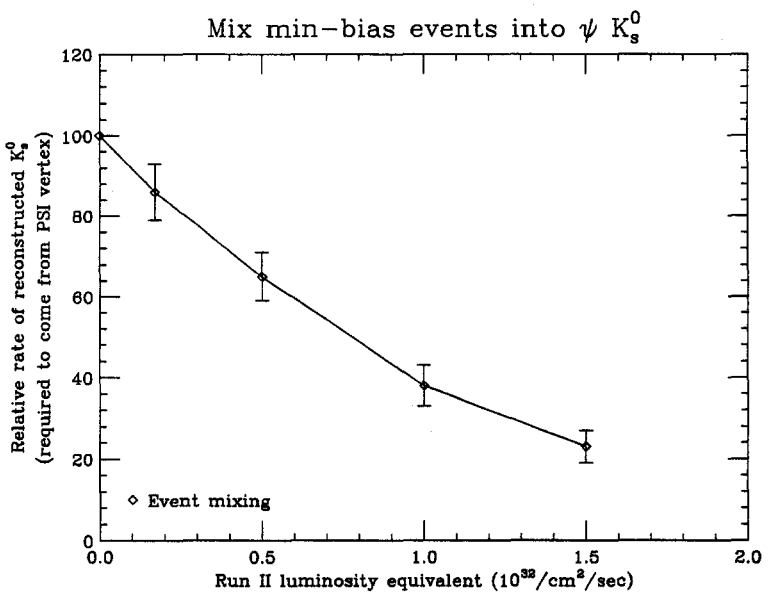

Figure 7: Relative K_s^0 reconstruction efficiency in J/ψ events, extrapolated to Run II luminosities by using minimum bias events mixed with J/ψ events from low luminosity data.

In the first study, $K_s^0 \to \pi^+\pi^-$ were reconstructed in $J/\psi \to \mu^+\mu^-$ events from low luminosity runs. Then minimum bias events were mixed in to simulate high luminosity running, and the efficiency of reconstructing the same K_s^0s was measured. Figure 7 shows the resulting drastic decrease in reconstruction efficiency, with only 40% of the originally reconstructed K_s^0s surviving at a luminosity of $10^{32} cm^{-2} sec^{-1}$. (This can be compared to an 80% survival rate for

the J/ψs).

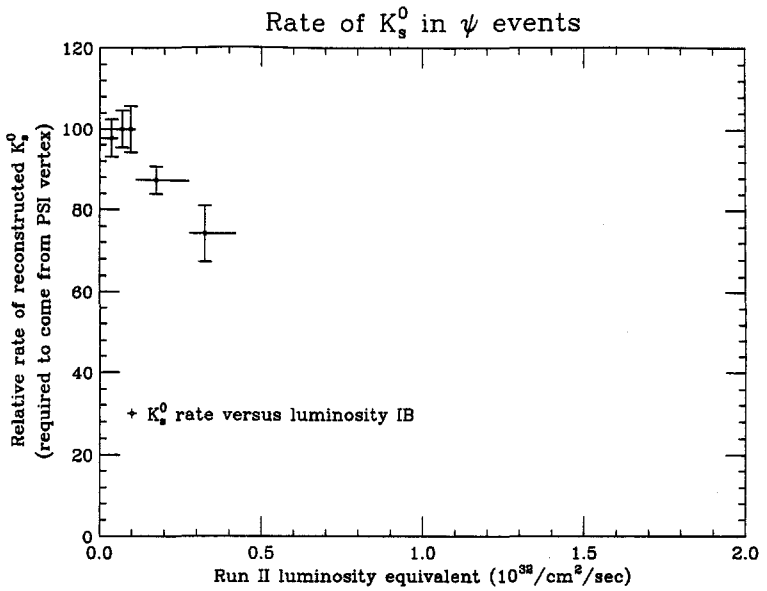

Figure 8: Relative K_s^0 reconstruction efficiency in J/ψ events in the present Run Ib data, scaled to Run II interactions per crossing.

The K_s^0 reconstruction efficiency can also be extracted directly from J/ψ event data without resorting to event mixing. Figure 8 plots the relative rate of finding K_s^0 in J/ψ events as a function of instantaneous luminosity in Run Ib data. The K_s^0 were required to come from the J/ψ vertex, and not the vertices of the extra minimum bias events. The Run Ib luminosity has been multiplied by a factor of three, to put it on an equivalent Run II luminosity scale. That is, by going to 36 bunches in Run II, each crossing will only have one sixth the amount of minimum bias event background as with the current six bunches, but the 750 ns CTC drift time integrates half the hits from the previous crossing and half the hits from the following crossing as well as the in-time hits, so the gain is only a factor of three. A significant degradation in efficiency can be seen even in the limited luminosity range of this technique, and it confirms the event mixing result.

2.4 Summary of tracking loss *without* an upgrade

At low luminosity, the CTC is a very efficient tracker. For instance, reconstruction efficiency for K^+ in $B \rightarrow J/\psi K^+$ in the pseudorapidity region less than 1 is 98%. Even in the very dense tracking environment of b-jets from top decay, the efficiency is around 87%. This high efficiency is critical, because the physics signal reconstruction efficiency is often the third, fourth, or fifth power of the single track reconstruction efficiency. At a luminosity of $10^{32} cm^{-2} sec^{-1}$ in Run IIa, the reconstruction efficiency for each primary track drops by around 10%. This will cause only a 20% loss of $J/\psi \rightarrow \mu^+\mu-$ events, but a 35% loss of SVX-tagged top events, and even larger losses for final states requiring reconstruction of higher multiplicities. Efficiency for non-primary tracks drops even faster, e.g. by 60% for K_s^0 in J/ψ events. The need to recover tracking efficiency is a strong motivation for tracking upgrades.

3 Fiber subsystem addition and expansion of SVX for Run IIa

The selected upgrade design for Run IIa of a fiber superlayer insert inside the inner radius of the CTC plus an expansion of the SVX II design from 4 layers to 5 layers is motivated by the need to fulfill the following functions:

Fibers

- The fiber superlayer compensates for the loss of inner CTC tracking layers; it regains tracking efficiency with the CTC for $|\eta| < 1$.
- The fiber track segment can be used in a level 1 trigger. (SVX II cannot because of readout time).

SVX 5th layer

- 5 SVX layers are required to make good quality 3D track segments:

  - Need 3 layers of SVX 90° stereo to have good vertexing resolution in Z.

  - Need 2 layers of small angle stereo to do the axial/stereo matching.

- 5 layers provide a robust vertex detector in the axial view:

  - Data studies show that 4 hit SVX(+CTC) tracks are higher purity than 3 hit tracks, 5 layers provide good efficiency for 4 hit tracks.

  - Monte Carlo studies show that the 5 layer design has high efficiency for segment finding.

Fibers + SVX 5th layer

- Fiber+SVX II stand alone tracking extends tracking to $|\eta|$=2, beyond the region covered by the CTC (albeit with lower P_t resolution).

3.1 The fiber subsystem

The proposed scintillating fiber system consists of 6 layers of axial fiber doublets, and 6 layers of small angle stereo doublets, at radii between 17 cm and 27 cm, as shown in Figure 9. Fiber diameter is chosen to be 500 microns, with 600 micron fiber to fiber spacing, as shown in Figure 10. Full details of the proposed

hardware system are in the companion document, *Proposal for an Intermediate Scintillating Fiber Tracker (IFT) for Run II: IFT Hardware.*

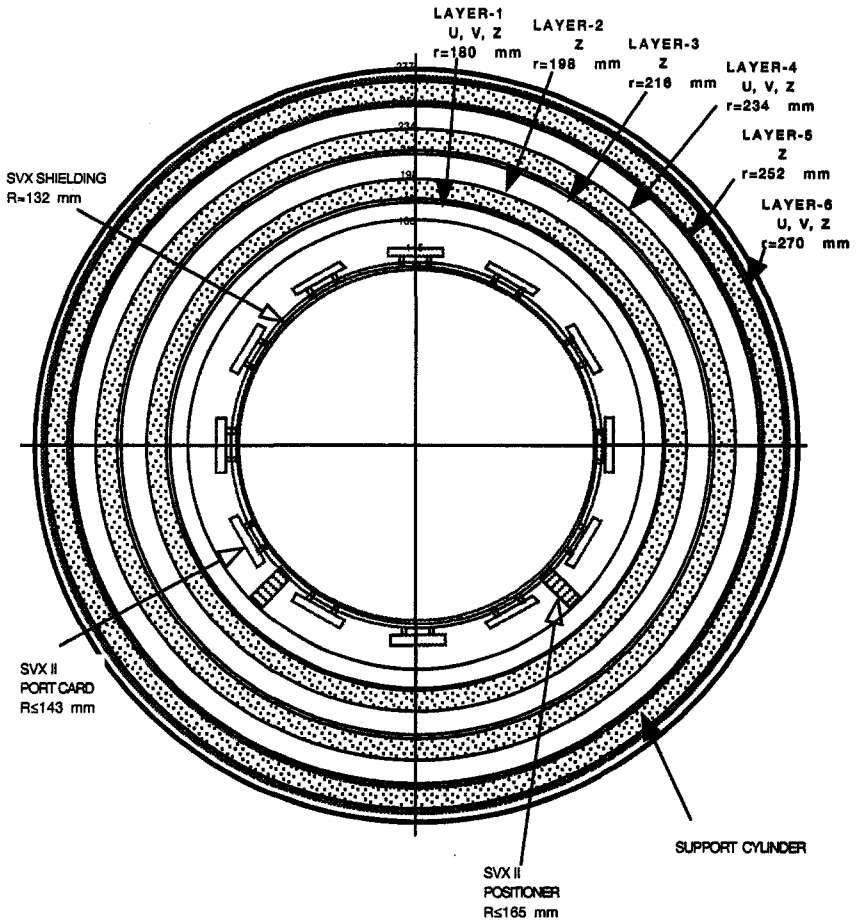

Figure 9: End view of scintillating fiber tracker.

The fiber system is a good match to the SVX and the outer layers of the CTC in terms of granularity, as can be seen in Figure 11.

The 500 micron fibers, which actually have 440 micron diameter active area, also will have reasonably low occupancy at L=$10^{32} cm^{-2} sec^{-1}$, as shown in Figure 12. The fiber occupancy is derived by scaling from CDF VTX detector occupancy. About half of the occupancy comes from the physics event. J/ψ events are used here, but top events have very similar occupancy. The other half of the hits are from the 2.7 minimum bias events per crossing that one

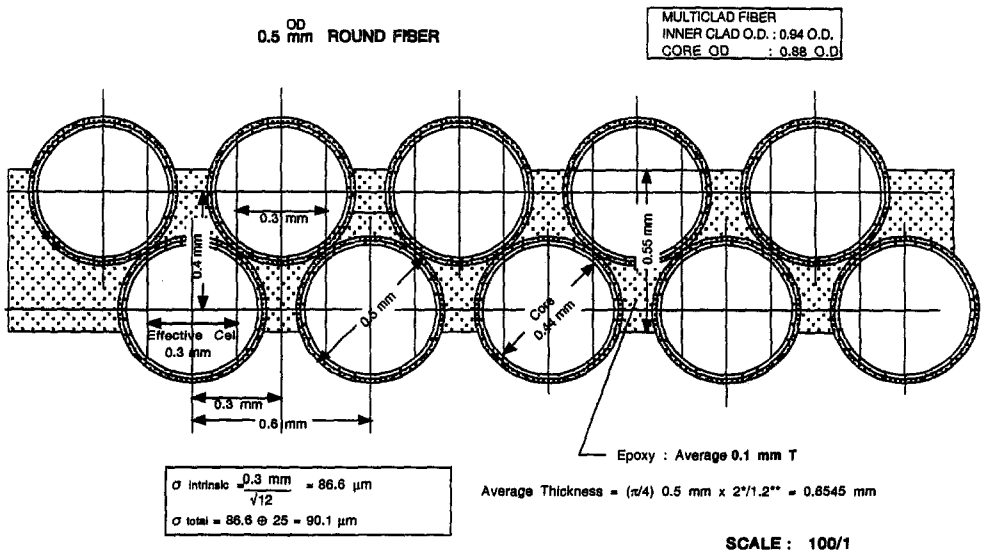

Figure 10: A scintillating fiber doublet layer.

will have with 396 ns bunch spacing in Run IIa. The CTC occupancy includes hits from twice as many minimum bias events, since it sees half the hits from adjacent crossings. Switching to 132 ns bunch spacing for Run IIb will cut the minimum bias occupancy for the fibers and SVX II down by a factor of three for the same luminosity, but doesn't affect the CTC occupancy.

Figure 13 compares the slope resolution of the CTC and fiber systems, using top Monte Carlo events, at the radius of the fibers. This gives some feeling of the pattern recognition help the fibers can give the CTC, in terms of a segment instead of just hit points. The resolutions are a good match. Note the growing tails in the CTC resolution as the luminosity is increased, reflecting the growing occupancy problems, while the fiber tails are stable.

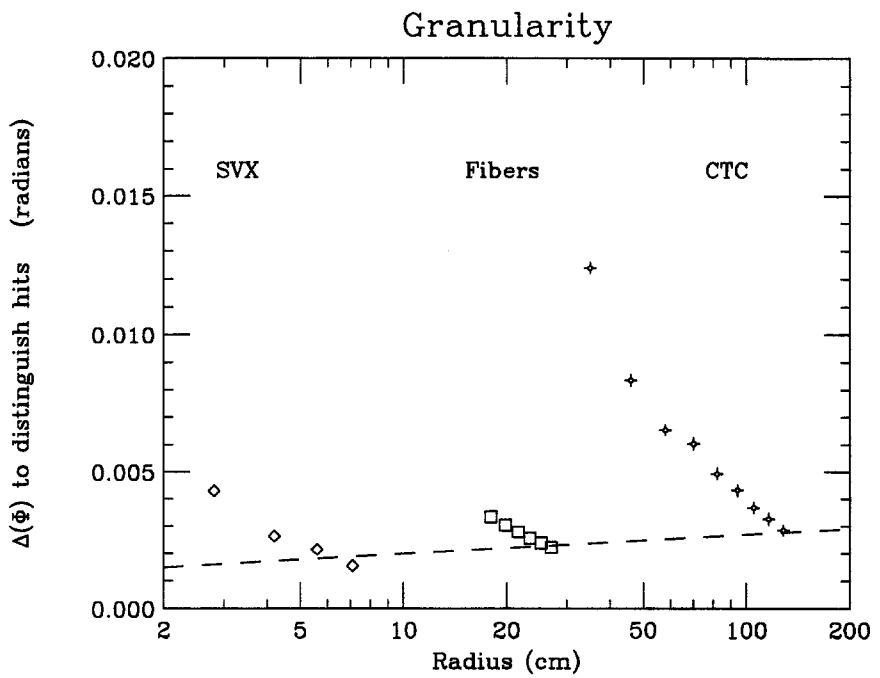

Figure 11: Rough comparison of the granularity of the tracking subsystems. A 'two-track' angular resolution is calculated by taking *a*) two times the axial strip width divided by the radius for the SVX, *b*) 600 microns (the singlet fiber spacing) divided by the radius for the fibers, *c*) the average pulse width divided by the radius for the CTC. The dashed line is meant to set the scale in a dense jet tracking environment; 10% of the time, there will be a second track less than that distance from a high P_t track in top events.

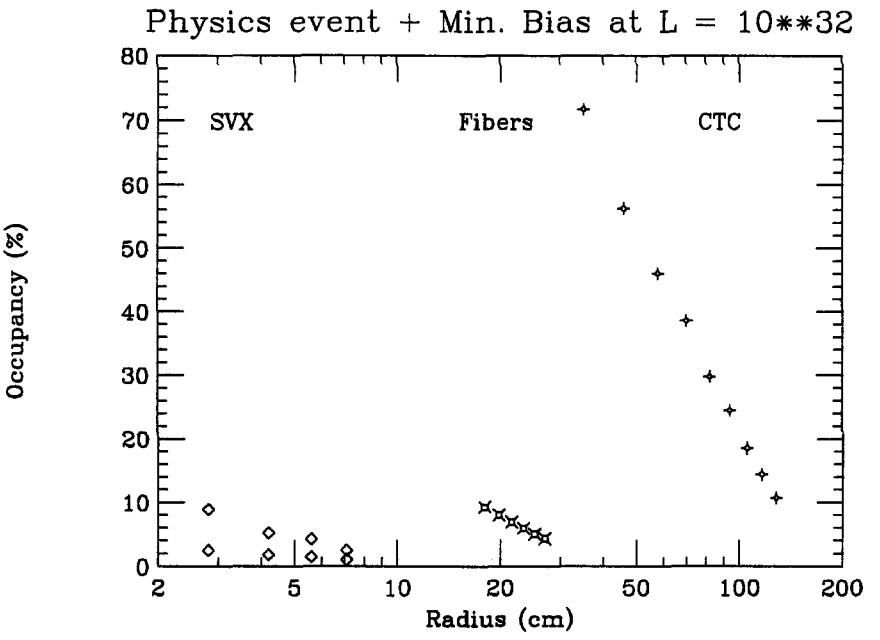

Figure 12: Occupancy in the tracking systems. For the SVX (diamonds), the upper points are for 90° stereo layers. The SVX occupancy is 'hit strips', as distinguished from read-out occupancy. (The nearest neighbors of hit strips are also read out, increasing read-out occupancy by about a factor of two).

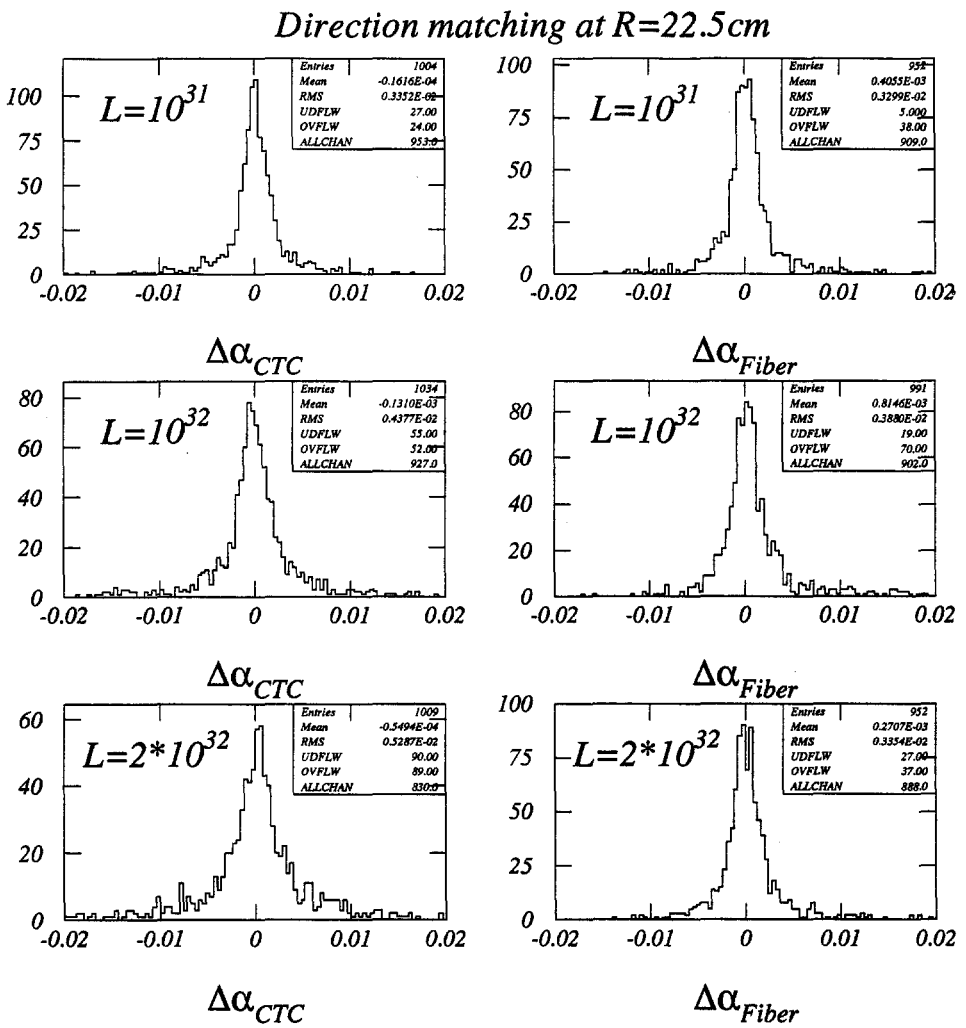

Figure 13: The difference between reconstructed angle and the angle of the generated track, for tracks from b-hadron decay in top Monte Carlo events. The left plots are tracks reconstructed with the CTC alone, extrapolated to the radius of the fibers; the right plots are reconstructed by the fiber system alone.

3.2 The SVX II subsystem

The 5-layer SVX II detector (Figure 14) is a natural extension of the previously proposed and approved 4-layer device [3]. Table 2 shows a comparison of design parameters between the present SVX′, the approved 4-layer SVX II, and the proposed 5-layer SVX II detectors. The additional 5th layer will match the wedge geometry defined by the inner 4 layers and be located at a radius of 10 - 11 cm from the beamline. The small angle stereo capabilities will allow standalone vertexing in r-z and the matching of hits between the r-ϕ and r-z coordinates. The width of the detectors in the 5th layer is approaching 6 cm and 6 inch wafer technology is already being developed and prototyped for fabrication of these detectors. A backup scheme using standard 4 inch wafers exists, whereby the 32 cm long ladders for the 5th layer are built with 6 rather than 4 detectors. Initial design studies indicate that the 64% increase in channel count from the extension of the 4 layer detector should not cause any problems in the mechanical construction, cooling, or readout of the device. As always, the material contribution of the detector will have to be minimized and carefully monitored in conjunction with the other upgrades. Given the similarity in the design and ladder fixturing, the construction schedule should be able to accomodate the 25% additional ladders composing the 5th layer without difficulty. As discussed in this document, we believe a 5-layer SVX II detector is required to achieve the necessary robustness and standalone tracking capability required for high luminosity data-taking at the Tevatron.

The cost estimate for the 5 layer SVX II system is shown in Table 3. While we are pursuing the development of detectors using 6 inch wafers, which could result in significant cost savings, the cost estimate for the design using more standard 4 inch wafers is used for planning purposes.

Detector Parameter	SVX′	4-layer SVX II	5-layer SVX II
Readout coordinates	r-Φ	r-Φ;r-z	r-Φ;r-z
Number of barrels	2	3	3
Number of layers per barrel	4	4	5
Number of wedges per barrel	12	12	12
Ladder length	25.5 cm	32.0 cm	32.0 cm
Combined barrel length	51.0 cm	96.0 cm	96.0 cm
Layer geometry	3° tilt	staggered radii	staggered radii
Radius innermost layer	3.0 cm	2.4 cm	2.4 cm
Radius outermost layer	7.8 cm	8.7 cm	10.7 cm
r-ϕ readout pitch (μm)	60;60;60;55	60;62;58;60	60;62;60;60;57
r-z readout pitch (μm)	-	150;133;133;150	150;133;60;150;57
Readout channel length (r-ϕ)	25.5 cm	16.0 cm	16.0 cm
r-ϕ readout chips/ladder	2;3;4;6	4;6;10;12	4;6;10;12;16
r-z readout chips/ladder	-	4;6;6;8	4;6;10;8;16
r-ϕ readout channels	46,080	147,456	221,184
r-z readout channels	-	110,592	202,752
Total number of channels	46,080	258,048	423,936
Total number of readout chips	360	2016	3312
Total number of detectors	288	576	720
Total number of ladders	96	144	180

Table 2: Comparison of the SVX′, 4-layer SVX II, and 5-layer SVX II detector geometries.

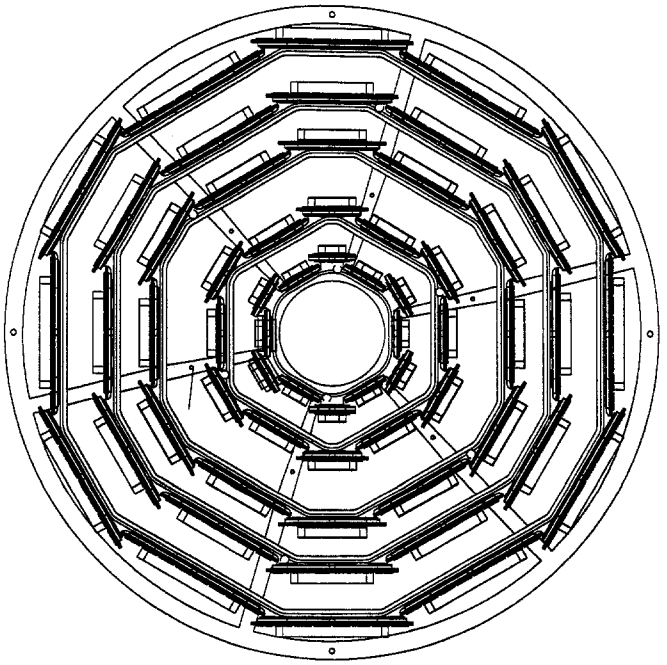

Figure 14: End view of the 5-layer SVX II detector.

SVXII 5-Layer Cost Estimate

Equipment Costs ($K)	4-Layer Cost Est		5-Layer Cost Est (6 inch wafers)		5-Layer Cost Est (4 inch wafers)	
		With contingency		With contingency		With contingency
Detectors	1951	2344	1960	2355	2690	3231
Mechanical Fabrication	1409	1560	1611	1785	1611	1785
DAQ Fabrication	2321	2854	3108	3822	3108	3822
Total	**5680**	**6758**	**6679**	**7962**	**7409**	**8838**
Additional development for small angle detectors			100	120	100	120
Incremental Cost for 5th Layer			**1099**	**1324**	**1829**	**2200**

Table 3: The cost estimate comparison for the addition of a 5th layer for the SVX II system.

3.3 CTC + fiber system performance

We have studied the efficacy of the fiber system in recovering CTC track reconstruction efficiency using top Monte Carlo events, overlayed with Monte Carlo minimum bias events to simulate high luminosity running. In this study, the extra minimum bias events were properly time shifted to correctly simulate the pattern of hits in the CTC from adjacent beam crossings with 396 ns bunch spacing. Table 4 shows the bottom line results of per track efficiency for b-daughter tracks. The fact that the CTC track reconstruction efficiency at low luminosity is 87% can be understood from Figure 11; of order 10% of the time tracks in the these dense jets are closer together than the CTC granularity. The drop in CTC tracking efficiency to 77% at L=$10^{32} cm^{-2} sec^{-1}$ is due to random occupancy from the extra minimum bias events. The efficiency of tagging a b-jet using secondary vertex reconstruction falls as about the third power of the track reconstruction efficiency, so the relative per track efficiency of (77%/87%) = (88%) going from low luminosity to L=$10^{32} cm^{-2} sec^{-1}$ implies a relative per event efficiency of around $(77\%/87\%)^3$ = 68%. This agrees reasonably with the 65% relative event efficiency seen previously in the event mixing studies.

Run	I	IIa	IIb
Luminosity ($cm^{-2} sec^{-1}$)	10^{31}	10^{32}	2x10^{32}
Track Eff. CTC	87%	77%	60%
Track Eff. CTC+fiber	93%	88%	80% 2D

Table 4: Per track reconstruction efficiency, tracks from b-daughters in top Monte Carlo events. Statistical errors are about 1%.

First, we examine the Run IIa implications of the fiber upgrade. The important point is that with the addition of the fibers in the pattern recognition and fitting, the reconstruction efficiency of 88% at L=$10^{32} cm^{-2} sec^{-1}$ is as good as the CTC-only reconstruction efficiency at low luminosity. Hence the fiber insert recovers the reconstruction efficiency for the Run IIa conditions!

Figure 15 shows the impact parameter resolution for the CTC-only tracks. As the inner layers degrade at high luminosity, the resolution is degrading. Figure 16 shows that the impact parameter resolution is significantly improved by the addition of the fiber system, as one would expect by adding high resolution

points at smaller radius. It also shows little degradation at high luminosity. Thus, although we have not run SVX pattern recognition with the CTC+fiber tracks, we are confident that the association will be good.

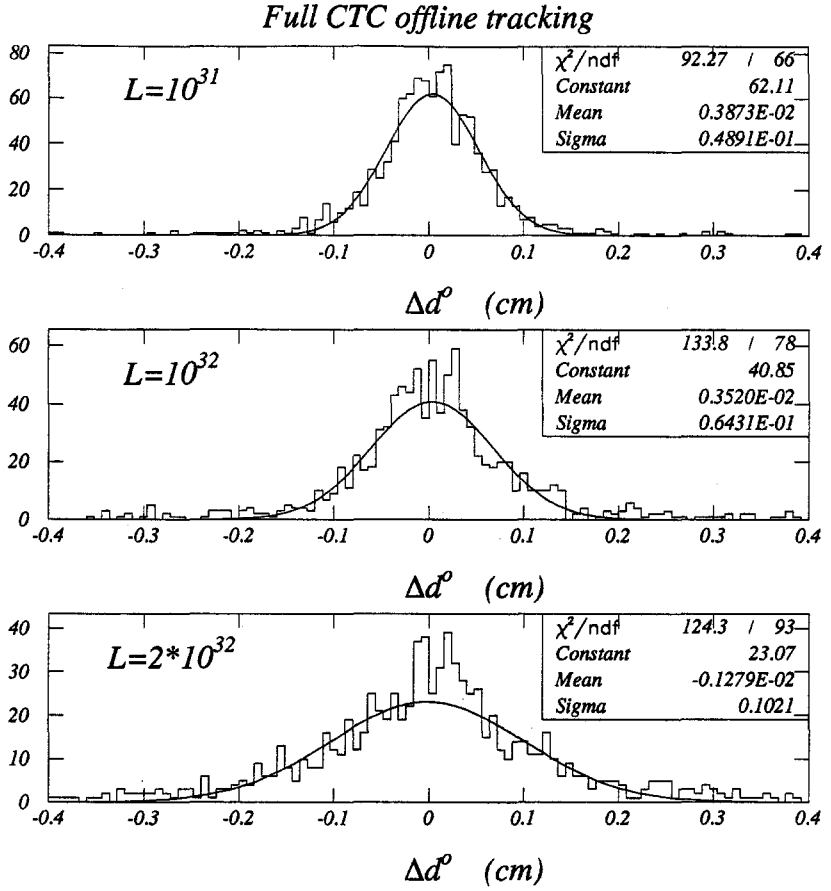

Figure 15: CTC impact parameter resolution: the difference between reconstructed and generated impact parameter for b-daughter tracks in top Monte Carlo events.

Figure 17 shows the number of correctly and incorrectly associated CTC hits on the tracks. The algorithm does a good job of limiting the number of incorrect hits associated with the tracks. However, we see even more clearly that at high luminosity the inner layers of the CTC have become useless.

Now lets look at the Run IIb efficiency in Table 4. The per track reconstruction efficiency drops to 80%, even with the fiber superlayer addition. This is for two dimensional, axial track reconstruction. For the other cases in the table, the stereo association to get 3D tracks is nearly 100% efficient given that a 2D axial track was found. In this case, the efficiency for 3D tracks was less;

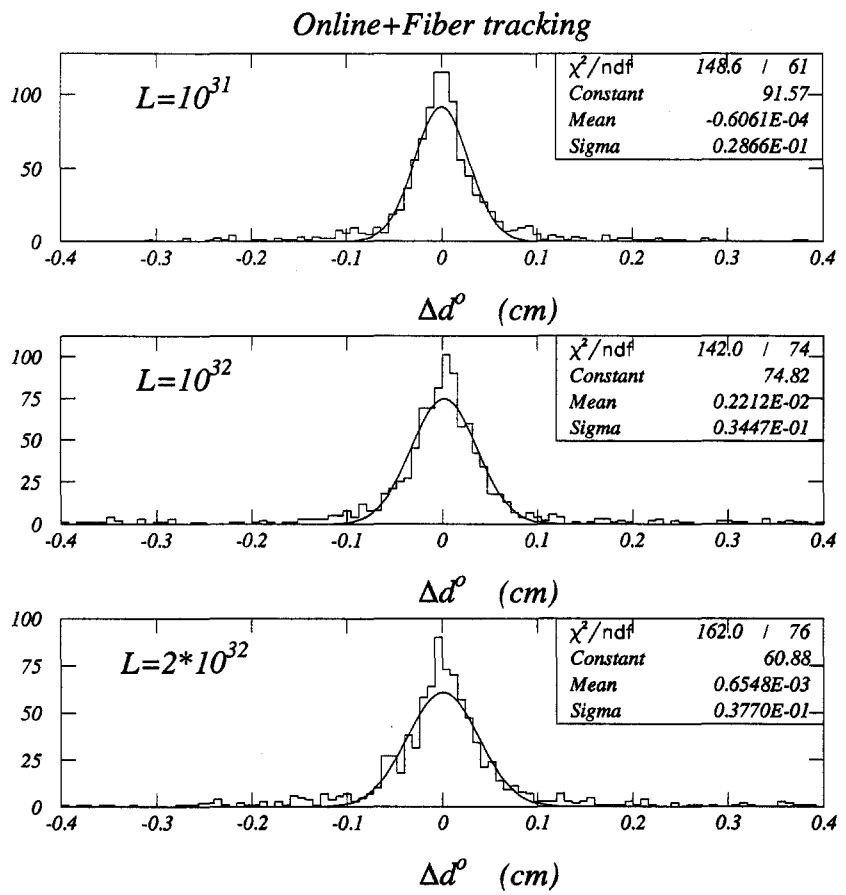

Figure 16: Impact parameter resolution of the CTC + fiber tracking system: the difference between reconstructed and generated impact parameter for b-daughter tracks in top Monte Carlo events.

but we have not yet used the stereo fibers to try to help the CTC stereo, which may bring the efficiency back up. Hence the 80% is an upper limit on the 3D track reconstruction. Once again, since the tag efficiency is proportional to the single track efficiency raised to a high power, this drop will seriously impact the CDF physics reach. Thus a replacement for the CTC will be needed when the luminosity becomes greater than $10^{32} cm^{-2} sec^{-1}$.

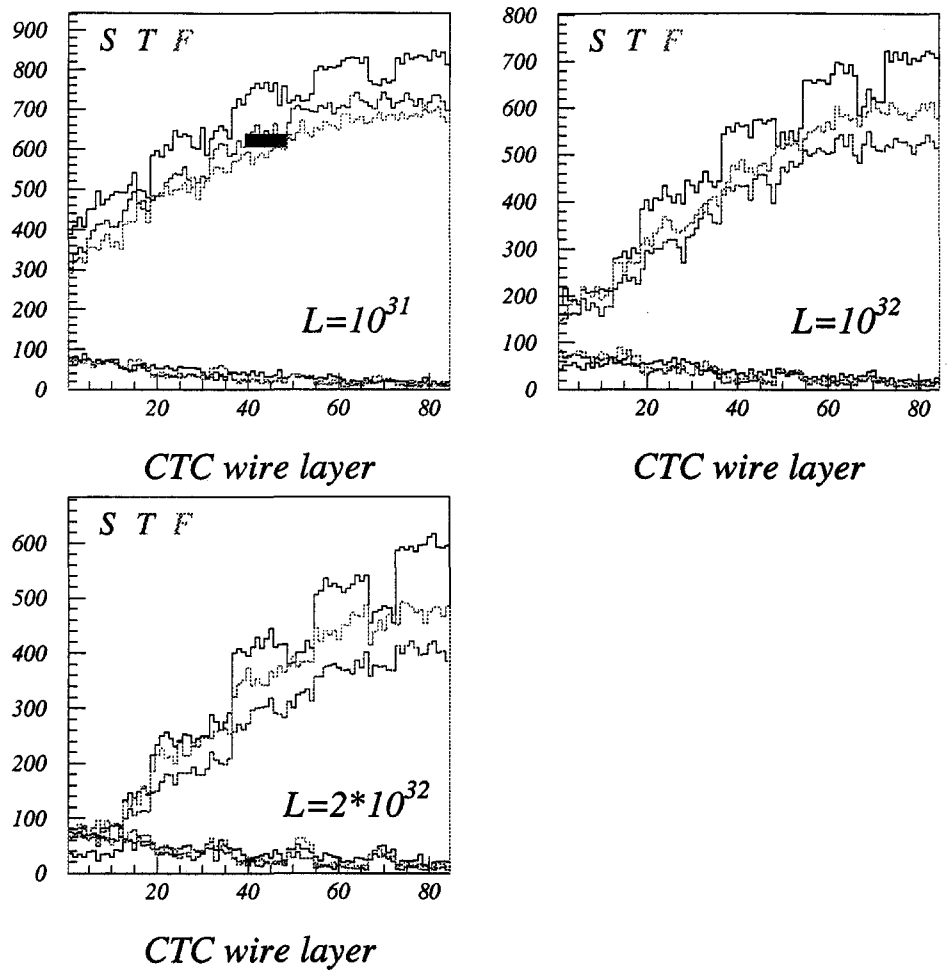

Figure 17: Parentage of used hits in the CTC, for the tracks from b decay in the top Monte Carlo samples. The upper curves show the number of correct hits used, the lower curves show the number of incorrect hits used. The curve labeled S used the standard offline CTC tracking, T used a stripped down version of CTC tracking, and F used the fiber segments to aid CTC reconstruction, in conjunction with the T version.

3.4 SVX II performance

Table 5 demonstrates the improvement in association of the axial and stereo hits in the SVX II with the modification of some layers to small angle stereo. This particular study was done with stand alone SVX II axial pattern recognition. There should be further improvement with the addition of the fiber stereo layers.

Stereo configuration	small angle stereo angle	purity 5 hit tracks	purity 4 hit tracks
90-90-90-90-90		36%	45%
90-90-s-90-s (*)	1°	73%	71%
90-90-s-90-s	2°	73%	70%

Table 5: For 5 layer SVX II stand alone track reconstruction, the percentage of the time that all of the stereo hits associated with a correctly found axial segment were from that same generated track. From $\bar{t}t$ Monte Carlo with 3 extra minimum bias interactions per event. (*) marks the proposed configuration.

Table 6 shows the increase in purity of tracks with the addition of the small angle stereo SVX II layers, for SVX II reconstruction driven with CTC tracks. The study starts with all CTC tracks with $P_t > 0.4\ GeV/c$ from Monte Carlo $\bar{t}t$ events with 2.7 minimum bias interactions per event, that passed through the SVX II fiducial acceptance. The efficiency for adding SVX II hits to these tracks is high. Tracks are then called 'pure', if all the SVX II hits associated with the track were actually generated by the track. In the 4-layer scheme, the purity of the axial hits is high, but the stereo association is significantly worse. The 5-layer small angle stereo scheme cuts the number of impure tracks down by about a factor of two, compared to the 4-layer all 90° stereo scheme, in spite of adding another layer which gives another chance to pick up a wrong hit. The table also shows that the impure tracks usually only have one wrong hit associated.

While the primary motivation for the addition of a fifth layer in the SVX II system comes from the need for sufficient stereo layers, the extra axial layer will also be very useful for improving the efficiency and quality of SVX reconstruction. To illustrate this, Table 7 gives a rough estimate from Run I data of the fraction of tracks with good SVX reconstruction, as a function of how many SVX hits were associated to CTC tracks. In jet triggered data, only a very small frac-

	4 layer SVX II 90-90-90-90	5 layer SVX II 90-90-s-90-s
tracking efficiency	97±1 %	99±1 %
axial track purity	93±1 %	95±1 %
$\leq$ 1 wrong axial hit		98±1 %
stereo track purity	82±1 %	90±1 %
$\leq$ 1 wrong stereo hit		98±1 %

Table 6: SVX II track efficiency and purity for CTC driven SVX II track reconstruction. Purity is defined here as the fraction of tracks in which all of the SVX II hit associations were correct. The '$\leq$ 1 wrong hit' entries allowed one wrongly associated hit in the case that 5 hits were associated.

tion of the tracks should have a physics induced impact parameter. The number of tracks with an impact parameter greater than, say, 3 times the calculated resolution is thus a rough estimate of the number of mis-reconstructions. As shown in the table, the quality improves tremendously with 4 hit tracks — however due to the cracks between barrels and dead channels, only about 75% of tracks end up with 4 hits in a 4 layer system. With a 5 layer system, nearly all real tracks should have 4 hits.

# SVX hits on track	2	3	4
Fraction with good reconstruction	14%	48%	84%

Table 7: Rough estimate of the fraction of tracks with good SVX reconstruction in jets: the fraction of tracks with impact parameter $< 3\sigma$ in random jets.

3.5 SVX II + fiber system performance

The fiber and SVX II subsystems will cover a much larger rapidity range than the CTC, so it is natural to ask what one can gain from using tracks which are not in the CTC fiducial acceptance. While the reconstruction code that combines fibers+SVX without the CTC is not yet ready, the results from stand

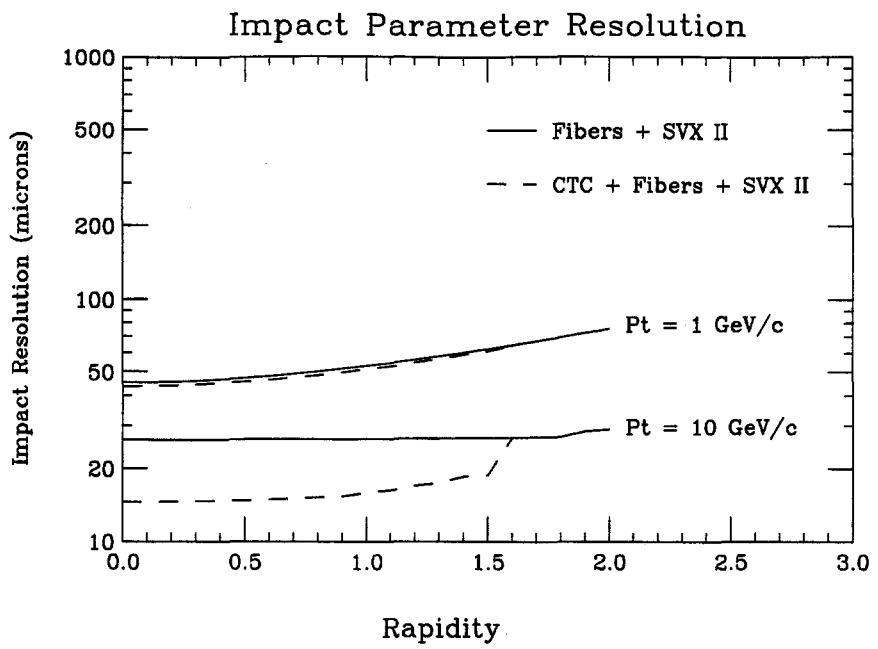

Figure 18: Calculated impact parameter resolution for SVX + fiber system standalone, compared to resolution using entire tracking system.

alone segment finders in each device indicate that there is a substantial gain to be made.

Looking once again at b-daughter tracks from top as an example, only 77% pass through the CTC outer layer but 97% are in the SVX II and fiber fiducial area. The current fiber segment finder is 90% (84%) efficient for these extra 2D (3D) tracks, with signal:background of 3 : 1. The 5 layer SVX segment finder, requiring 5 or 4 hits, is 97% efficient with signal:background of 1.2 : 1. The combination of these segments should greatly reduce the background, providing good quality efficient tracking. (We note that in a 4 Layer SVX system, the axial segment finder is only 82% efficient, with worse signal:background of 0.6 : 1.) Finally, Figure 18 indicates that the impact parameter resolution of the combined fiber+SVX system will be nearly as good as the CTC+SVX system. Hence, the fiber+SVX standalone tracking should significantly increase top tagging acceptance.

The fiber+SVX tracking should work even better in less dense tracking environments, to provide tracking of electrons into the upgraded plug calorimeter, to provide charge-vertex or jet-charge B flavor tagging, etc.

4 CTC replacement in Run IIb

The 750 ns drift time in the CTC, which causes it to see hits from out-of-time crossings, is what makes the CTC performance deteriorate faster than the fibers or SVX with increasing luminosity. The other properties of a gas tracker, low mass and relatively low cost to instrument a large volume, still are attractive. Simple scaling implies a gas tracker of similar scope to the CTC, but with a maximum drift time of 100 ns or less, would work well at L=3x$10^{32} cm^{-2} sec^{-1}$ with 132 ns bunch spacing. Two possible wire chamber replacements for the CTC, which meet this requirement, are currently under consideration.

4.1 Straw chamber

A straw tube chamber similar to the one planned for the SDC detector is one candidate. The large amount of R&D done for the SDC chamber gives one confidence in this solution. In fact, the CDF requirements would be less stringent than the SDC requirements. For CDF, the straw tubes would only be 3 meters long. The lower bunch crossing frequency means we could potentially use a conventional Argon-Ethane gas mixture instead of a fast gas. And the support structure is not quite as challenging.

Figure 19 shows a possible straw chamber configuration. It consists of 4 axial and 4 stereo superlayers. Each superlayer is 8 straws thick. The inner half of the chamber is made from 4 *mm* diameter straws, the outer half is made from 6 *mm* diameter straws.

A cost estimate for this configuration was made by scaling, item by item, from the SDC OTD Cost Estimate of March 1992. (E.g. straw tube material scales linearly with length, but support cylinder cost drops faster than linearly with radius, and program management costs were reduced less than linearly). A summary of the chamber costs, and comparison to the SDC costs, is shown in Table 8. An estimate of the electronics, trigger, and cabling costs in the CDF environment are added to the chamber costs in Table 9. The bottom line is $ 14.3 M for the entire straw system.

Another feature of the straw tube tracker is that, by using a faster gas, it could resolve a 60 ns bunch spacing. This would be important if there were further Tevatron improvements that allowed a bunch spacing less than 132 ns, with higher luminosity. This would double the instantaneous luminosity it could

WBS	Straw Chamber Cost Estimate (K$) Description	Material	Labor	EDIA	CDF 65712 channels Subtotal	SDC 141000 channels Subtotal
1.2.1	**Modules**				3110	7379
1.2.1.1	Axial Modules	690	765	100		
1.2.1.2	Stereo Modules	690	765	100		
1.2.2	**Support Structure**				2728	6007
1.2.2.1	Support Cylinders (4)	563	10	50		
1.2.2.2	Support Shim Rings (36)	750	50	50		
1.2.2.3	Cylinder Spaceframes	930	20	180		
1.2.2.5	External Support System	50	20	55		
1.2.3	**Cyl. and Frame Assy.**				194	363
1.2.3.1	Tooling and Preparation	4	27	5		
1.2.3.2	Assembly and Alignment	19	119	20		
1.2.4	**Modules into Support Struc.**				89	306
1.2.4.3	Module Instalation	2	30	30		
1.2.4.4	Alignment	2	25			
1.2.5	**Equiptment, Tooling & Fixture**				1636	5540
1.2.5.1	Module Assembly Tooling	50	200	100		
1.2.5.2	Support Structure Assy. Tooling	562	43	107		
1.2.5.4	Inspection and Align Tooling	60	10	15		
1.2.5.5	Surface Facility Assy. Tooling	172	24	50		
1.2.5.8	Electrical Function Test Equipt.	200	18	25		
1.2.6	**Utilities**				0	631
1.2.7	**Final Testing at CDF**				121	236
1.2.7.1	Leak Testing	4	22	2		
1.2.7.2	Functional Tests	43	32	10		
1.2.7.3	Alignment Tests	3	1	4		
1.2.9	**Gas System**				200	737
1.2.9.1	Cooling Gas	0	0	0		
1.2.9	Drift Gas	150	10	40		
1.2.10	**Facilities**				510	1678
1.2.10.1	Module Assembly Facility	150	150	0		
1.2.10.2	Support Assembly Facility	0	200	10		
1.2.11	**Program Management**				1300	1744
1.2.11.3	Reports	0	0	100		
1.2.11.4	Systems Engineering	40	0	250		
1.2.11.5	Project Engineer	80	0	500		
1.2.11.6	Safety Management	40	0	125		
1.2.11.7	Quality Management	40	0	125		
1.2.12	**R&D Effort**				260	1206
1.2.12.1	Construct Prototypes	30	30	0		
1.2.12.2	Other Efforts	100	0	100		
1.2	**TOTAL**	5424	2571	2153	**10148**	25827

Table 8: Cost of a straw tube chamber replacement for CTC, with SDC straw tracker cost estimate as a comparison, without contingency.

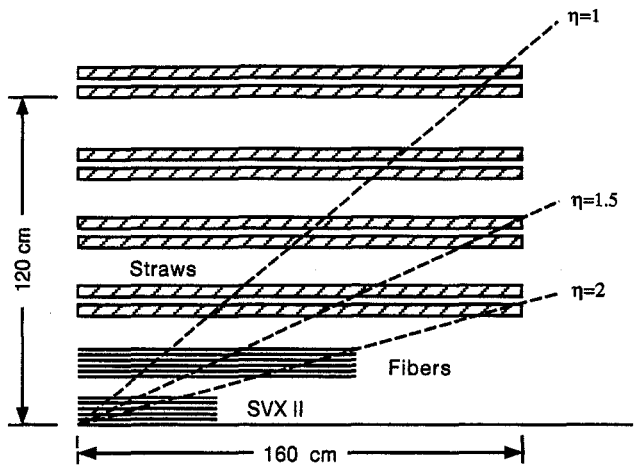

Figure 19: Quadrant view of a possible configuration for a straw chamber replacement of the CTC.

handle.

Straw System Cost		
Straw Chamber		$ 10,148 K
Electronics R&D		$ 450 K
Electronics	70K chan. at $46/chan.	$ 3,220 K
Trigger		$ 500 K
Total		**$ 14,318 K**

Table 9: Estimated cost of a straw tube chamber replacement for CTC, including electronics and trigger, without contingency.

4.2 CTC style chamber

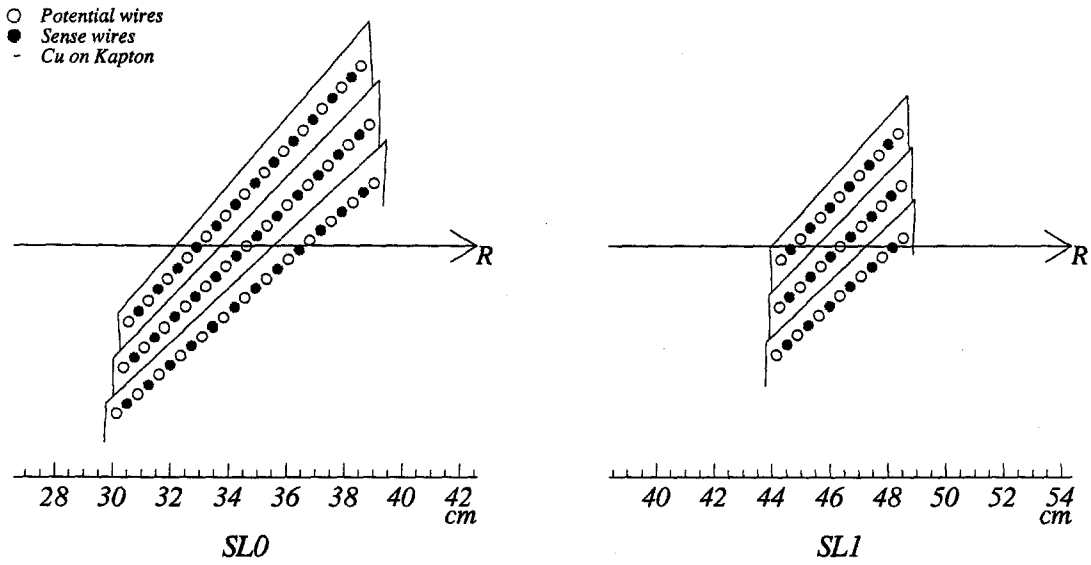

Figure 20: Possible configurations for axial and stereo cells of a CTC style CTC replacement.

By doubling the drift velocity, and making cells with one fourth the drift distance, one can reduce the drift time in CTC-like cells from 750 ns to under 100 ns. R&D is currently under way for such a chamber.

An exact copy of the CTC with 1/4 the cell width is impractical because of the field wires. i) They would produce too much tension on the end plates, ii) the wires would be massive enough to produce large multiple scattering, and iii) the field irregularities near the field plane then cover a significant fraction of the total available drift region. To get around this, the thought is to use copper coated kapton as field planes instead of field wires, as shown in Figure 20. The result would be a chamber with manageable tension, the same or slightly fewer radiation lengths of material than the CTC, and a smooth field plane.

An estimate of the cost, based on scaling of the costs to build the original CTC, and with inflation factored in, comes to $ 9.9M, as shown in Table 10. This is for a 9 superlayer device, the same as the CTC. It includes electronics and trigger, but not contingency.

R&D is being done to see if such a chamber can actually be built. If it can, it has the advantages that it could be instrumented to measure dE/dx, and it

	CTC cost	Scale factor to CTC II	Inflation factor	CTC II channels	Cost / channel	CTC II cost
M&S	$ 2,128 K	1.2	1.63			$ 4,162 K
Labor	$ 853 K	2	1.63			$ 2,781 K
Electronics	$ 818 K			24,624	$ 100.	$ 2,462 K
Trigger						$ 500 K
Total						**$ 9,906 K**

Table 10: Estimated cost of a CTC-style replacement for the CTC, including electronics and trigger, without contingency.

would have fewer radiation lengths of material than the straw option.

4.3 CTC replacement schedule

We will continue to study the above two options, with the goal of selecting one and submitting a conceptual design report in about one year.

Installation would occur around the year 2001. We note that the original CTC took about 3 years to build.

5 Cost summary

Table 11 summarizes the cost of the various upgrades. (Breakdowns of cost estimates can be found in in Table 3 for the SVX II, in Tables 8 and 9 for the straw chamber option, Table 10 for the CTC-style CTC replacement, and in the IFT Hardware document Table 8, for the fibers). The costs are expected to be split between the US, Italy, Japan, and Taiwan.

Run	Upgrades	Cost ($ FY 1995)
IIa	Fiber superlayer	$ 4.8M
	SVX II 5th layer	$ 1.8M
	Total	**$ 6.6M**
IIb	Straw tracker	$ 14.3M
	or	
	CTC II	$ 9.9M

Table 11: Cost Summary of Tracking Upgrade Proposals, without contingency.

References

[1] The CDF Collaboration, *Observation of Top Quark Production in $\overline{p}p$ Collisions with the CDF Detector at Fermilab*, Phys. Rev. Lett. **74**, 2626 (1995).

[2] *Expression of interest in a future collider detector in B0*, CDF Note 2436.

[3] *SVX II Upgrade Proposal*, CDF Note 1922.

Proposal for an

Intermediate Scintillating Fiber Tracker (IFT)

for Run II:

IFT Hardware

Version 2.2

March 26,1995

S. R. Amendolia, F. Bedeschi, G. Bellettini, V. Cavasinni, G. Chiarelli, B. Denby, V. Flaminio, A. Franceschi, S. Galeotti, G. L. Introzzi, A. Menzione, F. Raffaelli
University of Pisa and INFN

K. Hara, T. Kikuchi, S. Kim, K. Kondo, S. Miyashita, I. Nakano, M. Sano, K. Takikawa, K. Yasuoka
University of Tsukuba

M. Atac, P. Berge, M. Binkley, J. Elias, J. Hylen, J. C. Yun
Fermilab

C. Bromberg, J. Huston, R. Miller
Michigan State University

F. Abe, M. Mishina, Y. Morita
KEK

D. Cauz, G. Pauletta, L. Santi
University of Udine

Dario Bisello, Nicola Bacchetta
University of Padova

T. Okusawa, T. Yoshida
Osaka City University

Abstract

We propose a scintillating fiber tracking detector for the high luminosity conditions of Collider Run II where the performance of the inner layers of the central tracking chamber (CTC) will be compromised by high occupancies. The fiber tracker would be located in the intermediate radial space that is presently occupied by the vertex time projection (VTX) detectors. The proposed detector consists of six axial and six stereo cylindrical layers of scintillating fibers, where a layer is constructed as a half-cell staggered doublet of 500 micron diameter fibers. Six layers of axial doublets will provide excellent intermediate R-ϕ track segments that connect the track segments of the SVX II with those of the CTC unambiguously. Due to the fine granularity and hence low occupancy, such system can be fully efficient at very high luminosity. This will complement the inner superlayers of CTC which may be futher degraded by the high occupancy. The axial layers will also participate in triggering, providing precise track segments for use in Level 1 track finding and in Level 2 displaced vertex identification. The six additional doublet layers with stereo angle will each provide unambiguous space point because they are laid on top of the axial layers directly without radial distances, taking advantage of the extremely small fiber diameter. Such superlaye combination of the axial and stereo layers result in excellent 3D pattern recognition of the tracks in high multipicity environment, and can point back to the SVX II with fine Z-resolution. The fiber tracker will cover $|\eta|\leq 1.8$, backing up the four layers of SVX II, so that the central region is completely covered.

The technology and knowledge we have today are sufficient to build such a system. However once the project is approved we would like to carry out an intensive R & D towards further optimization and for detailed design throughout 1995. Further simulation will be made to optimize the layer configuration for the maximum tracking efficiency. We also have a good hope for reducing the material thickness and the cost.

A year and half starting from the beginning of 1996 should be adequate for the construction of the system and one year from mid 1997 will be devoted for the installation and debugging to be ready for Run II that is scheduled to start late 1998 to early 1999.

1. Introduction

The Tevatron has an exciting prospect of very high luminosity after the main injector is completed, up to a few times 10^{32} $cm^{-2}sec^{-1}$ or even higher, at $\sqrt{s}$ of 2 TeV . It enables us to explore the high energy frontier at least for the next decade. It is especially promising after the evidence for top quark production was seen by CDF and D0. In addition we have already proven the CDF's capability of studying B-physics. A robust tracking system operating at a few $x10^{32}$ $cm^{-2}sec^{-1}$ can possibly lead to probing into CP violation in CKM matrix elements.

Therefore it is the time to examine seriously the CDF's capability of maximal use of the luminosity that will be delivered by the Tevatron starting from Run II currently scheduled in late 1998 or early 1999.

One of the main concerns is the tracking system, which has been the most crucial element in the successful physics outcome of CDF. Due to the large drift distance in the CTC, up to ~4 cm, confusion of tracks has already been showing up in the inner super-layers even in the last run. In the future 36 x 36 bunch operation (bunch to bunch interval = 396 ns) and eventual 96 x 96 bunch operation (interval = 132 ns) of the Tevatron, the situation will further deteriorate not only due to the pile up of successive bunch crossings, but also due to the expected high luminosity by increased average number of interactions per bunch crossing up to 2.6. **Fig. 1** shows the average number of interactions per bunch crossing for various operating modes of the Collider.

The outer layers of the CTC will be functional for the immediate future and the new SVX II will provide excellent tracking at small radii immediately outside the beam pipe. Therefore it is imperative to improve tracking in the intermediate region with a detector that will connect the fine tracking by SVX II at small radii to the overall tracking by the outer layers of CTC.

An excellent candidate for such role is a scintillating fiber tracking system of fine granularity.

We propose to install a set of cylindrical scintillating fiber layers in the space between the outer envelope of SVX II and the inner tube of CTC ($r \approx 16.5 \sim 27.7$ cm) that is currently occupied by the VTX. The side view of the proposed scintillating fiber layers in the tracking volume is shown in **Fig. 2**. The basic element is a doublet layer of 0.5 mm OD scintillating fibers spaced by 0.6 mm and staggered layer to layer by a half spacing as illustrated in **Fig. 3**. Due to the staggering, the average thickness is 0.65 mm and virtually there is no inefficiency at the edge of the round fibers. 0.5 mm scintillating fiber with its

effective cell size of 0.3 mm will provide an R-ϕ resolution of the order of 100 μm which is a natural choice for the space between 50 μm silicon strips of SVX II and CTC, where the resolution is on the order of 200 μm per wire. 0.5 mm fibers are also necessary to avoid confusion in the pattern recognition in the high luminosity environment due to extremely high occupancy in this radial range. The estimated resolution of 90 μm for a single staggered doublet layer of 0.6 mm pitch comes as a result of a quadratic addition of the intrinsic resolution of ~87 μm (=0.3 mm/$\sqrt{12}$) and an alignment uncertainty conservatively taken as 25 μm.

A set of six axial layers will provide a stand-alone track segment with a redundancy of three hits. The system is perfectly cylindrical and seamless in azimuth. Preliminary simulation results indicate that four hit points are quite powerful in reconstructing the entangled tracks.

The proposed intermediate tracking layers also provide a track segment in R-Z. both for connecting the R-Z track segments measured by the SVX and the CTC and also to point back the SVX's 90° strips, possibly with its own small angle stereo strips, to find the corresponding track in R-Z view to help disentangle narrowly concentrated tracks. We propose to implement six doublet layers with $\pm\alpha°$ with respect to the beam axis, which is yet to be determined by a detailed simulation. Such superlayers of the axial and stereo fiber combination provide unambiguous space points because the stereo and the axil fibers are essentially at the same radius and the ghost probability is small due to the fine granularity.

Since the fibers are flexible, the stereo layer fibers can be helical and the choice of stereo angle is not limited by mechanical considerations. The limit comes from two factors: the Z-resolution improves rapidly with increasing the stereo angle up to ~10° (See **Fig. 4.**) but flattens out beyond, and the probability of finding ghosts increases almost linearly with the stereo angle (See **Fig. 5.**). If three layers are equally implemented with a combination of U- and V-layers of ± 3° (± 6°) , the Z-resolution is 2.1 mm (0.98 mm) when extrapolated to SVX outermost layer.

It should be pointed out that the configuration of the scintillating fiber layers is flexible because the radial thickness of each super layer is only a few mm and can be adjusted without compromising the performance much once the space required by the SVX II is finalized.

The idea of using scintillating fibers for tracking system is not new. However the following three prong advances in technology have made it a perfectly practical technique. Those are: a) the significant maturity of the solid state photon detector, VLPC, b) the recent

breakthrough in the commercially available fibers, and c) the development of the technology of fiber preparation through the CDF's endplug calorimeter upgrade project.

Because of these new technical circumstances, a scintillating fiber tracking system using 0.5 mm scintillating fibers will be highly efficient, both in individual layer detection efficiency for minimum ionizing particles and in the reconstruction efficiency with excellent pattern recognition capability. It should be reminded that scintillating fiber system is quite similar to SVX because it is more or less a discrete counting device. Other possible wire-based drift chamber type devices would need knowledge of the timing in addition to the registration of the wire positions.

Also the electronics is outside the detector structure and there is no need of mounting massive electronics boards at the end of the sensitive length. The only material in front of the endplug calorimeter face are the clear readout fibers. Plastic connectors for coupling the scintillating fibers to the readout clear fibers add a small mass of low atomic number material at the end of the active scinttilating fibers.

Finally we would like to point out that the scintillating fiber tracking system does not need high voltage or electrically active components within the tracking volume. Therefore, once installed and tested, primarily for the optical connections, the fiber tracker has no need for service accesses into the central tracking volume unless damaged by unexpected cause.

2. Recent Development in Technology

2.1 VLPC

Since the initial test[1)] that proved that VLPC was an excellent low level photon detector with high quantum efficiency (≤80%), built-in high gain (~10^5), high dynamic range (≥10^3), and very low noise (≤2 photo electrons) (See the spectrum measured on the fourth generation prototype, HISTE-IV in **Fig. 6**[2)]), there have been several small scale tests[3)] by various groups to prove the basic idea of using VLPC as the photon detector.

Simultaneously the conversion of the original military version SSPM to commercial version HISTE has steadily progressed at Rockwell, the company which is the sole holder of the proprietary patent of VLPC. The quantum efficiencies of the HISTE-I through IV are compared with that of SSPM in **Fig. 7**. The conversion was to suppress the infra-red sensitivity of SSPM and increase the quantum efficiency in the blue region.

Recently D0 group[2)] has made a successful operation of a 3,000-channel cosmic ray test stand using HISTE-IV. It demonstrated a large scale application of the scintillating fiber-VLPC system was quite manageable. Their result showed that the VLPC can be stably operated in He atmosphere of ~6.5° and the number of photoelectrons and the noise level for such large scale operation is essentially the same as what was observed by previous small scale tests by other people. It also demonstrated that the quantum efficiency of the HISTE-IV was ≥70 % to be compared to the ideal quantum efficiency of ~85% of SSPM. **Figs. 8a** and **8b** are the dependence of the quantum efficiency and the rate of the noise (≥1 p.e.) of SSPM and HISTE-V, respectively, on the operating voltage.

These facts eliminate some of the original negative perceptions against VLPC. There was a legitimate concern on the completion of the R&D by Rockwell that it might be terminated at an arbitrary moment. The HISTE-V chips have been produced recently and the preliminary results of the evaluation show that the quantum efficiency is on the order of 70% and the noise level is as good as SSPM as originally hoped for. Furthermore Rockwell now sees market of VLPC in medical and other applications besides the high energy physics. Therefore, although there could still be a valid concern on the reliability of Rockwell as the sole supplier, in regard to the pricing and the delivery schedule, the very basic doubt on the wisdom of relying on the VLPC as the only adequate photon detector has been already crossed out.

2.2 Fiber Development

A major breakthrough was made on the plastic optical fiber technology at about the time when CDF started the endplug calorimeter upgrade project. Kuraray, one of the companies specialized in the plastic optical fibers and scintillators, found a technique to apply another low refractive index cladding over the ordinary PMMA cladding. After initial trials, now it is well established and all the fibers we use in the ongoing endplug upgrade are such "multiclad" fibers to be distinguished from ordinary "single-clad" fibers. **Fig. 9** illustrates the structure of the multiclad and single clad fibers.

The material for the outer cladding is fluorinated-PMMA with n=1.42 which is not new. It has been used as the cladding for PMMA core (n=1.49) plastic fibers for short distance optical connections for computers. Though it is obvious that a cladding with such lower refractive index will yield a larger light trapping aperture because of larger total internal reflection angle, it was materialized only after a technique was developed to use PMMA as an inner cladding because the fluorinated-PMMA does not adhere well directly to the core material, polystyrene (n=1.59). It still have achieve the same total internal reflection angle because according to Snell's law of refraction, the total internal reflection is determined by the smallest reflactive index, 1.42 of the outer cladding in this case, among multiple layers of different indices. Only slight sacrifice is made because the intermediate layer takes, though small, finite thickness, 6% of OD, out of the diameter of the fiber otherwise could be used as the core.

With

$$n_{core} = 1.59 \text{ and } n_{outer\ clad} = 1.42,$$

the total reflection angle within the core, measured with respect to the fiber axis, is

$$\theta^{multi}_{total} = \cos^{-1}\left(\frac{1.42}{1.59}\right) = 26.74°$$

to be compared with

$$\theta^{single}_{total} = \cos^{-1}\left(\frac{1.49}{1.59}\right) = 20.43°$$

for single clad fiber.

This in turn makes the solid angle in one direction

$$\begin{aligned}\Omega^{multi} &= \frac{1}{2}\left\{1 - \cos\left(\frac{n_{clad}}{n_{core}}\right)\right\} \\ &= \frac{1}{2}\left\{1 - \frac{1.42}{1.59}\right\} \\ &= 5.35\ \%\end{aligned}$$

to be compared with

$$\Omega^{single} = \frac{1}{2}\{1 - \frac{1.49}{1.59}\}$$
$$= 3.14\ \%.$$

Therefore the "aperture" of the multiclad fiber is 60% larger after taking account of the 6% smaller core diameter compared to a single-clad fiber of the same diameter. In order to use small diameter fibers necessitated for better resolution and low occupancy, this is an important advantage. **Fig. 10** is an illustration of such relationship.

2.3 Tools and Techniques for Fiber Preparation

The endplug calorimeter upgrade project[4)] is in the last phase of the production of the scintillator tile/fiber panels. Panels for E.M. section have been all made and the production of the hadronic section is going to be finished by the end of the year.

This upgrade project is the first large scale use of optical plastic fibers for a real calorimeter and is significantly different from other type of fiber-based detectors because individual fiber is a link of a chain that determines the calorimeter uniformity in a few to several % level. Therefore they were prepared with a highly systematic way and the necessary tools and techniques were developed prior to the mass production. At every step, the qualities of the fibers were quantitatively monitored.

First of all, we have obtained a set of statistically significant data on the commercial fibers and found that they were very much satisfactory in terms of tolerances in various parameters.

The tools we developed include single-fiber finishing diamond machine, connector finishing diamond machine, and fusion splicing machine. They have been heavily used throughout the production process and the results have been remarkably consistent. The mirroring of the fiber end is not what we have developed but our massive use proved the quality of aluminum sputtering for mirroring simultaneously proving the quality of the fiber finishing.

We have been monitoring the quality of the commercial fibers carefully because it is the basis of whole technology. We now know that the uniformity of the roundness and the diameter are excellent. **Fig. 11** is a microscope photograph of a cross section of a scintillating fiber cut by the diamond fly-cutting machine and **Figs. 12a** and **b** are the histograms of the measured diameter sampled over 16 km and 20 km of the fibers, respectively. Further detailed data taken online in the process of drawing 0.9 mm OD clear fibers were submitted by KURARAY. The diameter was mesured at every cm over the delivered 50 km and the result were a) mean value = 0.90135 mm with b) R.M.S. =

0.591 % after rejecting c) 238 points that exceeded 40 μm limit. The histograms for every 2.2 km were all well symmetric around mean value with well behaving tail. The mean values of those 25 histograms (one histogram was missing.) ranged between 0.8966 and 0.9092 mm. From such data, we can safely specify the diameter tolerance of ±2 % as the real maximum.

The light output and the attenuation length, which are dependent on the purity and the concentration of the fluor and the mechanical uniformity of the core-cladding structure, has also been very consistent. **Fig. 13** is a histogram of the light output from fibers sampled over the entire period the production of E.M. tile/fiber panels. A ~70 cm long fiber was sampled at every 150 meter waveshifter fiber over the total of 16 km and inserted into a piece of scintillator tile. Using a Sr^{90} source shining the tile, the light output from 30 cm pigtail was mesured by a phototutbe. The R.M.S. variation is 2.9 % for 116 entries. Obviously the result is a combined effect of the diamter tolerance and the fluor concentration uniformity.

Fig. 14 is a histogram of the reflectivity[4)] of the mirrors made by aluminum-sputtering on the end of waveshifetr fibers. The measurement was made by directly comparing the light output before and after the mirroring. Therefore the quality of the fiber end finishing together with the mirroring should be the main factor with small measurement accuracy. The entries with 0.8 or lower in the reflectivity are due to faulty operation of the aluminum sputtering machine at one time due to contamination by other metal.

Most of these tools and techniques are what we need to use for the fiber tracking and the endplug calorimeter upgrade project has been an immensely valuable experience on how to handle fine fibers for optical system and how to monitor them.

As a conclusion of this chapter, we find that scintillating fiber tracking is a viable solution for the tracking in the intermediate radial region where fine granularity is essential. Fine granularity directly means a sizable number of channels, but we have the technique and experience to handle such large numbers of fine optical fibers.

3. Conceptual Configuration

3.1 Overall Design

Since the design of the SVX II has not been finalized, we take the non-"Draconian" 4-layer design* and the CTC's inner tube as the "default" boundary condition.

*It is not difficult to accommodate the 6-layer design as currently presented without changing the performance of the scintillating fiber tracking we propose.

The 4-layer design calls for the leg of the "positioner" at 165 mm as the largest radius and the CTC's inner tube ID is 277 mm. Therefore we assume that the proposed intermediate fiber tracking occupies the radial range between 165 mm and 270 mm. The sensitive length in Z-direction is 1.6 meter as the default design whcih may be extended to 2.2 meter if the simulation results allow larger occupancy without sacrificing the reconstruction efficiency.

As the default design until the configuration is optimized by a detailed simulation, there will be six super layers built on a composite materail cylinder and each layer is separated by 18 mm. Therefore the radii of those layers are at r=180, 198, 216, 234, 252, and 270 mm. The composition of these layers is : (U, V, Z), (Z), (Z), (U, V, Z), (Z), (U, V, Z). The sketch of the r-ϕ profile is shown in **Figs.15a**.

There are three concentric cylinders each carrying an odd nubered super layer and a successive even numbered super layer. In each cylinder, the odd numbered super layers is on the inner suface of ~18 mm thick RHACELL core and the even numbered layer is on the outer surface of it., each epoxied over a carbon fiber cloth. The procedure of assemblying such structure is to start with the innermost carbonfiber cloth spread over a collapsable mandrel and the structural layeres are built over it one by one. The carbon fiber cloth will provide a strength along the plane of the memblane and the ROHACELL core will provide the thickness perpendicular to the memblane to provide the strength against the bending moment. Excellent long term stability is expected due to near zero value of the thermal expansion coefficient of the carbon fiber.

44 μm thick carbon fiber cloth woven out of 7 μm fibers is commercially available and it should makes a strong composite structure with ROHACELL # 31, with perforation to remove 2/3 of the material. The perforation will not have much effect on the strength because of the strength of the carbon fibers in the membrane. The subsequent layers are built identically increasing the radius by 18 mm each

time. Thus we will have three independent shells which are supported at the both ends. If necessary it is imaginable to have a low mass ring which supports and adjusts the mid point.

As shown in **Fig.15b**, in those layers that consist of axial, Z-, and stereo, U- and V-, layers, the fiber layers are laid directly over the others and epoxied. The stereo layers are with $+\alpha°$ and $-\alpha°$ with respect to the Z-axis.

Each of the fiber layers is a staggered "doublet" layer of 0.5 mm^{OD} scintillating fibers spaced at 0.6 mm center to center as shown in **Fig. 3**. The effective sensitive cell is therefore about 0.3 mm considering the core of the fiber to be 0.44 mm. Therefore the expected resolution is ~0.3 mm/$\sqrt{12}$ = 0.87 μm. If we assume a tolerance of ~25 μm which is a conservative estimate including all the effect, especially the tolerance of the fiber diameter, 2% of the OD or 10 μm as the maximum, and the positioning accuracy of 25 μm** or better, the overall resolution is estimated to be 90 μm.

** Fiber positioning of D0 group's exercise. After the fiber position is measured as a gentle function of the position in Z and corrected in the software by parametrization, the residue was ~10 μm.

The material thickness is tabulated in **Table 1**. The total weight is about 14 kg per meter in the length evenly distributed along the axis and in azimuth..

The structural strength is being studied by finite element analysis, and, though preliminary, it has been shown that such structure is highly rigid. If the cylinder is supported at the both ends, naturally the sag is the largest at the midpoint along the axis. The entire cross section of the cylinder saggs by 50 μm without deforming the circular shape. Therefore the structure is very strong and the sag is almost negligible, or could be easily corrected with a small numbre of parameters. In this calculation the length of the cylinder was 2.2 meter and was supported at the both ends assuming a flange inserted into the structure at each end. The result for 3.1 meter is in the same range.

In the above analysis the fibers are taken as a simple load. Although a super layer consists of an axial fiber doublet layer and one or two stereo doublet layers with certain angles epoxied together make a complete cage, most of the strength is from the carbon fiber cloth.

A separate study was made in which a cylinder was assumed to be made by only a single layer of 64 μm carbon fiber cloth and optical fiber layers, U, V, and Z, all epoxied together. Even such a structure turned out to be strong enough and the maximum sag at the midpoint was 20 μm. Therefore the above result is

convincing. Test is being carried out to find out the strength with realistic arrangement of 0.5 mm fibers.

Furthermore, it seems possible that the entire structure is laid in the carbon fiber plastic tube of the CTC's inner wall. The load to the wall is calculated to be be ~1/2 or smaller of the total weight, ~42 kg provided the cylinder is supported at the place of the CTC's endplates. Such scheme might be needed if the SVX II needs to be supported by the intermediate scintillating fiber tracker. Such scenario will be studied futher. A mechanism for precise alignment is also under study.

The advantage of such design of three independent shells each carrying two super layers is that all fiber layers are accessible after they are completed either by a radioactive source or by a UV or X-ray source directly. Therefore the calibration of each fibers to find out whether there is any damage is trivial. Futhermore, using proper collimator and or trigger counter of fine resolution, possibly another set of scintillating fibers or silicon strips, it is possible to survey all the fiber positones as constructed. Then after three shells are assembled into a single structure, the overall alignment can be made with cosmic rays before seeing real events in the collision hall. Naturally real events will be used at least for the confirmation of the alignment over entire azimuthal angles.

I is also possible to imagine an in situ calibration/monitoring moving a light source or radiaoactive source in the gaps between the shells.

Table 1. Material Thickness

Radii mm	Thickness mm	Material	Density	X_0 (Comment)	Rad L
First Layer	(Average thickness of fiber doublet $= \frac{\pi}{4}$ x 0.5 mm x 2 x $\frac{1}{1.2}$ + 0.1 mm (Epoxy) = 0.7545 mm)				
179.5	0.044	Carbon Fiber Cloth (44 μm)	2.265 g/cm^3	18.8 cm (Solid Graphite)	0.0234
179.5	0.1	Epoxy	1.16~1.2 g/cm3	34.4 cm (Plexiglass)	0.0291
179.5~180.5	1	Fiber Doublet (Z)	1.032 g/cm3	42.4 cm (Polystyrene)	0.1779
	0.1	Epoxy			0.0291
180.5~181.5	1	Fiber Doublet (V)			0.1779
	0.1	Epoxy			0.0291
181.5~182.5	1	Fiber Doublet (U)			0.1779
Sub Total	3.0				0.6444 %
Spacer					
182.5	0.1	Epoxy			0.0291
182.5~197.5	15	ROHACELL #31	1/3 x 31 mg/cm3	40.55 g/cm^2	0.0382
197.5	0.1	Epoxy			0.0291
	0.044	Carbon Fiber Cloth			0.0234
Sub Total	15				0.1198 %
2nd Layer					
197.5	0.1	Epoxy			0.0291
197.5~198.5	1	Fiber Doublet (Z)			0.1779
Sub Total	1				0.2070 %
3rd Layer					
215.5	0.044	Carbon Fiber Cloth			0.0234
215.5	0.1	Epoxy			0.0291
215.5~216.5	1	Fiber Doublet (Z)			0.1779
Sub Total	1				0.2304 %
Spacer					
216.5	0.1	Epoxy			0.0291
216.5~233.5	17	ROHACELL #31	1/3 x 31 mg/cm3		0.0433
233.5	0.1	Epoxy			0.0291
	0.044	Carbon Fiber Cloth			0.0234
Sub Total	17				0.1249 %

4th Layer						
233.5	0.1	Epoxy				0.0291
233.5~234.5	1	Fiber Doublet (Z)	1.032 g/cm3	42.4 cm	(Polystyrene)	0.1779
	0.1	Epoxy				0.0291
234.5~235.5	1	Fiber Doublet (V)				0.1779
	0.1	Epoxy				0.0291
235.5~236.5	1	Fiber Doublet (U)				0.1779
Sub Total	3.0					0.6210 %
5th Layer						
251.5	0.044	Carbon Fiber Cloth				0.0234
251.5	0.1	Epoxy				0.0291
251.5~252.5	1	Fiber Doublet (Z)				0.1779
Sub Total	1					0.2304 %
Spacer						
252.5	0.1	Epoxy				0.0291
252.5~269.5	17	ROHACELL #31	1/3 x 31 mg/cm3			0.0433
269.5	0.1	Epoxy				0.0291
	0.044	Carbon Fiber Cloth				0.0234
Sub Total	17					0.1249 %
6th Layer						
269.5	0.1	Epoxy				0.0291
269.5~270.5	1	Fiber Doublet (Z)	1.032 g/cm3	42.4 cm	(Polystyrene)	0.1779
	0.1	Epoxy				0.0291
270.5~271.5	1	Fiber Doublet (V)				0.1779
	0.1	Epoxy				0.0291
271.5~272.5	1	Fiber Doublet (U)				0.1779
Sub Total	3.0					0.6210 %
Light Shield						
	0.04	Tedler Film	1.39 g/cm3	28.7 cm	(Mylar)	0.0139
TOTAL	**107.5**					**2.9 % X_0**

WEGHT/SHELL : 3.6~5.0 kg/meter : Fibers : 0.203g / m x (15,616~ 21,760) = 3.2~4.4 kg/m,
: ROHACELL : 2π (18~27)cmx1mx17mmx1/3x31mg/cm^3 = .2~.3kg/m
: Carbon Fiber : 2π x 2(18~27)cm x.044 mmx2.265g/cm^{3}x1m = .2~.3kg

The numbers of fibers are shown in **Table 2** for the assumed radii. Total of ~57,000 fibers is necessary for such configuration.

Table 2. Number of Fibers

(Default Configuration)

Radii	Views	Circumference	No. of Fibers /Doublet layer	No.of Views
180 mm	U, V, Z	1,130.97 mm	3,770/View	x 3
198 mm	Z	1,244.07 mm	4,147/View	
216 mm	Z	1,357.16 mm	4,524/View	
234 mm	U, V, Z	1,470.27 mm	4,901/View	x 3
252 mm	Z	1,583.36 mm	5,278/View	
270 mm	U, V, Z	1,696.46 mm	5,655/View	x 3
Total				**56,927 Fibers**

The scintillating fibers are each mirrored at one end and the other end is connected to a 5 meter long, 0.8 mm diameter clear fiber. The sizable step in diameter of the clear fibers was necessary considering the tolerance of the alignment of the fibers at the junction and the better transmission for the larger diameter fibers through 5 meter path length to the VLPC.

The connection is made by optical connector which is a simple extrapolation of the 10-fiber connectors developed for endplug upgrade project although the number of fibers will be 128 per connector. Based on our experience, the alignment tolerance is in the range of 10 μm. The junction between the connectors is filled with a 25 μm thick film of soft RTV for index matching that eliminate Fresnel reflection which other wise cost 10 % in the light transmission through air gap.

Light shielding is provided by black Tedlar film covering the inside and the outside of the entire stack. The film continues to cover the clear fibers routed through "30° crack between the endplug structure and the central structure to the end of the clear fiber bundles at the entrance into the cryostat to be mounted on the rear face of the endwall. The space at the end of the cylinder needed for such connections expected to be within the space curren ly used by CTC, namely 5 cm for the endplate, and 10 cm for the high voltage and preamp boards in Z-direction*.

*The test made for the endplug upgrade project has consistently proved that the bending 0.83 mm fibers does not affect the light transmission even in long term if the radius is larger than 2 cm.

4. Optical Readout by VLPC

4.1 VLPC

The photon detector is VLPC which is an acronym of silicon device, Visible Light Photon Counter. A microscope photograph is shown in **Fig. 16**. The characteristic of VLPC is summarized in **Table 3**.

The HISTE-V produced recently is 70 ~ 75 % in quantum efficiency according to the preliminary evaluation and it is expected to achieve ~80 % close to the military version SSPM's QE of 85 %.

The noise level has been shown to be ≤1 photoelectron. The gain was ~20,000 for HISTE-IV and became 80,000 for HISTE-V with the operating DC voltage of 6.5 V. The linearity and the repetition rate is only dependent on the areal saturation by the number density of photons each creating an avalanche of about 10 μm in lateral profile. Though the area within such an avalanche is saturated for ~10 μ sec, the accidental overlap of two photons hitting the same spot within the cell, 1 mm round for our choice, is extremely small** especially for the fiber tracking in which average number of photons is expected to be ~10 per MIP.

**A test showed no saturation up to 3,000 photons into one cell.

The rise and fall time is faster than a few ns. Therefore the output pulse shape is dominated by the amplifier's rise time and the decay time of the scintillator fluor of ~10 ns in exponential decay time constant.

The operating point has to be ~6°~7° K which can be provided by holding the VLPC in a He gas atmosphere slightly above liquid He level. It has been demonstrated that maintaining the temperature within ±0.5°*** for stable operation is not difficult with a simple temperature monitor and a resistor as a heater.

*** If cooled lower than 6°, the quantum efficiency drops and at temperature higher than 7° the noise level increases though the quantum efficiency does not increase beyond a plateau. See **Fig. 8b**.

4.2 Cassette and Cryostat

Since the VLPC has to be kept in a cryostat, the signal light brought by 5- meter long clear fiber has to be guided into the surface of VLPC by another clear fiber bundle from the top of the cryostat down into the cryostat in an assembly dubbed "cassette". **Fig. 17** is an illustration of the cassette.

Table 3 Characteristics of VLPC

Effective Quantum Efficiency	≥ 70%
Noise of ≥1 Photoelectron	≤ 5 k Hz
Average Gain	≥ 8 x 10^4
Gain Dispersion	≤ 30 % for single photoelectron
Dynamic Range	10^3 (Linear)
Pulse Rise Time	≤ 3 ns
After Plulse	none (≤0.01 %)
Saturation Pulse Rate	2.5 x 10^7 Hz
Average Current	(200 + 300 cc.) nA
Average Power	~ 1.3 μW
Operating Voltage	6 ~ 7 V
Breakdown Voltage	7.5 V
Operating Temperature	6° ~ 7 ° K
Dynamic Range	10^3 (Linear)
Magnetic Field Effect	None up to 1.2 Tesla
Neutron Damage Level	≥ 10^{10} n/cm2

The connection of the fiber bundles at the top of the cassette is again made by an optical connector. The clear fiber in the cassette is chosen to be 0.9 mm in diameter that provides a plenty tolerance for connecting with incoming 0.8 mm fiber and allows an unavoidable tolerance for connecting with VLPC.

The clear fiber surface does not touch the VLPC in order to avoid possible damage of the VLPC because of the quite different thermal expansion coefficients**** between plastic and silicon.

****The thermal expansion coefficient of commonly used plastic, including polystyrene, is $20 \times 10^{-6}/°C$ or 1.6 % for 300°C temperature change whereas for silicon it is $3 \times 10^{-6°}/C$ or smaller than 0.1 % for 300°C change.

The jump from 0.9 mm of the fiber diameter to 1 mm diameter sensitive aperture of VLPC allows ~30 μm tolerance in the alignment, which is inclusive of the fiber diameter tolerance of 2 % or 18 μm, the ~20 μm clearance of the hole on the fiber holder at the fiber end facing VLPC, and the relative alignment error between the fiber end holder and the VLPC of ~25 μm, and the gap up to ~75 μm between the end of the fiber and the VLPC surface. It should be reminded that the envelope of the light cone, once exiting from the fiber, becomes

$$\sin^{-1}\left[\, 1.59 \times \sin\{ \cos^{-1}(\frac{1.42}{1.59})^* \}\,\right] = 45.7°. \qquad (\ ^*\cos^{-1}(\frac{1.42}{1.59}) = 26.7° \ )$$

Such arrangement is illustrated in the cartoon in **Fig. 18.** .

Therefore a conservative allowance of the gap between the fiber end and the VLPC, which is not easy to control, necessitates the seemingly large step from the diameter of the fiber to the VLPC sensitive area.

VLPC's are made into 8-cell chips, as shown in **Fig. 19**. The sensitive round window is 1 mm^D and the center-to-center spacing is 1.05 mm. Each cell is connected to a square pad for micro-wire bonding. **Fig. 20** is a photograph taken under a microscope with a magnification of 50. Sixteen such 8-cell chips are laid in a row making up 128 channels corresponding to a single cassette that houses 128 channels of incoming fibers. The back of the VLPC chips is soldered onto an aluminum nitride substrate with each of the VLPC cells micro bonded to the printed lines on the substrate. A cable connecting these lines carry the signal through the cassette to the outside of the cryostat where the readout electronics board is mounted. A common DC bias voltage of 6~7 V is supplied to the soldered VLPC backing with respect to the readout pads.

By implementing simple "buffer" with felt around and inside the cassette, the top of the cassette can be at room temperature without dew condensation while the bottom of the cassette, ~20 long, is exposed to the temperature of the VLPC, i.e., 6.5°K.

The aluminum nitride substrate was chosen as a material that has the same thermal expansion coefficient as the VLPC which is a silicon device so that there will be no mechanical stress on the VLPC chips.

The substrate is also expected to provide uniform temperature to the VLPC chips since the VLPC's power consumption is only $\leq 1.5\ \mu$ Watt.

The cassette, with the incoming fibers and output cables, naturally brings in heat from the outside. Therefore a careful thermal design has to be incorporated with the cassette design. Based on the successful experience, the substrate will be soldered onto an oxygen-free copper tray and the whole assembly will be housed in a high purity ($\geq$ 99.999 %) aluminum casing which is cooled by penetrating pipes of two-phase liquid He. The pure aluminum casing is to provide well-controlled 4.2°K environment to the copper tray The chamber is also filled with He gas. The substrate is cooled to the desirable operating temperature 6°~7°K by He gas being cooled by the surrounding aluminum casing at 4.2°K. He gas flows upward through the vertical column of the cassette to "pre-cool" the fiber and cable bundles so that the proper temperature gradient between the top of the cassette and the bottom is maintained to minimize the heat flow from the outside.

The necessary operating temperature is maintained to ±5° around the required temperature by a sensor-heater pair, each a small resistor, connected to a simple temperature monitor-controller on the outside. However it has been learned that a proper adjustment of the relative position of the copper tray with respect to the aluminum casing and also the adjustment of the gas flow through the cassette at the outlet can bring the temperature close to the desired value without much activating the heater thus minimizing the He consumption.

It has been known from the past tests that the proper operating temperature and the voltage do not vary element to element within the same production batch and the gain variation is within ~10 % with the same operating condition.

We take the design of the substrate developed by D0 as a default design. The design has incorporated what has been learned in the past tests and, in our judgment, it is a well-thought design. Also there is a possibility that Rockwell provides the substrate with all VLPC chip's micro-bonded and tested. It is natural to expect that by combining our order with D0's order, the price will be significantly reduced.

Fig. 21 is a drawing of the cryostat developed by D0 which houses 12 cassettes corresponding to 1536 channels. Again we take this design as the default although there could be some change dependent on detailed assessment of the boundary conditions on how they are mounted at the back of the endwall.

5. Choice of Fibers and Optical Consideration

5.1 Choice of Fibers

In Run II, luminosity of up to ~2 x10^{32} $cm^{-2}sec^{-1}$ is expected. Even if the number of bunches is increased to 96 x 96 with bunch spacing of 132 ns, the average number of the interactions, taking 46 mb as cross section of the "visible" interactions, becomes 2.6 per bunch crossing. Any high PT collision event generates about 3 MIP equivalent number of tracks. 0.5 mm OD fibers are necessary for such condition in order to avoid the confusion in the pattern recognition directly with its small granularity and indirectly by suppressing the occupancy or the ghost probability.

However one has to be sure about the expected number of photoelectrons for MIP.

First, multiclad fiber is definitely favored because of the 60 % larger "aperture" as discussed in earlier chapter, and also superior mechanical properties. Due to the mechanical strength and the flexibility of the outer cladding material, fluorinated polymer, multiclad fibers are much more flexible and durable than single clad fibers whose cladding, PMMA is known to be brittle. Though the multiclad fiber has PMMA as the inner cladding it is secured and well protected by the outer cladding. Possibly due to such mechanical stability which most likely prevent unnoticed micro-cracks of PMMA, the attenuation lengths of the multiclad fibers are consistently better than that of single-clad fibers whose PMMA clad is exposed without protection. **Fig. 22** is a comparison of the attenuation curves of a multiclad fiber and a single clad fiber.

The scintillating fiber will be 1,500 PPM 3HF fiber, with 1% PTP as the primary fluor. 1,500 PPM has been measured[5)] to be optimum for the light output for a 1 meter or longer fiber. **Fig. 23** is a test result showing that the peak light output is obtained at ~1,500 PPM for 1 meter, 2 meter and 3 meter points. Once the fiber is longer than ~20 cm there is not much change in the output spectrum due to its large Stokes shift that is the unique feature of 3HF fiber. In case of ordinary scintillation fluors with small Stokes shifts, there is always non-negligible overlap between the absorption spectrum and the emission spectrum. Therefore along the path of the emitted light through the fiber, the shorter wave length end of the emitted light is gradually absorbed by the overlapping long wave length end of the absorption band. This is observed as a fast decay component in the attenuation curve. In contrast, 3HF has uniquely long Stokes shift due to its proton transfer mechanism and there is no overlapping between the absorption band and the emission band. Therefore the observed attenuation curve is well described by a single, long exponent and also the measured spectrum at 20 cm and 3 meter is not much different in

shape, as shown in **Fig. 24**. Also due to the spectrum peaking at green, 530 nm, the attenuation length is uniquely long, 5 meter for 0.83 mm multiclad scintillating fiber and 7 meter in a clear fiber as shown in **Fig. 22**. This also means that it is the strongest fiber found so far being less susceptible to the possible radiation damage[6].

The optimum value for the primary fluor PTP has also determined experimentally to be 1 %.

The rise time of 3HF is about the same as any other scintillating fiber, ≤ a few ns, and the decay time constant is ~12 ns. **Figs. 25a** and **b** show the oscilloscope trace of the signal from 3HF and its integration, respectively.

Long term stability of 3HF has been studied[7] recently. If it is exposed to UV containing light source at an intensity over certain threshold level, there is a noticeable degradation in the, light output. On the other hand there is no permanent damage if the light intensity does not exceed certain limit. The condition for fiber tracking is far below such "threshold" and no damage is expected as long as the material is not exposed to open day light or strong fluorescent lamp.

**Recently two other scintillation fluors have been synthesized and tested in a fiber. The result is similar to that of 3HF. However the concentration is half, for the optimum light output, of that of 3HF for "Vinyl 3HF" and further 1/4 for "FG231". Also "FG231" has a decay constant of ~10 ns and we are still investigating whether this type of fluor can be made into brighter fiber.

5.2 Optical Consideration

Table 4 is a step-by-step account of the number of photoelectrons. The starting point is the number of photons generated by a MIP that is, according to particle booklet, 1 photons/100 eV energy deposit. From various test results, this number well holds, on conservative side, for the number of photons in a 1500 ppm 3 HF (1% PTP) fibers. The light capturing aperture of a multiclad fiber is 5.35 % as discussed in Chapter 2, and taking 0.5 mm OD, the average number of photons to be "captured" is 33.7 for a MIP traversing the fiber perpendicularly at the edge of a 0.3 mm effective cell of the core.

Though the fiber is 1.6 meter long the far end is helped both by the angle of the traversal of the particle and also by the mirror. Therefore the weakest signal is from 90°, or η=0 point. The attenuation length of 0.5 mm 3HF fiber, 3.37 m is an interpolation of the data of 0.7 ~1.0 mm fibers and 60 μm fiber[8].

Table 4 <NUMBER OF PHOTOELECTRONS>

0.5 mm OD (Core = .88 OD = .44 mm),

0.6 mm Spacing Staggered Doublet

Effective Cell =.3 mm, Min Thickness at the Edge=.7315 D_{core}

3HF(1500 ppm, 1% PTP), Double Clad

1 photon /100 eV energy loss

$\langle dE \rangle_{min}$ = .5 mmx0.88*x.7315** x 1.032 g/cm^3 x 1.9 MeV/(g/cm^3)
*Core OD, **Min thickness
= 63.1 keV
=> 631 photons

Magnetic field effect (+7%) => 675 Photons

Fiber Capturing Efficiency : One direction $\frac{1}{2}(1-\frac{1.42}{1.59})$ = 5.346 %

No. of photons : **36.9 Photons**

		Far End	Midpoint
Length of 3HF to spliced point = L		1.6 m	.8 m
$\theta = \tan^{-1}(\frac{R}{L/2})$	:	19.29°	90°
(L = 1.6, R = 0.28 m)		(η=1.77)	(η = 0)
Angle Factor = 1/sin θ	:	3.03	1
Attenuation thru **3HF** = $\exp(-\frac{L}{3.37*})$	:	0.622	0.788
(* Fiber diameter dependence: L = 1.015 exp(2.4 D))			
Mirroring factor = 1+ Reflectance x $\exp\{-\frac{2x(1.6-L)}{3.37*}\}$			
Reflectance = 0.9	:	1.9	1.56
Attenuation thru **5-m 0.8 mm Clear Fiber**	:	$\exp(-\frac{9**}{12})$ = 0.472	
(**3.6 m to exit to the rear end from r = 20 cm at z=0.8 m , 3.3 meter from 9 O'ck point to 12 O'ck point on the endplug surfac along the 30° crack, and 2 meter as the extra routing)			
Transmission thru Connectors	:	$(0.95)^2$ = 0.903	
Transmission from clear fiber to VLPC	:	0.85	
Quantum Efficiency of VLPC	:	70 %	
Overall Attenuation Factor	:	0.908	0.311
<No. of Photoelectrons>	:	**33.5**	**11.5**

Detection Effic./Layer (≥2 pe**): ≥ 99.8 %**
(****Rockwell's spec for D0 : Noise ≥1 pe : 5,000 counts/sec)

Possible Improvement:
(Q.E. = 80 %) : **(38)** **(13)**

The length of the 0.8 mm clear fiber is taken for the worst case in which the fibers exit the "30°" crack at 9 O'ck point and reaches 12 O'ck point where the cryostat will be mounted routed in a circular path along the "30°" crack. A measured attenuation length for 0.83 mm clear fiber is used.

The reflectivity of the mirror is what has been measured in the end plug upgrade project (See **Fig. 14**) and the transmission through the connectors is the conservative side of the measured values. The transmission through the gap between the clear fiber and the VLPC is a value measured on a connector with air gap.

The quantum efficiency of the VLPC is what has been measured for the HISTE-5.It should be reminded that D0 cosmic ray test was made with HISTE IV which is ~62 % in quantume efficiency with the same measurment.

Taking all this effect into account the overall transmission is 0.3 for the 90° point yielding ~11 photoelectrons. This is the average value at the edge of the sensitive cell of the core for the longest possible clear fiber.

Landau fluctuation and Poisson statistics have to be taken into account to evaluate the detection efficiency. Landau distribution as generated by GEANT, as shown in **Fig. 26** for 0.5 mm polystyrene has a steep tail on the lower side and therefore does not make sizable contribution to degrading the signal compared to Poisson fluctuation. After these two effects are convoluted, the single layer efficiency is plotted in **Fig. 27** for various values of the average number of photoelectrons.

The specification for the noise level being discussed with Rockwell for D0's order, based on the data of HISTE-4 and HISTE-5, is that the noise of ≥1 pe must be 5,000 counts/sec or less. Considering that such number is low enough not to disturb the system performance, the threshold can be conservatively taken at ≥2 pe . Therefore the single layer detection efficiency is ≥99.9 %. It should be reminded again that the above estimate is for the edge of the effective 0.3 mm cell and for the longet route for the clear fibers. Therefore the overall efficiency is much higher than this value and therefore we have enough margin for unexpected decrease of the light due to unforeseen cause.

6. Signal Readout and Electronics

With the gain of ≥80,000 and the average number of photoelctrons to be ≥10, SVX II chip will be adequate for the signal readout providing the signal integrated over ~100 ns* and AD conversion.

*Out of 132 ns cycle, ~25 ns is necessary for the preparation.

It should be noted that rad-hardnes is not required, early non-rad-hard version in the chain of evolution of SVX II chips is adequate for the IFT.

In order to get fast signal outputs for low level triggering as discussed in the next chapter, a front end signal splitter/discriminator circuit dubbed "precursor chip" being developedby UC Davis group for D0 is counted on. The circuit splits the signal from VLPC into two ways, one for the input of SVX II chip and the other for discriminator input. A gate of ~30 ns will be applied at the discriminator to eliminate curling low momentum tracks beyond the necessary readout time. The path length-averaged speed of the transmission within the multiclad fiber is 5.6 ns/m which creates maximum of 18 (25) ns time difference between the direct and mirror-reflected signal for the nearest point on the ±0.8 (± 1.1) meter long sincitllating fiber. However the weakest signal is from the midpoint of the fiber whose reflected signal arrives at the near end 11 (15) ns later than the direct signal from the near end. Therefore the gate may be closed before the latest reflected signal from the near end. The effect of the gate width on the triggering efficiency which might be affected by not waiting the tail of the 3HF scintillation signal will be studied in near future.

7. Level 1 and Level 2 Triggers

Application of tracking requirements for trigger decisions at the earliest practical point in the multilevel trigger structure has been a major factor in CDF trigger strategies. The price to pay for delaying track requirements is in purchasing more bandwidth for the subsequent levels and/or imposing large prescale factors and/or raising physics thresholds. Scintillating fiber detection elements are intrinsically prompt and can easily be used at the first level trigger. The information can also be reused at higher levels of the trigger for pattern recognition algorithms such as tagging secondary vertices or finding the softer leg of a J/ψ candidate. Studies of the performance and optimization of utilizing fiber information in the Run II trigger system are just beginning; the following is an overview description of scintillating fiber participation in the first and second level trigger systems from more of a hardware perspective.

7.1 Level 1

It is our view that tracking information will be required for Level 1 decisions because of the physics goals that require low thresholds for leptons and particular processes like a B decaying to two pions. Without another "handle", the beam conditions of Run II may force the thresholds and prescale factors to unacceptably high values to stay within the Level 1 bandwidth limit. For the intermediate fiber tracker, there is a front end electronics prerequisite before the information can be used at Level 1. The front end electronics proposed is the SVX II readout chip which does not produce prompt hit bits for use by a trigger. A signal splitter or pickoff chip is needed in front of the SVX II chip to produce the prompt signals. At present, work is in progress on such a front end chip at U. C. Davis for the D0 fiber tracker trigger system.

Level 1 stiff track information will be generated by the XFT system working on prompt hit bit information from the CTC. Information from the intermediate fiber tracker would be added to the XFT road search in place of superlayer zero. As shown by A. Baumbaugh for the SDC design, processing the hit bits from fiber superlayers and linking between superlayers is a straightforward operation which can be realized using field programmable gate arrays. Track segments binned in transverse momentum and phi would be available in less than 100 nsec after the crossing, and then saved in a pipeline fashion for later inclusion in the XFT track finding process. Finalization of the fiber diameters and

superlayer radii would include the requirement of proper matching to the ϕ-granularity of the XFT system.

Using simple combinatorial logic, signals from the six axial layers of the IFT can be used to provide hits in 720 phi bins at a radius of 22 cm as an additional input to the XFT processor. In addition, a full standalone IFT trigger, which will also give the above mentioned 720 phi bins as a by product, is being studied by the Pisa and Udine groups. The output of the trigger, in addition to the 720 phi hits, will be the number of tracks found in a set of positive and negative Pt bins (number of bins to be determined).

The current plan is to divide the 6 axial layers into 192 identical phi wedges each containing 150 fibers (excluding overlap regions). The actual numbers will depend upon the final choices of superlayer radii, fiber pitch within the ribbons, and the choice of definition of the overlap regions between wedges (e.g., wedge shaped or butterfly shaped regions) and are not yet decided; however, the exact choice will not influence dramatically our conclusions.

Each wedge will be served by 2 standard cell gate array chips which enumerate all possible track combinations of hits in 5 or 6 layers. A simple simulation has shown that the number of patterns to store is well within the capabilities of existing technology for standard cell gate array chips with of the order of 200 pins. As opposed to the D0 design, we prefer standard cell gate arrays to field programmable gate arrays (FPGA) because experience in the Pisa group has shown that the FPGA's have significantly reduced density and require a very large programming effort. In order to accommodate possible misalignments of fibers or routing errors it is planned to have the fiber signals pass through an on-chip multiplexing layer before passing to the standard cell units, which will allow a remapping of the fiber signals afferent to the chip. The addressable multiplexor lines into the chip will thus allow a certain amount of 'programmability' even in this technically 'nonprogrammable' technology.

Because the standard cell approach enumerates all possible coincidences, the momentum resolution obtained should approach that obtainable offline. Studies of resolution, efficiency, and fake trigger rate are still under study. A cost estimate of this solution is given below.

In addition to the gate array solution, we are also investigating a solution using a neural network-like algorithm. This algorithm can be thought of as making use of 'fuzzy' coincidences between 5 or 6 'groups' of fibers in the different layers, instead of between individual fibers. In order to retain some of the information on the relative positions of the individual fibers, each one enters into the coincidence with an analogue weight which is exponential in its distance from the center of the fiber group. The algorithm is described in

more detail in a University of Udine internal note (available from G. Pauletta, U. Udine). Preliminary results indicate that the achievable momentum resolution is nearly on a par with that obtained offline. The advantage of this algorithm is that the total number of coincidences required is reduced by about 3 orders of magnitude as compared to the gate array solution, thus implying a much simpler chip design. Possible disadvantagess are: 1) The analogue weights may prove difficult (or, at least, expensive) to realize in silicon; and 2) The algorithm is more susceptible to problems caused by high occupancy. Studies are currently underway to evaluate the algorithm and its potential advantages and disadvantages. We do not yet have a price estimate for this solution. The preliminary study has some 300 chips with about 150 inputs each; therefore the cost should not be radically different from that of the gate array solution.

For either solution, it is foreseen to route the discriminated VLPC signals on ribbon cables to large multiwire patch panels which re-route the signals into the gate arrays. Whichever solution is finally adopted, it is important to reiterate that the existence of a trigger makes certain restrictions on the geometry of the detector and the readout path. Probably all fiber ribbons will have the same pitch. This puts restrictions on the ratios of the chosen superlayer radii since a fiber pattern periodic in phi is required for the trigger; i.e., it must be possible to divide the detector into *identical* wedges in order to ensure that a single gate array design will be able to serve for all trigger chips. The routing scheme chosen for the signals must then carefully preserve the geometry of the detector: the standard cell coincidences must operate on groups of signals which come from the same phi slice; coincidences may *not* span chip boundaries. As the design of the IFT becomes finalized, it will be important to keep these restrictions in mind in order not to compromise the very important ability of the IFT to participate in the level-1 trigger of CDF.

The estimated cost of the IFT Gate Array Trigger, with 6 axial fiber layers,192 Phi wedges, 150 fibers per wedge, 2 Gate arrays per wedge is:

Gate Array Chips	$120,000
(includes design, development, prototyping, test runs, contingencies)	
Trigger Cables	$ 8,000
(128 conductor)	
Multiwire Trigger Patch Panel Boards	$ 35,000
Power supplies for above	$ 12,000
VME Interfaces	$ 15,000
Total	$190,000

7.2 Level 2

In Level 2 trigger processing, the fibers would be treated in the same way as is planned for the SVX II strips. Adding hits from the axial fiber layers improves the pattern recognition, reduces ghosts and helps with the impact parameter resolution function. Basically, the fibers would be included in the Silicon Vertex Trigger (SVT) as if they were somewhat long strips. The ϕ granularity of 0.5 mm fibers at a radius of 25 to 30 cm is comparable to that of 50 μm pitch strips at a radius of 25 to 30 mm. The data source is also the same as for the SVX II, a trigger-friendly version of the SVX chip; no special new hardware is needed. As was the case for Level 1, the final choices for fiber diameters and superlayer radii include a requirement for proper matching to the phi- granularity of the SVT system.

8. Fiber Layer Assembly Procedure

8.1 Fiber Ribbon

The first process for making fiber layers is to make a ribbon of 128 fibers. Fibers are laid down onto a tray with 128 grooves of the cross section shown in **Fig. 28.** After the fibers of the first layer are laid into the grooves, the second layer fibers are laid down keyed between the first layer fibers. Narrow bridges with identical grooves as the base plate are placed at regular intervals on top of the second layer fibers to guarantee the positioning of fibers. After all the fibers are in place, epoxy is applied. The adjacent fibers are touching each other so that the spacing is maintained primarily by the fibers but not by the epoxy.

Connector is mounted on one end and polished with a diamond fly cutter. The other end is also cured with epoxy, fly cut with diamond machine, and mirrored.

Such process will guarantee the regular spacing between the fibers and when it is transferred from the ribbon making jig, the straightness within the fiber plane is not going to be disturbed if the ribbon is transported by a rigid beam using vacuum suction cups which act to the ribbon only vertically.

Such method has already been routinely practiced by Purdue group[9)] for D0, though for 0.835 mm fibers, and the result is quite satisfactory although there is a room for improvement in the accuracy of the of the fiber positioning and also the operation can be much simplified by proper jigs.

Currently both at Pisa and Fermilab, grooved plates are made/being made and ribbon making is practiced with 0.5 mm fibers. **Fig. 29** shows the shape of the groove being expored at Fermilab. This has a much deeper grooves which may ease the operation by better securing the fiber in the grooves. The profile of the grooves can be changed by grinding the tool bit to a proper shape and the first try of round grooves yielded deep groove of a round bottom quite precisely fitting round 0.5 mm diameter gauge pin as shown in the photograph shown in **Fig. 30.**

8.2 Final Mounting

The ribbon is then transferred to the cylinder and epoxied. The rotational positioning of the cylinder is well controlled by a stepping motor. Commercially available stepping motor with an accuracy of 10 seconds (0.048 mrad) gives 13 μm resolution for the fiber ribbon for the largest radius, 27 cm. The fiber positions can be inspected prior to applying epoxy by temporarily tacking the ribbon.

The process of laying down stereo layers is not different from the process for straight axial layers except that the fiber ribbon is laid onto the cylinder at an angle and therefore the cylinder needs to be rotated while the fibers are laid down and epoxied over the entire length.

9. Light Pulsing Monitoring System

We propose to monitor the stability of the response on a channel-by-channel basis by periodically exposing the fibers of each IFT layer to an extended pulsed source of ultraviolet (U/V) light. Extended sources will consist of quartz fibers from which cladding will have been partially removed over a length corresponding to the circumference of an IFT layer. The fibers will be fed by a pulsed U/V laser.

It has been verified in the laboratory that an extended source of U/V light can be created in this manner. The cladding was etched away from one side of a 600 micron diameter fiber by means of a sharp pointed instrument over a length of 60 cm (corresponding to the circumference of an IFT layer) near the end of a 30m long quartz fiber which was optically coupled to a pulsed nitrogen laser. It was verified that; (a) the intensity of the light escaping from the damaged fiber was sufficient to excite the scintillating fibers and (b) that the attenuation length, although dereased by partial removal of the fiber cladding, is nevertheless long enough to enable a sufficiently uniform distribution of U/V light over a length corresponding to the circumference of an IFT layer. (Details of the test can be found in a note obtainable from G. Pauletta).

One partially exposed quartz fiber per IFT layer will be introduced into the detector via the 33 degree crack and the partially exposed end of each fiber will be wrapped around an IFT layer and fixed with the exposed side in contact with the layered fibers. The fibers will be pulsed periodically by means of a pulsed U/V laser. Laser pulses will be shorter than the decay time of the fiber scintillator so that the time dependence of the channel response to the U/V stimulus can also be monitored. Laser power will be sufficient to generate more than 10**4 photons per pulse in order to have a better than 1% check of the channel response stability. The laser instability of ~ 3% will be factored out by viewing the end of each fiber with a PIN diode and dividing the laser-generated signals from the VLPC's by the PIN-diode output. It has been verified that one can monitor stability to better than 0.3% by means of this technique.

A similar technique will be used to monitor the upgraded plug calorimeter reponse, and the IFT monitor can be integrated into the plug monitor if the laser power is upgraded from that presently forseen for the plug, thereby saving considerable expense.

The cost of the proposed monitor comes mainly from the cost of upgrading the laser and of acquiring and etching the additional quartz fiber. A breakdown of the estimate is as follows:

laser upgrade	$ 20,000
quartz fiber	$ 14,000
PIN diodes	$ 2,000
other materials	$ 10,000
fiber etching	$ 5,000
machine shop	$ 5,000
tech time	$ 10,000
total	$ 66,000

10. R & D

In order to optimize the system and finalize the design in detail, we need to carry out some R & D in the earliest possible future.

The R & D can be reasonably well phased into the overall schedule taking advantage of the different degree of the needs of the R & D.

The longest time required for the fabrication is for the fiber lay-down process. Fortunately fiber ribbon making is one of the least of the needs for technical exploration and also it is almost independent of the development of the other components. Therefore the ribbon making can be started at an early phase in parallel with the process of finalizing the design of other components.

There are items that appears to need expertise of the outside company. The first of such items is the support cylinder whose good dimensional accuracy with long term stability is the basis of the tracking accuracy. The R & D on such item needs to be started at the earliest possible point.

Most of the works need engineering and a few technicians for prototyping in addition to the financial support.

We are also hoping to carry out a beam test of a prototype segment of about 1500 fibers to find out the real parameters such as R-ϕ and Z resolution, the detection

efficiency,and the effect of δ-rays, simultaneously gaining an experience on such system including the cryogenics and readout electronics.

The following is the list of the components that need R & D. In order to meet the dead line for the installation and debugging in 1997 through 1998, most of the R & D has to be finished by mid 1996.

Table 6 R & D

Items	Comments
Fiber Ribbon Making	Already underway. Minor both in the complexity and in the cost. Due to totally different fiber diameter we have to do the job independent of D0.
Support Cylinder	Major task. The prototype cylinder made by SSC related R&D showed excellent precision and strength but much more than what we need in terms of material thickness. There is a significant room for reducing the material thickness for our application.
Fiber Mounting on the Cylinder	Major task. Needs CORDEX machine long enough to survey 3.1 meter length. Needs early study and practice with ordinary (card board) cylinder.
VLPC substrate	Wait for D0 design to be completed within a few months. Most likely it satisfies our needs. Slightly differnt design is being studied at Pisa.
Cassette	Wait for D0 design to be completed. Most likely the design needs to be modified because of our specific constraint.
Cryostat	First wait for D0 design to be completed. It is possible that we need to modify it significantlly for our specific constraint.
Support structure	Major task. Need engineering for overall structure compatible with/including SVX II.
Readout electronics	Expecting SVX II chips to be completed in time. Expecting input splitter/discriminator chip, "prcursor chip", for fast signals for Level-1 trigger be completed in time for D0.

11. Cost Estimate

3

Table 8 COST ESTIMATE

Fiber Layers

Radii	Views	Circumference $2\pi R$	No. of Fibers $\frac{2\pi R}{0.6}$ x2		No. of Views	No. of Cassettes per View		(128 chan/cassette) Total
177.23 mm	U, Z	1,113.57 mm	3,712 / View	x	2	29 / View	x 2	= 58
195.57 mm	V, Z	1,228.80 mm	4,096 / View	x	2	32 / View	x 2	64
213.90mm	U, Z	1,343.97 mm	4,480 / View	x	2	35 / View	x 2	70
232.24 mm	V, Z	1,459.21 mm	4,864 / View	x	2	38 / View	x 2	76
250.57 mm	U, Z	1,574.38 mm	5,248 / View	x	2	41 / View	x 2	82
268.91 mm	V, Z	1,689.61 mm	5,632 / View	x	2	44 / View	x 2	88
Total			**56,064 Fibers**					**438 Cassettes**

Labor

	Engineer	Technician
Cassette	1 x 2 months	2 x 12 months
Cryostat	1 x 2	
Cylinder/Fiber Ribbon Mounting	1 x 1	3 x 4
Support structure	1 x 2	2 x 1
Cryogenics/Plumbing	1 x 1	2 x 1
Fiber Ribbon Making		2 x 12
Cable Making		2 x 6
Cabling		2 x 1
Installation/Debugging		3 x 6
Integration	1 x 2	
R & D	1 x 12	1 x 18
Miscellaneous	1 x 2	2 x 18
TOTAL	2 person-year $120 k (@$60k/yr/person)	150 person-months≈12.5 person-year $375 k(@$30k/person/yr)

COST ESTIMATE (cont.)

Scintillation Fibers	: 3HF(1500PPM)+PTP(1%), 0.5 mm, 2.2 meter each (*KURARAY Price List :$0.34/meter)	$0.75*	x 57,000	$ 42.6	k
Clear Fiber	: 0.8 mm, 7.4 meter (**KURARAY Price List : $0.57/meter)	$4.22**	x 57,000	$ 240.4	k
Cassette+VLPC	: D0 style, 1024 channel, assembled	$50,000	x 60	$ 3,000	k
Cryostat/Plumbing	:	$5 / chan	x 57,000	$ 285	k
Support Cylinder	: ROHACELL(#31)+Carbon Fiber Cloth			$ 5	k
Support Structure	:			$ 20	k
Fiber Ribbon Jig	: Grooved Plate	$1.5 k	x 4	$ 6	k
CMM Accessary	:			$ 20	k
Fiber Mounting Jig	:			$ 50	k
Electronics					
SVX II Chips	: 128 chan/chip	$100	x 480	$ 48	k
Port Cards	:	$3 k	x 22	$ 66	k
G-link $ fibers	:			$ 50	k
VME SAR/SRC boards:				$ 25	k
Miscellaneous	:			$ 25	k
Test stand				$ 50	k
Trigger				$ 190	k
Light Pulsing System				$ 66	k
Miscellaneous				$ 50	k
Labor	:			$ 495	k
TOTAL				**$4,784**	**k**

12. Summary

We propose to install a set scintillating fiber tracking layers in the intermediate radial range between SVX II and CTC for Run II. This will not only remedy the inefficiency of the inner superlayers of CTC but furthermore provide a powerful link between SVX II and CTC in a very high luminosity environment expected in Run II.

We envision six layers of axial layers and six layers of stereo layers as a default each consisting of a half-cell staggered layer of 0.5 mm OD scintillating fibers. Preliminary study indicates such a system is quite necessary and adequate.

Thanks to the recent development in technology and CDF's experince through endplug calorimeter upgrade project, the necessary technology and knowledge are in hand to build such a sytem.

Detailed account of the conception of such system is described.

Futher simulation study is necessary to optimize the tracking efficiency. Also an intensive R & D is desirable to optimize the mechanical aspect and finalize the design.

The parameters of the proposed scintillating fiber tracking layers, IFT, are listed in **Table 9**.

Table 9. Intermediate Scintillating Fiber Tracking Layers (IFT) Parameter Summary

Multiclad Fiber Parameters

Outer Cladding	:	Fluorinated PMMA (n=1.42)
		$\Delta r = 0.03 \times OD$
Inner Cladding	:	PMMA (n=1.49)
		$\Delta r = 0.03 \times OD$
Sensitive Core	:	Polystyrene (n=1.59)
		$D = 0.88 \times OD$
Total Int Refl Angle	:	$\cos^{-1}(\frac{1.42}{1.59}) = 26.7°$
Capturing Aperture	:	$\frac{1}{2}(1-\frac{1.42}{1.59}) = 5.35\ \%$

Scintillating Fiber
- Multiclad
- PTP 1%
- 3HF 1500 PPM
- 0.5 mmOD
- 3.1 m

Clear Fiber (Scintillating Fiber - Cryostat Entrance)
- Multiclad
- 5.8 m

Clear Fiber in Cassette
- Multiclad
- 0.9 mm^{OD}

VLPC

Sensitive Window	: 1 mm^{D}
QE	: ≥ 70 %
Gain	: ≥8x 10^4
Noise (≥1 photoelectrons)	: ≤5kHz/sec
Operating Temperature	: 6.5°~7° K

VLPC Chip
- 8 cells/chip
- 1.5 mm x 9.0 mm

Substrate
- 16 chips/substrate = 128 channels/substrate
- 12.5 mm x 50 mm

Cassette
- 8 substrate/cassette = 128 channel/cassette

<u>Tracking Layer Configuration</u>

0.5 mm scintillating Fiber, 0.6 mm Spacing,
Staggered Doublet

References

1) M. Atac, J. Park, D. Cline, D. Chrisman, D. Petroff, and E. Anderson
Nucl. Inst. Meth. A314 (1992) 56.

2) Y. M. Park,
D0 Note

3) B. Baumbaugh, et al.
Nucl. Inst. Meth. A345 (1994) 271

4) G. Appollinari, P. de Barbaro, and M. Mishina,
Proceedings; 4th Int. Conf. on Calorimetry in High Energy Physics,
La Biodola, Isola d'Elba, Italy, 1993, P 200.
P. de Barbaro, et al.,
CDF Note 2778.

5) J. Park, D. Chrisman, M. Atac, and M. Mishina
To be published in IEEE NS proceedings.

6) A. Bros and A. Pla-Dalmau
Nucl. Inst. Meth. Phys. Res. A327(1993)337.
A. Bross, C.L. Kim
Private communication.

7) M. Ching and S. Margulies,
To be published in the Proc. of Scintillating Fiber Workshop
University of Notre Dame, 1993.

8) C. D'Ambrosio, et al.,
Nucl. Inst. Meth. Phys. Sci. A345(1994)279.

9) B. Howell, D. Koltick, C. Cooper, J. Hinson, T. Crone, and D. Michael,
D0 Note 2009.
D. S. Koltick,
To be published in the proceedings of Scintillating Fiber Workshop
University of Notre Dame, 1993. Purdue University Report PU-94-677.

Figure Captions

Fig. 1 Average number of interactions per bunch crossing for various operating conditions.

Fig. 2 Side view of the proposed Scintillating Fiber Tracking Layers (IFT) in the tracking volume.

Fig. 3 Basic composition of the half-spacing staggered doublet layer of 0.5 mm^{OD} scintillating fibers with 0.6 mm spacing. Effective cell size is 0.3 mm.

Fig. 4 Single doublet-layer Z-resolution of stereo layers.

Fig. 5 Dependence of the Z-resolution and the ghost probability on the stereo angle.

Fig. 6 Pulse height spectrum of HISTE IV measured by D0 cosmic ray test[2)].

Fig. 7 Quantum efficiency of HISTE's I through IV compared with SSPM.

Fig. 8 Dependence of the quantum efficiency and the noise rate (≥1 pe) on the operating voltage

- a SSPM
- b HISTE V

Fig. 9 Structure of multiclad and single-clad fibers.

Fig. 10 Internal total reflection in multiclad and single clad fibers.

Fig. 11 Microscope photograph of an end of scintillating fiber (3HF) finished with diamond fly-cutter.

Fig. 12 Histograms of the diameter of commercial fibers:

- a 1 mm^{OD} sampled over 16 km.
- b 0.830 mm^{OD} sampled over 20 km.

Fig. 13 Histogram of light output from waveshifter doped fibers sampled at every 150 meter over the total of 16 km used for the production of E.M. section of the new end plug calorimeter. ~70-cm long Y-11 waveshifter fibers were inseterd into a scintillator tile with Sr90 souce as the light source and the output from 30-cm long tail out of the tile is measured by a phototube.

Fig. 14 Reflectivity of mirrored ends of the fibers[4)] sampled over the production period of the hadronic section tile/fiber assemblies. Cross hatched histogram corresponds to the data taken when the aluminum spattering vessel was contaminated.

Fig. 15 R-ϕ cross sectional views of the proposed intermediate scintillating fiber tracking layers.

a Overall cross section.
b Individual super layer and material thickness.
Fig. 16 Microscope photograph of VLPC.
Fig. 17 Cassette.
Fig. 18 Illustration of the steps of fiber diameters.
Fig. 19 8-cell VLPC chip.
Fig. 20 Photograph of VLPC cell with 50X magnification.
Fig. 21 Cryostat design of D0.
Fig. 22 Attenuation curve of multiclad fiber and single clad fiber.
Fig. 23 Light output vs. concentration of 3HF fiber.
Fig. 24 Comparison of the spectra at 0.2-meter and 3-meter points.
Fig. 25 Time structure of the signal from 3HF scintillating fiber.
a Oscilloscope trace.
b Integrated over time.
Fig. 26 Landau distribution of 0.5 mm thick scintillator generated by GEANT.
Fig. 27 Detection efficiency vs. threshold number of photoelectrons.
Fig. 28 Cross sectional view of a grooved tray for fiber ribbon making.
Fig. 29 Profile of round-bottom fiber groove.
Fig. 30 Microscope photograph of a trial round-bottom groove.

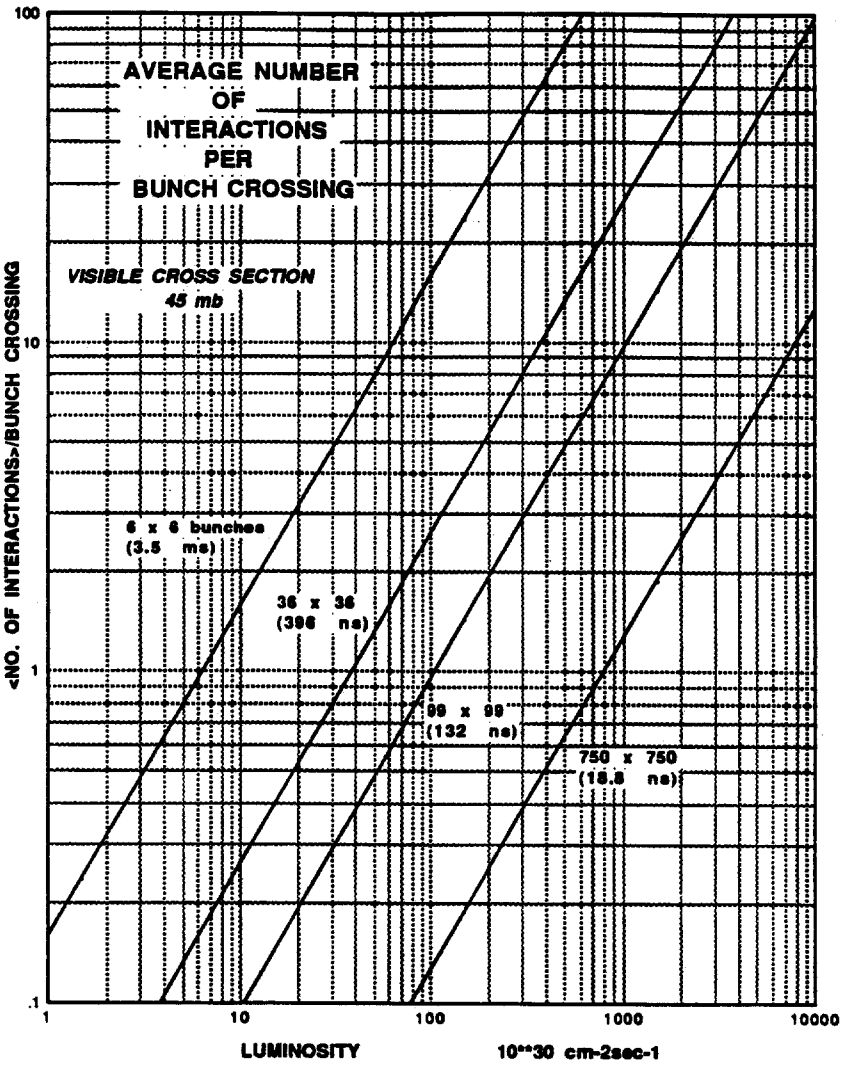
AVERAGE NUMBER
OF
INTERACTIONS
PER
BUNCH CROSSING
VISIBLE CROSS SECTION
45 mb
6 x 6 bunches
(3.5 ms)
36 x 36
(396 ns)
99 x 99
(132 ns)
750 x 750
(18.8 ns)
<NO. OF INTERACTIONS>/BUNCH CROSSING
100
10
1
.1
1
10
100
1000
10000
LUMINOSITY
10**30 cm-2sec-1

Fig. 1

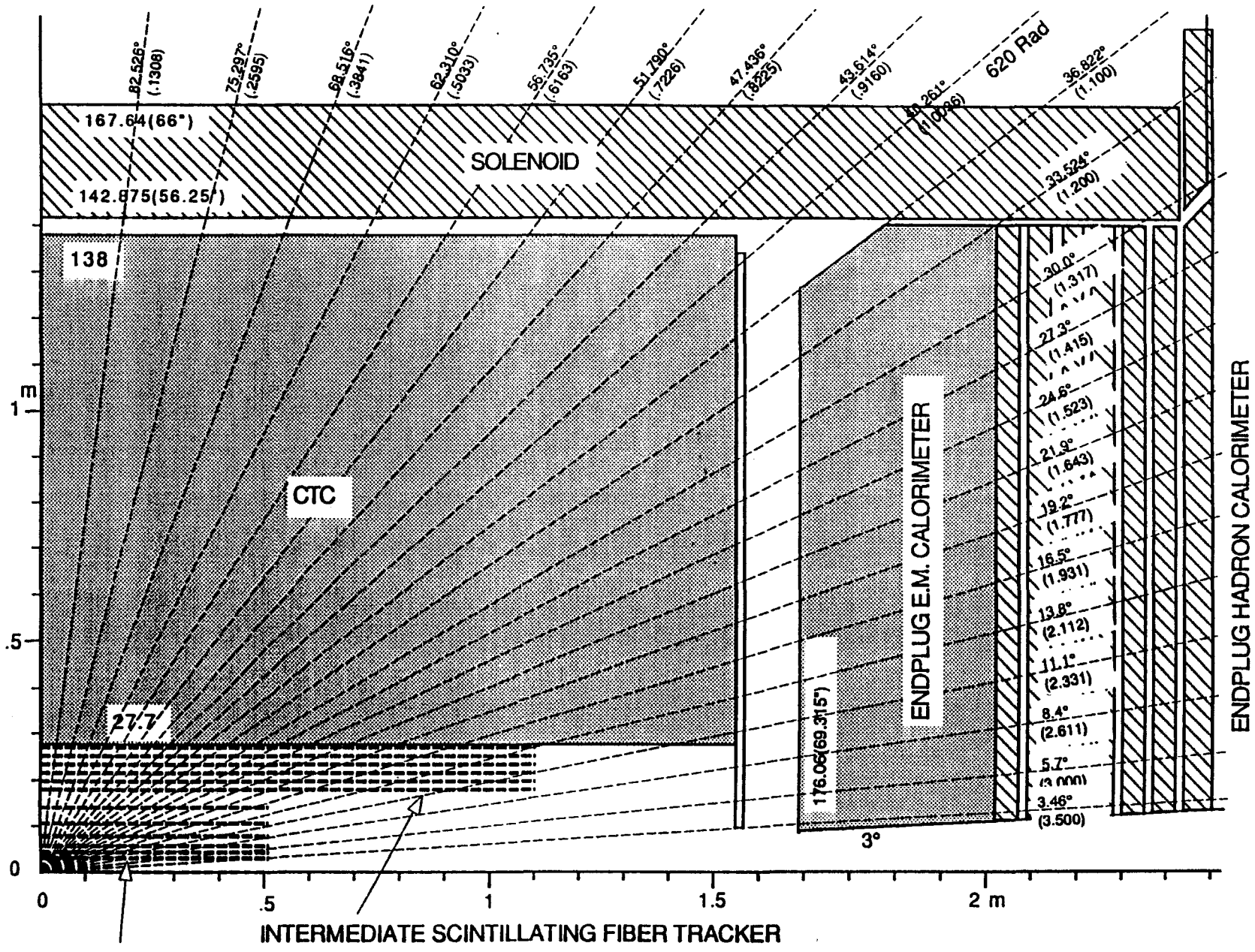
82.526° (.1308)
75.297° (.2595)
68.516° (.3841)
62.310° (.5033)
56.735° (.6163)
51.790° (.7226)
47.436° (.8225)
43.614° (.9160)
40.261° (1.0086)
620 Rad
36.822° (1.100)
33.524° (1.200)
167.64(66")
142.875(56.25")
SOLENOID
138
CTC
27.7
176.06(69.315")
ENDPLUG E.M. CALORIMETER
ENDPLUG HADRON CALORIMETER
30.0° (1.317)
27.3° (1.415)
24.6° (1.523)
21.9° (1.643)
19.2° (1.777)
16.5° (1.931)
13.8° (2.112)
11.1° (2.331)
8.4° (2.611)
5.7° (3.000)
3.46° (3.500)
3°
1 m
.5
0
0
.5
1
1.5
2 m
INTERMEDIATE SCINTILLATING FIBER TRACKER
SVX II

Fig. 2

0.5 mm OD ROUND FIBER

MULTICLAD FIBER
INNER CLAD O.D. : 0.94 O.D.
CORE OD : 0.88 O.D.

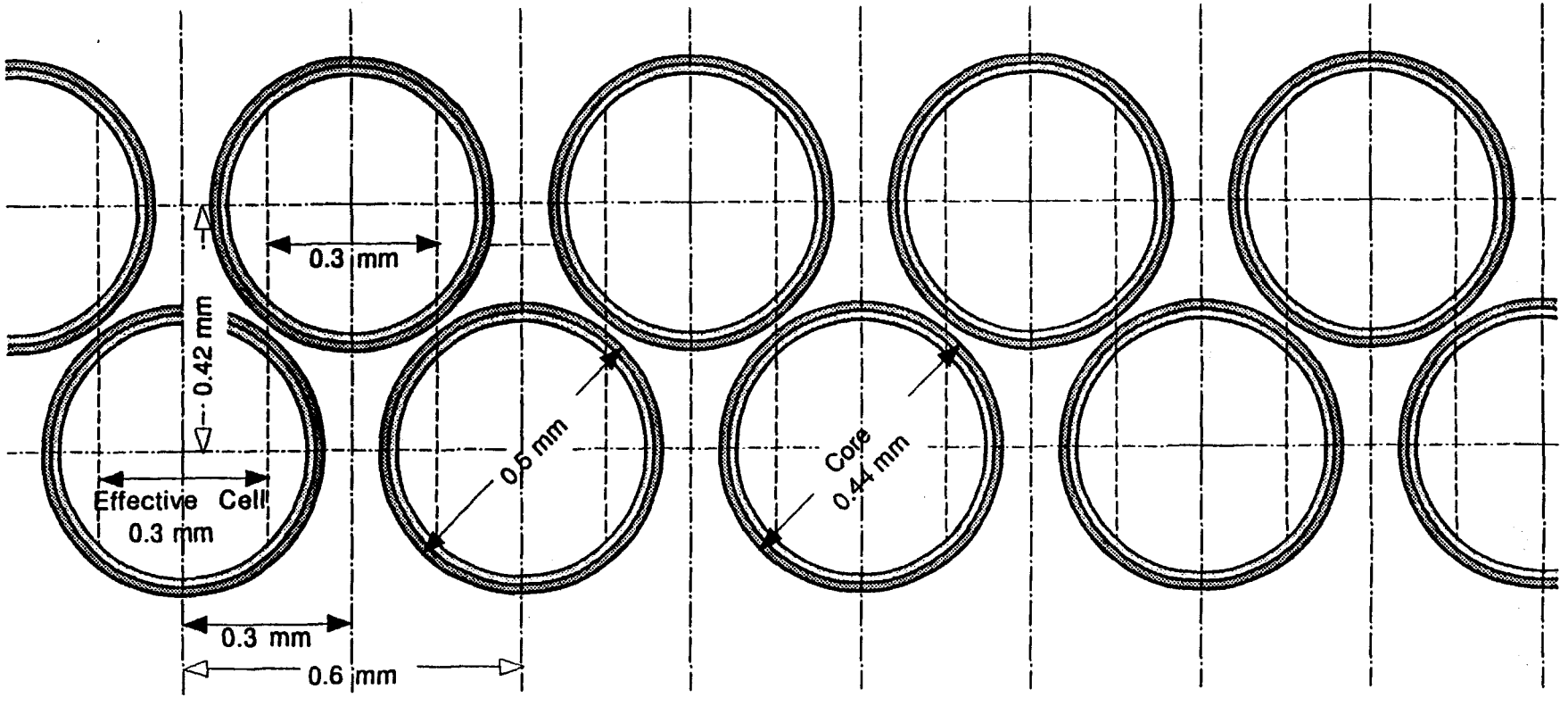

$$\sigma_{\text{intrinsic}} = \frac{0.3\ \text{mm}}{\sqrt{12}} = 86.6\ \mu\text{m}$$

$$\sigma_{\text{total}} = 86.6 \oplus 25 = 90.1\ \mu\text{m}$$

Average Thickness = $(\pi/4)$ 0.5 mm x 2*/1.2** = 0.6545 mm

Fig 3

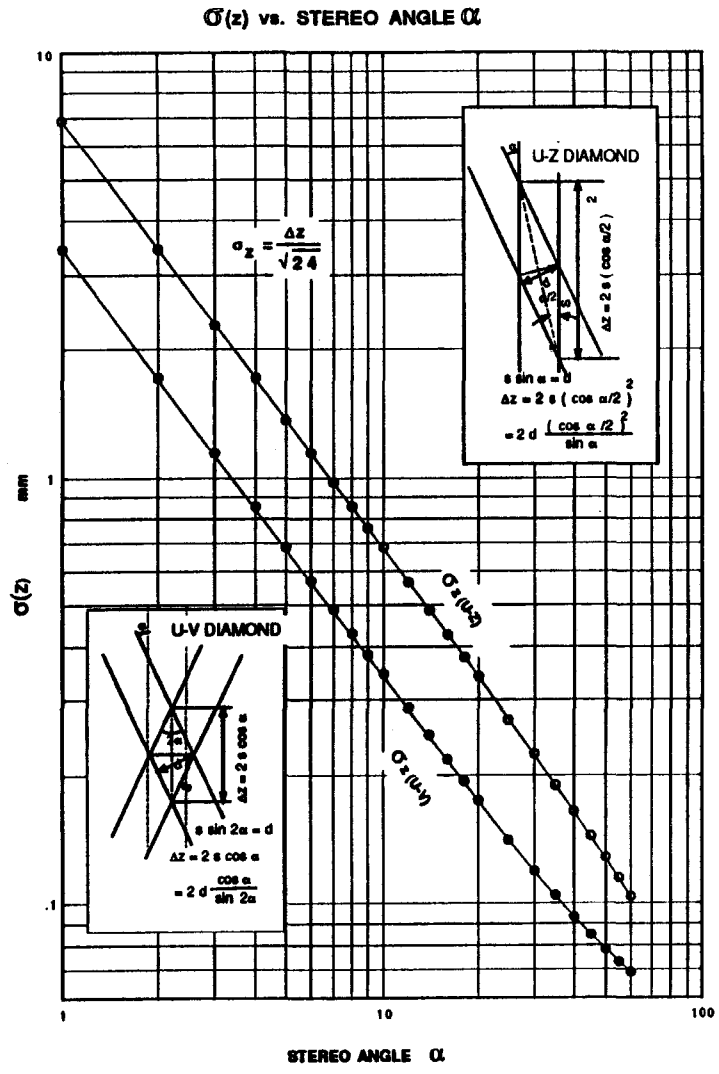
σ(z) vs. STEREO ANGLE α
σ(z) mm
STEREO ANGLE α
U-Z DIAMOND
U-V DIAMOND
σz(U-Z)
σz(U-V)

Fig. 4

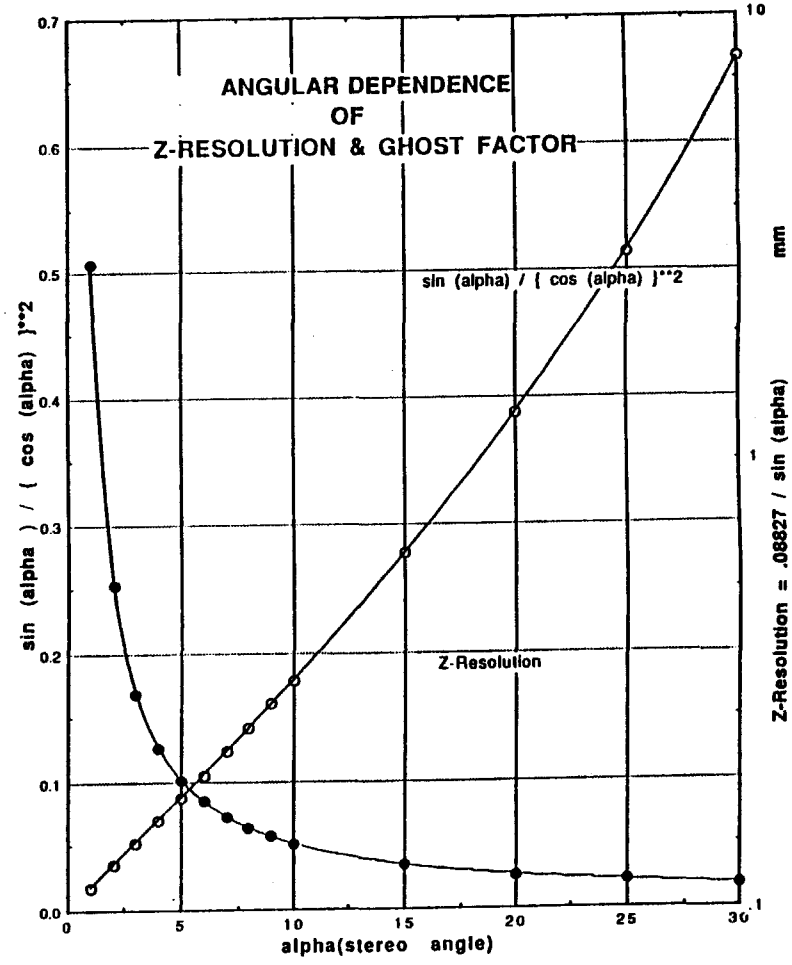
ANGULAR DEPENDENCE
OF
Z-RESOLUTION & GHOST FACTOR
sin (alpha) / (cos (alpha))**2
Z-Resolution
sin (alpha) / (cos (alpha))**2
Z-Resolution = .08827 / sin (alpha)
mm
alpha(stereo angle)

Fig.5

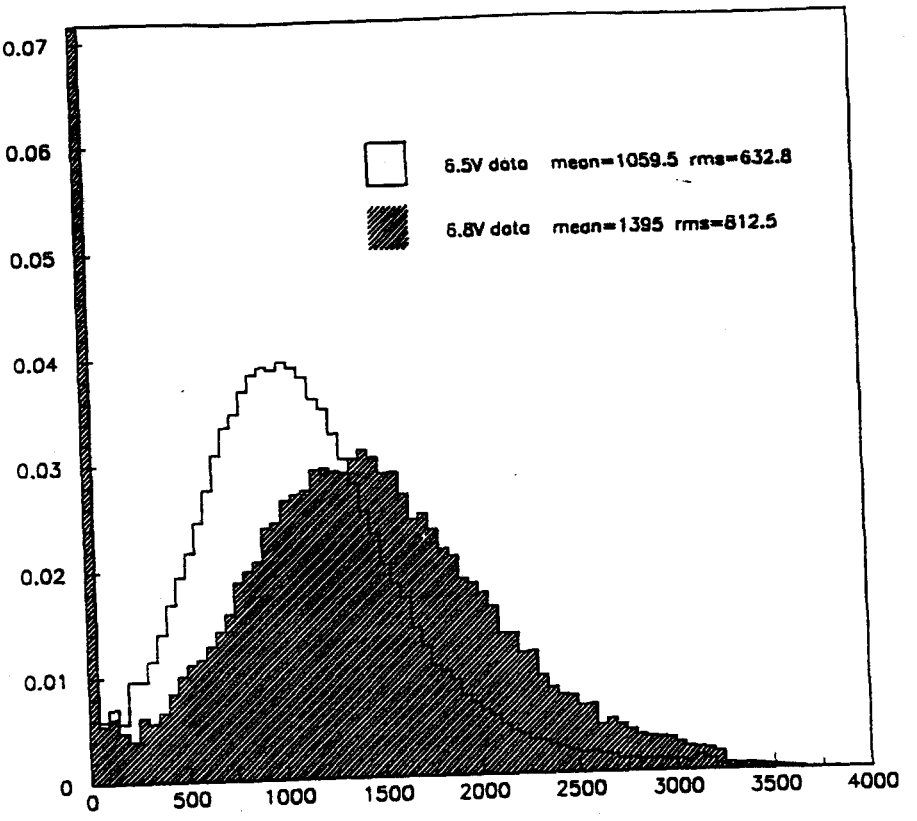
6.5V data mean=1059.5 rms=632.8
6.8V data mean=1395 rms=812.5
0.07
0.06
0.05
0.04
0.03
0.02
0.01
0
0
500
1000
1500
2000
2500
3000
3500
4000

Fig.6

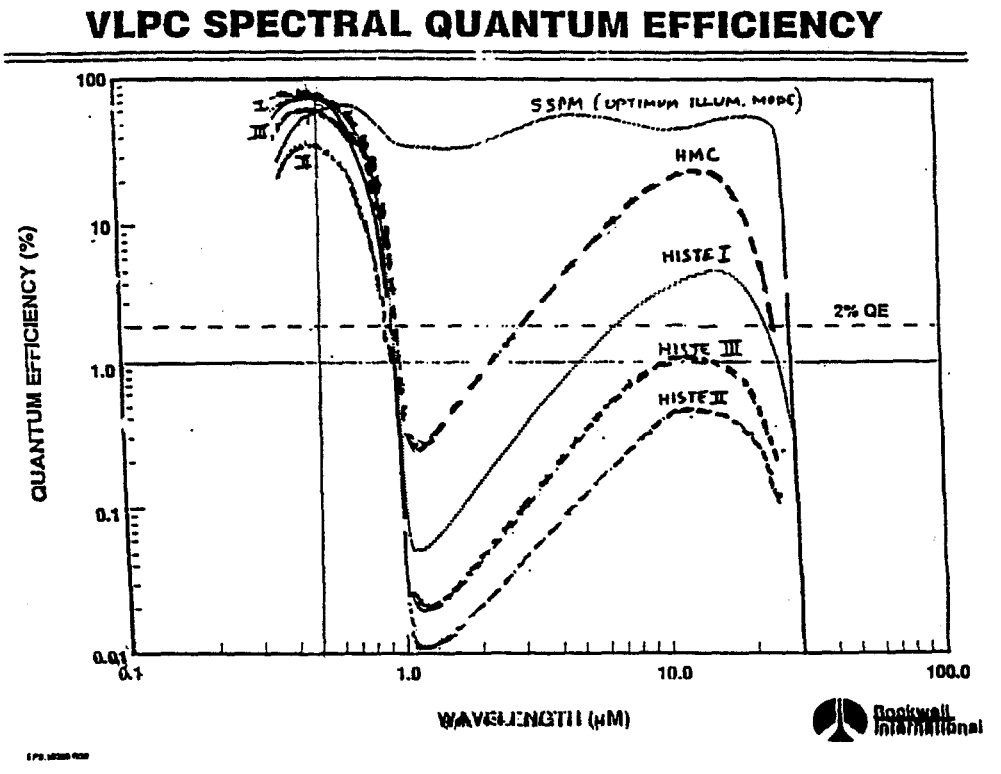
VLPC SPECTRAL QUANTUM EFFICIENCY
SSPM (OPTIMUM ILLUM. MODE)
HMC
HISTE I
HISTE III
HISTE II
2% QE
QUANTUM EFFICIENCY (%)
100
10
1.0
0.1
0.01
0.1
1.0
10.0
100.0
WAVELENGTH (μM)
Rockwell International

Fig.7

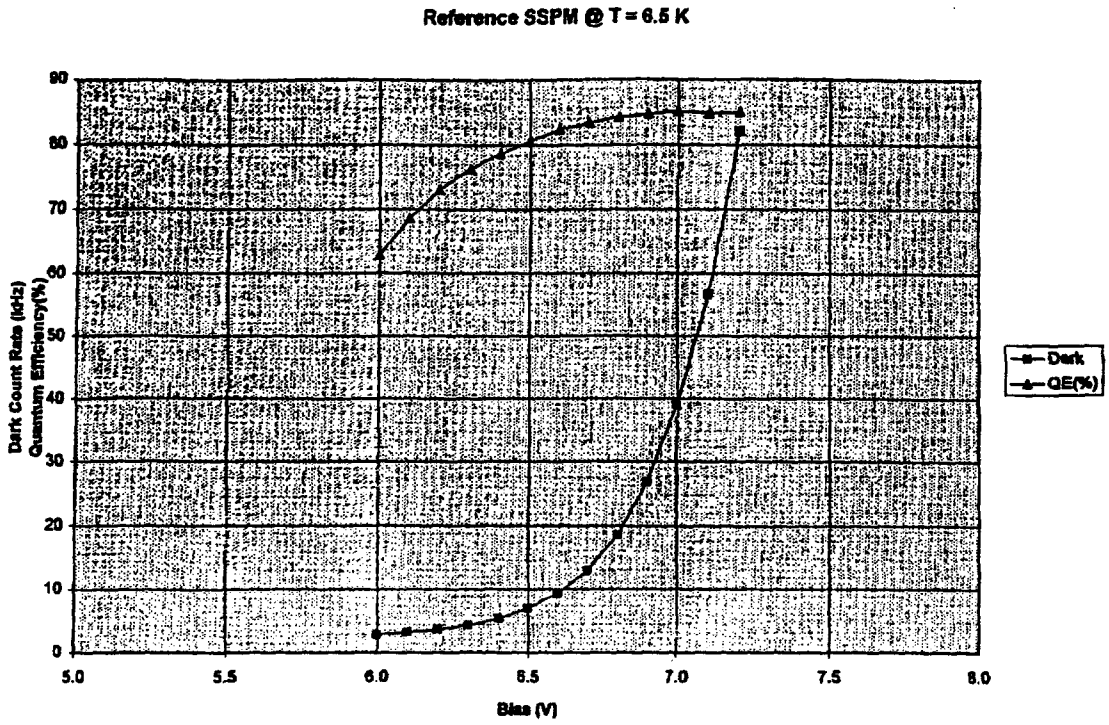
Reference SSPM @ T = 6.5 K
Dark Count Rate (kHz)
Quantum Efficiency(%)
Bias (V)
Dark
QE(%)
0
10
20
30
40
50
60
70
80
90
5.0
5.5
6.0
6.5
7.0
7.5
8.0

Fig.8 a

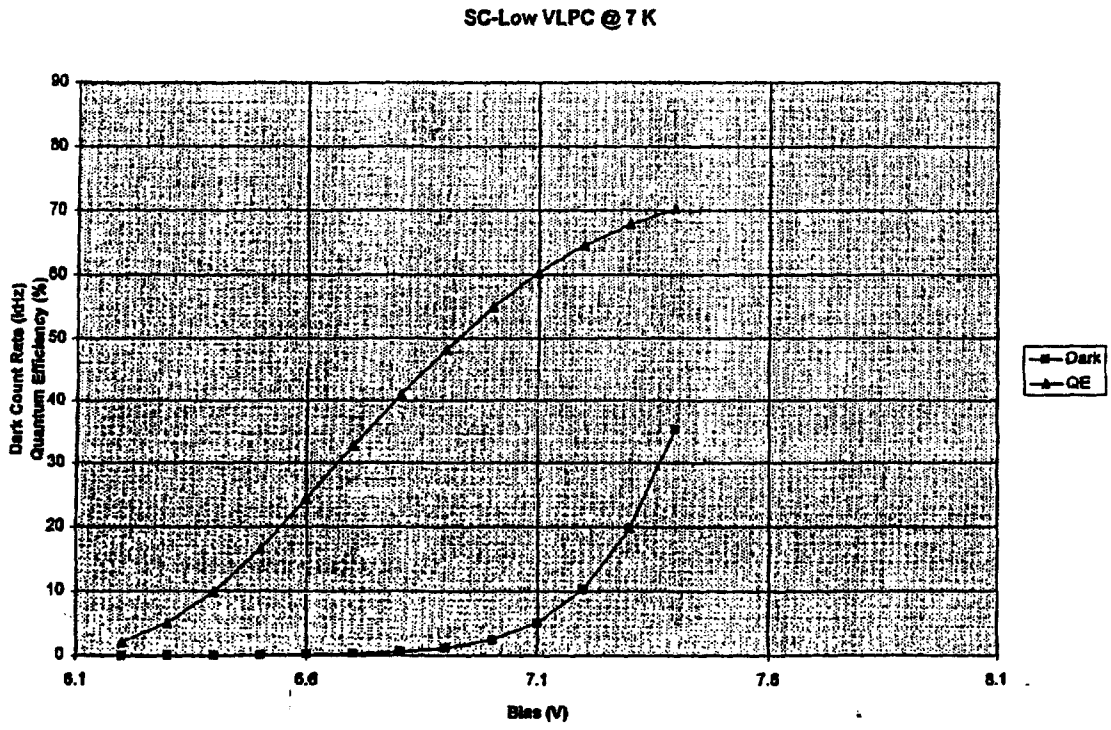
SC-Low VLPC @ 7 K
Dark Count Rate (kHz)
Quantum Efficiency (%)
Bias (V)
Dark
QE
0
10
20
30
40
50
60
70
80
90
6.1
6.6
7.1
7.6
8.1

Fig.8 b

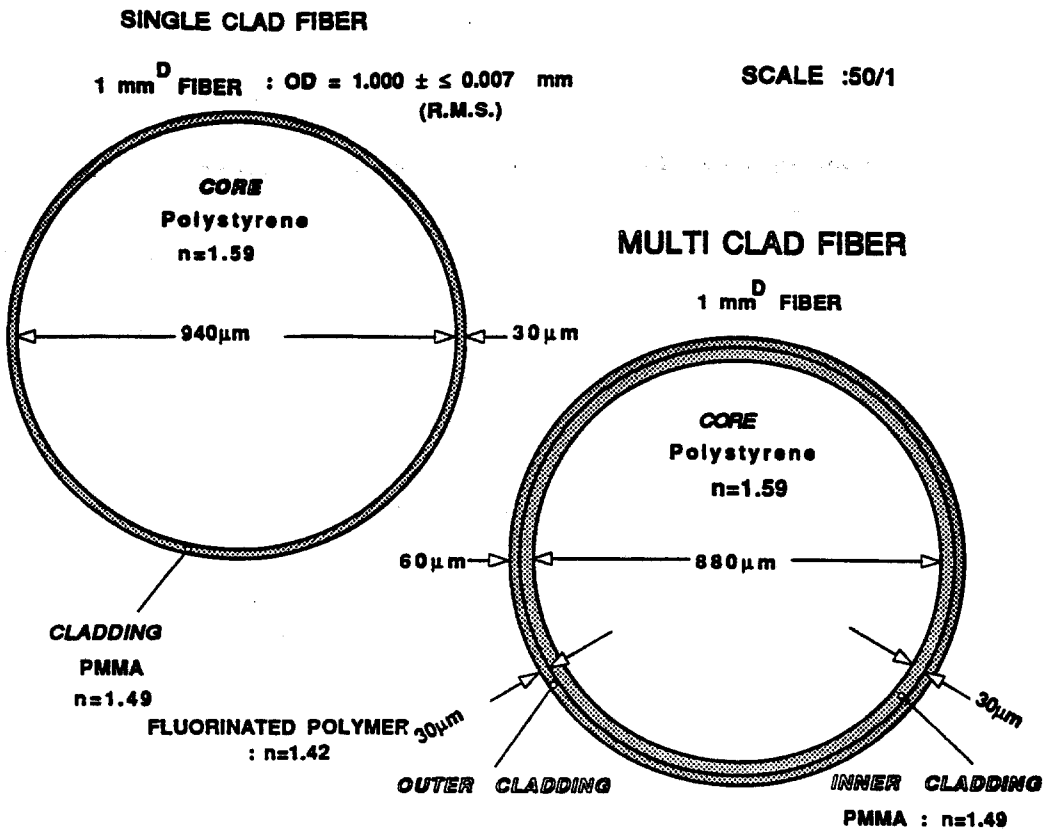

Fig.9

SNELL'S LAW OF REFRACTION

$n_1 \sin\theta_1 = n_2 \sin\theta_2 = \ldots = n_4 \sin\theta_4 = \ldots$

TOTAL INTERNAL REFLECTION

$\theta_4 = 90° \rightarrow \sin\theta_4 = 1$

$\sin\theta_1 = \frac{n_4}{n_1}$

FRACTIONAL SOLID ANGLE : ONE DIRECTION

$\Omega = 2\pi(1 - \cos\theta')/4\pi$

$= (1 - \sin\theta)/2$

$= (1 - n_2/n_1)/2$

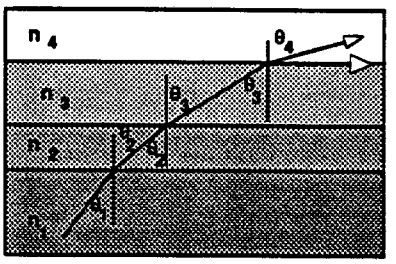

SINGLE CLAD FIBER

n_1 = 1.59 (Popistyrene)

n_4 = 1.49 (PMMA)

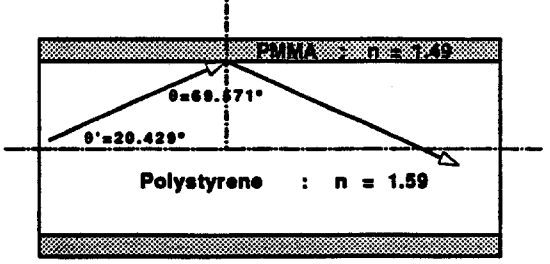

Polystyrene / PMMA

Ω = (1 - 1.49/1.59)/2 = 3.14 %

MULTICLAD FIBER

n_1 = 1.59 (Polystyrene)

(n_2 = 1.49 (PMMA))

n_4 = 1.42 (Fluorinated polymer)

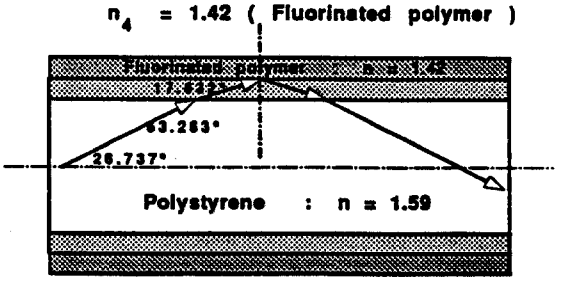

Polystyrene / Fluorinated polymer

Ω = (1- 1.42/1.59)/2 = 5.34 %

Fig.10

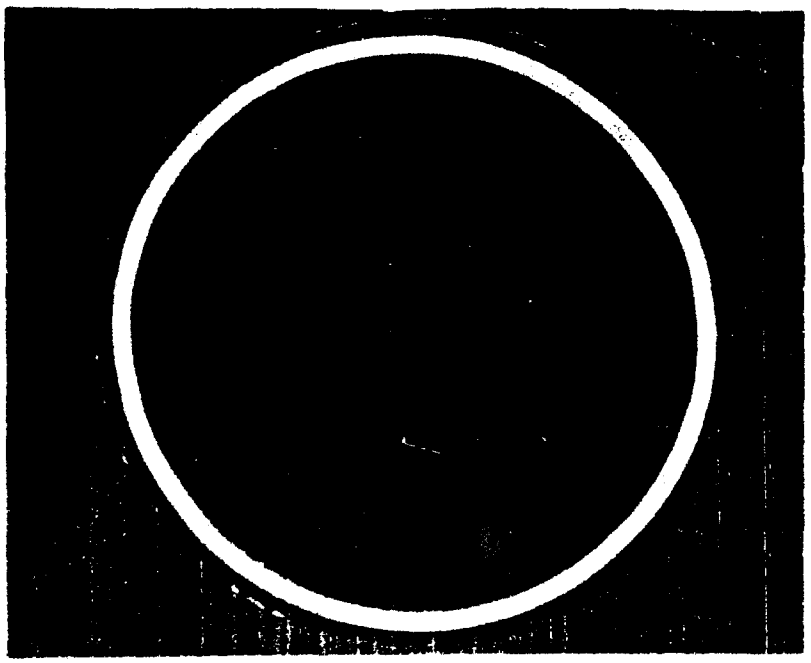

Fig.11

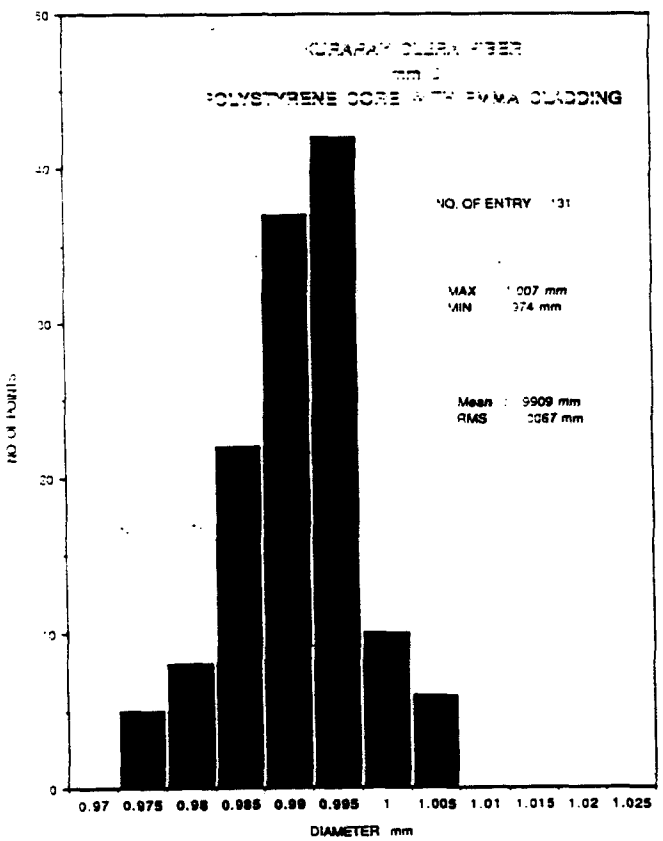

Fig.12 a

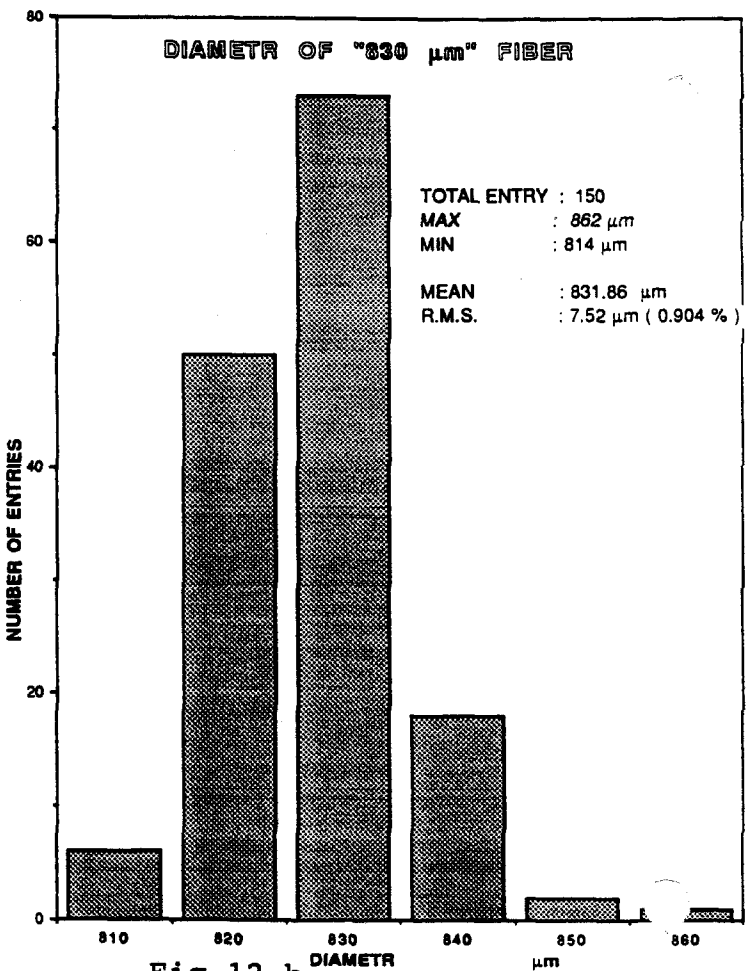

Fig.12 b

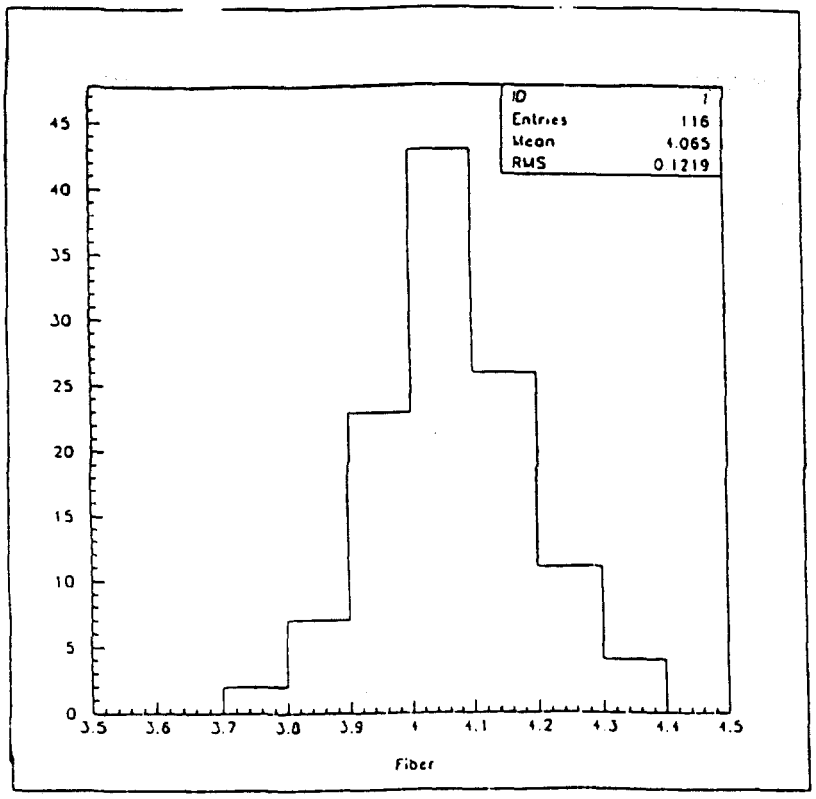
ID 1
Entries 116
Mean 4.065
RMS 0.1219
45
40
35
30
25
20
15
10
5
0
3.5
3.6
3.7
3.8
3.9
4
4.1
4.2
4.3
4.4
4.5
Fiber

Fig.13

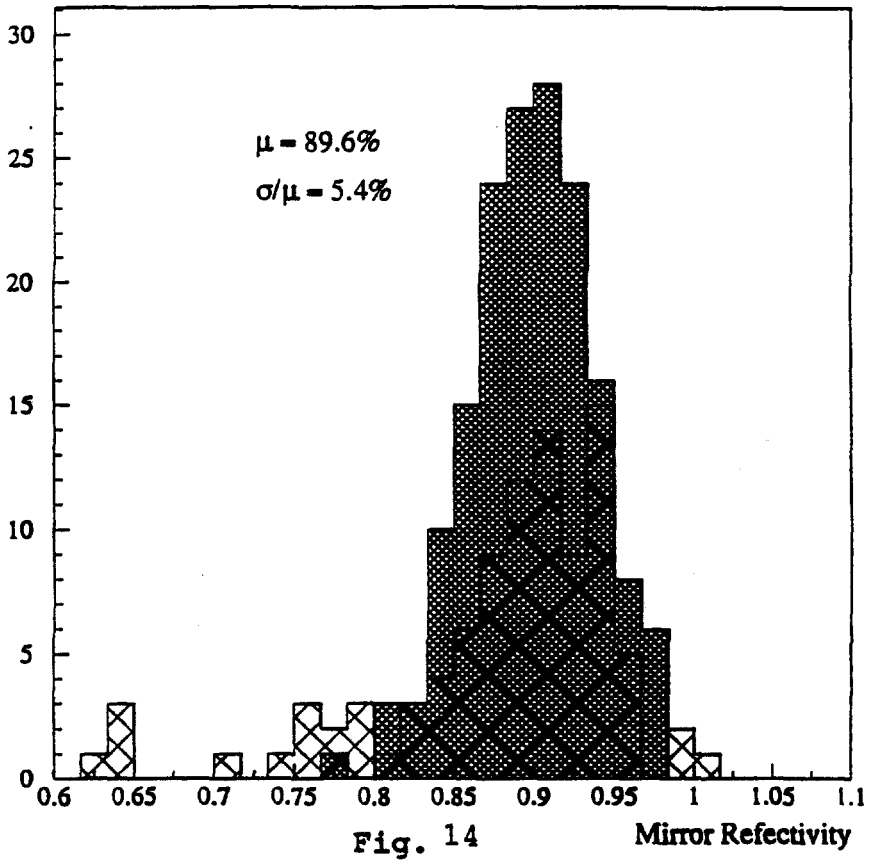
μ = 89.6%
σ/μ = 5.4%
30
25
20
15
10
5
0
0.6
0.65
0.7
0.75
0.8
0.85
0.9
0.95
1
1.05
1.1
Mirror Refectivity

Fig. 14

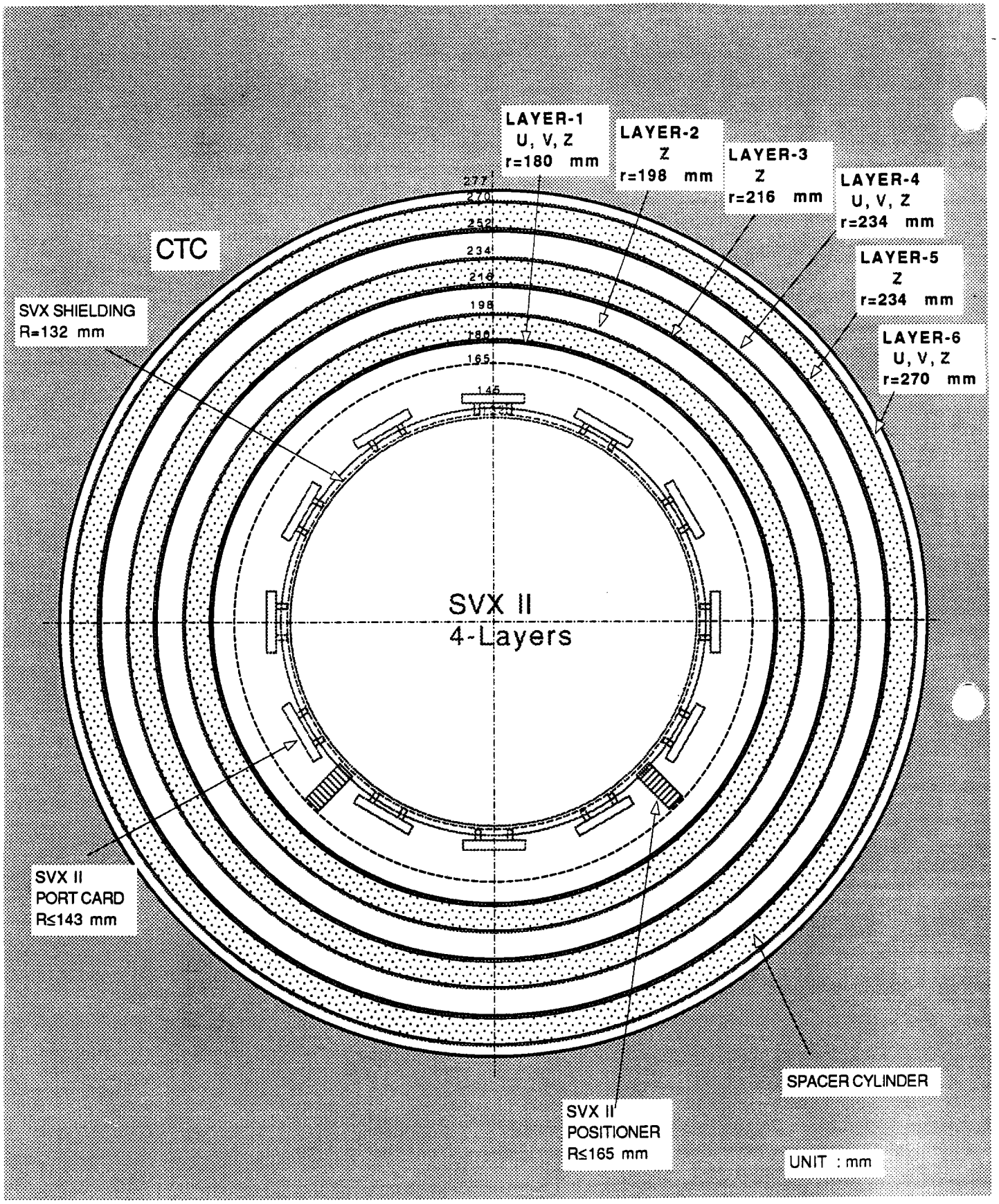
LAYER-1
U, V, Z
r=180 mm
LAYER-2
Z
r=198 mm
LAYER-3
Z
r=216 mm
LAYER-4
U, V, Z
r=234 mm
LAYER-5
Z
r=234 mm
LAYER-6
U, V, Z
r=270 mm
CTC
SVX SHIELDING
R=132 mm
277
270
252
234
216
198
180
165
146
SVX II
4-Layers
SVX II
PORT CARD
R≤143 mm
SPACER CYLINDER
SVX II
POSITIONER
R≤165 mm
UNIT : mm

Fig. 15 a

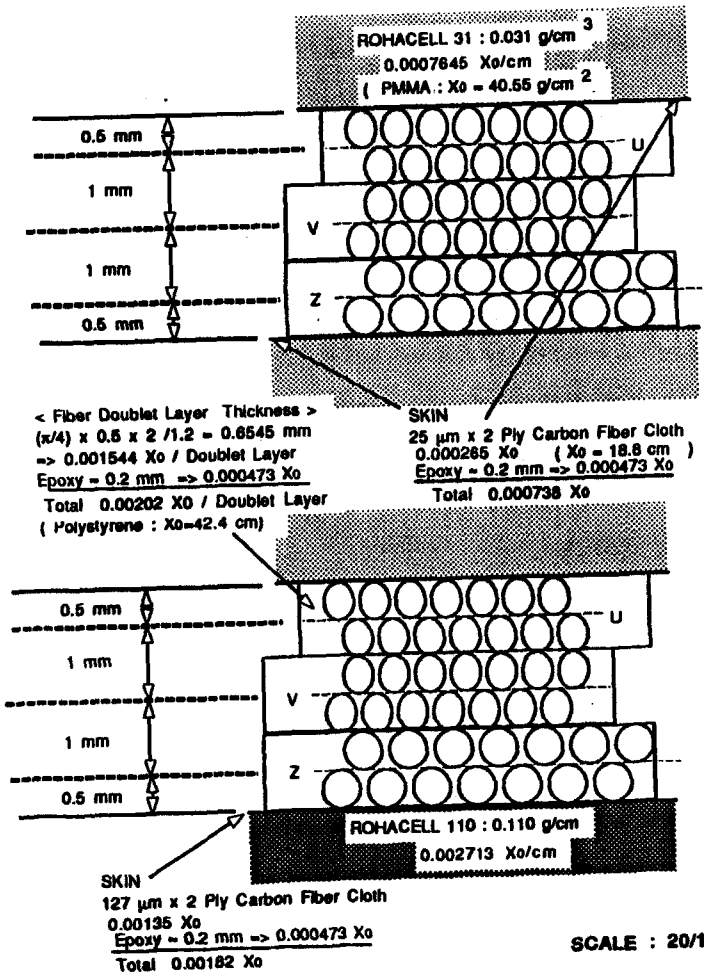

Fig.15 b

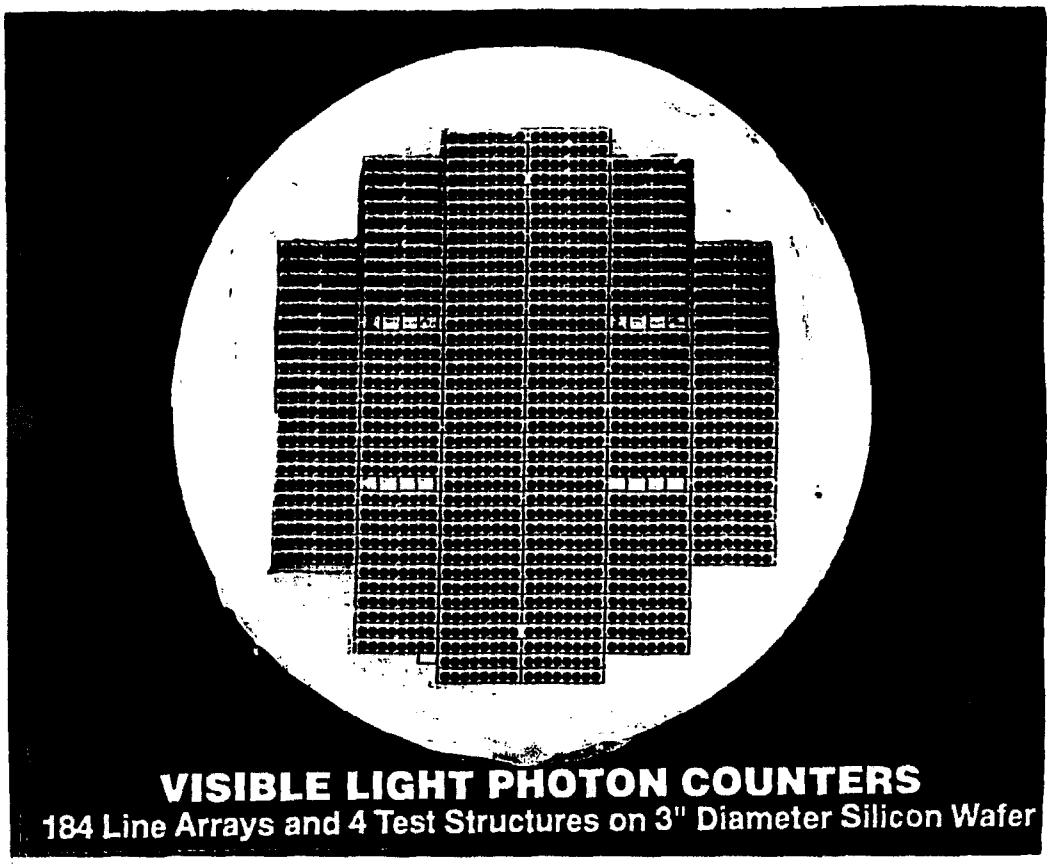

Fig. 16

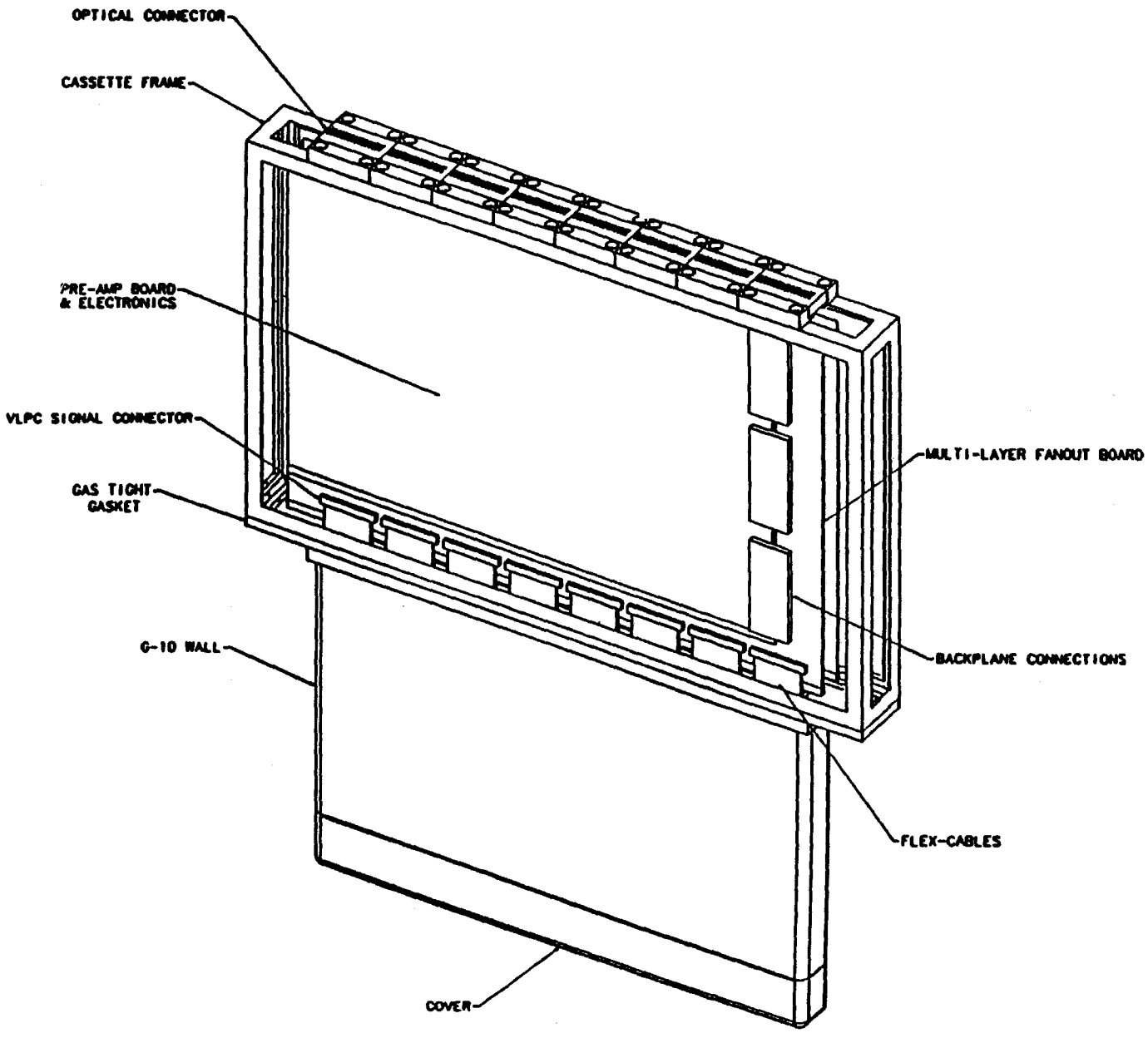

FIGURE #2: OVERALL CASSETTE LAYOUT

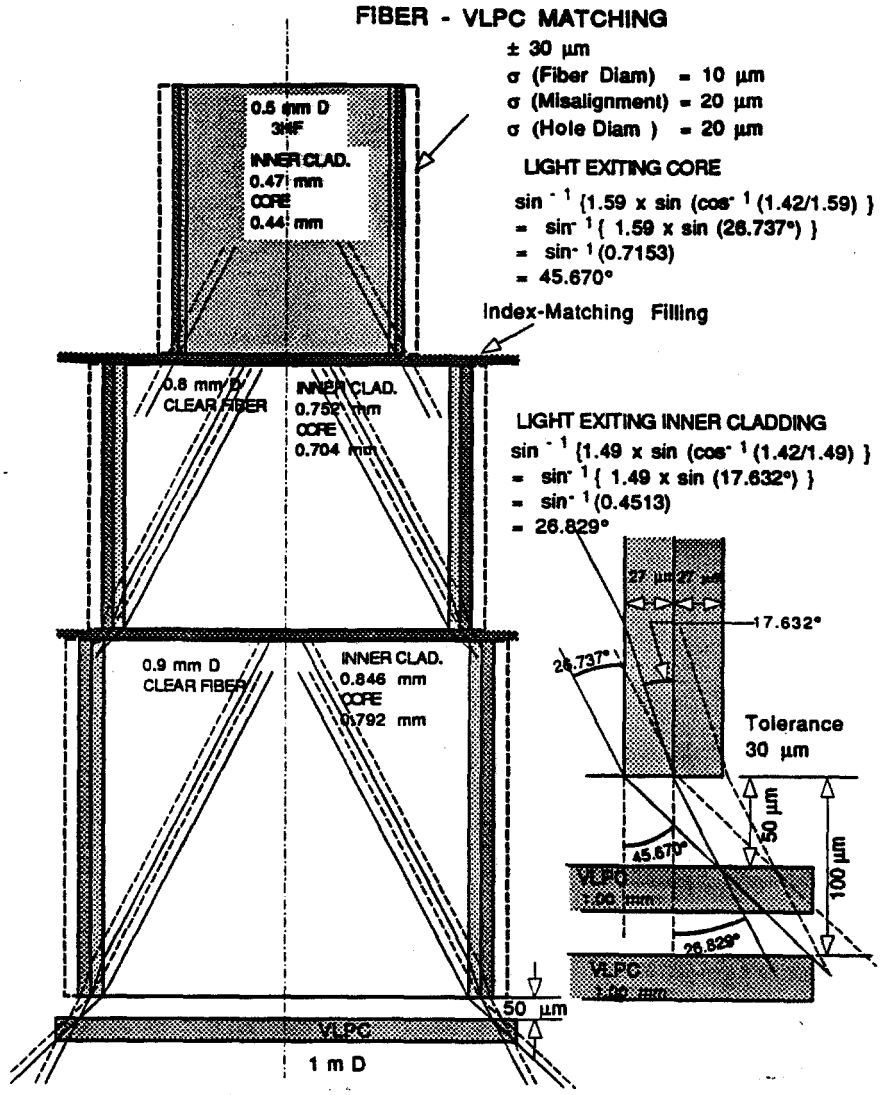
FIBER - VLPC MATCHING
± 30 µm
σ (Fiber Diam) = 10 µm
σ (Misalignment) = 20 µm
σ (Hole Diam) = 20 µm
LIGHT EXITING CORE
sin⁻¹ {1.59 x sin (cos⁻¹ (1.42/1.59) }
= sin⁻¹ { 1.59 x sin (26.737°) }
= sin⁻¹ (0.7153)
= 45.670°
Index-Matching Filling
0.5 mm D
3HF
INNER CLAD.
0.47 mm
CORE
0.44 mm
0.8 mm D
CLEAR FIBER
INNER CLAD.
0.752 mm
CORE
0.704 mm
LIGHT EXITING INNER CLADDING
sin⁻¹ {1.49 x sin (cos⁻¹ (1.42/1.49) }
= sin⁻¹ { 1.49 x sin (17.632°) }
= sin⁻¹ (0.4513)
= 26.829°
0.9 mm D
CLEAR FIBER
INNER CLAD.
0.846 mm
CORE
0.792 mm
17.632°
26.737°
Tolerance
30 µm
50 µm
100 µm
45.670°
VLPC
1.00 mm
26.829°
VLPC
1.00 mm
50 µm
VLPC
1 m D

Fig. 18

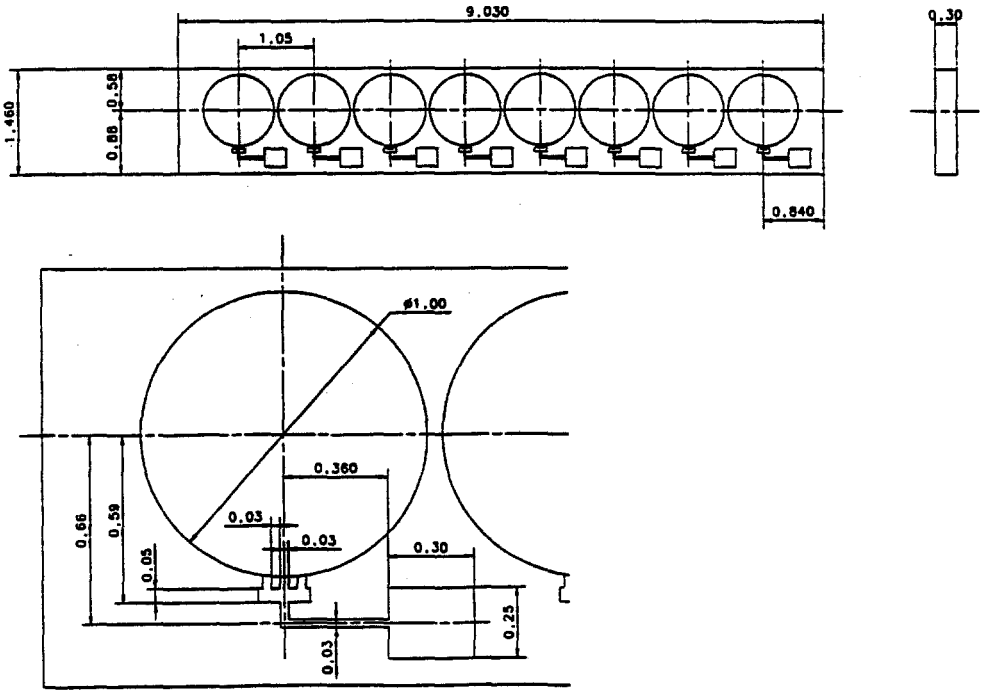
9.030
1.05
0.30
1.460
0.58
0.88
0.840
ø1.00
0.360
0.66
0.59
0.03
0.03
0.05
0.30
0.25
0.03

Fig. 19

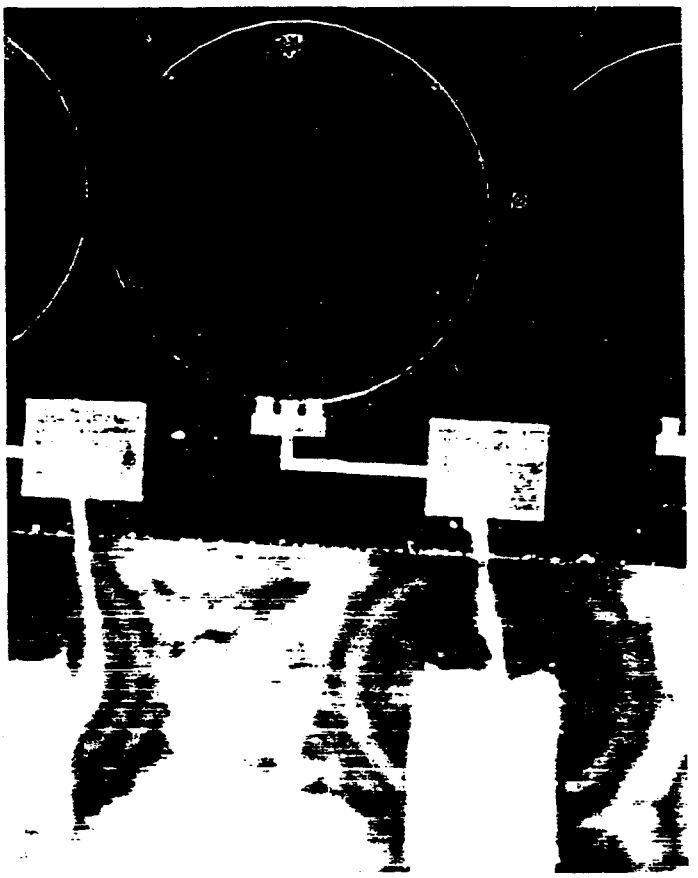

Fig. 20

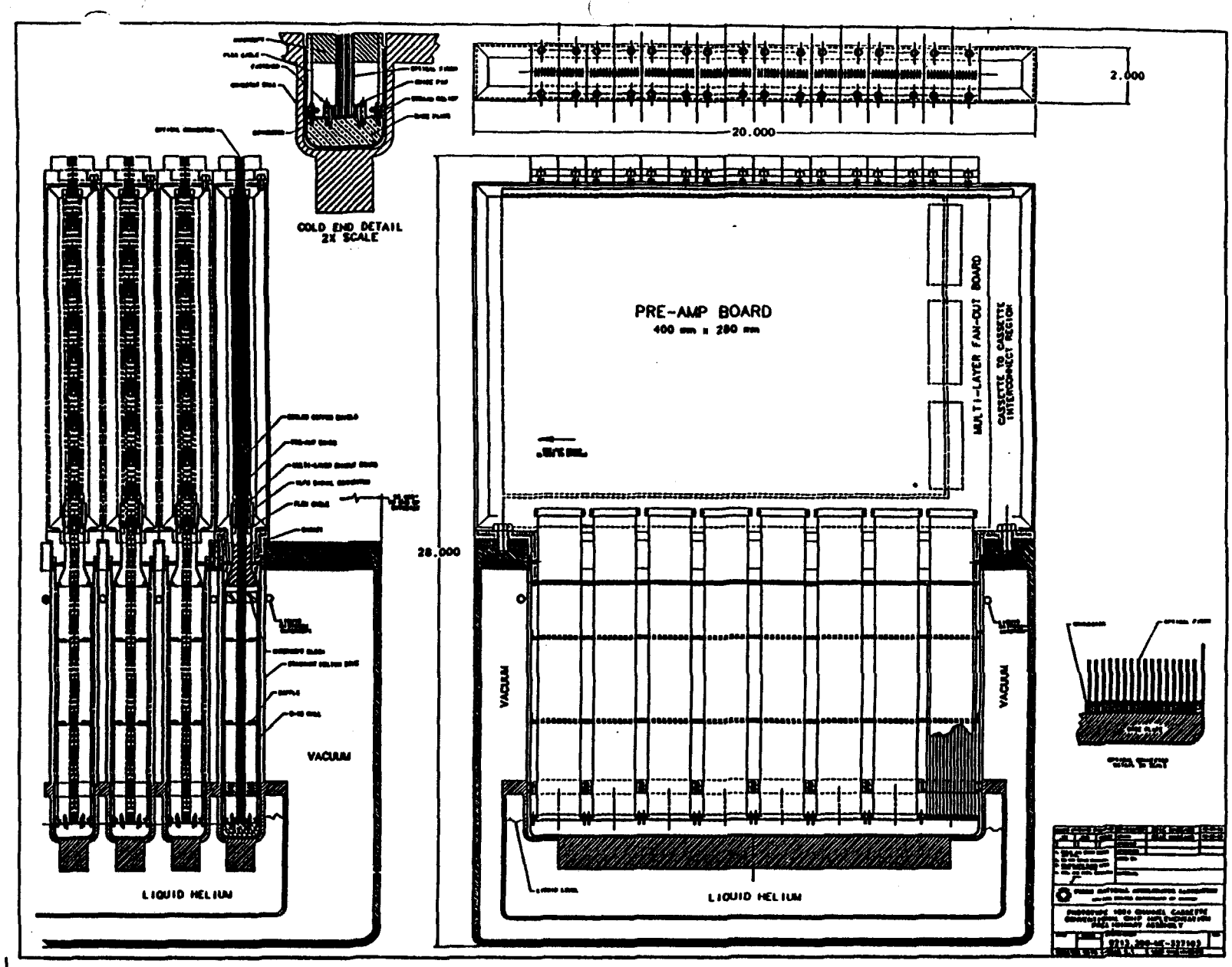

FIGURE #3: PRELIMINARY ASSEMBLY OF CASSETTE

Fig. 21

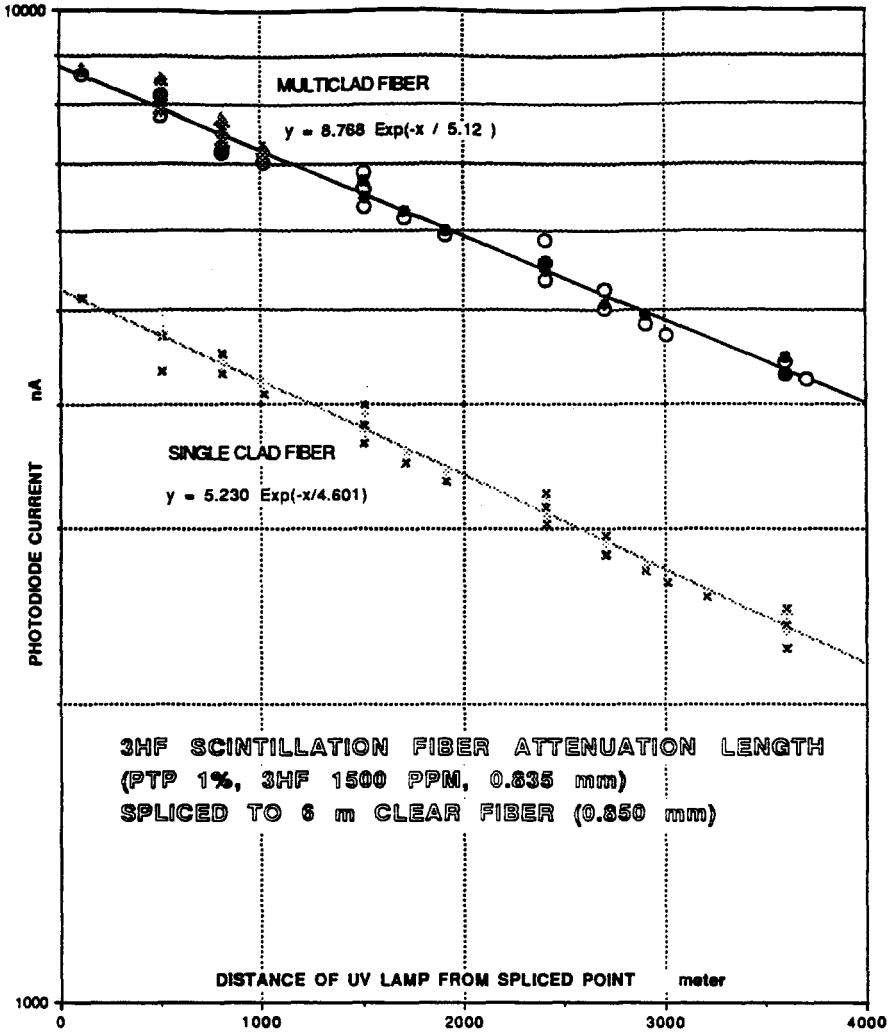

Fig. 22 a

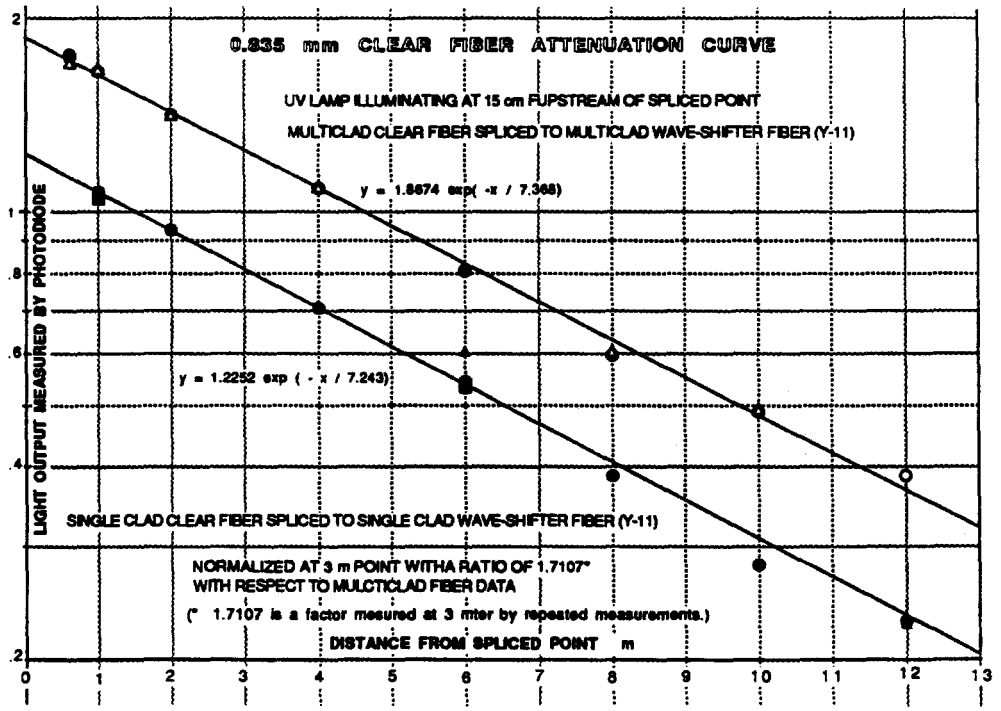

Fig. 22 b

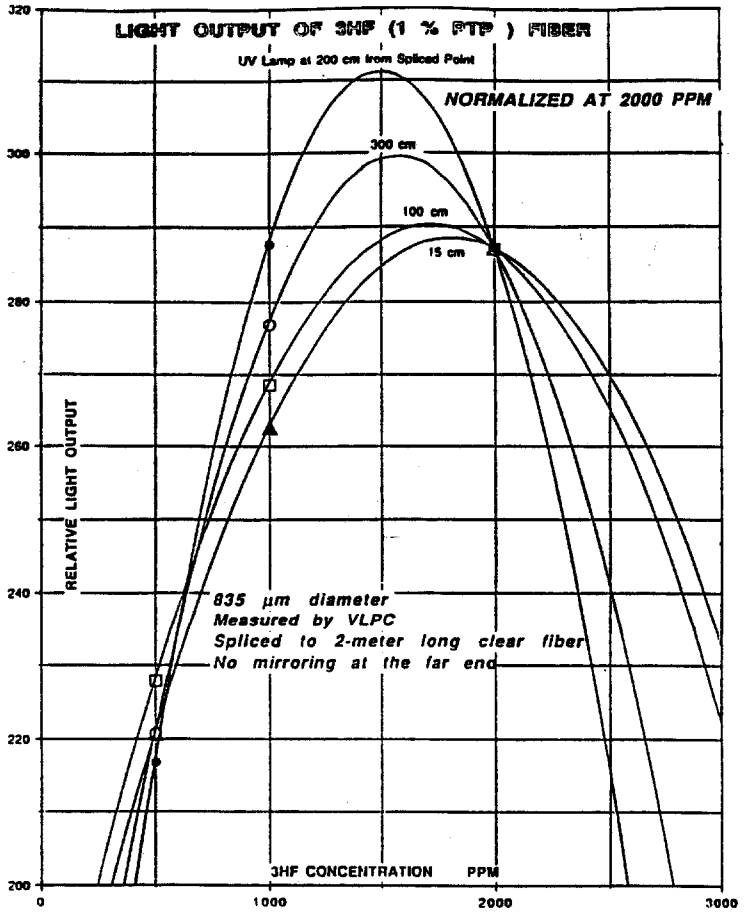
LIGHT OUTPUT OF 3HF (1 % PTP) FIBER
UV Lamp at 200 cm from Spliced Point
NORMALIZED AT 2000 PPM
300 cm
100 cm
15 cm
RELATIVE LIGHT OUTPUT
835 µm diameter
Measured by VLPC
Spliced to 2-meter long clear fiber
No mirroring at the far end
3HF CONCENTRATION PPM
320
300
280
260
240
220
200
0
1000
2000
3000

Fig. 23

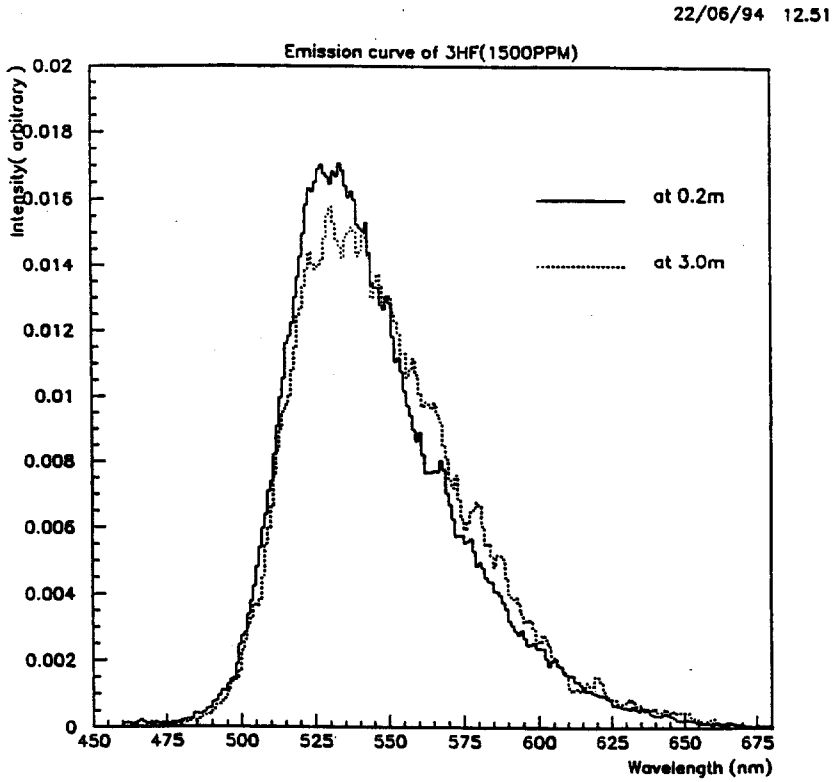
22/06/94 12.51
Emission curve of 3HF(1500PPM)
Intensity(arbitrary)
at 0.2m
at 3.0m
Wavelength (nm)
0.02
0.018
0.016
0.014
0.012
0.01
0.008
0.006
0.004
0.002
0
450
475
500
525
550
575
600
625
650
675

Fig.24

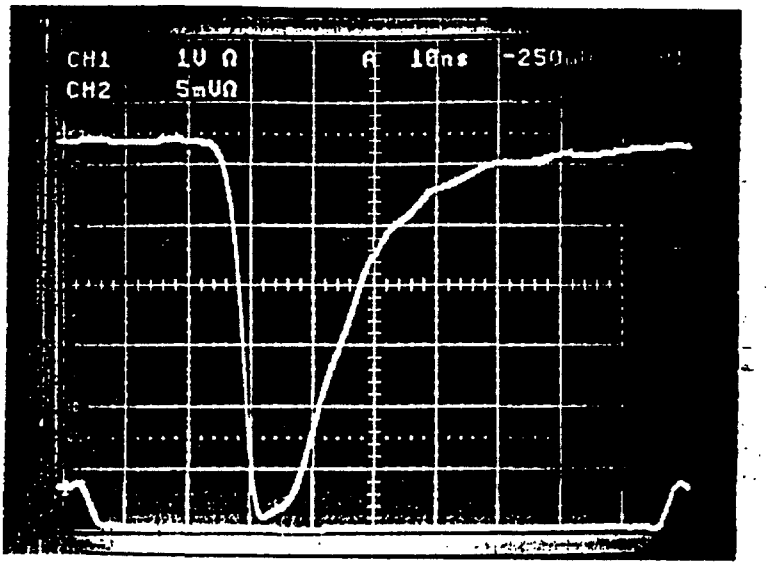

Fig. 25 a

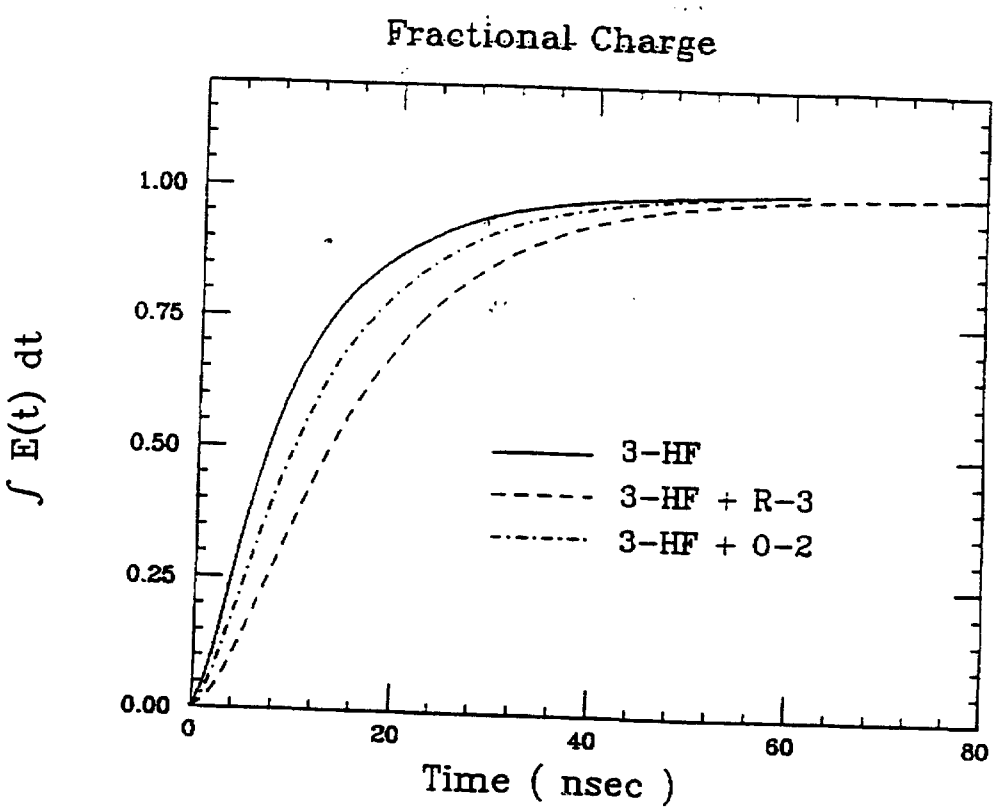

Fig. 25 b

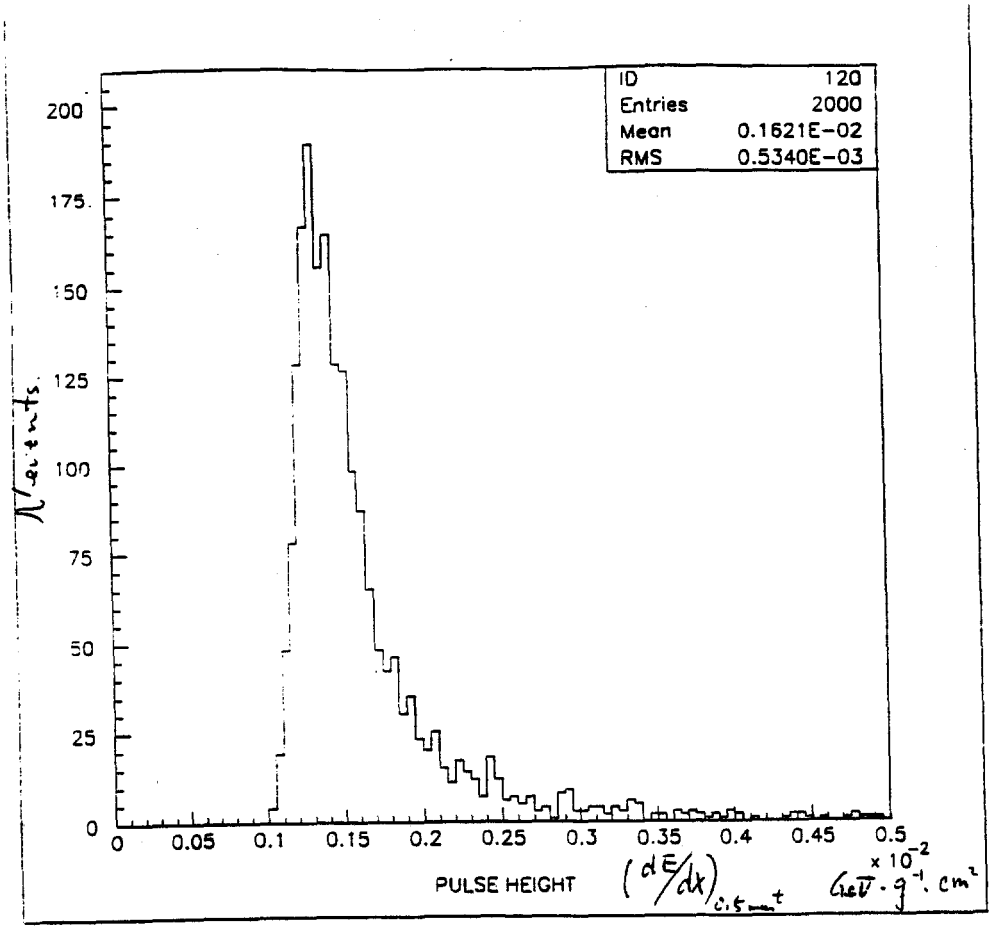
ID 120
Entries 2000
Mean 0.1621E-02
RMS 0.5340E-03
PULSE HEIGHT
x 10^-2

Fig. 26

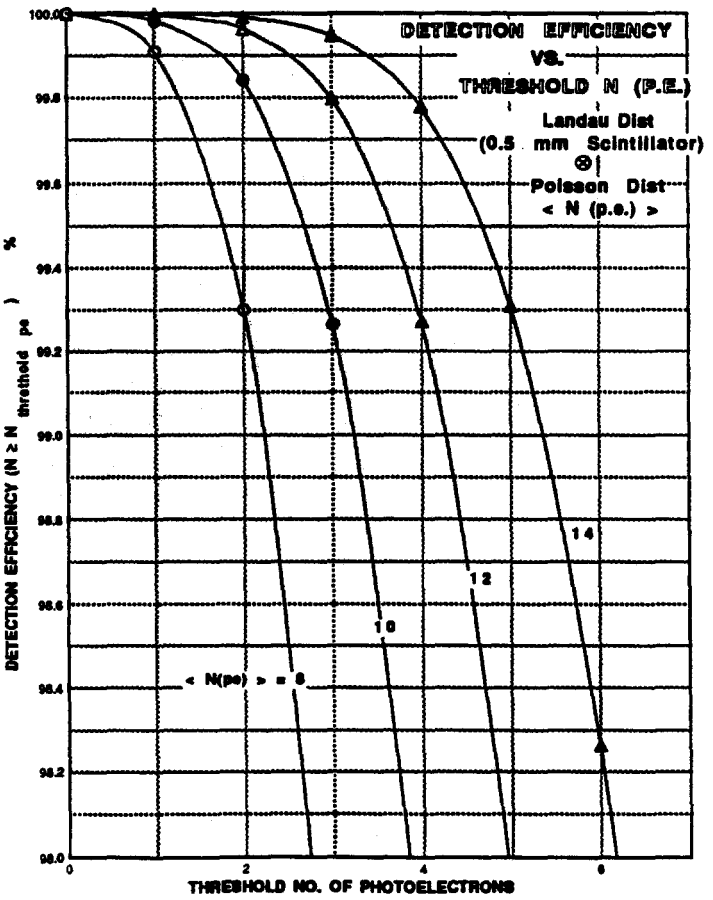
DETECTION EFFICIENCY
VS.
THRESHOLD N (P.E.)
Landau Dist
(0.5 mm Scintillator)
⊗
Poisson Dist
< N (p.e.) >
< N(pe) > = 8
10
12
14
DETECTION EFFICIENCY (N ≥ N threshold pe) %
THRESHOLD NO. OF PHOTOELECTRONS

Fig. 27

GROOVED TRAY

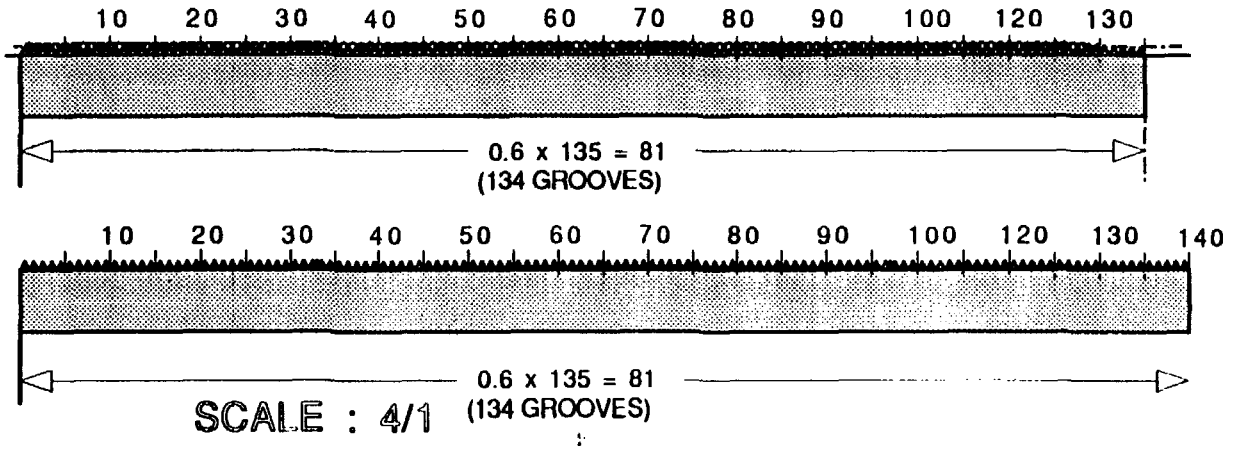

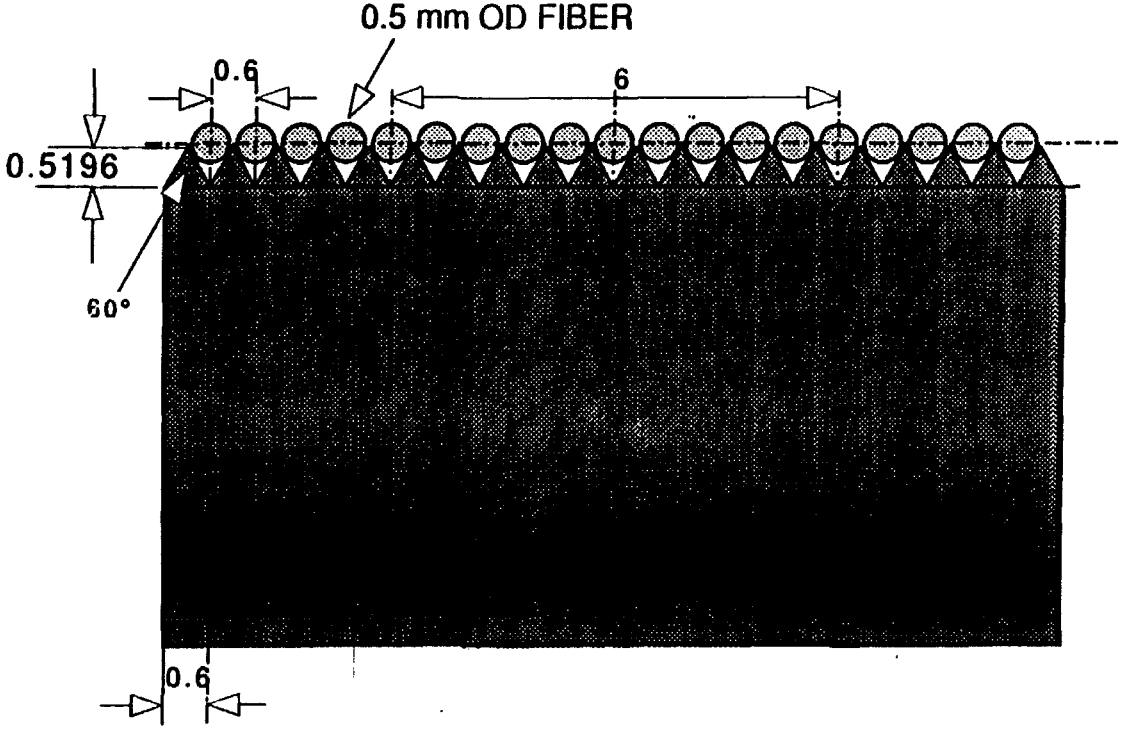

SCALE : 20/1

UNIT : mm

Fig 28

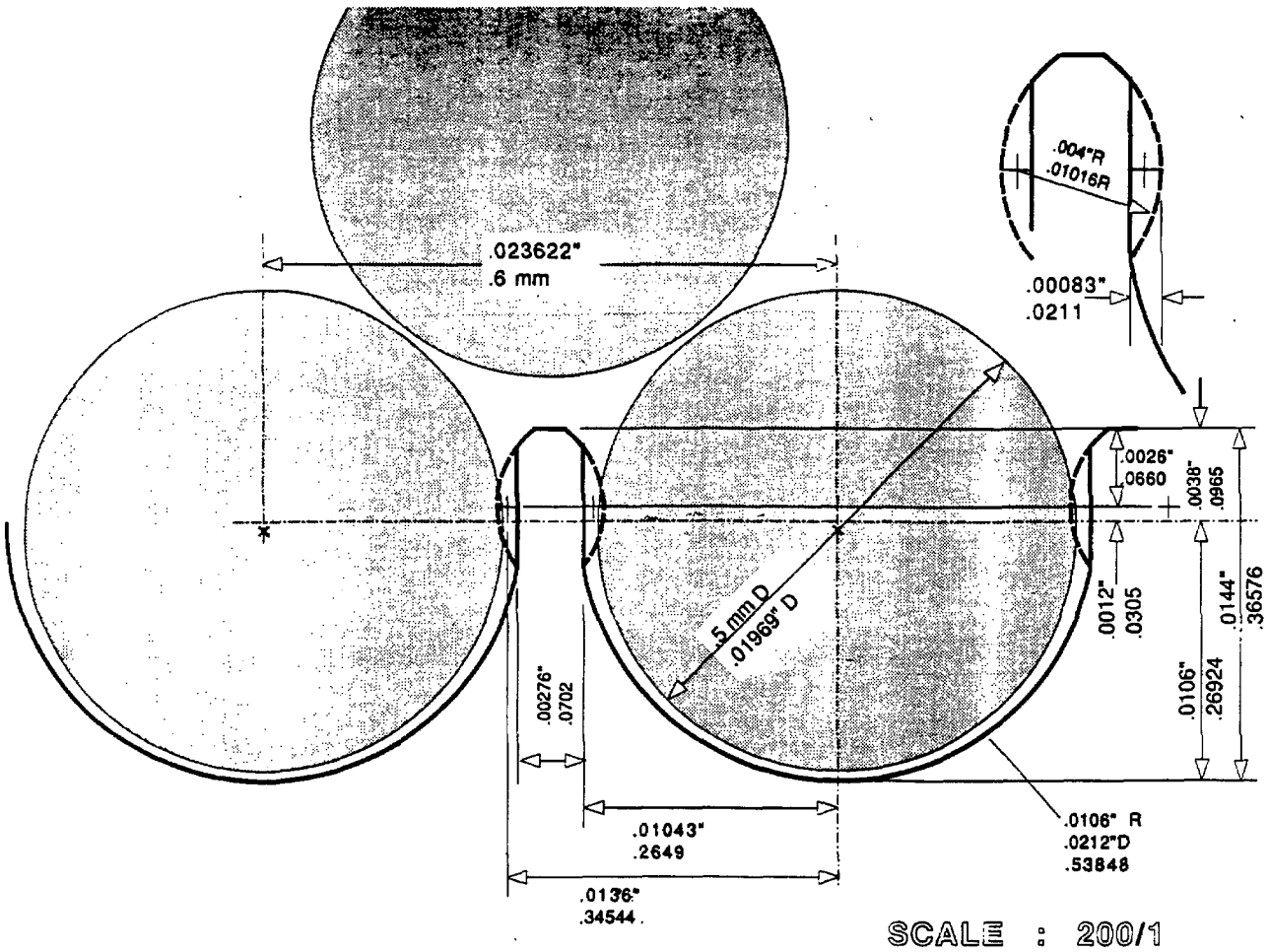
.023622"
.6 mm
.004"R
.01016R
.00083"
.0211
.0026"
.0660
.0038"
.0965
.5 mm D
.01969" D
.0012"
.0305
.0144"
.36576
.0106"
.26924
.00276"
.0702
.01043"
.2649
.0136"
.34544
.0106" R
.0212"D
.53848
SCALE : 200/1

Fig. 29

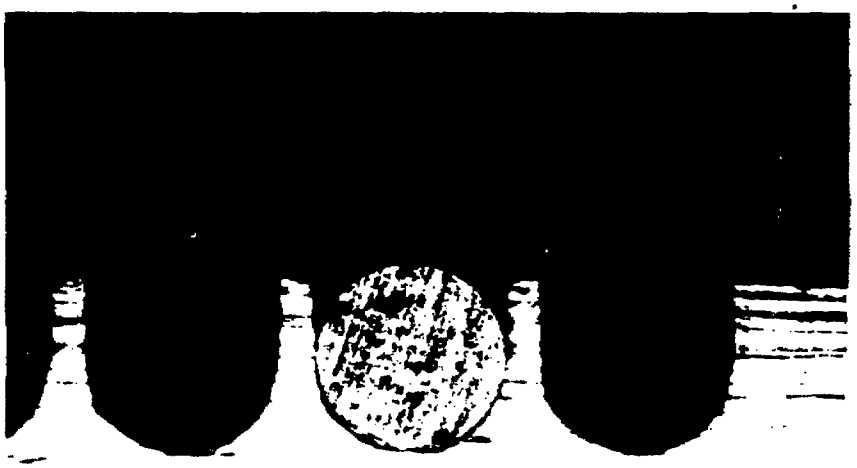

Fig. 30